

nature

THE INTERNATIONAL WEEKLY JOURNAL OF SCIENCE

EBOLA: DID WE LEARN?

*How to beat this epidemic
and prepare for the next*



GREEN SYNTHESIS

CHEMISTRY IN THE SLOW LANE

*Let time do all
the hard work*

PAGE 20

NEUROSCIENCE

REDEFINING FEAR

*Have we got it wrong on
the nature of anxiety?*

PAGE 34

MATERIALS

DESIGNER MAGNETS

*Inducing magnetism in
copper and manganese*

PAGES 42 & 69

NATURE.COM/NATURE

6 August 2015 £10

Vol. 524, No. 7563



THIS WEEK

EDITORIALS

WORLD VIEW Invest to energize West African research capacity **p.7**

LIKE! Social network helps botanists to identify unknown sundew **p.8**

FOSSIL FIND Lizards of the Caribbean have endless sequels **p.9**



Trial and triumph

The success of an Ebola vaccine trial shows that clinical trials can be done under the difficult field conditions of an epidemic — if there is enough political and regulatory will.

This is a big week in the fight against Ebola: a clinical trial of an Ebola vaccine in Guinea has reported a promising outcome. It is fantastic news — even the most cautious disease experts are hopeful that a corner has been turned.

What now? In a special collection of articles this week, *Nature* analyses the vaccine breakthrough and looks more broadly at the prospects for future control of epidemic threats. It is not all good news, and there are bound to be setbacks, but those who value the role of research in improving human welfare — and those who argue for broader recognition of that role among policymakers — can now walk a little taller.

Make no mistake: conducting an efficacy trial of a vaccine or a drug during an epidemic is difficult, to put it mildly. In the past, delays in getting regulatory approval for trials meant that outbreaks were usually over before the trial even started, so drugs and vaccines needed to treat the outbreak, or future ones, could not be tested.

Running a clinical efficacy trial in the arduous field conditions of an epidemic zone is no mean feat either. Yet against the odds, an international team of researchers not only did just that, but also showed that one shot of the vaccine had 100% efficacy — none of those vaccinated at the start of the trial developed Ebola ten days after receiving the vaccine (A. M. Henao-Restrepo *et al.* *Lancet* [http://dx.doi.org/10.1016/S0140-6736\(15\)61117-5](http://dx.doi.org/10.1016/S0140-6736(15)61117-5); 2015).

That such a vaccine could be clinically tested — a process that

usually takes years — in a short space of time and without the facilities of a sophisticated research hospital must rewrite the rules for how drug trials for infectious-disease threats are conducted. Faced with the urgency of Ebola, international collaborations of scientists, regulators, pharmaceutical companies and non-governmental organizations — and, to its credit, the World Health Organization, which had a leading role — pulled together with unprecedented speed to push vaccines and drugs through testing and into field trials.

Roll-out of the vaccine to more people will provide data to confirm its effectiveness. But by vaccinating the families, friends, health-care workers and others who come into contact with infected people, Ebola outbreaks could be stopped in their tracks — the same strategy that was used to eradicate smallpox in the 1970s. This means that this vaccine can, in principle, be deployed immediately to help to end the Ebola epidemic in West Africa. As aptly conveyed by the trial's French name, '*Ebola, ça suffit!*' ('Ebola, that's enough!'), it is time to finish the job.

The job remains, because even if Ebola has faded from the headlines, it is far from over. Eighteen months after it began, the epidemic continues to cause 20–30 cases a week. It could flare up at any time or spread to as-yet-unaffected countries in the region, taking the situation back to square one. Although vaccines will need to be developed against the four other species of Ebola virus, the efficacy of this vaccine against the Zaire species — if confirmed — means that never again should an Ebola epidemic occur on the same scale as in West Africa. ■

Driving test

'Gene drive' techniques have the potential to alter whole populations. Regulators must catch up.

Last year, researchers and policy experts expressed concerns about a — then hypothetical — way to use cutting-edge genetic techniques to rapidly alter entire populations of plants or animals. Such a technique, called a gene drive, could lead to unanticipated ecological consequences, they cautioned (K. A. Oye *et al.* *Science* **345**, 626–628; 2014). The authors discussed safety guidelines, made general policy recommendations, and met with some criticism: why raise alarm over a technique that did not yet exist?

Less than a year later, it did exist. Two groups have now published examples of gene drives engineered using CRISPR, a versatile and relatively easy system that allows researchers to make changes to genomes with pinpoint precision (see page 16). Crucially, it enabled a designated mutation to copy itself from one chromosome in a pair to the other, ensuring that it was passed to offspring and allowing it to spread rapidly

through a population (V. M. Gantz and E. Bier *Science* **348**, 442–444 (2015) and J. E. DiCarlo *et al.* Preprint at <http://doi.org/6k2>; 2015).

Engineering a lab animal or agricultural crop is one thing. Wielding the power to alter an entire wild population is quite another. The process understandably raises concern. But it could hold great benefit: mosquitoes could be tweaked so that they cannot carry malaria, or an endangered species could be saved by wiping out an invasive competitor.

Last week, the debate gained momentum when the US National Academy of Sciences held its first meeting to evaluate the potential benefits and risks of gene drives. As is often the case by the time such controversies start to attract mainstream attention, specialist researchers have been thrashing out the issue for years. These discussions have already produced various sets of guidelines on the use of gene drives, and the academy and others should use this literature as a starting point.

What is new is the advent of CRISPR. This adds extra dimensions to the debate, because it makes gene drives much easier and could dramatically accelerate the timeline for a potential release — accidental or intentional. Researchers and funding agencies should take note, and efforts to understand the ecological consequences of a gene drive should be made an urgent priority. Regulators and the wider world need to keep pace with the rapid development of CRISPR technology, and there is little time to waste. ■



Train Africa's scientists in crisis response

To prevent future epidemics, a new international effort must boost West Africa's scientific and public-health capacity, says Christian Bréchet.

Stamping out the Ebola outbreak in West Africa was always going to be difficult, and so it is proving. But the world is already talking about what to do 'post-Ebola'. Although there is general agreement on what needs to be improved — chiefly, local capacity and health care — to ensure a better response to the next epidemic there have been few concrete actions. Why? Because all global movements must start with a nucleus, around which broader efforts can aggregate. This has not yet been established. Here, I describe how the Pasteur Institute in Paris could form part of such a nucleus, and collaborate with the relevant national and international stakeholders.

The institute has joined with the Chinese Center For Disease Control and Prevention (China CDC) to convert talking into tangible action. In consultation with the governments of Guinea, Liberia and Sierra Leone — the countries that have been devastated by Ebola — our collaboration will invest in public health, education and research in the region to address the urgent needs highlighted by the Ebola epidemic.

Our main aim is to revitalize these countries' overextended health systems within five years, by improving science education and the training of health-care professionals. Our secondary objective is to strengthen research facilities, field surveillance and laboratory analysis to track and combat emerging and re-emerging infectious disease.

The Pasteur Institute has worked in West Africa for almost a century, partly as a legacy of France's history in the region. It has sites in Senegal's capital Dakar and in Abidjan, capital of Côte d'Ivoire, and it will soon open a centre in Conakry, Guinea. As such, the institute has been deeply involved in the international efforts to fight Ebola, particularly in Guinea.

The China CDC gained enormous experience in infectious-disease response during the 2003 outbreak of severe acute respiratory syndrome (SARS), and it has applied this expertise in the Ebola crisis, working under the leadership of deputy director-general George Gao. China and the Pasteur Institute have worked together during the crisis, and this collaboration forms the foundation of the new initiative.

The Ebola outbreak exposed the lack of local expertise. There was a shortage of skilled scientists and health-care workers able to diagnose the disease, for example. Our initiative will aim to help local authorities to revamp graduate training in science and public health in regional universities — including in Senegal and Côte d'Ivoire — and throughout the Pasteur network in Africa.

We aim to train more students in emerging infectious diseases, global public health and veterinary medicine. We will offer direct training, long-distance learning and internships

for students to work in Pasteur labs and with our teams in the field. Where needed, we will help to build facilities with the latest training technologies.

Surveillance has proved a real problem in the Ebola outbreak, and an important goal of our initiative is to train a substantial pool of skilled local professionals in techniques such as epidemiology so that they can do research-based disease tracking. By working with international partners we plan to improve access to modern equipment for medical biologists and other scientists in Africa.

We will also work to provide extra training for existing African scientists by funding postdoctoral fellowships and training at approved laboratories and facilities in West Africa. Today's professors will train tomorrow's students, so it is crucial that we establish more research

opportunities for local scientists. We hope that encouraging them to develop projects with international partners will generate a virtuous circle to ensure the sustainability of a research programme for public health.

The fellowships will cover a range of scientific disciplines, from outbreak investigation and rapid response to quality assurance. There are currently not enough — if any — of these opportunities in poor countries such as Guinea and Liberia. These nations need a new generation of African doctors, nurses, lab technicians and PhD-trained scientists. We will also provide funding to encourage the brightest African postdoctoral scientists who have trained abroad to return.

It is important that response to future disease outbreaks is informed by new knowledge about basic science. The joint project will fund collaborations between African scientists and inter-

national organizations that focus on the various components of an epidemic: the pathogen, vector, environment and host genetics.

Infectious-disease outbreaks will continue to occur. We must capitalize on the current political momentum and the will of international agencies and take steps to make lasting improvements to education, research and surveillance in West Africa and change the way the next outbreak unfolds.

The Pasteur Institute and the China CDC want to provide a foundation for this international effort. We appeal to other governmental and international organizations, African networks and funders to join us. Together, we can rebuild and establish the scientific and medical capacity and infrastructure that West Africa needs to recover from this outbreak, and to ensure that it is prepared for the next one. ■ SEE EDITORIAL P.5, NEWS FEATURE P.22, COMMENT P.27 & P.29

Christian Bréchet is president of the Pasteur Institute in Paris.
e-mail: christian.brechot@pasteur.fr

OUR MAIN AIM IS TO
REVITALIZE
THESE COUNTRIES'
OVEREXTENDED
HEALTH
SYSTEMS
WITHIN
FIVE YEARS.

➔ **NATURE.COM**
For Nature's special
on Ebola, see:
nature.com/ebola

RESEARCH HIGHLIGHTS

Selections from the
scientific literature

PARTICLE PHYSICS

Only left-handed particles decay

Only subatomic particles with a left-handed spin decay as a result of one of the fundamental forces, confirming that the Universe has a left-hand bias.

A team working on the LHCb experiment looked at the decay of trillions of subatomic particles known as Λ_b^0 baryons emerging from collisions at the Large Hadron Collider at CERN, Europe's particle-physics laboratory near Geneva, Switzerland. During this decay, a bottom quark from the baryon can turn into an up quark. The team confirmed that the weak nuclear force — one of the four fundamental forces in the Universe — causes only bottom quarks with left-handed spin to decay into up quarks, as predicted by the standard model of particle physics.

Previous measurements had suggested that right-handed quarks might also decay in this way, which, if true, would have called for new fundamental forces of nature.

Nature Phys. <http://doi.org/6kg> (2015)

CONSERVATION

Better estimates of extinction risk

Using an improved method for calculating the extinction risk of species could lower the risk estimates for about one in ten threatened species.

The influential Red List from the International Union for Conservation of Nature (IUCN) groups thousands of threatened plants and animals into different categories of extinction risk. Lucas Joppa at Microsoft Research in Redmond,

Washington, and his colleagues analysed different methods of calculating the 'extent of occurrence' (EOO) for 21,763 species of mammals, birds and amphibians on the Red List. The EOO is the total area over which a species might be found — the smaller the area, the greater the vulnerability of that species.

Past assessments often used EOO calculation methods that the IUCN now considers outdated. The researchers found that applying the IUCN-approved method would lower the risk category of many threatened animals for 14–15% of mammals,

7–8% of birds and 12–15% of amphibians.

Conserv. Biol. <http://doi.org/6jq> (2015)

MICROBIOLOGY

Microbes ramp up red-meat risk

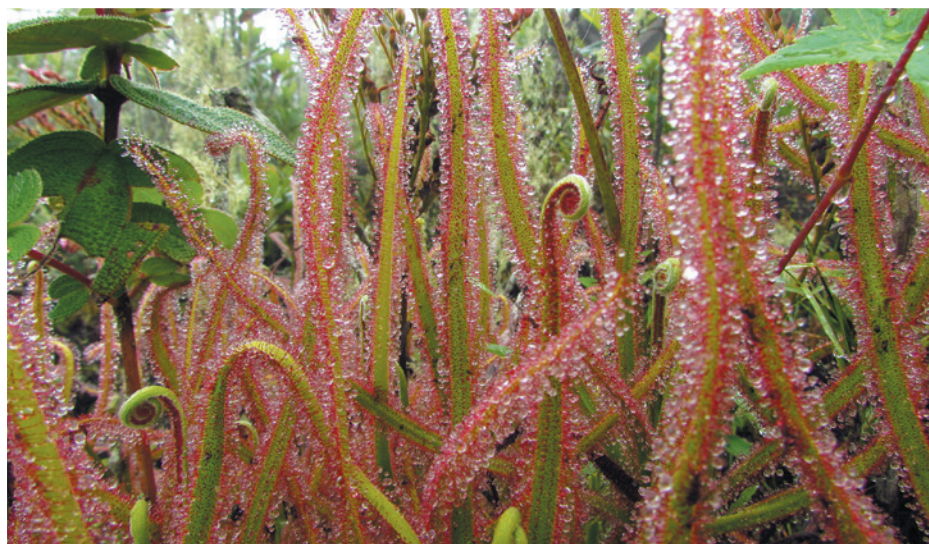
Microbes in the gut help to boost the risk of colon cancer when haem, the pigment found in red meat, is present.

Haem in the diet has been linked to an increased risk of colon cancer — the pigment damages cells lining the gut, which leads to excessive cell proliferation. Noortje Ijssennagger at University

habitat on a single mountain. The plant has stems roughly 1.5 metres long and is the largest *Drosera* species in the Americas. The team found many insects trapped in a sticky substance produced by the plant's red tentacles, which cover the leaves.

The sundew is considered critically endangered, because coffee and eucalyptus plantations threaten its habitat.

Phytotaxa 220, 257–267 (2015)



PAULO MINATEL GONELLA

PLANT BIOLOGY

New carnivorous plant found on Facebook

A new species of insect-eating sundew plant (*Drosera magnifica*; pictured) has been identified after an amateur naturalist posted photographs of it on Facebook.

Paulo Minatel Gonella at the University of São Paulo in Brazil and his colleagues were alerted to the photos on the social network, and travelled to southeastern Brazil to study the carnivorous species, which grows in a narrowly defined

Medical Center Utrecht in the Netherlands and her colleagues fed mice a diet containing haem and found that animals that also received antibiotics did not have this gut damage or increased cell proliferation. Haem increased the level of a bacterium called *Akkermansia muciniphila*, which breaks down the gut mucus lining, exposing gut cells to the damaging haem. Gut bacteria that produce sulfide also degrade this mucus barrier.

Using a biomarker to monitor gut mucus degradation could be a way to gauge colon-cancer risk, the authors say. *Proc. Natl Acad. Sci. USA* <http://doi.org/6jp> (2015)

GLACIOLOGY

Greenland glaciers have hidden depths

Greenland's glaciers may be more susceptible to global warming than was thought.

Eric Rignot of the University of California, Irvine, and his colleagues used sonar to analyse the depths and profiles of three glaciers terminating in fjords in western Greenland. They found that the glaciers reach hundreds of metres farther down into the ocean than current maps suggest, allowing the ice to come into contact with a deep layer of warm Atlantic water. This leads to melting and the formation of deep cavities that probably boost the chances of large glacier chunks breaking off.

The authors note that these processes are not included in current ice-sheet models, and suggest that estimates of Greenland's contribution to sea-level rise will need to be increased.

Geophys. Res. Lett. <http://doi.org/6dn> (2015)

PALAEOLOGY

Lizards evolved at snail's pace

Lizards of the Caribbean islands have changed little over millions of years.

Only three fossils of *Anolis* lizards have previously been studied, but now Emma Sherratt at the University of New England in Armidale, Australia, and her colleagues have analysed a further 17 fossils entombed in amber (pictured) from the Dominican Republic. The specimens, which are 15 million to 20 million years old, revealed that the animals were uniquely adapted to the different parts of the trees that they inhabit, much as they are today. For instance, lizards that lived on twigs tended to be small with short limbs.



Other fossils resembled larger lizards that live near the base of tree trunks and those found around the crowns of trees.

The findings suggest that communities can remain remarkably stable over long evolutionary timescales.

Proc. Natl Acad. Sci. USA <http://doi.org/6hk> (2015)

GEOPHYSICS

Ancient roots of Earth's magnetism

Earth may have developed a magnetic field as early as four billion years ago — more than half a billion years earlier than was thought.

John Tarduno at the University of Rochester in New York and his colleagues measured faint magnetic signals of iron-bearing minerals trapped inside zircon crystals up to four billion years old from the Jack Hills region of Western Australia. They found that the magnetic field fluctuated in strength, from a value similar to today's field (around 25 microteslas) to about 12% of that.

An ancient magnetic field when the planet was only about 500 million years old would have been a good, if imperfect, shield against the solar wind. This could have made the young planet more hospitable to life, the authors say.

Science 349, 521–524 (2015)

MATERIALS

Scaling up pure graphene growth

Researchers have found a way to grow and transfer crystals of graphene more efficiently compared with other methods.

Pure graphene comprises one-atom-thick sheets of carbon that have desirable electronic properties, and is best made by stripping a single layer of atoms off a graphite crystal.

However, the process is hard to scale up for industrial use

SOCIAL SELECTION

Popular topics on social media

A way to solve irreproducibility?

A growing backlog of psychology findings that have never been reproduced has shaken confidence in the field. One possible remedy is to require PhD students to replicate at least one study from their own specialism as part of their education, write UK psychologists Brian Earp and Jim Everett in an opinion piece in *Frontiers in Psychology*. “Best suggestion I’ve heard [with respect to] the replication crisis in psychology. Plus seems like just smart pedagogy,” tweeted Jonathan LaTourelle, a PhD student in the philosophy of cognitive science at Arizona State University in Tempe. But ethicist Owen Schaefer at the University of Oxford, UK, suggested in a comment on a blog post that the proposal could end up “disproportionately burdening” graduate students.

➔ **NATURE.COM**
For more on
popular papers:
go.nature.com/bowwby

Front. Psychol. <http://dx.doi.org/10.3389/fpsyg.2015.01152> (2015)

and other, more scaleable methods introduce contaminants. So Christoph Stampfer at RWTH Aachen University in Germany and his colleagues synthesized a layer of graphene on copper, and used a compound called hexagonal boron nitride to peel the graphene off and transfer it to another substrate. This yielded crystals with fewer flaws than those made using other techniques, and the copper could be used again to produce more graphene.

The resulting material has electronic properties that rival the best graphene made by other, less scaleable methods, the authors report.

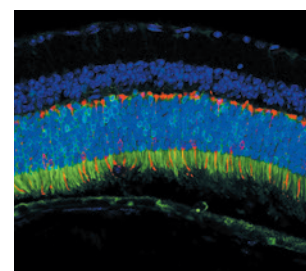
Sci. Adv. 1, e1500222 (2015)

VIROLOGY

Ancestral virus for gene therapy

An ancient virus reconstructed by researchers could make gene therapy more efficient.

Viruses are used in such therapies to deliver functioning genes to diseased cells in the body, but better viruses are needed to transfer genes more efficiently. Luk Vandenbergh of the Massachusetts Eye and Ear



Infirmity in Boston and his colleagues analysed the amino-acid sequences of the proteins that coat 75 adeno-associated viruses (AAV), 5 of which are being tested in human gene-therapy trials. They predicted how the structure of these proteins might have evolved, and came up with protein sequences for 9 AAVs that might have been ancestors of the current viruses. They synthesized the ancient AAVs and found that one, Anc80, could efficiently transfer genes to muscles and the retina in mice (pictured), and to the liver in both mice and monkeys.

Anc80 did not trigger any negative side effects in these animals that would prevent it from delivering genes to cells. *Cell Rep.* <http://doi.org/6j6> (2015)

➔ **NATURE.COM**
For the latest research published by Nature visit:
www.nature.com/latestresearch

LIVIA CARVALHO

ETTORE MORONE

SEVEN DAYS

The news in brief

RESEARCH

Ebola vaccine

An experimental Ebola vaccine seems to confer total protection against infection in people who are at high risk of contracting the virus, according to a trial in Guinea (A. M. Henao-Restrepo *et al. Lancet* [http://dx.doi.org/10.1016/S0140-6736\(15\)61117-5](http://dx.doi.org/10.1016/S0140-6736(15)61117-5); 2015). The vaccine, developed by the Public Health Agency of Canada and licensed to drug company Merck, is made from a livestock virus that has been engineered to produce an Ebola protein. The trial included two arms: of the 2,014 people who received the vaccine immediately, none developed Ebola ten days after getting the vaccine. There were 16 infections in the 2,380 people who were given the vaccine 3 weeks later. See page 13 for more.

Rice retraction

A paper claiming that the genetically engineered crop Golden Rice was an effective vitamin A supplement in children in China was retracted from *The American Journal of Clinical Nutrition* on 29 July. The journal retracted the paper (G. Tang *et al. Am. J. Clin. Nutr.* **96**, 658–664; 2012) because the authors, led by Guangwen Tang of Tufts University in Boston, Massachusetts, did not fulfil ethical requirements. Among other things, the journal says, they did not provide evidence that they had ethical approval for their experiments. The authors filed an injunction last year to stop the retraction, but were denied one by a Massachusetts court on 17 July.

EVENTS

White rhino dies

Just four northern white rhinos (*Ceratotherium simum cottoni*) remain in the world



HAWAII DEPT. LAND AND NATURAL RESOURCES

Arrests in Hawaii over telescopes

Protests over telescope building on Hawaii's mountains led to the arrest on the night of 30 July of more than 20 demonstrators on the island of Maui, where a 4.2-metre solar telescope is under construction on Haleakala. Seven protesters were also arrested at Mauna Kea on Big Island, in the latest escalation in the

stand-off over adding the planned Thirty Meter Telescope (TMT) to the 13 telescopes near the summit of Mauna Kea, which is sacred to Native Hawaiians. Protestors are also expected at the International Astronomical Union meeting in Honolulu from 3 to 14 August. Construction of the TMT remains on hold indefinitely.

after a female named Nabiré died at the Dvůr Králové Zoo in the Czech Republic on 27 July. The northern white rhino is a subspecies of the white rhino, which numbers around 20,000 in the wild. The zoo reported that Nabiré died when a large cyst inside her ruptured. This leaves one male and two female northern white rhinos in Kenya and one female in San Diego, California.

Crash investigation

SpaceShipTwo, a rocket plane owned by spaceflight company Virgin Galactic, broke up during a test flight in October 2014 because the co-pilot activated a braking system too soon. In its 28 July report on the crash, the US National Transportation

Safety Board stated that the plane's designer, Scaled Composites in Mojave, California, failed to account for human error in the pre-flight hazard analysis that it provided to federal aviation regulators. This omission ultimately led to the accident.

Anthrax grounded

The US shipping company FedEx says that it will stop carrying dangerous pathogens, or 'select agents'. The move comes after the US military announced in May that it had accidentally shipped live anthrax spores to nearly 200 labs in 9 countries. According to *USA Today*, which revealed the announcement on 29 July, FedEx is one of only two companies that ship select

agents, leaving researchers concerned that it will be difficult to transport samples in the case of an epidemic. FedEx says that it carried at least one of the live anthrax samples, from Dugway Proving Ground in Utah.

POLICY

Punish poaching

In a resolution passed by its general assembly on 30 July, the United Nations asked its members to step up the fight against wildlife crime. The decree expresses "serious concern" over the poaching of rhinos and elephants in Africa and urges member states to strengthen legislation to prevent and prosecute illegal trade. The resolution follows the London

KIERAN DODDS/PANOS

Declaration of February 2014, in which 41 nations agreed to deem poaching a serious crime — a technical UN term designed to result in harsher punishment for offenders.

US emissions curb

US President Barack Obama announced landmark regulations on 3 August to curb greenhouse-gas emissions from power plants. The regulations, developed by the US Environmental Protection Agency (EPA), call for a 32% reduction in emissions from the 2005 level by 2030. The target is stricter than the one proposed in June last year, which laid out a 30% cut. US states must now develop plans for how to reach the targets and submit them to the EPA by September 2016. See go.nature.com/fbidf5 for more.

Chimp ruling

Chimpanzees are not legal persons, a New York court ruled on 29 July. The activist group Nonhuman Rights Project had filed a suit in 2013 on behalf of two research chimpanzees at Stony Brook University in New York, arguing that the animals were being unlawfully detained. In her decision, judge Barbara Jaffe wrote that she was bound by legal precedent. But she did not discount the group's argument, saying



that the judicial system is slow to embrace change, but chimpanzees might one day gain legal rights.

PEOPLE

Physics spy suspect

A Russian physicist who worked in the Netherlands is under suspicion of having passed confidential information to the Russian intelligence service. Photonics and quantum-computing researcher Ivan Agafonov, who denies the allegations, worked at the Eindhoven University of Technology (TUE). A statement published by the TUE on 28 July says that the university was informed by Dutch intelligence services in July 2014 that Agafonov was in contact with Russian intelligence services. The statement adds that the university has terminated Agafonov's employment,

and Dutch authorities have revoked his residency permit on suspicion of espionage.

Telescope head

The president of the Giant Magellan Telescope Organization (GMTO) has stepped down. Physicist Ed Moses led the GMTO for less than a year. He left the post to deal with family matters, according to a 28 July statement by the governing board. Efforts to build the US\$1-billion telescope — which is scheduled for first light in 2022 — will be led by Patrick McCarthy, an astronomer at the Las Campanas Observatory in La Serena, Chile, who has previously helped to lead the GMTO, until a replacement is appointed.

Intelligence chief

Jason Matheny has been made director of the US Intelligence Advanced Research Projects Activity (IARPA), the agency announced on 3 August. IARPA funds high-risk, high-pay-off research for the US intelligence agencies. Matheny, who previously founded biotechnology organizations working to develop lab-grown meat, has directed IARPA's efforts to forecast events and scientific advances. He will be the agency's third director since it was founded in 2006.

COMING UP

9–13 AUGUST

Researchers with an interest in how light can be used to probe anything from nanoscale sensors to the outer cosmos meet in San Diego, California, at the SPIE Optics + Photonics conference. go.nature.com/48vevv

8–12 AUGUST

The 12th World Congress on Inflammation convenes in Boston, Massachusetts. Discussions will cover the latest research on the role of inflammation in disease and ways to control or halt it. inflammation2015.org

9–13 AUGUST

How do logic and relativity interconnect? Find out at the 2nd Logic, Relativity and Beyond conference in Budapest, Hungary. go.nature.com/st8s87

FACILITIES

Ecology funding cut

The US National Ecological Observatory Network (NEON) — a countrywide project to measure the effects of climate change — will cancel its experiment to monitor how streams respond to simulated environmental stressors. The move comes after the National Science Foundation told programme managers on 31 July that it was changing the scope of the project. NEON has a budget of US\$433.7-million over 5 years. It is constructing more than 100 data-collection sites around the United States, but it has faced charges of mismanagement (see *Nature* <http://doi.org/6k5j>; 2014).

➔ NATURE.COM

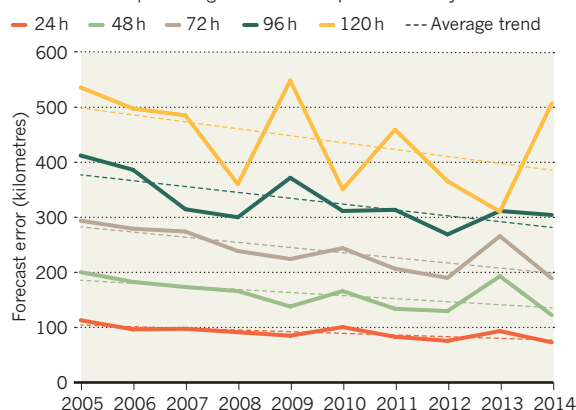
For daily news updates see: www.nature.com/news

TREND WATCH

This month marks the tenth anniversary of Hurricane Katrina's landfall along the northern Gulf of Mexico coast. The destruction left by the hurricane prompted the US National Oceanic and Atmospheric Administration (NOAA) and other scientists to put more effort into developing tools and techniques to improve the accuracy of their forecasts. The forecast error on NOAA's hurricane-path predictions two days ahead of landfall decreased from 204 kilometres in 2005 to 120 kilometres in 2014.

IMPROVING HURRICANE PREDICTION

NOAA's ability to predict where a hurricane in the Atlantic basin will hit in the hours preceding landfall has improved steadily.



SOURCE: NATIONAL HURRICANE CENTER

NEWS IN FOCUS



CANCER Physical-oncology programme accused of losing its way **p.14**

NEUROSCIENCE Scrap of mouse brain reconstructed in full detail **p.17**

OCEAN ACIDIFICATION Weak experiments create uncertainty for sea life **p.18**

PATIENCE IS A VIRTUE Can chemists become greener by taking their time? **p.20**

SEAN HAWKEY/WHO



A pioneering clinical trial in Guinea could provide a model for use in future disease outbreaks.

INFECTIOUS DISEASE

Ebola on trial

Rapid development of an effective vaccine has implications for the epidemic in West Africa and for clinical-trial policy.

BY DECLAN BUTLER, EWEN CALLAWAY & ERIKA CHECK HAYDEN

When Ebola broke out in West Africa in December 2013, triggering the largest-ever epidemic of the disease, there was no vaccine or drug that had been shown to be safe and effective in people. Just 20 months later, a vaccine seems to confer total protection against infection, according to the preliminary results of a trial in Guinea that were published on 31 July (A. M. Henao-Restrepo *et al. Lancet* [http://dx.doi.org/10.1016/S0140-6736\(15\)61117-5](http://dx.doi.org/10.1016/S0140-6736(15)61117-5); 2015). *Nature* looks at the implications of the trial's success for the ongoing epidemic, which has killed more than 11,000 people, as well as for how future clinical trials are conducted in outbreaks.

How did the vaccine come about?

Called rVSV-ZEBOV, it consists of a livestock virus that has been genetically engineered to masquerade as the Ebola virus (see 'Masters of disguise'). It was developed by the Public Health Agency of Canada, licensed to the pharmaceutical company Merck and tested by an international collaboration of funders, scientists, companies, organizations and governments, including the World Health Organization (WHO). The trial was carried out in Guinea, where the epidemic began, and used a 'ring' design in which contacts of infected people — such as members of the same household — are vaccinated, as are any subsequent contacts of those

➔ **NATURE.COM**
For *Nature's* special on Ebola, see nature.com/ebola

people. It comprised two groups: one received immediate vaccination and the other received the vaccine three weeks later.

What did the trial find?

Of the 2,014 contacts (of 48 people infected with Ebola) who received the vaccine immediately, none developed Ebola after a 10-day window — enough time for the body to summon an immune response to the vaccine and for any pre-existing Ebola infections to have revealed themselves. (A few people did develop the disease between 1 and 10 days after vaccination.) By comparison, 16 people out of the 2,380 contacts (from 42 cases) in the control group became infected during this time. The vaccine was therefore deemed to have provided 100% protection against the virus in this trial.

100% protection sounds too good to be true.

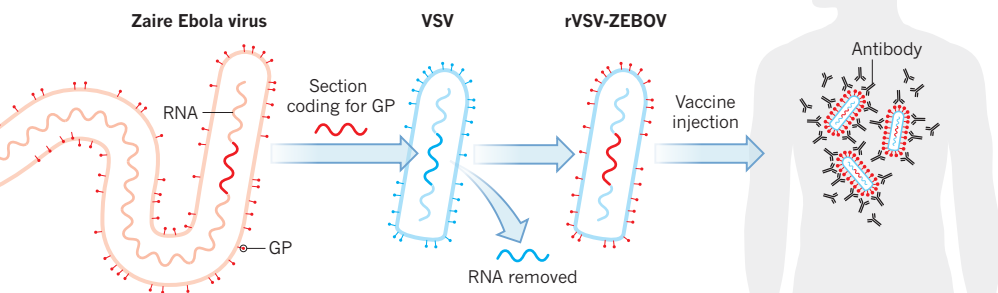
It probably is. The study was quite small, so the true protection rate may be slightly lower, says Marie-Paule Kieny, assistant director-general for health systems and innovation at the World Health Organization (WHO). An independent committee overseeing the trial considered the preliminary results so convincing that the control group was dropped on 26 July, and all contacts are now being vaccinated immediately. This will yield more data on the true levels of protection. But there is already excitement about the vaccine. "The results as reported are so striking that even if there are some issues in the study, it appears very likely that it's effective," says Jesse Goodman, a former US Food and Drug Administration official who is now at Georgetown University in Washington DC.

For how long does the vaccine work?

That is unknown. The trial was designed to test whether ring vaccination could snuff out outbreaks, and the several weeks of protection that it is known to provide is enough to do this. "That's good news for an outbreak situation," says Adrian Hill, director of the Jenner Institute at the University of Oxford, UK, who is involved in testing a different Ebola vaccine. However, he says, it remains to be seen whether the protection lasts any longer. "Will it work at six months? This trial doesn't tell us that" Longer-term — ideally lifelong — immunity is needed for a vaccine to provide sustained protection to health workers and other high-risk groups during an epidemic, or to mass-vaccinate populations should Ebola become endemic. ►

MASTERS OF DISGUISE

The rVSV-ZEBOV vaccine is made by genetically engineering a weakened form of vesicular stomatitis virus (VSV) so that it impersonates the Zaire species of Ebola virus, which caused the epidemic in West Africa.



1. Researchers snip out the RNA that codes for the virus's surface glycoprotein (GP), which allows the virus to latch onto human cells.

2. They then remove the stretch of RNA that codes for the VSV's surface protein and replace it with that for the Ebola GP.

3. The resulting vaccine tricks the human immune system into mounting a response against the Zaire Ebola virus.

► Other vaccine trials, including the one that Hill is involved in, are testing for longer-term protection. But the fall in the number of Ebola cases — to 20–30 per week over the past few months — means that the trials may struggle to provide clear results.

Could the rVSV-ZEBOV vaccine help to end the epidemic in West Africa?

The vaccine will continue to be used in Guinea as part of the clinical trial. Many researchers hope that it will be used in Liberia and Sierra Leone too, to end the epidemic — although case numbers have plummeted, there is a continued risk of flare-ups as well as of spread to nearby countries (see page 27). However, some regulatory hurdles need to be cleared first. Deployment in those nations could occur as part of an expanded clinical-trial regime or through emergency authorization by regulators, says

Gregory Hartl, a spokesperson for the WHO. The authorities there are now considering whether the available data are sufficient to license the vaccine for use outside a clinical-trial setting, a process that could take weeks to months, according to the WHO.

Is it unusual to do a trial during an outbreak?

Yes. Getting clinical trials approved by regulators usually takes years, as does conducting the gold standard of randomized controlled trials. That means that outbreaks tend to be over before trials can even begin. Clinical trials are also usually done in well-equipped research hospitals, and quality trials have generally been considered impossible to carry out in the often-atrocious field conditions of deadly outbreaks (see *Nature* 513, 13–14; 2014). The urgency of tackling Ebola changed all that. In September, the WHO-supported collaboration pulled out

all the stops to accelerate testing of treatments and vaccines that had shown promise in animals. It cut through the red tape and came up with trial designs that could quickly provide data at least good enough to inform efforts to control the outbreak. The rVSV-ZEBOV trial is one of several that came about as a result.

Can the fast-track approach be applied to other diseases?

Hill suggests that vaccines could quickly be developed for many other epidemic threats. He recommends that research on vaccines against such pathogens be accelerated so that clinical trials can be done now to test their safety; those that pass muster would be stockpiled, ready for efficacy tests as soon as an outbreak occurs. Pathogens considered priority health threats include Marburg virus, which is in the same family as Ebola, and the viruses that cause Middle East respiratory syndrome (MERS), Lassa fever and chikungunya.

Are lessons likely to be learned from rVSV-ZEBOV's success?

The hope is that it will provide a model for dealing with future outbreaks. "This is illustrating that it is feasible to develop vaccines much faster than we've been doing," says Hill. And there seems to be support for change at the highest level. Margaret Chan, director-general of the WHO, said on 31 July that the agency is developing a "blueprint" for accelerated development of measures to counteract potential epidemics. The plan aims to reduce the time from the recognition of an outbreak to availability of countermeasures to four months or less, and would include putting trial designs and regulatory approvals in place in advance of an outbreak. "No one wants to see clinicians, doctors, left empty-handed ever again," said Chan. ■

ONCOLOGY

Cancer–physics project accused of losing ambition

Trailblazers of physical oncology complain that US National Cancer Institute programme has lost sight of its mission.

BY GABRIEL POPKIN

An ambitious initiative that has deployed physics in the fight against cancer since 2009 has awarded a second round of grants. But some pioneers of the field, known as physical oncology, protest that the US

National Cancer Institute (NCI) has lost sight of the programme's original vision.

In June, the NCI announced that it would give each of four Physical Sciences-Oncology Centers (PS-OCs) around US\$2 million a year for five years. But the funded projects are too unambitious to produce major paradigm

shifts, argues Robert Austin, a physicist at Princeton University in New Jersey who helped the NCI to lay the groundwork for the programme, and whose centre was not funded in the second round.

The programme is "losing patience with those of us who want to understand the

fundamentals”, says Austin.

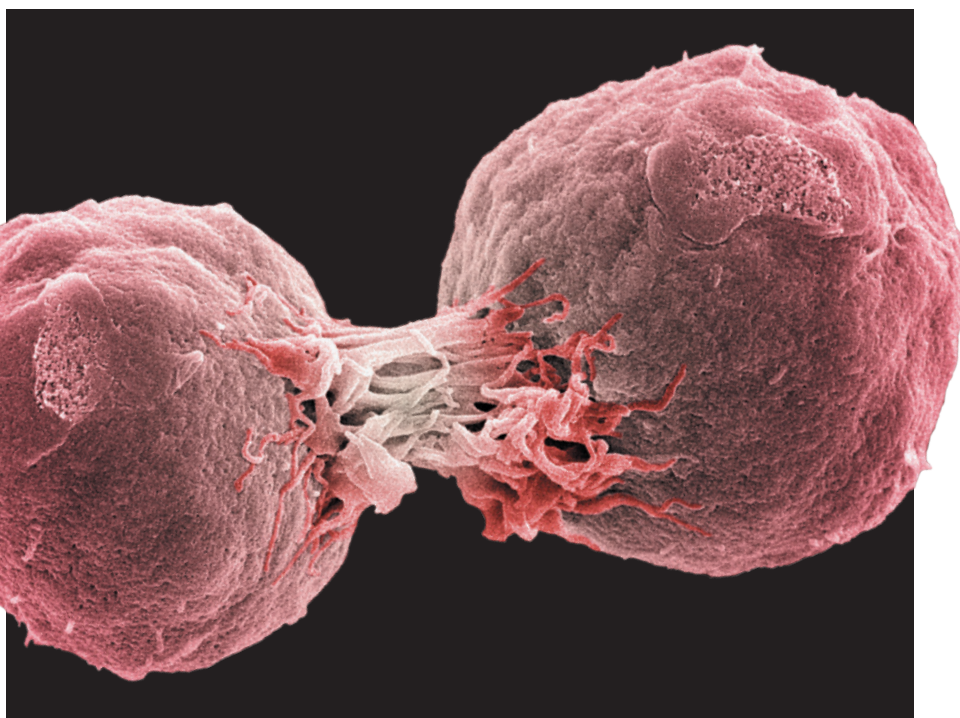
NCI officials say that the latest awards, along with two rounds of funding planned for later this year or next year, show the institute’s continuing commitment to the interdisciplinary approach. “The fact that this programme is renewed, while it’s not in the same original form, is still an indication of support,” says Larry Nagahara, a former director of the programme who left the NCI for Johns Hopkins University in Baltimore, Maryland, this month. Officials insist that there has been no move away from physics, although the programme also embraces related fields such as engineering and applied mathematics. “We’re sort of agnostic on the spectrum of research that people are working on,” says current programme head Sean Hanlon.

The PS-OC programme was largely the brainchild of Anna Barker, who in 2007–08, as a deputy director at the NCI, set up workshops that helped to lay the programme’s intellectual foundation. She and other proponents pointed out that although billions of dollars of research investment into drugs and therapies have reduced mortality for some cancers, they have not produced a fundamental understanding of the disease. Programme leaders proposed to open a new front in the war on cancer by recruiting physicists to study cancer as a physical rather than strictly biological phenomenon.

A DIFFERENT PERSPECTIVE

In 2009, the NCI gave grants averaging \$2.5 million a year for 5 years to 12 centres, each co-directed by a physical scientist and a cancer biologist. Some researchers attempted to re-envision cancer from the bottom up. For example, physicist Paul Davies of Arizona State University in Tempe, who along with Austin was involved in the initial programme workshops (see *Nature* 474, 20–22; 2011), has proposed that a cell becomes cancerous when it reverts to a primitive evolutionary state. He is investigating whether ancient genes become activated during cancer development (P. C. W. Davies and C. H. Lineweaver *Phys. Biol.* 8, 015001; 2011). Austin has explored the evolution of drug resistance by using microfluidic devices to expose tumour cells to chemical gradients (A. Wu *et al. Proc. Natl Acad. Sci. USA* 110, 16103–16108; 2013), and has suggested that cancer might result from environmental stress rather than from genetic mutations.

Others have sought to develop or refine mathematical or biophysical tools for cancer research. At the Dana-Farber Cancer Institute in Boston, Massachusetts, for example, researchers have built computer simulations to predict which genetic and cellular changes are most likely to lead to certain cancers, and which treatment approaches are most likely to succeed. Other centres have used advanced



Cell division and other cancer processes are being studied by physicists looking for fundamental insights.

microscopy and spectroscopy. Such projects are valuable, but do not seek the kind of fundamental understanding of cancer that is the hallmark of the physics approach, says Herbert Levine, a physicist at Rice University in Houston, Texas, who studies cancer but has not received PS-OC funding.

The awards announced in June went to existing centres at Northwestern University in Chicago, Illinois, and Dana-Farber, as well as to two new ones — at Columbia University in New York City and the University of Pennsylvania in Philadelphia. Neither Austin nor Davies had their proposals funded. Those decisions may reflect the tangible results

“The lofty goal of helping find a new set of directions in biology — I don’t think they quite got there.”

produced by less paradigm-challenging projects, Levine says. He thinks that projects seeking fundamental breakthroughs, such as Austin’s, need more time to achieve their

visions. “The lofty goal of helping find a new set of directions in biology with the help of physicists, computer scientists, whatever — I don’t think they quite got there.” Barker, who left the NCI in 2010 and is now at Arizona State, says that the PS-OCs have made progress in a number of areas, including understanding cancer evolution, predicting when a cell will become metastatic and developing biomarkers for cancer. But she agrees that five years was probably too short for the more ambitious efforts. “For these large consortia, it takes about the first three years to get them all working together, to get a common language in place,

to get common core resources developed,” she says. “In terms of judging the programme, I’d like to have seen it a couple years hence.”

NCI programme managers say that the plan was always to reopen the funding competition after five years, rather than simply to extend existing sites. More researchers applied for the second round of funding, they say, and there was not enough money for everyone. But they point out that physical oncologists now have more funding options. “I think most people will find somewhere to have their work supported,” says Hanlon, whether through future PS-OC awards, other NCI programmes or external sources.

Levine, for example, has funding from the state of Texas and has been involved in a partnership between the US National Science Foundation and private donors. The Francis Crick Institute, set to open this year in London, promises to bring more physicists into biomedical research (see *Nature* 509, 544–545; 2014). Austin and Davies say they may look overseas or to private foundations to continue their work.

NCI programme managers say that the diversification of funding sources shows that the field is gaining support and recognition. They also point to the journal *Convergent Science Physical Oncology*, launched in June by IOP Publishing of Bristol, UK, and to standing sessions on physics and the evolution of cancer at the American Physical Society’s annual March meeting and at meetings of the American Association for Cancer Research. “Those types of sessions didn’t exist five years ago — now you can find them at several of these meetings,” says Nagahara. “That’s a sign of success.” ■



Malaria-carrying mosquitoes (*Anopheles gambiae*) are a prime target for gene-editing techniques.

BIOTECHNOLOGY

Caution urged over DNA editing in wild

Method for rapidly altering gene pools could harm ecosystems.

BY HEIDI LEDFORD

“Crap!” That was the first word out of Kevin Esvelt’s mouth as he scanned a paper¹ published in *Science* last March. The work described the use of a gene-editing technique to insert a mutation into fruit flies that would be passed on to almost all of their offspring. Although intriguing, the report made Esvelt feel uneasy: if engineered flies escaped from a lab, the mutation could spread quickly through a wild population.

But that was exactly what exhilarated molecular biologist Anthony James at the University of California, Irvine. “Holy mackerel!” he wrote to the study’s authors. “Can we use it in mosquitoes?”

On 30 July, the US National Academy of Sciences, Engineering, and Medicine (NAS) held the first in a series of meetings meant to find ways to balance the promise and perils of the technique, called ‘gene drive’. The method can rapidly modify not just a single organism but a whole population, by inserting a desired genetic modification into an organism along with DNA that increases the rate at which the

change is passed to the next generation. The technique could be used to render mosquitoes unable to carry malaria parasites or to wipe out harmful invasive species, but it could also have unanticipated environmental costs and might be impossible to reverse. “Once this is out there, you cannot call it back,” says Walter Tabachnick, a population geneticist at the University of Florida in Vero Beach.

The idea of gene drive has been around for more than a decade². But its practicality was given a huge boost around three years ago with the arrival of CRISPR, a gene-editing technique that allows precise changes to an organism’s DNA³.

The *Science* paper¹, by developmental biologist Ethan Bier and his student Valentino Gantz at the University of California, San Diego, used CRISPR to insert a modification into genes on both chromosomes in a pair, so that when the flies bred, they would pass the modification on to practically all of their offspring.

The work came out of a desire to develop

“How do you test such a system, and how do you do it safely?”

a system that would make it easier to study genetic changes in organisms that are difficult to breed in the laboratory. Because CRISPR has been shown to work in a wide range of creatures, researchers hope one day to be able to engineer wild populations in much the same way.

DAVID SCHARF/CORBIS

CALL FOR CONCERN

Mindful of both the potential and the risks, Esvelt, a bioengineer at Harvard Medical School in Boston, Massachusetts, brought together a group of scientists to write a Comment in *Science*⁴, published last week, laying out the need for multiple containment strategies for gene-drive research that is done in the laboratory. Meanwhile, the NAS meeting marks the start of a 15-month search for ways to minimize the risk in advance of field releases. Because no one is known to have made CRISPR work in mosquitoes — the mostly likely organism for the application of the technology — the committee has some time to do its work.

But there is still urgency, noted Todd Kuiken, who explores the interface of science and policy at the Wilson Center, a think tank in Washington DC. CRISPR gene-drive technology is developing at a breakneck pace, and has the potential to dramatically alter ecosystems in unexpected ways. At the meeting, Kuiken used the invasion of Asian carp into some US lakes as an example of how little is known about some wild ecosystems. “While this is an invasive species, it’s also an established species,” he says. “I don’t think we have a good understanding of how we evaluate what happens when we remove a species from as large an ecosystem such as this.”

Meanwhile, Esvelt and his colleagues are studying the CRISPR gene-drive system in the nematode *Caenorhabditis elegans* to learn more about what happens to a population as engineered DNA is passed down through generations, accumulating mutations as it goes. They are also testing ways to make sure that a gene drive can be countermanded once it has been set loose.

These issues need immediate attention, says geneticist Daniel Wattendorf at the US Defense Advanced Research Projects Agency (DARPA) in Arlington, Virginia. Security concerns may mean that DARPA needs to start working on the technology before guidelines are drawn up, he adds.

And Tabachnick remains concerned that these preparations may not suffice. “How do you test such a system, and how do you do it safely?” he asks. “I’m not convinced that any of this work could ever possibly provide the assurance of safety that one might demand.” ■ **SEE EDITORIAL P.5**

1. Gantz, V. M. & Bier, E. *Science* **348**, 442–444 (2015).
2. Burt, A. *Proc. R. Soc. Lond. B* **270**, 921–928 (2003).
3. Jinek, M. et al. *Science* **337**, 816–821 (2012).
4. Akbari, O. S. et al. *Science* <http://dx.doi.org/10.1126/science.aac7932> (2015).

NEUROSCIENCE

Scrap of brain seen in full detail

Mouse map is step towards reconstructing human brain.

BY ALISON ABBOTT

Six years might seem like a long time to spend piecing together the structure of a speck of tissue vastly smaller than a bead of sweat. But that is how long it took a team led by cell biologist Jeff Lichtman at Harvard University in Cambridge, Massachusetts, to create the first complete reconstruction of a piece of tissue in the mammalian neocortex.

The reconstruction (N. Kasthuri *et al.* *Cell* **162**, 648–661; 2015) is essentially a 3D digital map that allows biologists to see the detail and relative positions of every individual cell part in a piece of tissue measuring 1,500 cubic micrometres, helping to reveal how the brain works.

It is a far cry from reconstructing all of the 100 billion or so cells that make up the entire human brain, which is one of neuroscientists' ultimate goals. But Christof Koch, president of the Allen Institute for Brain Science in Seattle, Washington, notes that the various technologies involved will speed up "tremendously" over the next decade: "I would call this a very exciting promissory note."

Lichtman's team has its sights set on a further challenge: reconstructing a cubic millimetre of rodent neocortex — a piece of tissue more than 600,000 times larger than the present achievement. The researchers will do that work as part of a consortium that in July received preliminary approval for funding by the US government agency IARPA (Intelligence Advanced Research Projects Activity), which promotes high-risk, high-pay-off research.

The neocortex is the most recently evolved brain region, and is of particular interest to

neuroscientists. As with other brain areas, its function is determined by how individual neurons are connected to each other through structures called synapses. These structures, which can be seen only with an electron microscope, allow chemical or electrical signals to pass between cells and can be pruned or created anew as an animal attunes itself to its environment.



Individual cell parts are visible in this 3D map of a tiny piece of mouse brain.

Reconstructing this level of detail required a multistep procedure. A diamond blade shaved a region of mouse neocortex called the somatosensory cortex into several thousand slices, which were continuously rolled onto a single long strip of special plastic tape at a rate of 1,000 sections every 24 hours. The sections were then imaged with a scanning electron microscope powerful enough to capture even the tiny vesicles that contain the chemical signalling molecules in synapses, known as neurotransmitters.

To reconstruct the scrap of tissue, the team homed in at the highest resolution around the finger-like dendrites of two neighbouring neurons. The researchers aligned the relevant digital images so that the parts of each cell in each

slice coincided with their positions on adjacent slices. To follow the individual cells through the different slices, they developed computer programs to assign a particular colour to every cell and to trace each one, either automatically or with input from researchers.

The volume of tissue used was too small to contain an entire cell, but large enough to contain fragments of more than 1,600 neurons and of other brain cells of at least six different types, as well as around 1,700 synapses.

One feature revealed by this reconstruction, which is now freely available to the scientific community, was that one neuron does not form synapses with another neuron just because the two happen to be physically close to each other, as some neuroscientists had assumed. Instead, the cells have clear preferences for particular neighbours. This had already been observed in the retina and in the hippocampus, both of which are evolutionarily older than the neocortex. The answer to what confers these preferences may be found in ongoing studies

to identify the molecular components of each synapse, says neuroscientist Seth Grant at the University of Edinburgh, UK.

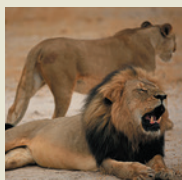
The Lichtman team is now working on similarly sized reconstructions of the cortical tissue from six-day-old mice, to see whether synapses behave the same way in an earlier stage of development, and on reconstructing a piece of human brain acquired during surgery.

As well as improving our understanding of the brain, such reconstructions could inspire new methods of computing. The consortium that is currently negotiating with IARPA is based at Harvard and at the Massachusetts Institute of Technology (MIT) in Cambridge and consists of 13 labs. Under the preliminary contract, the consortium would be part of IARPA's Machine Intelligence from Cortical Networks (MICrONS) programme and would receive tens of millions of dollars over five years, says MICrONS head Jacob Vogelstein. The general goal of the programme, he says, "is to revolutionize machine learning by reverse-engineering from codes discovered in the brain". He adds: "IARPA also invests in neuroscience because we are interested as well in understanding cognition — how people behave and make decisions." ■



**MORE
ONLINE**

Q&A



Charismatic lion's death highlights struggles of conservationists
go.nature.com/dwlz6h

MORE NEWS

- Philae's comet discoveries create series of conundrums
go.nature.com/aq3roz
- Four-legged snake fossil sparks legal investigation
go.nature.com/3r6ldh
- Earth's ancient magnetic field just got a lot older
go.nature.com/sqjlso

NATURE PODCAST



Ending Ebola; the biology of ancient organisms; and scientists and the nuclear bomb
nature.com/nature/podcast

MATERIALS SCIENCE

Stanene makes its debut

Graphene's tin cousin may conduct without heat loss.

BY CHRIS CESARE

Two years after physicists predicted that tin should be able to form a mesh just one atom thick, researchers report that they have made it¹. The thin film is called stanene (from the Latin *stannum* meaning tin, which also gives the element its chemical symbol, Sn) and is the latest cousin of graphene, the honeycomb lattice of carbon atoms that has spurred thousands of studies into related 2D materials (see *Nature* **522**, 274–276; 2015).

In theory, stanene has a talent that graphene does not: at room temperature, electrons should be able to travel along the edges of the tin mesh without colliding with other electrons and atoms as they do in most materials. This makes the film what physicists call a topological insulator, and means that it should be able to conduct electricity without losing energy as waste heat, according to predictions² made in 2013 by Shou-Cheng Zhang, a physicist at Stanford University in California, who is a co-author of the latest study.

A thin film of stanene might be the perfect highway along which to ferry current in electric circuits, says Peide Ye, a physicist and electrical engineer at Purdue University in West Lafayette, Indiana. “I’m always looking for something not only scientifically interesting but that has potential for applications in a device,” he says. “It’s very interesting work.”

But Zhang and his colleagues at four universities in China cannot yet confirm stanene’s predicted exotic properties. They created the mesh by vaporizing tin in a vacuum and allowing the atoms to waft onto a supporting surface made of bismuth telluride. Although this surface allows 2D stanene crystals to form, it also interacts with them, creating the wrong conditions for a topological insulator, says Zhang. He has already co-authored another paper³ examining which surfaces would work better. ■

1. Zhu, F. F. *et al.* *Nature Mater.* <http://dx.doi.org/10.1038/nmat4384> (2015).

2. Xu, Y. *et al.* *Phys. Rev. Lett.* **111**, 136804 (2013).

3. Xu, Y., Tang, P. & Zhang, S.-C. Preprint at <http://arxiv.org/abs/1507.00419> (2015).



Marine snails from the US West Coast show signs of shell weakening as a result of ocean acidification.

OCEAN ACIDIFICATION

Seawater studies come up short

Experiments fail to predict size of acidification's impact.

BY DANIEL CRESSEY

As the oceans’ chemistry is altered by rising levels of atmospheric carbon dioxide, the response of sea-dwellers such as fish, shellfish and corals is a huge unknown that has implications for fisheries and conservationists alike. But the researchers attempting to find an answer are often failing to properly design and report their experiments, according to an analysis of two decades of literature.

Oceans absorb much of the CO₂ emitted by human activities such as coal burning. This leads to a variety of chemical changes, such as making waters more acidic, which are referred to as ocean acidification.

The United Nations has warned that ocean acidification could cost the global economy US\$1 trillion per year by the end of the century, owing to losses in industries such as fisheries and tourism. Oyster fisheries in the United States are estimated to have already lost millions of dollars as a result of poor harvests, which can be partly blamed on ocean acidification.

The past decade has seen accelerated attempts to predict what these changes in pH will mean for the oceans’ denizens — in particular, through experiments that place organisms in water tanks that mimic future ocean-chemistry scenarios.

Yet according to a survey published last month by marine scientist Christopher Cornwall, who studies ocean acidification at the University of Western Australia in Crawley, and ecologist Catriona Hurd of the University of Tasmania in Hobart, Australia, most reports of such laboratory experiments either used inappropriate methods or did not report their methods properly (C. E. Cornwall and C. L. Hurd *ICES J. Mar. Sci.* <http://dx.doi.org/10.1093/icesjms/fsv118>; 2015).

Cornwall says that the “overwhelming evidence” from such studies of the negative effects of ocean acidification still stands. For example, more-acidic waters slow the growth and worsen the health of many species that build structures such as shells from calcium carbonate. But the pair’s discovery that many of the experiments are problematic makes it difficult

to assess accurately the magnitude of effects of ocean acidification, and to combine results from individual experiments to build overall predictions for how the ecosystem as a whole will behave, he says.

The survey, published in the journal *ICES Journal of Marine Science*, was based on a search of the Scopus database of research papers. Cornwall and Hurd analysed 465 studies published between 1993 and 2014 that manipulated seawater chemistry and found that experiments often failed to implement widely accepted measures to ensure quality.

For instance, to ensure robustness, manipulation studies should use multiple arrays of independent ocean-mimicking tanks. And in experiments that compare sea animals under acidified conditions with controls, these tanks should be randomized to remove bias. But the pair found that in several papers, researchers used one main seawater tank to supply multiple, supposedly independent smaller tanks.

CHEMICAL ERRORS

The researchers also found mistakes in basic chemistry: some authors simply added acid to a tank and ignored other chemical changes that result from the absorption of CO₂, such as increased levels of carbonates. Although the frequency of these chemistry errors has dropped since the 2010 publication of an international

'best practice' guide for ocean-acidification experiments (see go.nature.com/sp5kgn), the researchers found no evidence for improvements in the design of tank arrays.

Bayden Russell, an ocean-acidification researcher at the University of Hong Kong who reviewed drafts of the latest paper, has also noticed that some researchers fail to take into account the complexities of ocean acidifica-

"Truly rigorous designs are logistically complex and expensive."

tion when designing their experiments. "It is these complexities that will drive ecosystem responses to ocean acidification," he says.

Overall, Cornwall and Hurd found that in only 27 cases could they be certain that an appropriate experimental design had been used, and in 278 cases, the design was clearly inappropriate. The remaining studies had insufficient detail on experimental set-up — a problem in itself, note the researchers.

The pair present a series of recommendations for well-designed experiments and suggest a checklist of details that should be included in papers to allow replication of experiments, including which chemicals were used to manipulate the seawater chemistry and the configuration of tank arrays.

Ove Hoegh-Guldberg, director of the

Global Change Institute at the University of Queensland in St Lucia, Australia, suggests that researchers also need to take account of natural variations in temperature and CO₂ in experimental set-ups and ensure that experiments that manipulate acidity also simulate the accompanying rise in temperature from global warming, which many do not.

PRESSURE TO PUBLISH

Russell thinks that most research groups are now trying to use appropriate designs, but says that there are still problems, which he attributes to a variety of factors. "Unfortunately, truly rigorous designs are logistically complex and expensive in both set-up costs and ongoing maintenance time," he says. "When superimposed on the increasing pressure to publish rapidly, and in top journals, some researchers or research groups are still attempting to publish what I would consider sub-standard research."

Jonathan Havenhand, who works on marine invertebrates at the University of Gothenburg in Sweden and who co-authored the 2010 guide, welcomes the latest paper: "Everybody should know the stuff that's in Cornwall and Hurd's paper. It's good that they wrote it. It's disappointing that they had to."

Havenhand suspects the paper will be highly cited. "Whether people are going to be happy to be citing it, I don't know." ■



SLOW CHEMISTRY

BY XIAOZHI LIM

Slow, solid-state reactions used by lichens and Renaissance pigment-makers could help to make chemistry greener.

Cristina Mottillo is in no rush. She pours finely ground white powder into a Petri dish, carefully rolls it flat with the side of a small glass vial, then seals it into a chamber where the heat and humidity are like those on a sweltering summer day in the tropics. “Now,” she says, “we wait.”

Over the next four days, with no further effort from Mottillo, the three chemicals in that powder will gradually turn into ZIF-8: a stable, porous compound called a metal-organic framework that could find widespread use in carbon capture and storage, and that is worth more than 100 times the raw materials’ original value. “The reactants do all the work,” says Mottillo, a chemistry PhD student at McGill University in Montreal, Canada.

This is a radical departure from standard chemical-synthesis methods, which typically involve dissolving, heating and stirring ingredients in a solution to encourage them to react quickly. These techniques are fast and well understood, but they tend to consume large amounts of chemicals

and energy, and pose a major environmental challenge. An estimated 50–80% of all chemical waste produced by industry and university labs consists of solvents left over from synthesis, separation and purification.

For around two decades, a worldwide ‘green chemistry’ movement has been trying to find ways to minimize these toxic waste streams. But Mottillo is one of a handful of scientists starting to adopt an approach that is radical even by the movement’s standards. Her PhD supervisor, McGill chemist Tomislav Friščić, describes it as “lazy man’s chemistry”: let a mix of solid reactants sit around undisturbed while they spontaneously transform themselves. More properly called slow chemistry, or even just ageing, the approach requires few, if any, hazardous solvents and uses minimal energy. If planned properly, it also consumes all the reagents in the mix, so that there is no waste and no need for chemical-intensive purification.

Such processes have been known for millennia: rusting iron is a familiar example, as is the decades-long weathering process that produced the Statue of Liberty’s green patina. But only now are scientists starting to understand these processes and learn how to control them to obtain the products they want. In the past decade, research groups have used such techniques to produce valuable products, including organometallic complexes, pharmaceuticals, simple organic compounds and photoluminescent materials. Proponents such as Friščić are hoping to make many more.

“The ultimate goal,” he says, “is really to clean up the chemical manufacturing industry.”

SLOW AND STEADY

That could take a while: even the most ardent advocates agree that ageing faces an uphill struggle for credibility. Students are taught that good chemistry frequently starts with the right solvent: molecules in solution can react much faster than they otherwise would, because they are free to tumble and collide with one another, which facilitates the

Lichens make acids that react with solid rock in processes that chemists are trying to mimic.

FRANS LANTING/ROBERT HARDING PICTURE LIBRARY

SOURCES: 1 DAY: J. TIAN ET AL. *J. AM. CHEM. SOC.* **133**, 1399–1404 (2011); D. BRAGA ET AL. *CRYSTENGCOMM* **9**, 879–881 (2007); 4 DAYS: REF. 2; 1 WEEK: REF. 3; 1 MONTH: L. L. LI ET AL. *ARCH. PHARM. RES.* **31**, 381–389 (2008); 1 YEAR: M. R. LEE & I. PARSONS *CHEM. GEOL.* **161**, 385–397 (1999)

making and breaking of bonds. But slow chemistry happens in solids, where, by definition, everything is held rigidly in place. “People tend to think of a stone as a grave for molecules,” says Dario Braga, a solid-state chemist at the University of Bologna, Italy.

But that is not true. Solid-state reactions can take months or years, but they do exist in nature. In Western Australia, deposits of bird guano reacting with copper sulfide minerals in rocks have formed moolooite: an uncommon green copper oxalate mineral. Lichens living on rock often secrete a mixture of simple, weak organic acids that slowly react with minerals to produce complex metal–organic materials, which give the lichens some protection from invasive microorganisms.

Well into the nineteenth century, ageing was used to produce lead white, a pigment that is among the most widely used in art history. Manufacturers placed rolled-up sheets of lead over buckets containing a small amount of vinegar, and then left the buckets on a bed of manure in a shed. The metal would slowly react with water vapour in the air and carbon dioxide from the manure, turning into a white material now known to be a mixture of lead carbonate and lead hydroxide. The vinegar acted as a catalyst, and the decomposing manure kept the shed warm enough for the process to proceed at a reasonable rate. After about three months, the pigment was scraped off, washed and ground into a fine powder. It was used in paintings such as Leonardo da Vinci’s *Mona Lisa* (around 1506) and Johannes Vermeer’s *Girl with a Pearl Earring* (1665).

But the recent surge in slow chemistry has nothing to do with art. One factor has been interest from the pharmaceutical industry, which would like better control over the ageing processes that can slowly degrade drugs in pill form (see ‘Slow, slower, slowest’). Another is that solid-state chemistry is no longer the mystery it once was. Reactions in solids tend to be much more complex than those in liquids, where molecules quickly diffuse into a uniform mixture. Solids are often poorly mixed agglomerations of very different particles, and are riven with cracks and other structural defects, where chemical reactions can take place in different ways and at different rates. But rapid improvements in imaging techniques such as X-ray crystallography, nuclear magnetic resonance scanning and electron microscopy are now giving chemists a better understanding of how those reactions proceed in real time, and what they eventually produce.

Such insights, in turn, have helped proponents to streamline and improve on natural ageing processes, while countering the perception that ageing is too slow and unpredictable to be of practical use. “It’s not slow if you plan in advance,” insists Friščić, whose group is trying to better understand and exploit ageing reactions. Mottillo’s experiments in the green synthesis of metal–organic frameworks, for example, are an attempt to accelerate the chemistry between minerals and lichen acids.

PRACTICAL MAGIC

Another student in Friščić’s group has used a different ageing process to synthesize various metal–organic materials from oxides of main-group metals, transition metals and lanthanides — solids that tend to have very high melting points and low solubility. The researchers found that each metal oxide ages at a different speed¹, so they have patented this as a way to isolate the metals from one another: the ageing products are less dense than the oxides, so they will float in an intermediate-density liquid while the remaining oxides sink. Metal oxides, says Friščić, are ideal reagents because they are cheap, safe, widely available and produce only water as a by-product. Other metal salts, such as chlorides or nitrates, produce acids that end up as toxic waste. Furthermore, many metals occur naturally as oxides that have to be leached from ore with strong acids; with ageing, says Friščić, one could bypass that step, and make valuable metal–organic frameworks directly from rocks. He and his team are working on scaling this process up to bring it to the metal extraction and separation industry.

As for speed, says Friščić, “we can get reactivity going if we use a few tricks” — most of them quite straightforward. One is to put the samples in a humid atmosphere: water vapour can migrate through holes in the solid structures, acting as a lubricant to help atoms or molecules inside the solid to diffuse, react or even rearrange into new structures.

Another technique is to increase the temperature to, say, 45 °C — a far

SLOW, SLOWER, SLOWEST

Ageing reactions happen on a wide range of timescales.

1 DAY

- The antibiotic clarithromycin changes phase in carbon dioxide.
- Synthesis of milligrams of small, iron-based organometallic compounds.

4 DAYS

- Synthesis of 10 grams of zinc- or cobalt-based metal–organic frameworks.

1 WEEK

- Synthesis of milligrams of copper-based luminescent polymer.

1 MONTH

- Aspirin degrades at 60 °C and 90% humidity.

3 MONTHS

- Lead-white pigment produced from lead.

1 YEAR

- Lichen acids etch rock to a depth of 0.3–30 micrometres.

20 YEARS

- Green patina covers the Statue of Liberty as a result of an oxidation reaction between copper, oxygen and water vapour.

cry from the hundreds of degrees typical of industrial reaction vessels, but enough to make the ageing process run faster. “If we were living in India, we could potentially do it outside,” says Mottillo. And a third trick is to do what the lichens cannot, and grind the reactants together into a fine, homogeneous mixture to increase the surface area of the particles, where they touch each other and can react. That is how Mottillo was able to complete her ZIF-8 synthesis in days instead of weeks².

Braga and his group have used ageing, or vapour digestion as they call it, to make a variety of materials by exposing solid reactants in a vial to solvent vapour. For example, by letting solid copper(I) iodide sit with an organic compound for about a week in water, acetonitrile or toluene vapour, they obtained three new copper-based polymers that glow after exposure to ultraviolet light³. Such compounds could be used in light-emitting diodes and screen displays. But even more important, says Braga, is that copper(I) iodide is notoriously difficult to dissolve in common solvents; vapour digestion offers a way to make it and other insoluble materials more accessible to chemistry.

Braga and Friščić are still not sure exactly what is happening in these reactions. But Dominik Cinić, an assistant professor at the University of Zagreb, is applying their method to organic synthesis, a branch of chemistry that conventionally relies on energy- and chemical-intensive methods. Cinić’s group has demonstrated⁴ that vapour digestion can be used to synthesize Schiff bases, small organic molecules containing a carbon–nitrogen double bond. The team’s next goal is to use the method in a one-step synthesis of amines: nitrogen-containing organic compounds that are used in many dyes and drugs, and that typically require two or three synthesis steps.

Everyone working on ageing-based synthesis concedes that there is a long way to go. The mechanisms are not yet well understood and there are no good computational models to

speed up research. Furthermore, sceptics doubt that the chemical industry can ever do without solvents entirely. Walter Leitner, a green chemist at RWTH Aachen University in Germany, points out that ageing research has had the most success in inorganic synthesis — which has historically had a much smaller environmental impact than organic synthesis, where the most solvents are used. In organic synthesis, he says, the most practical target a green chemist can aim for is to find ways to replace toxic solvents with environmentally benign ones such as water.

Still, such objections have not discouraged Friščić. “Everything you can do in solution, you can do with ageing, and more,” he declares. At the moment, he is exploring the mechanisms behind ageing by monitoring reactions as they happen.

“All that one needs to do,” he says, “is to explore.” ■

XiaoZhi Lim is a freelance writer in Singapore.

1. Qi, F., Stein, R. S. & Friščić, T. *Green Chem.* **16**, 121–132 (2014).
2. Mottillo, C. et al. *Green Chem.* **15**, 2121–2131 (2013).
3. Braga, D., Grepioni, F., Maini, L., Mazzeo, P. P. & Ventura, B. *New J. Chem.* **35**, 339–344 (2011).
4. Cinić, D., Brekalo, I. & Kaitner, B. *Green Chem.* **48**, 11683–11685 (2012).



THE NEXT TIME

THE WORLD IS ILL-PREPARED FOR THE NEXT EPIDEMIC OR PANDEMIC. BUT THE HORROR OF THE EBOLA OUTBREAK IN WEST AFRICA MAY DRIVE CHANGE.

By Declan Butler

If there was one point last year when public-health experts held their breath, it was when a Liberian man infected with Ebola virus flew to Lagos, Nigeria, in July. Ebola was already raging uncontrolled through impoverished countries in West Africa, killing half of those it infected. Now a vomiting man had carried it straight to the heart of Africa's largest megacity — with 21 million inhabitants, many of whom live in slums. Experts were horrified at the prospect that the virus might rip through the city — and then, because Lagos is an international travel hub, spread farther afield.

"The last thing anyone in the world wants to hear is the two words, 'Ebola' and 'Lagos' in the same sentence," said Jeffrey Hawkins, the US consul general in Nigeria, at the time.

In the end, this apocalyptic scenario did not play out. Because Nigeria is a focus of global efforts to eradicate polio, it has a decent infrastructure of virology labs and epidemiologists and the capacity to run large public-awareness campaigns. Authorities quickly repurposed this toolbox to tackle Ebola, and the outbreak was contained with just 20 cases in all. The number of infections from Ebola in Guinea, Liberia, and Sierra Leone has dropped from its peak of hundreds of cases per week, to 20 or 30. But what has not faded is the fear that, at some point in the future, the world will face an outbreak of a deadly disease that spreads much more easily between people than Ebola does, and so results in an epidemic or pandemic that is even more terrible than that in West Africa.

Quite what that disease will be, no one knows. One worst-case scenario is that of an influenza virus as deadly as the one behind the 1918 pandemic, which raced across the world killing as many as 50 million people. Other virus families also keep researchers awake. Poxviruses are one: smallpox was eradicated in 1980 after killing some 300 million people in the twentieth century, but there are many animal poxviruses that could evolve to replace it. Paramyxoviruses are another major worry: the family includes Nipah virus and Hendra virus, both of which have triggered small outbreaks that caused serious illness and death. But uncertainty prevails. "Second on the list is the one we haven't thought of, and at the very top is the one we can't imagine," says infectious-disease specialist David Morens at the US National Institute of Allergy and Infectious Diseases in Bethesda, Maryland.

The Ebola epidemic has spurred researchers and public-health experts to call for a major overhaul of the world's approach to epidemic threats. What's needed, they argue, is better monitoring for the emergence and re-emergence of pathogens, and beefed-up health systems in the many poor countries that are often on the frontline of epidemics. They want to see nimble task forces that are able to respond rapidly and forcefully to outbreaks, and a multibillion-dollar global fund to quickly develop countermeasures such as drugs and vaccines.

At the same time, the risks need to be kept in perspective, say researchers. History shows that new pathogens that pose a large epidemic threat are "very rare," says Adrian Hill, a specialist in infectious diseases and director of the Jenner Institute in Oxford, UK. So are those that quickly kill many of those infected — the type that film plots thrive on. Many emerging epidemics, such as that of multidrug-resistant tuberculosis, move more slowly, yet cumulatively can kill many more people than the acute outbreaks that attract most of the media and political attention. But when they happen, large, acute epidemics can cause devastating loss of life and major economic damage, and the panic and chaos they generate can do more harm than the pathogen itself. The Ebola epidemic is not over, and there are concerns it could spike again.

"Ebola has been a wake-up call, not just for Africa, but for the world," said Margaret Chan, director-general of the World Health Organization (WHO) in March. "The world must never again find itself in such a position."

The greatest new epidemic threats are unknown pathogens that spread easily — for example, through the air — and to which humans have little or no immunity. The world's last brush with anything coming close was in late 2002, when the virus causing severe acute respiratory syndrome (SARS) caused an outbreak in humans in Guangdong province, China, then quickly fanned out into 29 countries — infecting at least 8,098 people and killing 774 of them — before a massive international response brought it under control. If that virus had spread just a bit more easily, it might have killed many more. "SARS probably came close to becoming an out-of-control pandemic," says Morens. "I think of SARS as one of our scariest close calls."

HOW TO DETECT THREATS

Like SARS, which is thought to have originated in bats, most future infectious diseases will come from animals; some three-quarters of new human diseases have emerged this way. Scientists suspect that the current Ebola outbreak originated when the virus passed from fruit bats to a

"SARS PROBABLY CAME CLOSE TO BECOMING AN OUT-OF-CONTROL PANDEMIC. I THINK OF SARS AS ONE OF OUR SCARIEST CLOSE CALLS."

two-year-old boy playing in a forested region of southern Guinea; Middle East respiratory syndrome (MERS), a viral disease that emerged in 2012, is probably transmitted by camels. And just last month, researchers reported that three squirrel breeders in Germany who had died of encephalitis were killed by a novel bornavirus that had been carried by the animals.

In theory, this knowledge could help the world to prepare. Scientists could carefully monitor viruses in animal populations and in people living nearby to identify potential threats, such as any that show some ability to cross the species barrier. Such basic research might allow scientists to get a head start on developing vaccines and drugs. But the science of predicting such threats is in its infancy. Scientists know little about what allows an animal pathogen to infect humans or to then spread between them, processes that depend on many factors, including its ability to enter human cells and replicate there. "Of all our gaps in knowledge, the worst gap is how little we know about the mechanisms of emergence," says Morens.

To make matters worse, the vast majority of infectious-disease research and surveillance is in developed countries, but most emerging and re-emerging diseases are in the developing world. "We need to be where the diseases are, and where they are likely to emerge, studying them at their source, not sitting in labs in US science buildings," says Morens, who is currently working on Ebola in Guinea.

Robert Garry, a virologist at Tulane University in New Orleans, Louisiana, is working with African scientists in an international project — the African Center of Excellence for Genomics of Infectious Diseases, based at Redeemer's University in Redemption City, Nigeria. The project, which began in May last year, is taking blood samples from villagers in the region who have fevers, and using next-generation genetic sequencing of the samples to discover new pathogens, as well as developing diagnostics for both new and known ones. Supported by the US National Institutes of Health and the World Bank, it has an initial four-year budget of around US\$8 million.

Researchers do have some clues to guide their search for threats. They know that factors such as geography, climate and culture can help to identify hotspots of disease emergence, with most at lower latitudes. And it is clear that a major driver is contact between animals and humans. The EcoHealth Alliance, an international network of scientists centred in New York City, and the US Agency for International Development's Emerging Pandemic Threats programme are carrying out viral sampling

Graves dug in
Freetown, Sierra
Leone, to cope with
those dying from Ebola
in late 2014.

from animals and people in hotspots across the world, and trying to tease out how farming, trade, deforestation and hunting and consumption of bushmeat influence the emergence of diseases.

Such projects have led to the discovery of hundreds of viruses including arenaviruses, phleboviruses, coronaviruses and rhabdoviruses — and are likely to yield many more in the future, says Garry. But even when researchers do find new viruses, it is difficult to say which of them might pose a major threat. Few people would have anticipated that HIV/AIDS, the world's largest recent pandemic, would be caused by a retrovirus, part of a viral family that had not previously been associated with major infectious disease, Garry says (see 'Emerging threats').

Some hints can be found by examining the affinity of viruses for receptors on human cells and assessing how well they spread between animals in the lab. These approaches are perhaps most advanced for flu viruses, which cause pandemics every few decades, of varying severity. Researchers around the world try to rank the potential pandemic risk of flu viruses using a battery of criteria, including the pathogens' ability to infect or transmit between ferrets, whether they can bind to human receptors, and to what extent the human population has immunity. This information is used to prioritize the development of vaccines against those that seem more threatening. But it cannot predict which flu viruses might go pandemic.

Researchers know that more could and should be done. One of the most important tasks is to establish local medical and research systems that can quickly analyse what is going on when a cluster of people suddenly comes down with serious disease. Such systems, which are often underdeveloped in poorer countries, require a trained local workforce of microbiologists, epidemiologists and clinical scientists, and diagnostics laboratories capable of testing clinical samples for a wide range of diseases. These could be implemented in a low-income country for as little as \$12 million annually, according to Jeremy Farrar, director of the UK biomedical charity the Wellcome Trust, who helped to establish such a system in Vietnam.

But right now, surveillance systems are just as limited as scientists' knowledge of emerging threats. So the current reality is that we will probably be alerted to the next human epidemic or pandemic only once it is well under way.

HOW TO RESPOND

At that point, the world must respond — fast. For Ebola, it did not. The initial outbreaks occurred in December 2013, but Ebola was only identified as the cause at the end of March 2014, by which point the outbreak had already spread. Early alarms by the humanitarian organization Médecins Sans Frontières (MSF; also known as Doctors Without Borders) were ignored, and the international response did not kick into high

gear until September (see *Nature* **513**, 469; 2014). "Ebola spun out of control because of a lack of political leadership, will and accountability — not because of insufficient funding, early-warning systems, coordination or medical technologies," Joanne Liu, international president of MSF, told a gathering of health leaders in May.

This was not how it was meant to be. In 2005, all 196 countries adopted a set of laws called the International Health Regulations, which were designed to improve the response to disease outbreaks. The regulations — effectively the world's emergency action plan — were spurred by the SARS epidemic, and by outbreaks of H5N1 avian flu virus.

But Ebola revealed how weak the regulations are. They mostly tasked individual countries with dealing with outbreaks — setting targets for them to reinforce their capacities for disease surveillance and response by 2012 — but did not include support to help the poorest countries reach those goals. This weakness has long been recognized, but not acted on — an "elephant in the emergency room," says David Fidler, a specialist in international and national security law at Indiana University Bloomington. Ten years after the treaty was adopted, two-thirds of its signatories have yet to meet the targets.

The regulations also failed to create an international rapid-response group to deal with a major outbreak. The WHO has never had outbreak-response teams on the scale needed to deal with an epidemic as large as Ebola, says Fidler, and what capacity it had has been slashed by budget and staff cuts. "What we are seeing in the Ebola crisis is the lack of a global public-health expeditionary capability that can handle something on a country or regional scale," he says.

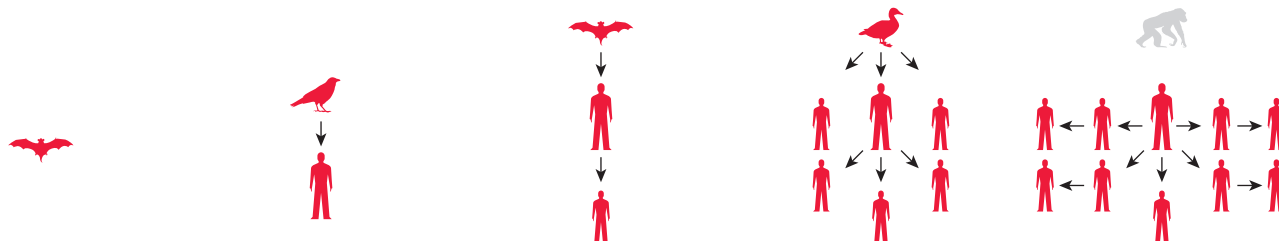
Governments and international organizations are now considering a raft of proposals to prevent the next serious outbreak from growing into an epidemic. These include boosting financial support for surveillance and outbreak response in low- and middle-income countries, and reform of the WHO, which has come under fire for its slow response to Ebola. One idea is to create a Centre for Emergency Preparedness and Response within the WHO but autonomous from it to avoid the agency's notorious politicization and bureaucracy. The body would link to other United Nations' agencies, the World Bank, philanthropic organizations, non-governmental organizations and industry. It would create an international reserve force that could be rapidly deployed to an outbreak, and be able to call up the planes and helicopters often needed to quickly ship large amounts of medical equipment to regions in need.

The World Bank, the WHO and other organizations are also working on the idea of a Pandemic Emergency Facility that could swiftly send contingency funds to cover the efforts of the WHO, governments and other bodies in the event of a serious outbreak.

The question now is whether these grand plans will become a reality. Many people hoped that these and other measures to reinforce outbreak

EMERGING THREATS

The size and severity of disease outbreaks depends on where the causal agent sits in an evolutionary spectrum, ranging from animal viruses that have yet to leap to humans, to pathogens that have evolved to spread easily between humans.



1. Animals only
Potential threats, including pathogens from families that have caused human disease in the past.

Examples:
poxviruses, paramyxoviruses.

2. Limited spread
Pathogens that pass from animals to humans but do not spread further.

Examples:
H5N1 flu, Nipah, rabies.

3. Small outbreaks
Pathogens that spill over and then spread between just a few people.

Examples:
MERS, Marburg.

4. Large outbreaks and epidemics
Pathogens that spill over into large numbers of people, or spread between many people.

Examples:
Chagas disease, cholera, Ebola.

5. Human only
Animal pathogens that have evolved to become human viruses.

Examples:
HIV/AIDS, measles, tuberculosis.



Public-health experts fear a repeat of the 1918 flu pandemic which killed as many as 50 million people.

NATIONAL MUSEUM OF HEALTH AND MEDICINE/SPL

preparedness and response would receive firm pledges at the June summit of G7 industrialized countries in Germany. But although the summit produced supportive language, it did not make concrete decisions, something that disappoints Manica Balasegaram, executive director of MSF's Access Campaign in Geneva, Switzerland. "We need money put on the table, we need political commitment and funding," he says.

But Farrar says that the high-level political attention is a good sign. He notes that the G7 has previously delivered on major public-health initiatives, such as helping to create the multibillion-dollar Global Fund to Fight AIDS, Tuberculosis and Malaria in 2002, two years after it was first proposed. What emerged from the G7 this year "has to be seen as setting a tone and a direction," Farrar says. "What's key is what then comes out of the language."

HOW TO GET VACCINES AND DRUGS

Even if the world reacts quickly to an emerging outbreak, it has to have effective tools to deploy. A vaccine could have stopped Ebola in its tracks, but the only ones available had not been tested in humans. Drugs, too, were stuck in the experimental phase. In this and other outbreaks, health-care workers often have to rely on centuries-old public-health measures, such as quarantine, chemical disinfection and encouraging hand washing — essential, but often not enough.

If a worst-case epidemic hit tomorrow, the script would probably be the same. The problem, say public-health officials, lies in how global drug and vaccine development is set up. The process is left largely to major pharmaceutical companies, which are geared towards treating those who can pay — developed-world inhabitants with mostly developed-world diseases — rather than to addressing the most pressing global health needs, which are often infectious diseases in the developing world. "What humanity actually needs isn't part of the equation," says Morens. "It's what can make big bucks."

That there were even candidate vaccines and drugs for Ebola was largely down to spending on biodefence rather than concerns about global health, says Balasegaram. And there are few, if any, effective drugs and vaccines for a host of other epidemic threats and neglected diseases ranging from SARS to dengue — leaving the world defenceless against almost all the pathogens most likely to cause the next epidemic.

After Ebola, "there is a real opportunity to change the status quo," says Jean-François Alesandrini, a spokesman for the Drugs for Neglected Diseases Initiative (DNDi), a non-profit body working on long-ignored diseases such as leishmaniasis.

In a paper published in May, leading researchers and public-health officials proposed the creation of an international not-for-profit pharmaceutical body, bringing together research organizations,

► NATURE.COM
For Nature's special on Ebola, see:
nature.com/ebola

supportive of the proposal — which is crucial, because such ventures typically need access to the vast drug libraries, vaccine-technology platforms and manufacturing capacity that only industry possesses.

Within such a scheme, Hill favours the immediate and accelerated development of vaccines against priority threats such as MERS and Marburg — a virus from the same family as Ebola that kills most of those it infects. He suggests foregoing the slow, costly animal studies that require high biosafety and biosecurity labs to contain the viruses, and instead developing small batches of vaccine that could be put directly through phase I safety and dosage testing in humans. If the vaccines were safe, and generated a good immune response, it is likely they would work, he says. Stockpiles could then be created, ready for phase II efficacy trials to start as soon as an outbreak occurs — so that it "can be nipped in the bud", Hill says. Researchers are encouraged by the announcement this week that a clinical trial of an Ebola vaccine has had positive results (see page 13).

But that still leaves the unknown pathogens, which are harder to prepare for. One option in such an outbreak would be to transfuse patients with the plasma of survivors, whose blood is often rich in antibodies specific to the virus, says Ian Lipkin, a virologist and outbreak specialist at Columbia University in New York. In many cases, this technique could provide a quick, ready-made therapy to an unknown pathogen, bypassing the years of research it can take to find drugs or vaccines.

The approach gained prominence during the Ebola outbreak: clinical trials of 'convalescent plasma' for Ebola began in West Africa in December (see *Nature* <http://doi.org/6dr>; 2014), and results are expected in coming months (*Nature* **517**, 9–10; 2015). Lipkin would like to see the infrastructure for collecting and processing blood and plasma improved in poorer countries, where it is often lacking.

Ideally, say researchers, clinical-trial designs would also be approved by regulators before an outbreak so that a trial could launch straight away (see page 29). This is already being done by researchers in the International Severe Acute Respiratory and Emerging Infection Consortium, an international network of outbreak specialists based in Oxford that aims to develop generic clinical-trial protocols that can be adapted to any epidemic threat.

Reforming the world's epidemic response systems is not going to be easy, and public-health specialists are well aware that impetus might be lost as the Ebola epidemic fades from the limelight. But they also think that the shocking events in West Africa — bodies on the streets, nationwide quarantines, economies collapsing — have left an indelible mark.

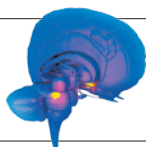
The West African epidemic has been a "game-changer" in how the world prepares for a serious epidemic, says Morens. The era after Ebola, he hopes, will be very different from the one before it. ■

Declan Butler is a senior reporter for Nature in France.

COMMENT

EPIDEMICS Have people and processes ready to do clinical trials in crises **p.29**

NEUROSCIENCE A haunting tour of the fringes of human experience **p.32**



PRODUCTIVITY Social values are distorted as scientists are driven harder **p.35**

OBITUARY David Raup, palaeobiology revolutionary, remembered **p.36**

MICHAEL DUFF/AP



People in Sierra Leone queue for food in March, during a country-wide lockdown intended to curb Ebola.

Finish the fight against Ebola

Leaders and health agencies are talking about ‘lessons learned’ from West Africa’s Ebola epidemic. But a major push is needed to end the outbreak, urges **Joanne Liu**.

Numbers of cases refusing to diminish, new communities being infected, bodies buried in secret. Sound familiar? It should. But these are not just scenes from last year’s Ebola epidemic. They are playing out today in West Africa.

As head of Médecins Sans Frontières (MSF; also known as Doctors Without Borders), which has treated one-third of reported Ebola cases in the outbreak, I have witnessed how a lack of political will undermined the response in the early days of the epidemic. Now, fatigue and a waning focus are threatening the final push to end it.

In the past few months, a stream of inter-governmental panels has been convened to appraise the international response to the epidemic — by the World Health Organization (WHO), the World Bank and the

G7 industrialized nations, among others. Meanwhile, an ever-growing list of philanthropic and academic institutions is preparing reports about ‘lessons learned’, to prevent future outbreaks. These include Harvard University in Cambridge, Massachusetts, and the Institute of Medicine, a US non-governmental organization (NGO).

Yet the Ebola epidemic in West Africa is far from under control. In the past three months alone, the number of cases — around 330 — is more than the third largest Ebola outbreak in history. Liberia, which was declared ‘Ebola-free’ in May, reported six cases by the end of June. And 20–27 cases have been confirmed across Guinea and Sierra Leone each week from mid-June

to mid-July. A large proportion of these cases cannot be traced back to the lists of people known to have been in contact with infected people. Over the past two months, cases have also emerged in Guinea’s Boke province, which borders Guinea-Bissau, a country with a weak health system and almost non-existent epidemiological surveillance and laboratory blood-testing capacity.

Equally concerning is that governments and aid agencies are still failing to earn the trust of some communities in their efforts to combat the epidemic, even though numerous experiences in the past 18 months have demonstrated just how crucial this is. On 29 May, for instance, the Red Cross was forced to withdraw workers from the north Guinea town of Kamsar in Boke after two Red Cross cars and an employee’s home were attacked, ►

► **NATURE.COM**
For Nature’s special
on Ebola, see:
nature.com/ebola

► and a warehouse containing equipment to enable safe burials was burnt down.

Albert Einstein defined insanity as doing the same thing over and over again, and expecting different results. As a global health community, we cannot talk about fighting future epidemics more effectively when we have failed to incorporate the lessons learned in this outbreak to bring it under control.

Getting to 'no new cases in at least 42 days' — twice the longest known incubation period for Ebola and the way in which the WHO defines the end of the epidemic — will require a major push. Ministries of health and aid agencies must do more to engage and empower communities in efforts to combat the disease, and to re-establish people's trust in government officials and health workers. The surveillance systems to locate and track new Ebola cases across Sierra Leone, Guinea and Liberia need to be properly supported — including in the districts that have not had an Ebola case for months. Governments, donors and NGOs must rebuild basic health-care infrastructure so that the countries affected can better deal with Ebola and the many other illnesses and conditions common to life in West Africa.

IN HINDSIGHT

In April 2014, near the start of the outbreak, MSF teams faced hostility in Guinea. There were cases of people in forest regions throwing rocks at ambulances. Such clashes have continued sporadically, involving our teams and those of other organizations.

These attacks were not a surprise. Such events had been seen in previous haemorrhagic-fever outbreaks and during the 2010 cholera outbreak in Haiti. In the Ebola epidemic, strangers showed up in villages in what looked like space suits and took away loved ones, with only around half being seen again. At the peak of the epidemic, people were often not told when their relatives had died or were not given the chance to bury their dead according to custom.

From these incidents, from our community teams, and from the success of other international aid organizations, such as the Red Cross, we have learned how important it is to have the support of community leaders, both elected and traditional. Community buy-in to access affected or at-risk villages and towns, and talking through the importance of safe burials with families, is crucial. Since autumn 2014, MSF teams have often carried out only one or two burials each day to allow enough time to explain to relatives of people who died from Ebola the importance of wearing protective clothing and disinfecting the body.

"There may be around 4,000 extra maternal deaths each year in the region."

ALL OR NOTHING

Six measures to end Ebola

Isolate and care for patients. Quarantine infected people and provide medical and psychosocial support for patients and their families.

Make burials safe. Disinfect corpses and ensure that people burying them wear protective clothing.

Engage communities. Work with communities to help them understand the nature of Ebola, how to protect themselves and how to stem transmission of the disease.

Support disease surveillance. Implement mechanisms to locate new cases easily, track probable transmission pathways, and identify sites that require disinfection.

Trace contacts. Monitor those who have had contact with infected people to ensure quick referral for care if they fall ill.

Re-establish health-care systems. Make medical care available for people with illnesses and conditions other than Ebola. [J.L.](#)

In the village of Téliélé in Guinea, from May to July 2014, MSF ran an Ebola treatment centre near where the village elders stayed during the day. This allowed villagers and relatives to see their loved ones and how they were being cared for. Other initiatives, such as building windows in treatment centres to allow people to interact with infected family members, were received positively.

The Liberian government similarly recognized the importance of engaging communities in a dialogue about Ebola. When the country was declared Ebola-free in early May, President Ellen Johnson Sirleaf acknowledged that the forced quarantine of West Point, an impoverished neighbourhood in the capital, Monrovia, may have done more damage than good by fuelling mistrust (in August 2014, tens of thousands of people in West Point were cordoned off for ten days without access to basic health care).

Yet patients and at-risk communities continue to be treated at best as victims and at worst as biohazards and disease vectors, rather than as central to bringing the epidemic under control. The government of Sierra Leone is still using coercive measures as the main tool to fight the outbreak. As soon as a case is confirmed, people who have been in contact with the patient are put in quarantine in their homes or in special facilities for 21 days. In Port Loko, quarantine has been imposed more forcefully, with security guards being stationed in front of the homes of people thought to be infected to prevent them or their families from leaving.

In Guinea, quarantines — known locally as *cerclage* (encirclement) — started in July in some villages in the Forecariah and Boke provinces. From late June to late July, 25% of the cases in Sierra Leone and Guinea were identified after those infected had died in their communities, suggesting that people are still not recognizing or reporting the disease, or seeking care in specialized centres.

In the ongoing effort to combat Ebola, more needs to be done to rewrite the public-health narrative. It must move from one that has been infused with fear to one that recognizes the hope for survival that supportive care can offer infected people.

RACE TO REBUILD

A major threat to bringing the current epidemic under control is the devastation to the public-health systems in all three countries (see 'Six measures to end Ebola'). The nations, with help from the international community, must re-establish basic health-care and public-health measures such as infection control, precautions for handling blood and other bodily fluids, as well as triage. (Triage involves setting up systems through which patients can be quickly tested for various diseases and assigned to isolation areas until a diagnosis has been made.)

The epidemic has left already-fragile health systems in tatters: at least 509 local health workers have died in the three affected countries, and routine vaccination programmes for diseases such as measles, rubella, tetanus and polio have all but ground to a halt in Sierra Leone and Guinea. Liberia restarted vaccinations efforts only in May.

From January to June, there were 850 measles cases in Liberia alone, and more than 500 children contracted whooping cough over a similar period. The reluctance of parents to bring their children to health facilities to receive the regular schedule of vaccinations has undermined immunization rates.

Malaria probably killed 10,900 more people in the three countries in 2014 than it would have done had the outbreak not happened, owing to the drop off in care¹. Efforts to reduce maternal mortality rates in the countries — which already have some of the highest in the world — have faced a tremendous setback. An evaluation by the World Bank estimates that the loss of health

DANIEL BEREHUJAK/GETTY

workers to Ebola will increase maternal mortality by 38% in Guinea, 74% in Sierra Leone and 111% in Liberia. In other words, there may be around 4,000 extra deaths each year in the region² if current levels of care continue.

Reinstating non-Ebola related health care, and re-establishing people's trust in it, is crucial to ending the epidemic — as well as to preventing a fresh wave of hardship for the people of West Africa. Without proper triage, people infected with Ebola may infect those who have a more treatable condition, such as malaria. Moreover, people with various diseases and conditions may avoid seeking care for fear of being infected with Ebola.

The departure in early July of French military medical teams from Guinea is worrying, as is the proposed withdrawal of Portuguese government teams supporting laboratory capacity in Guinea-Bissau. International efforts must be redoubled; United Nations agencies, foreign aid teams and NGOs should not yet pull out of West Africa.

Financial mechanisms being designed to combat future outbreaks, such as the World Bank's Pandemic Emergency Facility, should be deployed immediately to allow affected countries and neighbouring ones to bolster their epidemic response and preparedness. Neighbouring nations should be incentivized to do active surveillance without worrying about the potential economic impact of declaring cases. And if multilateral financial instruments are not ready, then developed economies such as the United States, Canada, the European Union and Japan, should fill the gaps. And preliminary results from a vaccine trial in Guinea, released on 31 July, are very promising³.

This year, I have been invited to participate in several expert panels focused on learning from this epidemic, to prevent history from repeating itself. Today, all the ingredients that enabled last year's devastation are still with us: rainy seasons, an uncoordinated response, fear and distrust. We need to push through the fatigue and complacency, and put everything we have learned into action to end this epidemic. We must finish the fight against Ebola. ■ **SEE NEWS FEATURE P.22**

Joanne Liu is international president of Médecins Sans Frontières in Geneva, Switzerland.

e-mail: joanne.liu@geneva.msf.org

1. Walker, P. G. T. *et al.* *Lancet Infect. Dis.* **15**, 825–832 (2015).
2. Evans, D. K., Goldstein, M. & Popova, A. *Lancet Glob. Health* **3**, e439–e440 (2015).
3. Henao-Restrepo, A. M. *et al.* *Lancet* [http://dx.doi.org/10.1016/0140-6736\(15\)61117-5](http://dx.doi.org/10.1016/0140-6736(15)61117-5) (2015).



Physicians in Liberia attend to a person ill with suspected Ebola.

Embed research in outbreak response

Testing Ebola treatments in West Africa's epidemic happened too late. Research response during future outbreaks must be more nimble, says **Trudie Lang**.

One year ago this month, the World Health Organization (WHO) declared the Ebola outbreak in West Africa a public-health emergency. A tremendous national and international response followed as it became clear that the epidemic would be on a scale never seen before with this disease.

As part of that response, in September 2014, my colleagues and I were funded to establish protocols for clinical trials to evaluate possible treatments. We are part of the Epidemic Disease Research Group Oxford and were

funded by the Wellcome Trust, a biomedical charity in London.

Within an unprecedented 12 weeks, we had protocols approved by ethics committees, drugs to hand, and staff trained and ready to begin trials at a treatment centre in Liberia. It was thanks to an extraordinary collaborative effort involving the University of Oxford, UK, the WHO, Médecins Sans Frontières (MSF; also known as Doctors Without Borders), researchers in West Africa and many others.

But another six weeks then passed before we could start giving the drug to patients, mostly because of bureaucratic and logistical barriers (see 'Timeline to a clinical trial'). ▶

➔ **NATURE.COM**
For Nature's special on Ebola, see: nature.com/ebola

► There is still no proven treatment for Ebola a year after the WHO announcement — in part because of the kinds of stumbling blocks we encountered. As the rate of new infections slowed, it became clear that there would not be enough patients to test our drug on, and we stopped the trial in February.

Government leaders must give the WHO the money and the support it needs to ensure that the world is 'research ready' for the next outbreak. A properly funded and empowered WHO could oversee the design and implementation of an on-call global task force of clinical-trial staff. It could also establish working groups to draw up template contracts so that agreements between the various players in a clinical trial can be signed off at speed. Most importantly, it could orchestrate outbreak research.

CLINICAL COMPLEXITY

It usually takes at least 18 months to set up a clinical trial. Myriad scientific, technical, regulatory and legal challenges must be resolved before any data can be collected¹. This is why there are no proven treatments for diseases such as Ebola — there had never been any clinical trials conducted during a disease outbreak^{2,3}. Yet by mid-November — just three months after the WHO declared the outbreak a public-health emergency — we were ready to start testing the effects of brincidofovir on patients in Liberia in a treatment centre run by MSF.

We achieved this in part by devising a clean and pragmatic protocol — it demanded no extra blood or other sampling over what would be carried out anyway as part of a patient's standard care (see 'Three successes').

Phase II and III trials, conducted since 2012 in the United States and involving about 1,000 people, had already shown that

brincidofovir could clear certain viral infections from children and adults without causing worrying side effects⁴⁻⁶. And we knew that it would anyway be difficult to distinguish side effects of the drug from symptoms of an Ebola infection. So we decided

"An international, neutral body needs to be put in charge of outbreak research."

to monitor only serious and unexpected side effects, and otherwise only verify whether patients were alive seven days after receiving the treatment (deaths from Ebola usually occur in the first few days after being admitted to a treatment centre.)

Once it had been confirmed that a person was infected, staff first needed to take the patient through the process of informed consent. They then gave enrolled patients the tablets and made observations; if the patient vomited after taking the drug, for instance, staff would need to give them a second dose.

Anything more complex, such as attempting to assess all the drug's possible side effects, would have meant monitoring several variables, from blood pressure to pain, in hundreds of patients. This would have increased both the risk of infection for the staff taking the measurements and the chance of introducing errors into the data.

Another factor that speeded things up was the astounding way that everyone on the ground came together. The research ethics committees that we worked with in both Liberia and Sierra Leone must have been flooded with requests from the research groups wanting to conduct trials. Yet we received detailed and high-quality reviews of our proposals within days of submitting them — a process that would normally have taken at least three months.

However, we encountered major stumbling blocks when dealing with the following four issues.

Difficulties in deploying African staff.

We knew that hundreds of people in Africa, including nurses, clinicians and pharmacists, had the skills and experience to set up and conduct a robust clinical trial. So in October, we put out a call for clinical-trial staff on the Global Health Network (www.theglobalhealthnetwork.org) — an online forum for medical researchers in low- and middle-income countries. Within 24 hours, we had received more than 250 replies from experienced African staff.

Just a few days later, we realized that we would not be able to secure visas for the responders fast enough to ensure them adequate care should they become infected. In the end, we employed staff from the United Kingdom, Australia, France, Ireland and elsewhere — people who could be repatriated quickly if necessary. Although the visa problems did not stall progress, it would have been more appropriate and better for strengthening Africa's research capacity and international ties if we had been able to use the skilled workers from African countries.

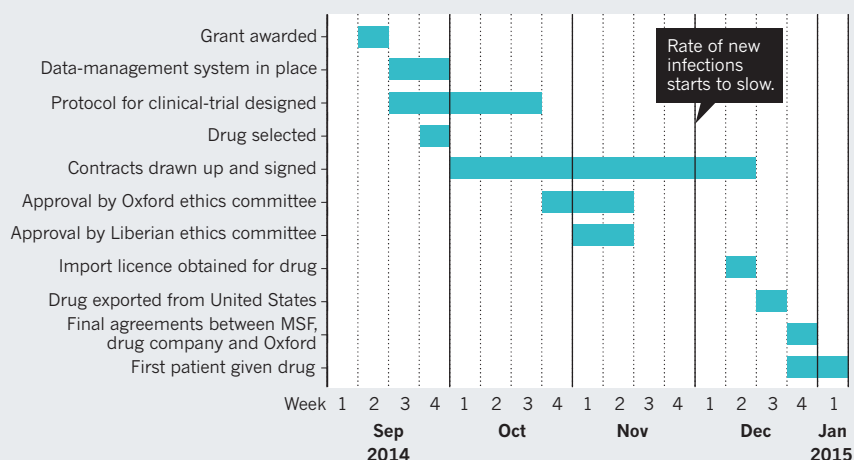
Delays over contracts. In mid-November, we were again hampered by bureaucracy. A major difficulty was getting the legal contracts drawn up and agreed to by the various parties involved — the University of Oxford, the drug company Chimerix of Durham, North Carolina (which was supplying the brincidofovir), and MSF. MSF has shown tremendous leadership in the response to the Ebola epidemic but — appropriately — the organization is geared to delivering aid, not to facilitating research. Just as the epidemic began to show signs of slowing, we were delayed by six crucial weeks while waiting for contracts to be processed through MSF's systems, which took longer than seemed necessary.

An unorchestrated 'land grab.' By the end of 2014, five research groups, including ours, were ready to start clinical trials for candidate treatments. This meant that humanitarian agencies such as MSF, Save the Children and GOAL, as well as local health-care leaders, had to make difficult choices about what research to do where.

For the trial that we conducted in Liberia, staff worked in pairs on 45-minute rotations to avoid overheating in the full-body suits that they had to wear in the treatment centre's 'red zone'. This meant that two trial staff could attend to only about five patients at one time. An obvious solution would have been to run the trial across multiple treatment centres simultaneously — but getting access to more centres was not feasible because of the complexity of the procedures and the

TIMELINE TO A CLINICAL TRIAL

During the Ebola epidemic, some of the steps in going from receiving grant money to testing a candidate drug on a patient were achieved in record time. Other steps, such as getting agreement on contracts, must be completed much more quickly in the next epidemic.





In future, visa issues must not prevent African health workers from helping with clinical trials.

time involved. Although the various teams of researchers worked hard to collaborate, for instance by standardizing methods and sharing data, on the ground it felt as if we were in a chaotic 'land grab' for sites and patients.

READY FOR NEXT TIME

Despite the lack of a proven treatment for Ebola, our efforts and those of other researchers over the past year will have been worth it if they help to ensure that, next time, the global community is better prepared. Humanitarian organizations routinely mobilize diverse groups of people, including local workers, to help to deliver aid after earthquakes or tsunamis; research teams need to be mobilized just as quickly.

First, an on-call global task force consisting of, say, 100–200 clinical-trial staff spread across five different countries should be established. This could be funded by agencies such as the Wellcome Trust, or by philanthropic organizations, such as the Bill & Melinda Gates Foundation (which partners with medical humanitarian charities). These people should be employed in everyday studies and be trained for outbreak research so that they can be deployed immediately to coordinate a trial in the event of an epidemic. Research centres that are well positioned and located to handle outbreaks could collaborate and provide the missing diagnostic capacity by making their laboratory expertise known and available.

Second, contractual agreements between parties with stakes in a clinical trial will always be necessary. Probable snagging points — such as concerns over drug pricing or data ownership — are easy to predict and should be addressed to some degree ahead of time. According to one contract template, the company providing the drug would have, say, exclusive access to the data for a limited amount of time; in another, the data would be made public as soon as they are generated.

Finally, an international, neutral body needs to be put in charge of outbreak research. Before the next outbreak, such a body could hammer out the details of crisis trial staffing and contracts. Most importantly, this organization could set the research priorities during an epidemic and ensure that adequate numbers of sites and patients are allocated to the different teams involved. The WHO is the obvious agency to do this but it currently lacks the necessary funds, mandate and support.

In the case of the Ebola epidemic, instead of having multiple research groups, each struggling to complete their trial because of insufficient numbers of patients, the WHO could have directed all the teams to recruit patients for an agreed prioritized trial. This would have been a better approach scientifically and ethically. If a trial is stopped because of insufficient numbers of participants, then every patient who has taken part in it has taken a risk needlessly.

EBOLA CLINICAL TRIALS

Three successes

The trial conductors (the Epidemic Disease Research Group Oxford) showed that clinical trials do not have to be expensive, slow and difficult.

The clinical staff employed did an incredible job. Many had never been to Africa before, and were plunged into gruelling conditions. Their willingness to leave their families and work long hours without dropping standards speaks to the feasibility of an on-call global task force for clinical trials.

The research teams set a precedent for data sharing, spurred by the International Severe Acute Respiratory and Emerging Infection Consortium. Teams agreed on what endpoints to measure in trials and standardized the types of data collected. They also shared experiences in meetings led by the World Health Organization, teleconferences and on a dedicated website (www.ebolaclinicaltrials.org). **TL**

To obtain a solid evidence base for the treatment, prevention and management of infectious diseases, everyone involved in outbreak response — aid agencies, ministries of health, health-care workers on the ground — needs to have research embedded in their plans long before an epidemic takes hold. Only then can experimental treatments be tested within days, not months. ■ **SEE NEWS FEATURE P.22**

Trudie Lang is professor of global health research at the Centre for Tropical Medicine and Global Health, University of Oxford, UK. e-mail: trudie.lang@ndm.ox.ac.uk

1. Lamberti, M. J., Brothers, C., Manak, D. & Getz, K. *Ther. Innov. Regul. Sci.* **47**, 101–109 (2013).
2. *Nature* **513**, 143–144 (2014).
3. Cohen, J. *Science* **346**, 911 (2014).
4. Florescu, D. F. & Keck, M. A. *Expert Rev. Anti. Infect. Ther.* **12**, 1171–1178 (2014).
5. Matthes-Martin, S., Boztug, H. & Lion, T. *Expert Rev. Anti. Infect. Ther.* **11**, 1017–1028 (2013).
6. Painter, W. et al. *Antimicrob. Agents Chemother.* **56**, 2726–2734 (2012).

CLARIFICATION

The Comment 'Agree on biodiversity metrics to track from space' (A. K. Skidmore *et al. Nature* **523**, 403–405; 2015) referred to Copernicus as a European Space Agency (ESA) initiative. In fact, it is a European programme to which ESA contributes.



ELOY GOMEZ PHOTOGRAPHY/GETTY

NEUROSCIENCE

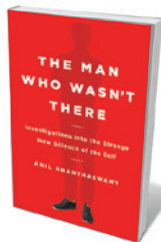
In the blink of an I

Douwe Draaisma is impressed by a study on the science behind ‘maladies of the self’.

It might happen while you are lecturing. All of a sudden, you hear yourself talking: an autopilot version of yourself seems to have taken over. With rising panic, you struggle to get back in, praying that what this autopilot has to say makes sense.

Who — or what — is the ‘yourself’ that does the talking? And who is the ‘I’ that anxiously tries to regain control? Are there temporarily two selves? Or is there still a single self, experienced from the outside? In most cases, the ‘split’ dissolves quickly and you slip back into the driver’s seat. You have experienced a brief spell of depersonalization.

Depersonalization can also be pathological, sometimes linked to epilepsy, and can last for minutes or even hours. To science writer Anil Ananthaswamy, chronic types of



The Man Who Wasn't There: Investigations into the Strange New Science of the Self
ANIL ANANTHASWAMY
Dutton: 2015

dissociation belong to “maladies of the self”, a set of experiences, conditions and syndromes that offer a window on what constitutes a self. For *The Man Who Wasn't There*, Ananthaswamy interviewed patients, psychiatrists and neuroscientists, charting how the self is affected in people with autism spectrum disorder, dementia, epilepsy or schizophrenia, and examining out-of-body experiences, doppelgänger hallucinations and phantom sensations. Much of the book reads like a travelogue, an exploration of the fringes of human experiences with Ananthaswamy a dependable guide, as in his celebrated *The Edge of Physics* (Gerald Duckworth, 2010). However elusive the experiences may seem, he keeps analysis close to the findings of modern neuroscience and psychiatry.

Ananthaswamy hears intimate, sometimes heartbreaking stories about what it means to experience a condition’s symptoms. He has a gift for weaving these through the technicalities of neuroscientific literature. Autobiographies hinging on conditions such as Asperger’s syndrome and schizophrenia are proliferating, but there is little to fill the void between such accounts and the scientific

literature. Linking experiences with experiments, and individuals with numbers, Ananthaswamy bridges that gap convincingly.

Possibly the most harrowing malady of the self is Cotard’s syndrome, in which a person, often with severe depression, believes that he or she has died. Ananthaswamy presents the case of 48-year-old Graham. After a failed attempt to electrocute himself, he became convinced that he was brain dead. Scans showed severe loss of activity in the frontal and parietal regions of the brain — structures supporting the ‘default mode network’, which allows one to remember and maintain the feeling that there is an ‘I’ that acts and experiences. Investigators speculated that antidepressants — or depression — could dampen activity in these brain areas but held that neither hypothesis could explain the extent of the lowered metabolism. Cotard’s syndrome is philosophically unsettling, because it questions the axiomatic certainty of the Cartesian ‘I think, therefore I am’. Yet, Ananthaswamy observes, there must still be an ‘I’ that

NATURE.COM

For more on science in culture see:
nature.com/booksandarts

experiences the delusion of being dead.

More common, but equally ghostly, are phantom experiences. After amputation of a limb, some people still feel itching or pain from it, probably due to activity in the now-vacant part of their cortical 'map', the neurological representation that supports their body image. Lesser known is the inverse, body integrity identity disorder, in which a

"Ananthaswamy hears intimate, sometimes heartbreaking stories about what it means to experience symptoms."

person feels that a healthy body part is foreign to them. The disorder may cause severe suffering. Quite a few desperate people have taken it into their own hands to get rid of the prob-

lematic body part, and have bled to death.

In a moving chapter, Ananthaswamy travels with 'David' to an Asian surgeon who relieves him of a leg that has felt odd since childhood. Afterwards, David finally feels at one with his bodily self. Swiss neuropsychologist Peter Brugger suggests that a limb that feels foreign may be the result of a cortical map that never included it in the first place.

There are many such inversions in *The Man Who Wasn't There*. They make intriguing associations. Could the feeling of a split self in depersonalization be the inverse of the ecstatic feeling of oneness with the world sometimes experienced during an epileptic seizure originating in the temporal lobe? (The brain region that is hyperactive during ecstatic seizures, the anterior insula, is underactive during chronic depersonalization, which seems to point in this direction.) Is the loss of a self supported by personal memories in Alzheimer's disease analogous to the scrambling of the self in schizophrenia? And could the trouble that some people with autism spectrum disorder have in intuiting the mental states of others — which has been called a deficient theory of mind — also cause the less sophisticated introspective skills that they may have?

Ananthaswamy does not end with a list of conclusions about the location, structure or organization of a hypothetical self. One could hardly expect him to: most of the research is in flux, and has been especially so since the introduction of sophisticated imaging techniques. Instead, he gives a sense of the many forces — hormonal, chemical, psychological, social — that modulate the self-as-experienced. One finishes the quest with a sense of paradox that the concept of self, often seen as elusive if not illusory, is so eminently suited to tightening these various narrative threads. ■

Douwe Draaisma is professor of the history of psychology at the University of Groningen in the Netherlands. His latest book is *Forgetting*. e-mail: d.draaisma@rug.nl

Books in brief



Katrina: After the Flood

Gary Rivlin SIMON & SCHUSTER (2015)

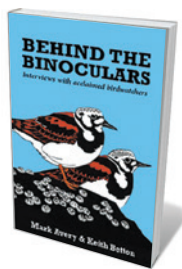
Ten years ago this month, New Orleans lay drowning, its levees breached by the storm surge from Hurricane Katrina. One million people were displaced and, despite federal preparedness exercises, the administration responded sluggishly. Journalist Gary Rivlin sweeps from street to boardroom in this history of the aftermath, studded with figures such as polarizing New Orleans mayor Ray Nagin and seething with egregious political failings that deepened racial inequality during the city's recovery. As Rivlin sharply reminds, overcoming disasters is very much an issue of governance.



The Black Mirror: Looking at Life Through Death

Raymond Tallis YALE UNIVERSITY PRESS (2015)

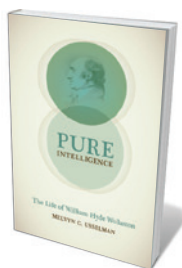
Death may be unimaginable, but former geriatric specialist Raymond Tallis explores it imaginatively nonetheless. Inspired by novelist E. M. Forster's line from *Howards End* (1910), "Death destroys a man; the idea of death saves him", Tallis's meditation on his future corpse is a meshed march of philosophical musings and bald physical detail. As he sifts a lifetime's worth of sensory and emotional memory, Tallis's prose stuns like poetry — from the "crackling, rebellious stretching as paper balls unscrunch" to the self's continuity despite the "distracted, multiple" nature of life. Enchanting.



Behind the Binoculars: Interviews with Acclaimed Birdwatchers

Mark Avery and Keith Betton PELAGIC (2015)

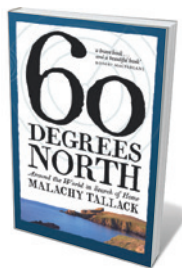
Whether spotting golden eagles in Idaho or long-tailed tits in London, professional birdwatchers are a rare breed — observational dynamos wedded to their craft. Wildlife campaigner Mark Avery and birdwatcher Keith Betton have captured 20 stories (including their own) from British luminaries such as wagtail expert Stephanie Tyler and birder extraordinaire Lee Evans. This is both a serious overview of the field and a flock of delights, from the shot of a youthful Betton with three young song thrushes balancing on his forearm to fond memories of first binoculars, whether Leica Ultravids or Swarovskis.



Pure Intelligence: The Life of William Hyde Wollaston

Melvyn C. Usselman UNIVERSITY OF CHICAGO PRESS (2015)

He was crucial to the development of crystallography, and discovered the amino acid cystine and the elements palladium and rhodium. Yet scientific polymath William Hyde Wollaston (1766–1828) is largely forgotten. This meticulous biography, the life's work of late chemist Melvyn Usselman, reveals a man of indefatigable curiosity and methodological genius. As we see Wollaston crafting analytical instruments for Arctic expeditions, stargazing or showing scientific writer Mary Somerville the uses of a goniometer, we can only concur with Usselman that this was a "man worth knowing".



Sixty Degrees North: Around the World in Search of Home

Malachy Tallack POLYGON (2015)

If you follow Shetland's latitude of 60° N around the world, you will encounter cultures "challenged by climate, by landscape, by remoteness". So writes Shetlander Malachy Tallack in this powerful memoir detailing how, unmoored by his father's death, he traversed that line to explore geographies inner and outer. Whether in Alaska's Kenai peninsula dodging bears or among the Even people in "huge, cold and utterly strange" Siberia, Tallack is forever testing the psychological dynamics of the sense of belonging. **Barbara Kiser**

Inside the fear factor

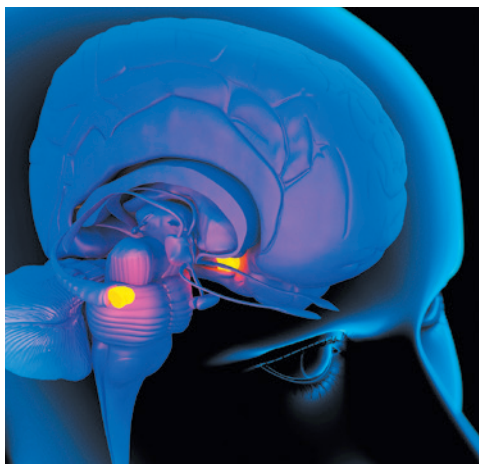
Susanne Ahmari applauds neuroscientist Joseph LeDoux's redefinition of anxiety.

Some 40 million people worldwide have been diagnosed with anxiety disorders. In *Anxious*, Joseph LeDoux presents a rigorous, in-depth guide to the history, philosophy and scientific exploration of this widespread emotional state. An eminent neuroscientist and author of *The Emotional Brain* (Simon & Schuster, 1996) and *The Synaptic Self* (Viking, 2002), he offers a magisterial review of the role of mind and brain in the generation of both unconscious defensive responses and consciously expressed anxiety.

LeDoux looks first at how our understanding of anxiety has evolved. He starts with ancient etymology (the Greek *angh* signified constriction) and moves on to Sigmund Freud's view of anxiety as the "root of most if not all mental maladies", and philosopher Søren Kierkegaard's perspective on it as existential, evolving from the dread that stems from freedom of choice. He then lays out the core distinction between fear and anxiety. Fear he defines as anticipation of danger from a physically present threat (a grizzly bear in front of you); anxiety, as anticipation of an uncertain threat (potential predators roaming outside your tent).

But although 'fear' and 'anxiety' are excellent descriptors of conscious feelings, LeDoux shows, they should not be used to describe the unconscious mental processes and neural circuits associated with these emotions. Instead of thinking of those processes as "fear stimuli activate a fear system to produce fear responses", he proposes conceptualizing them as "threat stimuli elicit defense responses via activation of a defensive system". This is a subtle distinction, and LeDoux makes an excellent case that it is an important foundation for rigorous research into the neural underpinnings of the conscious and unconscious processes that subserve anxiety.

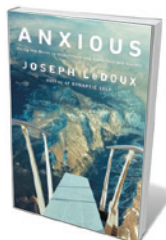
He ranges broadly and deeply across molecular neuroscience, psychology and philosophy, yet his methodical approach keeps his argument clear. He starts with a cogent description of threat processing and conditioning based on the 'fight vs flight vs freeze' framework, and moves on to the neural circuits thought to underlie these responses. He gives a clear precis of the possible mental processes behind anxiety disorders (such as impaired ability to discriminate between threat and safety). He then launches into his central thesis: that emotional states of mind such as consciously expressed anxiety are not inherited from our evolutionary



The brain's amygdalae (yellow) are key to anxiety.

ancestors. He argues that decades of animal research have failed to show that animals can consciously express feeling-states — in part because of their limited prefrontal cortical development and lack of verbal language. He does not rule out the possibility that animals can consciously feel emotions, but states that "it is not sufficient to provide evidence ... that the behavior in question is consistent with the existence of a conscious experience. One also has to show that the behavior cannot be accounted for by processes that work nonconsciously." A dog may look ecstatic when given a meaty bone, but it is difficult to prove scientifically that it feels what we think of as ecstasy.

The clinical importance of this distinction becomes clear in subsequent chapters, in which the unconscious and conscious brain processes involved in expressing fear and anxiety are ascribed to distinct neural circuits that may have different roles in the pathology and treatment of anxiety disorders. For



Anxious: Using the Brain to Understand and Treat Fear and Anxiety
JOSEPH LEDOUX
Viking: 2015.

example, when a hiker encounters a snake, information is rapidly and unconsciously sent from the eyes through the sensory thalamus to the amygdala, which can trigger the hiker to freeze before she is aware of the problem. In a slower process, the visual cortex receives the same information from the thalamus, leading to conscious awareness

and identification of the snake. In people with anxiety disorders such as post-traumatic stress disorder, the unconscious rapid path to the amygdala may be too strong, leading to perception of threats when none exist.

LeDoux's views jibe with those of many researchers investigating the underpinnings of anxiety disorders, but they are not always acknowledged in the media and elsewhere. Importantly, *Anxiety* highlights that, although it may not be possible to study the verbally based human emotional experience using animal models, wise use of those models is crucial for progress towards treatments. They remain our only direct window into the molecules, cells and circuits that guide emotions.

Neuroscientists, psychologists, philosophers and psychiatrists will find this exquisitely referenced book particularly useful. It is also a must-read for young investigators, and anyone perusing the footnotes will be rewarded with an insider's view of the state and evolution of anxiety research. LeDoux's charming personal asides give an impression of having a conversation with a world expert.

LeDoux ends on a high note, describing how cutting-edge research on the neural substrates of anxiety is being translated into new approaches for psychiatric treatment. He discusses, for example, the use of drugs that modulate glutamate-based synaptic transmission to aid exposure therapy for conditions including phobias — a clinical improvement discovered through studies of threat-learning in rats. He also proposes adaptations to therapy protocols that could improve the efficacy of existing treatment. He suggests adjusting the timing of exposure-therapy sessions to maximize consolidation of new learning; sessions scheduled at night, for example, would allow that to happen during sleep without interference from the events of the day.

Such ideas are unproven, and potentially difficult to translate into practice given current constraints on mental-health clinics and care providers. But they are a good example of the transformative potential of cross-talk between basic neuroscience researchers and clinicians. It is only through such synergistic collaborations that we will make significant advances in the treatment of anxiety. ■

Susanne Ahmari is director of the Translational OCD Laboratory at the University of Pittsburgh in Pennsylvania. She integrates cutting-edge neuroscience with clinical studies to develop treatments. e-mail: ahmarise@upmc.edu

ROGER HARRIS/SPL

Correspondence

Social impacts of science metrics

Metrics used to gauge a researcher's productivity and importance to science can come at a social cost (J. Wilsdon *Nature* **523**, 129; 2015). Too often, such metrics are underpinned by values of questionable worth.

Any quantitative measure of productivity will reward people who choose to work long hours, build large research teams and minimize their commitments to teaching, review panels and university committees.

The use of such metrics can discourage people from sharing responsibilities and time with their partners or spouses, from investing in and enjoying their children's lives, and from participating in their local communities. Researchers can feel forced to sacrifice 'unproductive' recreational pursuits such as holidays, sport, music, art and reading — activities that other metrics correlate highly with creativity and quality of life (see also J. Overbaugh *Nature* **477**, 27–28; 2011).

We need a more nuanced approach to academic evaluations for hiring, promotion and tenure. The emphasis on quantitative measures of productivity places unfair burdens on scientists and their families, and it discourages some students from pursuing academic careers.

Stephen C. Harvey *University of Pennsylvania, Philadelphia, USA.*
steharv@mail.med.upenn.edu

Protect the young from e-cigarettes

Democratic state senator Mark Leno is to be commended for trying to sustain California's leading position in protecting young people from the harmful effects of tobacco and nicotine, in all its forms (see *Nature* **523**, 267; 2015). Contrary to industry claims, the use of electronic

cigarettes is increasing among young people who have never smoked before (R. E. Bunnell *et al. Nicotine Tob. Res.* **17**, 228–35; 2015), and not just among adult smokers searching for a less harmful alternative to cigarettes.

Some e-cigarettes are designed to look like cigarettes, come in flavours that appeal to children and adolescents, and are promoted and sold in shops and pharmacies that are frequented by young people. Electronic cigarettes also deliver addictive nicotine; more research is needed on the safety of their other ingredients.

Until more is known about these largely unregulated products, legislation similar to the bill that failed in California should be widely introduced to keep e-cigarettes and other electronic nicotine-delivery devices out of the hands of young people.

Linda Richter *CASAColumbia, New York, USA.*
lrichter@casacolumbia.org

Support Nepal to rebuild sustainably

A government report on Nepal's earthquakes on 25 April and 12 May, which caused around 8,600 deaths and displaced at least 2.8 million people, rightly prioritizes the reconstruction of buildings and infrastructure (see go.nature.com/pdksq6). However, it overlooks the impact of large-scale restoration work on the fragile environment and imperilled ecosystems. The importance of this was learned from the extensive rebuilding in Aceh, Indonesia, after the 2004 Indian Ocean tsunami.

A report on rebuilding in Aceh recommended addressing environmental degradation early in the redesign process to limit potential damage during reconstruction, with a view to minimizing deforestation and exploitation

of natural resources (see <http://go.nature.com/xpaxju>).

Likewise, the international aid community should support Nepal in using environmentally friendly reconstruction methods. The government must regulate the extraction of clay soil — in demand for producing trillions of fire bricks — because this can trigger landslides and erode fragile terrain. It should impose carbon-emissions standards on brick kilns and make them cleaner and more efficient, to cut pollution and wood consumption. (Deforestation has claimed around two-thirds of Nepal's natural forest in 30 years.) Controlling the excavation of gravel and sand from river beds would reduce the risk of diverting important currents, and would protect river ecosystems.

Shiva Raj Mishra *Nepal Development Society, Chitwan, Nepal.*
nedsnepal@gmail.com

Plant collections find strength in numbers

Preserved plant collections in the United States may be under threat (*Nature* **523**, 16; 2015), but there are grounds for optimism. Many herbaria, including those at our own institutions, are assembling digitized specimens in increasingly popular open databases. They are joining together to promote their value for research, teaching and other services, including the formal identification of species and to raise public awareness.

Online information from plant collections is attracting positive attention, especially among younger scientists. Student interest is opening the eyes of university administrators. And crowdsourcing is educating a wide range of individuals as they collect information for herbarium databases.

The Society of Herbarium

Curators is an example of an international advocacy organization founded to preserve and promote endangered collections (www.herbariumcurators.org). Its regional networks reach out to groups that were previously under-represented in the botanical community, such as state and federal agencies, and schoolchildren and teachers.

The society is developing community standards of curation and is ensuring that herbaria are fully used and not orphaned by their institutions. We advise every herbarium director to become a member: our strength lies in numbers.

Conley K. McMullen *James Madison University Herbarium, Harrisonburg, Virginia, USA.*
Andrea Weeks *Ted R. Bradley Herbarium, George Mason University, Fairfax, Virginia, USA.*
mcmullck@jmu.edu

High-rise buildings worsened heatwave

This summer's heatwave in Pakistan was the worst in more than 30 years, and caused the deaths of more than 1,200 people in Karachi alone. The city is an urban heat island that can reach temperatures up to 15°C warmer than those of its rural surroundings. Urgent and fundamental reform of local governance is needed to protect the city's population of 22 million.

Despite the 2010 Sindh High Density Development Board Act, high-rise development in Karachi has continued unabated. Besides obstructing life-saving sea breezes, these developments compound the city's water and electricity shortages. Buildings are poorly ventilated and cheaply constructed from materials that are unable to cope with extreme temperatures.

Abdur Rehman Cheema *COMSATS Institute of Information Technology, Islamabad, Pakistan.*
arehmancheema@gmail.com

NETWORK SCIENCE

Destruction perfected

Pinpointing the nodes whose removal most effectively disrupts a network has become a lot easier with the development of an efficient algorithm. Potential applications might include cybersecurity and disease control. [SEE LETTER P.65](#)

ISTVÁN A. KOVÁCS
& ALBERT-LÁSZLÓ BARABÁSI

An enduring truth of network science is that the removal of a few highly connected nodes, or hubs, can break up a complex network into many disconnected components¹. Sometimes, a fragmented and inactive network is more desirable than a functioning one. Consider, for example, the need to eliminate bacteria by disrupting their molecular network or by vaccinating a few individuals in a population to break up the contact network through which a pathogen spreads. In a quest to find the silver bullets that can effectively dismantle large networks, Morone and Makse² (page 65 of this issue) have developed an algorithm that achieves this by identifying sets of network nodes known as influencers.

It is not certain whether targeting and removing network hubs — defined as the nodes with the largest number of links — can inflict maximum disruption on a network. It may be more effective to eliminate a combination of hubs and central, but less-well-connected, nodes. The removal of hubs is usually preferred because they are easy to locate, whereas identifying the optimal set of nodes for

which deletion would cause maximum damage is a non-deterministic polynomial-time hard (NP-hard) problem³. This means that it is computationally feasible only for small networks. Morone and Makse attack the problem of network disruption by mapping the integrity of a tree-like random network into optimal percolation^{4,5} theory. From this, they derive an energy function with a minimum that corresponds to the set of nodes that need to be eliminated, to yield a network whose largest cluster is as small as possible. Although identifying this minimum is still an NP-hard problem, the authors were inspired by the energy function's shape to find a simple algorithm that offers an approximate solution.

To do this, Morone and Makse introduce the concept of collective influence, which is the product of the node's reduced degree (the number of its links minus one) and the sum of the reduced degrees of the nodes that are a certain number of steps away from it (Fig. 1). Collective influence describes how many other nodes can be reached from a given node, assuming that nodes of high collective influence have a crucial role in the network. The collective-influence-based algorithm then sequentially removes nodes, starting with those that have the highest collective influence

(known as influencers) and recalculating the collective influence of the rest following each operation. The authors show that, for large networks, removing the set of influencers identified by this algorithm is more effective in fragmenting a network than removing the hubs, or than removing nodes that are identified through other algorithms, such as PageRank⁶ or closeness centrality⁷. The set of influencers identified by the authors contains many nodes with few connections. This highlights the fact that the importance of a node in ensuring a network's integrity is determined not only by the number of direct links it has to other nodes, but also by which other nodes it is connected to.

The collective-influence algorithm is remarkable for its computational complexity because it requires only $N^2 \log N$ computations to dismantle a network that contains N number of nodes. Its complexity is reduced to $N \log N$ if, instead of individual nodes, a fixed fraction of the total is removed at each step of the computation. The authors compare their method to the predictions of spin-glass theory, which was originally developed to describe the properties of disordered magnets and has found a range of applications in network analysis. They conclude that the nodes prioritized

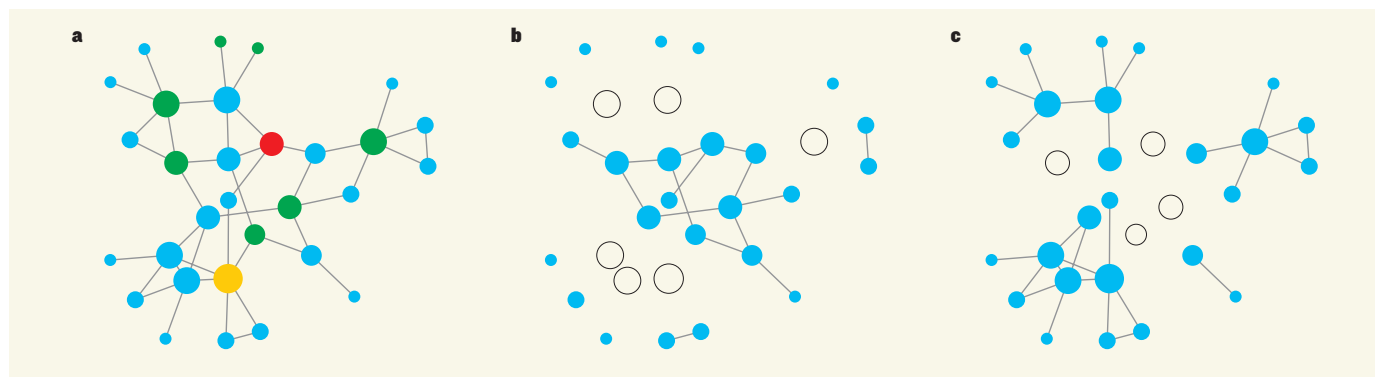


Figure 1 | Optimal network demolition. Morone and Makse² introduce an algorithm that allows them to efficiently dismantle networks. The authors define the collective influence of a network node as the product of its reduced degree (the number of its nearest connections, k , minus one), and the total reduced degree of all nodes at distance d from it (defined as the number of steps from it). **a**, In this network, for $d=2$, the red node with $k=4$ has the highest collective influence, because the total reduced degree of the nodes at $d=2$ from it (green and yellow circles) is 21. This yields a collective influence of $3 \times 21 = 63$. The most connected hub, with $k=6$ (yellow circle), has a

collective influence of 60. **b**, Removing the 6 nodes with the highest k (white circles) causes considerable damage to the network, but leaves a sub-network that contains 12 nodes unperturbed. **c**, By contrast, the algorithm developed by the authors allows them to identify a set of nodes (known as influencers) according to their collective influence. Using this, the removal of four influencer nodes (white circles) results in a fragmented network in which the largest connected cluster that remains has only ten nodes. This illustrates the algorithm's effectiveness over conventional methods for prioritizing network destruction.

by the collective-influence algorithm represent an approximate solution, which has a size close to that of the theoretical optimal solution. On the basis of spin-glass theory, we expect that the collective-influence solution has only a small overlap with the optimal solution, and hence must be treated with caution. However, the influencers found by collective influence are more effective in destroying a network than nodes selected by other methods. So even though the collective-influence method is approximate, it is faster and more efficient.

As with any new algorithm, open questions abound. The collective-influence algorithm has only one free parameter — the distance, expressed in the number of steps, from any given node. At zero distance, the collective influence of a node is equal to the square of its reduced degree, and so in this case the algorithm simply removes the hubs. To improve the algorithm's accuracy, one must choose a non-zero distance — but one that is not too large, because for large distances the boundaries of the network are reached, diminishing a node's collective influence (the collective influence approaches zero). Although Morone and Makse find that any distance greater than one works, a firm criterion for choosing an optimal value is lacking and would be desirable. Finally, because the authors designed their algorithm to work on networks that are locally tree-like, further work and quantitative evidence are needed on its expected accuracy for networks with loops, such as most social networks.

The collective-influence algorithm, just like similar algorithms, removes a node together with all its links. However, for many systems, node removal is too drastic an intervention. Softer touches, such as removing or rewiring specific links, are more tractable and desirable. For example, these approaches are relevant for networks in biological cells, in which many diseases are caused by mutations that result in deletion of links rather than the complete removal of nodes⁸. Understanding such 'edgetic' effects, and designing algorithms that can detect the minimum number of links to delete so as to achieve a given outcome, remains a challenge for future work.

The identification of optimal influencers, at either the node or the link level, is the first step towards building networks that would be robust against both attacks and failures. Mastering the design principles of such super-robust networks could have profound implications for anything from cybersecurity to the design of an attack- and error-tolerant power grid, and may even allow us to develop drugs that can rescue a cellular network from its diseased state with minimal side effects. ■

István A. Kovács and Albert-László Barabási are at the Center for Complex Network Research and in the Department of Physics, Northeastern University, Boston,

Massachusetts 02115, USA.

e-mail: alb@neu.edu

1. Albert, R., Jeong, H. & Barabási, A.-L. *Nature* **406**, 378–382 (2000).
2. Morone, F. & Makse, H. A. *Nature* **524**, 65–68 (2015).
3. Garey, M. R. & Johnson, D. S. in *Computers and Intractability: A Guide to the Theory of*

NP-completeness (Freeman, 1979).

4. Hashimoto, K. *Adv. Stud. Pure Math.* **15**, 211–280 (1989).
5. Karrer, B., Newman, M. E. J. & Zdeborová, L. *Phys. Rev. Lett.* **113**, 208702 (2014).
6. Brin, S. & Page, L. *Proc. 7th Int. World Wide Web Conf.* **30**, 107–117 (1998).
7. Freeman, L. C. *Soc. Networks* **1**, 215–239 (1978–79).
8. Sahni, N. et al. *Cell* **161**, 647–660 (2015).

DIABETES

A smart insulin patch

A microneedle-containing patch that is designed to sense elevated blood glucose levels and to respond by releasing insulin could offer people with diabetes a less-painful and more-reliable way to manage their condition.

OMID VEISEH & ROBERT LANGER

Diabetes is widely recognized as one of the biggest medical challenges of the twenty-first century, afflicting more than 280 million people globally¹. People with diabetes must tirelessly self-monitor their blood glucose levels and inject the correct dose of the glucose-lowering hormone insulin to keep their blood glucose levels in the

normal range². This treatment regime involves challenges — it requires painful and inconvenient subcutaneous injections, is imprecise, and can cause serious problems if insulin dosage is not closely tuned to the patient's immediate physiological needs³. Reporting in *Proceedings of the National Academy of Sciences*, Yu et al.⁴ describe a glucose-responsive microneedle patch that can be painlessly applied to the skin and that releases insulin as blood glucose levels increase.

'Smart' glucose-responsive insulin-based therapies involve the automatic release of insulin in response to increases in blood glucose concentration. Smart therapies can improve disease control and limit the potential for excessively low blood glucose levels, which is a potentially deadly effect of excessive insulin dosing³. To mimic the physiological needs of a patient accurately, such therapies must respond rapidly to elevated glucose levels, and must release insulin with kinetics that closely mirror those of a healthy pancreas.

One type of smart therapy makes use of microcomputer-controlled insulin-delivery systems. These systems couple implantable continuous glucose monitors (CGMs) to automated pumps, and administer insulin through a subcutaneously inserted cannula tube. They are currently being evaluated in the clinic, and have shown promise in helping patients to achieve their target blood glucose level more regularly^{5,6}. However, the sensors of current CGMs must be calibrated many times a day using hand-held glucometers. They produce blood-glucose measurements that lag behind true blood glucose levels by 5–15 minutes, hampering efforts to maintain a healthy range³. They are also the size of pagers, and the implanted sensors and cannula increase the risk of infection and require frequent maintenance and replacement to combat the body's immune response, increasing inconvenience, discomfort and cost to the patient³.

The microneedle-patch device developed by Yu and colleagues is a 6-millimetre-square

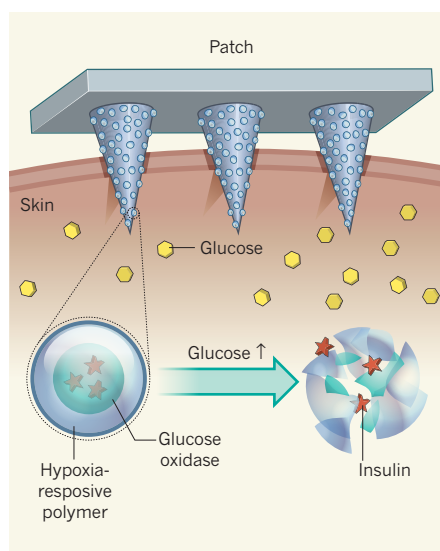


Figure 1 | A microneedle patch to monitor glucose and release insulin. Yu et al.⁴ have developed a smart insulin-releasing patch made of 121 nanoparticle-containing microneedles. The patch painlessly penetrates the interstitial fluid between subcutaneous skin cells. The nanoparticles in each needle contain insulin and the glucose-sensing enzyme glucose oxidase, which converts glucose to gluconic acid. These molecules are surrounded by a hypoxia-responsive polymer. Increases in glucose oxidase activity in response to glucose elevation produce a low-oxygen environment in the nanoparticles, which is sensed by the hypoxia-responsive polymer, triggering disassembly of the nanoparticles and the release of insulin.

relative of cyanase genes from nitrite-oxidizing bacteria. Because this single isolate is the only ammonia oxidizer ever found to produce cyanase, it is probable that along its evolutionary journey it acquired the cyanase gene by horizontal transfer from a nitrite-oxidizing partner during nitrification.

Nitrification is a cornerstone of the global nitrogen cycle because it both removes ammonia and produces nitrate, the latter fuelling many other pathways, including the eventual return of nitrogen gas to the atmosphere. Unabated nitrification, however, has undesirable environmental effects, such as soil acidification, nitrate toxicity in drinking water, algal overgrowth (eutrophication) and oxygen depletion in coastal marine systems ('dead zones'), and it contributes to global warming⁴.

Although chemical fixation of nitrogen gas to ammonia by the Haber–Bosch process revolutionized global agriculture by circumventing the limitations of biological nitrogen fixation, we have now entered a period in which human sources of fixed nitrogen exceed all natural sources combined. This has brought the global nitrogen cycle to its current and serious state of imbalance⁵. The main regulatory focus for stemming runaway impacts of nitrification and nitrate has been the control of ammonium-based fertilizers — how these are applied and how to maximize their uptake by plants. Palatinszky and colleagues' findings raise the question of whether cyanate should join ammonia (and urea, the only other known energy-providing substrate for ammonia oxidizers) as a key controller of the nitrification process.

Scholars of prebiotic chemistry have demonstrated that cyanide can act as a building block and substrate for generating essential components of living cells⁶. Extant microorganisms⁷ and plants⁸ have been identified that produce cyanide, take it up from the environment, transform it or even assimilate it. These findings argue for an ongoing and significant role of cyanide and its derivatives as nutrients and scaffolds for biopolymerization. Palatinszky and colleagues' results elevate the role of cyanate (and perhaps cyanide as its reduced precursor) from a building block (and toxin) to an energy-supplying molecule. This places cyanate (and cyanide) in a new evolutionary context — one could envisage ecosystems here or on extrasolar planets in which a cyanate–cyanide cycle could support both assimilatory and dissimilatory modules of nitrogen metabolism.

Cyanate on its own is chemically unstable and does not persist in large quantities in the environment. However, it can stably persist at low concentrations in seawater⁹ and is produced inside cells by the decomposition of urea and the metabolite carbamoyl phosphate¹⁰. Nitrifying microorganisms, particularly in the oceans, are geared towards survival at extremely low nutrient levels. Palatinszky *et al.* suggest that nitrite-oxidizing bacteria either

produce more cyanate as a by-product of their distinctive metabolism or import cyanate on a continuous basis. Both of these possibilities argue that this involvement of cyanate supports the formation and metabolism of nitrifying partnerships even when ammonia is scarce.

Thus, this report is a good reminder that microorganisms defy our strict categorizations into functional and phylogenetic groups because they evolve and survive in complex geochemical contexts. Nitrifying consortia provide an excellent illustration that microbial partnerships are dynamic and sometimes mysterious, and often challenge our predefined boundaries. ■

Lisa Y. Stein is in the Department of Biological Sciences, University of Alberta,

Edmonton, Alberta T6G 2E9, Canada.
e-mail: lisa.stein@ualberta.ca

1. Bernhard, A. *Nature Educ. Knowl.* **3**, 25 (2010).
2. Ward, B. B. in *Nitrification* (eds Ward, B. B., Arp, D. J. & Klotz, M. G.) 3–8 (ASM Press, 2011).
3. Palatinszky, M. *et al.* **524**, 105–108 (2015).
4. Galloway, J. N., Leach, A. M., Bleeker, A. & Erisman, J. W. *Phil. Trans. R. Soc. B* **368**, 20130120 (2013).
5. Rockström, J. *et al.* *Nature* **461**, 472–475 (2009).
6. Patel, B. H., Percivalle, C., Ritson, D. J., Duffy, C. D. & Sutherland, J. D. *Nature Chem.* **7**, 301–307 (2015).
7. Luque-Almagro, V. M. *et al.* *Biochem. Soc. Trans.* **39**, 269–274 (2011).
8. Yu, X.-Z. *Int. J. Environ. Sci. Technol.* **12**, 763–774 (2015).
9. Widner, B., Mulholland, M. R. & Mopper, K. *Anal. Chem.* **85**, 6661–6666 (2013).
10. Purcarea, C. *et al.* *J. Biol. Chem.* **278**, 52924–52934 (2003).

This article was published online on 29 July 2015.

CLIMATE SCIENCE

Uncertain future for vegetation cover

How will Earth's vegetation cover respond to climate change, and how does this compare with changes associated with human land use? Modelling studies reveal how little we still know, and act as a clarion call for further work.

ALMUT ARNETH

Vegetation and soil take up and release large amounts of carbon dioxide, and are thus key players in the climate system. Writing in *Global Biogeochemical Cycles*, Davies-Barnard *et al.*¹ describe results from an Earth-system model that incorporates a dynamic component representing vegetation and the associated carbon cycle. They used this to investigate how change of vegetation in response to global warming and increasing atmospheric CO₂ levels compares, in terms of area and carbon uptake, with the effects of human land use — particularly deforestation and reforestation — over the coming decades. In total, the projected changes strongly depend on the type and location of future land-use change, and on the magnitude of climate change.

In most parts of the world, humans have greatly altered the type of vegetation that dominates the landscape. Further large changes in land cover are expected as demand for food, timber and biofuels grows, and as the climate warms. Knowledge about the location of dominant vegetation cover in the future is needed for many reasons. Enhanced vegetation growth and the expansion of vegetation cover into new regions owing to climate change takes up CO₂ from the atmosphere, whereas large amounts of this greenhouse gas are lost from

vegetation and soil following deforestation. Changes in vegetation cover also alter the way in which incoming solar radiation is reflected or absorbed at the land surface, and how it subsequently warms the surface and leads to evaporation and transpiration of water. Taken together, vegetation and soil influence climate change globally and regionally.

Despite this, only the most recent (fifth) report by the Intergovernmental Panel on Climate Change (IPCC) has simultaneously considered the effects of land-use change and of dynamically changing vegetation and soil processes — at least in a few simulations² of future climate change using Earth-system models. By contrast, stand-alone vegetation models have been used for some years to assess the combined effects of natural vegetation dynamics and deforestation³. However, climate scientists have rarely attempted to systematically disentangle the two, especially with respect to the area covered.

In their modelling study, Davies-Barnard and colleagues show how three scenarios that consider both land-use change and climate change lead to substantial regional discrepancies in where, and by how much, vegetation cover expands or decreases (Fig. 1). The model shows that climate-change effects are larger in boreal forest than in tropical forest, and become more important towards the end of the twenty-first century. In fact, the one outcome

that emerges from all three scenarios is the poleward expansion of boreal forest, a finding that has also been reported in previous work (see ref. 3, for example). By contrast, tropical forests are more affected by land-use change than are boreal ones, and the effects become evident in the next few decades, but the direction and speed of change depends greatly on the scenario — for example, the ratio of the land area adopted for crop and pasture lands to the area of reforestation.

Thus, a complex picture emerges in which changes in vegetation cover depend on the speed of vegetation's response to human-induced forcing, whether warming and higher atmospheric CO₂ levels stimulate the expansion of forest cover, and the relative size of areas of deforestation and reforestation. To complicate matters further, the magnitude and direction of vegetation-area change and ecosystem carbon changes are not proportional to each other. The regional differences associated with each scenario count, and not just because of their effects on climate. Changes in land cover will affect species and habitat diversity, but also water supplies, food provision, air quality and other services that society derives from ecosystems. A better understanding of where and when we can expect land-cover changes is therefore needed to develop sustainable land-management strategies.

As Davies-Barnard and co-workers note, there are several caveats to their analysis, some of which relate to the vegetation and carbon-cycle model used. In their study, the nitrogen and carbon cycles do not interact; such a lack of interaction can affect not only future carbon-cycle projections², but also how simulated vegetation cover responds to climate and atmospheric CO₂ changes⁴. Furthermore, the representation of croplands is highly simplified in their model, and does not consider crop-management practices that are known to affect the carbon content of soil.

Another caveat is that forest-management practices, the dynamics of forest regrowth and tree-age distributions are not accounted for in the authors' model, but these are important for carbon cycling in ecosystems. And only net land-use changes — the net area that undergoes a change from one time period to the next — are considered, even though the accuracy of estimates of total land-use change and carbon-cycle calculations can be substantially improved when the more-detailed, multidirectional changes that occur within a region are accounted for^{5,6}. We do not know the degree to which Davies-Barnard and colleagues' results would be affected if all of these caveats were explicitly addressed. Their study will therefore stimulate and challenge scientists to account for land-use and land-cover change much more realistically than is done at present.

Even more interesting is how much the study's findings depend on the envisaged future world. In the fifth IPCC report, four

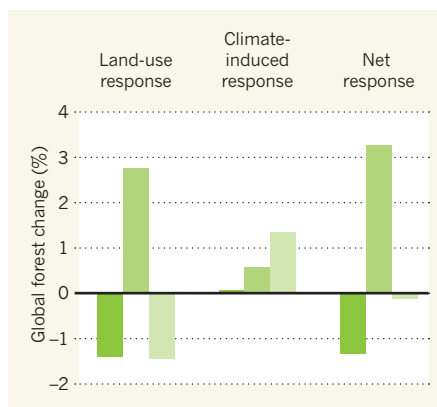


Figure 1 | Simulations of future forest cover. Davies-Barnard *et al.*¹ have used a computational model to investigate how the change of vegetation cover in response to global warming and increasing atmospheric CO₂ levels compares with the effects of land use (deforestation and reforestation) over the coming decades. The graphs depict changes in the percentage of the global land area covered by forest in 2100, using three different scenarios of climate change and land use; results from each scenario are shown in a different colour. The results differ greatly for each scenario. (Adapted from ref. 1.)

future anthropogenic emission scenarios (known as representative concentration pathways) were each realized by a different integrated assessment model, which combines knowledge about aspects of climate change and economics into a single framework. The uncertainties associated with projections of land-use change are therefore unknown, even though different outcomes of land-use change are feasible for each of the scenarios. However, the uncertainties in land-use change — in terms of the total area, location and direction of change — will need to be considered to develop land-based policies for mitigating and adapting to the effects of climate change.

SYNTHETIC BIOLOGY

Ribosomal ties that bind

The ribosome is the cellular complex of proteins and RNA molecules that synthesizes proteins. An artificial ribosome in which the two main subunits are tethered together creates opportunities for engineering this process. [SEE LETTER P.119](#)

JOSEPH D. PUGLISI

To engineer a system is to demonstrate a mastery of physical understanding. Mechanical engineers harness a deep understanding of fundamental physics to design new motors. Similarly, biologists are using the current explosion in information about molecular structure and function to engineer biological systems. The ribosome — the

Scientists are addressing this issue by developing a broader range of land-use change projections, using different integrated assessment models, for each of the representative concentration pathways used in the IPCC report⁷. In addition, projections from global and regional models of land-use change that are conceptually different from integrated assessment models are emerging or are under development^{8–10}. We will soon be able to test how components of the future carbon cycle and the climate, and of many other crucial ecosystem properties, will alter when a range of CO₂ levels and climate changes are combined with various land-use-change scenarios. This will help us to answer the overarching question of how to share a finite resource: the land. ■

Almut Arneth is in the Department of Environmental Atmospheric Research, Institute of Meteorology and Climate Research, Karlsruhe Institute of Technology, Garmisch-Partenkirchen 82467, Germany. e-mail: almut.arneth@kit.edu

1. Davies-Barnard, T., Valdes, P.-J., Singarayer, J. S., Wiltshire, A. & Jones, C. D. *Global Biogeochem. Cycles* **29**, 842–853 (2015).
2. Ciais, P. *et al.* in *Climate Change 2013: The Physical Science Basis. Contribution of Working Group I to the Fifth Assessment Report of the Intergovernmental Panel on Climate Change* (eds Stocker, T. F. *et al.*) 465–570 (Cambridge Univ. Press, 2013).
3. Storch, S. *et al.* *Glob. Change Biol.* **14**, 2015–2039 (2008).
4. Wärlind, D., Smith, B., Hickler, T. & Arneth, A. *Biogeosciences* **11**, 6131–6146 (2014).
5. Stocker, B. D., Feissli, F., Strassmann, K. M., Spahni, R. & Joos, F. *Tellus B* **66**, 23188 (2014).
6. Wilkenskjeld, S., Kloster, S., Pongratz, J., Raddatz, T. & Reick, C. H. *Biogeosciences* **11**, 4817–4828 (2014).
7. O'Neill, B. C. *et al.* *Clim. Change* **122**, 387–400 (2014).
8. van Asselen, S. & Verburg, P. H. *Glob. Change Biol.* **18**, 3125–3148 (2012).
9. Murray-Rust, D. *et al.* *Environ. Model. Software* **59**, 187–201 (2014).
10. Arneth, A., Brown, C. & Rounsevell, M. D. A. *Nature Clim. Change* **4**, 550–557 (2014).

macromolecular complex containing RNAs and proteins that translates the genetic code — represents one of nature's most sophisticated machines. Engineering ribosomes would enable experimental manipulation of protein synthesis and provide deeper insights into cellular and molecular biology. On page 119 of this issue, Orelle *et al.*¹ describe drastic, but simple, engineering of functional ribosomes, in which two separate subunits are linked as one.

Comprehensive genomic profiles of small cell lung cancer

A list of authors and affiliations appears at the end of the paper

We have sequenced the genomes of 110 small cell lung cancers (SCLC), one of the deadliest human cancers. In nearly all the tumours analysed we found bi-allelic inactivation of *TP53* and *RBI*, sometimes by complex genomic rearrangements. Two tumours with wild-type *RBI* had evidence of chromothripsis leading to overexpression of cyclin D1 (encoded by the *CCND1* gene), revealing an alternative mechanism of Rb1 deregulation. Thus, loss of the tumour suppressors *TP53* and *RBI* is obligatory in SCLC. We discovered somatic genomic rearrangements of *TP73* that create an oncogenic version of this gene, *TP73Δex2/3*. In rare cases, SCLC tumours exhibited kinase gene mutations, providing a possible therapeutic opportunity for individual patients. Finally, we observed inactivating mutations in *NOTCH* family genes in 25% of human SCLC. Accordingly, activation of Notch signalling in a pre-clinical SCLC mouse model strikingly reduced the number of tumours and extended the survival of the mutant mice. Furthermore, neuroendocrine gene expression was abrogated by Notch activity in SCLC cells. This first comprehensive study of somatic genome alterations in SCLC uncovers several key biological processes and identifies candidate therapeutic targets in this highly lethal form of cancer.

Small cell lung cancer (SCLC) accounts for approximately 15% of all lung cancers, arises in heavy smokers, and the tumour cells express neuroendocrine markers. Although chemotherapy is initially effective in the treatment of SCLC, recurrence arises rapidly in the vast majority of cases, usually killing the patient within only a few months¹. SCLC is rarely treated by surgery and few specimens are available for genomic characterization. Previous studies applying mostly exome sequencing in a limited number of tumour specimens have revealed only a few recurrently mutated genes^{2,3}.

We hypothesized that complex genomic rearrangements, which are undetectable by exome sequencing, might further contribute to the pathogenesis of SCLC and thus performed whole-genome sequencing of 110 human SCLC specimens (Supplementary Tables 1–4). One of the hallmarks of SCLC is the high frequency of mutations in *TP53* and *RBI* (refs 2–7). As mice lacking *Trp53* and *Rb1* in the lung develop SCLC^{8,9}, we also sequenced 8 of these murine SCLC tumours in order to identify mutations that may promote SCLC development following loss of *Trp53* and *Rb1* and that may overlap with such accessory genes in human SCLC¹⁰ (Supplementary Table 5).

Samples and clinical data

We collected 152 fresh-frozen clinical tumour specimens obtained from patients diagnosed with stage I–IV SCLC under institutional review board approval (Supplementary Table 1 and Extended Data Fig. 1). The tumour samples were enriched for earlier stages and consisted of primary lung ($n = 148$) and metastatic tumours ($n = 4$) obtained by surgical resection ($n = 132$), biopsy ($n = 4$), pleural effusion ($n = 1$) or through autopsy ($n = 15$). We performed whole-genome sequencing on 110 of these tumours and their matched normal DNA. A total of 42 cases were excluded from the analysis because of insufficient quality or amount of DNA. Most of these 110 tumours were treatment-naïve, with only five cases obtained at the time of relapse. We analysed transcriptome sequencing data in 71 of the 110 specimens that had undergone genome sequencing and in 10 additional specimens. Finally, 103 of the 110 genome-sequenced specimens and 39 additional specimens were analysed by Affymetrix 6.0 SNP arrays (Supplementary Table 1 and Extended Data Fig. 1). Eight tumour samples from preclinical SCLC mouse models were analysed

by whole-exome sequencing ($n = 6$) or whole-genome sequencing ($n = 2$) (Supplementary Table 5).

Recurrent somatic alterations in SCLC

SCLC genomes exhibited extremely high mutation rates^{2,3} of 8.62 nonsynonymous mutations per million base pairs (Mb). C:G>A:T transversions were found in 28% of all mutations on average, a pattern indicative of heavy smoking (Fig. 1a and Supplementary Tables 2 and 3). The smoking history or clinical stage of the tumours did not correlate with the type and number of mutations (Extended Data Fig. 2). The median tumour content was 84% (Extended Data Fig. 3a and Supplementary Table 2). By contrast, murine SCLC tumours showed a low number of somatic alterations (on average 28.5 protein-altering mutations per sample on average)¹⁰ (Supplementary Table 5).

In order to assess the amount of genetic heterogeneity of SCLC, we developed a subclonality score, which can be interpreted as the probability that an arbitrary point mutation in a randomly selected cancer cell is subclonal throughout the entire tumour (Methods). A reliable reconstruction of the subclonal architecture was possible in 55 of the cases (Extended Data Fig. 3b). A comparison to lung adenocarcinoma¹¹ indicated a threefold lower subclonal diversity in SCLC ($P = 0.00023$, Extended Data Fig. 3b), pointing to pronounced differences in the evolution of SCLC and lung adenocarcinoma^{12,13}. In contrast to adenocarcinomas, the level of heterogeneity in SCLC did not correlate with clinical stage (Extended Data Fig. 2b).

We applied several analytical filters in order to identify mutations with a probable relevance in SCLC biology in the context of the high load of background mutations² (Extended Data Fig. 1, Supplementary Table 6 and Methods). They include (I) analyses of significance determined by a comparison of observed and expected mutation rates followed by a correction for expressed genes, (II) a survey of regional clustering of mutations that may indicate mutational targeting of functionally enriched areas in tumour suppressors or proto-oncogenes, (III) determination of genes that are enriched for likely damaging mutations, (IV) a comparison with genes whose biological relevance has been established in SCLC mouse models, and (V) a listing of genes with a likely therapeutic relevance or that are otherwise

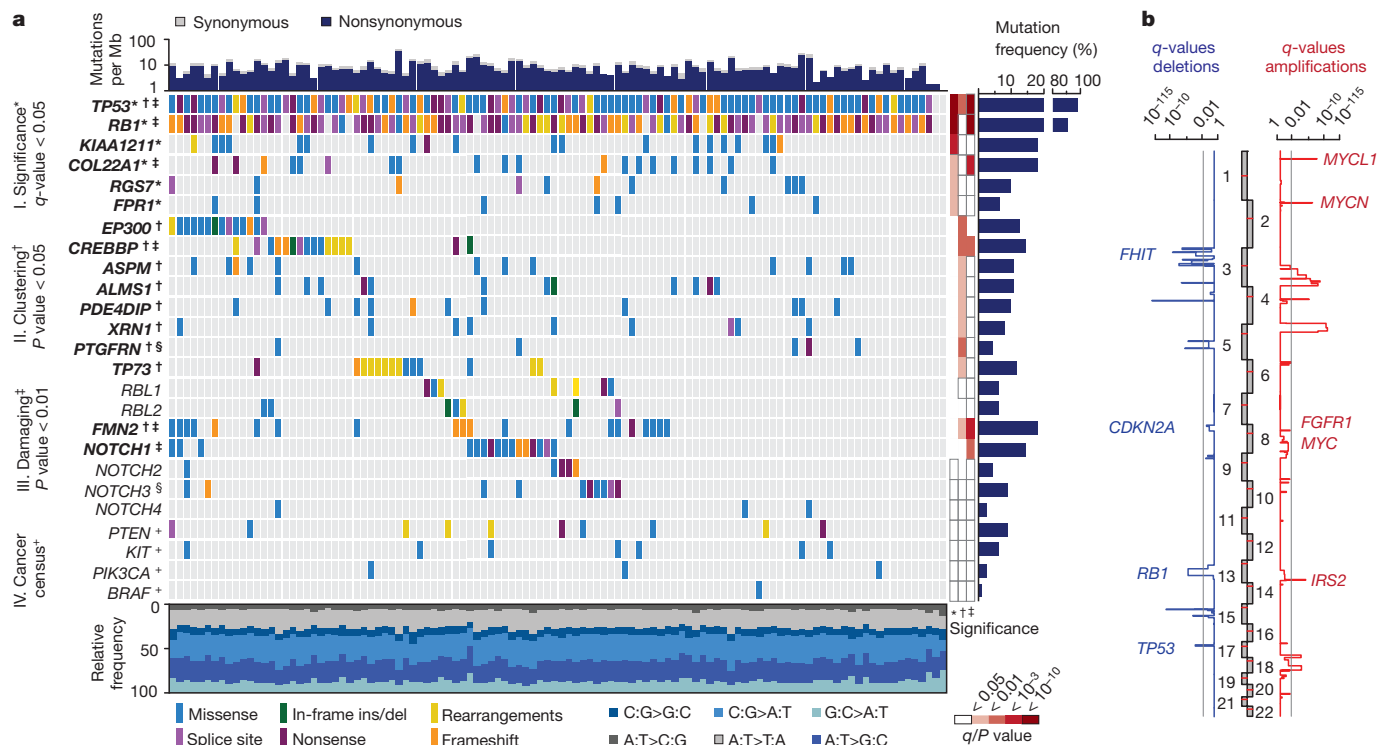


Figure 1 | Genomic alterations in small cell lung cancer. **a**, Tumour samples are arranged from left to right. Alterations of SCLC candidate genes are annotated for each sample according to the colour panel below the image. The somatic mutation frequencies for each candidate gene are plotted on the right panel. Mutation rates and type of base-pair substitution are displayed in the top and bottom panel, respectively. Significant candidate genes are highlighted in bold (*corrected q -values < 0.05, † P < 0.05, ‡ P < 0.01). The

frequently affected by genetic alterations in human cancers (that is, genes in the Cancer Gene Census¹⁴ and COSMIC¹⁵ database).

Among the significantly mutated genes (I), (q -values < 0.05, Methods) were *TP53* and *RB1* (refs 4–7), *KIAA1211* and *COL22A1*, as well as *RGS7* and *FPR1*, both of which are involved in G-protein-coupled receptor signalling (Fig. 1a).

Locally clustered mutations (II) are indicative of functional selection (P < 0.05, Supplementary Table 6, Methods)^{2,16}. Of all genes, Fig. 1a lists those alterations that occurred in more than 8% of the samples, were otherwise affected by recurrent genomic rearrangements (Supplementary Table 4), or were mutated in *Trp53*^{-/-}, *Rb1*^{-/-} or *Trp53*^{-/-}, *Rb1*^{-/-}, *Rbl2*^{-/-} SCLC tumours arising in mice^{8,9} (Supplementary Table 5). Confirming previous results and our analytical strategy, the histone acetyltransferase genes *CREBBP* and *EP300* exhibited significantly clustered mutations and recurrent inactivating translocations (Fig. 1a and Extended Data Fig. 3c)^{2,3}. Furthermore, significant mutation clustering occurred in genes with functional roles in the centrosome (*ASPM*, *ALMS1* and *PDE4DIP*), in the RNA-regulating gene *XRN1* and the tetraspanin gene *PTGFRN*; the latter was also mutated in murine SCLC (Extended Data Fig. 3c). The *TP53* homologue *TP73*, which was also affected by recurrent somatic rearrangements (Fig. 1a), also showed clustered mutations.

In the group of significantly damaged genes (III) we also found *TP53*, *RB1*, *CREBBP* and *COL22A1*, further highlighting their likely biological relevance in SCLC. Additional inactivating mutations occurred in *FMN2* and *NOTCH1* (P < 0.01). *NOTCH* family genes were recurrently mutated with a pattern of frequent inactivation. *Notch3* was also mutated in a *Trp53*^{-/-}, *Rb1*^{-/-}, *Rbl2*^{-/-} mouse tumour (Fig. 1a, Supplementary Table 5 and Methods).

Of the genes with an established role in murine SCLC (IV), we confirmed *PTEN*^{10,17}. *RBL1* and *RBL2*, which are closely related to *RB1* (ref. 9), similarly exhibited inactivating translocations and

respective level of significance is displayed as a heatmap on the right panel. Genes that are also mutated in murine SCLC tumours are denoted with a § symbol. Mutated cancer census genes of therapeutic relevance are denoted with a + symbol. **b**, Somatic copy number alterations determined for 142 human SCLC tumours by single nucleotide polymorphism (SNP) arrays. Significant amplifications (red) and deletions (blue) were determined for the chromosomal regions and are plotted as q -values (significance < 0.05).

mutations (Fig. 1a, Extended Data Fig. 3d and Supplementary Table 4). Mice with inactivation of *Trp53*, *Rb1* and *Rbl2* develop SCLC with shorter latency than mice lacking *Trp53* and *Rb1* alone⁹, thus validating *RBL2* as another accessory tumour suppressor in SCLC.

Given the lack of therapeutic options in SCLC, we sought mutations that are known oncogenic drivers in other cancers and sometimes associated with response to targeted drugs (V)^{14,15}. Of these, we found mutations in four tumours with a potential therapeutic implication, including mutations in *BRAF*¹⁸, *KIT*^{19,20} and *PIK3CA*²¹ (Extended Data Fig. 3e). Thus, genotyping of SCLC patients may reveal individual patients who might have a possible benefit from targeted therapeutic intervention.

Across these five categories, mutations in *CREBBP*, *EP300*, *TP73*, *RBL1*, *RBL2* and *NOTCH* family genes were largely mutually exclusive (Fig. 1a), suggesting that they may exert similar pro-tumorigenic functions in the development of SCLC. We did not observe significant correlations of global mutational signatures (for example, predominance of C:G>A:T transversions) with the mutational status of these genes (Extended Data Fig. 2b). Furthermore, mutations in these genes were not significantly associated with the total number of mutations, overall survival or other clinical parameters (Extended Data Fig. 4). The mutation status of 22 of the most frequently mutated genes was confirmed in an independent data set (Methods and Supplementary Table 7).

By analysing somatic copy number alterations, we confirmed previously known genomic losses within 3p pointing to focal events on 3p14.3–3p14.2 (harbouring *FHIT*⁵) and 3p12.3–3p12.2 (harbouring *ROBO1* (ref. 22)) (Fig. 1b, Extended Data Fig. 5a and Supplementary Table 8)^{5,22,23}. *FHIT* expression was also reduced in cases with focal deletions (Extended Data Fig. 5b). In addition to homozygous losses in the *CDKN2A* locus (Extended Data Fig. 5c), amplification of the *MYC* family genes⁵, *MYCL1*, *MYCN* and *MYC*, as well as of the

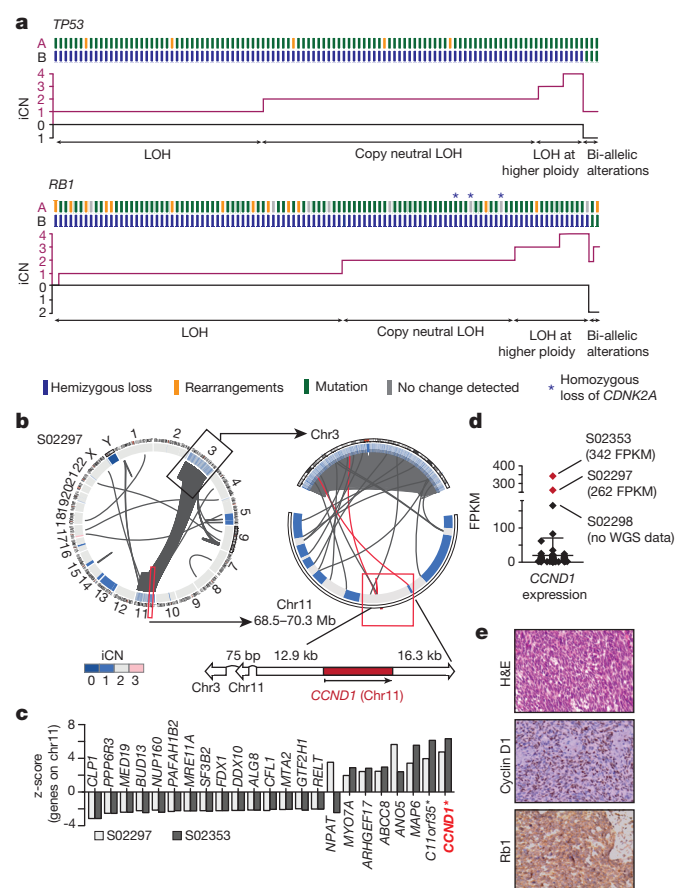


Figure 2 | Universal bi-allelic inactivation of *TP53* and *RB1* in human SCLC. **a**, Alterations of *TP53* and *RB1* were determined based on whole-genome sequencing data of 108 SCLC cases. Samples are plotted from left to right. Alleles A and B are represented for each case and colour-coded according to the somatic alteration. The integral copy number (iCN) state of each allele is plotted; hemizygous losses are annotated as loss of heterozygosity (LOH), copy-neutral LOH or LOH at higher ploidy. Samples retaining allele A and B show alterations on both alleles (bi-allelic alterations). **b**, Circos plot of case S02297 showing intra- and interchromosomal translocations between chromosome 3 and 11. The copy number state of the respective chromosomal regions (iCN) is plotted as a heatmap. The genomic context of *CCND1* (on chromosome 11) is highlighted. **c**, Significantly differentially expressed genes encoded on chromosome 11 are analysed in both chromothripsis cases in comparison to all other tumours. Positive and negative z-scores show upregulation and downregulation of genes, respectively ($P < 0.05$; * q -value < 0.05). **d**, Distribution of *CCND1* expression over 81 SCLC samples. Chromothripsis cases are highlighted in red. **e**, Haematoxylin and eosin (H&E) and immunohistochemistry staining for cyclin D1 and Rb1 for sample S02297. Original magnification, $\times 400$.

tyrosine kinase gene, *FGFR1* (refs 2, 24), and *IRS2* were recurrent genomic events (Fig. 1b). Focal *IRS2* amplifications occurred in 2% of the cases (Extended Data Fig. 5d, e).

Universal inactivation of *TP53* and *RB1*

Inactivating mutations in *TP53* and *RB1* have been shown to affect up to 90% and up to 65% of SCLC, respectively^{2–7}. By contrast, our whole-genome sequencing analyses revealed that both genes were altered in all but two cases that exhibited signs of chromothripsis²⁵ (Figs 1 and 2). *TP53* and *RB1* alterations were mostly inactivating (Supplementary Table 9 and Extended Data Fig. 6a). Missense mutations in *TP53* affected the functionally critical DNA binding domain, while *RB1* was frequently altered by complex genomic translocations. Many mutations in *RB1* occurred at exon–intron junctions, which caused protein-damaging splice events as confirmed by transcriptome

sequencing (Extended Data Fig. 6b–e and Supplementary Tables 10 and 11). In the 108 tumours without chromothripsis, *TP53* and *RB1* had bi-allelic losses in 100% and 93% of the cases, respectively. Inactivating events included mutations, translocations, homozygous deletions, hemizygous losses, copy-neutral losses of heterozygosity (LOH) and LOH at higher ploidy (Fig. 2a, Extended Data Fig. 6 and Supplementary Table 9). Loss of *CDKN2A* occurred in cases with both bi-allelic inactivation of *TP53* and *RB1* and hemizygous loss of *RB1* (Fig. 2a). Although emerging data supports a continuum model of inactivation of tumour suppressors across multiple cancers, *TP53* and *RB1* follow the classical discrete ‘two-hit paradigm’ pattern of Knudson-type tumour suppressors in SCLC^{26,27}.

The two tumours affected by chromothripsis displayed a similar pattern of massive genomic rearrangements between chromosomes 3 and 11 (Fig. 2b and Extended Data Fig. 7a), but lacked shared fusion transcripts in the transcriptome sequencing data, suggesting that a particular fusion is not a common target (Extended Data Fig. 7b and Supplementary Table 12). Of the genes on chromosomes 3 and 11, *CCND1* (encoding cyclin D1) was retained (Fig. 2b and Extended Data Fig. 7a) resulting in significant *CCND1* overexpression in both tumours, but not in the other SCLC specimens (Fig. 2c, d and Supplementary Table 13). Immunohistochemistry confirmed high expression of cyclin D1 and a lack of nuclear Rb1 (Fig. 2e, Extended Data Fig. 7c). There were fewer proliferating Ki67-positive cells in these two cases. As cyclin D1 negatively regulates Rb family proteins²⁸, these findings suggest that chromothripsis in cases with wild-type *RB1* may compensate for genomic loss of *RB1*.

Together, our findings provide evidence for the notion that complete genomic loss of both *TP53* and *RB1* function is obligatory in the pathogenesis of SCLC.

Oncogenic genomic events affecting *TP73*

We analysed the genome sequencing data for the presence of clustered chromosomal breakpoints that may indicate a common biological target (Supplementary Table 14)²⁹ and found 5 major clusters affecting *RB1*, as well as regions on chromosomes 1, 3 (3q26), 6 (affecting *CDKAL1*) and 22 (Fig. 3a). Breakpoints in chromosome 22 caused inactivating translocations of *TTC28* (Extended Data Fig. 8a)³⁰. Breakpoints also clustered downstream of the L1HS retrotransposon in SCLC, further supporting a role for this element in cancer^{31,32}, (Extended Data Fig. 8b). Breakpoints on chromosomes 3, 6 and 22 did not result in changes of expression of the affected genes (Supplementary Table 10).

By contrast, genomic breakpoints affecting chromosome 1 clustered precisely in the *TP73* locus in 7% of the cases ($n = 8$). To our surprise, several breakpoints were recurrently located in introns 1, 2 and 3 of *TP73*. In two cases, breakpoints led to complex intrachromosomal rearrangements (Extended Data Fig. 8c and Supplementary Table 4), while the majority of breaks caused intragenic fusions and, thus, exclusion of either exon 2, or exons 2 and 3, which were all somatic (Fig. 3b and Extended Data Fig. 8d). Some rearrangements were copy-neutral events, while others occurred on the background of copy number gains (Extended Data Fig. 8e). One tumour sample revealed genomic exclusion of exon 10 (Fig. 3b). Analyses of transcriptome sequencing data confirmed that these rearrangements created the N-terminally truncated transcript variants p73 Δ ex2 and p73 Δ ex2/3, as well as p73 Δ ex10 (ref. 33) (Fig. 3c, d and Supplementary Table 11). Genomic validation and comparative profiling of transcript variants confirmed that p73 Δ ex2/3 were not naturally occurring splice variants in SCLC and were only found in cases with genomic rearrangements (Fig. 3d and Supplementary Table 11). Some tumours expressed p73 Δ ex2, in which we failed to identify genomic rearrangements (Supplementary Table 11).

p73 Δ ex2 and p73 Δ ex2/3 lack a fully competent transactivation domain and are known tumour-derived variants of *TP73* (ref. 33). p73 with N-terminal truncations has dominant negative functions

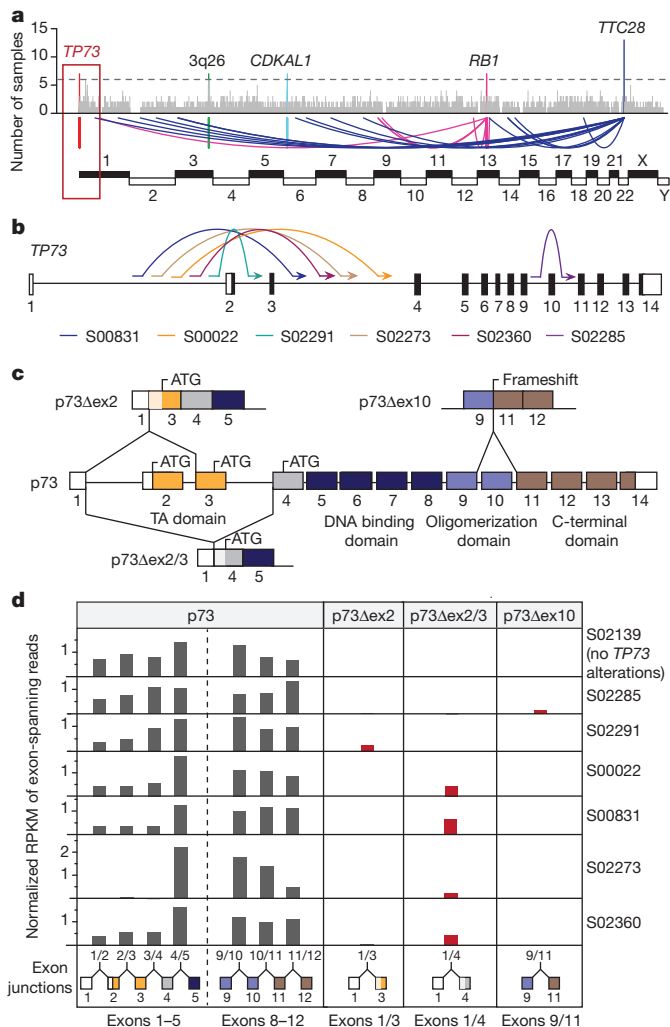


Figure 3 | Recurrent rearrangements generating oncogenic variants of *TP73*. **a**, Genomic breakpoints identified by whole-genome sequencing were mapped to their chromosomal locations. Recurrent breakpoints ($n > 6$ samples) are highlighted in colours. **b**, Schematic representation of the *TP73* locus (hg19) illustrating intragenic translocations. Coding and non-coding regions of the annotated exons are shown as black and white boxes, respectively. **c**, Schematic representation of exons encoding p73, p73Δex2, p73Δex2/3 and p73Δex10. **d**, Exon skipping events were assessed in the transcriptome data of samples with genomic translocations resulting in p73Δex2, p73Δex2/3 and p73Δex10 transcript variants. S02139 served as a reference sample without *TP73* alterations. The expression of uncommon exon combinations is highlighted in red.

on wild-type p73 and p53, and is a confirmed oncogene *in vivo*^{34,35}. p73Δex10 results in an early stop codon; C-terminal truncations can similarly exert dominant-negative effects on wild-type p73 (ref. 33).

Altogether, *TP73* was somatically altered by mutations and genomic rearrangements in 13% of the cases (Fig. 1 and Extended Data Fig. 8c–e). To our knowledge, this is the first study describing p73Δex2/3 variants to emerge as a consequence of precise genomic rearrangements.

Tumour suppressive roles of Notch in SCLC

In an unsupervised hierarchical clustering analysis of transcriptome sequencing data (Methods), we observed two major clusters of SCLC tumours (Fig. 4a and Extended Data Fig. 9a). The majority (77%, $n = 53/69$) of tumours exhibited high expression of the neuroendocrine markers *CHGA* (chromogranin A)¹ and *GRP* (gastrin releasing peptide)⁵, had high levels of *DLK1* (ref. 36), a non-canonical inhibitor of Notch signalling³⁶, and *ASCL1*, a lineage oncogene of neuroendo-

crine cells whose expression is inhibited by active Notch signalling (Extended Data Fig. 9b)^{37,38}. The remaining cases (23%, $n = 16/69$) also expressed *SYP* (synaptophysin) or *NCAM1* (CD56), thus confirming that all tumours were of the typical SCLC subtype¹ (Extended Data Fig. 9c). Furthermore, no significant difference in the distribution of the major known SCLC mutations (for example, *TP53*, *RB1* or *CREBBP*) existed between the two transcriptional subtypes (Extended Data Fig. 9a). Thus, although all SCLC tumours shared the most frequent mutations as well as key neuroendocrine markers, the majority had a gene expression pattern suggestive of low Notch pathway activity (high levels of *ASCL1* and *DLK1*).

Mutations affected *NOTCH* family genes in both human and murine SCLC (Fig. 1a and Supplementary Table 5). The mutations did not cluster significantly in any individual domains, but frequent damaging mutations occurred in the extracellular domain (Fig. 4b and Extended Data Fig. 10a), suggesting that *NOTCH* may be a tumour suppressor in SCLC. Overall, the *NOTCH* family was affected by genomic alterations in 25% of human SCLC (Fig. 1).

Based on these observations and emerging evidence that activation of Notch signalling may inhibit the expansion of neuroendocrine tumour cells^{39,40}, we examined the consequences of Notch pathway activation in *Trp53;Rb1;Rbl2* conditional triple-knockout (TKO) mice⁹. We crossed *Rosa26^{Lox-stop-Lox-Notch2ICD}* (*LSL-N2ICD*) mice that conditionally express an activated form of Notch2 (Notch2 intracellular domain, N2ICD) to TKO mice and found a significant reduction in the number of tumours that arose in the presence of N2ICD ($P < 0.001$; Fig. 4c). Similar results were obtained upon activation of Notch1, reflecting a general inhibition of SCLC initiation by active Notch signalling (Extended Data Fig. 10b). The recombination efficiency of an innocuous inducible reporter allele (*Rosa26^{mT/mG}*) by Cre was much greater than that of the *N2ICD* allele, providing further support for a strong negative selection against active Notch signalling during SCLC development (Extended Data Fig. 10c–e). Importantly, the inhibitory effects of Notch observed in the early stages of tumorigenesis correlated with a prolongation of survival of the mutant mice expressing N2ICD (Fig. 4d). Similarly, ectopic expression of N1ICD in both mouse and human SCLC cell lines significantly inhibited their growth (Fig. 4e and Extended Data Fig. 10f).

SCLC tumours in TKO mice showed typical patterns of neuroendocrine differentiation with high expression of synaptophysin and *Ascl1*. Consistent with the notion that Notch regulates neuroendocrine differentiation in SCLC, overexpression of N2ICD resulted in the upregulation of *Hes1* and abrogated expression of neuroendocrine markers (Extended Data Fig. 10g). Similarly, N1ICD induced upregulation of Notch targets (for example, *Hes1*, *Hey1*, *Hey2*) in murine SCLC cells (Fig. 4f, Extended Data Fig. 10h and Supplementary Table 15), as well as gene expression signatures consistent with cell cycle inhibition (Extended Data Fig. 10i). Ectopic expression of N1ICD inhibited cell cycle progression in murine and human SCLC cell lines (Extended Data Fig. 10j, k). This cell cycle inhibition is reminiscent of what has been seen in other contexts where Notch activation acts as a tumour suppressor^{41,42}.

Altogether, our analyses involving genome and transcriptome sequencing of human and murine SCLC tumours, as well as studies in genetically manipulated mice, identify and validate Notch as a tumour suppressor and master regulator of neuroendocrine differentiation in SCLC.

Discussion

Here we provide a comprehensive analysis of somatic genome alterations in SCLC, identifying many novel candidate genes, some of which may have therapeutic implications. Such alterations with immediate therapeutic consequences are rare but present in SCLC (for example, in *BRAF* or *KIT*), suggesting that individual patients may benefit from genotyping and subsequent targeted kinase inhibitor therapy. We further discovered recurrent expression of p73Δex2/3 in SCLC and

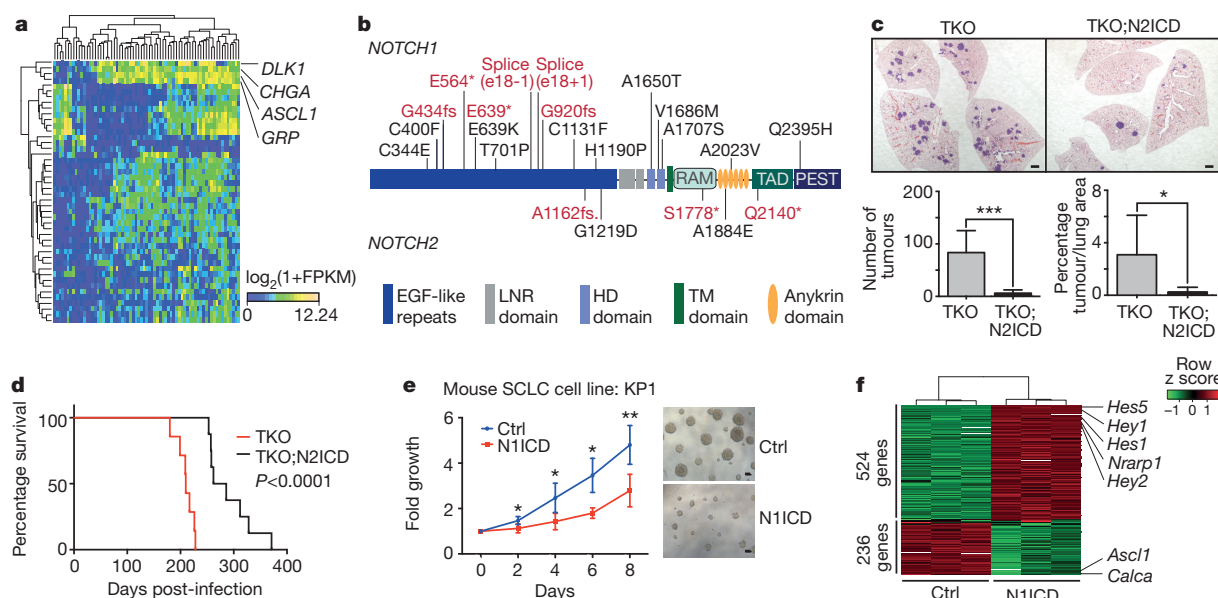


Figure 4 | Notch is a tumour suppressor and a key regulator of neuroendocrine differentiation in SCLC. **a**, Unsupervised expression analysis of human SCLC tumours. Tumour samples are arranged in columns and grouped by the expression of differentially expressed genes (rows). Expression values are represented as a heatmap; yellow and blue indicate high and low expression, respectively. **b**, Schematic representation of *NOTCH1* and *NOTCH2*. Somatic mutations are mapped to the respective protein domains. Damaging and missense mutations are highlighted in red and black, respectively. **c**, Representative H&E images of lungs from *Trp53;Rb1;Rb2* triple-knockout (TKO) or TKO;N2ICD (Notch2) mice collected 3 months after Ad-Cre instillation. Scale bar, 1 mm. Tumours were quantified for each genotype ($n = 8$). Statistical significance was determined by two-tailed unpaired Student's *t*-test. **d**, Survival analysis of TKO ($n = 7$, median

survival = 210 days) and TKO;N2ICD ($n = 8$, median survival = 274 days) mice. Statistical significance was determined by log-rank test. **e**, Cell viability assay of the murine SCLC cell line KP1 transfected with a N1ICD (Notch1) expression plasmid or empty vector control (Ctrl) (3 independent biological replicates with 3 technical replicates each). Fold growth is normalized to day 0; representative images were taken on day 8. Scale bar, 50 μ m. Statistical significance was determined by two-tailed paired Student's *t*-test. **f**, Mouse SCLC cells were transfected with control or N1ICD and analysed 48 h after transfection by gene expression microarrays. The heatmap describes differentially expressed genes in control or N1ICD-transfected cells ($n = 3$, each); red and green indicate high and low expression, respectively. * $P < 0.05$; ** $P < 0.01$; *** $P < 0.001$. Data are represented as mean \pm s.d.

established a genetic mechanistic basis for this oncogenic variant. *TP73 Δ ex2/3* has recently been demonstrated to function as an oncogene^{34,35} and therapeutic options were identified to restrict p73-dependent tumour growth *in vivo*, including in *Trp53*-deficient tumours³⁵. Given the frequent occurrence of genomic *TP73* alterations in SCLC, such approaches may potentially be promising in SCLC tumours. Our results furthermore provide proof for universal

bi-allelic inactivation of *TP53* and *RB1*, thereby establishing these two genes as obligatory tumour suppressors in SCLC.

Our genomic analyses also identified *NOTCH* family genes as tumour suppressors and master regulators of neuroendocrine differentiation in SCLC, and we validated this finding *in vivo* in a pre-clinical mouse model of this disease. Our observations may thus provide an initial link between Notch and the neuroendocrine phenotype in SCLC. In contrast to the involvement of *TP73* and *NOTCH* family genes (Fig. 5), the functional role of most of the other newly discovered genes (for example, *KIAA1211*, *COL22A1*, *ASPM*, *PDE4DIP* or *PTGFRN*) is much less clear. Although our analytical filters support their involvement in the tumour pathogenesis, functional experiments will be required to clarify their biological role.

In summary, we have provided the first, to our knowledge, comprehensive genomic analysis of SCLC, implicating several previously unknown genes and biological processes (Fig. 5) in the pathogenesis of this disease as possible targets for more efficacious targeted therapeutic intervention against this deadly cancer.

Online Content Methods, along with any additional Extended Data display items and Source Data, are available in the online version of the paper; references unique to these sections appear only in the online paper.

Received 15 January; accepted 15 June 2015.

Published online 13 July 2015.

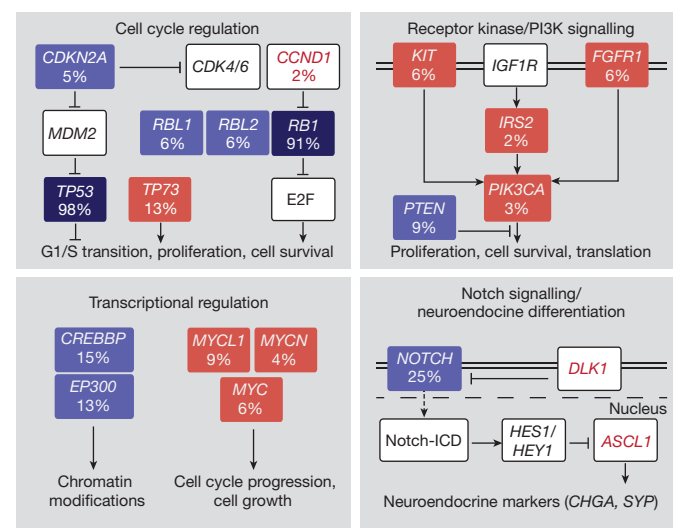


Figure 5 | Signalling pathways recurrently affected in SCLC. Red and blue boxes denote genes with activating and inactivating alterations, respectively. Deep blue boxes highlight the bi-allelic inactivation of *TP53* and *RB1*. Genes found expressed at high levels are shown in red font.

- van Meerbeeck, J. P., Fennell, D. A. & De Ruyscher, D. K. Small-cell lung cancer. *Lancet* **378**, 1741–1755 (2011).
- Peifer, M. *et al.* Integrative genome analyses identify key somatic driver mutations of small-cell lung cancer. *Nature Genet.* **44**, 1104–1110 (2012).
- Rudin, C. M. *et al.* Comprehensive genomic analysis identifies *SOX2* as a frequently amplified gene in small-cell lung cancer. *Nature Genet.* **44**, 1111–1116 (2012).
- Takahashi, T. *et al.* p53: a frequent target for genetic abnormalities in lung cancer. *Science* **246**, 491–494 (1989).

5. Wistuba, I. I., Gazdar, A. F. & Minna, J. D. Molecular genetics of small cell lung carcinoma. *Semin. Oncol.* **28**, 3–13 (2001).
6. Horowitz, J. M. *et al.* Frequent inactivation of the retinoblastoma anti-oncogene is restricted to a subset of human tumor cells. *Proc. Natl Acad. Sci. USA* **87**, 2775–2779 (1990).
7. Mori, N. *et al.* Variable mutations of the RB gene in small-cell lung carcinoma. *Oncogene* **5**, 1713–1717 (1990).
8. Meuwissen, R. *et al.* Induction of small cell lung cancer by somatic inactivation of both Trp53 and Rb1 in a conditional mouse model. *Cancer Cell* **4**, 181–189 (2003).
9. Schaffer, B. E. *et al.* Loss of p130 accelerates tumor development in a mouse model for human small-cell lung carcinoma. *Cancer Res.* **70**, 3877–3883 (2010).
10. McFadden, D. G. *et al.* Genetic and clonal dissection of murine small cell lung carcinoma progression by genome sequencing. *Cell* **156**, 1298–1311 (2014).
11. Imielinski, M. *et al.* Mapping the hallmarks of lung adenocarcinoma with massively parallel sequencing. *Cell* **150**, 1107–1120 (2012).
12. Zhang, J. *et al.* Intratumor heterogeneity in localized lung adenocarcinomas delineated by multiregion sequencing. *Science* **346**, 256–259 (2014).
13. de Bruin, E. C. *et al.* Spatial and temporal diversity in genomic instability processes defines lung cancer evolution. *Science* **346**, 251–256 (2014).
14. Futreal, P. A. *et al.* A census of human cancer genes. *Nature Rev. Cancer* **4**, 177–183 (2004).
15. Forbes, S. A. *et al.* COSMIC: exploring the world's knowledge of somatic mutations in human cancer. *Nucleic Acids Res.* **43**, D805–D811 (2015).
16. Lawrence, M. S. *et al.* Mutational heterogeneity in cancer and the search for new cancer-associated genes. *Nature* **499**, 214–218 (2013).
17. Yokomizo, A. *et al.* PTEN/MMAC1 mutations identified in small cell, but not in non-small cell lung cancers. *Oncogene* **17**, 475–479 (1998).
18. Holderfield, M., Deuker, M. M., McCormick, F. & McMahon, M. Targeting RAF kinases for cancer therapy: BRAF-mutated melanoma and beyond. *Nature Rev. Cancer* **14**, 455–467 (2014).
19. Hibi, K. *et al.* Coexpression of the stem cell factor and the c-kit genes in small-cell lung cancer. *Oncogene* **6**, 2291–2296 (1991).
20. Hirota, S. *et al.* Gain-of-function mutations of c-kit in human gastrointestinal stromal tumors. *Science* **279**, 577–580 (1998).
21. Shibata, T., Kokubu, A., Tsuta, K. & Hirohashi, S. Oncogenic mutation of *PIK3CA* in small cell lung carcinoma: a potential therapeutic target pathway for chemotherapy-resistant lung cancer. *Cancer Lett.* **283**, 203–211 (2009).
22. Angeloni, D. *et al.* Analysis of a new homozygous deletion in the tumor suppressor region at 3p12.3 reveals two novel intronic noncoding RNA genes. *Genes Chromosomes. Cancer* **45**, 676–691 (2006).
23. Kovatich, A. *et al.* Molecular alterations to human chromosome 3p loci in neuroendocrine lung tumors. *Cancer* **83**, 1109–1117 (1998).
24. Weiss, J. *et al.* Frequent and focal *FGFR1* amplification associates with therapeutically tractable *FGFR1* dependency in squamous cell lung cancer. *Sci. Transl. Med.* **2**, 62ra93 (2010).
25. Korbel, J. O. & Campbell, P. J. Criteria for inference of chromothripsis in cancer genomes. *Cell* **152**, 1226–1236 (2013).
26. Knudson, A. G. Two genetic hits (more or less) to cancer. *1, Nature Rev. Genet.* **1**, 157–162 (2001).
27. Berger, A. H., Knudson, A. G. & Pandolfi, P. P. A continuum model for tumour suppression. *Nature* **476**, 163–169 (2011).
28. Beasley, M. B. *et al.* The P16/cyclin D1/Rb pathway in neuroendocrine tumors of the lung. *Hum. Pathol.* **34**, 136–142 (2003).
29. Northcott, P. A. *et al.* Enhancer hijacking activates *GF11* family oncogenes in medulloblastoma. *Nature* **511**, 428–434 (2014).
30. The Cancer Genome Atlas Network. Comprehensive molecular characterization of human colon and rectal cancer. *Nature* **487**, 330–337 (2012).
31. Pitkänen, E., Cajuso, T., Katainen, R., Kaasinen, E. & Välimäki, N. Frequent L1 retrotranspositions originating from *TTC28* in colorectal cancer. *Oncotarget* **5**, 853–859 (2014).
32. Helman, E., Lawrence, M. L. & Stewart, C. Somatic retrotransposition in human cancer revealed by whole-genome and exome sequencing. *Genome Res.* **24**, 1053–1063 (2014).
33. Jancalek, R. The role of the *TP73* gene and its transcripts in neuro-oncology. *Br. J. Neurosurg.* **28**, 598–605 (2014).
34. Tannapfel, A. *et al.* Autonomous growth and hepatocarcinogenesis in transgenic mice expressing the p53 family inhibitor DNP73. *Carcinogenesis* **29**, 211–218 (2008).
35. Venkatanarayan, A. *et al.* IAPP-driven metabolic reprogramming induces regression of p53-deficient tumours *in vivo*. *Nature* **517**, 626–630 (2015).
36. Falix, F. A., Aronson, D. C., Lamers, W. H. & Gaemers, I. C. Possible roles of *DLK1* in the Notch pathway during development and disease. *Biochim. Biophys. Acta* **1822**, 988–995 (2012).
37. Ball, D. W. Achaete-scute homolog-1 and Notch in lung neuroendocrine development and cancer. *Cancer Lett.* **204**, 159–169 (2004).
38. Augustyn, A. *et al.* *ASCL1* is a lineage oncogene providing therapeutic targets for high-grade neuroendocrine lung cancers. *Proc. Natl Acad. Sci. USA* **111**, 14788–14793 (2014).
39. Sriuranpong, V. *et al.* Notch signaling induces cell cycle arrest in small cell lung cancer cells. *Cancer Res.* **1**, 3200–3205 (2001).
40. Wael, H. *et al.* Notch1 signaling controls cell proliferation, apoptosis and differentiation in lung carcinoma. *Lung Cancer* **85**, 131–140 (2014).
41. Rangarajan, A. *et al.* Notch signaling is a direct determinant of keratinocyte growth arrest and entry into differentiation. *EMBO J.* **20**, 3427–3436 (2001).
42. Qi, R. *et al.* Notch1 signaling inhibits growth of human hepatocellular carcinoma through induction of cell cycle arrest and apoptosis. *Cancer Res.* **63**, 8323–8329 (2003).

Supplementary Information is available in the online version of the paper.

Acknowledgements We are grateful to all the patients who contributed their tumour specimens. We thank the computing center of the University of Cologne (RRZK) for providing the CPU time on the DFG-funded supercomputer ‘CHEOPS’, as well as for the support. We thank S. Artavanis-Tsakonas and S. Fre for the gift of the mice with inducible NICD expression. We thank C. Nguyen, J. Berg, J. Heuckmann, F. Malchers, C. Lovely and A. Bernsheim for scientific discussions and advice. We thank Genentech/gRED for providing raw sequencing data from a previously published study³. Some tumors in these studies were provided by the LungBiobank Heidelberg, member of the NCT-Tissue bank, the biomaterial bank Heidelberg and the biobank platform of the German Center for Lung Research, Heidelberg, Germany. This work was supported by the German Cancer Aid (Deutsche Krebshilfe) as part of the small cell lung cancer genome sequencing consortium (grant ID: 109679 to R.K.T., M.P., R.B., P.N., M.V. and S.A.H.). Further support was provided by the Korea Research Foundation (KRF 2011-0030105; grant to S.J.J.). Additional funding was provided by the NIH (5R01CA114102-08 to J.S.), the German Ministry of Science and Education (BMBF) as part of the NGFNplus program (grant 01GS08101 to R.K.T., J.W. and P.N.) and as part of the e:Med program (grant no. 01ZX1303A to R.K.T., J.W., C.R., R.B. and M.P. and grant no. 01ZX1406 to M.P.), by the Deutsche Forschungsgemeinschaft (DFG; through TH1386/3-1 to R.K.T. and KFO-286 to P.N.), by the German federal state North Rhine Westphalia (NRW), by the European Union (European Regional Development Fund: Investing In Your Future) as part of the PerMed NRW initiative (grant 005-1111-0025 to R.K.T., J.W. and R.B.), by SFB832 (TP6 to R.K.T., TP5 to L.C.H.), by the Deutsche Krebshilfe as part of the Oncology Centers of Excellence funding program (to R.B., R.K.T. and M.S.), by the EU-Framework program CURELUNG (HEALTH-F2-2010-258677 to R.K.T., J.W., J.K.F., L.R., M.S.C. and E.B.), by Stand Up To Cancer—American Association of Cancer Research Innovative Research Grant (SU2C-AACR-IR60109 to R.K.T.), by the German Consortium for Translational Cancer Research (DKTK) Joint Funding program, by the National Cancer Center Research and Development Fund (NCC Biobank: 23A-1, to T.K., J.Y. and R.I.), by the Italian Ministry of Health (Ricerca Corrente RC1303LO57 and GR program 2010-2316264 to L.A.M.), by the Roy Castle Lung Cancer Foundation UK (to J.K.F.), by the AIRC/MGAF grant 12983 (to L.A.M.) and by A*STAR in Singapore (scholarship to J.S.). J.S. is the Harriet and Mary Zelencik Scientist in Children's Cancer and Blood Diseases.

Author Contributions J.G., J.S.L., M.P., J.S. and R.K.T. conceived the project, analysed and interpreted the data, and wrote the manuscript. J.G., J.S.L., J.S., F.L., R.M., S.P., D.E., B.Pü, M.S.W., J.O.K., J.A., C.B., M.B. and P.S. designed experiments. J.G., J.S.L., I.D., C.M., A.T., R.M., S.-M.C., D.K., D.E., I.V., D.S., B.Pi, P.S., C.B., P.M.S. and M.Bog performed experiments. J.G., M.P., J.S.L., S.A.H., M.V., M.S.W., J.O.K., Y.C., X.L., D.V., M.W., N.H. and M.Bos performed data analysis. E.B., W.D.T., R.B., L.H., L.O., S.P., S.J.J. and G.K. performed pathology review. E.B., W.D.T., L.O., A.N.K., Y.Y. and V.T. conducted further immunohistochemistry studies. F.L., L.F.-C., G.B., S.M., D.S., V.A., U.L., T.Z., S.A., M.H., J.W., P.N. and C.R. helped with logistics. S.J.J., N.S.J., K.-S.P., D.Y., J.Y., T.K., R.I., K.T., M.N., T.M., H.H., P.A.S., I.P., Y.C., A.S., C.-M.C., Y.-H.K., P.P.M., Y.Z., D.J., M.K., G.M.W., P.A.R., B.S., I.K., M.L., L.A.M., A.I.T., J.K.F., M.J., J.Kn., E.C.-V., L.R., U.P., O.-T.B., M.L.-I., E.T., J.Kö, M.Sc, J.B., M.Sa, M.S.-C., H.B.S., Y.Y., S.P., L.H., R.B. and E.B. contributed with murine and human tissue samples.

Author Information Affymetrix SNP 6.0, whole-genome, and transcriptome sequencing on human specimen have been deposited at the European Genome-phenome Archive under the accession code EGAS00001000925. Whole-exome and whole-genome sequencing data of murine SCLC tumors can be accessed through (<http://www.translational-genomics.uni-koeln.de/scientific-resources/>). Microarray data on mouse cell lines is accessible through Gene Expression Omnibus (GEO) accession number GSE69091. Reprints and permissions information is available at www.nature.com/reprints. The authors declare competing financial interests: details are available in the online version of the paper. Readers are welcome to comment on the online version of the paper. Correspondence and requests for materials should be addressed to R.K.T. (roman.thomas@uni-koeln.de), J.S. (julsage@stanford.edu) or M.P. (mpeifer@uni-koeln.de).

Julie George^{1*}, Jing Shan Lim^{2*}, Se Jin Jang³, Yupeng Cun¹, Luka Ozretić⁴, Gu Kong⁵, Frauke Leenders¹, Xin Lu¹, Lynnette Fernández-Cuesta^{1†}, Graziella Bosco¹, Christian Müller¹, Ilona Dahmen¹, Nadine S. Jahchan², Kwon-Sik Park², Dian Yang², Anthony N. Karnezis⁵, Dedeeepa Vaka², Angela Torres², Maia Segura Wang¹, Jan O. Korbel¹, Roopika Menon⁸, Sung-Min Chun³, Deokhwan Kim³, Matt Wilkerson¹⁰, Neil Hayes¹¹, David Engelmann¹², Brigitte Pützer¹², Marc Bos¹, Sebastian Michels¹³, Ignacia Vlasic¹⁴, Danila Seidel¹, Berit Pinther¹, Philipp Schaub¹, Christian Becker¹⁵, Janine Altmüller^{15,16}, Jun Yokota^{17,18}, Takashi Kohno¹⁷, Reika Iwakawa¹⁷, Koji Tsuta¹⁹, Masayuki Noguchi²⁰, Thomas Muley^{21,22}, Hans Hoffmann²¹, Philipp A. Schnabel^{22,23}, Iver Petersen²⁴, Yuan Chen²⁴, Alex Soltermann²⁵, Verena Tischler²⁵, Chang-min Choi²⁶, Yong-Hee Kim²⁷, Pierre P. Massion²⁸, Yong Zou²⁸, Dragana Jovanovic²⁹, Milica Kontić²⁹, Gavin M. Wright³⁰, Prudence A. Russell³¹, Benjamin Solomon³², Ina Koch³³, Michael Lindner³³, Lucia A. Muscarella³⁴, Annamaria la Torre³⁴, John K. Field³⁵, Marko Jakopovic³⁶, Jelena Knezevic³⁷, Esmeralda Castaños-Vélez³⁸, Luca Ros³⁹, Ugo Pastorino⁴⁰, Odd-Terje Brustugun^{41,42}, Marius Lund-Iversen⁴³, Erik Thunnissen⁴⁴, Jens Köhler^{45,46}, Martin Schuler^{45,46}, Johan Botling⁴⁷, Martin Sandelin⁴⁷, Montserrat Sanchez-Céspedes⁴⁸, Helga B. Salvesen^{49,50}, Viktor Achter⁵¹, Ulrich Lang^{51,52}, Magdalena Bogus⁵³, Peter M. Schneider⁵³, Thomas Zander⁵⁴, Sascha Ansen⁵³, Michael Hallek^{13,55}, Jürgen Wolf¹³, Martin Vingron⁵⁶, Yasushi Yatabe⁵⁷, William D. Travis⁵⁸, Peter Nürnberg^{15,55,59}, Christian Reinhardt¹⁴, Sven Perner⁹, Lukas

Heukamp⁴, Reinhard Büttner⁴, Stefan A. Haas⁵⁶, Elisabeth Brambilla⁶⁰, Martin Peifer^{1,59}, Julien Sage² & Roman K. Thomas^{1,4}

¹Department of Translational Genomics, Center of Integrated Oncology Cologne–Bonn, Medical Faculty, University of Cologne, 50931 Cologne, Germany. ²Departments of Pediatrics and Genetics, Stanford University, Stanford, California 94305, USA. ³Department of Pathology and Center for Cancer Genome Discovery, University of Ulsan College of Medicine, Asan Medical Center 88, Olympic-ro 43-gil, Songpa-gu, Seoul 138-736, Korea. ⁴Department of Pathology, University Hospital Cologne, 50937 Cologne, Germany. ⁵Department of Pathology, College of Medicine, Hanyang University, 222 Wangsimniro, Seongdong-gu, Seoul 133-791, Korea. ⁶Vancouver General Hospital, Terry Fox laboratory, Vancouver, British Columbia V5Z 1L3, Canada. ⁷European Molecular Biology Laboratory, Genome Biology Unit, 69117 Heidelberg, Germany. ⁸Institute of Pathology, Center of Integrated Oncology Cologne–Bonn, University Hospital of Bonn, 53127 Bonn, Germany. ⁹Center for Cancer Genome Discovery, University of Ulsan College of Medicine, Asan Medical Center 88, Olympic-ro 43-gil, Songpa-gu, Seoul 138-736, Korea. ¹⁰Department of Genetics, Lineberger Comprehensive Cancer Center, The University of North Carolina at Chapel Hill, North Carolina 27599-7295, USA. ¹¹UNC Lineberger Comprehensive Cancer Center School of Medicine, University of North Carolina at Chapel Hill, North Carolina 27599-7295, USA. ¹²Institute of Experimental Gene Therapy and Cancer Research, Rostock University Medical Center, 18057 Rostock, Germany. ¹³Department I of Internal Medicine, Center of Integrated Oncology Cologne–Bonn, University Hospital Cologne, 50937 Cologne, Germany. ¹⁴Department of Internal Medicine, University Hospital of Cologne, 50931 Cologne, Germany. ¹⁵Cologne Center for Genomics (CCG), University of Cologne, 50931 Cologne, Germany. ¹⁶Institute of Human Genetics, University Hospital Cologne, 50931 Cologne, Germany. ¹⁷Division of Genome Biology, National Cancer Center Research Institute, Chuo-ku, Tokyo 1040045, Japan. ¹⁸Genomics and Epigenomics of Cancer Prediction Program, Institute of Predictive and Personalized Medicine of Cancer (IMPPC), Barcelona 08916, Spain. ¹⁹Department of Pathology and Clinical Laboratories, National Cancer Center Hospital Chuo-ku, Tokyo 1040045, Japan. ²⁰Department of Pathology, Faculty of Medicine, University of Tsukuba, Ibaraki 305-8575, Japan. ²¹Thoraxklinik at University Hospital Heidelberg, Amalienstrasse 5, 69126 Heidelberg, Germany. ²²Translational Lung Research Center Heidelberg (TLRC-H), Member of German Center for Lung Research (DZL), Amalienstrasse 5, 69126 Heidelberg, Germany. ²³Institute of Pathology, University of Heidelberg, Im Neuenheimer Feld 220, 69120 Heidelberg, Germany. ²⁴Institute of Pathology, Jena University Hospital, Friedrich-Schiller-University, 07743 Jena, Germany. ²⁵Institute of Surgical Pathology, University Hospital Zürich, 8091 Zürich, Switzerland. ²⁶Department of Oncology, University of Ulsan College of Medicine, Asan Medical Center, 88, Olympic-ro 43-gil, Songpa-gu, Seoul 138-736, Korea. ²⁷Department of Thoracic and Cardiovascular Surgery, University of Ulsan College of Medicine, Asan Medical Center, 88, Olympic-ro 43-gil, Songpa-gu, Seoul 138-736, Korea. ²⁸Thoracic Program, Vanderbilt-Ingram Cancer Center PRB 640, 2220 Pierce Avenue, Nashville, Tennessee 37232, USA. ²⁹University Hospital of Pulmonology, Clinical Center of Serbia, Medical School, University of Belgrade, 11000 Belgrade, Serbia. ³⁰Department of Surgery, St. Vincent's Hospital, Peter MacCallum Cancer Centre, 3065 Melbourne, Victoria, Australia. ³¹Department of Pathology, St. Vincent's Hospital, Peter MacCallum Cancer Centre, 3065

Melbourne, Victoria, Australia. ³²Department of Haematology and Medical Oncology, Peter MacCallum Cancer Centre, 3065 Melbourne, Victoria, Australia. ³³Asklepios Biobank für Lungenerkrankungen, Comprehensive Pneumology Center Munich, Member of the German Center for Lung Research (DZL), Asklepios Fachkliniken München-Gauting 82131, Germany. ³⁴Laboratory of Oncology, IRCCS Casa Sollievo della Sofferenza, Viale Cappuccini, 71013 San Giovanni, Rotondo, Italy. ³⁵Roy Castle Lung Cancer Research Programme, Department of Molecular and Clinical Cancer Medicine, Institute of Translational Medicine, The University of Liverpool Cancer Research Centre, 200 London Road, L69 3GA Liverpool, UK. ³⁶University of Zagreb, School of Medicine, Department for Respiratory Diseases Jordanovac, University Hospital Center Zagreb, 10000 Zagreb, Croatia. ³⁷Laboratory for Translational Medicine, Rudjer Boskovic Institute, 10000 Zagreb, Croatia. ³⁸Charité Comprehensive Cancer Center, Charité Campus Mitte, 10115 Berlin, Germany. ³⁹Tumor Genomics Unit, Department of Experimental Oncology and Molecular Medicine, Fondazione IRCCS — Istituto Nazionale Tumori, Via Venezian 1, 20133 Milan, Italy. ⁴⁰Thoracic Surgery Unit, Department of Surgery, Fondazione IRCCS Istituto Nazionale Tumori, 20133 Milan, Italy. ⁴¹Institute of Clinical Medicine, Faculty of Medicine, University of Oslo, N-0424 Oslo, Norway. ⁴²Department of Oncology, Norwegian Radium Hospital, Oslo University Hospital, N-0310 Oslo, Norway. ⁴³Department of Pathology, Norwegian Radium Hospital, Oslo University Hospital, N-0310 Oslo, Norway. ⁴⁴Department of Pathology, VU University Medical Center, 1007 MB Amsterdam, The Netherlands. ⁴⁵West German Cancer Center, Department of Medical Oncology, University Hospital Essen, 45147 Essen, Germany. ⁴⁶German Cancer Consortium (DKTK), 69120 Heidelberg, Germany. ⁴⁷Departments of Immunology, Genetics and Pathology, and Medical Sciences, Respiratory, Allergy and Sleep Research, Uppsala University, 75185 Uppsala, Sweden. ⁴⁸Genes and Cancer Group, Cancer Epigenetics and Biology Program (PEBC), Bellvitge Biomedical Research Institute (IDIBELL), 08908 Hospitalet de Llobregat, Barcelona, Spain. ⁴⁹Department of Clinical Science, Center for Cancer Biomarkers, University of Bergen, N-5058 Bergen, Norway. ⁵⁰Department of Gynecology and Obstetrics, Haukeland University Hospital, N-5058 Bergen, Norway. ⁵¹Computing Center, University of Cologne, 50931 Cologne, Germany. ⁵²Department of Informatics, University of Cologne, 50931 Cologne, Germany. ⁵³Institute of Legal Medicine, University of Cologne, 50823 Cologne, Germany. ⁵⁴Gastrointestinal Cancer Group Cologne, Center of Integrated Oncology Cologne–Bonn, Department I for Internal Medicine, University Hospital of Cologne, 50937 Cologne, Germany. ⁵⁵Cologne Excellence Cluster on Cellular Stress Responses in Aging-Associated Diseases (CECAD), University of Cologne, 50931 Cologne, Germany. ⁵⁶Computational Molecular Biology Group, Max Planck Institute for Molecular Genetics, 14195 Berlin, Germany. ⁵⁷Department of Pathology and Molecular Diagnostics, Aichi Cancer Center, 464-8681 Nagoya, Japan. ⁵⁸Department of Pathology, Memorial Sloan-Kettering Cancer Center, New York 10065, USA. ⁵⁹Center for Molecular Medicine (CMMC), University of Cologne, 50931 Cologne, Germany. ⁶⁰Department of Pathology, CHU Grenoble INSERM U823, University Joseph Fourier, Institute Albert Bonniot 38043, CS10217 Grenoble, France. †Present address: Genetic Cancer Susceptibility Group, Section of Genetics, International Agency for Research on Cancer (IARC-WHO), 69008 Lyon, France.

*These authors contributed equally to this work.

METHODS

Human lung tumour specimens. The institutional review board of the University of Cologne approved this study. We collected and analysed fresh-frozen tumour samples of 152 SCLC patients, which were provided by multiple collaborating institutions as fresh-frozen tissue specimen, frozen sections or as genomic DNA extracted from fresh-frozen material (Extended Data Fig. 1). Human tumour samples were obtained from patients under IRB-approved protocols following written informed consent.

The fresh-frozen SCLC samples were primary tumours diagnosed as stage I–IV tumours, and snap-frozen after tissue sampling. All tumour samples were pathologically assessed to have a purity of at least 60% and no extensive signs of necrosis. Additionally, these tumour samples were reviewed by at least two independent expert pathologists and the diagnosis of SCLC was histomorphologically confirmed by H&E staining and immunohistochemistry for chromogranin A, synaptophysin, CD56 and Ki67. Matching normal material was provided in the form of EDTA-anticoagulated blood or adjacent non-tumorigenic lung tissue (Supplementary Table 1). The matched normal tissue was confirmed to be free of tumour contaminants by pathological assessment. Furthermore, tumour and matching normal material were confirmed to be acquired from the same patient by short tandem repeat (STR) analysis conducted at the Institute of Legal Medicine at the University of Cologne (Germany), or confirmed by subsequent SNP 6.0 array and sequencing analyses. Patient material was stored at -80°C .

Whole-genome sequencing was performed on 110 SCLC fresh-frozen tumour samples and matched normal material. Additionally, we analysed RNA-seq data of 81 SCLC primary tumours (Extended Data Fig. 1 and Supplementary Table 1), among which 20 cases were previously published^{2,43}. Furthermore, we studied the copy-number alterations of a total of 142 fresh-frozen tumour specimen by Affymetrix SNP 6.0, among which 74 cases were described before⁴⁴.

Clinical correlation studies were performed with the study cohort of 110 SCLC patients considering age of diagnosis, gender, tumour stage, surgery, treatment with chemotherapeutics, smoking status, smoking history and overall survival (Extended Data Figs 2 and 4 and Supplementary Table 1). The median follow-up time for this cohort of 110 SCLC patients was 69 months, and 31% of the patients were alive at the time of last follow-up (Extended Data Fig. 2a and Supplementary Table 1). Smoking status was available for 88% ($n = 97$) of the patients; 63% ($n = 69$) reported a smoking history amounting to a median of 45 pack-years. Patients with a known smoking history were further subcategorized to heavy smokers (>30 pack-years), average smokers (10–30 pack-years) and light/never smokers (<10 pack-years).

Primary findings on somatic mutations were further studied in a second independent cohort consisting of 112 SCLC cases. This validation cohort refers to the exome sequencing data of 28 fresh-frozen SCLC primary tumours and 9 SCLC cell lines^{2,3} which were re-analysed in this present study (Supplementary Table 7). Additionally, we performed targeted sequencing on 8 fresh-frozen and 67 formalin fixed paraffin embedded (FFPE) samples from SCLC patients (Supplementary Table 1).

Mouse SCLC models and tumour samples. Mice were maintained according to practices prescribed by the NIH (Bethesda, MD) at Stanford's Research Animal Facility, accredited by the Association for the Assessment and Accreditation of Laboratory Animal Care (AAALAC). The *Trp53;Rb1* double-knockout (DKO) and the *Trp53;Rb1;Rb2* triple-knockout (TKO) mouse models for SCLC have been previously described^{8,9}. Mice were bred onto a mixed genetic background composed of C57BL/6, 129/SvJ and 129/SvOla. SCLC tumours were induced in 8-week-old mice by intratracheal instillation with 4×10^7 plaque-forming units (p.f.u.) of adenovirus expressing the Cre recombinase (Ad-Cre, Baylor College of Medicine, Houston, TX).

Whole-genome and whole-exome sequencing was performed on 8 murine SCLC tumours isolated from DKO and TKO mice. Primary tumours and metastases were dissected, snap-frozen, and stored at -80°C . The material was pathologically confirmed to have a tumour content of at least 90%. The respective tail tissue was similarly processed and served as a normal reference for 6 tumour samples (Supplementary Table 5). Average mutation rates were calculated for cases with tumour-normal pairs ($n = 6$).

SCLC tumours expressing the activated intracellular domain (ICD) of Notch1 (Notch1 ICD, N1ICD) and Notch2 (Notch2 ICD, N2ICD) were analysed in mouse models. *Rosa26^{Lox-stop-Lox-Notch1ICD}* (*LSL-N1ICD*) or *Rosa26^{Lox-stop-Lox-Notch2ICD}* (*LSL-N2ICD*) mice were obtained from Spyros Artavanis-Tsakonas and Exelixis. These mice are similar to recently published *Rosa26^{+/LSL-Notch3ICD}* mice⁴⁵. *Rosa26^{+/LSL-N1ICD}* or *Rosa26^{+/LSL-N2ICD}* mice were crossed with TKO mice. TKO or TKO;*Rosa26^{+/LSL-N1ICD}* mice were infected with Ad-Cre at week 8 and their survival was monitored. The sample size was chosen based on our experience with these mouse models of cancer (a minimum of 3–5 mice usually ensures statistical significance if the phenotypes are robust). We used

both males and females in these experiments, littermates served as controls. Tumour initiation was studied three months after Ad-Cre instillation. The lungs were fixed and tumour burden was quantified using ImageJ software. To control for the efficiency of deletion, we also crossed TKO mice to *Rosa26^{mT/mG}* reporter mice⁴⁶. For all tumour quantifications, the investigator was blinded to the genotypes when the H&E pictures were taken, and during the quantification of tumour number and area. No samples or animals were excluded from the analyses, and no randomization was performed.

DNA and RNA extractions. Nucleic acids were extracted from fresh-frozen tissue specimen which were processed to 15–30 sections each of 20 μm thickness at a cryostat maintaining a temperature of -20°C (Leica). In the case of FFPE samples, 6–10 sections of 10 μm thickness were prepared.

DNA was extracted from fresh-frozen tissues, EDTA blood, or FFPE samples using the Gentra Puregene DNA extraction kit (Qiagen) following the protocol of the manufacturer. DNA isolates were hydrated in TE-buffer and confirmed to be of high molecular weight (>10 kb) by agarose gel electrophoresis. Genomic DNA from fresh-frozen samples with evident signs of degradation were excluded from further sequencing studies.

For RNA extractions, tissue sections were first lysed and homogenized with the Tissue Lyzer (Qiagen). Subsequent RNA extractions were performed with the Qiagen RNeasy Mini Kit according to the instructions of the manufacturer. The RNA quality was assessed at the Bioanalyzer 2100 DNA Chip 7500 (Agilent Technologies) and samples with a RNA integrity number (RIN) of over 7 were further analysed by RNA-seq.

Next-generation sequencing. All sequencing reactions were performed on an Illumina HiSeq 2000 instrument (Illumina, San Diego, CA, USA).

Whole-genome sequencing. Whole-genome sequencing was performed with DNA extracted from fresh-frozen tumour and normal material. Short insert DNA libraries were prepared with the TruSeq DNA PCRfree sample preparation kit (Illumina) for paired-end sequencing at a minimum read length of 2×100 bp. Human DNA libraries were sequenced with the aim to obtain a coverage of minimum $30\times$ for both tumour and matched normal. Murine DNA libraries of tumour and matched normal were both sequenced to a coverage of $25\times$.

Whole-exome sequencing. Whole-exome sequencing was performed on fresh-frozen tissue specimen from mice. The enrichment for the exome was performed with the SureSelectXT Mouse All Exon kit (Agilent) following the protocol of the manufacturer. The exon-enriched libraries were subjected to paired-end sequencing with a read-length of 2×100 bp. Both tumour and normal material was sequenced to a minimum coverage of $60\times$.

RNA-sequencing. RNA-sequencing (RNA-seq) was performed with RNA extracted from fresh-frozen human tumour tissue samples. cDNA libraries were prepared from poly(A) selected RNA applying the Illumina TruSeq protocol for mRNA. The libraries were then sequenced with a 2×100 bp paired-end protocol to a minimum mean coverage of $30\times$ of the annotated transcriptome.

Targeted enrichment sequencing. Targeted enrichment sequencing was performed on human FFPE and fresh-frozen tumour and normal specimen for the purpose of validating genome alterations in an independent cohort. The custom probe design was constructed with SureDesign (Agilent Technologies) enriching for the exons of 22 genes of interest. DNA libraries were prepared with the SureSelect XT reagent kit according to the manufacturer's instructions (Agilent Technologies) and sequenced with the aim to obtain a coverage of at least $200\times$.

Dideoxy sequencing for validation of somatic alterations. If available, RNA-seq or exome sequencing was used to validate somatic mutations determined by genome sequencing. Alternatively, dideoxynucleotide chain termination sequencing (Sanger sequencing) was performed to validate mutations, genomic rearrangements, and chimaeric fusion transcripts. Primer pairs were designed to amplify the target region encompassing the somatic alteration. The PCR reactions were performed either with genomic DNA, whole-genome amplified DNA or cDNA. The amplified products were subjected to Sanger sequencing and the respective electropherogram was analysed with Geneious (<http://www.geneious.com>).

Copy number analysis by Affymetrix SNP 6.0 arrays. Human DNA extracted from fresh-frozen tumour specimen was hybridized to Affymetrix Genome-Wide Human SNP array 6.0 following the manufacturer's instructions. The signal intensities were processed to analyse for chromosomal gene copy number data. Raw copy number signals and segmented copy number data were computed following the procedure described previously²⁴.

The raw, unsegmented copy number signals were used to analyse for significant copy number alterations applying the method CGARS⁴⁷. Significant amplifications were determined with the upper quantiles 0.25, 0.15, 0.1, and 0.05; deletions were computed in reference to the 0.25 lower quantile. The significance threshold was set at a q -value of 0.05 (Supplementary Table 8).

Data processing. The raw sequencing reads of human and mouse samples acquired from whole-genome, whole-exome or targeted enrichment sequencing were aligned to the respective human (NCBI37/hg19) or mouse reference genome (NCBI37/mm9). The alignment was performed with the BWA aligner⁴⁸ (version 0.6.1-r104). Concordant read-pairs were identified as potential PCR duplicates and were subsequently masked in the alignment file. The quality of the sequencing data was determined and is summarized in Supplementary Table 2.

The whole-genome sequencing data of human samples was analysed for purity and ploidy with methods previously described² (Extended Data Fig. 3a and Supplementary Table 2).

Somatic mutations and copy number alterations were determined with our in-house analysis pipeline^{2,49}. The calling of somatic mutations in human samples was further improved by filtering the identified variant against the sequencing data of more than 500 normal samples (including exome or genome sequencing data). Additionally, an estimation of human DNA library contamination was implemented to enhance sensitivity and specificity of mutation calling.

Analysis of significantly mutated and biologically relevant genes. The significance of recurrently mutated genes was analysed for the whole-genome sequencing data set of 110 human SCLC samples (Extended Data Fig. 1a).

As previously described², the analysis first estimated the background mutation rate for each gene and corrected for its expression by referring to the RNA-seq data of 81 human primary SCLC tumour specimen analysed in the present study. The analysis included those genes which had FPKM values (fragments per kilobase of exon per million fragments mapped) of over 1 in at least 50 samples. Following corrections for the occurrence of synonymous mutations, significantly mutated genes were determined with q -values of <0.05 (Fig. 1a, Extended Data Fig. 1a (filter I) and Supplementary Table 6).

Mutations that cluster within a gene are defined as a mutational hotspot similar to our previously described method². Here we used an analytical derivation of the test statistics, rather than resampling. To this end, the mutated positions are rescaled to lie within zero and one (using the protein length). Under the null hypothesis of having no particular mutational hotspot, the rescaled mutated positions are uniformly distributed between zero and one, thus its expected value is 0.5. We therefore chose the final statistics as sum over the modulus of the rescaled position minus 0.5. This allows that the distribution under the null hypothesis can analytically be calculated; hence, also the P values. The analysis was calculated for genes that were significantly mutated in at least 5% of the samples with $P < 0.05$ (Fig. 1a, Extended Data Fig. 1a (filter II) and Supplementary Table 6). In order to further filter for the genes of relevance, subsequent analysis considered those genes recurrently mutated in more than 8% ($n > 8$) samples. The called genes were scored for their relevance by either analysing recurrent translocations affecting these genes (Supplementary Table 4) or by comparison with the mouse SCLC mutation data to identify alterations in common genes (Supplementary Table 5).

Additionally, recurrent mutations were scored for the accumulation of clearly damaging mutations in which splice site, frameshift and nonsense mutations were considered as damaging mutations. Here, we restricted the aforementioned significance analysis only to this class of mutations (by restricting the background mutation rate only to damaging mutations) and determined significance at $P < 0.01$ (Fig. 1a, Extended Data Fig. 1a (filter III) and Supplementary Table 6).

Genetic alterations were further scored for their relevance by comparison with genes that were functionally characterized in genetically engineered mouse models (GEMM) for SCLC^{9,10}, or by comparing somatic mutations in SCLC with mutations in other cancer types reported in the Cancer Gene Census¹⁴ and in COSMIC (catalogue of somatic mutations in cancer)¹⁵ (Fig. 1a, Extended Data Fig. 1a (filter IV and V) and Supplementary Table 6). Additionally, the sequencing data of mouse SCLC specimen was used to identify alterations in common genes.

Analysis of subclonal architecture. To determine the subclonal architecture from genome sequencing data, we first computed the cancer cell fraction (CCF; that is, the fraction of cancer cells carrying a particular mutation) of each called somatic point mutation. To this end, we first estimated the tumour purity, absolute copy numbers, and subclonal copy number changes using our previously described method² and computed for each mutation the expected allelic fraction under clonality assumption. The quotient between the observed allelic fraction of a mutation with its corresponding expected allelic fraction then yields the CCF. To assess the clonal and subclonal populations we next identified distinct clusters in the CCF profile and assigned each mutation to the cluster of highest probability. In order to provide a measure for the subclonal architecture, we proposed the following score:

$$\text{Subclonality score} = \frac{\sum_{i=1}^{nc} \phi_i m_i}{\sum_{i=0}^{nc} \phi_i m_i}$$

where $i = 0$ represents the clonal population, $i = 1, \dots, nc$ the subclonal populations; ϕ_i is the CCF of each population (thus, $\phi_0 \approx 1$), and m_i is the number of mutations

assigned to cluster i . This subclonality score can be interpreted as the probability that a randomly selected mutation present in a single cancer cell is subclonal throughout the entire tumour.

As a low sequencing depth limits the robust identification of subclonal populations, we computed the genome-wide average contribution of a single mutated read to the CCF. For a given tumour purity p , average ploidy π , and mean coverage c , this measure is given by:

$$\text{Average increase of CCF per read} = \frac{2(1-p) + p\pi}{pc}$$

The smaller the average increase of CCF per read, the more accurately the subclonality score can be determined since more subclonal mutations can be called from the sequencing data. In this study, the most limiting factor for assessing the subclonal diversity is the relatively low sequencing depth ($35\times$ on average). We therefore used this measure to select the samples that are suitable for a reliable calculation of the subclonality score. To this end, we systematically scanned from the average increase of CCF per read from large to small values and detected the point of the most prominent change in the distribution of the subclonality score (Supplementary Table 2).

Analysis of genomic breakpoints. Genomic rearrangements were reconstructed from the whole-genome sequencing data of 110 human SCLC samples following the procedure as previously described^{12,49}. The genomic rearrangements called from each tumour sample were further filtered against a library of 110 normal genomes to thus minimize the detection of false-positive rearrangements. Genomic breakpoints of SCLC candidate driver genes are listed in Supplementary Table 4.

The genomic breakpoints of all samples were mapped to their chromosomal locations and recurrent breakpoints clustering within the range of 100 kb were identified with a similar approach described previously²⁹ (Supplementary Table 14).

Processing and analysis of RNA-seq data. RNA-seq data was processed as previously described^{2,49} to detect chimaeric transcripts and to determine the transcriptional abundance of annotated transcript variants. In brief, paired-end RNA-seq reads were mapped to the human reference genome (NCBI37/hg19) using GSNAP. Potential chimaeric fusion transcripts were identified by discordant read pairs and by individual reads mapping to distinct chromosomal locations. The sequence context of rearranged transcripts was reconstructed around the identified breakpoint and the assembled fusion transcript was then aligned to the human reference genome to determine the genes involved in the fusion.

Cufflinks was used to determine the expression levels of annotated transcripts referring to unique paired-end reads which align within the expected mapping distance. The expression is represented as FPKM values (Supplementary Table 10).

Transcript splicing analysis. RNA-seq data was used to analyse for alternative splicing events of *TP53*, *RB1* and *TP73* caused by exon skipping or intron retention (Supplementary Table 11). The paired-end reads were mapped to the reference genome (hg19) using STAR mapper. In reference to the annotation of exon junctions provided from UCSC genes and RefSeq the following parameters were applied: ref 1, options: -alignIntronMin 20, -alignIntronMax 500000, -outFilterMismatchNmax 10, and -chimSegmentMin 10. The coordinates of reads potentially crossing exon boundaries were derived from the respective "SJ.out.tab" file and compared to the reference annotation. Subsequently, junction read counts were assigned to all transcripts containing the respective exon combination. If the exon combination is novel, read counts were assigned to those transcripts sharing one of the exons contributing to the novel junction. For subsequent analyses the transcript with the highest number of junction read counts was used as a reference. Additionally, for exon combinations unique to alternative transcripts a representative transcript was selected based on total read counts. The read counts of each exon junction were normalized to the reads per kilobase per million mapped reads (RPKM) per sample. These expression values were further normalized per gene by dividing by the average expression of the exons of the reference transcript. Potentially novel exon combinations were rejected if the average expression of the reference transcript was <2 or if their expression were $<10\%$ of the reference transcript expression.

Differential expression for outlier studies. Differential gene expression analysis was performed to compare the transcriptional profile of the two chromothripsis cases (S02297 and S02353) with other non-chromothripsis SCLC cases and to thus identify outliers in the expression profile. The expression was analysed by computing z -scores for all samples referring to the RPKM values and using the R function 'scale'; RPKM values smaller than 3 were set to 0. In order to prioritize for genes differentially expressed in the two samples S02297 and S02353, genes were ranked by their respective z -scores. Statistical testing was performed for genes on Chr 3 and Chr 11, respectively. The P values were then combined from the two samples using Fisher's method and corrected for multiple hypothesis testing by using the Benjamini-Hochberg approach. Differentially

expressed genes with a $P < 0.05$ and q -values < 0.01 are provided in Supplementary Table 13.

Unsupervised expression clustering. Unsupervised clustering was performed with RNA-seq data of 69 SCLC cases for which matching genome sequencing data was available (Fig. 4a and Extended Data Fig. 9a). As expression values are approximately following log-normal distribution, we transformed raw FPKM of each transcript by $\log_2(1 + \text{FPKM})$. The resulting expression scores were then searched for a high and low expression characteristic over the samples. To this end, expression scores of each transcript were divided into two states using k -means clustering. To prevent an accumulation of artificial signals, only transcripts with at least 6 samples in each state and having a state-averaged fold change larger than 3 are considered for further analysis. A t -test is then computed between the two states of the remaining transcripts and corrected for multiple hypothesis testing using the false discovery rate framework. Next, transcripts having a q -value smaller than 0.01 were selected. For genes with multiple transcript variants, the transcript with the smallest q -value was chosen as representative transcript. Then, invariant genes were removed (having a standard deviation across all samples < 2). To improve clustering, only genes that share a similar pattern of the two states in at least 6 other genes are finally selected (using a Fisher's exact test with a significance threshold of 10^{-6}). Using the determined list of transcripts/genes, hierarchical clustering (Euclidean distance, complete linkage) was performed on the raw expression scores.

IRS2 amplification FISH assay. A fluorescence *in situ* hybridization (FISH) assay was used to detect and confirm *IRS2* amplifications at the chromosomal level. We performed a signal detection approach, with two probes on chromosome 13: the reference probe is located on the centromeric region of chromosome 13 (Empire Genomics, Art.Nr.: CHR13-10-GR) and was labelled with green 5-fluorescein dUTP to produce a green signal; the target probe is located on the *IRS2* locus spanning 13q33.3–34 and was labelled with biotin to produce a red signal using the CTD-2083015 BAC clone (Life Technologies, CA, USA). As previously described²⁴, slides of FFPE and fresh-frozen samples of tumour tissues were prepared, stained and analysed at a fluorescence microscope (Zeiss, Jena, Germany) with a 63 \times oil immersion objective. A non-amplified nucleus showed one red target signal for every corresponding green reference signal, with a red/green ratio of 1:1 (Extended Data Fig. 5e). High-level amplifications were determined for at least 10 red signals. In some cases the red signals were observed as clusters in the cells. At least 100 nuclei per case were evaluated.

Immunohistochemistry. Immunohistochemistry was performed on human tumour FFPE samples to analyse for the protein expression of Rb, cyclin D1, p53, p14 (ARF), and p16. The staining was performed with the BenchMark XT automated immunohistochemistry slide staining system (Roche). The following antibodies and conditions were applied: Rb (C-15) rabbit polyclonal (Santa Cruz; FFPE retrieving conditions: 60 min at pH 6.0; dilution: 1:500; incubation: 60 min, 37 °C); Cyclin D1 clone SP4 rabbit monoclonal (Microm France; FFPE retrieving conditions: 90 min at pH 8.4; dilution: 1:200; incubation: 60 min, 37 °C); p53 clone DO7 mouse monoclonal (Dako; FFPE retrieving conditions: 60 min at pH 8.4; dilution: 1:25; incubation: 60 min, 37 °C); p14 ARF clone 4C6/4 mouse monoclonal (Cell Signaling; FFPE retrieving conditions: 60 min, water-bath 98 °C at pH 6.0; manual immunohistochemistry staining with Novolink Max polymer detection system (Leica); dilution: 1:4,000; incubation: overnight, 4 °C); p16 INK4 Ab-7 clone PO7 mouse monoclonal (Neomarkers; FFPE retrieving conditions: 60 min at pH 8.4; dilution: 1:800; incubation: 60 min, room temperature).

For immunohistochemistry on mouse tumour FFPE samples, sections were permeabilized for antigen retrieval by microwaving in a citrate-based antigen unmasking solution (Vector Laboratories). The following antibodies were used: GFP (Invitrogen; A11122; dilution: 1:400), RFP/Tomato (Rockland Immunochemicals; 600-401-379; dilution: 1:500), Notch2 (Cell Signaling; 5732; dilution: 1:200), Hes1 (Cell Signaling; 11988; dilution: 1:200), Ascl1 (BD Biosciences; 556604; dilution: 1:200) and Synaptophysin (Neuromics; MO20000; dilution: 1:200). Sections were developed with DAB (Vector Labs) and counterstained with haematoxylin.

Cell lines, tissue culture and transfections. Mouse (KP1) and human (NJH29, NCI-H82 and NCI-H187) SCLC cell lines were grown in RPMI-1640 media supplemented with 10% bovine growth serum (BGS) (Fisher Scientific) and penicillin-streptomycin-glutamine (Gibco), as described before⁵⁰. KP1, NJH29 were generated at Stanford. NCI-H82 and NCI-H187 were purchased from ATCC. These cells grow as suspension spheres or aggregates in culture. All cell lines were maintained at 37 °C in a humidified chamber with 5% CO₂. All cell lines tested negative for mycoplasma infection. For transient expression of Notch ICD, cells were trypsinized and transfected with either MigR1-IRES-GFP (Ctrl) or MigR1-Notch1-ICD-IRES-GFP (NICD) using Lipofectamine 2000 (Life Technologies). The plasmids were gifts from W.S. Pear (University of Pennsylvania, Philadelphia). Then 48 h after transfection, cells were trypsinized and resuspended in phosphate-buffered saline (PBS) containing 10% BGS and 1 $\mu\text{g ml}^{-1}$ 7-aminoactinomycin D (Life Technologies) that labels dead cells. Live GFP⁺ cells were then sorted for subsequent experiments using a BD FACSaria fluorescence-activated cell sorting (FACS) machine.

Gene expression and microarray analysis. Gene expression and microarray analyses were performed with the mouse cell line KP1 transiently transfected with MigR1-IRES-GFP (Ctrl) or MigR1-Notch1-ICD-IRES-GFP (NICD).

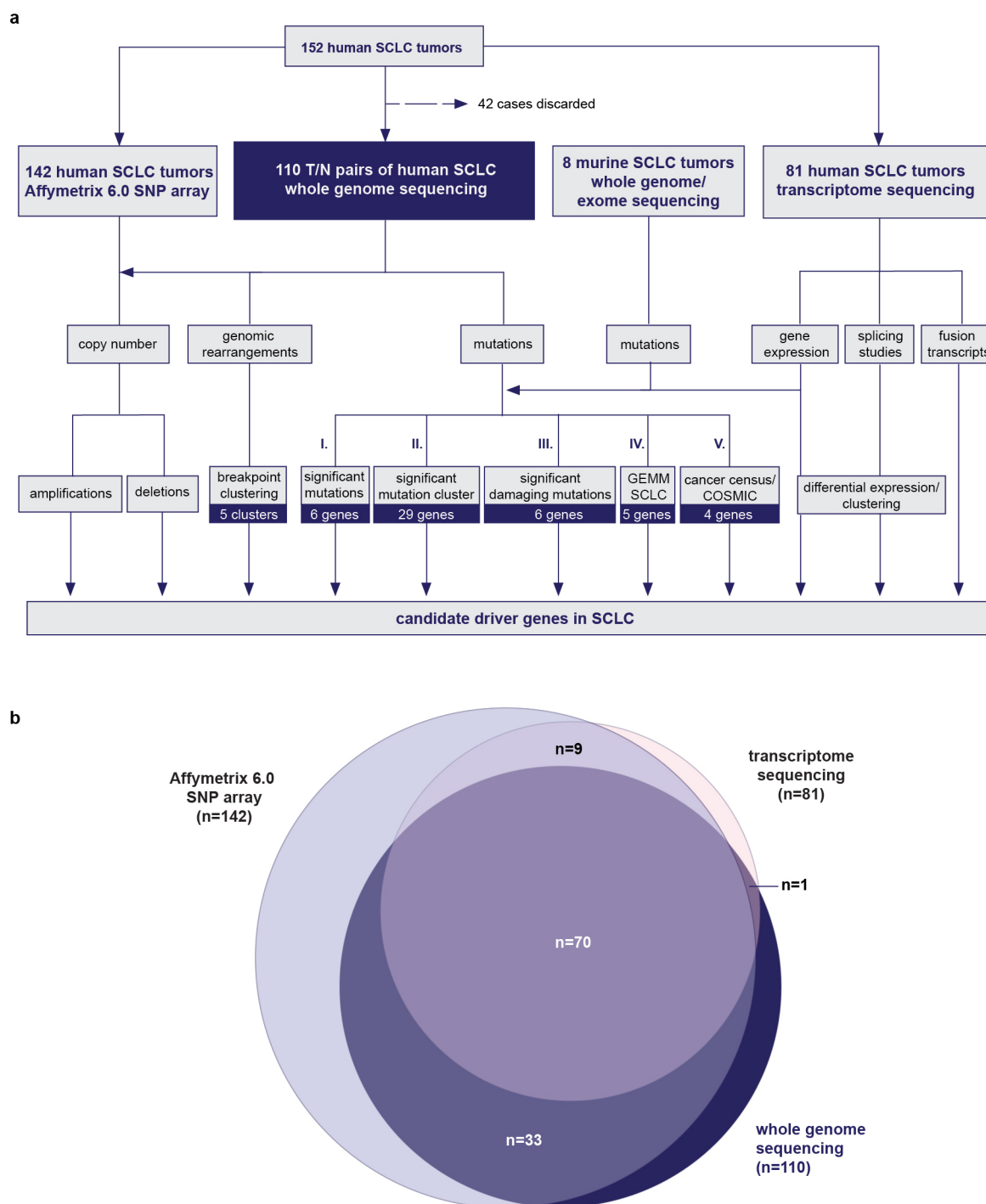
Then 1×10^5 GFP⁺ cells were sorted and the RNA isolated using the AllPrep DNA/RNA micro kit (Qiagen). RNA quality assessment using the 2100 Bioanalyzer (Agilent) as well as the subsequent cDNA preparation steps for microarray analysis were performed at the Stanford Protein and Nucleic Acid (PAN) facility using the GeneChip Mouse Gene 2.0 ST Array (Affymetrix). For gene expression analysis, the Robust Multichip Average (RMA) Express 1.0.4 program was used for background adjustment and quantile RMA normalization of the 41,345 probe sets encoding mouse genome transcripts. Linear models for microarray data (LIMMA) was used to compare Ctrl or NICD samples on RMA normalized signal intensities. Only genes with an adjusted P value of 0.05 or less were considered as significantly differentially expressed. A total of 769 probes accounting for 760 genes were significant, and the expression levels of these genes were represented as a heatmap using the heatmap.2 function in R. The analysis was performed in triplicates. A list of significant genes is provided in Supplementary Table 15.

MTT cell viability assay. Sorted GFP⁺ cells were seeded at 1×10^4 per well in 96-well plates. The MTT reagents (Roche) were added on days 0, 2, 4, 6 and 8 for mouse SCLC cell lines or on days 0, 2, 4 and 6 for the human SCLC cell line NJH29. The absorbance wavelength was 570 nm with a reference wavelength of 650 nm.

EdU incorporation assay. Transfected cells were treated with 10 μM EdU (5-ethynyl-2'-deoxyuridine) (Life Technologies) for 3 h before trypsinization for FACS. 1×10^5 live, GFP⁺ cells were sorted and labelled with EdU using the Click-iT EdU Pacific Blue flow cytometry assay kit (Life Technologies). Cells were then run through the BD FACSaria to analyse for per cent EdU incorporation.

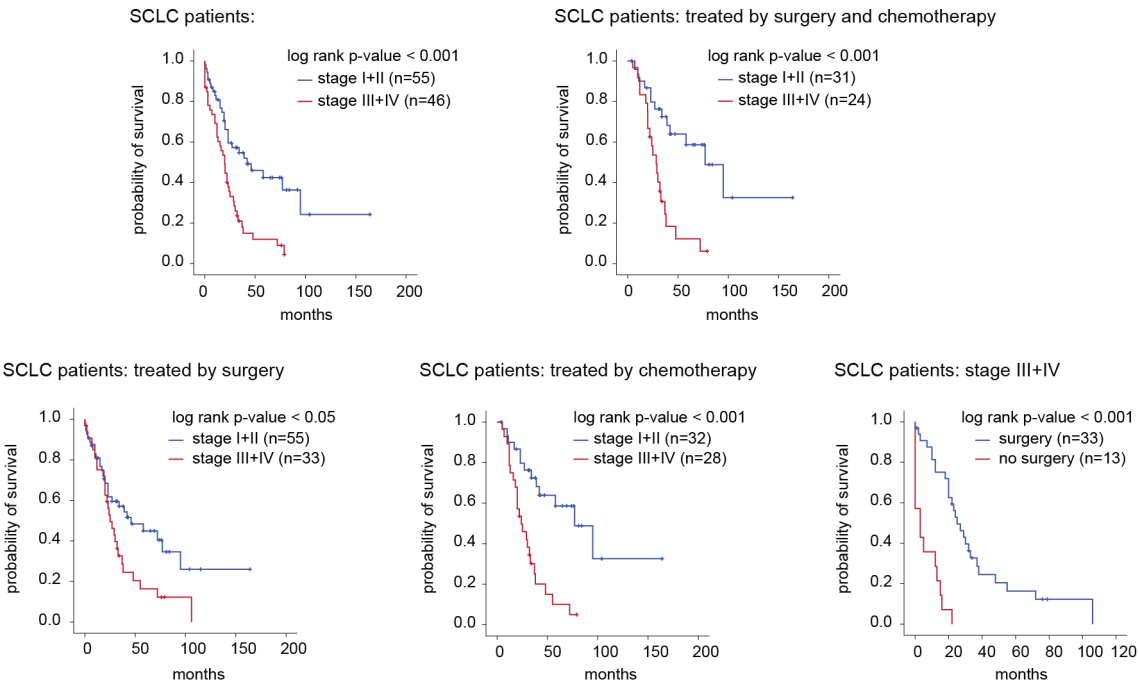
Data reporting. No statistical methods were used to predetermine sample size.

43. Iwakawa, R. *et al.* Genome-wide identification of genes with amplification and/or fusion in small cell lung cancer. *Genes Chromosomes Cancer* **52**, 802–816 (2013).
44. Seidel, D. A genomics-based classification of human lung tumors. *Sci. Transl. Med.* **5**, 209ra153 (2013).
45. Lafkas, D. *et al.* Notch3 marks clonogenic mammary luminal progenitor cells in vivo. *J. Cell Biol.* **203**, 47–56 (2013).
46. Muzumdar, M. D., Tasic, B., Miyamichi, K., Li, L. & Luo, L. A global double-fluorescent Cre reporter mouse. *Genesis* **45**, 593–605 (2007).
47. Lu, X., Thomas, R. K. & Peifer, M. CGARS: cancer genome analysis by rank sums. *Bioinformatics* **30**, 1295–1296 (2014).
48. Li, H. & Durbin, R. Fast and accurate short read alignment with Burrows–Wheeler transform. *Bioinformatics* **25**, 1754–1760 (2009).
49. Fernandez-Cuesta, L. *et al.* Frequent mutations in chromatin-remodelling genes in pulmonary carcinoids. *Nat. Commun.* **5**, 3518 (2014).
50. Jahchan, N. S. *et al.* A drug repositioning approach identifies tricyclic antidepressants as inhibitors of small cell lung cancer and other neuroendocrine tumors. *Cancer Discov.* **3**, 1364–1377 (2013).



Extended Data Figure 1 | Genomic analyses in SCLC tumours. a, Schematic detailing the genomic study and number of samples as well as various steps of analyses for the identification of candidate genes in SCLC. **b**, Illustration of the number of samples analysed in this study.

a



b

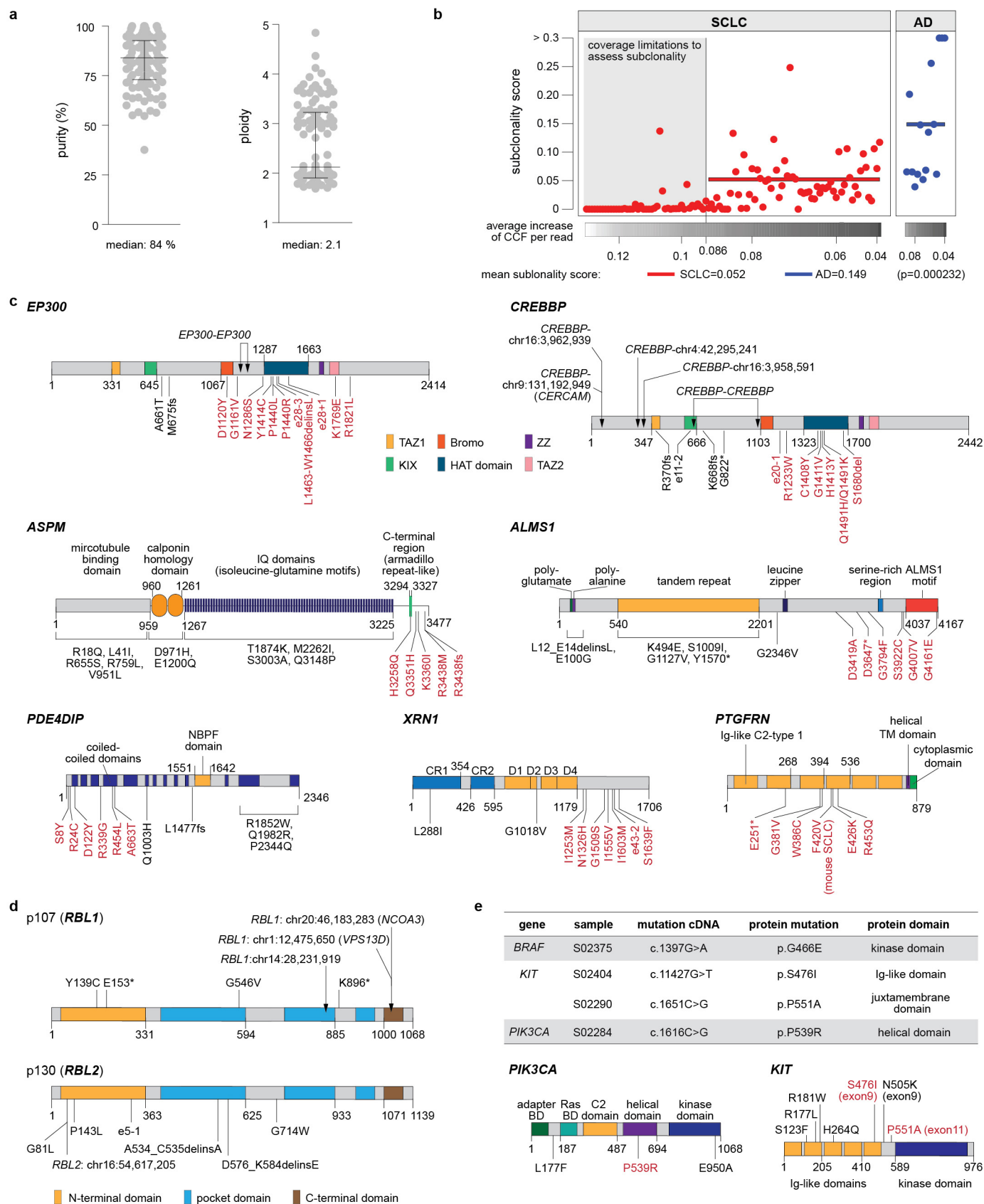
item tested*	clinical stage (early: stage I and II, late: stage III and IV)
non-synonymous mutations (n=109)	p-value: 0.855
C:G>A:T transversion rate (n=109)	p-value: 0.908
subclonality (n=55)	p-value: 0.723

item tested*	smoking category based on pack-years (light/never, average, heavy smoker)
non-synonymous mutations (n=69)	p-value: 0.164
C:G>A:T transversion rate (n=69)	p-value: 0.737

* Kruskal-Wallis test

Extended Data Figure 2 | Clinical molecular-correlation analyses.
a, Survival analysis of SCLC patients based on clinical stage and treatment options (surgery and/or chemotherapy). Statistical significance was determined by log-rank test. **b**, Analyses of clinical stage and smoking status and the

respective effect on number and type of mutations, as well as mutational subclonality in tumours. Statistical significance was determined by Kruskal-Wallis analysis.

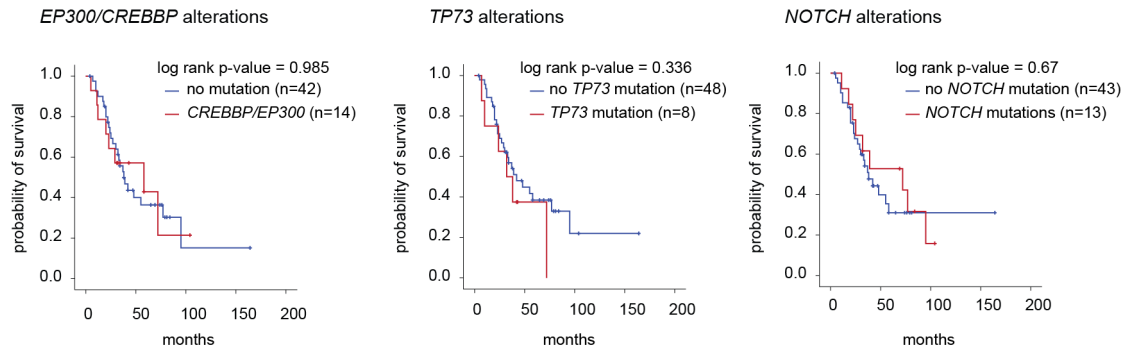


Extended Data Figure 3 | Genomic characterization of SCLC tumours.

a, Purity and ploidy determined in SCLC tumours by whole-genome sequencing presented as dot density plots showing median and the interquartile range (IQR) **b**, Subclonal architecture of SCLC in comparison to lung adenocarcinoma (AD). Whole-genome sequencing data of SCLC and of adenocarcinoma ($n = 15$)¹¹ was analysed for the presence of subclonal populations using clustering of the derived cancer cell fraction (CCF) of all single nucleotide mutations. To compare the emerging subclonal structure, we derived a subclonality score that takes into account the CCF of each sub-population as well as its mutational burden (see Methods). In order to prevent the low sequencing coverage (35× for SCLC and 63× for AD) from causing a systematic underrepresentation of the subclonal diversity in the mutation calls, we computed the contribution of a single read to the CCF on

genome-wide average. After systematically determining a threshold within the average increase of CCF per read values (see Methods for details), we determined the group of samples for which a reliable estimation of the subclonality score is not possible (grey area). The subclonality scores of the remaining SCLC cases were then compared to those of the adenocarcinoma cases ($P = 0.000232$; Mann–Whitney test). **c**, Schematic representation of candidate genes with significant clustering of mutations in respective protein domains. Somatic mutations and genomic translocations are mapped to the respective protein regions. Hotspot mutations are highlighted in red. **d, e**, Genomic alterations in the *RB1* family proteins p107 (*RBL1*) and p130 (*RBL2*) (**d**), and in *KIT* and *PIK3CA* (**e**). Somatic mutations in therapeutic target genes are listed and mapped to the protein domains of *KIT* and *PIK3CA*. Mutations with potential therapeutic implications are highlighted in red.

a SCLC patients: treated by surgery and chemotherapy.



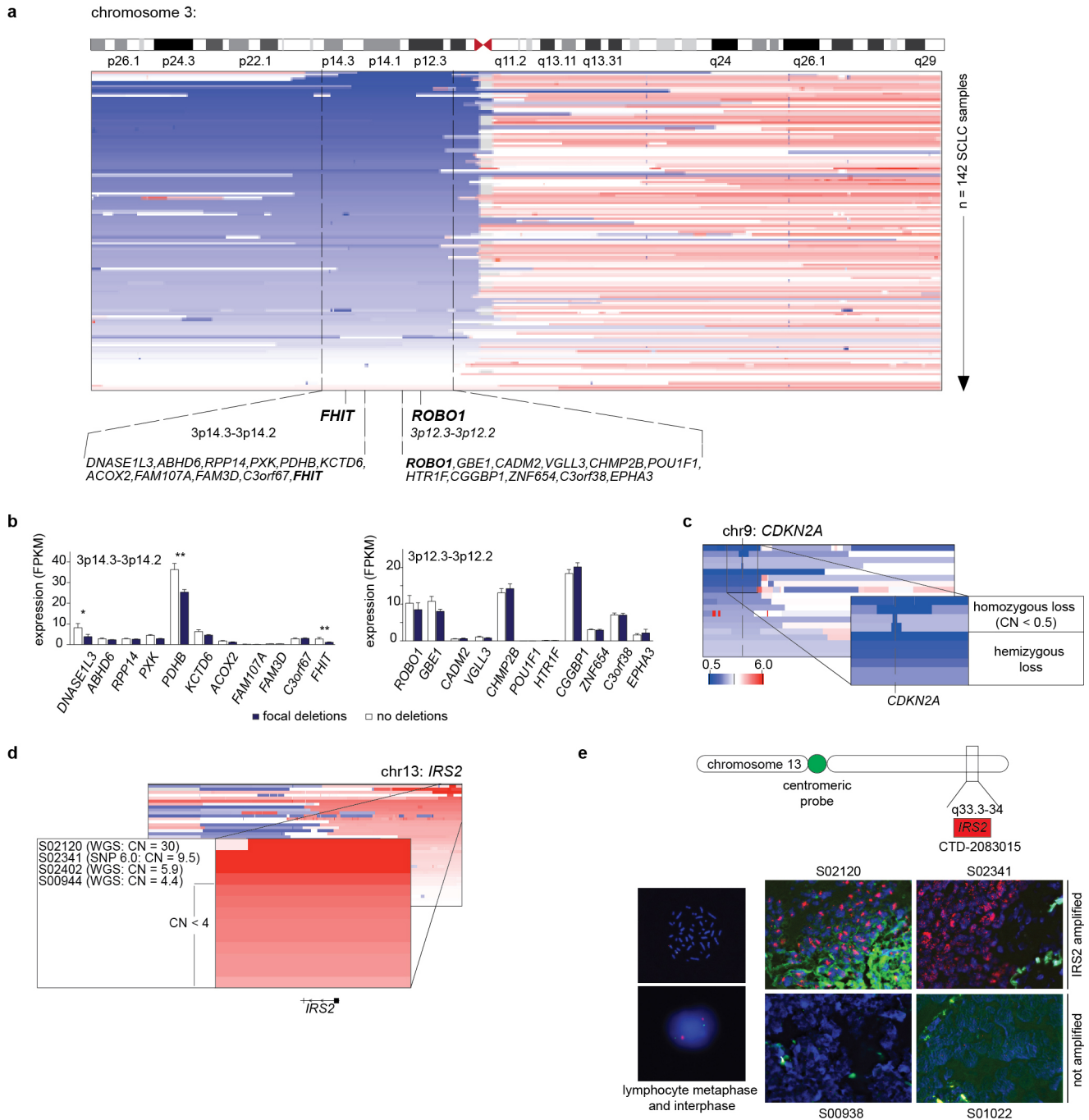
b

item tested*	<i>CREBBP/EP300</i>	<i>TP73</i>	<i>NOTCH</i>
age	p-value: 0.740	p-value: 0.983	p-value: 0.215
sex	p-value: 0.764	p-value: 0.984	p-value: 0.409
C:G>A:T transversion rate	p-value: 0.237	p-value: 0.985	p-value: 0.365
clinical stage (early: stage I and II, late: stage III and IV)	p-value: 0.509	p-value: 0.983	p-value: 0.308
non-synonymous mutations	p-value: 0.424	p-value: 0.983	p-value: 0.257
subclonality (n=55)	p-value: 0.839	p-value: 0.994	p-value: 0.124
smoking category based on pack-years (light/never, average, heavy smoker)	p-value: 1.0	p-value: 1.0	p-value: 0.382

* multinomial logistic regression

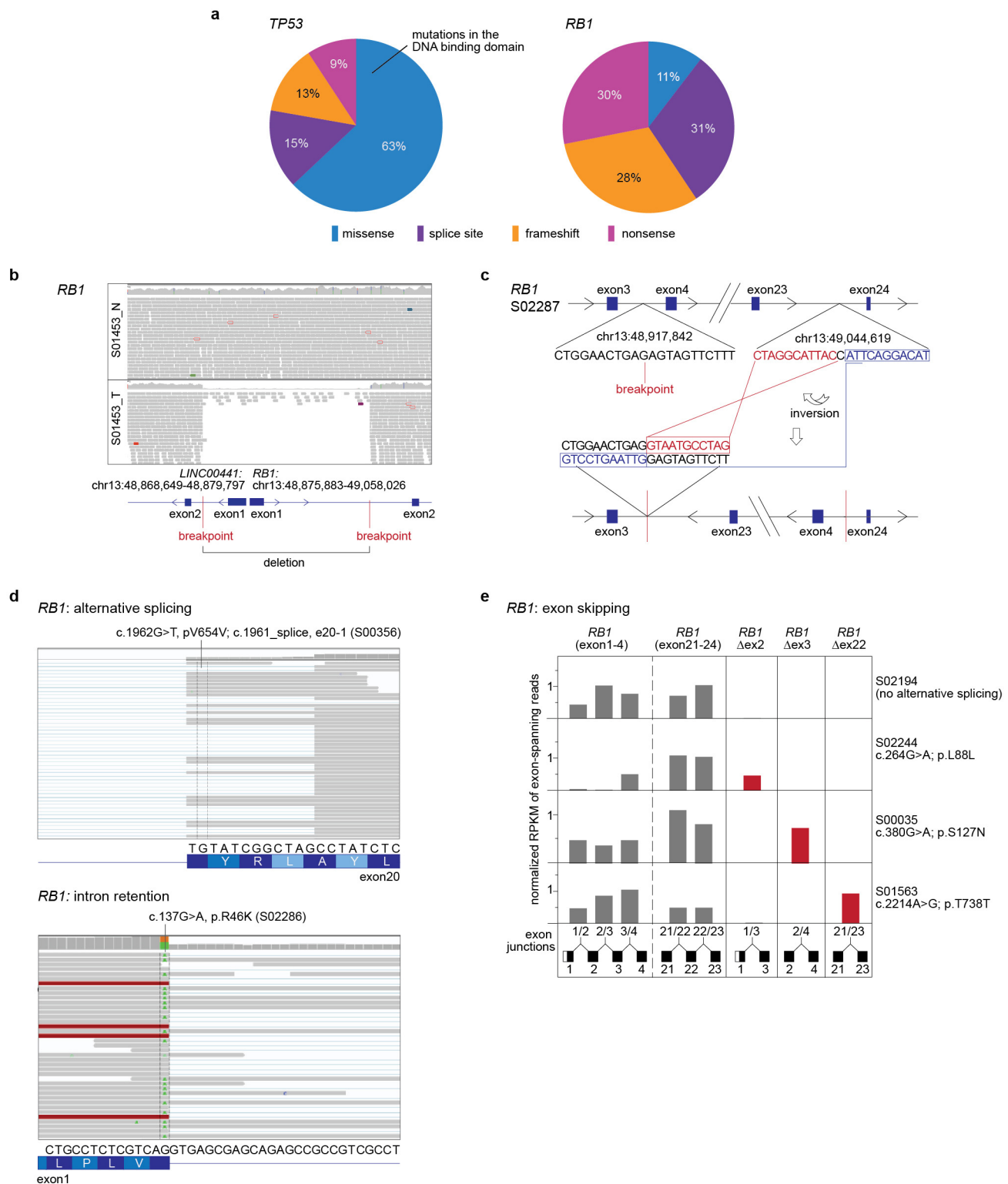
Extended Data Figure 4 | Clinical molecular-correlations of significantly mutated genes. **a**, Survival analysis of SCLC patients based on the status of *CREBBP/EP300*, *TP73* or *NOTCH* alterations. Statistical significance was

determined by log-rank test. **b**, Analysis of *CREBBP/EP300*, *TP73* and *NOTCH* alterations and their effect on clinical and genetic parameters. Statistical significance was analysed by multinomial logistic regression.



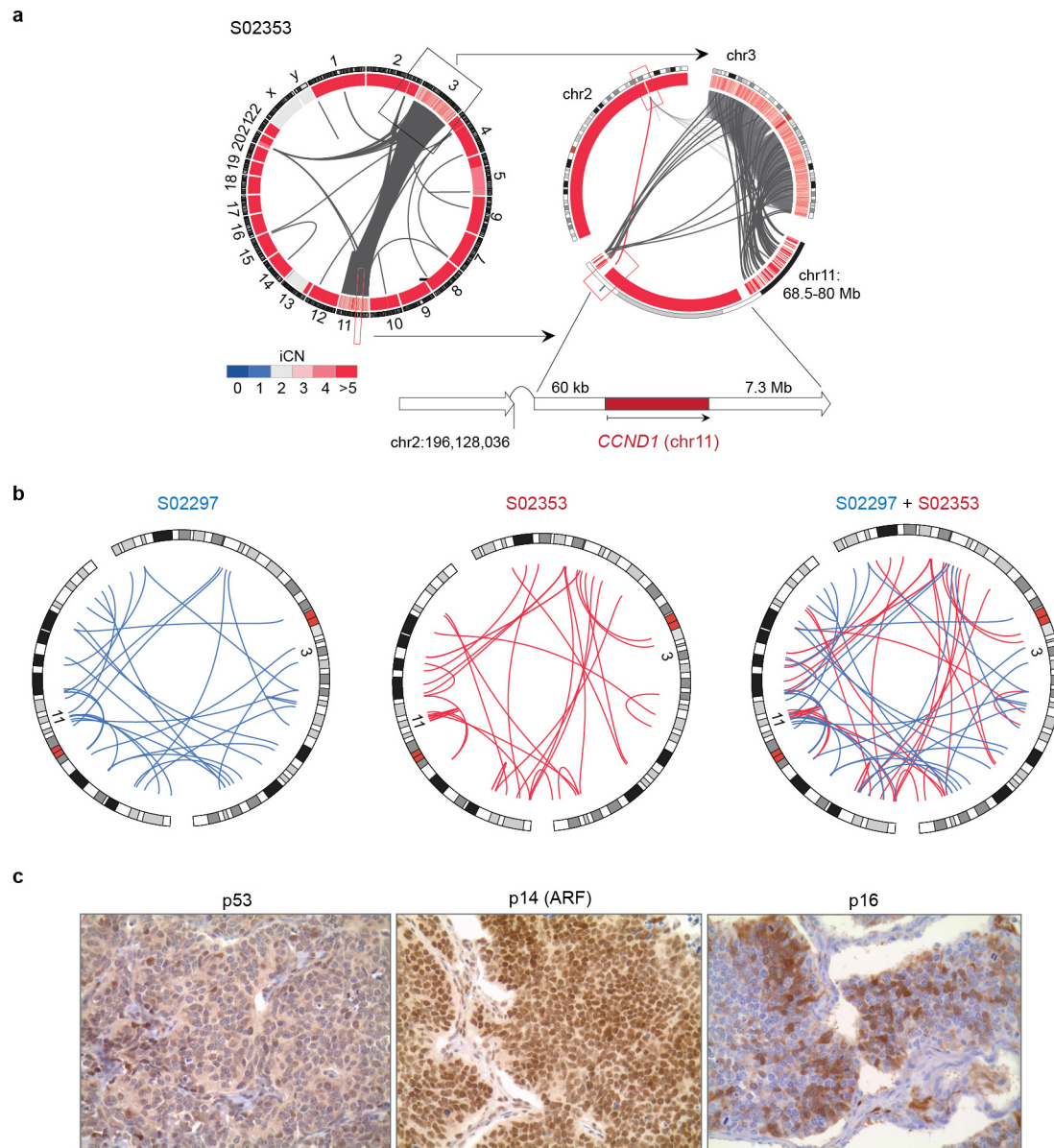
Extended Data Figure 5 | Significant somatic copy number alterations in SCLC. **a**, Deletions of the chromosomal arm 3p point to the 3p14 (*FHIT*) and 3p12 (*ROBO1*) locus. **b**, Expression analyses of genes encoded on the 3p14.3–3p14.2 and 3p12.2–3p12.2 locus. Histogram displaying the expression of samples with focal deletions (blue) and samples without any copy number alterations (white). Mean and standard error of the mean is plotted for each gene in each group. Significant differences were determined by Mann–Whitney test; * $P < 0.05$; ** $P < 0.01$. **c**, **d**, Focal deletions of the *CDKN2A* (**c**) and focal amplifications of *IRS2* (**d**) were found on chromosome 9 and 13, respectively.

The copy number (CN) states were computed from SNP array (SNP 6.0) and from whole-genome sequencing (WGS) data. The samples are sorted according to their amplitude of deletions or amplifications. **e**, Amplifications of *IRS2* were determined by FISH analysis. *IRS* amplifications were quantified based on the ratio of red signals (*IRS2*-specific probe) to green signals (centromere probe for chromosome 13). Lymphocyte spreads and SCLC tumours without detectable *IRS2* amplifications served as negative controls. Scale bar, 100 μm .



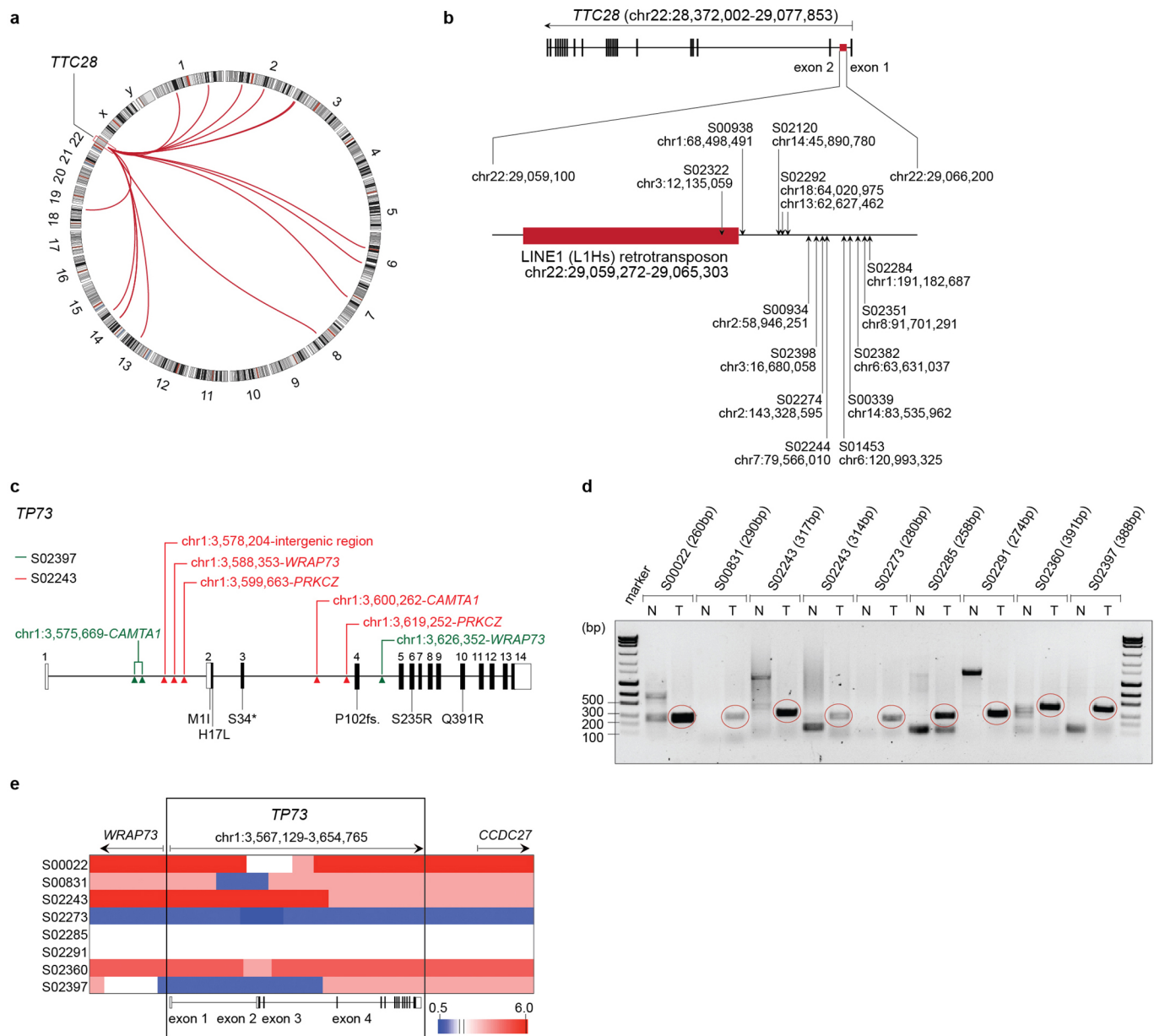
Extended Data Figure 6 | *TP53* and *RB1* alterations in SCLC. **a**, Distribution of somatic mutations in *TP53* and *RB1* according to the colour panel provided. **b**, **c**, Complex genomic rearrangements in *RB1* showing homozygous deletions of exon 1 (**b**) or inversions within the *RB1* gene (**c**). **d**, **e**, Annotated silent or missense mutations in *RB1* occur at intron-exon junctions resulting in

alternative splicing, intron retention (**d**) or exon skipping events (**e**). The coverage at the respective exon junctions is quantified as RPKM values. Sample S02194 is not holding any mutations at intron-exon junctions and is displayed as an example for unaltered splicing of *RB1*.



Extended Data Figure 7 | Chromothripsis in human SCLC. **a**, Circos plot of the chromothripsis sample S02353 showing intra- and interchromosomal rearrangements between chromosome 3 and 11. The integral copy number state (iCN) is plotted as a heatmap and assigned to the respective chromosomal regions. The chromosomal context of *CCND1* (on chromosome 11) is

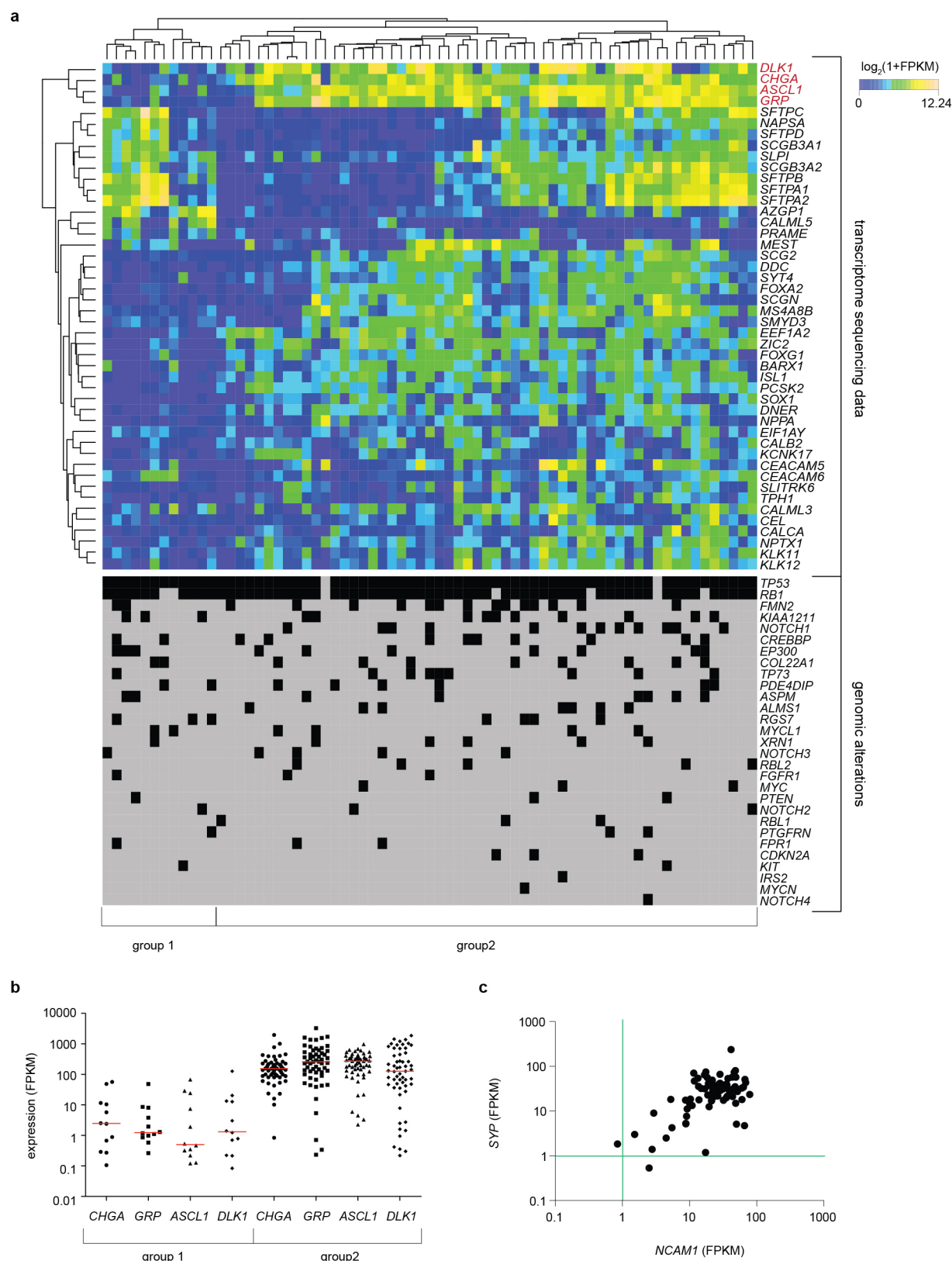
highlighted. **b**, Circos plots displaying fusion transcripts identified in the SCLC chromothripsis cases (Supplementary Table 12) are represented as blue (S02297) or red (S02353) lines for genes located on chromosome 3 and 11. **c**, Immunohistochemistry staining for p53, p14 (ARF) and p16 on FFPE material of the chromothripsis sample S02297. Original magnification, $\times 400$.



Extended Data Figure 8 | Recurrent genomic translocations in SCLC.

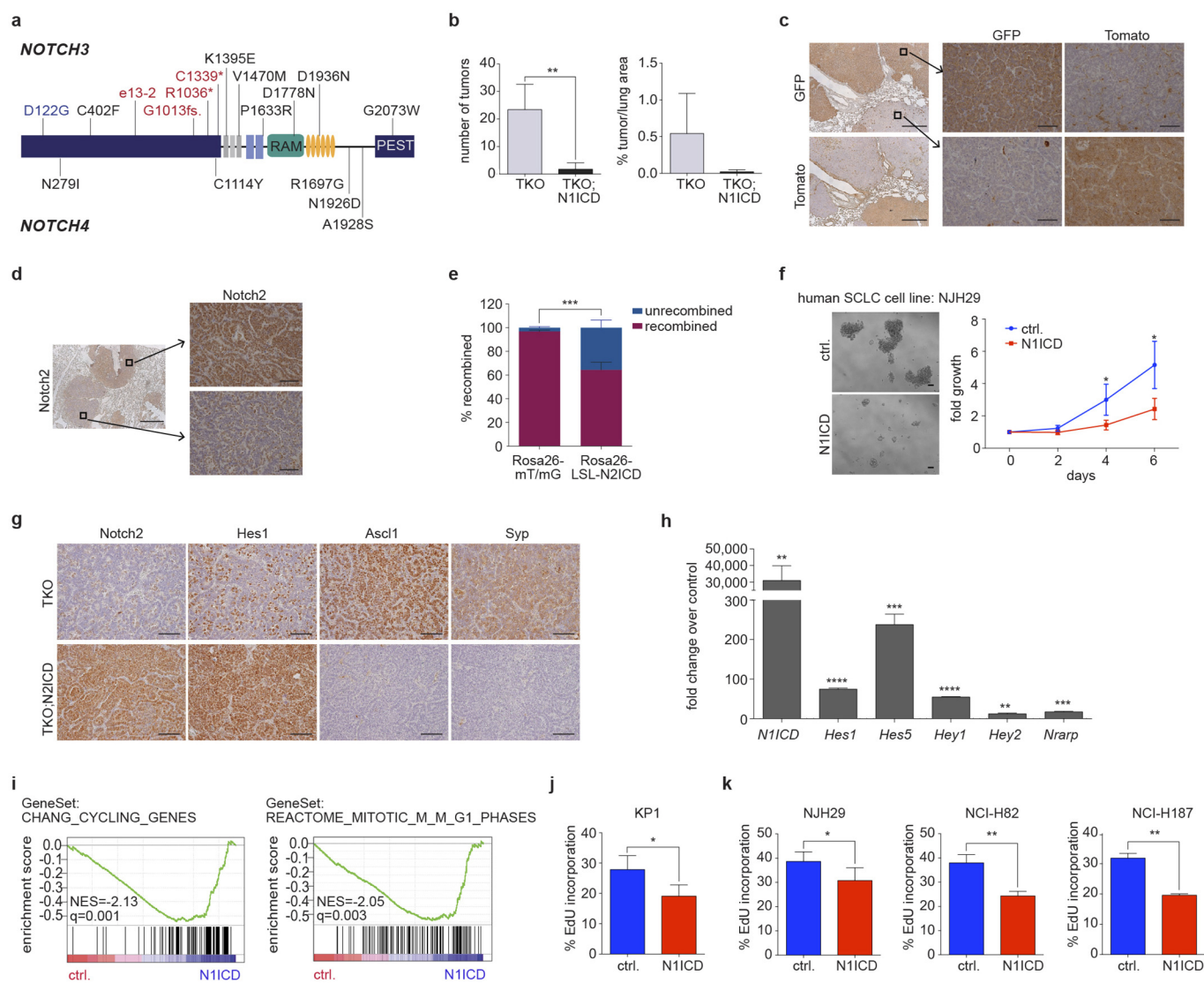
a, Recurrent genomic translocations ($n = 14$) affecting chromosome 22 are illustrated as a Circos plot highlighting the respective rearrangements as red connecting lines. **b**, Breakpoints in chromosome 22 map to intron 1 of *TTC28* and cluster downstream of the LINE1 (L1Hs) retrotransposon. Each arrow indicates the sample and the respective chromosomal position the segment translocates to. **c**, Schematic representation of the *TP73* locus (hg19) describing complex intrachromosomal rearrangements of *TP73* identified for S02397 and

S02243. Recurrent somatic mutations identified in Fig. 1a are mapped to the respective exons. **d**, Validation of somatic *TP73* translocations. Genomic regions involved in the *TP73* rearrangements were amplified in matched normal (N) and tumour (T) samples. The expected band size is indicated in brackets. The respective PCR products were subjected to Sanger sequencing to confirm the genomic breakpoint. **e**, Copy-number state of the *TP73* gene in samples involved in genomic translocations.



Extended Data Figure 9 | Transcriptome profile of human SCLC tumours.
a, Unsupervised hierarchical clustering of transcriptome sequencing data of 69 SCLC specimens as described in Fig. 4a. Each sample is annotated for the genomic alterations described in Fig. 1. Black filled boxes describe the presence of a genomic event. **b**, Expression values of *CHGA*, *GRP*, *ASCL1* and *DLK1*

(FPKM) are represented as dot density plots for the subgroups identified in (a). Red lines highlight the median value for each group. **c**, Expression values of the neuroendocrine markers *SYP* (synaptophysin) and *NCAM1* (CD56) plotted as scatter plots for all SCLC samples. Green lines indicate thresholds for no expression (FPKM < 1).



Extended Data Figure 10 | Notch is a tumour suppressor in SCLC regulating neuroendocrine differentiation. **a**, Somatic mutations identified in *NOTCH3* and *NOTCH4* are mapped to the protein domains. Damaging mutations are highlighted in red. Mutations found in murine SCLC tumours are highlighted in blue. **b**, Quantification of tumour lesions and per cent tumour area to lung in TKO ($n = 5$) and TKO;N1ICD ($n = 4$) mice 3 months after Ad-Cre instillation. Statistical significance was determined by two-tailed unpaired Student's *t*-test. **c**, Representative immunohistochemistry for GFP or tdTomato in lungs from TKO;*Rosa26^{mT/mG}* mice approximately 6 months after tumour induction. Left scale bar, 500 μ m; right and middle: scale bar, 50 μ m. **d**, Representative immunostaining for Notch2 in lungs from TKO;*Rosa26^{N2ICD}* mice approximately 6 months after tumour induction. Left scale bar, 500 μ m; right scale bar, 50 μ m. **e**, Quantification of the per cent recombination at the *Rosa26* locus in TKO;*Rosa26^{mT/mG}* ($n = 6$) and TKO;*Rosa26^{N2ICD}* mice ($n = 10$; two-tailed unpaired Student's *t*-test). **f**, Cell

viability assay of the human SCLC cell line NJH29 transfected with a N1ICD (Notch1) expression plasmid or empty vector control (Ctrl) (3 independent biological replicas with 3 technical replicas each). Fold growth was normalized to day 0; representative images were taken on day 6. Scale bar, 50 μ m. **g**, Immunohistochemistry staining in FFPE embedded tissues of TKO and TKO;N2ICD mice. Scale bar, 50 μ m. **h**, Quantitative RT-PCR validation of *Notch1* induction and the expression of common Notch target genes after N1ICD transfection in murine SCLC cells (three biological replicas; two-tailed paired Student's *t*-test). **i**, Mouse SCLC cells transfected with control or N1ICD (Notch1) were analysed 48 h later by gene expression microarrays. Gene Set Enrichment Analysis (GSEA) was performed on these data; selected significant gene sets are displayed. **j, k**, EdU analysis of mouse (j) and human (k) SCLC cells (three independent biological replicas with three technical replicas each; two-tailed paired Student's *t*-test). * $P < 0.05$; ** $P < 0.01$; *** $P < 0.001$. Data are represented as mean \pm s.d.

HipBA–promoter structures reveal the basis of heritable multidrug tolerance

Maria A. Schumacher^{1*}, Pooja Balani^{2*}, Jungki Min¹, Naga Babu Chinnam¹, Sonja Hansen^{2†}, Marin Vulić^{2†}, Kim Lewis² & Richard G. Brennan¹

Multidrug tolerance is largely responsible for chronic infections and caused by a small population of dormant cells called persisters. Selection for survival in the presence of antibiotics produced the first genetic link to multidrug tolerance: a mutant in the *Escherichia coli* *hipA* locus. HipA encodes a serine–protein kinase, the multidrug tolerance activity of which is neutralized by binding to the transcriptional regulator HipB and *hipBA* promoter. The physiological role of HipA in multidrug tolerance, however, has been unclear. Here we show that wild-type HipA contributes to persister formation and that high-persister *hipA* mutants cause multidrug tolerance in urinary tract infections. Perplexingly, high-persister mutations map to the N-subdomain-1 of HipA far from its active site. Structures of higher-order HipA–HipB–promoter complexes reveal HipA forms dimers in these assemblies via N-subdomain-1 interactions that occlude their active sites. High-persistence mutations, therefore, diminish HipA–HipA dimerization, thereby unleashing HipA to effect multidrug tolerance. Thus, our studies reveal the mechanistic basis of heritable, clinically relevant antibiotic tolerance.

Bacterial multidrug tolerance (MDT) is largely responsible for the inability of antibiotics to eradicate infections and is caused by a subpopulation of phenotypic variants called persisters¹. Because bactericidal antibiotics target processes in metabolically active cells, persisters, which are dormant, survive^{1,2}. Persisters that resume growth after antibiotic removal lead to recurrent infections, especially those caused by biofilms^{1,3–5}. Hence, MDT represents a significant threat to human health. However, elucidation of the mechanisms that drive MDT has been hampered by the rarity of persisters; typically only one in 10⁵ cells becomes a persister. The first persister locus, *hipA7*, was identified in *E. coli* three decades ago⁶. The *hipA7* locus, which leads to a 1,000-fold increase in persisters, contains two mutations, G22S and D291A, in the HipA protein⁷. HipA is a 440-residue protein that is co-transcribed with the 88-residue helix–turn–helix containing HipB DNA-binding protein^{6–15}. HipB forms a complex with HipA and promoter DNA, neutralizing the MDT activity of HipA. Thus, HipA and HipB form a toxin–antitoxin module^{16–18}.

Recent data revealed HipA is a serine–protein kinase^{11–13} that phosphorylates glutamyl-transfer RNA synthase^{14,15}, inhibiting protein synthesis and driving cells into dormancy. Formation of the HipA–HipB–*hipBA* promoter complex, which consists of several HipA and HipB molecules bound to multiple operator sites, maintains HipA in an inactive state and mediates transcription autorepression^{9,10}. However, the mechanisms involved in these inhibitory activities are not understood. Mutants in *hipA* have been used as a convenient model to study persisters^{17,19}, but it has been unclear whether the kinase plays a role in MDT *in vivo*. Here we show that wild-type (WT) HipA contributes to persister formation, and that *hipA7* high-persister mutants are found in patients with urinary tract infections (UTIs). The molecular basis for the high-persister phenotypes was revealed by structures of higher-order HipA–HipB–*hipBA* promoter complexes, emphasizing the importance of structural studies on fully assembled transcription promoter complexes in elucidating complex biological regulatory mechanisms.

HipA contributes to antibiotic tolerance

E. coli HipA was the first bona fide MDT-inducing protein identified⁶. Ectopic overexpression of the native HipA protein increases persister production. However, deletion of the *hipA* gene produces no phenotype⁹, either because of redundant mechanisms of persister formation or because HipA does not play a role in antibiotic tolerance^{19–21}. However, if only a small fraction of cells expressing HipA become persisters, this would be overlooked in studies on bulk populations. We therefore examined the correlation between *hipBA* expression and persister formation in single cells using a plasmid-encoded promoter_{*hipBA*}–green fluorescent protein (GFP) fusion, which reports chromosomal *hipBA* expression. Fluorescence-activated cell sorting (FACS) of this population showed a random distribution, and dim, middle and bright cells were collected and exposed to ofloxacin (Fig. 1a). Survival was considerably better in bright cells and depended on the presence of the chromosomal *hipBA* locus, suggesting that stochastic expression of the *hipBA* operon indeed causes persister formation. Analysis of the *hipA7* mutant showed a similar pattern but shifted to higher levels of expression (Fig. 1a). These results demonstrate that *hipA* contributes to persister formation in WT *E. coli*, and that the *hipA7* mutation somehow leads to elevated expression of the *hipBA* operon.

HipA causes MDT UTIs

The *hipA7* mutant was originally obtained in the Moyed laboratory by selecting for increased antibiotic tolerance and has been widely used as a model for studying persisters⁶. To obtain additional higher-persister HipA mutants, we performed a similar selection for increased tolerance to a combination of ampicillin and cefotaxim. To enrich for high-persister mutants, surviving cells were cultured and challenged again with antibiotics. Whole-genome sequencing identified an additional *hipA* allele, P86L, which displayed a high-persister phenotype similar to *hipA7* (Fig. 1b and Extended Data

¹Department of Biochemistry, Duke University School of Medicine, Durham, North Carolina 27710, USA. ²Antimicrobial Discovery Center, Northeastern University, Department of Biology, Boston, Massachusetts 02115, USA. [†]Present addresses: Helmholtz Centre for Infection Research, Inhoffen Strasse 7, 38124, Braunschweig, Germany (S.H.); Seres Therapeutics, Cambridge, Massachusetts 02142, USA (M.V.).

*These authors contributed equally to this work.

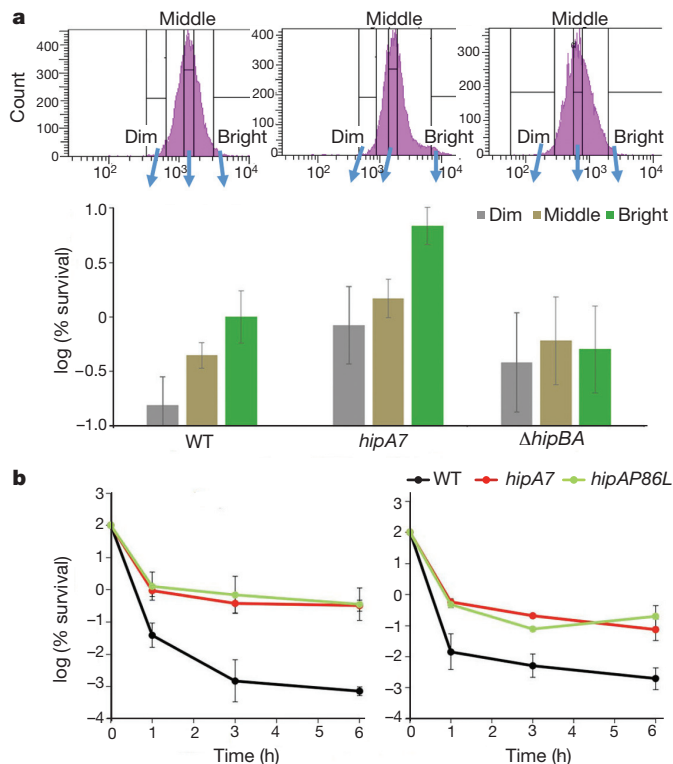


Figure 1 | Expression of *hipA* leads to persister formation. **a**, GFP expression levels of plasmid carrying promoter *hipBA*–GFP construct in WT, *hipA7* and Δ *hipBA* strains. One hundred thousand FACS-sorted cells were collected representing dim, middle and bright populations and survival to ofloxacin was measured. **b**, Exponentially growing cultures were treated with ampicillin (left panel) or ciprofloxacin (right panel). Samples were taken at indicated times and surviving bacteria were determined by colony count. Values in **a** and **b** are an average of at least three biological replicates; error bars, s.d.

Fig. 1). Given the dramatically improved survival of these mutants in the presence of antibiotics, we reasoned that such strains might be selected for not only in the laboratory, but also in nature.

UTIs are the most common chronic infections in humans and are caused primarily by *E. coli*^{22,23}. It has been suggested that the recurrent

nature of such UTI infections may be driven by drug tolerance²⁴. Indeed, dormant *E. coli* cells tolerant to antibiotics are present within the bladder epithelium. However, the mechanism of their tolerance is unknown. We therefore screened a library of 477 *E. coli* isolates, both commensal and from patients with UTIs, in search of *hipA* mutations. Strikingly, sequencing of the *hipA* genes revealed 23 *hipA7* mutants (both G22S and D291A substitutions were present in these mutants) and a *hipA*(P86L) mutant (Supplementary Table 1). Deletion of the *hipA7* allele in a UTI isolate caused a sharp decline in antibiotic tolerance, confirming the functionality of this mutation (Fig. 2a). Next, we examined the antibiotic tolerance of *E. coli hipA7* that had infected human bladder cells. A strain deleted in *hipA7* showed a sharp decrease in the level of persisters surviving treatment with ciprofloxacin, an antibiotic routinely used to treat UTIs (Fig. 2b). Thus, these data provide evidence that *hipA* mutations, including *hipA7*, are important players in clinically relevant *E. coli* MDT infections.

Mapping *HipA* high-persister mutants

In addition to *hipA*(P86L) and *hipA7* (*hipA*(G22S–D291A)), *hipA*(D88N), which was isolated in an earlier laboratory screen⁷, also leads to a high-persister phenotype. For *hipA7*, MDT is conferred by the G22S mutation, while D291A has a dampening effect (M.V., unpublished observations). Notably, each of these high-persister mutations map to HipA N-subdomain-1, which contains a unique fold (Fig. 2c)¹¹. In the structure of HipA–HipB bound to a single operator, Gly22, Pro86 and Asp88 are far from the HipA active site and HipB interacting surface (Fig. 2c)¹¹. However, data suggest that when HipA is assembled with HipB on the *hipBA* promoter, which contains multiple operators, its MDT activity is inhibited^{9,10} by some unknown mechanism(s).

Characterization of *hipBA* promoters

The *hipBA* system appears widespread among Gram-negative species. However, only the *E. coli hipBA* promoter has been characterized. This promoter contains four operators bound by HipB with the consensus TATCCN₈GGATA^{9–11}. To identify additional *hipBA* promoters, we searched the genomes of multiple bacteria (see Methods). These analyses revealed *hipBA* promoters and *hipB* and *hipA* genes in numerous Gram-negative bacteria. Intriguingly, all promoters contained two to four operators that are separated by 10 base pairs (bp), except for the O2 and O3 operators in *E. coli* and *Shigella sonnei*, which are linked by a 21 or 22 bp spacer (Fig. 3a). To deduce the

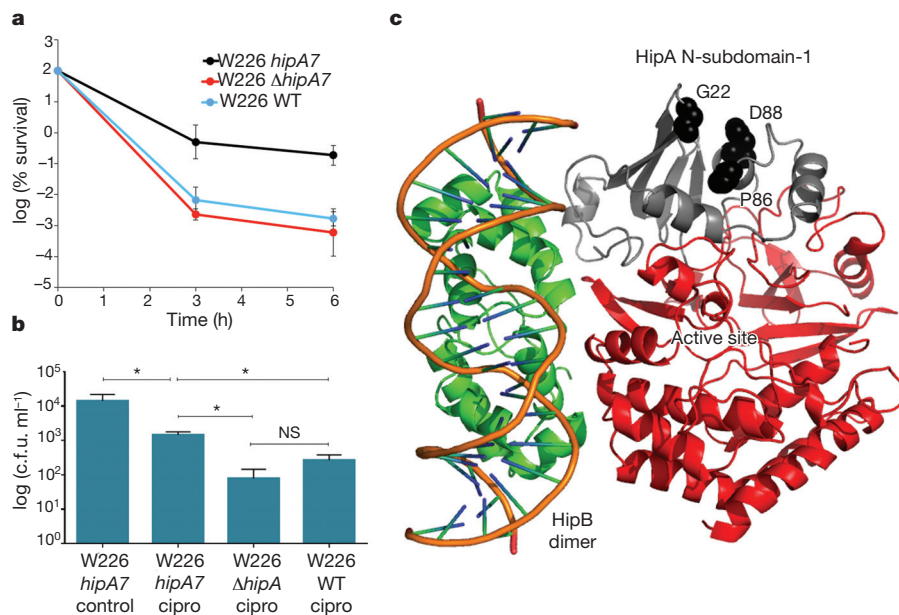


Figure 2 | Mutants in *hipA7* are found among pathogenic and commensal strains of *E. coli* and cause a high-persister phenotype in clinical isolates and bladder cells. **a**, The *hipA7* allele confers a high-persister phenotype to an exponentially growing clinical isolate of *E. coli* treated with ciprofloxacin. **b**, *E. coli* infecting HTB-9 human bladder cells. Strains (W226 *hipA7*, W226 Δ *hipA7* and W226 WT) were treated with ciprofloxacin (cipro). **P* < 0.05; NS, non-significant; c.f.u., colony-forming units. **c**, HipA high-persister mutation sites, G22S, P86L and D88N, localize to the N-subdomain-1, far from the active site, DNA and HipB dimer. Values in **a** and **b** are an average of at least three biological replicates; error bars, s.d.

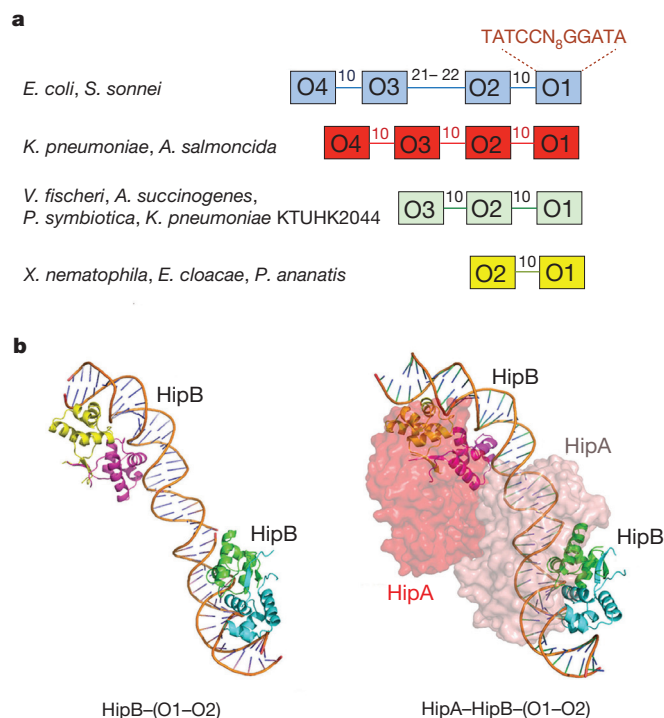


Figure 3 | Structures of HipB-(O1-O2) and HipA-HipB-(O1-O2) complexes. **a**, The *hipBA* promoter organization in various bacteria. Notable features are the conservation of the operator sequence and 10 bp spacing between operators (indicated) except *E. coli* and *S. sonnei*, which contain 21 or 22 bp O2-O3 linkers. **b**, The HipA-HipB-DNA structure (right) is shown in the same orientation as the HipB-(O1-O2) complex (left) with HipA molecules (red and pink) shown as transparent surfaces. Both structures adopt the same extended conformation.

molecular mechanisms of *hipBA* autorepression and higher-order promoter assembly, we next determined structures of HipB and the HipA-HipB complex bound to the ‘minimal’ *hipBA* promoter composed of the O1-O2 operators.

Structures of HipB bound to either a 48 or a 50 bp *hipBA* promoter were obtained to 3.35 and 3.50 Å resolution, respectively (Extended Data Table 1, Extended Data Fig. 2a and Fig. 3b). Specific binding by HipB dimers induces $\sim 70^\circ$ bends in consecutive operators as well as significant DNA deformations in the 10 bp linker, which results in the HipB dimers being positioned on opposite faces of the DNA (Fig. 3b). Thus, unlike previous suggestions that HipB binding to multiple *hipBA* operators might lead to DNA wrapping¹¹, both HipB-(O1-O2) structures reveal that, although the DNA is significantly distorted, the HipB-(O1-O2) complexes are extended (Extended Data Fig. 3a). That this structure is also formed in solution is supported by atomic force microscopy (AFM) experiments, which show HipB dimer pairs as single irregular spheres on closely spaced O1-O2 and O3-O4 sites on an extended DNA template (Extended Data Fig. 3b-d).

Structure of the HipBA-promoter complex

A HipA-HipB-(O1-O2) structure was next obtained to 3.77 Å resolution (Extended Data Table 2 and Extended Data Fig. 2b) and revealed the same extended conformation as the HipB-(O1-O2) complexes, with each HipA contacting the side of one HipB dimer (Figs 3b and 4a, b). As noted, it was unclear how HipA kinase activity is maintained in an inactive state in the promoter complex as the HipA active sites are exposed in the structure of HipA-HipB bound to a single operator¹¹. The HipA-HipB-(O1-O2) structure reveals why complex formation and, more pointedly, why the extended conformation of the complex are essential to HipA inhibition.

Specifically, the HipB-induced bends in the O1 and O2 operators juxtapose the normally monomeric HipA molecules, allowing them to dimerize. Strikingly, HipA dimerization, which buries $\sim 1,000$ Å² of surface area, blocks the active sites of each HipA molecule (Fig. 4a, b). Further, HipA dimerization positions the active sites in proximity, probably precluding the extrusion of the HipA P-loop, which can be *trans*-autophosphorylated, causing HipA inactivation (Extended Data Fig. 4)¹². While it is possible that structural changes in the P-loops and adjacent activation regions might allow them to access the extruded state, this seems unlikely, and preventing inadvertent P-loop ejection and phosphorylation would keep HipA primed for catalysis upon promoter release.

Mechanism for high-persister phenotype

As previously noted¹¹, Asp291 is located close to the HipB-HipA interface (Fig. 4b) but the roles of the HipA higher-persister mutations located on N-subdomain-1 were unclear (Fig. 2c). The HipA-HipB-(O1-O2) structure provides an explanation for these high-persister mutations as it reveals that N-subdomain-1 constitutes the majority of the HipA dimerization interface in the complex. N-subdomain-1 regions involved in dimerization include residues 20-25 and 53-90, both of which encompass the high-persister mutations. C-domain residues 263 and 270 provide the only additional dimer contacts. Although the detailed locations of the atoms in the HipA side chains cannot be discerned at this resolution, Gly22, Pro86 and Asp88 are positioned precisely at the dimer interface in the HipA-HipB-(O1-O2) structure. In high-resolution HipA structures, Asp88 and Pro86 participate in helical capping and hence stabilization of the relatively short $\alpha 4$ helix, which is important in HipA dimer contacts (Extended Data Fig. 5a, b and Fig. 4c). The two Gly22 residues directly abut and form the nexus of the dimer (Extended Data Fig. 5b). Modelling shows that substitution of this glycine to any other residue would lead to steric clash between subunits in the dimer (Fig. 4c).

The HipA-HipB-(O1-O2) structure also explains previous DNase I footprinting data showing that HipA makes multiple DNA contacts⁹. In the HipA-HipB-(O1-O2) structure, the DNA-facing surface of the HipA dimer is electropositive, and residues Lys3, Lys27, Arg49, Asn51 and Thr53 from HipA N-subdomain-1 and Lys379 and Arg382 from the C-domain are positioned to make DNA phosphate contacts (Extended Data Fig. 6). Notably, in the HipA-HipB-(O1-O2) structure, although the crystallization mixture contained a 2:2 HipB:HipA ratio, HipA molecules are only bound to HipB subunits facing the 10 bp spacer. This binding arrangement not only allows HipA-HipA dimerization, but also HipA-DNA contacts and hence would be predicted to be energetically favoured over binding to the outside-facing HipB subunits. Regardless, previous studies showed HipA is capable of binding HipB with a 2:2 ratio¹¹. It is possible that HipA molecules bound at the outer edges of promoter regions that do not dimerize could be active. To this point, however, studies indicate that HipB and HipA expression in cells is extremely low; it has been estimated that the *hipA* and *hipB* genes, which contain an unusual number of non-optimal codons and are under the control of a non-optimal promoter, may be transcribed only ~ 0.25 times per generation⁹. Expression analyses also suggest that HipB may be present at higher concentrations than HipA⁹. Thus, while the ratio of HipA to HipB and their intracellular concentrations, free and DNA-bound, are not known, multiple mechanisms appear to have been selected to ensure low protein levels, in particular of HipA, including possibly insufficient amounts of HipA to occupy the outside-facing HipB subunit.

Combined, our structural data suggest a molecular explanation for the *hipA7* high-persister phenotype identified decades ago⁶ as they predict that mutation of residues in the HipA-HipA interface, particularly the G22S substitution, would impair this dimerization, thereby disfavoring HipA-HipB-(O1-O2) complex formation. To test this structural hypothesis, we examined the HipA-HipA

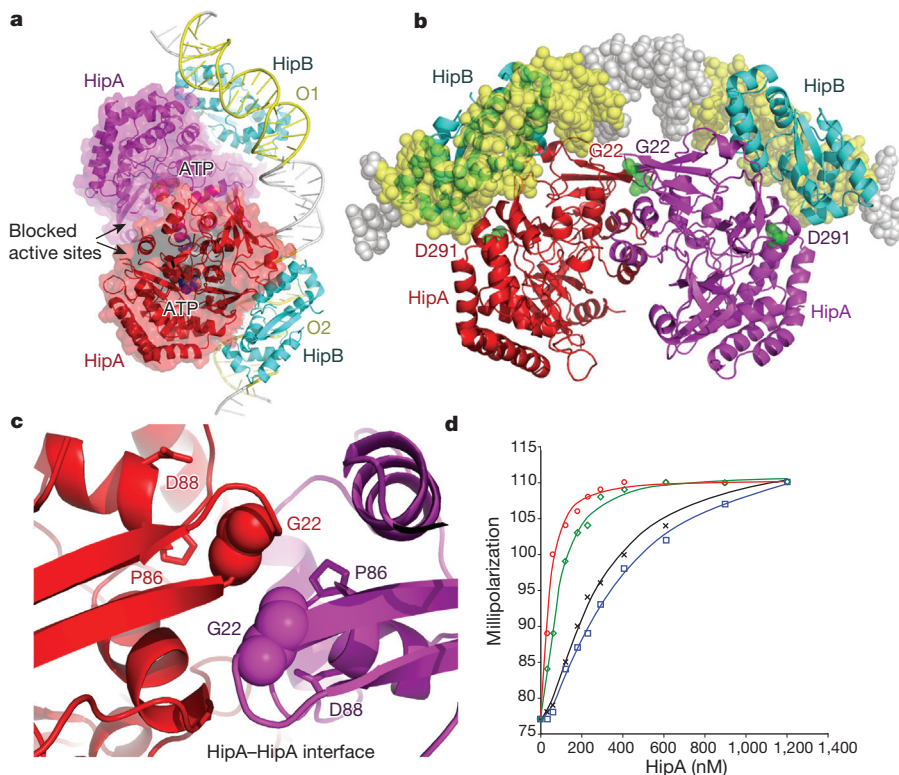


Figure 4 | Dimerization-mediated inhibition of HipA and structural mechanism underlying the high-persistence phenotype of N-subdomain-1 mutations. **a**, HipA-HipB-(O1-O2) structure. The HipA active sites, denoted by ATP molecules, which are not present in the structure, are occluded by HipA dimerization. **b**, Locations of HipA7 high-persistence mutations in the HipA-HipB-(O1-O2) complex. Gly22 and Asp291 are shown as green spheres. **c**, Close up of HipA dimer interface. Gly22 residues (spheres) are positioned precisely at the dimer centre. High-persistence mutations, D88N and P86L, shown as sticks, also localize to this interface. **d**, Representative binding isotherms of WT HipA (red plot), HipA(G22S) (blue plot), HipA(D88N) (green plot) and HipA(P86L) (black plot) and the HipB-(O1-O2) complex. Values in this figure are averages of three experiments.

interaction in the context of a fluorescently labelled O1-O2 DNA (F-O1-O2) complexed with HipB (Methods). Wild-type HipA bound the HipB-(F-O1-O2) complex with a dissociation constant (K_d) of 50 ± 5.7 nM, while the mutants displayed reduced binding, with K_d values of 374 ± 40 nM, 280 ± 80 nM and 87 ± 6.0 nM for HipA(G22S), HipA(P86L) and HipA(D88N), respectively (Fig. 4d). That HipA(D88N) was not as affected in its binding is consistent with previous data showing this mutation causes a less severe persistence phenotype⁷. Thus, these data support the structural mechanism for the high-persistence phenotype and explain the increased HipA protein expression in *hipA7* strains (Fig. 1a). Simply, there is less HipA7 bound at the promoter and HipA is required for full repression of the *hipBA* operon^{9,10}.

Models for HipBA-promoter complexes

The HipA-HipB-(O1-O2) structure reveals that the conserved 10 bp linker between operators provides appropriate spacing for HipA dimerization. However, in the *E. coli* and *S. sonnei* *hipBA* promoters, O2 and O3 are separated by 21 and 22 bp, respectively, which modelling indicates is too long to allow HipA-HipA contacts. To gain insight into HipA-HipB organization on the O2-O3 region of the promoter, we determined the structure of a HipA-HipB-(O2-O3) complex to 3.99 Å. Remarkably, the structure showed that the 21 bp DNA linker is disordered and apparently extruded, thereby allowing the HipA molecules to form the same dimer as observed in the O1-O2 complex (Extended Data Fig. 7a, b). Thus, while ~10 bp may be an energetically optimal inter-operator spacing to allow HipA-HipA contacts, the addition of an extra turn of DNA helix does not preclude the formation of HipA dimers. Combining this result with the HipA-HipB-(O1-O2) structure allows us to generate models for higher-order bacterial HipA-HipB-*hipBA* promoter complexes (Fig. 5).

The *hipBA* transcription repression mechanism

In addition to controlling the MDT activity of HipA, HipA-HipB-promoter complex formation also mediates transcription autorepression⁹. Bacterial RNA polymerase (RNAP) is recruited to promoters via specific interactions between its σ -factor and the -35 and

-10 boxes²⁵⁻²⁸. In the *E. coli* *hipBA* promoter, these elements are located at the 5' and 3' ends of O2¹⁰. The HipB-(O1-O2) structure includes the -10 and most of the -35 element. Thus, to gain insight

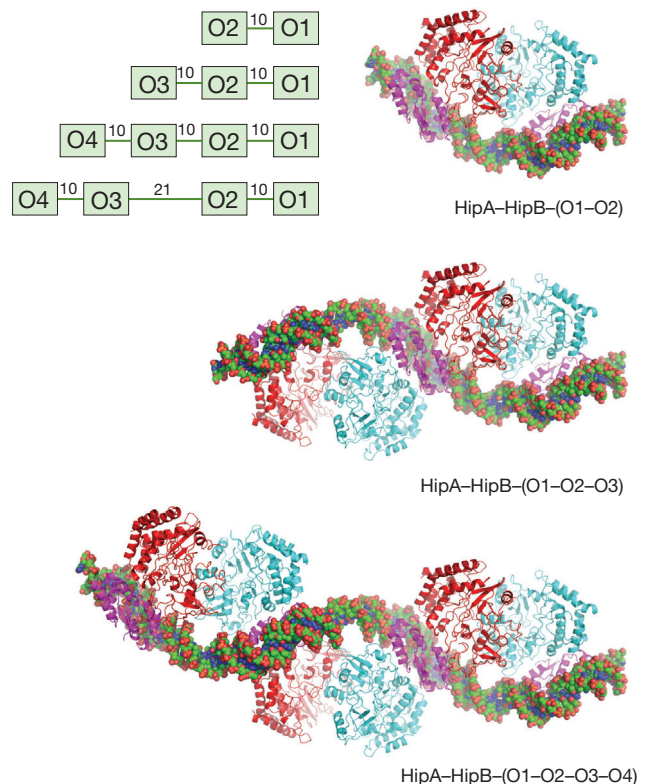


Figure 5 | Structures of fully assembled HipA-HipB-*hipBA* promoter complexes. Left: schematic organizations of *hipBA* promoters ascertained by bioinformatic analyses. Right: structure of the HipA-HipB-(O1-O2) complex (top) and deduced structures of the HipA-HipB-(O1-O2-O3) (middle) and HipA-HipB-(O1-O2-O3-O4) (bottom) complexes.

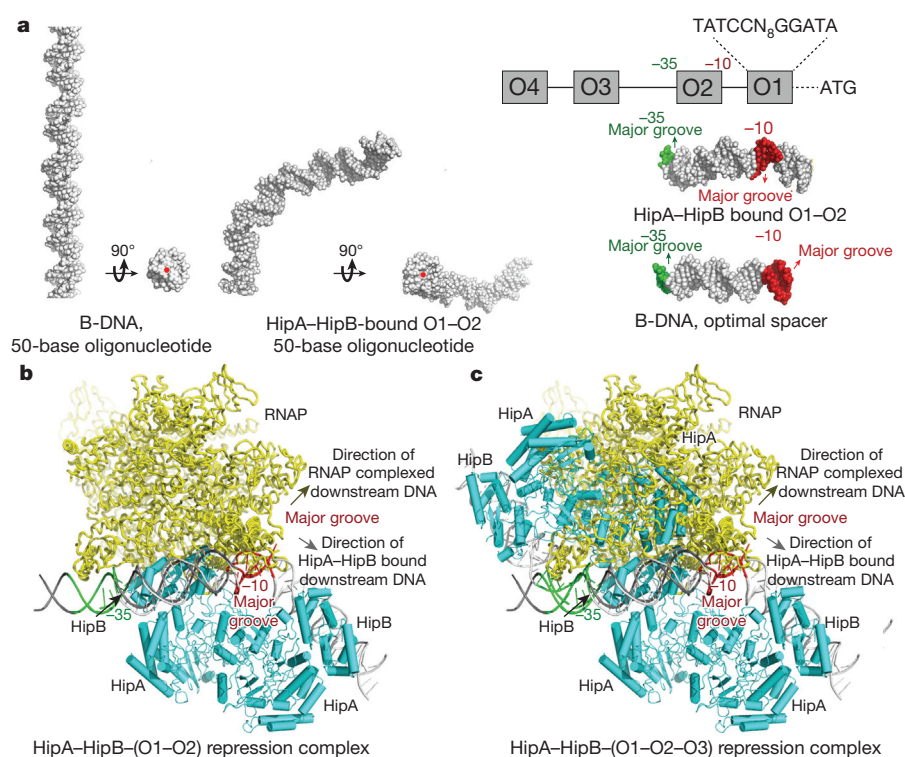


Figure 6 | Molecular mechanisms of HipB and HipA-HipB-mediated transcription repression of the *hipBA* operon. **a**, Comparison of HipA-HipB-bound DNA and canonical B-DNA structures (left). O2 encompasses the -35 and -10 boxes of the *hipBA* promoter and is dramatically distorted by HipB-HipA binding, consequently reconfiguring the major and minor groove positions to preclude σ -factor binding (right). **b**, Superimposition of the -35 and -10 elements of the HipA-HipB-(O1-O2) and RNAP holoenzyme-DNA complexes (1L9Z)²⁵ reveals HipB-RNAP steric clash and reorientation of downstream DNA. **c**, Superimposition of the -35 and -10 elements of the modelled HipA-HipB-(O1-O2-O3) and RNAP holoenzyme-DNA complexes reveals additional HipA- σ clash.

into the mechanism(s) of HipB and HipA-HipB autorepression, we analysed the DNA conformation surrounding O2 and overlaid HipA-HipB-promoter structures onto the RNAP holoenzyme-DNA structure. These analyses show that HipB-induced DNA distortions in O2 repositions the -35 and -10 boxes to lie on opposite faces of the DNA, probably precluding productive RNAP binding (Fig. 6a). Further, these superimpositions demonstrated that HipB, and to a lesser degree HipA, would sterically block RNAP access to the -35 box (Fig. 6b). HipA-HipB-mediated DNA distortion also bends the DNA downstream of -10 opposite to the direction used by RNAP to initiate transcription. Finally, superimposition of the HipA-HipB-(O1-O2-O3) complex onto the RNAP holoenzyme-DNA complex shows that the HipA molecule bound between O2 and O3 would sterically impede RNAP binding (Fig. 6c).

Our analyses indicate that HipB and HipA-HipB promoter-binding present a strong physical roadblock for RNAP binding and misalign key promoter elements. These findings suggest that the positions of the -35 and -10 boxes in the *E. coli hipBA* promoter have evolved to ensure highly efficient repression and hence might be similarly organized in other *hipBA* promoters. Indeed, we found that *hipBA* promoters in which the -35 and -10 elements could be readily predicted harbour the same relative positioning as found in the *E. coli* promoter (Extended Data Fig. 8), suggesting a conserved *hipBA* autorepression mechanism across Gram-negative bacteria.

Discussion

Persisters are the main culprits responsible for recalcitrance of chronic infections to antibiotic therapy^{1,4,5,29}. RNA endonuclease toxin-antitoxin modules, which use mRNA-degrading RNases to inhibit translation, have been shown to be expressed in persisters^{30,31} and deleting ten of them sharply decreases antibiotic tolerance²¹. We show here by single-cell analysis that tolerance increases in a small population of *E. coli* stochastically overexpressing HipA alone. Moreover, this kinase becomes the dominant factor determining tolerance in *hipA7* mutants, where it accounts for 99.9% of all persisters. We also show that *hipA7* mutants are present in *E. coli* isolates from patients with UTIs, providing a direct link with this particular

mechanism of persister formation and the clinical manifestation of disease. Target modification is the most common mechanism by which bacteria acquire resistance to antibiotics. The UTI *hipA7 E. coli* described in this study provides a precedent to a parallel evolutionary mechanism imparting increased tolerance to antibiotics.

Mutations in *hipA* that lead to a high-persister phenotype and UTIs localize to HipA N-subdomain-1, a surface exposed region distal to the HipA kinase active site and HipB binding region. Our structural studies reveal the importance of this region as they show that when HipA forms higher-order promoter complexes with HipB and multiple operators in *hipBA* promoters, the kinase forms dimers via interactions between operator-adjacent N-subdomains-1. Critically, the formation of these HipA dimers blocks their active sites. Hence, mutations in this HipA-HipA interface would liberate HipA from its inactive state, leading to increased persistence. These structures also explain the basis for *hipBA* autorepression, as HipB-HipA binding to the promoter distorts critical promoter elements required for productive RNAP binding and functions as a roadblock to efficient transcription. Finally, in general, the structural mechanisms by which promoters containing multiple DNA-binding elements are regulated are poorly understood, as structures have largely been determined for individual transcription-factor-DNA complexes. Our studies emphasize the importance of visualizing higher-order assemblies to understand not only the mechanisms of transcription regulation fully, but also how the functions of the DNA-bound regulatory proteins themselves and, in turn, cellular physiology are impacted by assembly formation.

Online Content Methods, along with any additional Extended Data display items and Source Data, are available in the online version of the paper; references unique to these sections appear only in the online paper.

Received 1 March; accepted 12 June 2015.

Published online 29 July 2015.

- Lewis, K. Persister cells. *Annu. Rev. Microbiol.* **64**, 357–372 (2010).
- Maisonneuve, E. & Gerdes, K. Molecular mechanisms underlying bacterial persisters. *Cell* **157**, 539–548 (2013).
- Lewis, K. Persister cells, dormancy and infectious disease. *Nature Rev. Microbiol.* **5**, 48–56 (2007).

4. Mulcahy, L., Burns, J., Lory, S. & Lewis, K. Emergence of *Pseudomonas aeruginosa* strains producing high levels of persister cells in patients with cystic fibrosis. *J. Bacteriol.* **192**, 6191–6199 (2010).
5. Conlon, B. P. *et al.* Activated ClpP kills persisters and eradicates a chronic biofilm infection. *Nature* **503**, 365–370 (2013).
6. Moyed, H. S. & Bertrand, K. P. *hipA*, a newly recognized gene of *Escherichia coli* K-12 that affects frequency of persistence after inhibition of murein synthesis. *J. Bacteriol.* **155**, 768–775 (1983).
7. Korch, S. B., Henderson, T. A. & Hill, T. M. Characterization of the *hipA7* allele of *Escherichia coli* and evidence that high persistence is governed by (p)ppGpp synthesis. *Mol. Microbiol.* **50**, 1199–1213 (2003).
8. Moyed, H. S. & Broderick, S. H. Molecular cloning and expression of *hipA*, a gene of *Escherichia coli* K-12 that affects frequency of persistence after inhibition of murein synthesis. *J. Bacteriol.* **166**, 399–403 (1986).
9. Black, D. S., Irwin, B. & Moyed, H. S. Autoregulation of *hip*, an operon that affects lethality due to inhibition of peptidoglycan or DNA synthesis. *J. Bacteriol.* **176**, 4081–4091 (1994).
10. Black, D. S., Kelly, A. J., Mardis, M. J. & Moyed, H. S. Structure and organization of *hip*, an operon that affects lethality due to inhibition of peptidoglycan or DNA synthesis. *J. Bacteriol.* **173**, 5732–5739 (1991).
11. Schumacher, M. A. *et al.* Molecular mechanisms of HipA-mediated multidrug tolerance and its neutralization by HipB. *Science* **323**, 396–401 (2009).
12. Schumacher, M. A. *et al.* Role of unusual P-loop ejection and autophosphorylation in HipA-mediated persistence and multidrug tolerance. *Cell Rep.* **2**, 518–525 (2012).
13. Correia, F. F. *et al.* Kinase activity of overexpressed HipA is required for growth arrest and multidrug tolerance in *Escherichia coli*. *J. Bacteriol.* **188**, 8360–8367 (2006).
14. Germain, E., Castro-Roa, D., Zenkin, N. & Gerdes, K. Molecular mechanism of bacterial persistence by HipA. *Mol. Cell* **52**, 248–254 (2013).
15. Kaspy, I. *et al.* HipA-mediated antibiotic persistence via phosphorylation of the glutamyl-tRNA-synthetase. *Nature Commun.* **4**, 3001 (2013).
16. Yamaguchi, Y. & Inouye, M. Regulation of growth and death in *Escherichia coli* by toxin–antitoxin systems. *Nature Rev. Microbiol.* **9**, 779–790 (2011).
17. Balaban, N. Q. Persistence: mechanisms for triggering and enhancing phenotypic variability. *Curr. Opin. Genet. Dev.* **21**, 768–775 (2011).
18. Hayes, F. & Van Melder, L. Toxins-antitoxins: diversity, evolution and function. *Crit. Rev. Biochem. Mol. Biol.* **46**, 386–408 (2011).
19. Rotem, E. *et al.* Regulation of phenotypic variability by a threshold-based mechanism underlies bacterial persistence. *Proc. Natl Acad. Sci. USA* **107**, 12541–12546 (2010).
20. Hansen, S., Lewis, K. & Vulić, M. Role of global regulators and nucleotide metabolism in antibiotic tolerance in *Escherichia coli*. *Antimicrob. Agents Chemother.* **52**, 2718–2726 (2008).
21. Maisonneuve, E., Shakespeare, L. J., Jorgensen, M. G. & Gerdes, K. Bacterial persistence by RNA endonucleases. *Proc. Natl Acad. Sci. USA* **108**, 13206–13211 (2011).
22. Shilling, J. D. & Hultgren, S. J. Recent advances into the pathogenesis of recurrent urinary tract infections: the bladder as a reservoir for uropathogenic *Escherichia coli*. *Int. J. Antimicrob. Agents* **19**, 457–460 (2002).
23. Blango, M. G. & Mulvey, M. A. Persistence of uropathogenic *Escherichia coli* in the face of multiple antibiotics. *Antimicrob. Agents Chemother.* **54**, 1855–1863 (2010).
24. Mysorekar, I. U. & Hultgren, S. J. Mechanisms of uropathogenic *Escherichia coli* persistence and eradication from the urinary tract. *Proc. Natl Acad. Sci. USA* **103**, 14170–14175 (2006).
25. Campbell, E. A., Westblade, L. F. & Darst, S. E. Regulation of bacterial RNA polymerase sigma activity: a structural perspective. *Curr. Opin. Struct. Biol.* **11**, 121–127 (2008).
26. Murakami, K. S. & Darst, S. A. Bacterial RNA polymerases: the whole story. *Curr. Opin. Struct. Biol.* **13**, 31–39 (2003).
27. Murakami, K. S., Masuda, S., Campbell, E. A., Muzzin, O. & Darst, S. A. Structural basis of transcription initiation: an RNA polymerase holoenzyme–DNA complex. *Science* **296**, 1285–1290 (2002).
28. Feklistov, A. & Darst, S. A. Structural basis for promoter –10 element recognition by the bacterial RNA polymerase σ subunit. *Cell* **147**, 1257–1269 (2011).
29. LaFleur, M. D., Qi, Q. & Lewis, K. Patients with long-term oral carriage harbor high persister mutants of *Candida albicans*. *Antimicrob. Agents Chemother.* **54**, 39–44 (2010).
30. Keren, I., Shah, D., Spoering, A., Kaldalu, N. & Lewis, K. Specialized persister cells and the mechanism of multidrug tolerance in *Escherichia coli*. *J. Bacteriol.* **186**, 8172–8180 (2004).
31. Shah, D. V. *et al.* Persisters: a distinct physiological state of *E. coli*. *BMC Microbiol.* **6**, 53–62 (2006).

Supplementary Information is available in the online version of the paper.

Acknowledgements We thank the Advanced Light Source and their support staff. The Advanced Light Source is supported by the Director, Office of Science, Office of Basic Energy Sciences, Materials Sciences Division, of the US Department of Energy at the Lawrence Berkeley National Laboratory. We also thank the Broad Institute and funding from the NIAID–GSCID for whole-genome sequencing, and A. E. Stapleton and J. R. Johnson for the UTI *E. coli* strains. This work was supported by an MD Anderson Trust Fellowship (to M.A.S.), the Welch Foundation (G-0040) and Duke University School of Medicine (to R.G.B.), and by National Institutes of Health grants T-R01 AI085585 and R01 GM061162 and by an Army Research Office instrumentation grant W911NF-09-1-0278 (to K.L.).

Author Contributions M.A.S. and R.G.B. designed and analysed the structural and biochemical studies. P.B. and K.L. designed and analysed the genetic studies. M.A.S. performed the X-ray crystallographic and biochemical studies. P.B. performed genetic and cell culture studies. S.H. performed the *hipBA* expression analysis. M.V. assisted with genetic analyses. J.M. performed bioinformatics analyses. N.B.C. purified proteins for structural studies. M.A.S., R.G.B., P.B. and K.L. wrote the manuscript.

Author Information Crystallographic coordinates and structure factor files have been deposited in the Protein Data Bank under accession numbers 4YG7, 4YG4 and 4YG1. Reprints and permissions information is available at www.nature.com/reprints. The authors declare no competing financial interests. Readers are welcome to comment on the online version of the paper. Correspondence and requests for materials should be addressed to M.A.S. (maria.schumacher@duke.edu), R.G.B. (Richard.brennan@duke.edu) or K.L. (k.lewis@neu.edu).

METHODS

Bacterial strain construction. The *hipA*P86L and *hipA*7 mutants in the WT (MG1655) background were constructed using the P1 transduction method³². The deletion mutant of *hipA* in uropathogenic *E. coli* W226 was constructed using a modified lambda Red recombination method³³. A kan/parE cassette under the control of a rhamnose promoter was used to replace *hipA*³⁴. Colonies were selected on Luria Bertani agar (LBA) + kanamycin plates and mutations confirmed by lack of growth on minimal-MOPS agar plates containing 0.5% rhamnose as a sole carbon source. For replacement of the kan/parE cassette with a WT *hipA*, the allele was amplified from WT MG1655 strain and inserted into target cells by transformation. Colonies that successfully replaced the cassette with the new *hipA* allele were selected on minimal-MOPS rhamnose agar plates. The mutants used for sorting were constructed by inserting a reporter plasmid (pUA66) obtained from the *E. coli* promoter library, which had a *hipA* promoter transcriptionally fused to GFP³⁵. The plasmids were transformed into a WT (MG1655) and *hipA*7 strain. The representative *E. coli* commensal and UTI clinical strains were obtained from H. Ochman, R. K. Selander and the ECOR reference collection^{36,37}. The UTI strains were obtained from A. E. Stapleton and J. R. Johnson.

Mutagenesis of WT *E. coli* to obtain high-persister mutants. An *E. coli* K12 MG1655 WT strain was used for the selection of *in vitro* *hip* mutants via a modified version of the original Moyed and Bertrand screen⁶. Briefly, a WT *E. coli* culture was grown overnight from a single colony. The overnight culture was diluted 1:500 in Luria Bertani broth (LBB) and grown for 2 h to an absorbance ($A_{600\text{ nm}}$) of 0.2. This culture was diluted 1:50 in LBB and regrown to $A_{600\text{ nm}} = 0.2$. The culture was diluted once again and regrown. The serial dilutions and regrowth allowed the removal of pre-existing persisters^{38,39}. After the third growth step, cultures were diluted 2:1 in 125 mM HEPES/KOH pH 7 in a 2 ml tube and mutagenized with $15\text{ }\mu\text{g ml}^{-1}$ ethyl methanesulfonate (EMS) for 45 min at 37 °C³⁴. EMS was removed by centrifugation and the cell pellet was resuspended in LBB and grown overnight to allow for segregation. The mutagenized pool was plated onto LBA and LBA with $100\text{ }\mu\text{g ml}^{-1}$ rifampicin. Colony-forming units were scored after incubation for 24 h and frequency of rifampicin-resistant mutants was calculated as a measure of efficiency of mutagenesis.

Enrichment for high-persister mutants from the mutagenized pools. To enrich for high-persister mutants, the mutagenized pool was diluted 1:750 in fresh medium and grown to mid-exponential phase before challenging with a combination of $100\text{ }\mu\text{g ml}^{-1}$ ampicillin and $50\text{ }\mu\text{g ml}^{-1}$ cefotaxime for 4 h. The challenge was done with two antibiotics to minimize the selection of resistant mutants. The cells were then washed twice with 1% NaCl, resuspended in fresh medium and grown overnight. This cycle of antibiotic treatment and regrowth was repeated two more times and the persister fractions were measured at the end of each cycle by plating the dilutions onto LBA and scoring the colony-forming units. After the final round of enrichment, $100\text{ }\mu\text{l}$ of the mutagenized pools were plated onto four LB plates and incubated overnight to allow colonies to grow. Twelve clones were selected randomly from well-isolated colonies and streaked for purity. Minimal inhibitory concentrations (MICs) of all clones for ampicillin, cefotaxime and ofloxacin were established to eliminate any possible resistant mutants. In addition, the growth rates of individual clones were tested to eliminate mutants with growth abnormalities. Ten mutants exhibited MICs and growth rates similar to the parent WT strain. The *hip* phenotype of the clones was tested in exponential phase with $100\text{ }\mu\text{g ml}^{-1}$ ampicillin, as well as in stationary phase with $5\text{ }\mu\text{g ml}^{-1}$ ofloxacin. Clones with increased antibiotic tolerance in both exponential and stationary phases were sent for whole-genome sequencing to identify mutated genes.

Growth rate and MIC measurement. The growth rates of the selected high-persister mutants were measured in LB broth. Overnight cultures were diluted 1:1,000 in fresh medium and grown for 6 h. Growth was measured by plating dilutions onto LB agar and counting colony-forming units per millilitre (c.f.u. ml⁻¹) every 30 min. To eliminate resistant mutants, the MICs of all selected clones were determined for ampicillin, cefotaxime and ofloxacin. The MIC measurements were made by standard MIC assays according to Clinical and Laboratory Standards Institute guidelines.

Selection of high-persister candidate clones. The high-persister clones for whole-genome sequencing were selected on the basis of three criteria: high-persister phenotype, WT MICs and WT growth rates. Nine clones that met these criteria were selected for whole-genome sequencing.

Whole-genome sequencing. Whole-genome sequencing was performed on DNA extracted from high-persister candidate strains using a Qiagen DNEasy DNA extraction kit. To identify the mutations responsible for the high-persister phenotype in the selected *in vitro* *hip* mutants, whole-genome sequencing of these strains was done at the Broad Institute (Cambridge, Massachusetts, USA) using Solexa sequencing technology. The genomes of the sequenced *hip* mutants were

compared with the WT parent strain to determine the SNPs generated by EMS mutagenesis.

Persister assays. Persister assays for exponentially growing cultures were done by diluting overnight cultures 1:100 in fresh medium and then growing the cultures to late exponential phase ($\sim 5 \times 10^7$ c.f.u. ml⁻¹). An aliquot of the culture was taken before the addition of antibiotic to measure the initial colony-forming unit counts. Antibiotic was then added and aliquots were removed at 1, 3 and 6 h time points, washed with 1% NaCl, serially diluted and plated onto LBA or MacConkey agar, as indicated.

Sorting persisters expressing GFP using FACS. Bacterial cultures containing the reporter plasmid were grown overnight from freezer stocks. The overnight cultures were further diluted 1:100 in fresh medium containing kanamycin and grown to late exponential phase. At this stage, cells were washed twice with sterile PBS and run through the FACS Aria II cell sorter. Individual cells were sorted on the basis of their GFP expression levels. Total cell population GFP levels were measured by analysing 10,000 cells per sample. The cell populations were divided into three fractions based on their intensity of fluorescence (dim, middle and bright) and sorted into separate tubes with each fraction containing 100,000 cells. The fractions were then individually resuspended into media containing $5\text{ }\mu\text{g ml}^{-1}$ ofloxacin for 3 h and the dilutions were plated onto LBA to count colony-forming units per millilitre.

***E. coli* infection of bladder cell cultures.** HTB-9 human bladder cells (American Type Culture Collection (ATCC) 5637) were obtained from ATCC and grown to 80% confluence in 24-well plates in RPMI1640 supplemented with 10% fetal bovine serum, 2 mM L-glutamine, 10 mM HEPES, 1 mM sodium pyruvate, 4,500 mg l⁻¹ glucose, and 1,500 mg l⁻¹ sodium bicarbonate, and incubated at 37 °C in a 5% CO₂ atmosphere. Cells were examined daily under the microscope to check for contamination and healthy growth. *E. coli* cultures for infection were grown in LBB for 24 h at 37 °C in static conditions to induce type 1 pilus formation, which is necessary for cell attachment. Once the bladder cell cultures reached the desired confluency, the cells were infected with the *E. coli* cultures as described in ref. 40. Infected cells were then washed twice with PBS2+, and fresh media containing either $2\text{ }\mu\text{g ml}^{-1}$ ciprofloxacin or $10\text{ }\mu\text{g ml}^{-1}$ gentamycin (control) was added to the appropriate wells to determine the persister fraction in the infected cells. After 6 h of incubation, the bladder cells were lysed with 1 ml of 0.4% Triton X-100 in PBS. All steps subsequent to lysis were performed on ice, to prevent loss of bacteria. The lysates were diluted and $10\text{ }\mu\text{l}$ were plated in triplicates on MacConkey agar to count survivors. Five hundred microlitres of the undiluted lysates were plated onto MacConkey agar plates to increase the limit of detection.

Statistical analysis. No statistical methods were used to predetermine sample size. The experiments were not randomized. The investigators were not blinded to allocation during experiments and outcome assessment.

The statistical significance for bladder cell experiments was calculated using unpaired two-tailed *t*-tests in GraphPad Prism 6 software. *P* values below 0.05 were considered significant.

Protein expression, purification and crystallization of HipB–(O1–O2), HipA–HipB–(O1–O2) and HipA–HipB–(O2–O3) complexes. HipB was purified in a single step via Ni-NTA chromatography. In all crystallization experiments, the His-tag was removed by thrombin cleavage. HipA(D309Q), in which the catalytic base, D309, was mutated to glutamine rendering the protein inactive, was expressed and purified as previously described⁴¹. HipA(D309Q) was used in all structural studies and hence will be referred to as HipA. To obtain HipB–DNA crystals, HipB was concentrated to 20 mg ml^{-1} and mixed at a stoichiometry of one DNA duplex to two HipB dimers. Two crystal forms of HipB–(O1–O2) complexes were obtained. The $P_{21}2_12_1$ form was grown using an O1–O2 DNA duplex with the sequence 5′-TTATCCGCTTAAGGGGATATTATAAGTTT TATCCTTTAGTGAGGATAA-3′. Crystals were produced by mixing the HipB–DNA solution, 1:1, with 38% MPD and 0.1 M sodium acetate pH 4.6. The resultant crystals were cryo-preserved straight from the drop for data collection. A C2 crystal form was obtained by combining HipB with a DNA containing an O1 site with a self-complementary 10 bp overhang designed to generate a 50 bp symmetric O1–O1 site (a pseudo-O1–O2 site). The DNA was mixed 1:1 with 20 mg ml^{-1} of HipB dimer and crystallized using 27% PEG 8000, 0.1 M MES pH 6.5. The crystals were cryo-preserved using the crystallization solution supplemented with 20% glycerol. Crystals of the HipA–HipB–(O1–O2) complex were obtained by using the self-complementary O1 site, which generated the 50 bp symmetric operator duplex. To crystallize the HipA–HipB–DNA complex, HipA, HipB dimer and DNA duplex were mixed 2:1:1 and added 1:1 (v:v) to 4 M sodium formate. The crystals took the tetragonal, space group $P_{43}2_12_1$. A 57-base oligonucleotide encompassing the *hipBA* O2–O3 site (5′-TATCCCGTAGAG CGGATAAGATGTGTTTCCAGATTGACTTATCCTCACTAAAGGATA-3′) was used to crystallize the HipA–HipB–(O2–O3) complex. To form the ternary

complex, HipA, HipB dimer and DNA duplex were mixed 4:2:1 and the solution combined with 1.3 M ammonium sulfate, 0.1 M citrate pH 5.6. The crystals were cryo-preserved by dipping them in the crystallization solution supplemented with 15% glycerol for several seconds before placement in the cryo-stream. All X-ray intensity data were collected at the Advanced Light Source beamline 8.3.1 and processed with MOSFLM.

Structure determinations of the HipB-(O1-O2), HipA-HipB-(O1-O2) and HipA-HipB-(O2-O3) complexes. The HipB-(O1-O2) complex structure was determined using the previously determined HipA-HipB-21-base oligonucleotide DNA structure¹¹, as a search model after removing HipA. There is a full 48 bp O1-O2 fragment and two HipB dimers in the asymmetric unit. Molecular replacement using Phaser produced two solutions and, after refinement, electron density for the DNA connecting the O1 and O2 operators was revealed and modelled. The structure was refined using CNS and Phenix^{41,42}. The HipB complex with the two-fold related O1 sites was also solved using the HipB dimer-O1 complex. One solution was obtained and crystal symmetry generated the extended complex. After refinement, density for the connecting DNA was evident and modelled. However, the value of R_{free} remained high (> 39%). After several rounds of refitting and refinement, clear electron density was observed for a non-specifically bound HipB dimer in which one HipB subunit makes semi-specific contacts while the other makes no base contacts. Notably, this non-specific complex may represent a snapshot of HipB interaction with DNA before forming a specific complex with the operator and concomitant bending. Addition of the extra HipB dimer led to convergence of refinement to a value of $R_{\text{free}} = 28.9\%$. The HipB-(O1-O2) form 1 crystal structure refined to final value of $R_{\text{work}}/R_{\text{free}} = 24.4\%/28.5\%$ with 91.1% of residues in the favoured region of the Ramachandran plot, while the HipB-(O1-O2) form 2 structure had a final value of $R_{\text{work}}/R_{\text{free}} = 24.8\%/28.9\%$ with 94.0% of residues in the most favoured region of the Ramachandran plot (Extended Data Table 1).

Freshly grown crystals of the HipA-HipB-(O1-O2) complex only diffracted to 10 Å. However, crystals in drops that had dried out over time diffracted to beyond 5 Å. Hence, systematic dehydration efforts were initiated and resulted in significantly improved diffraction and the ability to develop a cryo-condition. Data were collected to 3.77 Å resolution and the structure was solved by molecular replacement using the HipA-HipB-O1 structure. The structure could only be solved after removing one HipA (giving a HipA:HipB:DNA stoichiometry of one HipA subunit to one HipB dimer to one DNA duplex). Two solutions were obtained and used to construct the final model, which contained two HipA subunits, two HipB dimers and two O1 sites with the connecting spacer DNA. The model was minimally refined in Phenix after rigid body optimization⁴¹ (Extended Data Table 2). The HipA-HipB-(O2-O3) structure was solved by molecular replacement using the HipA-HipB dimer-O1 complex from the HipA-HipB-(O1-O2) structure. There were two HipA molecules and one HipB dimer in the asymmetric unit and half of the 57-bp oligonucleotide DNA. Crystallographic symmetry generated the full complex. Remarkably, electron density for the central 21 bp operator spacer region was mostly disordered. The structure was minimally refined in CNS⁴² (Extended Data Table 2).

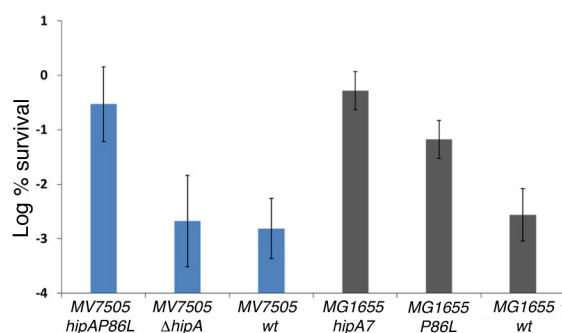
Identification and analyses of *hipBA* promoter. To locate and map putative *hipBA* operators within the promoters of enteric bacteria, the Regulatory Sequence Analysis Tools (RSAT)⁴³ program was used. The operator-based TATCCNNNNNNNGGATA sequence pattern was used as the search input.

Fluorescence polarization binding studies. Fluorescence-polarization-based binding assays⁴⁴ were performed in binding buffer consisting of 150 mM NaCl and 25 mM Tris-HCl pH 7.5. To assess the abilities of WT HipA, HipA(G22S), HipA(D88N) and HipA(P86L) to bind to the HipB-(O1-O2) complex, WT HipB was first titrated into the binding buffer containing 1 nM fluoresceinated O1-O2 DNA until saturation. Increasing concentrations of HipA protein were then

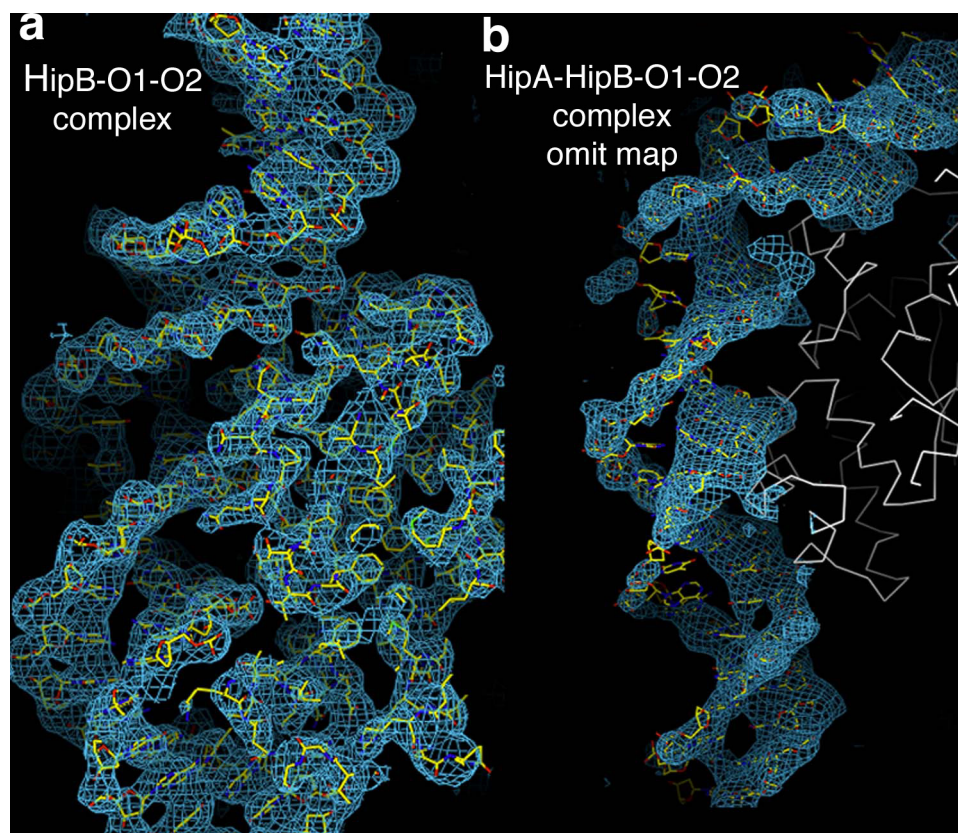
added to this complex. The data were plotted and fitted using KaleidaGraph. These analyses were conducted in triplicate (technical duplicates) with associated errors noted in the text.

AFM imaging of HipB-DNA complexes. A linear 1,811 bp DNA containing the entire 5' untranslated region and *hipBA* promoter, referred to as *phipBA*, was amplified using *E. coli* K12 MG1655 genomic DNA as a template and PCR primers (forward: 5'-ATAATAACTCGAGTCACCTACTACCGTATCTCGGCTTAA-3'; reverse: 5'-ATAATAATACATATGACCGTATAAGCCGCATGTCGAGATGGC-3'). The gel-purified *phipBA* was subcloned into the pET15b vector after digesting with XhoI and NdeI. To obtain large quantities of the resulting 500 bp DNA, PCR was performed using the pET15b-*phipBA* as a template and the primers 5'-AAGTTTAGGCATTACCACTCC-3' (forward) and 5'-ACCGTATAAGCCGCATGTCGA-3' (reverse), respectively. The amplified 500 bp DNA was gel purified using a Qiaquick gel extraction kit and the sequence was verified by DNA sequencing. AFM was performed as described⁴⁵ whereby 20 μM HipA and HipB were mixed in a 1:1 ratio in binding buffer (20 mM Tris pH 7.5, 200 mM NaCl). The HipA-HipB complex was then mixed with the 500 bp DNA at 4:1 or 8:1 ratios and incubated at 23 °C for 10 min before AFM analysis. The AFM data were collected after a sample was deposited on 1-(3-aminopropyl)silatrane (APS) mica⁴⁶ and incubated on this surface. Excess sample was washed off with de-ionized water and the resultant sample dried with argon gas. AFM images in air were acquired using a MultiMode AFM NanoScope IV system operating in tapping mode. Regular tapping-mode silicon probes with a spring constant of 42 N m⁻¹ and a resonant frequency between 300 and 320 kHz were used.

32. Miller, J. H. *A Short Course in Bacterial Genetics* 357–364 (Cold Spring Harbor Laboratory Press, 1992).
33. Datsenko, K. A. & Wanner, B. L. One-step inactivation of chromosomal genes in *Escherichia coli* K-12 using PCR products. *Proc. Natl Acad. Sci. USA* **97**, 6640–6645 (2000).
34. Maisonneuve, E., Shakespeare, L. J., Jørgensen, M. G. & Gerdes, K. Bacterial persistence by RNA endonucleases. *Proc. Natl Acad. Sci. USA* **108**, 13206–13211 (2011).
35. Zaslaver, A. A. *et al.* A comprehensive library of fluorescent transcriptional reporters for *Escherichia coli*. *Nature Methods* **3**, 623–628 (2006).
36. Ochman, H. & Selander, R. K. Standard reference strains of *Escherichia coli* from natural populations. *J. Bacteriol.* **157**, 690–693 (1984).
37. Duriez, P. *et al.* Commensal *Escherichia coli* isolates are phylogenetically distributed among geographically distinct human populations. *Microbiology* **147**, 1671–1676 (2001).
38. Lewis, K. *et al.* in *Biofilms, Infection and Antimicrobial Therapy* (eds Pace, J. *et al.*) 241–256 (Taylor & Francis, 2006).
39. Keren, L. N. *et al.* Persister cells and tolerance to antimicrobials. *FEMS Microbiol. Lett.* **230**, 12–18 (2004).
40. Blango, M. G. & Mulvey, M. A. Persistence of uropathogenic *Escherichia coli* in the face of multiple antibiotics. *Antimicrob. Agents Chemother.* **54**, 1855–1863 (2010).
41. Adams, P. D. *et al.* PHENIX: a comprehensive Python-based system for macromolecular structure solution. *Acta Crystallogr. D* **66**, 213–221 (2012).
42. Brünger, A. T. *et al.* Crystallography and NMR System: a new software suite for macromolecular structure determination. *Acta Crystallogr. D* **54**, 905–921 (1998).
43. Thomas-Chollier, M. *et al.* RSAT 2011: regulatory sequence analysis tools. *Nucleic Acids Res.* **39**, W86–W91 (2011).
44. Lundblad, J. R., Laurance, M. & Goodman, R. H. Fluorescence polarization of protein-DNA and protein-protein interactions. *J. Mol. Endocrinol.* **10**, 607–612 (1996).
45. Ni, L., Tonthat, N. K., Chinnam, N. & Schumacher, M. A. Structures of the *Escherichia coli* transcription activator and regulator of diauxie, XylR: an AraC DNA-binding family member with a LacI/GalR ligand-binding domain. *Nucleic Acids Res.* **41**, 1998–2008 (2013).
46. Shlyakhtenko, L. S. *et al.* Silatrane-based surface chemistry for immobilization of DNA, protein-DNA complexes and other biological materials. *Ultramicroscopy* **97**, 279–287 (2003).

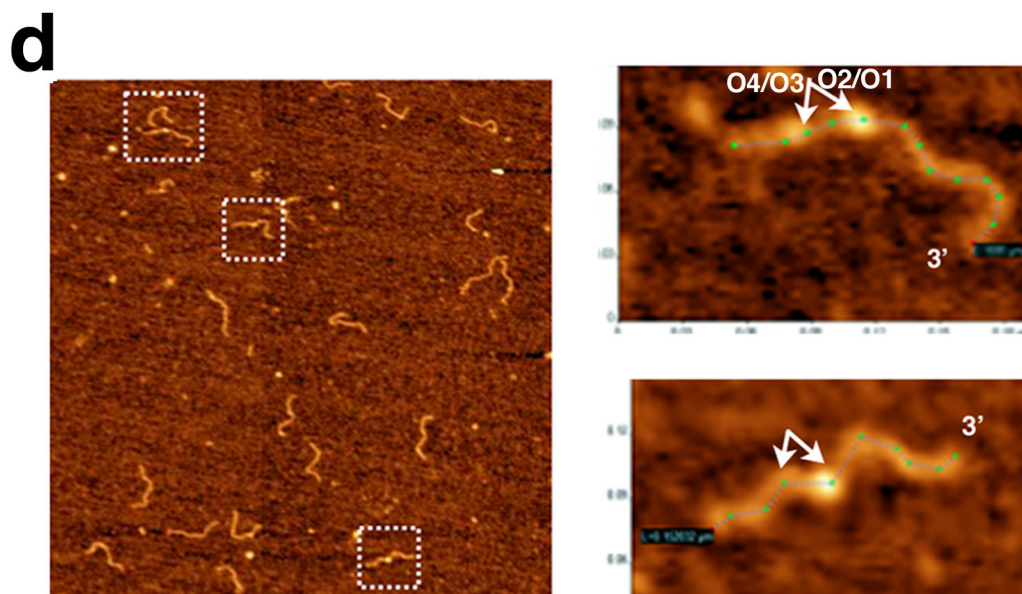
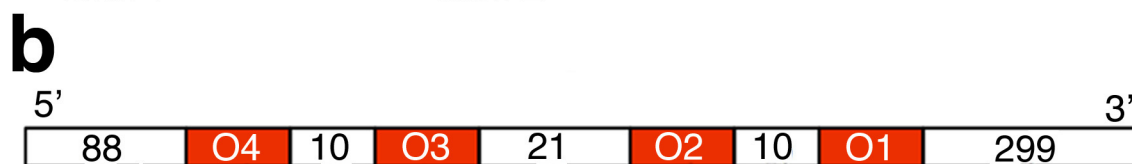
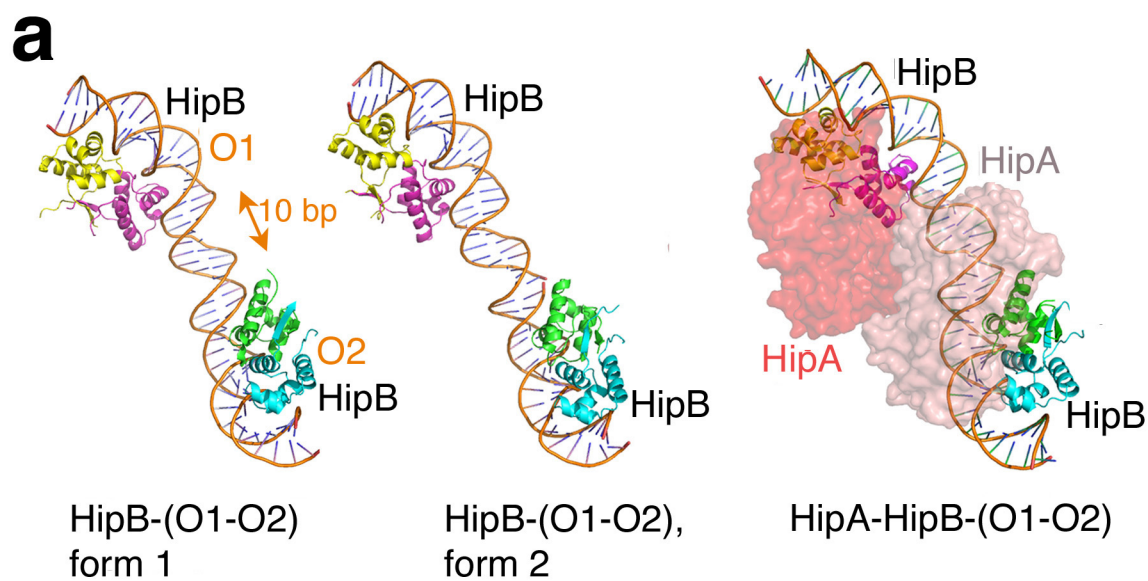


Extended Data Figure 1 | Validation of the persister phenotype of the *hipAP86L* mutant allele. Comparison of time-dependent survival of isogenic strains of *E. coli* to $100 \mu\text{g ml}^{-1}$ of ampicillin in exponential phase. MV7505 was the original EMS strain with the *hipAP86L* mutation, Δ *hipA* and WT *hipA* in the same background (MV7505 Δ *hipA* and MV7505 WT), MG1655 (WT) and known high-persister mutant (MG1655 *hipA7*). Overnight cultures of the strains were diluted 1:100 in fresh medium and, after 1.5 h of growth, treated with $100 \mu\text{g ml}^{-1}$ of ampicillin for 6 h. Values are an average of at least three individual biological replicates; error bars, s.d.



Extended Data Figure 2 | Electron density maps for HipB-(O1-O2) and HipA-HipB-(O1-O2) promoter complexes. **a**, Structure of HipB-(O1-O2) complex showing the final refined structure and composite omit map (blue mesh), contoured at 0.9σ and calculated to 3.35 Å resolution. **b**, $F_o - F_c$

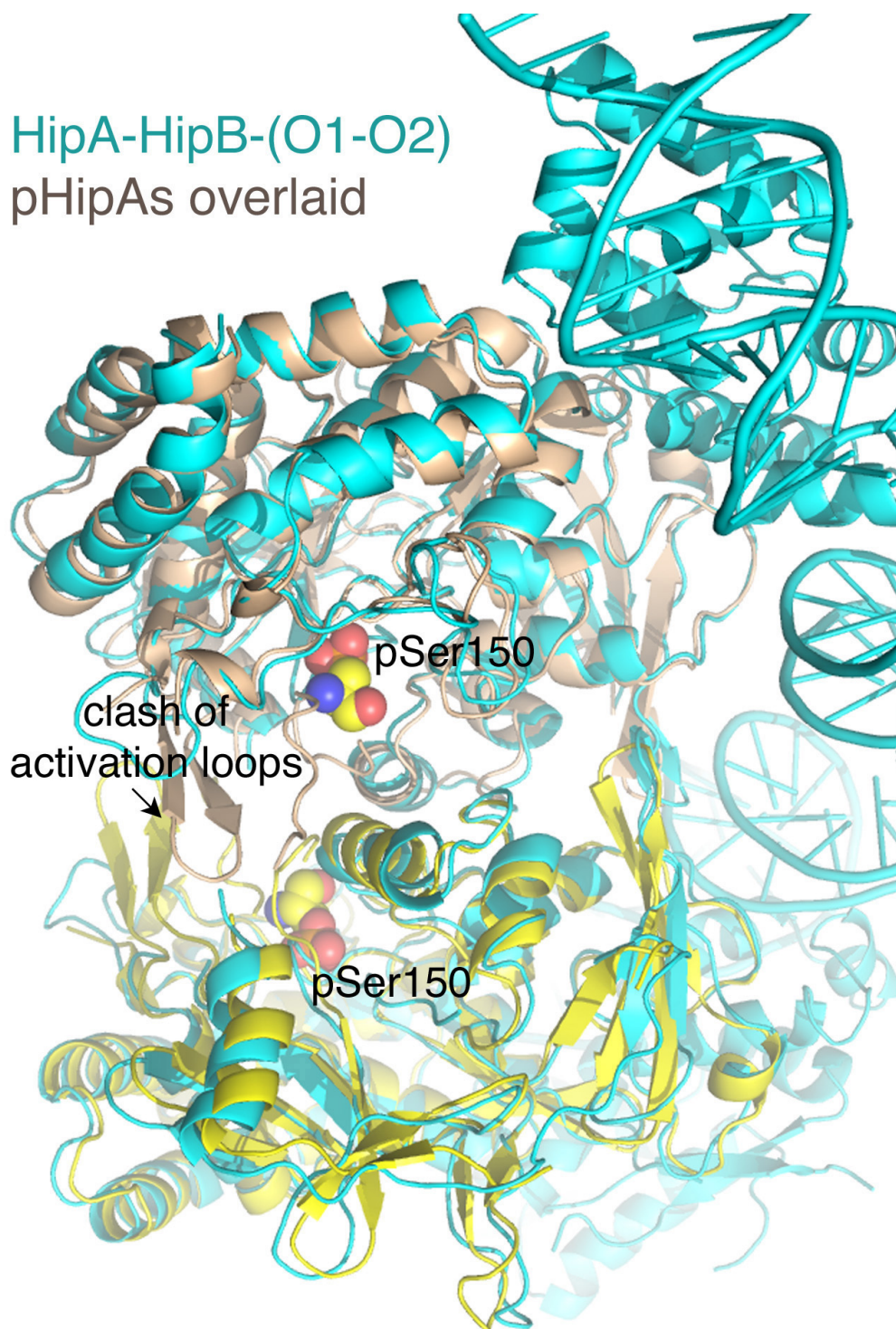
omit electron density map (blue mesh) contoured at 3.5σ to 3.77 Å resolution for the HipA-HipB-(O1-O2) complex in which the entire DNA molecule had been removed. The protein backbone is shown as white lines.



Extended Data Figure 3 | Higher-order HipB-*hipBA* and HipA-HipB-*hipBA* promoter complexes are extended. **a**, Comparison of HipB-(O1-O2) and HipA-HipB-(O1-O2) structures showing they adopt the same extended conformation. **b**, Schematic of the DNA site used in AFM experiments examining HipB interaction with O1-O2-O3-O4. The 5' and 3' DNA ends have an extra 88 bp and 299 bp, respectively, allowing for their differentiation. **c**, Possible models for HipB-promoter structures. Left: the wrapped model; right: the extended model, which has no cross-HipB contacts. In the wrapped model, the closely apposed HipB molecules would appear as a single 'blob'

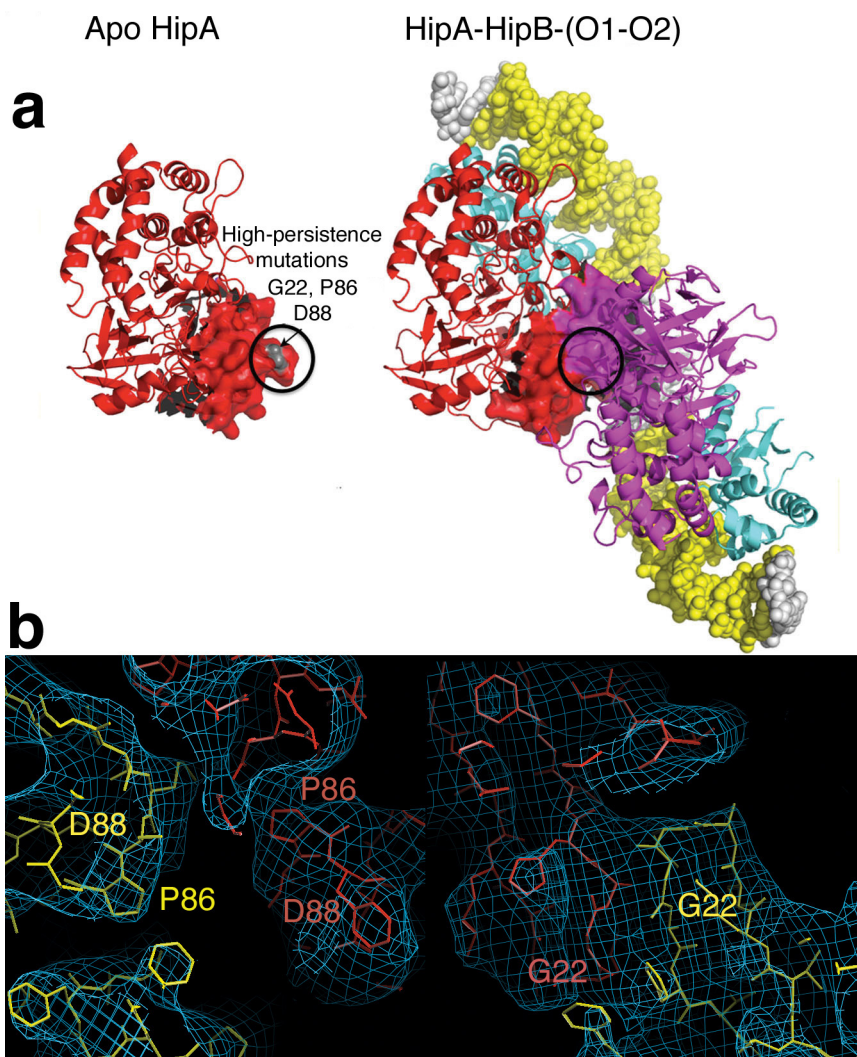
(indicated by dashed green line) bound to fish-hook DNA. In the extended, 'beads-on-a-string' model, the HipB dimers bound to O1-O2 and O3-O4 would be close in space, even if on opposite faces of the DNA; hence, given the resolution of AFM, they would appear as single dots on extended DNA. **d**, AFM images of HipB bound to the DNA schematized in **b**. The right panel shows two magnified images. HipB dimers bound to closely spaced O1-O2 or O3-O4 are observed as single dots (indicated by arrows), consistent with the extended model. The longer 3' end is evident in these images.

HipA-HipB-(O1-O2) pHipAs overlaid



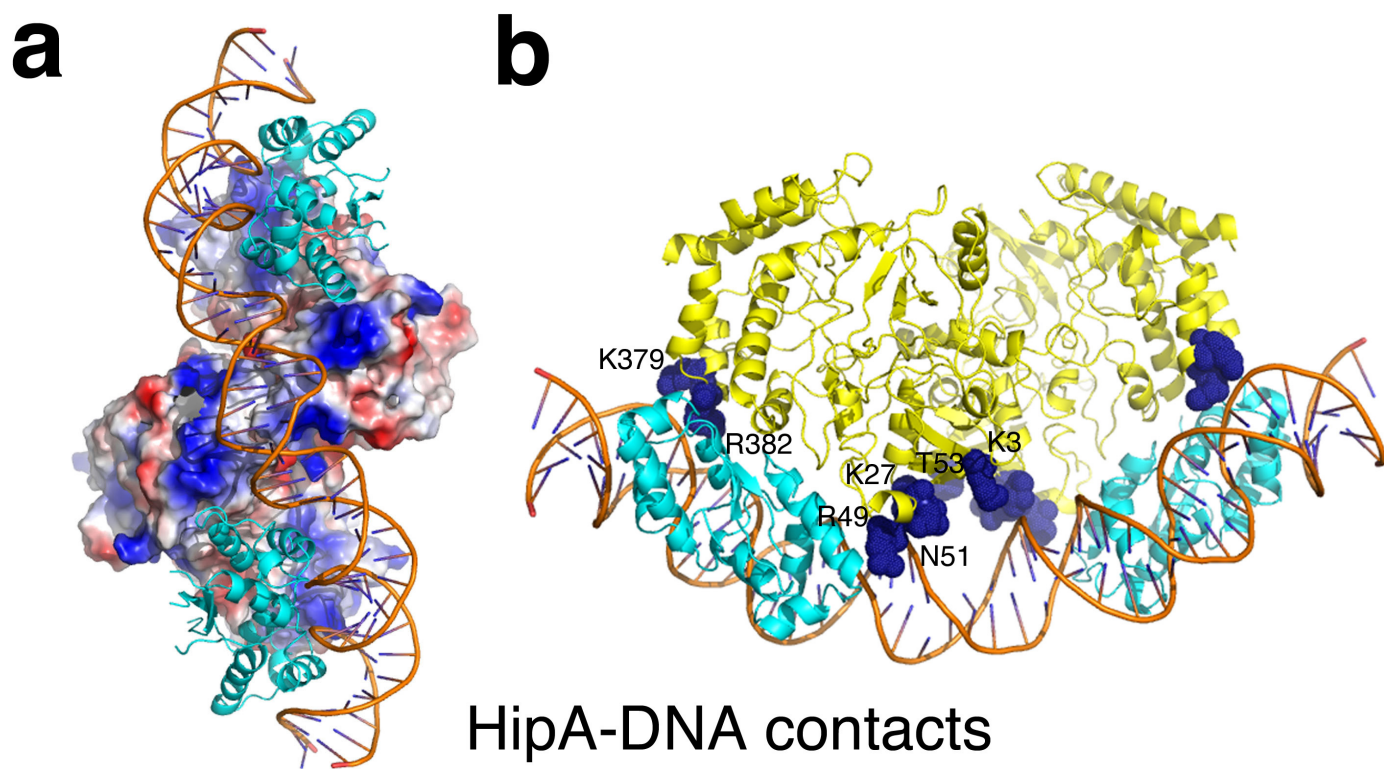
Extended Data Figure 4 | P-loop ejection in HipA higher-order promoter complexes. The HipA-HipB-(O1-O2) complex is coloured cyan and two phosphorylated HipA (pHipA) molecules, in which Ser150 is phosphorylated (shown as spheres) and the loop ejected from the active site pocket, are coloured yellow and beige. In pHipA the ejected P-loops stabilize the formation of

the activation loops. When the pHipA molecules are overlaid onto the promoter-bound HipA dimer, the ejected P-loops and the activation regions from neighbouring molecules would clash unless they were to adopt a different structure or conformation.



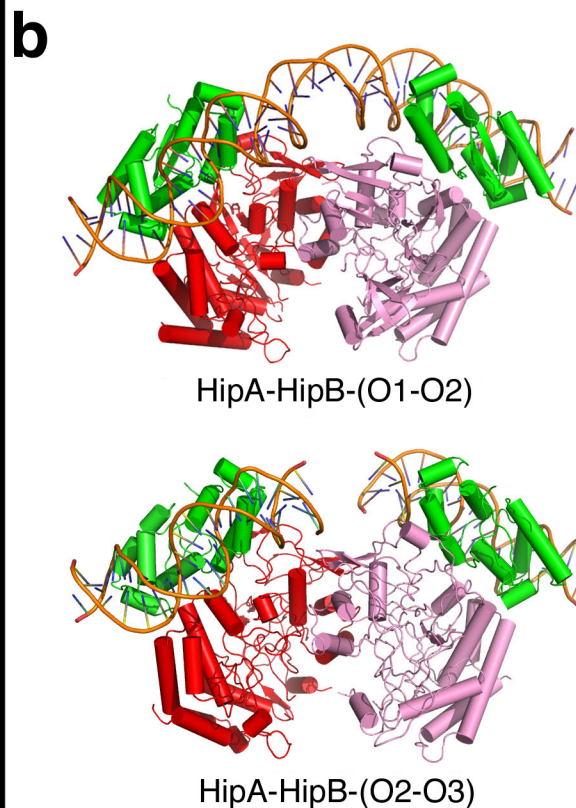
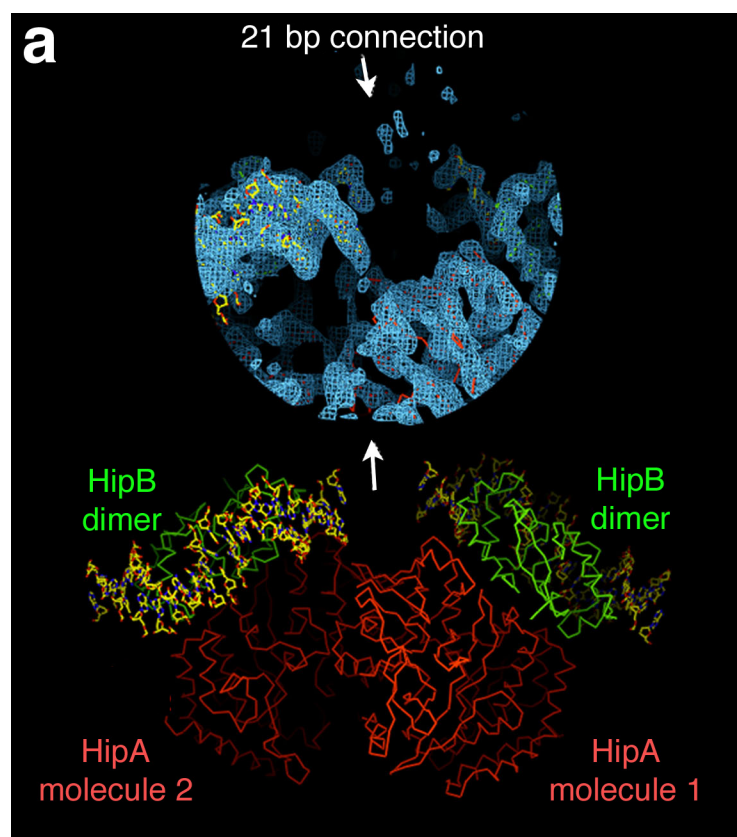
Extended Data Figure 5 | HipA N-subdomains-1 mediate dimerization in the HipA-HipB-promoter complex. **a**, Comparison of apo HipA with promoter complexed HipA showing that the high-persistence hotspot region in HipA mediates dimerization. Left: ribbon diagram of apo HipA with N-subdomain-1 shown as a red surface, and the location of mutations causing high-persistence coloured grey and circled. Right: HipA-HipB-(O1-O2) promoter structure. DNA operator sites are coloured yellow, HipB dimers are coloured cyan and HipA molecules are coloured red and magenta. The red HipA is shown in the same orientation as the apo HipA to the left. The

N-subdomain-1 high-persistence hotspot region is circled as in the apo structure. Note, this region forms the centre of HipA dimerization in the higher-order complex. **b**, Sigma-A-weighted $2F_o - F_c$ map showing a close up of residues in the HipA interface in the complex. The map is contoured at 0.8σ and calculated to 3.77 Å. Left: close up of the locations of Pro86 and Asp88 in the dimer interface. Right: location of Gly22 in the structure. The two-fold related Gly22 residues directly abut, indicating that any residue other than glycine would not allow stable formation of this dimer.



Extended Data Figure 6 | HipA contacts to DNA in the HipA-HipB-promoter complex. **a**, HipA-HipB-(O1-O2) complex with the DNA shown as an orange cartoon, HipB dimers as cyan ribbons and HipA molecules as electrostatic surface representations. The blue and red surfaces of HipA correspond to electropositive and electronegative regions, respectively. The

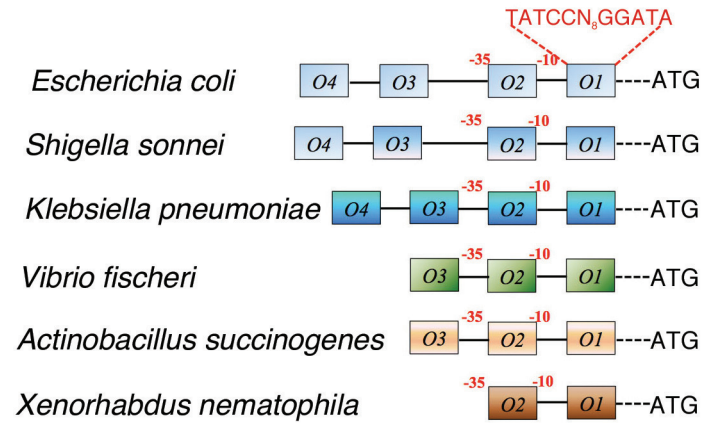
HipA regions in proximity to DNA are strikingly electropositive. **b**, HipA-HipB-(O1-O2) complex with DNA and HipB dimers shown and coloured as in **a**. HipA molecules are shown as yellow ribbons, with DNA interacting residues shown as spheres, coloured blue and labelled for one HipA subunit.



Extended Data Figure 7 | HipA dimers form in the HipA-HipB-(O2-O3) complex. **a**, Structure of the HipA-HipB-(O2-O3) complex. The overall structure is shown at the bottom of the panel, with the two HipA molecules depicted as red lines and the HipB dimers as green lines. The DNA is shown as sticks. The O2 and O3 operators are connected by a 21 bp linker, which is disordered in the structure. This is illustrated by the $2F_o - F_c$ map (blue mesh)

contoured at 1.0σ to 3.99 \AA , shown in the same orientation as the structure below. **b**, Comparison of the HipA-HipB-(O1-O2) and HipA-HipB-(O2-O3) complexes showing that they have identical higher-order structures in which the HipA monomers (red and pink) are brought into proximity to form the same dimer when complexed with HipB dimers and O1-O2 or O2-O3 promoter regions.

hipBA systems in Gram-negative bacteria



Extended Data Figure 8 | Schematic showing the results of the bioinformatic identification of the $-35/-10$ boxes of *hipBA* promoters in Gram-negative bacteria. The predicted promoters, their operator arrangement and the locations of the $-35/-10$ boxes for each bacterial species (labelled to the left)

are shown. The consensus HipB binding sequence is shown in red above the O1 operator site of the *E. coli* (MG1655) *hipBA* promoter. The transcription start site (ATG) is also shown for reference.

Extended Data Table 1 | Crystallographic statistics: HipB promoter complexes

	HipB-(O1-O2)/form1	HipB-(O1-O2)/form2
Data collection		
Space group	P2 ₁ 2 ₁ 2 ₁	C2
Cell dimensions		
<i>a</i> , <i>b</i> , <i>c</i> (Å)	293.9,54.5,47.7	100.7,68.9,78.3
α , β , γ (°)	90,90,90	90,93.1,90
Resolution (Å)	146.9-3.35	78.2-3.50
<i>R</i> _{sym}	0.092 (0.327)*	0.123 (0.723)
<i>I</i> / σ <i>I</i>	8.0 (2.0)	7.5 (1.5)
Completeness (%)	97.5 (97.2)	97.0 (97.0)
Redundancy	3.0 (3.1)	3.0 (2.8)
Refinement		
Resolution (Å)	146.5-3.35	78.2-3.50
No. reflections	11187	6749
<i>R</i> _{work} / <i>R</i> _{free} (%)	24.4/28.5	24.8/28.9
R.m.s deviations		
Bond lengths (Å)	0.009	0.014
Bond angles (°)	1.27	1.57

*Highest resolution shell is shown in parenthesis.

Extended Data Table 2 | Crystallographic statistics: HipA–HipB promoter complexes

	HipA-HipB-(O1-O2)	HipA-HipB-(O2-O3)
Data collection		
Space group	P4 ₃ 2 ₁ 2	P2 ₁ 2 ₁ 2 ₁
Cell dimensions		
<i>a</i> , <i>b</i> , <i>c</i> (Å)	228.2, 228.2, 130.8	214.0, 146.8, 53.8
α , β , γ (°)	90, 90, 90	90, 90, 90
Resolution (Å)	161.4–3.77	146.8–3.99
<i>R</i> _{sym}	0.100 (0.762)*	0.156 (0.608)
<i>I</i> / σ <i>I</i>	6.9 (1.4)	4.0 (1.6)
Completeness (%)	99.8 (99.4)	94.2 (95.7)
Redundancy	5.8 (3.9)	2.8 (2.9)
Refinement		
Resolution (Å)	161.4–3.77	146.8–3.99
No. reflections	35140	14066
<i>R</i> _{work} / <i>R</i> _{free} (%)	35.9/37.8	30.8/38.7
R.m.s deviations		
Bond lengths (Å)	0.013	0.012
Bond angles (°)	1.48	1.67

*Highest resolution shell is shown in parenthesis.

Influence maximization in complex networks through optimal percolation

Flaviano Morone¹ & Hernán A. Makse¹

The whole frame of interconnections in complex networks hinges on a specific set of structural nodes, much smaller than the total size, which, if activated, would cause the spread of information to the whole network¹, or, if immunized, would prevent the diffusion of a large scale epidemic^{2,3}. Localizing this optimal, that is, minimal, set of structural nodes, called influencers, is one of the most important problems in network science^{4,5}. Despite the vast use of heuristic strategies to identify influential spreaders^{6–14}, the problem remains unsolved. Here we map the problem onto optimal percolation in random networks to identify the minimal set of influencers, which arises by minimizing the energy of a many-body system, where the form of the interactions is fixed by the non-backtracking matrix¹⁵ of the network. Big data analyses reveal that the set of optimal influencers is much smaller than the one predicted by previous heuristic centralities. Remarkably, a large number of previously neglected weakly connected nodes emerges among the optimal influencers. These are topologically tagged as low-degree nodes surrounded by hierarchical coronas of hubs, and are uncovered only through the optimal collective interplay of all the influencers in the network. The present theoretical framework may hold a larger degree of universality, being applicable to other hard optimization problems exhibiting a continuous transition from a known phase¹⁶.

The optimal influence problem was initially introduced in the context of viral marketing¹, and its solution was shown to be NP-hard⁴ for a generic class of linear threshold models of information spreading^{17,18}. Indeed, finding the optimal set of influencers is a many-body problem in which the topological interactions between them play a crucial role^{13,14}. On the other hand, there has been an abundant production of heuristic rankings to identify influential nodes and ‘superspreaders’ in networks^{6–12,19}. The main problem is that heuristic methods do not optimize a global function of influence. As a consequence, there is no guarantee of their performance.

Here we address the problem of quantifying nodes’ influence by finding the optimal (that is, minimal) set of structural influencers. After defining a unified mathematical framework for both immunization and spreading, we provide its optimal solution in random networks by mapping the problem onto optimal percolation. In addition, we present CI (Collective Influence), a scalable algorithm to solve the optimization problem in large-scale real data sets. The thorough comparison with competing methods (Supplementary Information section I²⁰) ultimately establishes the better performance of our algorithm. By taking into account collective influence effects, our optimization theory identifies a new class of strategic influencers, called ‘weak nodes’, which outrank the hubs in the network. Thus, the top influencers are highly counterintuitive: low-degree nodes play a major broker role in the network, and despite being weakly connected, can be powerful influencers.

The problem of finding the minimal set of activated nodes^{17,18} to spread information to the whole network⁴ or to optimally immunize a network against epidemics¹¹ can be exactly mapped onto optimal percolation (see Supplementary Information section IIB). This mapping

provides the mathematical support to the intuitive relation between influence and the concept of cohesion of a network: the most influential nodes are the ones forming the minimal set that guarantees a global connection of the network^{5,9,10}. We call this minimal set the ‘optimal influencers’ of the network. At a general level, the optimal influence problem can be stated as follows: find the minimal set of nodes which, if removed, would break down the network into many disconnected pieces. The natural measure of influence is, therefore, the size of the largest (giant) connected component as the influencers are removed from the network.

We consider a network composed of N nodes tied with M links with an arbitrary-degree distribution. Let us suppose we remove a certain fraction q of the total number of nodes. It is well known from percolation theory²¹ that, if we choose these nodes randomly, the network undergoes a structural collapse at a certain critical fraction where the probability of existence of the giant connected component vanishes, $G = 0$. The optimal influence problem corresponds to finding the minimum fraction q_c of influencers to fragment the network: $q_c = \min\{q \in [0, 1]: G(q) = 0\}$.

Let the vector $\mathbf{n} = (n_1, \dots, n_N)$ represent which node is removed ($n_i = 0$, influencer) or left ($n_i = 1$, the rest) in the network ($q = 1 - 1/N \sum_i n_i$), and consider a link from i to j ($i \rightarrow j$). The order parameter of the influence problem is the probability that i belongs to the giant component in a modified network where j is absent, $v_{i \rightarrow j}$ (refs 22, 23). Clearly, in the absence of a giant component we find $\{v_{i \rightarrow j} = 0\}$ for all $i \rightarrow j$. The stability of the solution $\{v_{i \rightarrow j} = 0\}$ is controlled by the largest eigenvalue $\lambda(\mathbf{n}; q)$ of the linear operator $\hat{\mathcal{M}}$,

defined on the $2M \times 2M$ directed edges as $\mathcal{M}_{k \rightarrow \ell, i \rightarrow j} \equiv \frac{\partial v_{i \rightarrow j}}{\partial v_{k \rightarrow \ell}} \Big|_{\{v_{i \rightarrow j} = 0\}}$.

We find for locally tree-like random graphs (see Fig. 1a and Supplementary Information section II):

$$\mathcal{M}_{k \rightarrow \ell, i \rightarrow j} = n_i \mathcal{B}_{k \rightarrow \ell, i \rightarrow j} \quad (1)$$

where $\mathcal{B}_{k \rightarrow \ell, i \rightarrow j}$ is the non-backtracking matrix of the network^{15,24}. The matrix $\mathcal{B}_{k \rightarrow \ell, i \rightarrow j}$ has non-zero entries only when $(k \rightarrow \ell, i \rightarrow j)$ form a pair of consecutive non-backtracking directed edges, that is, $(k \rightarrow \ell, \ell \rightarrow j)$ with $k \neq j$. In this case $\mathcal{B}_{k \rightarrow \ell, \ell \rightarrow j} = 1$ (equation (13) in Supplementary Information). Powers of the matrix $\hat{\mathcal{B}}$ count the number of non-backtracking walks of a given length in the network (Fig. 1b)²⁴, much in the same way as powers of the adjacency matrix count the number of paths⁵. Operator $\hat{\mathcal{B}}$ has recently received a lot of attention thanks to its high performance in the problem of community detection^{25,26}. We show its topological power in the problem of optimal percolation.

Stability of the solution $\{v_{i \rightarrow j} = 0\}$ requires $\lambda(\mathbf{n}; q) \leq 1$. The optimal influence problem for a given q ($\geq q_c$) can be rephrased as finding the optimal configuration \mathbf{n} that minimizes the largest eigenvalue $\lambda(\mathbf{n}; q)$ (Fig. 1c). The optimal set \mathbf{n}^* of Nq_c influencers is obtained when the minimum of the largest eigenvalue reaches the critical threshold:

$$\lambda(\mathbf{n}^*; q_c) = 1 \quad (2)$$

¹Levich Institute and Physics Department, City College of New York, New York, New York 10031, USA.

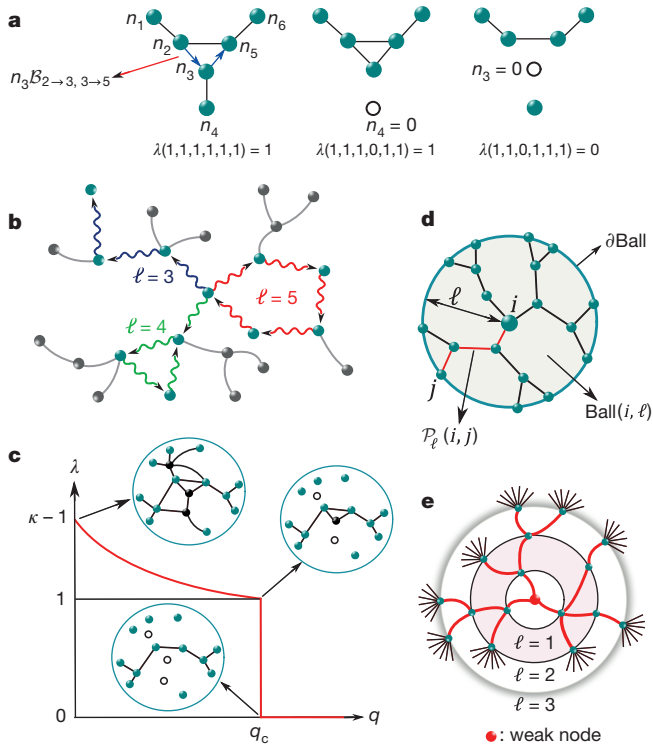


Figure 1 | The non-backtracking (NB) matrix and weak nodes. **a**, The largest eigenvalue λ of $\hat{\mathcal{M}}$ exemplified on a simple network. The optimal strategy for immunization and spreading minimizes λ by removing the minimum number of nodes (optimal influencers) that destroys all the loops. Left panel, the action of the matrix $\hat{\mathcal{M}}$ is on the directed edges of the network. The entry $\mathcal{M}_{2 \rightarrow 3, 3 \rightarrow 5} = n_3 \mathcal{B}_{2 \rightarrow 3, 3 \rightarrow 5} = n_3$ encodes the occupancy ($n_3 = 1$) or vacancy ($n_3 = 0$) of node 3. In this particular case, the largest eigenvalue is $\lambda = 1$. Centre panel, non-optimal removal of a leaf, $n_4 = 0$, which does not decrease λ . Right panel, optimal removal of a loop, $n_3 = 0$, which decreases λ to zero. **b**, A NB walk is a random walk that is not allowed to return back along the edge that it just traversed. We show a NB open walk ($\ell = 3$), a NB closed walk with a tail ($\ell = 4$), and a NB closed walk with no tails ($\ell = 5$). The NB walks are the building blocks of the diagrammatic expansion to calculate λ . **c**, Representation of the global minimum over \mathbf{n} of the largest eigenvalue λ of $\hat{\mathcal{M}}$ versus q . When $q \geq q_c$, the minimum is at $\lambda = 0$. Then, $G = 0$ is stable (still, non-optimal configurations exist with $\lambda > 1$ for which $G > 0$). When $q < q_c$, the minimum of the largest eigenvalue is always $\lambda > 1$, the solution $G = 0$ is unstable, and then $G > 0$. At the optimal percolation transition, the minimum is at \mathbf{n}^* with $\lambda(\mathbf{n}^*, q_c) = 1$. For $q = 0$, we find $\lambda = \kappa - 1$ ($\kappa = \langle k^2 \rangle / \langle k \rangle$), where k is the node degree) which is the largest eigenvalue of $\hat{\mathcal{B}}$ for random networks²⁵ with all nodes present ($n_i = 1$). When $\lambda = 1$, the giant component is reduced to a tree plus one single loop (unicyclic graph), which is suddenly destroyed at the transition q_c to become a tree, causing the abrupt fall of λ to zero. **d**, $\text{Ball}(i, \ell)$ of radius ℓ around node i is the set of nodes at distance ℓ from i , and ∂Ball is the set of nodes on the boundary. The shortest path from i to j is shown in red. **e**, Example of a weak node: a node with a small number of connections surrounded by hierarchical coronas of hubs at different ℓ levels.

The formal mathematical mapping of the optimal influence problem to the minimization of the largest eigenvalue of the modified non-backtracking matrix for random networks, equation (2), represents our first main result.

An example of a non-optimized solution corresponds to choosing n_i at random and decoupled from the non-backtracking matrix^{23,27} (random percolation²¹, Supplementary Information section IID). In the optimized case, we seek to derandomize the selection of the set $n_i = 0$ and optimally choose them to find the best configuration \mathbf{n}^* with the lowest q_c according to equation (2). The eigenvalue $\lambda(\mathbf{n})$ (from now on we omit q in $\lambda(\mathbf{n}; q) \equiv \lambda(\mathbf{n})$, which is always kept fixed) determines the growth rate of an arbitrary vector \mathbf{w}_0 with $2M$ entries after ℓ iterations of the matrix

$\hat{\mathcal{M}}: |\mathbf{w}_\ell(\mathbf{n})| = \langle \mathbf{w}_\ell | \mathbf{w}_\ell \rangle^{\frac{1}{2}} = |\hat{\mathcal{M}}^\ell \mathbf{w}_0| = \left\langle \mathbf{w}_0 \left| (\hat{\mathcal{M}}^\ell)^\dagger \hat{\mathcal{M}}^\ell \right| \mathbf{w}_0 \right\rangle^{\frac{1}{2}} \sim e^{\ell \log \lambda(\mathbf{n})}$. The largest eigenvalue is then calculated by the power method:

$$\lambda(\mathbf{n}) = \lim_{\ell \rightarrow \infty} \left[\frac{|\mathbf{w}_\ell(\mathbf{n})|}{|\mathbf{w}_0|} \right]^{1/\ell} \quad (3)$$

Equation (3) is the starting point of an (infinite) perturbation series that provides the exact solution to the many-body influence problem in random networks and therefore contains all physical effects, including the collective influence. In practice, we minimize the cost energy function of influence $|\mathbf{w}_\ell(\mathbf{n})|$ in equation (3) for a finite ℓ . The solution rapidly converges to the exact value as $\ell \rightarrow \infty$, the faster the larger the spectral gap. We find for $\ell \geq 1$, to leading order in $1/N$ (Supplementary Information section IIE):

$$|\mathbf{w}_\ell(\mathbf{n})|^2 = \sum_{i=1}^N (k_i - 1) \sum_{j \in \partial \text{Ball}(i, 2\ell - 1)} \left(\prod_{k \in \mathcal{P}_{2\ell - 1}(i, j)} n_k \right) (k_j - 1) \quad (4)$$

where $\text{Ball}(i, \ell)$ is the set of nodes inside a ball of radius ℓ (defined as the shortest path) around node i , $\partial \text{Ball}(i, \ell)$ is the frontier of the ball, $\mathcal{P}_\ell(i, j)$ is the shortest path of length ℓ connecting i and j (Fig. 1d), and k_i is the degree of node i .

The first collective optimization in equation (4) is $\ell = 1$. We find $|\mathbf{w}_1(\mathbf{n})|^2 = \sum_{i,j=1}^N A_{ij}(k_i - 1)(k_j - 1)n_i n_j$, where A_{ij} is the adjacency matrix (equation (39) in Supplementary Information). This term is interpreted as the energy of an antiferromagnetic Ising model with random bonds in a random external field at fixed magnetization, which is an example of a pair-wise NP-complete spin-glass whose solution is found in Supplementary Information section III with the cavity method²⁸ (Extended Data Fig. 2).

For $\ell \geq 2$, the problem can be mapped exactly to a statistical mechanical system with many-body interactions which can be recast in terms of a diagrammatic expansion, equations (41)–(49) in Supplementary Information. For example, $|\mathbf{w}_2(\mathbf{n})|^2$ leads to 4-body interactions (equation (45) in Supplementary Information), and, in general, the energy cost $|\mathbf{w}_\ell(\mathbf{n})|^2$ contains 2ℓ -body interactions. As soon as $\ell \geq 2$, the cavity method becomes much more complicated to implement and we use another suitable method, called extremal optimization (EO)²⁹ (Supplementary Information section IV). This method estimates the true optimal value of the threshold by finite-size scaling following extrapolation to $\ell \rightarrow \infty$ (Extended Data Figs 3, 4). However, EO is not scalable to find the optimal configuration in large networks. Therefore, we develop an adaptive method, which performs excellently in practice, preserves the features of EO, and is highly scalable to present-day big data.

The idea is to remove the nodes causing the biggest drop in the energy function, equation (4). First, we define a ball of radius ℓ around every node (Fig. 1d). Then, we consider the nodes belonging to the frontier $\partial \text{Ball}(i, \ell)$ and assign to node i the collective influence (CI) strength at level ℓ following equation (4):

$$\text{CI}_\ell(i) = (k_i - 1) \sum_{j \in \partial \text{Ball}(i, \ell)} (k_j - 1) \quad (5)$$

We notice that, while equation (4) is valid only for odd radii of the ball, $\text{CI}_\ell(i)$ is defined also for even radii. This generalization is possible by considering an energy function for even radii analogous to equation (4), as explained in Supplementary Information section IIG. The case of one-body interaction with zero radius $\ell = 0$ (equation (59) in Supplementary Information) leads to the high-degree (HD) ranking (equation (62) in Supplementary Information)¹⁰.

The collective influence, equation (5), is our second and most important result since it is the basis for the highly scalable and optimized CI algorithm which follows. In the beginning, all the nodes are present: $n_i = 1$ for all i . Then, we remove node i^* with highest CI_ℓ and set $n_{i^*} = 0$. The degree of each neighbour of i^* is decreased by one, and the procedure is repeated to find the new top CI node to remove. The algorithm is terminated when the giant component is zero (see Supplementary Information section V for implementation, and

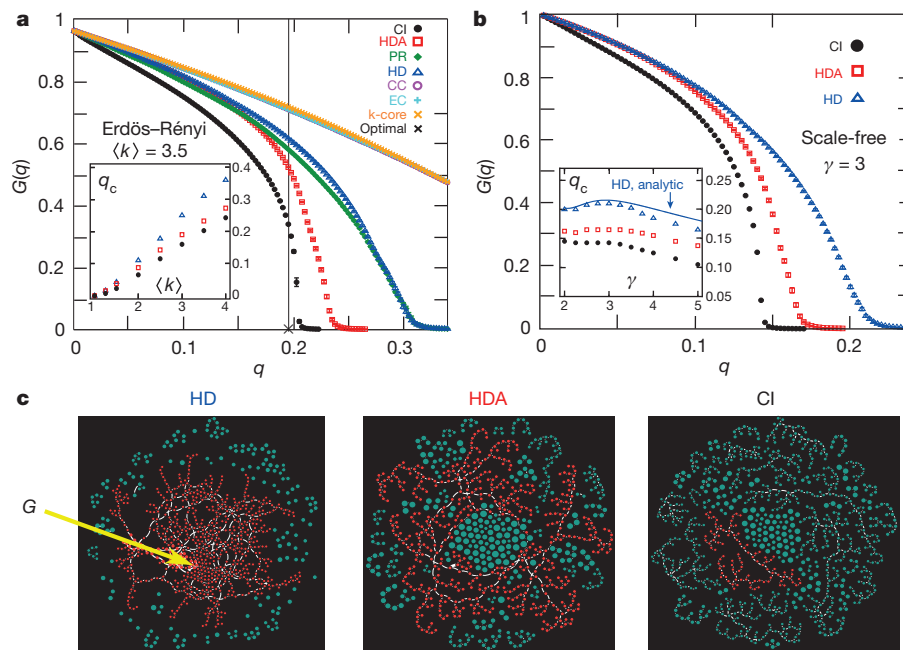


Figure 2 | Exact optimal solution and performance of CI in synthetic networks. **a**, $G(q)$ in an ER network ($N = 2 \times 10^5$, $\langle k \rangle = 3.5$, error bars are s.e.m. over 20 realizations). We show the true optimal solution found with EO ('x' symbol), and also using CI, HDA, PR, HD, CC, EC and k-core methods. The other methods are not scalable and perform worse than HDA and are treated in Supplementary Information sections VI and VII (Extended Data Figs 8, 9). CI is close to the optimal $q_c^{\text{opt}} = 0.192(9)$ obtained with EO in Supplementary Information section IV. Note that EO can estimate the extrapolated optimal value of q_c , but it cannot provide the optimal

configuration for large systems. Inset, q_c (obtained at the peak of the second-largest cluster) for the three best methods versus $\langle k \rangle$. **b**, $G(q)$ for a SF network with degree exponent $\gamma = 3$, maximum degree $k_{\max} = 10^3$, minimum degree $k_{\min} = 2$ and $N = 2 \times 10^5$ (error bars are s.e.m. over 20 realizations). Inset, q_c versus γ . The continuous blue line is the HD analytical result computed in Supplementary Information section IIG (Extended Data Fig. 1b). **c**, Example of SF network with $\gamma = 3$ after the removal of 15% of nodes, using the three methods HD, HDA and CI. CI produces a much reduced giant component G (red nodes).

Supplementary Information section VA for minimizing $G(q) \neq 0$. By increasing the radius ℓ of the ball we obtain better and better approximations of the optimal exact solution as $\ell \rightarrow \infty$ (for finite networks, ℓ does not exceed the network diameter).

The collective influence CI_ℓ for $\ell \geq 1$ has a rich topological content, and consequently tells us more about the role played by nodes in the network than the non-interacting high-degree hub-removal strategy at $\ell = 0$, CI_0 . The augmented information comes from the sum in the right hand side of equation (5), which is absent in the naive high-degree rank. This sum contains the contribution of the nodes living on the surface of the ball surrounding the central vertex i , each node weighted by the factor $k_j - 1$. This means that a node placed at the centre of a corona irradiating many links—the structure hierarchically emerging at different ℓ levels as seen in Fig. 1e—can have a very large collective influence, even if it has a moderate or low degree. Such ‘weak nodes’ can outrank nodes with larger degree that occupy mediocre peripheral locations in the network. The commonly used word ‘weak’ in this context sounds particularly paradoxical. It is, indeed, usually used as a synonym for a low-degree node with an additional bridging property, which has resisted a quantitative formulation. We provide this definition through equation (5), according to which weak nodes are, de facto, quite strong. Paraphrasing Granovetter’s conundrum³⁰, equation (5) quantifies the “strength of weak nodes”.

The CI-algorithm scales as $\sim O(N \log N)$ by removing a finite fraction of nodes at each step (Supplementary Information section VB). This high scalability allows us to find top influencers in current big-data social media and the minimal set of people to immunize in large-scale populations at the country level. The applications are investigated next.

Figure 2a shows the optimal threshold q_c for a random Erdős-Rényi (ER) network⁵ (marked by the vertical line) obtained by extrapolating the EO solution to $N \rightarrow \infty$ and $\ell \rightarrow \infty$ (Supplementary Information section IV). In the same figure we compare the optimal threshold against the heuristic centrality measures: high-degree (HD)⁹, high-degree

adaptive (HDA), PageRank (PR)⁷, closeness centrality (CC)⁶, eigenvector centrality (EC)⁶, and k-core¹² (see Supplementary Information section I for definitions). Supplementary Information sections VI and VII show the comparison with the remaining heuristics^{6,11} and the Belief Propagation method of ref. 14, respectively, which have worse computational complexity (and optimality), and cannot be applied to the network sizes used here. Remarkably, at the optimal value q_c predicted by our theory, the best among the heuristic methods (HDA, PR and HD) still predict a giant component ~ 50 – 60% of the whole original network. Furthermore, the influencer threshold predicted by CI approximates very well the optimal one, and, notably, CI outperforms the other strategies. Figure 2b compares CI in scale-free (SF) networks⁵ against the best heuristic methods, that is, HDA and HD. In all cases, CI produces a smaller threshold and a smaller giant component (Fig. 2c).

As an example of an information spreading network, we consider the web of Twitter users (Supplementary Information section VIII¹⁹). Figure 3a shows the giant component of Twitter when a fraction q of its influencers is removed following CI. It is surprising that a lot of Twitter users with a large number of contacts have a mild influence on the network. This is witnessed by the fact that, when CI (at $\ell = 5$) predicts a zero giant component (and so it exhausts the number of optimal influencers), the scalable heuristic ranks (HD, HDA, PR and k-core) still give a substantial giant component of the order of 30–70% of the entire network. These heuristics also, inevitably, find a remarkably large number of (fake) influencers, which is at least 50% larger than that predicted by CI (Fig. 3b and Supplementary Information section VIII). One cause for the poor performance of the high-degree-based ranks is that most of the hubs are clustered, which gives a mediocre importance to their contacts. As a consequence, hubs are outranked by nodes with lower degree surrounded by coronas of hubs (shown in detail in Fig. 3c), that is, the weak nodes predicted by the theory (Fig. 1e).

Finally, we simulate an immunization scheme on a personal contact network built from the phone calls performed by 14 million people in

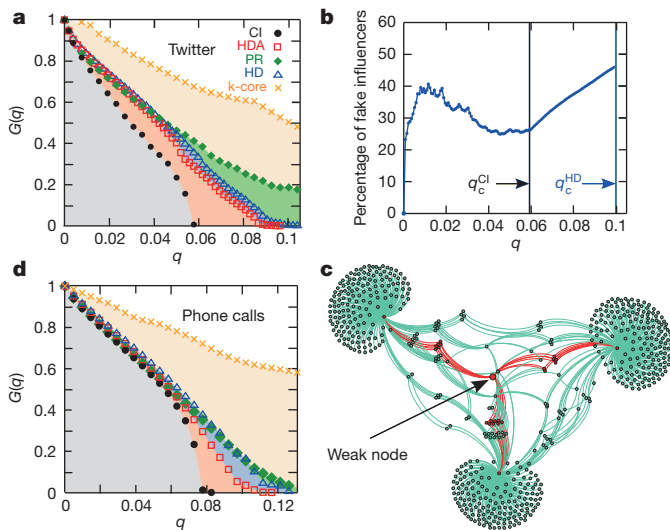


Figure 3 | Performance of CI in large-scale real social networks. **a**, Giant component $G(q)$ of Twitter users¹⁹ ($N = 469,013$) computed using CI, HDA, PR, HD and k-core strategies (other heuristics have prohibitive running times for this system size). **b**, Percentage of fake influencers or false positives (PFI, equation (120) in Supplementary Information) in Twitter as a function of q , defined as the percentage of non-optimal influencers identified by the HD algorithm in comparison with CI. Below q_c^{CI} , PFI reaches as much as $\sim 40\%$, indicating the failure of HD in optimally finding the top influencers. Indeed, to obtain $G = 0$, HD has to remove a much larger number of fake influencers, which at q_c^{HD} reaches PFI $\approx 48\%$. **c**, An example of the many weak nodes found in Twitter. These crucial influencers were missed by all heuristic strategies. **d**, $G(q)$ for a social network of 1.4×10^7 mobile phone users in Mexico representing an example of big data to test the scalability and performance of the algorithm in real networks. CI immunizes this social network using half a million fewer people than the best heuristic strategy (HDA), saving $\sim 35\%$ of the vaccine stockpile.

Mexico (Supplementary Information section IX). Figure 3d shows that our method saves a large number of vaccines or, equivalently, finds the smallest possible set of people to quarantine; our method therefore also outranks the scalable heuristics in large real networks. Thus, while the mapping of the influencer identification problem onto optimal percolation is strictly valid for locally tree-like random networks, our results may apply also to real loopy networks, provided the density of loops is not excessively large.

Our solution to the optimal influence problem shows its importance in that it helps to unveil hitherto hidden relations between people, as witnessed by the weak-node effect. This, in turn, is the by-product of a broader notion of influence, lifted from the individual non-interacting point of view^{6–12,19,20} to the collective sphere: influence is an emergent property of collectivity, and top influencers arise from the optimization of the complex interactions they stipulate.

Online Content Methods, along with any additional Extended Data display items and Source Data, are available in the online version of the paper; references unique to these sections appear only in the online paper.

Received 19 February; accepted 20 May 2015.

Published online 1 July 2015.

1. Domingos, P. & Richardson, M. Mining knowledge-sharing sites for viral marketing. In *Proc. 8th ACM SIGKDD Int. Conf. on Knowledge Discovery and Data Mining*, 61–70 (ACM, 2002); <http://dx.doi.org/10.1145/775047.775057>.

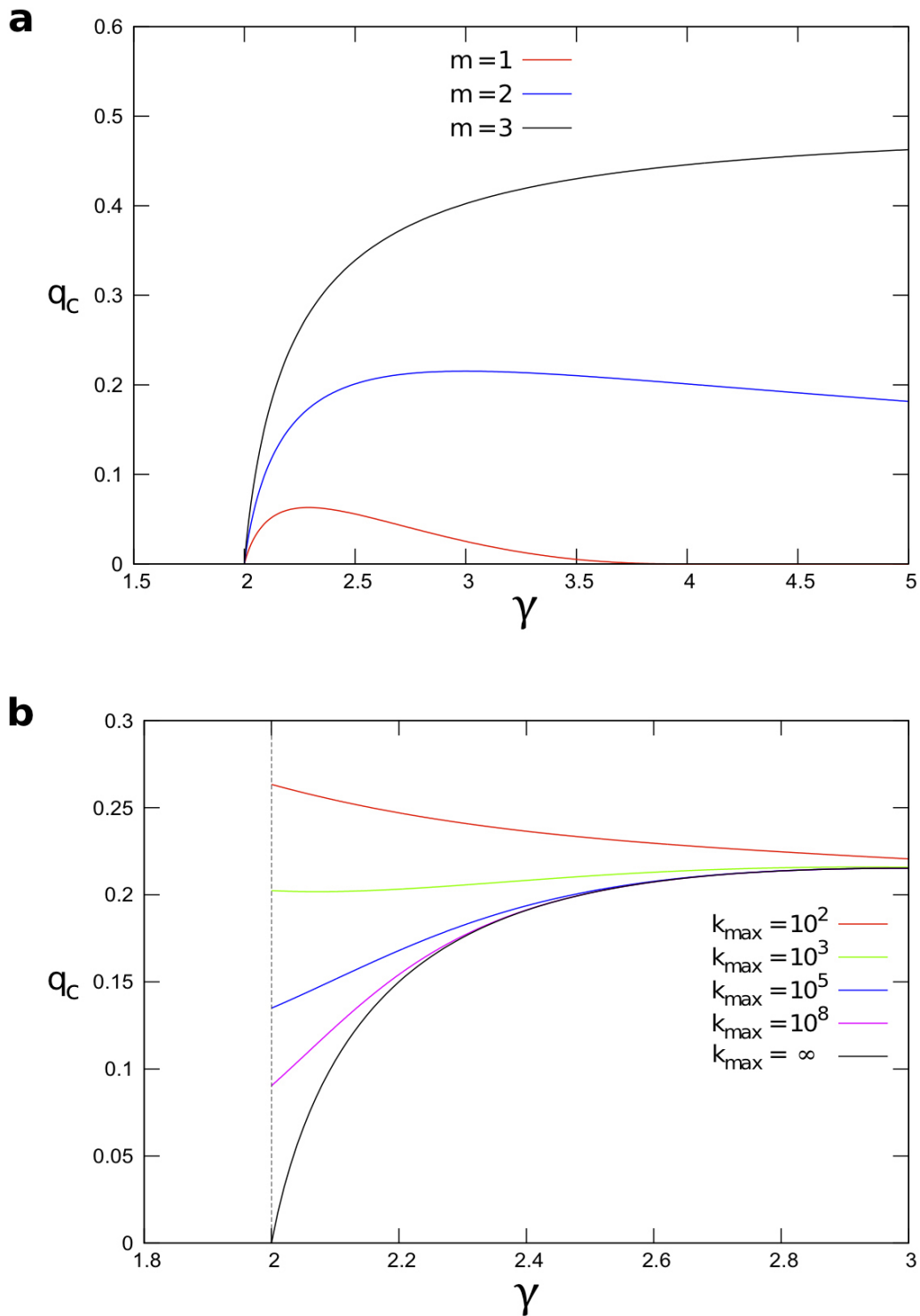
2. Pastor-Satorras, R. & Vespignani, A. Epidemic spreading in scale-free networks. *Phys. Rev. Lett.* **86**, 3200–3203 (2001).
3. Newman, M. E. J. Spread of epidemic disease on networks. *Phys. Rev. E* **66**, 016128 (2002).
4. Kempe, D., Kleinberg, J. & Tardos, E. Maximizing the spread of influence through a social network. In *Proc. 9th ACM SIGKDD Int. Conf. on Knowledge Discovery and Data Mining*, 137–143 (ACM, 2003); <http://dx.doi.org/10.1145/956750.956769>.
5. Newman, M. E. J. *Networks: An Introduction* (Oxford Univ. Press, 2010).
6. Freeman, L. C. Centrality in social networks: conceptual clarification. *Soc. Networks* **1**, 215–239 (1978).
7. Brin, S. & Page, L. The anatomy of a large-scale hypertextual web search engine. *Comput. Networks ISDN Systems* **30**, 107–117 (1998).
8. Kleinberg, J. Authoritative sources in a hyperlinked environment. In *Proc. 9th ACM-SIAM Symp. on Discrete Algorithms* (1998); *J. Assoc. Comput. Machinery* **46**, 604–632 (1999).
9. Albert, R., Jeong, H. & Barabási, A.-L. Error and attack tolerance of complex networks. *Nature* **406**, 378–382 (2000).
10. Cohen, R., Erez, K., ben-Avraham, D. & Havlin, S. Breakdown of the Internet under intentional attack. *Phys. Rev. Lett.* **86**, 3682–3685 (2001).
11. Chen, Y., Paul, G., Havlin, S., Liljeros, F. & Stanley, H. E. Finding a better immunization strategy. *Phys. Rev. Lett.* **101**, 058701 (2008).
12. Kitsak, M. *et al.* Identification of influential spreaders in complex networks. *Nature Phys.* **6**, 888–893 (2010).
13. Altarelli, F., Braunstein, A., Dall'Asta, L. & Zecchina, R. Optimizing spread dynamics on graphs by message passing. *J. Stat. Mech.* P09011 (2013).
14. Altarelli, F., Braunstein, A., Dall'Asta, L., Wakeling, J. R. & Zecchina, R. Containing epidemic outbreaks by message-passing techniques. *Phys. Rev. X* **4**, 021024 (2014).
15. Hashimoto, K. Zeta functions of finite graphs and representations of p-adic groups. *Adv. Stud. Pure Math.* **15**, 211–280 (1989).
16. Coja-Oghlan, A., Mossel, E. & Vilenchik, D. A spectral approach to analyzing belief propagation for 3-coloring. *Combin. Probab. Comput.* **18**, 881–912 (2009).
17. Granovetter, M. Threshold models of collective behavior. *Am. J. Sociol.* **83**, 1420–1443 (1978).
18. Watts, D. J. A simple model of global cascades on random networks. *Proc. Natl Acad. Sci. USA* **99**, 5766–5771 (2002).
19. Pei, S., Muchnik, L., Andrade, J. S. Jr, Zheng, Z. & Makse, H. A. Searching for superspreaders of information in real-world social media. *Sci. Rep.* **4**, 5547 (2014).
20. Pei, S. & Makse, H. A. Spreading dynamics in complex networks. *J. Stat. Mech.* P12002 (2013).
21. Bollobás, B. & Riordan, O. *Percolation* (Cambridge Univ. Press, 2006).
22. Bianconi, G. & Dorogovtsev, S. N. Multiple percolation transitions in a configuration model of network of networks. *Phys. Rev. E* **89**, 062814 (2014).
23. Karrer, B., Newman, M. E. J. & Zdeborová, L. Percolation on sparse networks. *Phys. Rev. Lett.* **113**, 208702 (2014).
24. Angel, O., Friedman, J. & Hoory, S. The non-backtracking spectrum of the universal cover of a graph. *Trans. Am. Math. Soc.* **367**, 4287–4318 (2015).
25. Krzakala, F. *et al.* Spectral redemption in clustering sparse networks. *Proc. Natl Acad. Sci. USA* **110**, 20935–20940 (2013).
26. Newman, M. E. J. Spectral methods for community detection and graph partitioning. *Phys. Rev. E* **88**, 042822 (2013).
27. Radicchi, F. Predicting percolation thresholds in networks. *Phys. Rev. E* **91**, 010801(R) (2015).
28. Mézard, M. & Parisi, G. The cavity method at zero temperature. *J. Stat. Phys.* **111**, 1–34 (2003).
29. Boettcher, S. & Percus, A. G. Optimization with extremal dynamics. *Phys. Rev. Lett.* **86**, 5211–5214 (2001).
30. Granovetter, M. The strength of weak ties. *Am. J. Sociol.* **78**, 1360–1380 (1973).

Supplementary Information is available in the online version of the paper.

Acknowledgements This work was funded by NIH-NIGMS 1R21GM107641 and NSF-PoLS PHY-1305476. Additional support was provided by ARL. We thank L. Bo, S. Havlin and R. Mari for discussions and Grandata for providing the data on mobile phone calls.

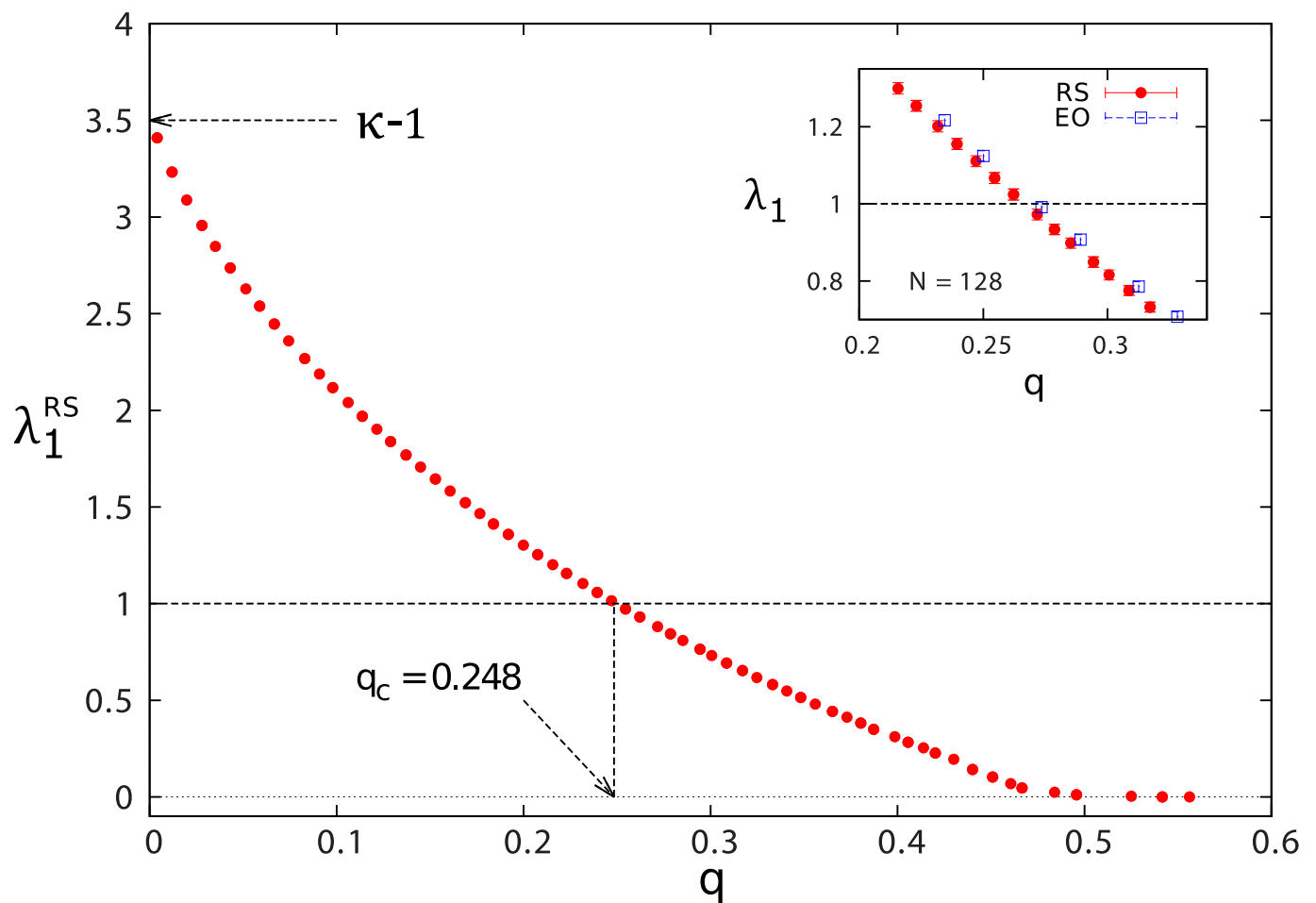
Author Contributions Both authors contributed equally to the work presented in this paper.

Author Information Reprints and permissions information is available at www.nature.com/reprints. The authors declare no competing financial interests. Readers are welcome to comment on the online version of the paper. Correspondence and requests for materials should be addressed to H.A.M. (hmake@lev.cuny.cuny.edu).



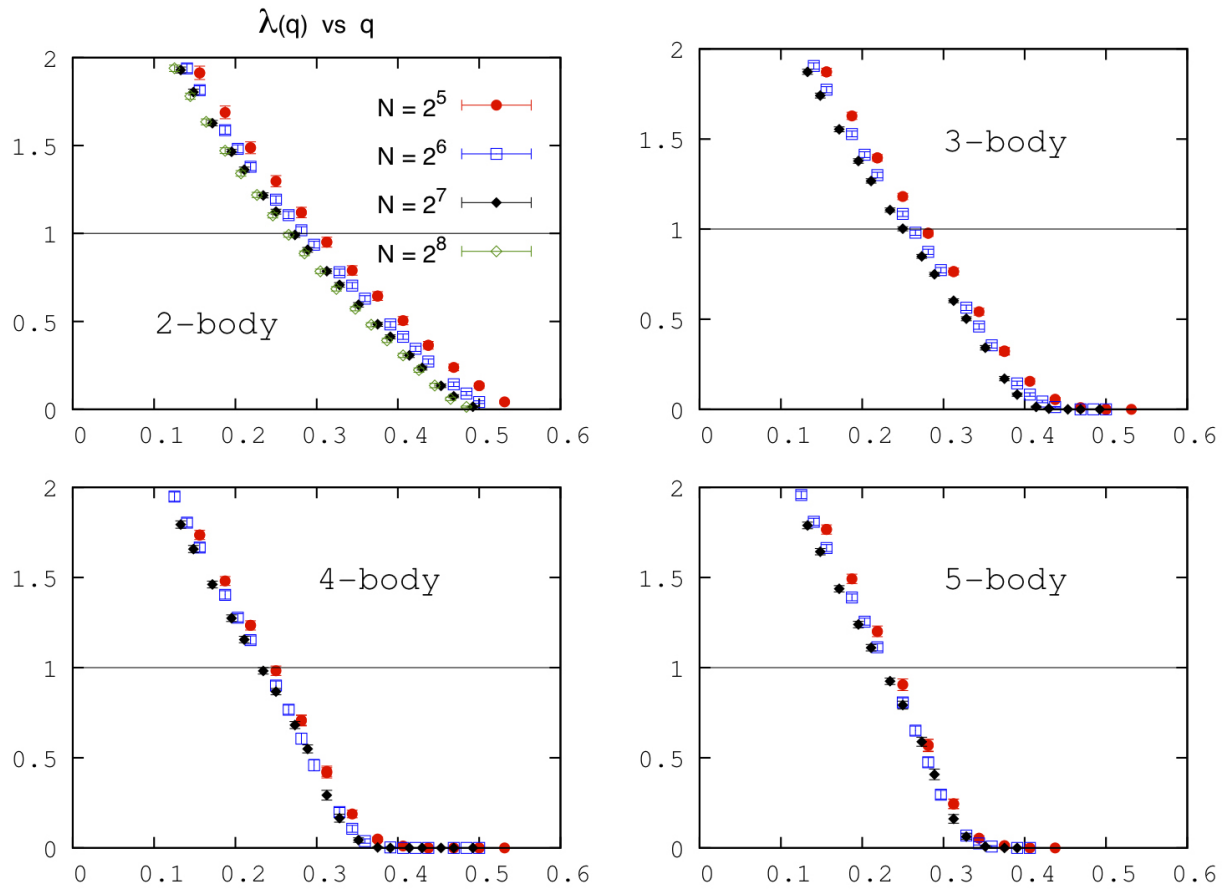
Extended Data Figure 1 | High-degree (HD) threshold. **a**, HD influence threshold q_c as a function of the degree distribution exponent γ of scale-free networks in the ensemble with $k_{\max} = mN^{1/(\gamma-1)}$ and $N \rightarrow \infty$. The curves refer to different values of the minimum degree m : 1 (red), 2 (blue), 3 (black). The fragility of SF networks (small q_c) is notable for $m = 1$ (the case calculated in ref. 10). In this case ($m = 1$), the network contains many leaves, and reduces to a star at $\gamma = 2$, which is trivially destroyed by removing the only single hub, explaining the general fragility in this case. Furthermore, in this same case, the network becomes a collection of dimers with $k = 1$ when $\gamma \rightarrow \infty$, which is still trivially fragile. This also explains why $q_c \rightarrow 0$ for $\gamma \geq 4$. Therefore, the fragility in the case $m = 1$ has its roots in these two limiting trivial cases. Removing the leaves ($m = 2$) results in a 2-core, which is already more robust.

For the 3-core $m = 3$, $q_c \approx 0.4$ – 0.5 provides a quite robust network, and has the expected asymptotic limit to a non-zero q_c of a random regular graph with $k = 3$ as $\gamma \rightarrow \infty$, $q_c \rightarrow (k - 2)/(k - 1) = 0.5$. Thus, SF networks become robust in these more realistic cases, and the search for other attack strategies becomes even more important. **b**, HD influence threshold q_c as a function of the degree distribution exponent of scale-free networks with minimum degree $m = 2$ in the ensemble where k_{\max} is fixed and does not scale with N . The curves refer to different values of the cut-off k_{\max} : 10^2 (red), 10^3 (green), 10^5 (blue), 10^8 (magenta), and $k_{\max} = \infty$ (black), and show that for a typical k_{\max} degree of 10^3 , for instance in social networks, the network is fairly robust with $q_c \approx 0.2$ for all γ . The curve with $m = 2$ and $k_{\max} = 10^3$ is replotted in the inset of Fig. 2b.



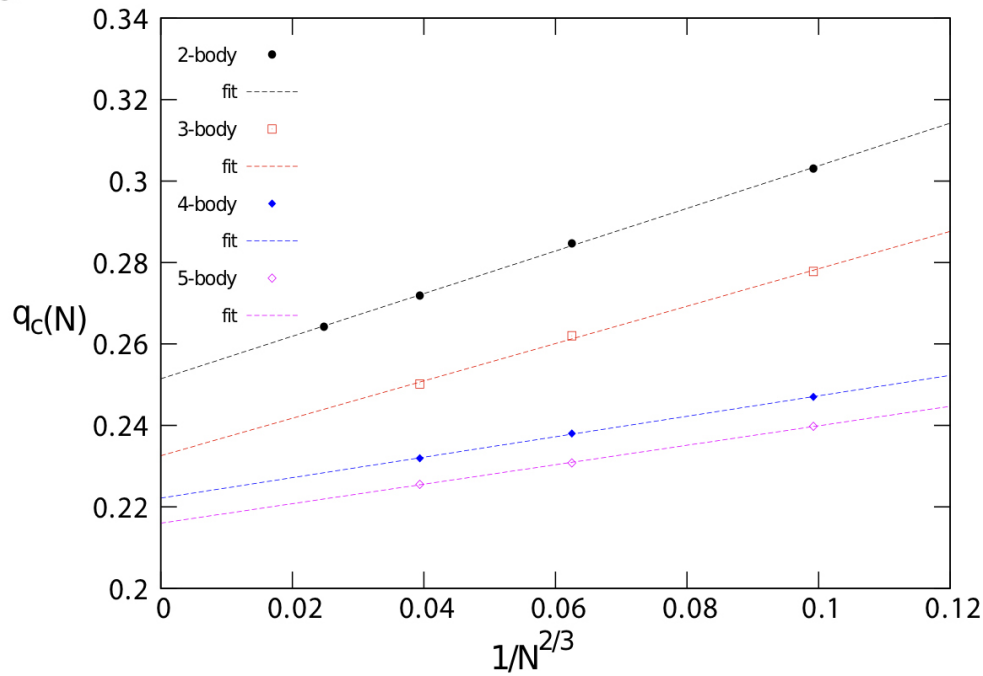
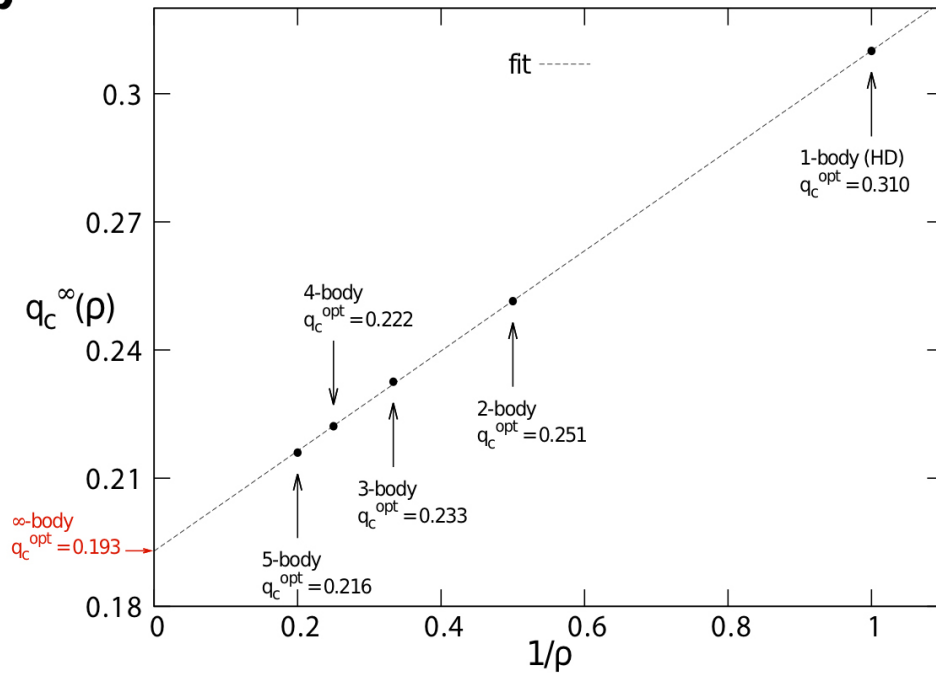
Extended Data Figure 2 | Replica Symmetry (RS) estimation of the maximum eigenvalue. Main panel, the eigenvalue $\lambda_1^{\text{RS}}(q)$, equation (92) in Supplementary Information for the two-body interaction $\ell = 1$, obtained by minimizing the energy function $\mathcal{E}(s)$ with the RS cavity method. The curve was computed on an ER graph of $N = 10,000$ nodes and average degree $\langle k \rangle = 3.5$

and then averaged over 40 realizations of the network (error bars are s.e.m.). Inset, comparison between the RS cavity method and EO (extremal optimization) for an ER graph of $\langle k \rangle = 3.5$ and $N = 128$. The curves are averaged over 200 realizations (error bars are s.e.m.).



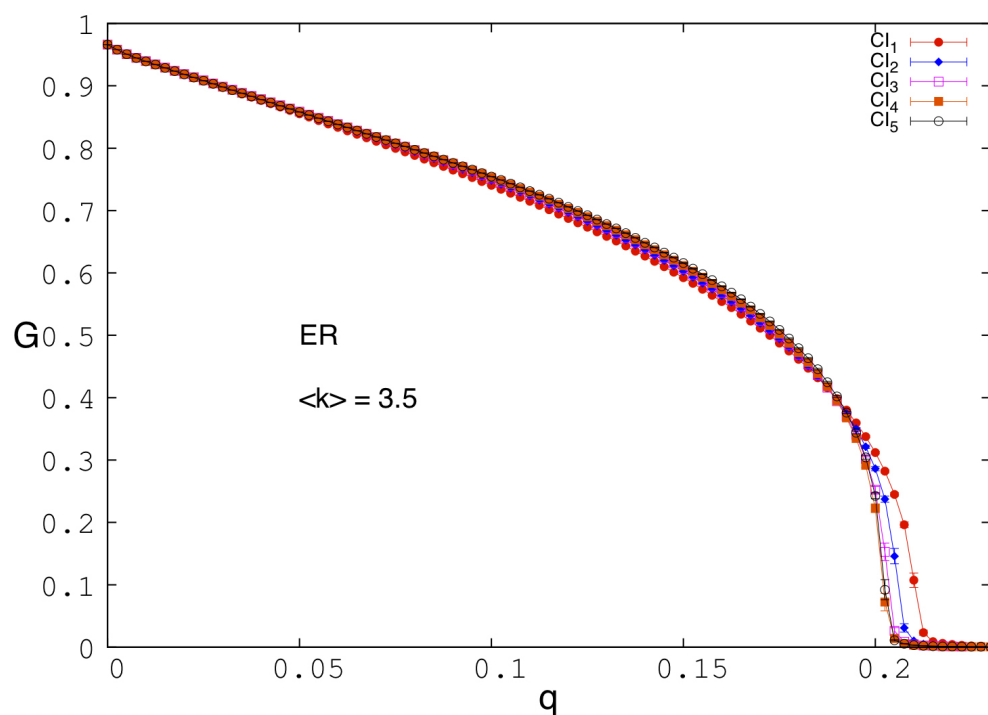
Extended Data Figure 3 | EO estimation of the maximum eigenvalue. Eigenvalue $\lambda(q)$ obtained by minimizing the energy function $\mathcal{E}(\mathbf{n})$ with τ EO (τ -extremal optimization), plotted as a function of the fraction of removed nodes q . The panels are for different orders of the interactions. The curves in

each panel refer to different sizes of ER networks with average connectivity $\langle k \rangle = 3.5$. Each curve is an average over 200 instances (error bars are s.e.m.). The value q_c where $\lambda(q_c) = 1$ is the threshold for a particular N and many-body interaction.

a**b****Extended Data Figure 4 | Estimation of optimal threshold q_c^{opt} with EO.**

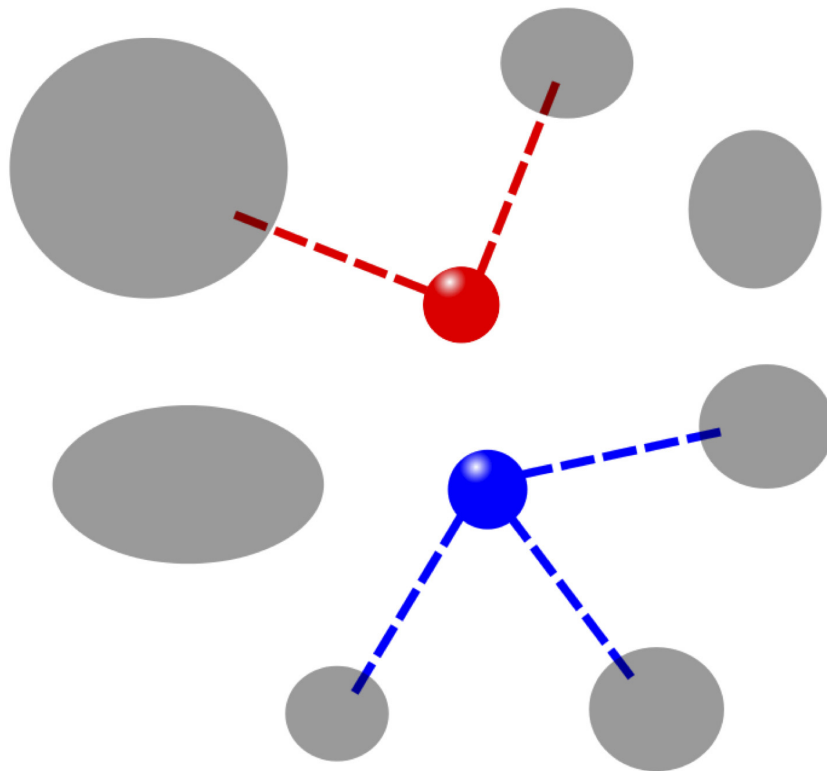
a, Critical threshold q_c as a function of the system size N , obtained with EO from Extended Data Fig. 3, of ER networks with $\langle k \rangle = 3.5$ and varying size. The curves refer to different orders of the many-body interactions. The data show a linear behaviour as a function of $N^{-2/3}$, typical of spin glasses, for each many-

body interaction ρ . The extrapolated value $q_c^{\infty}(\rho)$ is obtained at the y intercept. **b**, Thermodynamic critical threshold $q_c^{\infty}(\rho)$ as a function of the order of the interactions ρ from **a**. The data scale linearly with $1/\rho$. From the y intercept of the linear fit we obtain the thermodynamic limit of the infinite-body optimal value $q_c^{\text{opt}} = q_c^{\infty}(\rho \rightarrow \infty) = 0.192(9)$.



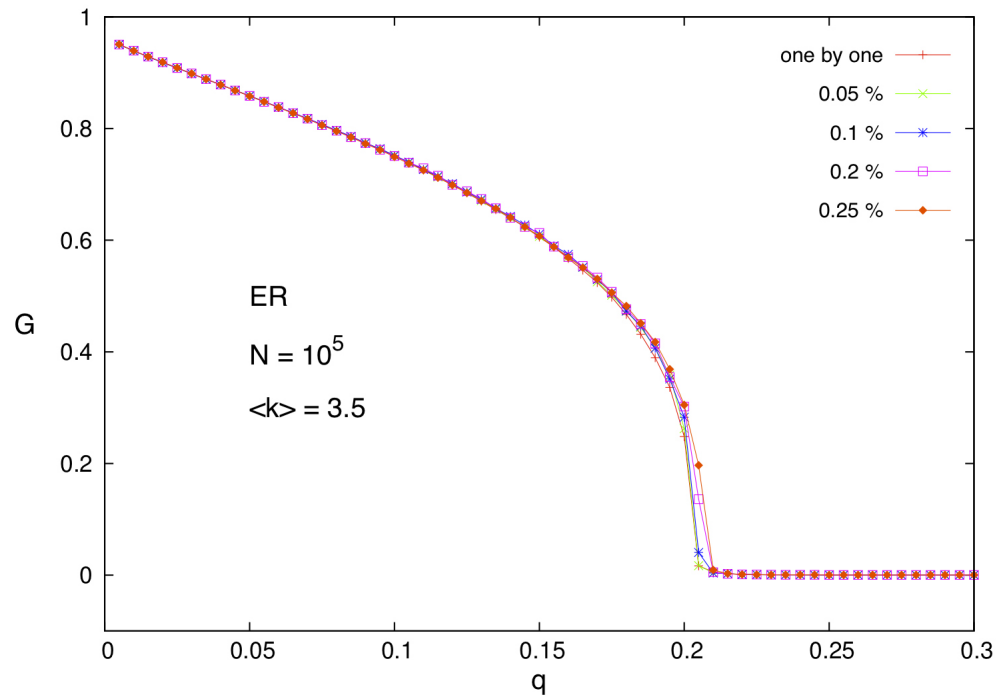
Extended Data Figure 5 | Comparison of the CI algorithm for different radii ℓ of the Ball(ℓ). We use $\ell = 1, 2, 3, 4, 5$, on a ER graph with average degree $\langle k \rangle = 3.5$ and $N = 10^5$ (the average is taken over 20 realizations of the network, error bars are s.e.m.). For $\ell = 3$ the performance is already practically indistinguishable from $\ell = 4, 5$. The stability analysis we developed to minimize q_c is strictly valid only when $G = 0$, since the largest eigenvalue of the

modified NB matrix controls the stability of the solution $G = 0$, and not the stability of the solution $G > 0$. In the region where $G > 0$ we use a simple and fast procedure to minimize G explained in Supplementary Information section VA. This explains why there is a small dependence on having a slightly larger G for larger ℓ , when $G > 0$ in the region $q \approx 0.15$.

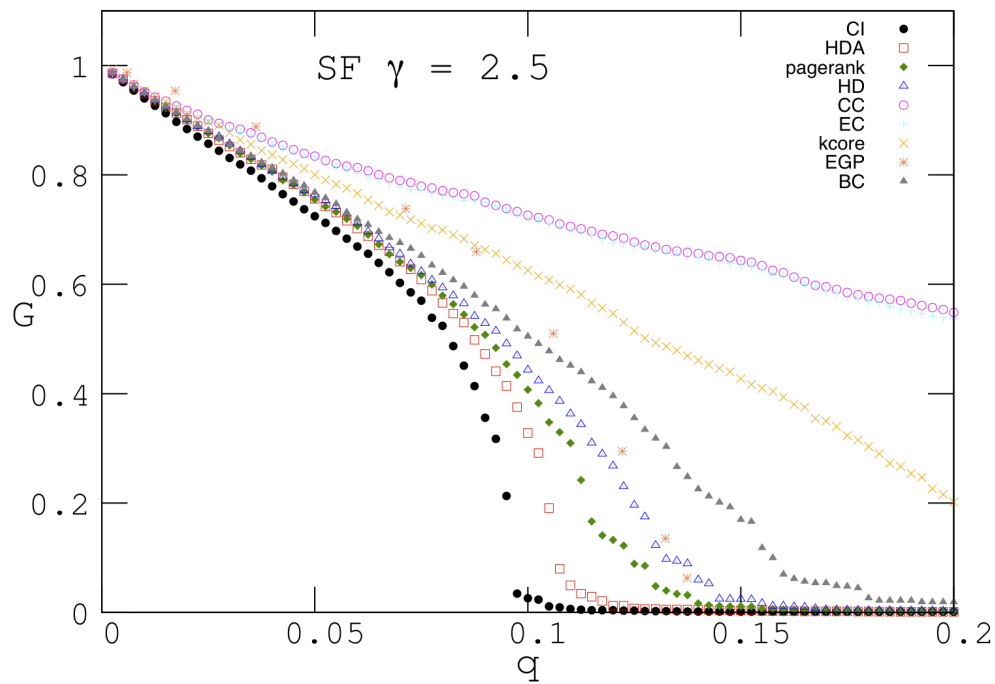


Extended Data Figure 6 | Illustration of the algorithm used to minimize $G(q)$ for $q < q_c$. Starting from the completely fragmented network at $q = q_c$, the Nq_c influencers are reinserted with their original degree and connected to their original neighbours with the following criterion: each node is assigned and index $c(i)$ given by the number of clusters it would join if it were reinserted

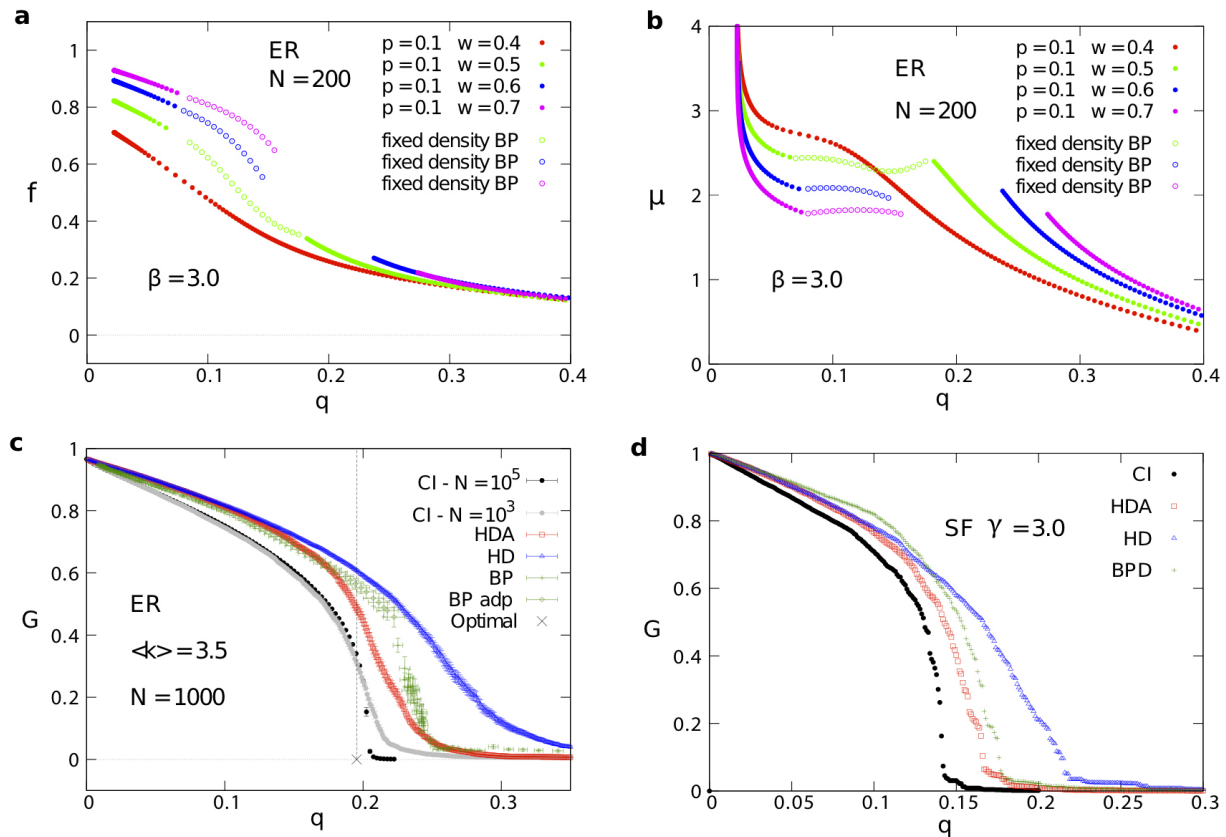
in the network. For example, the red node has $c(\text{red}) = 2$, while the blue one has $c(\text{blue}) = 3$. The node with the smallest $c(i)$ is reinserted in the network: in this case the red node. Then the $c(i)$ s are recalculated and the new node with the smallest $c(i)$ is found and reinserted. These steps are repeated until all the removed nodes are reinserted in the network.



Extended Data Figure 7 | Test of the decimation fraction. Giant component G as a function of the fraction of removed nodes q using CI, for an ER network of $N = 10^5$ nodes and average degree $\langle k \rangle = 3.5$. The profiles of the curves are drawn for different percentages of nodes fixed at each step of the decimation algorithm.



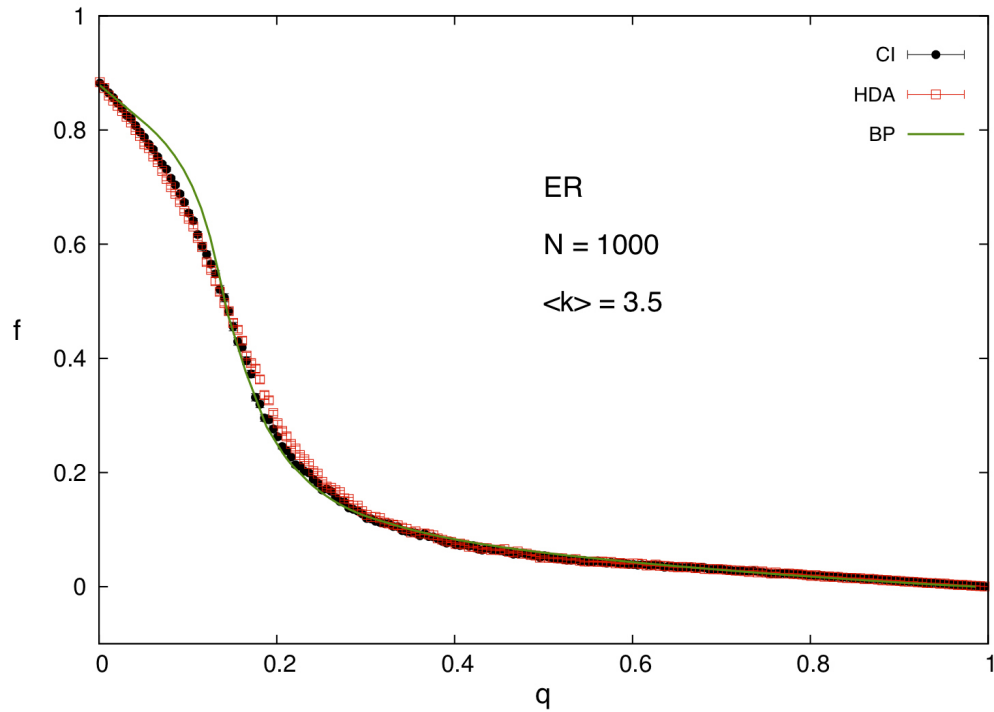
Extended Data Figure 8 | Comparison of the performance of CI, BC and EGP in destroying G . We also include HD, HDA, EC, CC, k-core and PR. We use a scale-free (SF) network with degree exponent $\gamma = 2.5$, average degree $\langle k \rangle = 4.68$, and $N = 10^4$. We use the same parameters as in ref. 11.



Extended Data Figure 9 | Comparison with BP for a network

immunization. **a**, Fraction of infected nodes f as a function of the fraction of immunized nodes q in the susceptible-infected-removed (SIR) model from the BP solution. We use an ER random graph of $N = 200$ nodes and average degree $\langle k \rangle = 3.5$. The fraction of initially infected nodes is $p = 0.1$ and the inverse temperature $\beta = 3.0$. The profiles are drawn for different values of the transmission probability w : 0.4 (red curve), 0.5 (green), 0.6 (blue), 0.7 (magenta). Also shown are the results of the fixed density BP algorithm (open circles). **b**, Chemical potential μ as a function of the immunized nodes q from BP. We use an ER random graph of $N = 200$ nodes and average degree $\langle k \rangle = 3.5$. The fraction of the initially infected nodes is $p = 0.1$ and the

inverse temperature $\beta = 3.0$. The profiles are drawn for different values of the transmission probability w : 0.4 (red curve), 0.5 (green), 0.6 (blue), 0.7 (magenta). Also shown are the results of the fixed density BP algorithm (open circles) for the region where the chemical potential is non-convex. **c**, Comparison between the giant components obtained with CI, HDA, HD and BP. We use an ER network of $N = 10^3$ and $\langle k \rangle = 3.5$. We also show the solution of CI from Fig. 2a for $N = 10^5$. We find in order of performance: CI, HDA, BP and HD. (The average is taken over 20 realizations of the network, error bars are s.e.m.) **d**, Comparison between the giant components obtained with CI, HDA, HD and BPD. We use a SF network with degree exponent $\gamma = 3.0$, minimum degree $k_{\min} = 2$, and $N = 10^4$ nodes.



Extended Data Figure 10 | Fraction of infected nodes $f(q)$ as a function of the fraction of immunized nodes q in SIR from BP. We use the following parameters: initial fraction of infected people $p = 0.1$, and transmission probability $w = 0.5$. We use an ER network of $N = 10^3$ nodes and $\langle k \rangle = 3.5$.

We compare CI, HDA and BP. All strategies give similar performance, owing to the large value of the initial infection p , which washes out the optimization performed by any sensible strategy, in agreement with the results shown in figure 12a of ref. 14.

Beating the Stoner criterion using molecular interfaces

Fatma Al Ma'Mari^{1*}, Timothy Moorsom^{1*}, Gilberto Teobaldi², William Deacon¹, Thomas Prokscha³, Hubertus Luetkens³, Steve Lee⁴, George E. Sterbinsky⁵, Dario A. Arena⁵, Donald A. MacLaren⁶, Machiel Flokstra⁴, Mannan Ali¹, May C. Wheeler¹, Gavin Burnell¹, Bryan J. Hickey¹ & Oscar Cespedes¹

Only three elements are ferromagnetic at room temperature: the transition metals iron, cobalt and nickel. The Stoner criterion explains why iron is ferromagnetic but manganese, for example, is not, even though both elements have an unfilled 3d shell and are adjacent in the periodic table: according to this criterion, the product of the density of states and the exchange integral must be greater than unity for spontaneous spin ordering to emerge^{1,2}. Here we demonstrate that it is possible to alter the electronic states of non-ferromagnetic materials, such as diamagnetic copper and paramagnetic manganese, to overcome the Stoner criterion and make them ferromagnetic at room temperature. This effect is achieved via interfaces between metallic thin films and C₆₀ molecular layers. The emergent ferromagnetic state exists over several layers of the metal before being quenched at large sample thicknesses by the material's bulk properties. Although the induced magnetization is easily measurable by magnetometry, low-energy muon spin spectroscopy³ provides insight into its distribution by studying the depolarization process of low-energy muons implanted in the sample. This technique indicates localized spin-ordered states at, and close to, the metal–molecule interface. Density functional theory simulations suggest a mechanism based on magnetic hardening of the metal atoms, owing to electron transfer^{4,5}. This mechanism might allow for the exploitation of

molecular coupling to design magnetic metamaterials using abundant, non-toxic components such as organic semiconductors. Charge transfer at molecular interfaces may thus be used to control spin polarization or magnetization, with consequences for the design of devices for electronic, power or computing applications (see, for example, refs 6 and 7).

Multifunctional materials with the spin degree of freedom, such as multiferroics, magnetic semiconductors and molecular magnets, have aroused interest as potentially transformative components in quantum technologies^{8–12}. Strategies used to bring magnetic ordering to these materials typically rely on the inclusion of magnetic transition metals, heavy elements with a large atomic moment or rare earths. In thin-film structures, proximity effects and coupling at interfaces have an essential role in determining magnetic and transport characteristics of the structures^{13,14}. This is especially the case for molecular spintronics^{15,16}, where organic thin films grown on Cu have demonstrated spin filtering¹⁷. The organic–magnetic coupling can propagate for long distances in systems such as nanoscale vortex-like configurations or nanoskyrmion lattices¹⁸.

We choose C₆₀ as a model molecule, owing to its structural simplicity and robustness as well as its high electron affinity. C₆₀/transition-metal complexes exhibit strong interfacial coupling between metal 3d_z electrons and molecular π -bonded *p* electrons. The potential created by the mismatch of molecular and metal work functions leads to a

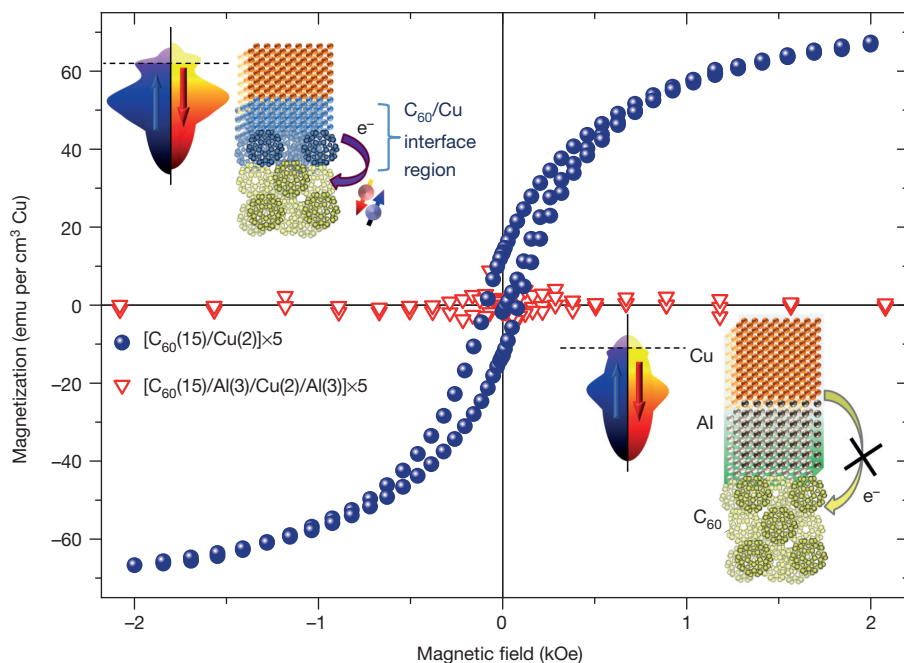


Figure 1 | Effect of molecular interfaces.

Schematics and room-temperature magnetization for a Ta(5)/[C₆₀(15)/Cu(2)]×5/Al(5) and a Ta(5)/[C₆₀(15)/Al(3)/Cu(2)/Al(3)]×5 sample; the numbers in parentheses are the film thicknesses in nanometres. The Cu-to-C₆₀ charge transfer and interface reconstruction results in substantial changes in the density of states (DOS) of the metallic film and a band splitting that leads to magnetic ordering. On the other hand, an Al spacer between both materials screens the charge transfer from the 3d transition metal and stops the band splitting. emu, electromagnetic unit.

¹School of Physics and Astronomy, University of Leeds, Leeds LS2 9JT, UK. ²Stephenson Institute for Renewable Energy, Department of Chemistry, University of Liverpool, Liverpool L69 3BX, UK.

³Laboratory for Muon Spin Spectroscopy, Paul Scherrer Institut, 5232 Villigen, Switzerland. ⁴School of Physics and Astronomy, SUPA, University of St Andrews, St Andrews KY16 9SS, UK. ⁵Photon Sciences Directorate, Brookhaven National Laboratory, Upton, New York 11973, USA. ⁶School of Physics and Astronomy, SUPA, University of Glasgow, Glasgow G12 8QQ, UK.

*These authors contributed equally to this work.

partial filling of the interface states^{19–21}. Other molecules with close electron affinity and the potential for $3d_z-p$ coupling could be used to similar effect. In the case of C_{60} on metallic substrates such as Cu films, the charge transfer from the metal can be of up to three electrons per molecule and leads to a metallization of the interface²². Magnetic polarization in fullerenes induced by spin injection or charge transfer may extend for long distances, owing to low spin–orbit coupling and the absence of a hyperfine interaction^{23,24}.

In the metal, it is expected that the charge transfer will be quickly screened by free electrons. A priori, there is no reason to suspect that a spin-unpolarized molecule would change the magnetic state of a metallic film. However, we find that the charge transfer and surface reconstruction at the interface²⁵ can lead to an emergent magnetization in both the metal and the molecule. Magnetometry measurements of C_{60} /Cu and C_{60} /Mn multilayers show hysteresis at room temperature. The magnetization disappears when all the transition-metal–molecular interfaces are decoupled via an Al or Al_2O_3 spacer layer (Fig. 1).

Changes in the density of states (DOS) of the metal may be larger close to the interface, but should be screened deeper within the material. If the film is thick enough, the bulk properties of the metal are expected to dominate and quench the magnetization. This effect is shown in Fig. 2: the magnetization of C_{60} /Cu and C_{60} /Mn multilayers decays once the metallic-film thickness exceeds 2–3 nm. Decreasing the coupling between the top and bottom interfaces of a metal layer may also play a role in quenching the magnetization.

The magnetization of C_{60} /Cu samples is 3–4 times stronger than that of C_{60} /Mn, which is probably due to the better lattice matching

and larger charge transfer between Cu and C_{60} (ref. 19). However, bulk Mn is paramagnetic and much closer to complying with the Stoner criterion than is diamagnetic Cu, owing to the larger exchange interactions and DOS at the Fermi level ($DOS(E_F)$)²⁶. This property may be correlated with the propagation length of the effect, which is five times greater in Mn than in Cu. C_{60} /Mn multilayers also show a larger paramagnetic slope of the magnetization than does decoupled Mn; see Supplementary Figs 1–4. Both systems exhibit anisotropy with an easy axis that lies in the plane of the film, and out-of-plane saturation fields of about 10–15 kOe at room temperature (inset of Fig. 2b). The Cu and Mn samples degrade with time, and the magnetization drops over several days or weeks depending on the layer structure and protective cap used (Supplementary Fig. 5).

To explore the dependence of magnetization on interfacial coupling, we fabricated samples with different numbers of C_{60} (15)/Cu(2.5) junctions (the numbers in parentheses are the film thicknesses in nanometres). The magnetic moment of these multilayers is proportional to the number of C_{60} /Cu interfaces, suggesting that the magnetism is due to molecular coupling (inset of Fig. 2a). However, the amount of Cu and C_{60} also increases as we grow more layers. To ensure that the magnetization is not simply proportional to the amount of material deposited, we performed a related set of measurements where the total sample thickness is kept constant: 9 nm of Cu and 81 nm of C_{60} , but split into different numbers of C_{60} /Cu repeats (Supplementary Fig. 6). In this case, the magnetism also increases with the number of interfaces; for example, the magnetic moment of $[C_{60}(16.2)/Cu(1.8)] \times 5$ is greater than the magnetic moment of $[C_{60}(27)/Cu(3)] \times 3$. However, trying to split the sample into Cu films that are $\lesssim 1.5$ nm thick results in discontinuous layers and a drop in the magnetization. This thickness and interface dependence of the magnetization could not arise from contaminants, and X-ray spectroscopy did not show the presence of impurities (Supplementary Figs 7–11).

Magnetometry measurements show that the magnetization is dependent on the thickness of the metal, but not on the thickness of the molecular film, as long as the latter is continuous and smooth (about 10–20 nm thick). However, magnetometry by itself cannot determine where the magnetization is located or how much of it corresponds to each material. Conversely, low-energy muon spin rotation (μ SR) provides a magnetic profile of the sample²⁷ and has been applied successfully to other metallo-molecular systems³. Here, a beam of almost fully polarized positive muons is moderated to keV energies so that their tunable stopping range is tens to hundreds of nanometres. The local polarization at the positive-muon stopping depth is probed through the detection of decay positrons, preferentially emitted along the muons' spin direction.

We use this technique to study two samples: multilayer A is a magnetic sample with the structure (from bottom to top) Ta(5)/ C_{60} (20)/Cu(2.5)/ C_{60} (50)/Au(10); multilayer B is a decoupled, diamagnetic reference sample with Al_2O_3 layers in between the Cu and C_{60} (Fig. 3a). The uppermost gold film slows injected positive muons and protects the inner layers from oxidation. The total sample structure is designed to allow the active layers to be probed with a range of accessible positive-muon energies and to maximize the stopping profile at the regions of interest, that is, close to the C_{60} /Cu interface. The Cu thickness is chosen to obtain the highest magnetization (Fig. 2a). Muon stopping profiles and further experimental details can be found in Supplementary Information section S.3 and Supplementary Figs 12–13.

Muons with 4 keV implantation energy probe the identical, uppermost C_{60} (50)/Au(10) layers of both samples. Nevertheless, the zero-field μ SR measurements at 250 K demonstrate a significant difference ($P < 0.001$) in the polarization of the implanted muons: for the magnetic multilayer-A sample, a fraction of approximately 10% of the muon-spin polarization is rapidly lost, which indicates that about 10% of the region sampled by the muons is affected by the magnetism (Fig. 3b). This result points to additional sources of magnetic flux in the multilayer-A sample. In this (uppermost C_{60} (50)/Au(10)) region,

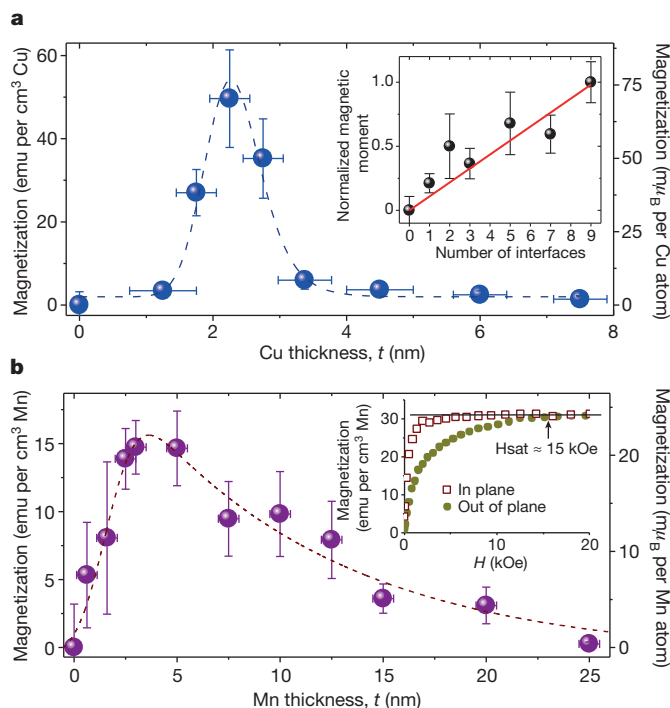


Figure 2 | Room-temperature magnetization for Cu and Mn films. Dashed lines are exponentially modified Gaussian fits. Error bars in thickness constitute the film roughness and in magnetization are calculated as the standard error of the mean. **a**, Dependence of the magnetization on the Cu-film thickness for a total of 145 samples with the structure Ta(5)/ $[C_{60}(10-20)/Cu(t)/C_{60}(10-20)] \times (1-5)/Al(5)$. Films with $t \lesssim 1-1.5$ nm are discontinuous. Inset, magnetic moment versus the number of C_{60} (15)/Cu(2.5) interfaces; they are roughly proportional. **b**, As for **a**, but for Mn, with 96 samples measured. The magnetization in Mn films is smaller than in Cu films, but propagates for a longer distance. Inset, out-of-plane and in-plane magnetization measurements of a $[C_{60}(15)/Mn(2.5)] \times 4$ sample as a function of magnetic field strength H . H_{sat} , magnetic field strength at which the magnetization saturates; emu, electromagnetic unit; μ_B , Bohr magneton.

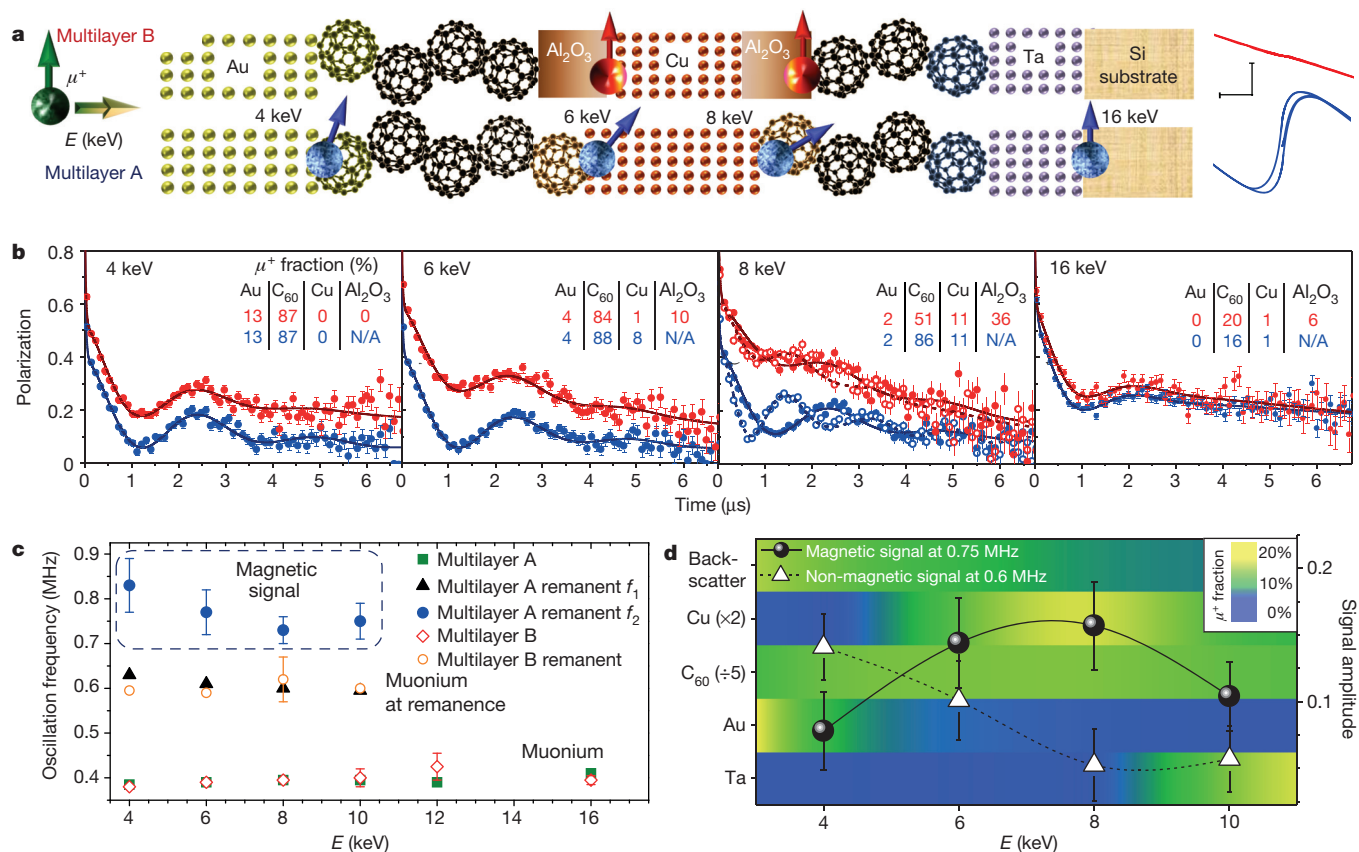


Figure 3 | Muon spin rotation (μ SR) spectroscopy at 250 K. Error bars are the standard error of the mean in about 10^6 events. **a**, Schematic of the experiment and the samples measured: multilayer A, [Ta(5)/C₆₀(20)/Cu(2.5)/C₆₀(50)/Au(10)]; and the control, multilayer B, [Ta(5)/C₆₀(20)/Al₂O₃(4)/Cu(2.5)/Al₂O₃(4)/C₆₀(50)/Au(10)]. Far-right, raw hysteresis loops; the horizontal scale bar represents 1 kOe and the vertical scale bar represents 100 emu per cm³ of Cu in multilayer A or B, as appropriate. **b**, Zero-field μ SR spectra for 4 keV, 6 keV, 8 keV and 16 keV muon implantation energies. Multilayer B is plotted in red; multilayer A is plotted in blue. Tables show the fraction of positive muons (μ^+) stopped in each layer in each sample. At 8 keV, zero-field spectra are shown before (closed symbols) and after (open symbols, remanent state) a magnetic field with a strength of 300 Oe was applied, evidencing clear differences in the multilayer-A sample. **c**, Oscillation

frequencies from fits to the data plotted in **b**. At remanence, a new signal f_2 at approximately 0.75 MHz is observed in the multilayer-A sample, in addition to the signal f_1 at 0.6 MHz that is observed for both samples, with f_2 attributed to the emergent magnetization. **d**, The polarization (signal) amplitude of the magnetic remanent signal at 0.75 MHz tracks the fraction of muons stopped in the Cu (maximum at 8 keV), whereas the signal associated with muonium at 0.6 MHz is anti-correlated to it. The markers correspond to the signal amplitude (measured by the right-hand axis) for the zero-field spectra at the given energy E . The background shading corresponds to the fraction of positive muons (μ^+) stopped in the given layer in multilayer A, beginning with backscattered muons, which do not decay in the film, and ending with those muons that enter the Ta seed layer; the shading for the Cu, C₆₀ and Au layers corresponds to the data shown in blue in the inset tables in **b**.

the additional flux most probably arises from stray dipolar fields, since at low temperatures (20 K) we find that 75% of the positive muons implanted in the C₆₀ layer form a bound electron–muon state called muonium, which is observed in a non-magnetic environment^{28,29}. This observation strongly indicates that the C₆₀ layer is, for the most part, free of magnetic moments, and suggests that the magnetism is localized at the Cu/C₆₀ interface. Owing to the presence of muonium in C₆₀, the data analysis is difficult, but further support for this scenario comes from the energy/depth dependence of the μ SR data at low and high temperatures. At 20 K, the observable muonium fraction decreases in the magnetic multilayer-A sample as the Cu layer is approached (Supplementary Fig. 14). Analogously, at 250 K, the difference between the spectra of the two samples increases for the 6-keV data and is even greater at 8 keV, the energy at which the muons most heavily sample the Cu layer (Fig. 3b). If the Cu were non-magnetic, then one would expect an overall increase of the muon polarization, which is not observed.

Another means of locating the magnetism in the multilayer-A sample is to study its μ SR response in the zero-field remanent state. Both samples contain an oscillation at 0.4 MHz, owing to the muonium formed in semiconducting C₆₀. After applying an external field of 300 Oe, this signal is shifted to 0.6 MHz, which we attribute to a small

residual field of approximately 0.3 Oe in the apparatus. Nonetheless, the remanent 8-keV μ SR spectra shown in Fig. 3b are clearly different from the virgin spectra for the magnetic multilayer-A sample, whereas only subtle changes are observed for the non-magnetic reference sample multilayer B. The new feature related to the remanent state of multilayer A is an additional oscillation at approximately 0.75 MHz, which is not observed for the non-magnetic multilayer B (Fig. 3c). This new frequency is explained by an additional magnetic field of 0.1 Oe at the muonium site in close proximity to the Cu layer. The amplitude of this signal follows the fraction of positive muons stopped in the Cu layer (Fig. 3d), whereas the non-magnetic signal at 0.6 MHz is anti-correlated to this fraction. Altogether, the low-energy μ SR data fully support the notion of a magnetic moment being localized in the metallic layer and the immediate Cu/C₆₀ interface.

To search for the origins of the induced magnetization, we modelled the Cu/C₆₀ interface using density functional theory (DFT); see Supplementary Information section S.4. The molecular roughness of the C₆₀ films has been accounted for via several interface models based on: (1) the single crystal 7-vacancy Cu(111) reconstruction²⁰; (2) C₆₀ encapsulation into adsorbed Cu(111) films (Cu{C₆₀}); and (3) Cu(111) growth into the pits of the C₆₀ film (C₆₀{Cu}); see Fig. 4a. Regardless of the adopted model variant (Supplementary Figs 15–19), we

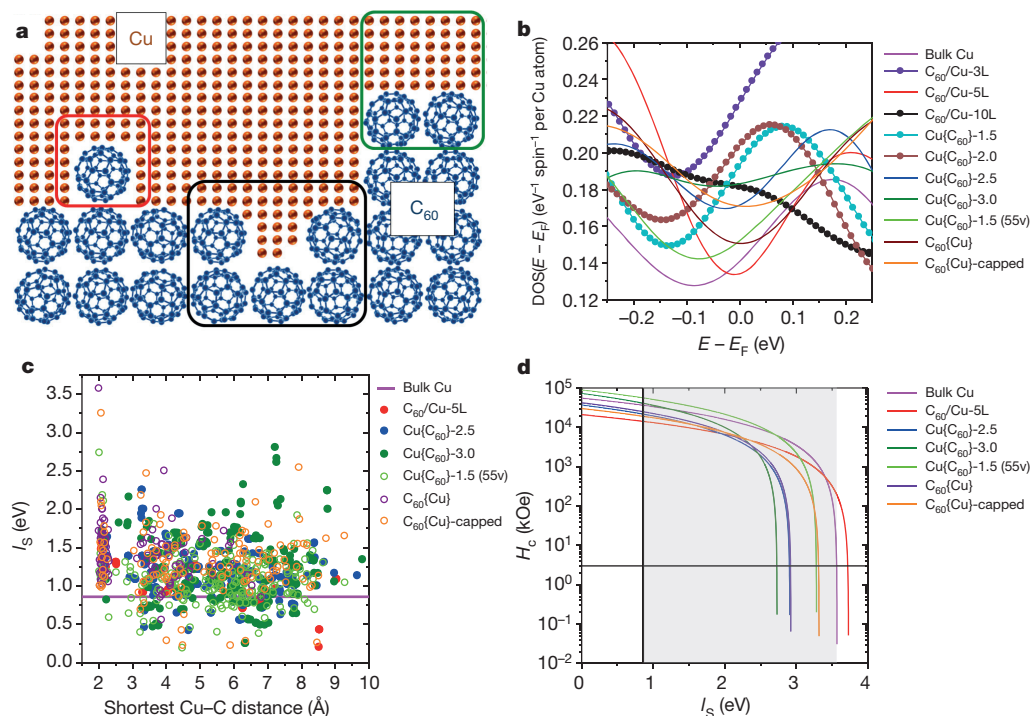


Figure 4 | DFT simulations and metamagnetic modelling. **a**, Schematic of the molecularly rough Cu/C₆₀ interface with: atomically flat C₆₀/Cu contacts (green square); C₆₀ inclusion in Cu film (Cu{C₆₀}; red square); and Cu inclusion in pits of the C₆₀ film (C₆₀{Cu}; black square). The optimized atomic structures are reported and labelled in Supplementary Figs 15–19. **b**, Total DOS per electronic spin state as a function of energy around the Fermi level (DOS($E - E_F$)) for bulk Cu and the Cu/C₆₀ interface models. In the Cu{C₆₀} models, ‘-1.5’, ‘-2.0’, ‘-2.5’ and ‘-3.0’ indicate the initial Cu–C distance (in ångströms); the Cu{C₆₀}-1.5 model with 55 Cu vacancies is denoted Cu{C₆₀}-1.5 (55v). In the atomically flat C₆₀/Cu contact models, ‘-3L’, ‘-5L’ and

‘-10L’ indicate the number of Cu layers in the model. In the C₆₀{Cu} models, ‘-capped’ refers to a structure that is topped with a continuous Cu layer. **c**, Atom-resolved analysis of the Stoner exchange integral I_S for the Cu atoms as a function of the shortest Cu–C₆₀ distance. I_S for bulk Cu is 0.86 eV. **d**, The critical magnetic field strength (H_c) for spontaneous ferromagnet metamagnetic transition as a function of I_S for the models computed to have positive curvature at DOS(E_F) in **b**. The horizontal black line marks a typical magnetic field strength during sample preparation. Shaded area represents the possible values for I_S in the different geometries, with the bulk value of 0.86 eV indicated by the vertical black line.

find a non-magnetic ground state for all the considered interfaces. With the exception of the thicker C₆₀/slab (‘slab’ refers to a finite, non-monoatomic layer) interfaces and the Cu{C₆₀} models that are prepared with short (1.5–2 Å) initial Cu–C distances, all the models exhibit positive curvature in DOS(E_F); see Fig. 4b. Within the mean-field itinerant-electron model (Supplementary Fig. 20), convex DOS(E_F) may lead, for sufficiently high external magnetic fields, to a spontaneous first-order paramagnetic-to-ferromagnetic metamagnetic transition. For the computed DOS(E_F) of the Cu/C₆₀ interface models, the critical magnetic field strength (H_c) for the metamagnetic transition sharply decreases with increasing values of the Stoner exchange integral (I_S) according to $[1 - I_S \text{DOS}(E_F)]^{3/2}$; see Fig. 4d.

Atom-resolved analysis of I_S reveals a change in the exchange strength at the Cu/C₆₀ interfaces of up to a factor of four (Fig. 4c). Magnetic hardening by up to a factor of three has been previously reported for magnetic cobalt atoms contacted to π -conjugated molecules⁵. The computed values of I_S (from 0.86 eV for bulk Cu to up to more than 2.5 eV for interfacial Cu atoms) suggest viable paramagnetic-to-ferromagnetic metamagnetic transitions for field strengths lower than 1 kOe for thin Cu layers (Fig. 4d). On this basis, we attribute the measured ferromagnetism to a transition of the Cu/C₆₀ system in magnetic fields with strengths of 0.3–5 kOe generated during sample deposition and preparation (see Methods). Our DFT calculations predict that 77–95% of the magnetization in the Cu/C₆₀ system will be distributed in the metal (Supplementary Table 8 and Supplementary Figs 21–26), in good agreement with the muon spectroscopy data.

Although the substantial electron transfer from the Cu layers to C₆₀ (≥ 1.6 electrons per C₆₀ molecule, depending on the model; Supplementary Table 7) is effective in altering the curvature of DOS(E_F)

and increasing I_S , the calculated DOS(E_F) $\times I_S$ product remains less than unity (Supplementary Table 6), which does not fulfil the Stoner criterion. However, despite not satisfying the Stoner criterion in the ground state, magnetometry and muon spectroscopy presented here provide conclusive evidence for the emergence of magnetism at Cu/C₆₀ interfaces. This is probably associated with a sharp decrease of five orders of magnitude in the ferro-metamagnetic critical field strength H_c as I_S increases that is made possible by C₆₀-induced magnetic hardening of Cu. Similar effects due to charge transfer could also take place in other hybrid metallo-organic¹⁷ and d^0 magnetic systems³⁰. To maximize this effect, it should be possible to look for molecules with large electron affinity such as polyoxometalates and metals with a large exchange integral such as zinc. However, good band and structural matching is needed to obtain noticeable results. Manipulating the charge transfer by applying electric potentials or using energy band matching may lead to applications in molecular memories or devices such as spin capacitors.

Online Content Methods, along with any additional Extended Data display items and Source Data, are available in the online version of the paper; references unique to these sections appear only in the online paper.

Received 11 December 2014; accepted 22 May 2015.

1. Stoner, E. C. Collective electron ferromagnetism. *Proc. R. Soc. London Ser. A* **165**, 372–414 (1938).
2. Stoner, E. C. Collective electron ferromagnetism. II. Energy and specific heat. *Proc. R. Soc. London Ser. A* **169**, 339–371 (1939).
3. Drew, A. J. *et al.* Direct measurement of the electronic spin diffusion length in a fully functional organic spin valve by low-energy muon spin rotation. *Nature Mater.* **8**, 109–114 (2009).
4. Vandewal, K. *et al.* Efficient charge generation by relaxed charge-transfer states at organic interfaces. *Nature Mater.* **13**, 63–68 (2014).

5. Callsen, M., Caciuc, V., Kiselev, N., Atodiressei, N. & Bluegel, S. Magnetic hardening induced by nonmagnetic organic molecules. *Phys. Rev. Lett.* **111**, 106805 (2013).
6. Moodera, J. S., Koopmans, B. & Oppeneer, P. M. On the path toward organic spintronics. *MRS Bull.* **39**, 578–581 (2014).
7. Raman, K. V. Interface-assisted molecular spintronics. *Appl. Phys. Rev.* **1**, 031101 (2014).
8. Beeler, M. C. *et al.* The spin Hall effect in a quantum gas. *Nature* **498**, 201–204 (2013).
9. Eerenstein, W., Mathur, N. D. & Scott, J. F. Multiferroic and magnetoelectric materials. *Nature* **442**, 759–765 (2006).
10. Powell, A. K. Molecular magnetism: a bridge to higher ground. *Nature Chem.* **2**, 351–352 (2010).
11. Geng, Y. *et al.* Direct visualization of magnetoelectric domains. *Nature Mater.* **13**, 163–167 (2014).
12. Warner, M. *et al.* Potential for spin-based information processing in a thin-film molecular semiconductor. *Nature* **503**, 504–508 (2013).
13. Maccherozzi, F. *et al.* Evidence for a magnetic proximity effect up to room temperature at Fe/(Ga,Mn)As interfaces. *Phys. Rev. Lett.* **101**, 267201 (2008).
14. Vobornik, I. *et al.* Magnetic proximity effect as a pathway to spintronic applications of topological insulators. *Nano Lett.* **11**, 4079–4082 (2011).
15. Barraud, C. *et al.* Unravelling the role of the interface for spin injection into organic semiconductors. *Nature Phys.* **6**, 615–620 (2010).
16. Sanvito, S. Molecular spintronics: the rise of spinterface science. *Nature Phys.* **6**, 562–564 (2010).
17. Raman, K. V. *et al.* Interface-engineered templates for molecular spin memory devices. *Nature* **493**, 509–513 (2013).
18. Brede, J. *et al.* Long-range magnetic coupling between nanoscale organic-metal hybrids mediated by a nanoskymion lattice. *Nature Nanotechnol.* **9**, 1018–1023 (2014).
19. Pai, W. W. *et al.* Optimal electron doping of a C₆₀ monolayer on Cu(111) via interface reconstruction. *Phys. Rev. Lett.* **104**, 036103 (2010).
20. Xu, G. *et al.* Detailed low-energy electron diffraction analysis of the (4 × 4) surface structure of C₆₀ on Cu(111): seven-atom-vacancy reconstruction. *Phys. Rev. B* **86**, 075419 (2012).
21. Tamai, A. *et al.* Electronic structure at the C₆₀/metal interface: an angle-resolved photoemission and first-principles study. *Phys. Rev. B* **77**, 075134 (2008).
22. Cho, S. W. *et al.* Origin of charge transfer complex resulting in ohmic contact at the C₆₀/Cu interface. *Synth. Met.* **157**, 160–164 (2007).
23. Zhang, X. *et al.* Observation of a large spin-dependent transport length in organic spin valves at room temperature. *Nature Commun.* **4**, 1392 (2013).
24. Moorsom, T. *et al.* Spin-polarized electron transfer in ferromagnet/C₆₀ interfaces. *Phys. Rev. B* **90**, 125311 (2014).
25. Tseng, T.-C. *et al.* Charge-transfer-induced structural rearrangements at both sides of organic/metal interfaces. *Nature Chem.* **2**, 374–379 (2010).
26. Janak, J. F. Uniform susceptibilities of metallic elements. *Phys. Rev. B* **16**, 255–262 (1977).
27. Morenzoni, E. *et al.* Implantation studies of keV positive muons in thin metallic layers. *Nucl. Instrum. Methods* **B192**, 254–266 (2002).
28. Ansaldo, E. J., Niedermayer, C. & Stronach, C. E. Muonium in fullerite. *Nature* **353**, 121 (1991).
29. Duty, T. L. *et al.* Zero-field μ SR in crystalline C₆₀. *Hyperfine Interact.* **86**, 789–795 (1994).
30. Coey, J. M. D. d^0 ferromagnetism. *Solid State Sci.* **7**, 660–667 (2005).

Supplementary Information is available in the online version of the paper.

Acknowledgements This work was supported by the Engineering and Physical Sciences Research Council through grants EP/K00512X/1, EP/K036408/1, EP/J01060X/1 and EP/I004483/1. Use of the N8 POLARIS (EPSRC EP/K000225/1), ARCHER (via the UKCP Consortium, EP/K013610/1), and the High Performance Computing (HPC) Wales facilities is acknowledged. Use of the National Synchrotron Light Source, Brookhaven National Laboratory, was supported by the US Department of Energy, Office of Science, Office of Basic Energy Sciences, under contract number DE-AC02-98CH10886.

Author Contributions F.A.M. and T.M. grew and characterized the samples, conducted the magnetometry and μ SR, and contributed to the data analysis; G.T. performed and analysed the DFT simulations; W.D. grew and characterized the Cu–C₆₀ multilayers; T.P., H.L., S.L. and M.F. contributed to the design, measurement and analysis of the μ SR experiments; D.A.M. contributed to the TEM images and structural analysis; G.E.S. and D.A.A. performed the X-ray magnetic circular dichroism and X-ray absorption spectroscopy measurements; M.A., M.C.W., G.B. and B.J.H. contributed to the sample structure and measurement setup; and O.C. designed the study, analysed the data and wrote the manuscript. All authors discussed the results and commented on the manuscript.

Author Information The data presented here are available at <http://dx.doi.org/10.5518/6>. Reprints and permissions information is available at www.nature.com/reprints. The authors declare no competing financial interests. Readers are welcome to comment on the online version of the paper. Correspondence and requests for materials should be addressed to O.C. (o.cespedes@leeds.ac.uk).

METHODS

Magnetic measurements were taken using a superconducting quantum interference device operated as a vibrating sample magnetometer (SQUID-VSM), model MPMS3 from Quantum Design with resolution better than 10^{-8} emu. The thin films were deposited on 0.5-mm thick Si/SiO₂ substrates. Metals were deposited by DC magnetron sputtering at a pressure of approximately 2.5 mbar (24 s.c.c.m. of Ar; 10^{-8} mbar base pressure) with a deposition rate of $1\text{--}3 \text{ \AA s}^{-1}$. C₆₀ films were deposited by thermal evaporation from a sublimed, 99.9%-purity source in an Al₂O₃ boat in the same chamber at approximately 10^{-8} mbar and with deposition rates of $0.5\text{--}1 \text{ \AA s}^{-1}$. Al₂O₃ films were grown via plasma oxidation of Al films: O₂ flow of 76 s.c.c.m., 35 mA current. Oxygen is highly detrimental to the emergent magnetism, and samples grown in a poor vacuum ($P_{\text{total}} \geq 2 \times 10^{-8}$ or $P_{\text{O}_2} \geq 5 \times 10^{-10}$ mbar) show no magnetization. Ta seed layers are used to decrease the sample roughness. Our thermally sublimed C₆₀ films are relatively rough when compared to sputtered metallic films (about 1 nm r.m.s. roughness for C₆₀ compared to <0.5 nm in metals). The metallic films are continuous and there is negligible diffusion into the molecular film as seen in low-angle X-rays (Supplementary Fig. 3). Cross-sections of representative samples were analysed by transmission electron microscopy, which showed that the metallic layers are continuous and the C₆₀ layers are polycrystalline (Supplementary Fig. 27). The films experience a magnetic field strength of approximately 0.3 kOe during growth, owing to an in-plane magnet and the field from the magnetron gun. They are also subject to field strengths of about 1–5 kOe during loading and centring in the SQUID-VSM, which is needed to position the sample with respect to the SQUID sensor.

Low-energy muon spin spectroscopy³¹ uses positive muons to provide a probe of local magnetization. Positive muons are implanted into a sample and decay into a detectable positron and a neutrino/anti-neutrino pair. Owing to charge-parity violation, there is a preferred direction of emission of the positrons along the muons' spin vector. Determining the direction of the positron decay allows us to determine the precession of the muon spin and, therefore, the local field at the muon implantation site. A polarized high-intensity beam of energetic (MeV) positive muons³² is obtained from the decay of π^+ , generated by a proton beam impinging on a graphite target. After moderation in a cryogenic solid Ar moderator where the beam polarization is conserved³³, the anti-muons are

re-accelerated electrostatically to keV energies and transported by electrostatic elements to the sample. Positrons emitted from muon decay are detected by two plastic scintillator rings and the difference between the fluxes observed at these two detectors is used to determine the instantaneous spin direction of implanted positive muons as a function of time. The muon asymmetry is then calculated using $A(t) = [N_L(t) - N_R(t)]/[N_L(t) + N_R(t)]$, where $N_{L,R}(t)$ are the background-corrected decay histograms of the left and right positron detectors, respectively. The error of each bin count n is given by the standard deviation of n . The errors of each bin in $A(t)$ are then calculated by standard error propagation.

Standard, fixed spin-moment³⁴ and non-collinear van der Waals corrected density functional theory simulations were done using the projected augmented wave method as implemented in the VASP program³⁵. We used the PBE exchange-correlation functional³⁶, a 400 eV plane-wave energy cut-off, (0.2 eV, first-order) Methfessel–Paxton electronic smearing³⁷, and a 10-symmetry-irreducible k -point grid for the single crystal 7-vacancy Cu(111) 4×4 reconstruction models. For the Cu{C₆₀} and C₆₀{Cu} 8×8 reconstruction models, only one k point was used. The adopted atomic-force threshold for geometry optimization was 0.02 eV \AA^{-1} . For the 7-vacancy model we relaxed the five topmost Cu layers together with all the atoms of the C₆₀ molecule. All the atoms of the Cu{C₆₀} and C₆₀{Cu} models were relaxed. In all cases, a vacuum separation of at least 12 \AA was present between replicated images of the interface models.

31. Bakule, P. & Morenzoni, E. Generation and applications of slow polarized muons. *Contemp. Phys.* **45**, 203–225 (2004).
32. Prokscha, T. *et al.* The new μ E4 beam at PSI: a hybrid-type large acceptance channel for the generation of a high intensity surface-muon beam. *Nucl. Instrum. Methods* **A595**, 317–331 (2008).
33. Morenzoni, E. *et al.* Generation of very slow polarized positive muons. *Phys. Rev. Lett.* **72**, 2793–2796 (1994).
34. Schwarz, K. & Mohn, P. Itinerant metamagnetism in YCO₂. *J. Phys. F Met. Phys.* **14**, L129–L134 (1984).
35. Kresse, G. & Furthmüller, J. Efficient iterative schemes for *ab initio* total-energy calculations using a plane-wave basis set. *Phys. Rev. B* **54**, 11169–11186 (1996).
36. Perdew, J. P., Burke, K. & Ernzerhof, M. Generalized gradient approximation made simple. *Phys. Rev. Lett.* **77**, 3865–3868 (1996).
37. Methfessel, M. & Paxton, A. T. High-precision sampling for Brillouin-zone integration in metals. *Phys. Rev. B* **40**, 3616–3621 (1989).

A zeolite family with expanding structural complexity and embedded isorecticular structures

Peng Guo^{1,2*}, Jiho Shin^{3*}, Alex G. Greenaway⁴, Jung Gi Min³, Jie Su^{1,2}, Hyun June Choi³, Leifeng Liu^{1,2}, Paul A. Cox⁵, Suk Bong Hong^{3,§}, Paul A. Wright^{4,§} & Xiaodong Zou^{1,2,§}

The prediction and synthesis of new crystal structures enable the targeted preparation of materials with desired properties. Among porous solids, this has been achieved for metal–organic frameworks^{1–3}, but not for the more widely applicable zeolites^{4,5}, where new materials are usually discovered using exploratory synthesis. Although millions of hypothetical zeolite structures have been proposed^{6,7}, not enough is known about their synthesis mechanism to allow any given structure to be prepared. Here we present an approach that combines structure solution with structure prediction, and inspires the targeted synthesis of new super-complex zeolites. We used electron diffraction to identify a family of related structures and to discover the structural ‘coding’ within them. This allowed us to determine the complex, and previously unknown, structure of zeolite ZSM-25 (ref. 8), which has the largest unit-cell volume of all known zeolites (91,554 cubic ångströms) and demonstrates selective CO₂ adsorption. By extending our method, we were able to predict other members of a family of increasingly complex, but structurally related, zeolites and to synthesize two more-complex zeolites in the family, PST-20 and PST-25, with much larger cell volumes (166,988 and 275,178 cubic ångströms, respectively) and similar selective adsorption properties. Members of this family have the same symmetry, but an expanding unit cell, and are related by hitherto unrecognized structural principles; we call these family members embedded isorecticular zeolite structures.

New porous materials with designed structures and properties have been synthesized from metal–organic frameworks (MOFs)¹ by assembling inorganic and organic building units of defined geometry to give frameworks with predictable topology and functionality^{2,3}. This degree of control is difficult to achieve for purely inorganic frameworks^{4,5}. Geometrically related structures have been prepared, for example using enlarged clusters^{9,10} or extended inorganic chains as building units¹¹, but the former requires major changes in framework chemistry and synthesis conditions and the latter uses organic templates that cannot be removed without structural collapse. For the most industrially important class of microporous materials, zeolites, which have fully connected frameworks of corner-sharing AlO₄ and SiO₄ tetrahedra, there are no examples where new structures have been designed and then directly prepared. Millions of energetically feasible hypothetical zeolite ‘structures’ have been predicted^{6,7}, but routes to their synthesis remain elusive.

Even when new zeolites are prepared, through exploratory synthesis, their structure solution takes time because they crystallize as powders. Nevertheless, complex zeolite structures can be solved, usually with help from an electron microscope¹². In one approach, powder X-ray diffraction (PXRD) intensity data are combined with structure factor phase information obtained from high-resolution transmission electron microscopy (HRTEM) images^{13–16}; in another, rotation electron diffraction (RED)^{17,18} is applied to crystals less than a

micrometre in size^{19–21}. Here, we used electron diffraction to solve a complex, unknown zeolite structure related to paulingite; using the ‘strong reflections’ method²², we discovered that this unknown zeolite structure and paulingite have the same structural ‘coding’. We extended this method to predict a family of highly complex zeolite frameworks with unit-cell volumes in excess of any previously reported volumes, and prepared two of them via rational synthesis.

ZSM-25, first reported in 1981⁸, was synthesized according to methods in the literature using Na⁺ and tetraethylammonium (TEA⁺) ions as structure directing agents (SDAs)²³, as part of our search for selective adsorbents (see Methods). It showed good CO₂ adsorption properties (described below), but its structure was not known. We therefore applied the RED method to ZSM-25 (NaTEA-ZSM-25) microcrystals (Fig. 1a, b, Methods, Extended Data Fig. 2a–c). The three-dimensional (3D) RED data revealed that ZSM-25 is body-centred cubic (unit-cell edge length $a = 42.3$ Å) with Laue symmetry $m\bar{3}m$. However, electron beam damage causes low data resolution and prevents structure solution using direct methods. The IZA Database of Zeolite Structures²⁴ lists three frameworks with the same Laue symmetry as ZSM-25: KFI (ZK-5), RHO (Rho) and PAU (paulingite) all have the same space group $Im\bar{3}m$. Further, we found that the strong reflections of ZSM-25 are distributed in the same regions of reciprocal space as those calculated for RHO and PAU (Fig. 1a–d, Extended Data Fig. 3), indicating the RHO, PAU and ZSM-25 structures are related. Strong reflections represent the main structural features of a crystal and can be used for structure solution²⁵. We therefore thought that it might be possible to phase the strong reflections of ZSM-25 from the known PAU structure, and thus solve its structure. The 21 strongest symmetry-independent reflections were identified, and their phases assigned to be those calculated from corresponding reflections of the PAU structure (Fig. 1c, d, Extended Data Table 1). All 16 symmetry-independent T atoms (T = Si, Al) were located from the 3D electron-density map using the 21 reflections: oxygen atoms were placed between the T atoms according to TO₄ tetrahedral geometry. The structure of as-made NaTEA-ZSM-25, including its aluminosilicate framework and extra-framework cation and water positions, was refined against synchrotron PXRD data (Fig. 2a, Methods).

The ZSM-25 framework can be considered an expanded version of PAU. Both are built of seven different cage types²⁴; these have the face symbols and three-letter codes $[4^{12}6^88^6]$ (*lta*), $[4^88^2]$ (*d8r*), $[4^{12}8^6]$ (*pau*), $[4^66^28^6]$ (*t-plg*), $[4^38^3]$ (*t-oto*), $[4^68^4]$ (*t-gsm*) and $[4^78^5]$ (*t-phi*); Fig. 2b. Face symbols give the number of faces per cage with the specified number of sides: for example, $[4^88^2]$ denotes cages with eight four-sided faces and two octagonal faces. The maximum ring size in each is eight, which establishes them as small-pore zeolites. The *lta* cages are connected via chains of alternating *d8r* and *pau* cages along unit-cell edges to form cubic scaffolds (Fig. 2c, d). The scaffold of

¹Inorganic and Structural Chemistry, Department of Materials and Environmental Chemistry, Stockholm University, SE-106 91 Stockholm, Sweden. ²Berzelii Centre EXSELENT on Porous Materials, Stockholm University, SE-106 91 Stockholm, Sweden. ³Centre for Ordered Nanoporous Materials Synthesis, School of Environmental Science and Engineering, POSTECH, Pohang 790-784, South Korea.

⁴EaStCHEM School of Chemistry, University of St Andrews, St Andrews KY16 9ST, UK. ⁵School of Pharmacy and Biomedical Sciences, University of Portsmouth, Portsmouth PO1 2DT, UK.

*These authors contributed equally to this work.

§These authors jointly supervised this work.

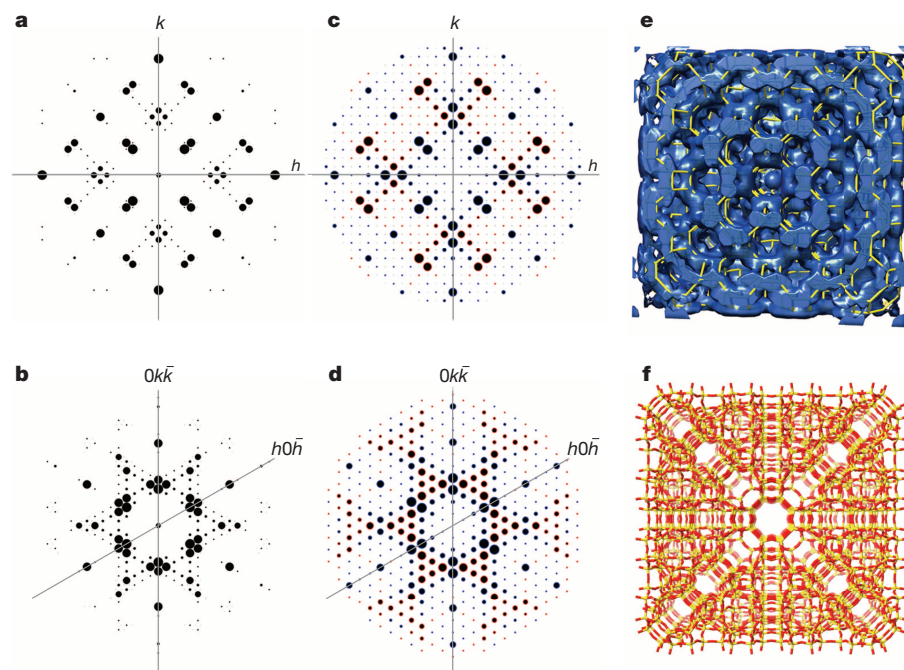


Figure 1 | Structure determination of ZSM-25 using the strong reflections approach. **a, b,** The 2D slice of $(hk0)$ (**a**) and $(hkh+k)$ (**b**) cut from the reconstructed 3D reciprocal lattice from the RED data. The symmetry $m\bar{3}m$ has been superimposed to allow for a better comparison. **c, d,** Simulated $(hk0)$ (**c**) and $(hkh+k)$ (**d**) diffraction patterns of the idealized PAU structure, with the structure factor phases marked in blue (180°) and red (0°). **e,** 3D map generated by using amplitudes obtained from RED of ZSM-25 and phases calculated from the structure of PAU. **f,** The framework structure of ZSM-25.

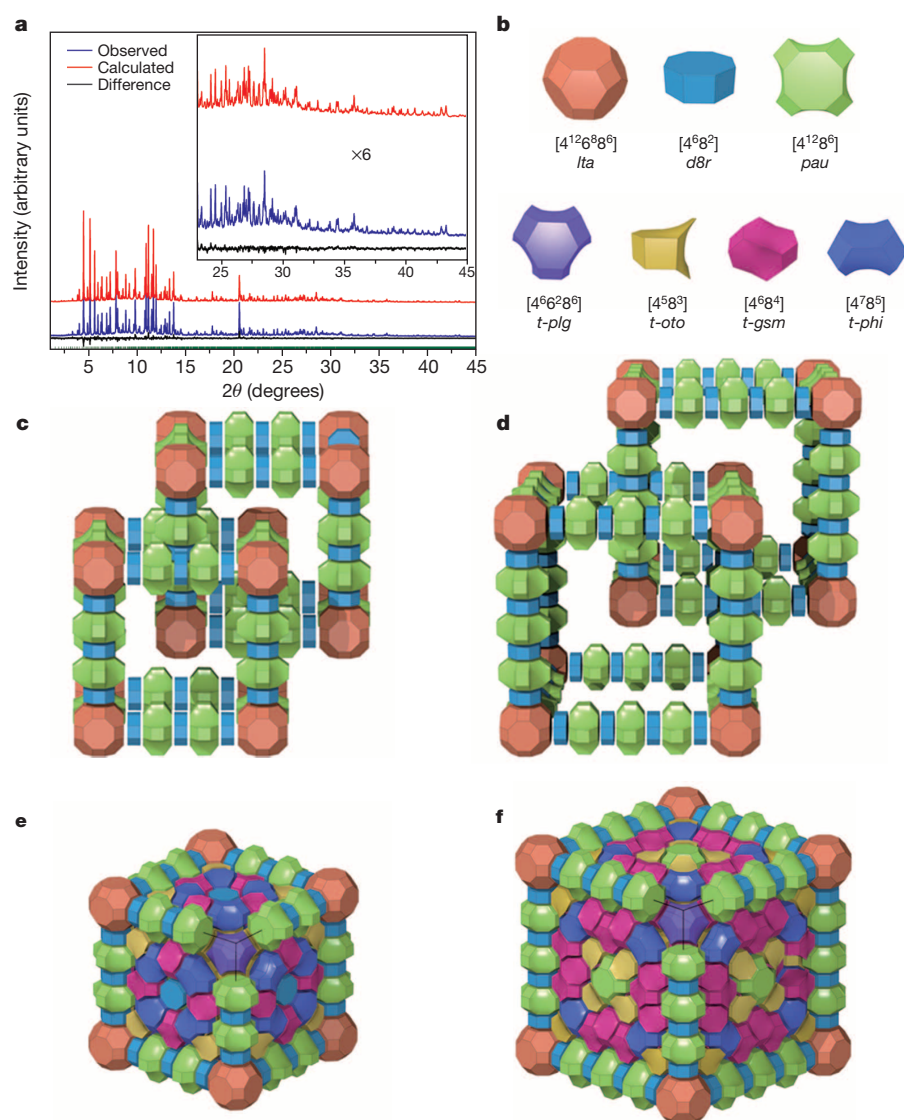


Figure 2 | PXRD profiles and description of the structure of ZSM-25. **a,** Rietveld refinement of as-made NaTEA-ZSM-25 (X-ray wavelength $\lambda = 0.63248 \text{ \AA}$). The inset intensities are scaled by a factor of six. **b,** The seven different cages, $[4^{12}6^88^6]$ (*lta*), $[4^88^2]$ (*d8r*), $[4^{12}8^6]$ (*pau*), $[4^66^28^6]$ (*t-plg*), $[4^58^3]$ (*t-oto*), $[4^68^4]$ (*t-gsm*) and $[4^78^5]$ (*t-phi*), found in ZSM-25, as solid tiles. **c, d,** The connectivity of the *lta*, *d8r* and *pau* cages in PAU (**c**) and ZSM-25 (**d**), showing the interpenetration of the two cubic scaffolds. The sequence is *lta*–*d8r*–*pau*–*d8r*–*pau*–*d8r*–*lta* for PAU and *lta*–*d8r*–*pau*–*d8r*–*pau*–*d8r*–*pau*–*d8r*–*lta* for ZSM-25. **e, f,** The 3D framework structure of PAU (**e**) and ZSM-25 (**f**) with *t-plg*, *t-oto*, *t-gsm* and *t-phi* cages embedded in the scaffolds.

ZSM-25 is extended from that of **PAU** by adding an extra pair of *pau* and *d8r* cages along each unit-cell edge, which expands *a* by approximately 10 Å. In accordance with the body-centred structure, each structure contains two such cubic scaffolds, interpenetrated. The space between the scaffolds is filled by the four other types of cages to form fully four-connected frameworks (Fig. 2e, f). All cages are interconnected via 8-ring windows. The structure of **RHO** can be obtained by removing two pairs of *pau* and *d8r* cages from each unit-cell edge, leaving only one *d8r* cage between the *lta* cages (Extended Data Fig. 6). **RHO**, **PAU** and ZSM-25 belong to the same family. **PAU** and ZSM-25 can be considered expanded versions of **RHO**. We call this the RHO family, and denote Rho to be the first generation (RHO-G1), paulinite the third (RHO-G3) and ZSM-25 the fourth (RHO-G4). It is interesting to predict the structure of other family members. While the structure of RHO-G2 with two *d8r* and one *pau* cages per unit-cell edge (*a* ≈ 25 Å) was generated previously^{26,27}, it is much more challenging to predict larger structures by modelling how the large space between the cubic scaffolds should be filled.

We anticipated that the structure relationship (structural ‘coding’) of the higher members of the RHO family would also be reflected in reciprocal space, and that this could be exploited for structure prediction. We found that the structure factors of the strong reflections for ZSM-25 and **PAU** are indeed very similar (Fig. 3a, Extended Data

Fig. 3). The framework of ZSM-25 could be predicted solely from the related **PAU** framework, without using any experimental diffraction data from ZSM-25 (Methods). We applied the same approach to predict the structures of other members: RHO-G2 from **PAU** (RHO-G3), RHO-G5 from ZSM-25 (RHO-G4) and RHO-G6 from RHO-G5 (Fig. 3b, c, Methods, Extended Data Fig. 5). The final energies per SiO₂ unit as a function of framework density for RHO-G1 to RHO-G6 are consistent with the trends observed for known structures (Supplementary Fig. 2, Supplementary Table 12), indicating that they are all energetically feasible. In principle, the number of members in the RHO family is limitless. New zeolites with ever-greater unit-cell volume and complexity are achieved by adding new pairs of *d8r* and *pau* cages, and their structures can be predicted using a similar approach.

Except for RHO-G1 and RHO-G2, all other members consist of the same seven cages (Fig. 3c, Extended Data Fig. 6, Supplementary Tables 13, 14) and every T atom is part of three 4-rings. We think that these common motifs arise as a consequence of a dominating aluminosilicate crystallization pathway. That both ECR-18 (**PAU**) and ZSM-25 were synthesized using TEA⁺ and Na⁺ as SDAs, together with K⁺ in the case of ECR-18, led us to speculate that the larger members (for example, RHO-G5 and RHO-G6) of this family could also be synthesized using these SDAs, in concert with other inorganic cations.

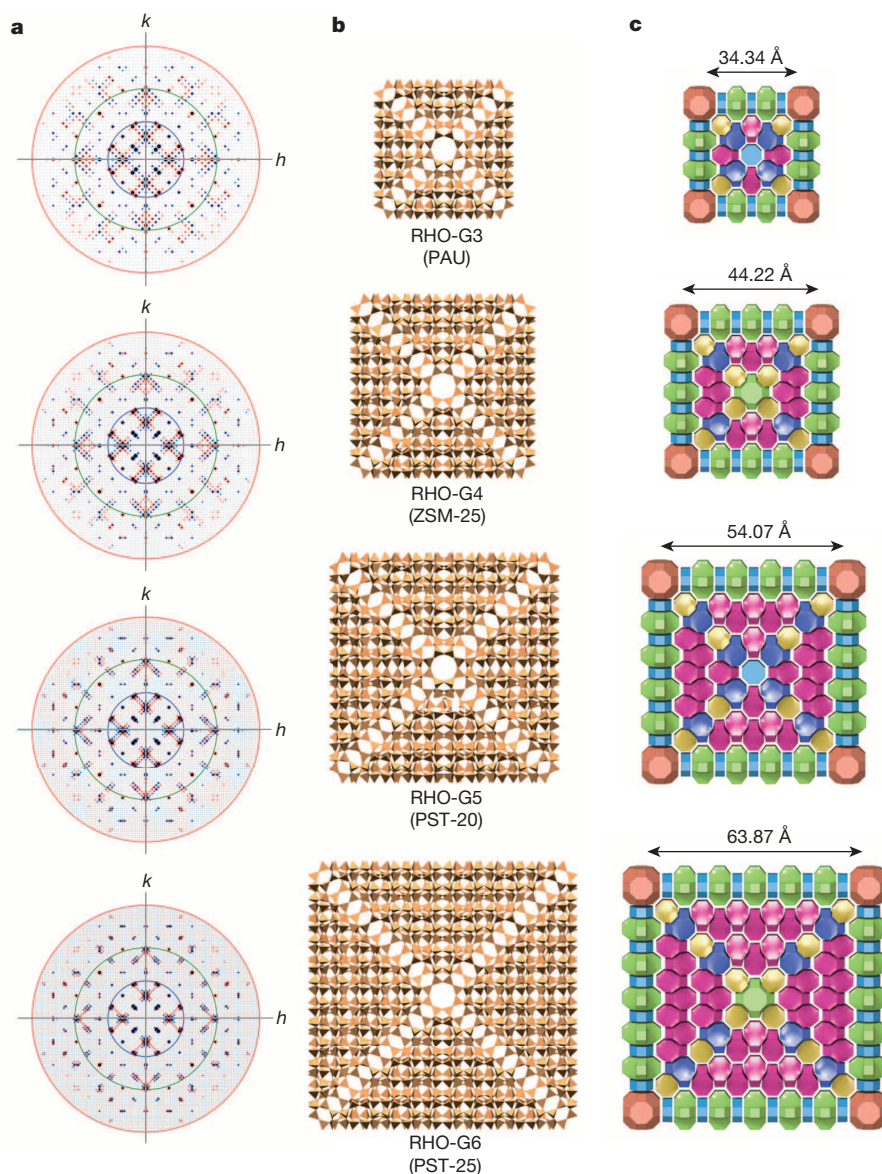


Figure 3 | Comparison of the reflection distributions and framework structures of RHO-G3 to RHO-G6. **a**, The (*hk*0) reciprocal plane showing the similar amplitude and phase distribution of the strong reflections of RHO-G3 to RHO-G6. Reflections in red have phases of 0°, while those in blue have phases of 180°. The red, green and blue circles correspond to *d*-spacings of 1.0 Å, 1.6 Å and 3.0 Å, respectively. **b**, **c**, Polyhedral (**b**) and tiling (**c**) representations of cross-sections (about 12 Å thick) of RHO-G3 to RHO-G6. The crystals corresponding to RHO-G3 to RHO-G6 were synthesized as ECR-18, ZSM-25, PST-20 and PST-25, respectively. The arrangement in the centre alternates every second structure in (**c**), that is, it is similar for RHO-G3 and RHO-G5, and RHO-G4 and RHO-G6.

Examination of the evolution of the numbers of different cages in the RHO family showed that the numbers of *t-oto*, *t-gsm* and *t-phi* cages grow much faster than those of the other four cage types (Supplementary Table 13). Furthermore, we were aware that the natural zeolites gismondine (GIS) and phillipsite (PHI), which contain *t-gsm* cages only (GIS) and *t-oto* and *t-phi* cages (PHI) as building units, possess substantial amounts of alkaline-earth cations such as Ca^{2+} and even Ba^{2+} as extra-framework cations²⁴. This prompted us to introduce small amounts of different alkaline-earth cations to the ZSM-25 synthesis mixture to promote the preferential formation of *t-oto*, *t-gsm* and *t-phi* cages and thus to favour crystallization of the more-complex members of the RHO family.

Following the strategy described above, we were able to synthesize the hypothetical RHO-G5 phase, denoted PST-20 (Methods, Extended Data Fig. 1b, Supplementary Tables 1, 2). Its successful synthesis was confirmed by RED (Extended Data Fig. 2d–f) and Rietveld refinement (Extended Data Fig. 4). Although the crystallization of PST-20 was sensitive to synthesis temperature and time, the presence of the alkaline-earth cations Ca^{2+} and, in particular, Sr^{2+} is required to direct its crystallization. A pure sample of PST-20 was successfully prepared by addition of Sr^{2+} to the synthesis gel. Subsequent structural analysis revealed that the Sr^{2+} cations are located mainly within the 8-rings of its *t-oto*, *t-gsm* and *t-phi* cages (Supplementary Fig. 6), validating our approach. Following the same rational approach, modification of the synthesis conditions by the addition of both Sr^{2+} and Ca^{2+} to the gel composition that gives ZSM-25 resulted, after hydrothermal treatment, in products that contained crystals of RHO-G6, the next, even more complex zeolite in the RHO family (Supplementary Fig. 9, Supplementary Table 3). Further work is in progress to obtain the pure form of this material, which we denote PST-25.

As with all members of this family, ZSM-25 and PST-20 (and PST-25) are accessible to molecules that can pass through 8-rings, and so they are potentially useful as small-molecule adsorbents. Removal of CO_2 from natural gas or from flue gases²⁸ is one area of current interest for small-pore zeolites. We found that NaTEA-ZSM-25 and Na^+ -exchanged NaSrTEA-PST-20 (denoted NaTEA-PST-20) show similarly high uptakes of CO_2 and low uptakes of N_2 and CH_4 (Fig. 4, Methods, Extended Data Table 2). The CO_2/CH_4 selectivity for all members of the RHO family is high, and much greater than that exhibited by the K-chabazite that we examined (Extended Data Table 2). We attribute this to the effect of cation gating, where cations blocking 8-ring windows in the structures are able to move to allow the passage of gas molecules that strongly interact with them, such as CO_2 , but remain in place in the presence of weakly interacting molecules^{29,30}. Moreover, the CO_2 uptakes remained the same over 100 adsorption–desorption cycles (insets of Fig. 4a, b). The CO_2 uptake at 1.0 bar and 298 K was 3.5 mmol g^{-1} for NaTEA-ZSM-25 and 3.2 mmol g^{-1} for NaTEA-PST-20. These CO_2 uptakes are somewhat lower than that of Na-Rho (4.5 mmol g^{-1} at 1.0 bar and 298 K), but they are comparable with those observed for other well studied small-pore zeolites such as K-chabazite (CHA, 3.6 mmol g^{-1}). More notably, although CO_2 adsorption on Na-Rho reached equilibrium only after about 2 h, uptake on NaTEA-ECR-18 was faster (equilibrating in 5 min), and NaTEA-ZSM-25 and NaTEA-PST-20 achieved equilibrium more quickly still (after about 2 min) (Fig. 4c). Given their selective adsorption, fast kinetics and long-term stability, NaTEA-ZSM-25 and NaTEA-PST-20 are of potential interest as CO_2 adsorbents.

Structure expansion in the RHO family operates at two levels (Fig. 3c, Extended Data Fig. 6, Supplementary Figs 4c, 5c). First, the twofold interpenetrated scaffold is expanded by inserting *pau* and *d8r* cages along each unit-cell edge. Second, the space between the scaffolds is filled by four other cage types to form rigid, fully four-connected frameworks. The former expansion is isorecticular, as seen in MOFs^{1–3}, whereas the latter filling occurs by embedding four different cages in the inter-scaffold space. We call frameworks resulting from this principle of structure expansion ‘embedded isorecticular’; the RHO family is

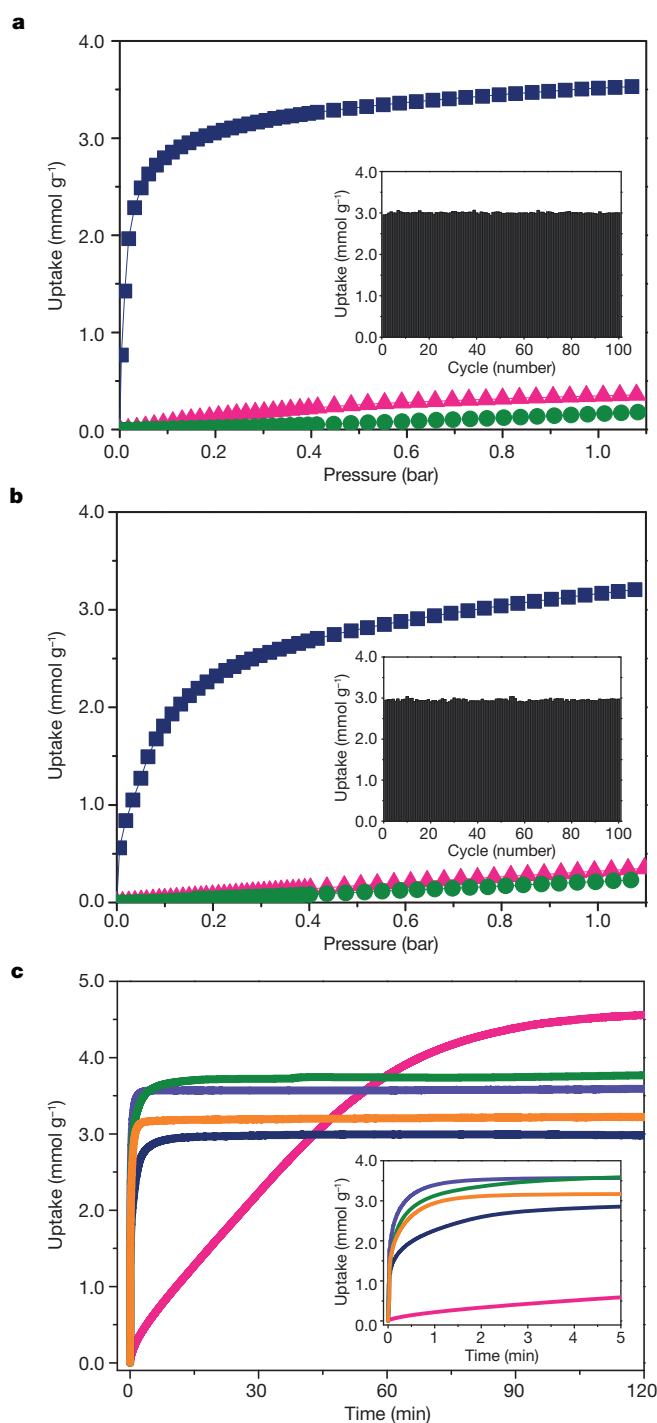


Figure 4 | Gas adsorption properties of NaTEA-ZSM-25 and NaTEA-PST-20. **a, b**, Adsorption isotherms at 298 K of CO_2 (navy), CH_4 (green) and N_2 (pink) for NaTEA-ZSM-25 (**a**) and NaTEA-PST-20 (**b**). Inset, CO_2 adsorption–desorption cycles at 343 K. **c**, CO_2 adsorption kinetics at 298 K and 1.2 bar of NaTEA-ZSM-25 (violet), NaTEA-PST-20 (orange), NaTEA-ECR-18 (navy), Na-Rho (pink) and K-chabazite (green). Inset, zoom of the CO_2 adsorption kinetics for the first 5 min.

the first example. Although other families of expanded structures have the same topology and enlarged pore sizes^{2,3,11} (Supplementary Fig. 4a, b), the RHO-family members have different topologies but similar pore sizes (Supplementary Fig. 5b, c, Supplementary Tables 10, 11). The structural relationships among the RHO-family members become clear in reciprocal space, through the similar amplitude and phase distribution of reflections. This structural ‘coding’ is useful both

for structure solution and for prediction of new family members. It has enabled the syntheses of new zeolites with huge unit cells from chemically relatively simple systems—ZSM-25, PST-20 and PST-25 are the largest zeolites so far by unit-cell volume—and it suggests a route to the rational synthesis of certain classes of zeolites.

Online Content Methods, along with any additional Extended Data display items and Source Data, are available in the online version of the paper; references unique to these sections appear only in the online paper.

Received 20 January; accepted 8 May 2015.

Published online 15 July 2015.

- Yaghi, O. M. *et al.* Reticular synthesis and the design of new materials. *Nature* **423**, 705–714 (2003).
- Eddaoudi, M. *et al.* Systematic design of pore size and functionality in isorecticular MOFs and their application in methane storage. *Science* **295**, 469–472 (2002).
- Deng, H. *et al.* Large-pore apertures in a series of metal-organic frameworks. *Science* **336**, 1018–1023 (2012).
- Davis, M. E. Ordered porous materials for emerging applications. *Nature* **417**, 813–821 (2002).
- Wang, Z., Yu, J. & Xu, R. Needs and trends in rational synthesis of zeolitic materials. *Chem. Soc. Rev.* **41**, 1729–1741 (2012).
- Foster, M. D. & Treacy, M. M. J., *Atlas of Prospective Zeolite Structures* <http://www.hypotheticalzeolites.net/> (2010).
- Deem, M. W. *Deem Database* <http://www.hypotheticalzeolites.net/DATABASE/DEEM/index.php> (2011).
- Doherty, H. G., Plank, C. J. & Rosinski, E. J. Crystalline zeolite ZSM-25. US patent 4,247 416 (1981).
- Férey, G. Building units design and scale chemistry. *J. Solid State Chem.* **152**, 37–48 (2000).
- Zou, X. D., Conradsson, T., Klingstedt, M., Dadachov, M. S. & O’Keeffe, M. A mesoporous germanium oxide with crystalline pore walls and its chiral derivative. *Nature* **437**, 716–719 (2005).
- Lin, H.-Y. *et al.* Crystalline inorganic frameworks with 56-ring, 64-ring, and 72-ring channels. *Science* **339**, 811–813 (2013).
- Willhammar, T., Yun, Y. F. & Zou, X. D. Structure determination: structural determination of ordered porous solids by electron crystallography. *Adv. Funct. Mater.* **24**, 182–199 (2014).
- Zou, X. D., Hovmöller, S. & Oleynikov, P. *Electron Crystallography: Electron Microscopy and Electron Diffraction* Ch. 9 (Oxford Univ. Press, 2011).
- Gramm, F. *et al.* Complex zeolite structure solved by combining powder diffraction and electron microscopy. *Nature* **444**, 79–81 (2006).
- Baerlocher, C. *et al.* Structure of the polycrystalline zeolite catalyst IM-5 solved by enhanced charge flipping. *Science* **315**, 1113–1116 (2007).
- Baerlocher, C. *et al.* Ordered silicon vacancies in the framework structure of the zeolite catalyst SSZ-74. *Nature Mater.* **7**, 631–635 (2008).
- Zhang, D. L., Oleynikov, P., Hovmöller, S. & Zou, X. D. Collecting 3D electron diffraction data by the rotation method. *Z. Kristallogr.* **225**, 94–102 (2010).
- Wan, W., Sun, J. L., Su, J., Hovmöller, S. & Zou, X. D. Three-dimensional rotation electron diffraction: software RED for automated data collection and data processing. *J. Appl. Crystallogr.* **46**, 1863–1873 (2013).
- Willhammar, T. *et al.* Structure and catalytic properties of the most complex intergrown zeolite ITQ-39 determined by electron crystallography. *Nature Chem.* **4**, 188–194 (2012).
- Martínez-Franco, R. *et al.* Synthesis of an extra-large molecular sieve using proton sponges as organic structure-directing agents. *Proc. Natl Acad. Sci. USA* **110**, 3749–3754 (2013).
- Hua, W. *et al.* A germanosilicate structure with $11 \times 11 \times 12$ -ring channels solved by electron crystallography. *Angew. Chem. Int. Edn* **53**, 5868–5871 (2014).
- Zhang, H., Zou, X. D., Oleynikov, P. & Hovmöller, S. Structure relations in real and reciprocal space of hexagonal phases related to i-ZnMgRE quasicrystals. *Phil. Mag.* **86**, 543–548 (2006).
- Hong, S. B. *et al.* Synthesis and characterization of zeolite ZSM-25. *Stud. Surf. Sci. Catal.* **135**, 186 (2001).
- Baerlocher, Ch. & McCusker, L. B. *Database of Zeolite Structures* <http://www.iza-structure.org/databases/> (2007).
- Karle, J. & Karle, I. L. The symbolic addition procedure for phase determination for centrosymmetric and non-centrosymmetric crystals. *Acta Crystallogr.* **21**, 849–859 (1966).
- Vaughan, D. E. W. & Strohmaier, K. G. Synthesis of ECR-18—a synthetic analog of paulingite. *Micropor. Mesopor. Mat.* **28**, 233–239 (1999).
- Blatov, V. A., Ilyushin, G. D., Lapshin, A. E. & Golubeva, O. Yu. Structure and chemical composition of the new zeolite ISC-1 from the data of nanocluster modeling. *Glass Phys. Chem.* **36**, 663–672 (2010).
- Rochelle, G. T. Amine scrubbing for CO₂ capture. *Science* **325**, 1652–1654 (2009).
- Shang, J. *et al.* Discriminative separation of gases by a “molecular trapdoor” mechanism in chabazite zeolites. *J. Am. Chem. Soc.* **134**, 19246–19253 (2012).
- Lozinska, M. M. *et al.* Cation gating and relocation during the highly selective “trapdoor” adsorption of CO₂ on univalent cation forms of zeolite Rho. *Chem. Mater.* **26**, 2052–2061 (2014).

Supplementary Information is available in the online version of the paper.

Acknowledgements We acknowledge financial support from the Swedish Research Council (VR), the Swedish Governmental Agency for Innovation Systems (VINNOVA), the Röntgen-Ångström Cluster through the project grant MATsynCELL, the Knut and Alice Wallenberg Foundation through the project grant 3DEM-NATUR, the NCRI (2012R1A3A-2048833) and BK 21-plus programmes through the National Research Foundation of Korea, and the UK EPSRC (EP/J02077X/1). We acknowledge the ESRF, Grenoble (ID31, A. N. Fitch; ID22, C. Drathen) and the PAL, Pohang (9B, D. Ahn) for synchrotron X-ray beam time. We thank L. B. McCusker and C. Baerlocher for suggestions about the Rietveld refinement. The TEM was financed by the Knut and Alice Wallenberg Foundation.

Author Contributions S.B.H. and P.A.W. identified and initiated the research project, which was developed and brought to a conclusion jointly by S.B.H., P.A.W. and X.Z. J.Sh., J.G.M., H.J.C. and S.B.H. carried out the zeolite synthesis and gas sorption work. P.G. conducted the TEM work. P.G., L.L. and X.Z. carried out the structure solution and structure prediction work. P.G., A.G.G., J.Su, P.A.W. and X.Z. made the Rietveld refinements. P.A.C. did the molecular modelling and energy calculations. P.G., J.Sh., S.B.H., P.A.W. and X.Z. wrote and corrected the manuscript.

Author Information The Crystallography Information Files (CIFs) are deposited at the Cambridge Crystallographic Data Centre (CCDC, <http://www.ccdc.cam.ac.uk>) with CCDC numbers: 1031577 for as-made NaTEA-ZSM-25, 1057085 for calcined NaTEA-ZSM-25, 1057832 for as-made NaSrTEA-PST-20 and 1039878 for Na⁺-exchanged NaSrTEA-PST-20. Reprints and permissions information is available at www.nature.com/reprints. The authors declare no competing financial interests. Readers are welcome to comment on the online version of the paper. Correspondence and requests for materials should be addressed to S.B.H. (sbhong@postech.ac.kr), P.A.W. (paw2@st-andrews.ac.uk) or X.Z. (xzou@mmk.su.se).

METHODS

Zeolite syntheses. ZSM-25 was synthesized from aluminosilicate gels with a very narrow range of $\text{SiO}_2/\text{Al}_2\text{O}_3$ and $\text{Na}_2\text{O}/\text{SiO}_2$ ratios in the presence of TEABr, as reported by several groups^{8,23,31}. In a typical synthesis of ZSM-25, 1.92 g of $\text{Al}(\text{OH})_3 \cdot 1.0\text{H}_2\text{O}$ were first mixed with a solution of 3.04 g of NaOH solution (50%, Aldrich) in 60.73 g of distilled water. To the resulting clear solution, 10.80 g of Ludox AS-40 (DuPont) and 11.15 g of TEABr (98%, Aldrich) were added. The resulting gel composition was $1.9\text{Na}_2\text{O} \cdot 1.0\text{Al}_2\text{O}_3 \cdot 5.2\text{TEABr} \cdot 7.2\text{SiO}_2 \cdot 390\text{H}_2\text{O}$. The final synthesis mixture was stirred at room temperature for one day, charged into Teflon-lined 23-ml autoclaves and heated at 408 K under rotation (60 r.p.m.) for 7 days.

PST-20 was synthesized using the organic SDA, TEA⁺, together with two inorganic SDAs, Na⁺ and Sr²⁺ cations. In a typical synthesis of PST-20, 1.92 g of $\text{Al}(\text{OH})_3 \cdot 1.0\text{H}_2\text{O}$ were first mixed with a solution of 3.04 g of 50% NaOH solution in 60.73 g of distilled water. To the resulting clear solution, 10.80 g of Ludox AS-40, 1.07 g of $\text{Sr}(\text{NO}_3)_2$ (Aldrich) and 11.15 g of TEABr were added. The resulting gel composition was $1.9\text{Na}_2\text{O} \cdot 0.5\text{SrO} \cdot 1.0\text{Al}_2\text{O}_3 \cdot 5.2\text{TEABr} \cdot 7.2\text{SiO}_2 \cdot 390\text{H}_2\text{O}$. If required, seed crystals (2 wt% of anhydrous raw materials) were added to this gel. The seed crystals used here were PST-20 zeolite containing a small amount of ZSM-25 (<20%, according to PXRD analysis), which was previously prepared at 418 K for 4 days. The final synthesis mixture was stirred at room temperature for one day, charged into Teflon-lined 23-ml autoclaves, and heated at 418 K under rotation (60 r.p.m.) for 2 days. Further details of PST-20 synthesis are given in Supplementary Tables 1 and 2.

The solid products were recovered by filtration, washed repeatedly with water, and then dried overnight at room temperature. As-made ZSM-25 and PST-20 samples were characterized by PXRD, and ²⁷Al and ²⁹Si solid-state magic-angle spinning NMR (Extended Data Fig. 1). The samples were calcined at 773 K in air for 8 h. PXRD patterns show that ZSM-25 retained its crystallinity but PST-20 lost crystallinity upon calcination. As-made PST-20 (NaSrTEA-PST-20) was refluxed twice in 1.0 M NaNO₃ solution at 353 K for 6 h (2.0 g solid per 100 ml solution) to ensure that it was in its Na⁺-TEA⁺ form (denoted NaTEA-PST-20). For comparison, ECR-18 (PAU), zeolite Rho (RHO), and chabazite (CHA) with similar Si/Al ratios were also synthesized according to the procedures reported in the literature^{26,32,33} and converted to their Na⁺ or K⁺ forms.

Collection of rotation electron diffraction (RED) data. For RED data collection, powders of as-made NaTEA-ZSM-25 and NaSrTEA-PST-20 samples were dispersed in absolute ethanol and treated by ultrasonic treatment for 2 min. A droplet of the suspension was transferred onto a carbon-coated copper grid and dried in air. The 3D RED data were collected on a JEOL JEM2100 TEM at 200 kV using the RED-data collection software¹⁸. A single-tilt tomography sample holder was used for the data collection. The electron diffraction frames were recorded on a 12-bit Gatan ES500W Erlangshen camera side-mounted at a 35 mm port. For NaTEA-ZSM-25, the tilt step was 0.10° and the exposure time was 3.0 s per electron diffraction frame. The tilt range was 76.71° and the total data collection time was about 70 min. Because NaSrTEA-PST-20 was more electron-beam sensitive than NaTEA-ZSM-25, a shorter data collection time (17 min) was used, with a larger tilt step (0.20°), a shorter exposure time (1.0 s per electron diffraction frame) and a tilt range of 49.98° (Supplementary Table 4).

The data processing was performed using the software RED-data processing¹⁸. The unit cell was determined from the positions of the diffraction spots detected in the electron diffraction frames. The RED data show that both NaTEA-ZSM-25 and NaSrTEA-PST-20 are body-centred cubic with the Laue symmetry of *m*3̄m (Extended Data Fig. 2). The unit-cell parameter determined from the RED data was *a* = 42.3 Å for NaTEA-ZSM-25 and *a* = 52.4 Å for NaSrTEA-PST-20 (Supplementary Table 4). The reflection conditions were deduced from the reconstructed reciprocal lattice to be *hkl*: *h* + *k* + *l* = 2*n*, *hk0*: *h* + *k* = 2*n*, *hkh*: *k* = 2*n*, *00l*: *l* = 2*n*. From the Laue symmetry and reflection conditions, the possible space groups are *I*432 (No. 211), *I*43̄m (No. 217), and *Im*3̄m (No. 229). The intensity for each reflection was extracted from the electron diffraction frame with the highest intensity value. The final list of reflections with the indices and intensity was output to an HKL file for SHELX³⁴.

Structure determination of ZSM-25. Three zeolite frameworks were identified that have the same Laue group as ZSM-25: ZK-5 (KFI, *a* = 18.75 Å), zeolite Rho (RHO, *a* = 15.03 Å) and paullingite³⁵ (PAU, *a* = 35.09 Å). The crystallographic structure factors were calculated from the atomic coordinates of the idealized framework given in the Database of Zeolite Structures²⁴. It was found that the strong reflections of ZSM-25 are distributed in the same locations in reciprocal space as those calculated from PAU (Fig. 2a–d). Twenty-one symmetry-independent reflections up to 2.5 Å resolution with amplitudes larger than 30% of the strongest reflection were identified from the RED data, and their phases were assigned to be those of structure factor phases calculated from corresponding reflections of the PAU structure (Fig. 2c, d, Extended Data Table 1). The

indices of the required corresponding reflections in the PAU structure were obtained by scaling according to the unit cells: $h_{\text{PAU}} = h_{\text{ZSM-25}} \times a_{\text{PAU}}/a_{\text{ZSM-25}}$, $k_{\text{PAU}} = k_{\text{ZSM-25}} \times a_{\text{PAU}}/a_{\text{ZSM-25}}$, $l_{\text{PAU}} = l_{\text{ZSM-25}} \times a_{\text{PAU}}/a_{\text{ZSM-25}}$ (Extended Data Table 1). The 3D electron-density map was calculated by inverse Fourier transformation from the amplitudes and phases of these strong reflections using the SUPERFLIP software (Fig. 2e)³⁶. All 16 symmetry-independent T atoms (T = Si, Al) were located from the 3D electron-density map using the software EDMA³⁷. The oxygen atoms were placed between the T atoms according to SiO₄ tetrahedral geometry. The final model is a four-connected 3D framework (Fig. 2f), which was geometrically optimized using TOPAS Academic 4.1³⁸. Every T atom is part of three 4-rings (in two different chains of 4-rings), accounting for the characteristic infrared and Raman spectra that have been reported previously for ZSM-25²³.

Rietveld refinement (ZSM-25 and PST-20) and profile fitting (PST-25). High-resolution PXRD data of as-made NaTEA-ZSM-25 were collected at room temperature at experimental station ID31 at the ESRF, Grenoble (X-ray wavelength λ = 0.632480 Å). PXRD data of calcined NaTEA-ZSM-25 (Extended Data Fig. 1a) was obtained in flat plate mode using a PANalytical X'Pert PRO diffractometer (λ = 1.5418 Å). High-resolution PXRD data of as-made and Na⁺-exchanged NaSrTEA-PST-20 were collected at 100 K at experimental station ID22 at the ESRF, Grenoble (λ = 0.40091 Å). The samples were sealed in glass capillaries of 0.7 mm diameter. Rietveld refinement was performed using TOPAS Academic V4.1³⁸. High-resolution PXRD data of a sample with a mixture of PST-25 and PST-20 (Run 18, Supplementary Table 3) were collected in flat-plate mode on the 9B beamline at the Pohang Acceleration Laboratory, South Korea (λ = 1.4640 Å). Profile fitting was performed in the 2 θ range of 10°–70° by the LeBail method³⁹ using the GSAS suite of programs⁴⁰.

For NaTEA-ZSM-25, the background was fitted with a 16th-order Chebyshev polynomial. The refinement was conducted using a Pearson VII peak profile function, followed by refinement of unit cell (*a* = 45.0711(3) Å) and zero-shift. The chemical formula was deduced from EDPS, TGA and CHN analyses to be $[(\text{N}(\text{C}_2\text{H}_5)_4)_{40}\text{Na}_{285}(\text{H}_2\text{O})_{600}][\text{Si}_{1115}\text{Al}_{325}\text{O}_{2880}]$. The organic TEA⁺ cations were suggested by molecular modelling to be located in the *pau* and *t-plg* cages (Supplementary Fig. 1 and Supplementary Table 5), and Na⁺ and water molecule positions were arrived at by comparison with the structure of as-made paullingite³⁵ and by difference Fourier analysis. Considering the ratio of Si/Al = 3.4, soft restraints were placed on the T–O distances (1.64 Å, T = Si, Al) and O···O distances (2.68 Å) within the TO₄ tetrahedra. All T positions were refined with the same, and fixed, occupancies. Additional Na⁺ cations and guest water molecules were located from the difference Fourier maps by fixing the framework of ZSM-25. All atomic positions were refined in the final cycles. The Debye–Waller factors of T, O, C and N atoms were fixed to 0.8, 1, 10 and 10, respectively, while those of Na⁺ and water molecules were refined. The final refinement converged to a weighted-profile-fit *R* factor *R*_{wp} = 0.0537, a profile-fit *R* factor *R*_p = 0.0414 and goodness of fit GOF = 2.87 (Fig. 3a, Supplementary Table 6).

There are 16 symmetry-independent T-atom positions, 40 oxygen-atom positions, four TEA⁺ locations, 13 Na⁺-cation positions and 24 water-molecule locations in NaTEA-ZSM-25. Most Na⁺ cations are located in the 8-rings of the *t-oto*, *d8r* and *t-gsm* cages; some of them are partially occupied and sometimes share the same positions with guest water molecules. A Na⁺ cation (Na12, occupancy of 0.51) is found at the 6-ring connecting the *lta* and *t-plg* cages. There are about 296 Na⁺ cations in one unit cell, which is consistent with the chemical analysis. The TEA⁺ cations are disordered in the *pau* and *t-plg* cages. The final refinement shows that there is one TEA⁺ in each *pau* cage, and 0.85 and 0.80 TEA⁺ in *t-plg* cages (there are two symmetry-independent *t-plg* cages). The *t-plg* cages contain both TEA⁺ cations and guest water molecules, with a total occupancy of 1.0. The final framework structure has reasonable T–O bond distances (1.64 ± 0.02 Å), O–T–O angles (109.3 ± 4.5°) and T–O–T angles (132–159°).

Rietveld refinement of the calcined, hydrated ZSM-25 was carried out in a similar way to that of NaTEA-ZSM-25, with the obvious difference that no TEA⁺ cations remain in the solid (*a* = 44.9242(16) Å, Supplementary Fig. 7 and Supplementary Table 7).

For as-made NaSrTEA-PST-20, the unit-cell formula derived by elemental analysis and structure refinement was $[(\text{N}(\text{C}_2\text{H}_5)_4)_{56}\text{Na}_{162}\text{Sr}_{210}(\text{H}_2\text{O})_{563}][\text{Al}_{638}\text{Si}_{2002}\text{O}_{5280}]$. The starting structure was based on the model of RHO-G5 established during the prediction of larger structures of the RHO family. The background was fitted with a 30th-order Chebyshev polynomial. The refinement was conducted using a TCHZ peak profile function, followed by refinement of unit cell (*a* = 55.0437(16) Å) and zero-shift. Soft restraints were placed on the T–O distances (1.64 Å, T = Si, Al) and O···O distances (2.68 Å) within the TO₄ tetrahedra. All T positions were refined with the same, and fixed, occupancies. The location of TEA⁺ cations was modelled using the positions obtained from the structural model of NaTEA-ZSM-25, where TEA⁺ cations were in the *pau* and

t-plg cages. The $\text{Na}^+/\text{Sr}^{2+}$ cations were either allocated from difference Fourier maps or placed in similar sites as those in NaTEA-ZSM-25. These cations were mostly in the 8-ring sites throughout the structure. When the fractional occupancies of cations refined to values considerably greater than 1 when input as ' Na^+ ', they were instead included as more strongly scattering Sr^{2+} cations and their occupancies were refined without any restrictions. Each Na^+ or Sr^{2+} site was then modelled with a mixed occupancy with water oxygen. In this way six sites were identified as unambiguously containing Sr^{2+} cations (Sr1–Sr6). Additional scattering identified from difference Fourier mapping was included as water oxygen. The Debye–Waller factors of T, O, Na/Sr, water molecules and C(N) in the TEA⁺ ions were fixed to 1, 1.5, 3, 4 and 5, respectively and all fractional atomic coordinates were refined in the final cycles. The refinement converged to $R_{\text{wp}} = 0.0791$, $R_p = 0.0569$ and $\text{GOF} = 4.396$ (Extended Data Fig. 4a, Supplementary Table 8).

For NaTEA-PST-20, the chemical formula obtained from the elemental analysis and structure refinement was $[(\text{N}(\text{C}_2\text{H}_5)_4)_{56}\text{Na}_{56}\text{Sr}_{11}(\text{H}_2\text{O})_{586}[\text{Al}_{638}\text{Si}_{2002}\text{O}_{5280}]]$; a small amount of Sr^{2+} cations still remained after the ion exchange. Rietveld refinement was carried out in a similar way to that of as-made NaSrTEA-PST-20 and the refined unit cell was $a = 55.0664(7)$ Å. The locations of TEA⁺ and Na⁺ cations were modelled using the positions obtained from the structure model of NaTEA-ZSM-25. Additional guest water molecules were located from the difference Fourier maps by fixing the framework of NaTEA-PST-20. The Debye–Waller factors of T, O, Na/Sr, water molecules and C(N) in the TEA⁺ ions were fixed to 1, 2, 3, 4 and 5, respectively and all fractional atomic coordinates refined in the final cycles. The refinement converged to $R_{\text{wp}} = 0.0883$, $R_p = 0.0653$ and $\text{GOF} = 3.59$ (Extended Data Fig. 4b, Supplementary Table 9).

During the refinement of NaTEA-PST-20, some unindexed peaks were identified, which could be attributed to the minor impurity phases ZSM-25 and (for some smaller peaks) the even larger RHO-family member RHO-G6. Thus, the structure models of NaTEA-PST-20 and NaTEA-ZSM-25 were both included in the refinement. Considering the complexity of the two structures and the number of parameters, only the TCHZ peak profile function, the zero-shift, the background with a 17th-order Chebychev polynomial, and the unit cells of the two structures were refined. The atomic positions and thermal parameters were fixed on the basis of the two structure models. The refinement was improved and converged to $R_{\text{wp}} = 0.0793$, $R_p = 0.0593$ and $\text{GOF} = 3.16$ (Supplementary Fig. 8, Supplementary Table 9), with 92.5 wt% of PST-20 and 7.5 wt% of ZSM-25 in the sample.

The synchrotron PXRD pattern of the sample from Run 18 (Supplementary Table 3 and Supplementary Fig. 9a) was compared to those calculated on the basis of the structure models of PST-20 and the hypothetical RHO-G6, which indicated that the sample is a mixture of RHO-G6 (denoted PST-25) and PST-20, with about 75% PST-25. The two-phase LeBail refinement based on PST-25 and PST-20 resulted in a good agreement between the observed and the calculated profiles (Supplementary Fig. 9b; $R_{\text{wp}} = 0.0221$, $R_p = 0.0142$), and the unit-cell parameters, $a = 55.0270(5)$ Å for PST-20 and $a = 65.0436(4)$ Å for PST-25.

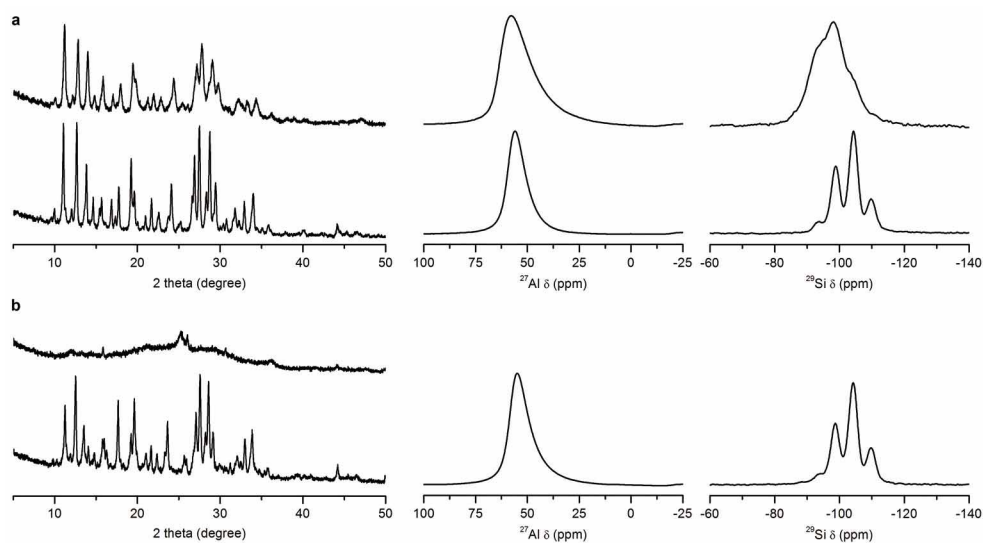
Prediction of ZSM-25 from PAU on the basis of strong reflections. Inspired by the successful structure solution of ZSM-25 by phasing the RED data using the related PAU structure, we investigated the possibility of deducing the structure of ZSM-25 solely from the PAU structure. We compared the structure factors calculated from the frameworks of PAU and ZSM-25, and found that the intensity distribution of reflections is similar and the phases of the strong reflections are the same, as shown in Fig. 3a and Extended Data Fig. 3. We selected the 133 strongest symmetry-independent reflections of PAU with normalized structure factor $E > 1.2$ and d -spacing $d > 1.00$ Å to predict the structure of ZSM-25 (Supplementary Table 15). The structure factor amplitudes and phases of these strong reflections were transposed to be those of a 'hypothetical' ZSM-25 by converting the reflection indices according to $h_{\text{ZSM-25}} = h_{\text{PAU}} \times a_{\text{ZSM-25}}/a_{\text{PAU}}$, $k_{\text{ZSM-25}} = k_{\text{PAU}} \times a_{\text{ZSM-25}}/a_{\text{PAU}}$, $l_{\text{ZSM-25}} = l_{\text{PAU}} \times a_{\text{ZSM-25}}/a_{\text{PAU}}$ and taking the nearest integers. A 3D electron-density map was calculated (Extended Data Fig. 5d), and all 16 T atoms and 31 out of 40 oxygen atoms in the asymmetric unit were located. A complete ZSM-25 framework could be obtained by adding the nine missing oxygen atoms geometrically between the T atoms (Extended Data Fig. 5e). Compared to the 3D electrostatic-potential map obtained from RED (Fig. 2e), the 3D electron-density map deduced from PAU (Extended Data Fig. 5d) has higher resolution so that most of the oxygen atoms could be resolved from the density map. This showed that the framework structure of ZSM-25 could be predicted solely from the related PAU framework, without using any ZSM-25 experimental diffraction data.

Prediction of new structures in the RHO family. The structure of RHO-G2 (Extended Data Fig. 5b) ($a \approx 25$ Å) was predicted previously^{26,27}. The prediction

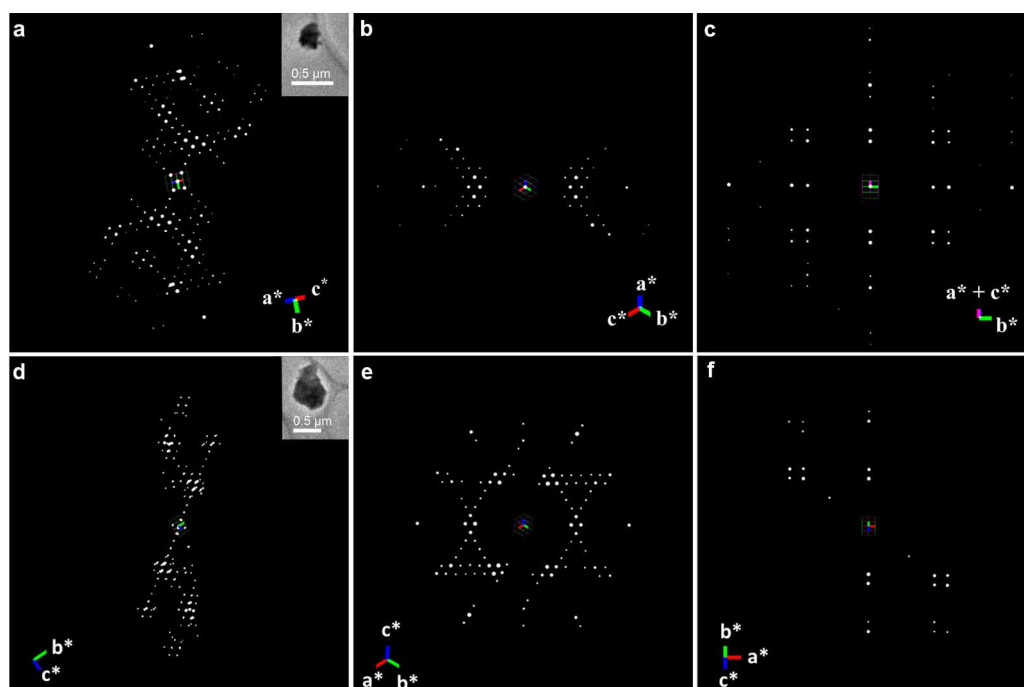
of larger structures, for example RHO-G5 ($a \approx 55$ Å), RHO-G6 ($a \approx 65$ Å) and so on, is very challenging. Although we know the unit cell, space group and partial structures (the cubic scaffolds) of RHO-G5 and RHO-G6, it is difficult to fill the remaining empty space between the cubic scaffolds by model building to complete these two structure models manually. We therefore used the strong reflections method we developed above to predict the structure model of RHO-G5 from RHO-G4, and the structure model of RHO-G6 from RHO-G5. Structure factor amplitudes and phases were calculated from the idealized structure model of RHO-G4 (ZSM-25). The 470 strongest reflections with $E > 1.2$ and $d > 1.00$ Å were selected (Supplementary Table 16). The indices of each strong reflection of RHO-G5 were calculated from the indices of the corresponding reflection of RHO-G4 according to $h_{\text{RHO-G5}} = h_{\text{RHO-G4}} \times a_{\text{RHO-G5}}/a_{\text{RHO-G4}}$, $k_{\text{RHO-G5}} = k_{\text{RHO-G4}} \times a_{\text{RHO-G5}}/a_{\text{RHO-G4}}$, $l_{\text{RHO-G5}} = l_{\text{RHO-G4}} \times a_{\text{RHO-G5}}/a_{\text{RHO-G4}}$. The 3D electron-density map was calculated by inverse Fourier transformation from the amplitudes and phases adopted from those of RHO-G4 using the SUPERFLIP software³⁶ (Extended Data Fig. 5f). All 29 T atoms and 44 out of 70 oxygen atoms in the asymmetric unit of RHO-G5 were located from the 3D map by using the EDMA software³⁷, and the remaining 26 oxygen atoms were added geometrically between the T atoms to complete the four-connected framework (Extended Data Fig. 5g). A similar approach was applied to generate the RHO-G6 structure based on the RHO-G5 structure. The 3D electron-density map (Extended Data Fig. 5h) was calculated using the 742 strongest reflections with $E > 1.2$ and $d > 1.00$ Å from the RHO-G5 structure, as given in Supplementary Table 17. The calculation of the indices of RHO-G6 follows the previous rules, $h_{\text{RHO-G6}} = h_{\text{RHO-G5}} \times a_{\text{RHO-G6}}/a_{\text{RHO-G5}}$, $k_{\text{RHO-G6}} = k_{\text{RHO-G5}} \times a_{\text{RHO-G6}}/a_{\text{RHO-G5}}$, $l_{\text{RHO-G6}} = l_{\text{RHO-G5}} \times a_{\text{RHO-G6}}/a_{\text{RHO-G5}}$. All 47 T atoms and 96 out of 112 oxygen atoms of RHO-G6 in the asymmetric unit were located from the 3D map, and the remaining 16 oxygen atoms were added geometrically between the T atoms to complete the four-connected framework (Extended Data Fig. 5i). All the structures in the RHO family were further energy-minimized in the pure SiO₂ forms using GULP (Supplementary Fig. 2, Supplementary Table 12), and are all energetically feasible. The corresponding unit-cell parameters for RHO-G1 to RHO-G6 are 14.77 Å, 24.58 Å, 34.40 Å, 44.22 Å, 54.07 Å and 63.87 Å, respectively. The energy difference from quartz was as predicted, on the basis of the results of earlier studies using GULP that show a clear trend between energy and framework density⁴¹. The lattice energies for the RHO family are comparable with those for other zeolite structures built from 4- and 6-rings only, for example SOD, LTA, FAU, MER, FAU, KFI, CHA, PHI. This indicates that all structures in the RHO family are energetically reasonable.

Gas adsorption experiments. The CO₂, CH₄, and N₂ adsorption isotherms of NaTEA-ZSM-25 and NaTEA-PST-20 were measured at 298 K and at pressures up to 1.2 bar using a Mirae SI nanoPorosity-XG analyser (Fig. 4a, b). Prior to the experiments, each zeolite sample was evacuated for 6 h at 523 K. Adsorption kinetics and adsorption-desorption cycling of CO₂ were performed using a Setaram PCTPro E&E analyser. Prior to the experiments, the zeolite sample was evacuated for 6 h at 473 K. While kinetics of CO₂ adsorption was determined at 298 K and 1.2 bar (Fig. 4c), cyclic CO₂ adsorption was repeated 100 times at 343 K and 1.2 bar in vacuum-swing-regeneration mode (Fig. 4a, b).

1. Totktarev, A., Harris, T., Kibby, C., Ione, K. & O'Rear, D. Studies on ZSM-25. In *Proc. 12th Int. Zeolite Conf.* Vol. 1 (eds Treacy, M. M. J. et al.) 2023–2030 (Materials Research Society, Cambridge Univ. Press, 1999).
2. Chatelain, T. et al. Synthesis and characterization of high-silica zeolite RHO prepared in the presence of 18-crown-6 ether as organic template. *Microporous Mater.* **4**, 231–238 (1995).
3. Coe, C. G., Gaffney, T. R. & Srinivasan, R. S. Chabazite for gas separation. US patent 4,925 460 (1990).
4. Sheldrick, G. M. A short history of SHELX. *Acta Crystallogr.* **A64**, 112–122 (2008).
5. Gordon, E. K., Samson, S. & Kamb, W. B. Crystal structure of the zeolite paulingite. *Science* **154**, 1004–1007 (1966).
6. Palatinus, L. & Chapuis, G. SUPERFLIP – a computer program for the solution of crystal structures by charge flipping in arbitrary dimensions. *J. Appl. Crystallogr.* **40**, 786–790 (2007).
7. Palatinus, L., Prathapa, S. J. & van Smaalen, S. EDMA: a computer program for topological analysis of discrete electron densities. *J. Appl. Crystallogr.* **45**, 575–580 (2012).
8. Young, R. A. (ed.) *The Rietveld Method* (Oxford Univ. Press, 1995).
9. Le Bail, A., Duroy, H. & Fourquet, J. L. Ab-initio structure determination of LiSbWO₆ by X-ray powder diffraction. *Mater. Res. Bull.* **23**, 447–452 (1988).
10. Larson, A. C. & Von Dreele, R. B. *General Structure Analysis System* (GSAS). Report No. LAUR 86-748 (Los Alamos National Laboratory, 2004).
11. Henson, N. J., Cheetham, A. K. & Gale, J. D. Theoretical calculations on silica frameworks and their correlation with experiment. *Chem. Mater.* **6**, 1647–1650 (1994).

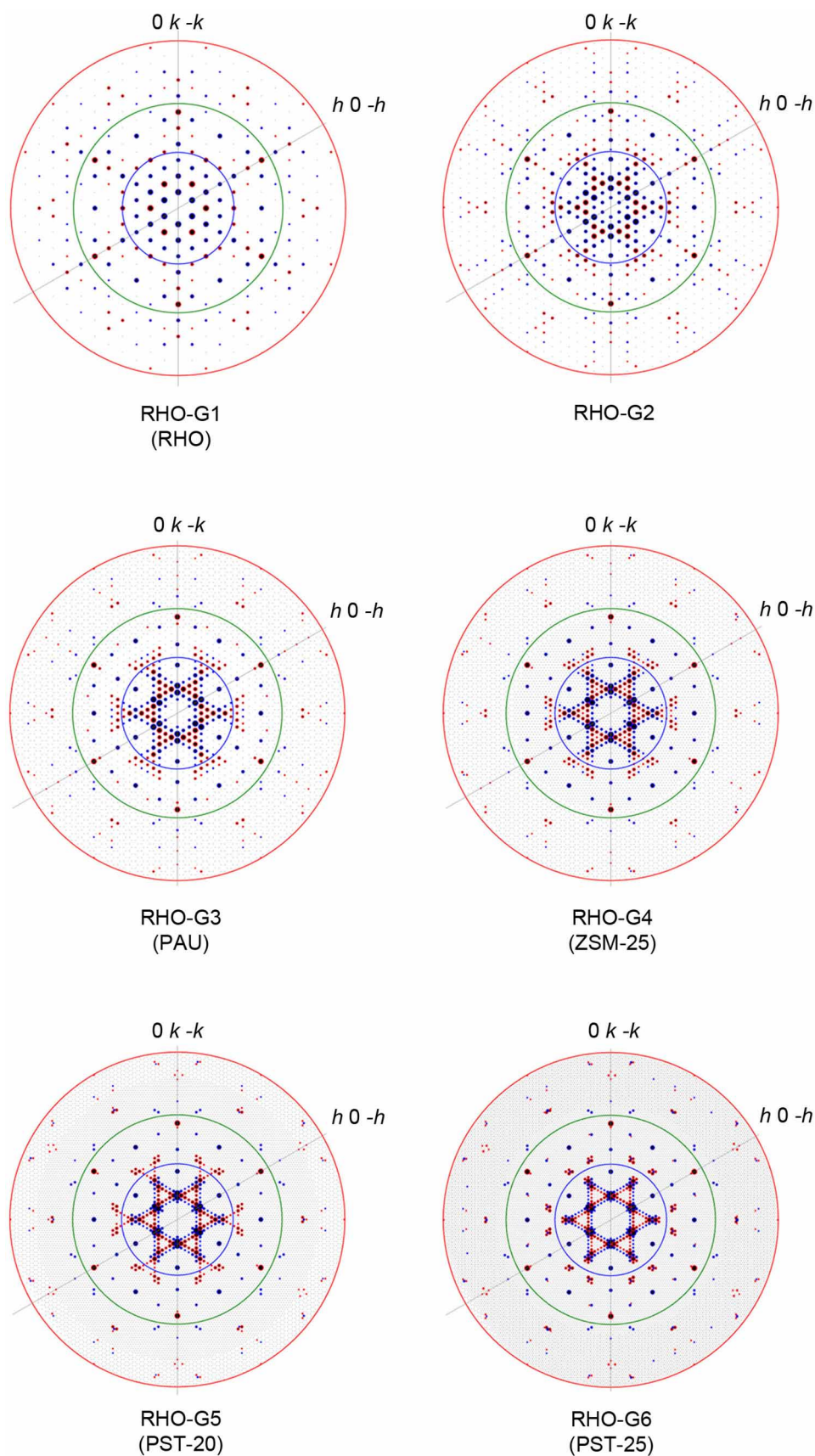


Extended Data Figure 1 | Characterization of ZSM-25 and PST-20 zeolites. a, b, PXRD patterns (left panels), ^{27}Al (middle panels) and ^{29}Si (right panels) magic-angle spinning NMR spectra of as-made (bottom plots within each panel) and calcined (top plots within each panel) ZSM-25 (**a**) and PST-20 (**b**).



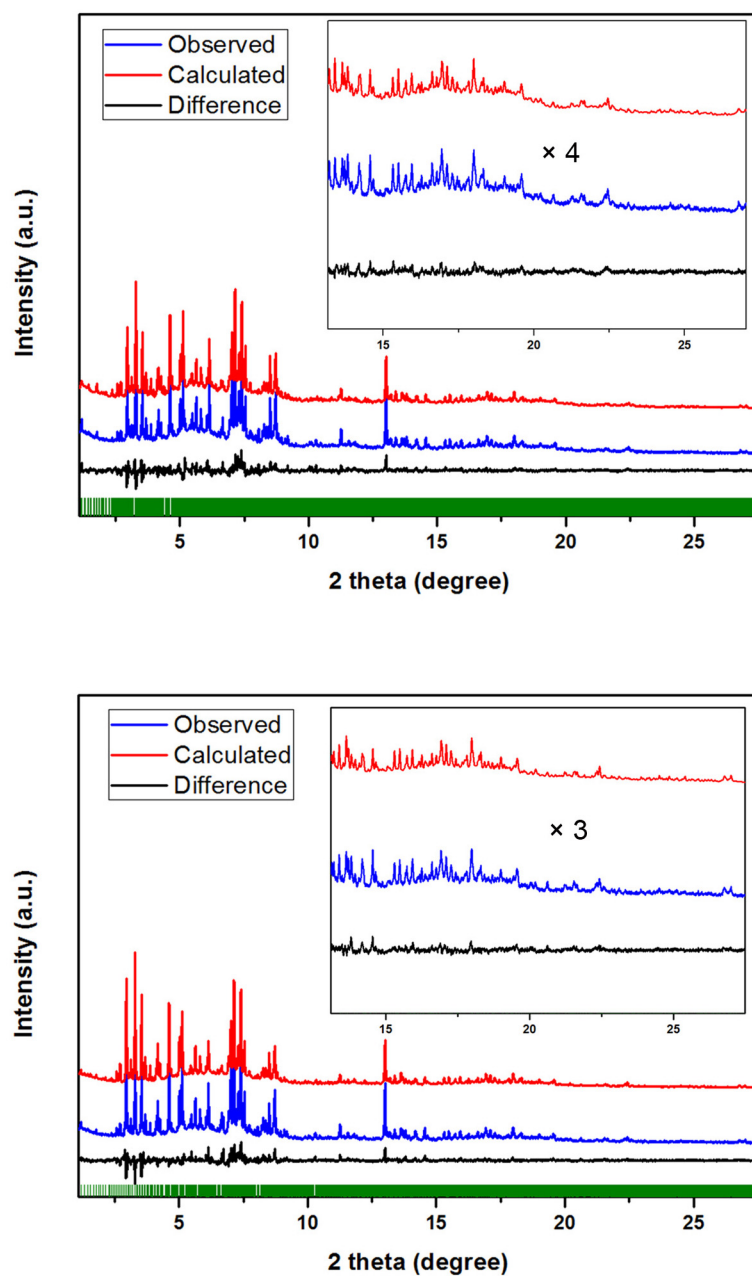
Extended Data Figure 2 | Reconstructed 3D reciprocal lattice from the RED data. **a–c**, NaTEA-ZSM-25 and **d–f**, NaSrTEA-PST-20. **a, d**, The 3D reciprocal lattice with the crystal inset. **b, c, e, f**, 2D slices cut from the reconstructed

3D reciprocal lattice showing the $(hk0)$ plane (**b, e**), (hkh) (**c**) and $(hk\bar{k})$ (**f**) reciprocal plane. The distributions of the strong reflections for NaTEA-ZSM-25 and NaSrTEA-PST-20 are similar to that of PAU.



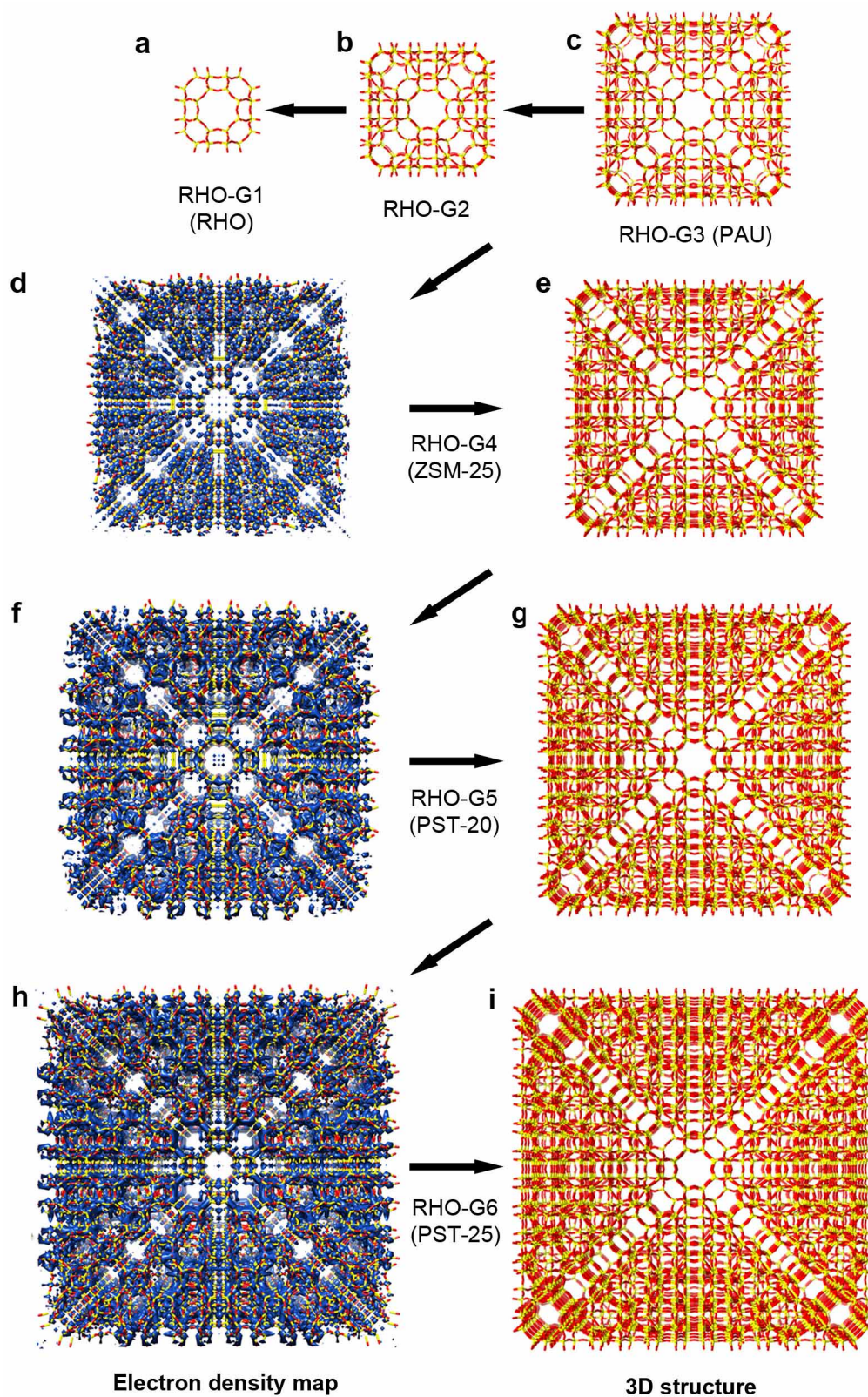
Extended Data Figure 3 | Structure factor amplitudes and phases calculated from the structure models of RHO-G1 to RHO-G6. The $(h\bar{k}h + \bar{k})$ reflections are shown. Reflections in red and blue have phases of 0° and 180° , respectively.

The red, green and blue circles correspond to d -spacings of 1.0 Å, 1.6 Å and 3.0 Å, respectively. The frameworks are idealized in the pure SiO_2 forms.



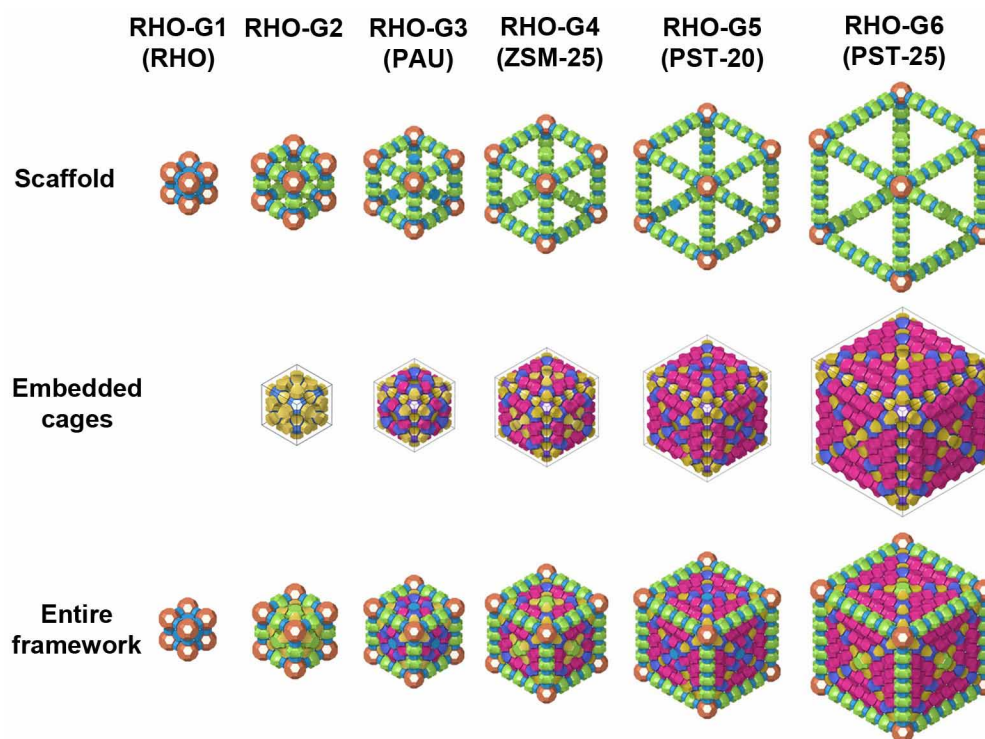
Extended Data Figure 4 | PXRD profiles for the Rietveld refinement of as-made and Na⁺-exchanged NaSrTEA-PST-20. Top, as-made NaSrTEA-PST-20. Bottom, Na⁺-exchanged NaSrTEA-PST-20 (denoted NaTEA-PST-20). The observed, calculated and difference curves are shown in blue, red and black,

respectively. The good agreement of observed and calculated data at high angles (inset) indicates that the framework structure is correct. The slight differences at lower angles are due to incomplete determination of the positions of all guest molecules/cations (X-ray wavelength $\lambda = 0.40091 \text{ \AA}$).



Extended Data Figure 5 | The prediction of the RHO-family members RHO-G1 to RHO-G6 from the structure of PAU (RHO-G3). The arrows indicate how the structures were predicted from their nearest generations. The 3D electron-density map of RHO- G_n ($n = 4-6$) was generated using the

structure factors of strong reflections from RHO- $G(n-1)$, which allowed a 3D structure model of RHO- G_n to be built. The structures of RHO-G1 and RHO-G2 were obtained from RHO-G3 by model building.



Extended Data Figure 6 | Tile representations of the structures of RHO-G1 to RHO-G6 in the RHO family. The structure expansion operates at two levels: first, a pair of *pau* and *d8r* cages is inserted along each unit-cell edge (top)

resulting in isoreticular expansion of the scaffold; and second, other cages are embedded (middle) in the inter-scaffold space. The resulting frameworks are denoted as 'embedded isoreticular zeolite structures' (bottom).

Extended Data Table 1 | Structure factor amplitudes and phases used for structure solution of ZSM-25

$h_{\text{ZSM-25}}$	$k_{\text{ZSM-25}}$	$l_{\text{ZSM-25}}$	$d_{\text{ZSM-25}}/\text{\AA}$	$ F_{\text{ZSM-25}} $ from RED data	Phase ϕ_{PAU}	h_{PAU}	k_{PAU}	l_{PAU}
4	0	4	8.0	17.7	180	3	0	3
0	18	0	2.5	16.2	180	0	14	0
5	1	4	6.9	14.2	0	4	1	3
5	0	5	6.4	13.0	180	4	0	4
9	0	9	3.5	12.8	180	7	0	7
5	13	0	3.2	12.3	0	4	10	0
4	14	0	3.1	12.1	0	3	11	0
8	4	4	4.6	10.9	0	6	3	3
0	10	0	4.5	10.2	180	0	8	0
10	5	5	3.7	9.5	0	8	4	4
0	8	0	5.6	8.8	180	0	6	0
8	5	5	4.2	8.2	180	6	4	4
1	9	0	5.0	7.6	0	1	7	0
4	13	1	3.3	7.3	180	3	10	1
4	4	10	3.9	6.7	180	3	3	8
6	2	4	6.0	6.1	0	5	2	3
13	0	13	2.4	6.0	180	10	0	10
5	2	3	7.3	5.9	0	4	2	2
1	14	5	3.0	5.8	180	1	11	4
7	3	4	5.2	5.3	0	5	2	3
1	4	3	8.8	5.3	180	1	3	2

Structure factor amplitudes of the strongest reflections obtained from RED data, and the corresponding reflections and structure factor phases in the PAU structure. The amplitudes $|F_{\text{ZSM-25}}|$ were calculated as the square-roots of the intensities extracted from RED. The indices of the corresponding reflections in the PAU structure were obtained: $h_{\text{PAU}} = h_{\text{ZSM-25}} \times a_{\text{PAU}}/a_{\text{ZSM-25}}$, $k_{\text{PAU}} = k_{\text{ZSM-25}} \times a_{\text{PAU}}/a_{\text{ZSM-25}}$, $l_{\text{PAU}} = l_{\text{ZSM-25}} \times a_{\text{PAU}}/a_{\text{ZSM-25}}$, where the unit cell $a_{\text{PAU}} = 35 \text{ \AA}$ and $a_{\text{ZSM-25}} = 45 \text{ \AA}$.

Extended Data Table 2 | Room-temperature CO₂/CH₄ and CO₂/N₂ selectivities

Materials	CO ₂ /CH ₄ selectivity		CO ₂ /N ₂ selectivity	
	0.1 bar	1.0 bar	0.1 bar	1.0 bar
NaTEA-PST-20	117	15	47	10
NaTEA-ZSM-25	331	22	43	10
NaTEA-ECR-18	105	11	49	9
Na-Rho	142	23	319	31
K-chabazite	13	3	42	7

The selectivities are measured at 0.1 bar and 1.0 bar for NaTEA-PST-20, NaTEA-ZSM-25, NaTEA-ECR-18, Na-Rho and K-chabazite. The CO₂/CH₄ and CO₂/N₂ selectivities are defined as $Q_{\text{CO}_2}/Q_{\text{CH}_4}$ and $Q_{\text{CO}_2}/Q_{\text{N}_2}$, respectively, where Q_{CO_2} , Q_{CH_4} , and Q_{N_2} are the respective equilibrium molar uptakes of CO₂, CH₄ and N₂ at a given pressure taken from the corresponding single component isotherms.

Conversion of amides to esters by the nickel-catalysed activation of amide C–N bonds

Liana Hie¹, Noah F. Fine Nathel¹, Tejas K. Shah¹, Emma L. Baker¹, Xin Hong¹, Yun-Fang Yang¹, Peng Liu¹, K. N. Houk¹ & Neil K. Garg¹

Amides are common functional groups that have been studied for more than a century¹. They are the key building blocks of proteins and are present in a broad range of other natural and synthetic compounds. Amides are known to be poor electrophiles, which is typically attributed to the resonance stability of the amide bond^{1,2}. Although amides can readily be cleaved by enzymes such as proteases³, it is difficult to selectively break the carbon–nitrogen bond of an amide using synthetic chemistry. Here we demonstrate that amide carbon–nitrogen bonds can be activated and cleaved using nickel catalysts. We use this methodology to convert amides to esters, which is a challenging and underdeveloped transformation. The reaction methodology proceeds under exceptionally mild reaction conditions, and avoids the use of a large excess of an alcohol nucleophile. Density functional theory calculations provide insight into the thermodynamics and catalytic cycle of the amide-to-ester transformation. Our results provide a way to harness amide functional groups as synthetic building blocks and are expected to lead to the further use of amides in the construction of carbon–heteroatom or carbon–carbon bonds using non-precious-metal catalysis.

The ability to interconvert functional groups is important in synthetic chemistry and many biological processes. Methodologies^{4,5} have been developed that enable chemists to strategically harness the reactivity of most functional groups. Likewise, breakthroughs in biochemistry have led to an understanding of how changes in functional groups regulate physiological processes⁶.

One particularly interesting dichotomy exists in considering the amide functional group¹, which is the key component of all proteins (Fig. 1a). Since Schwann's initial discovery of pepsin—the first enzyme to be discovered—in 1836, scientists have been intrigued by the ability of enzymes to break amide linkages^{3,6}. Such amide cleavage processes govern many cellular regulatory functions and are responsible for the degradation of proteins to amino acids^{1,3}. In contrast, the synthetic chemistry of amide-bond cleavage has remained underdeveloped, even though amides are well suited for use in multistep synthesis because of their stability under a variety of reaction conditions. Commonly used methods to break amide carbon–nitrogen (C–N) bonds include the reductive conversion of amides to aldehydes using Schwartz's reagent⁷ and the displacement of Weinreb's *N*-OMe-*N*-Me amides with organometallic reagents en route to ketones⁸. Following Pauling's seminal postulate regarding amide planarity², the poor reactivity of amides is now well understood as being a result of the strength of the resonance-stabilized amide C–N bond¹.

To circumvent the long-standing problem involving the low reactivity of amides and their modest synthetic use in C–N bond cleavage processes, we designed the general approach shown in Fig. 1b. The C–N bond of amide **1** undergoes activation by a transition-metal catalyst. Following oxidative addition, the resultant acyl metal species **2** is trapped by an appropriate nucleophile to furnish product **3**, with the release of amine **4**. This approach allows for the breakdown of amides, and renders amides useful synthetic building blocks. Although examples exist for the metal-catalysed C–heteroatom bond

activation of acid chlorides⁹, anhydrides⁹, and 2-pyridyl esters¹⁰, to our knowledge, the direct metal-catalysed activation of C–N bonds of amides is unknown. This is notable given the widespread use of

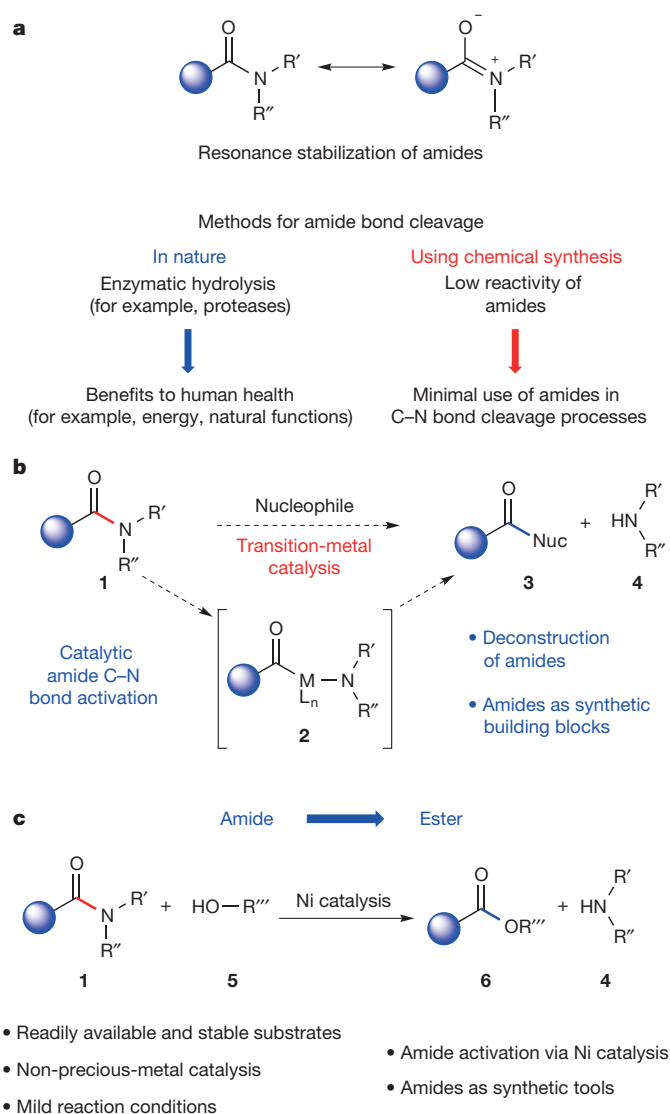


Figure 1 | Amide-bond cleavage using transition-metal catalysis. **a**, An illustration of the stability of amides and the contrast between how amides are used in nature and in chemical synthesis. **b**, Design of amide C–N bond activation to deconstruct amides and exploit them as synthetic building blocks (nuc, nucleophile; L_n , ligands coordinated to transition metal; blue spheres, R' , R'' , R''' , any carbon-based functional groups). **c**, Strategy for the conversion of amides to esters.

¹Department of Chemistry and Biochemistry, University of California, Los Angeles, California 90095, USA.

Entry		Calculated ΔG (kcal mol ⁻¹)	Calculated oxidative addition barrier with Ni/SIPr (kcal mol ⁻¹)	Temperature (°C)	Equivalents of MeOH	Yield of ester
1		+2.4	36.8	110	2.0	0%
2		0.0	36.2	110	2.0	0%
3		-1.1	34.0	110	2.0	23%
4		-6.1	31.9	110	2.0	22%
5		+3.1	39.0	110	2.0	0%
6		-4.3	30.6	110	2.0	55%
7		-6.8	26.0	110	2.0	>99%
8		-6.8	26.0	80	1.2	>99%

Figure 2 | Experimental and computational study of amide-bond activation during the conversion of benzamides **7 to methyl benzoate **8a**.** The ΔG values for the overall reactions were obtained using DFT calculations (assuming a temperature of 298 K). DFT methods were used to calculate oxidative addition barriers using Ni/SIPr as the metal/ligand combination. Reactions were carried out with bis(1,5-cyclooctadiene)nickel(0) (Ni(cod)₂, 10 mol%), SIPr (10 mol%), substrate (50.0 mg, 1.0 equiv.), methanol (1.2 or 2.0 equiv.), and toluene (1.0 M), for 12 h at the specified temperatures. Yields were determined by ¹H nuclear magnetic resonance (NMR) analysis using hexamethylbenzene as an internal standard. Me, methyl; OMe, methoxy; Ph, phenyl.

a

Entry	Amide substrate	Yield of methyl ester
1		88% (R = H)
2		80% (R = <i>p</i> -CF ₃)
3		92% (R = <i>p</i> -F)
4		90% (R = <i>p</i> -OMe)
5		90% (R = <i>p</i> -Me)
6		83% (R = <i>m</i> -Me)
7		89% (R = <i>o</i> -Me)
8		94%
9		94%

b

Entry	Ester product	Yield of ester
19		82%
20		64%
21		67%
22		90%
23		49%
24		88%

Entry	Ester product	Yield of ester
25		67%
26		65%
27		91%
28		74%

Figure 3 | Scope of our methodology. **a**, **b**, The scope of the amide-to-ester transformation was evaluated with respect to the amide substrate (**a**), and with respect to the alcohol nucleophile, using **7g** as the amide substrate (**b**). Reactions were carried out with Ni(cod)₂ (10 mol%), SIPr (10 mol%), substrate (100.0 mg, 1.00 equiv.), alcohol (1.2 equiv.), and toluene (1.0 M) at 80 °C for

12 h. Yields shown reflect the average of two isolated experiments, except for entry 10; the yield for entry 10 was determined by ¹H NMR analysis using hexamethylbenzene as an internal standard, owing to the volatility of the ester product. *t*-Bu, *tert*-butyl; *p*, *para*; *m*, *meta*; *o*, *ortho*.

transition-metal catalysis in organic synthesis, where there exist many examples of catalytic transformations occurring smoothly in the presence of amide linkages.

We validate the strategy outlined in Fig. 1b through the conversion of amides to esters (Fig. 1c). Amide to ester conversion, much like transamidation^{11,12}, remains a challenging and underdeveloped synthetic transformation. Amides are often stable enough that esterification is difficult and requires the use of harsh acidic or basic conditions, while employing a large excess of nucleophile (for example, using the alcohol nucleophile as a solvent)¹. Perhaps the most promising protocol to achieve amide-to-ester conversions is Keck's methylation/hydrolysis sequence¹³, although this methodology is limited to the synthesis of methyl esters. Esterifications using acyl aziridines¹⁴ and *N*-methylamides (albeit with activation by nitrosation)¹⁵ have also been reported. Here we demonstrate the nickel-catalysed conversion of amides to esters, which proceeds under exceptionally mild reaction conditions. In addition to establishing the scope of this methodology, we use density functional theory (DFT) calculations to predict whether the amide-to-ester conversion, or the reverse, is thermodynamically favoured. DFT calculations are also used to predict a plausible catalytic cycle. These experimental and computational studies not only substantiate the notion of using non-precious-metal catalysis for the activation of amide C–N bonds, but also lay the foundation for further studies aimed at the strategic manipulation of amides as synthetic building blocks using catalysis.

We examined the conversion of benzamides **7** to methyl benzoate **8a** both computationally (using the 'Gaussian 09' software; see Supplementary Information) and experimentally (Fig. 2). Because

amides are known for their stability, we assessed whether the amide-to-ester conversion could be rendered thermodynamically favourable by the judicious choice of amide *N*-substituents. Using DFT methods, we calculated the change in Gibbs free energy ΔG for the reaction of amides **7** with methanol to give esters **8a** and amines **4**. Whether this transformation is favourable or not depends on the nature of the *N*-substituents (entries 1–8). Methanolysis of Weinreb amide **7d** (entry 4) and *N*-arylated substrates **7f** and **7g** (entries 6–8) were found to be the most energetically favourable. In contrast, esterifications of *N*-alkyl amides **7a**, **7b**, and **7e** were deemed thermodynamically unfavourable. This is in line with the experimentally measured equilibrium constant for the reaction of *N,N*-dimethylbenzamide **7b** and methanol (entry 2), in which the reverse reaction is thermodynamically favoured (see Supplementary Information for further discussion)¹⁶.

Encouraged by the unique ability of nickel to catalyse the activation of strong aryl–heteroatom bonds^{17–19}, particularly those in phenol¹⁹, aniline^{20–22}, and phthalimide²³ derivatives, we also calculated the activation free energies for acyl C–N bond oxidative addition of each amide substrate using nickel catalysis. The barriers calculated for commercially available *N*-heterocyclic carbene ligand SIPr (entries 1–8) reveal that the oxidative addition barriers are reasonable in some cases. We studied these reactions experimentally using 10 mol% Ni(cod)₂, 10 mol% SIPr, 2.0 equivalents of methanol, and toluene as solvent at 110 °C for 12 h. There was good agreement between our observations and computational predictions. No reaction or low yields were seen for substrates **7a**–**7e** (entries 1–5). However, when the calculated ΔG and the oxidative addition barrier were favourable, substantial formation of product **8a** was observed (entries 6 and 7). Coupling of substrate **7g**

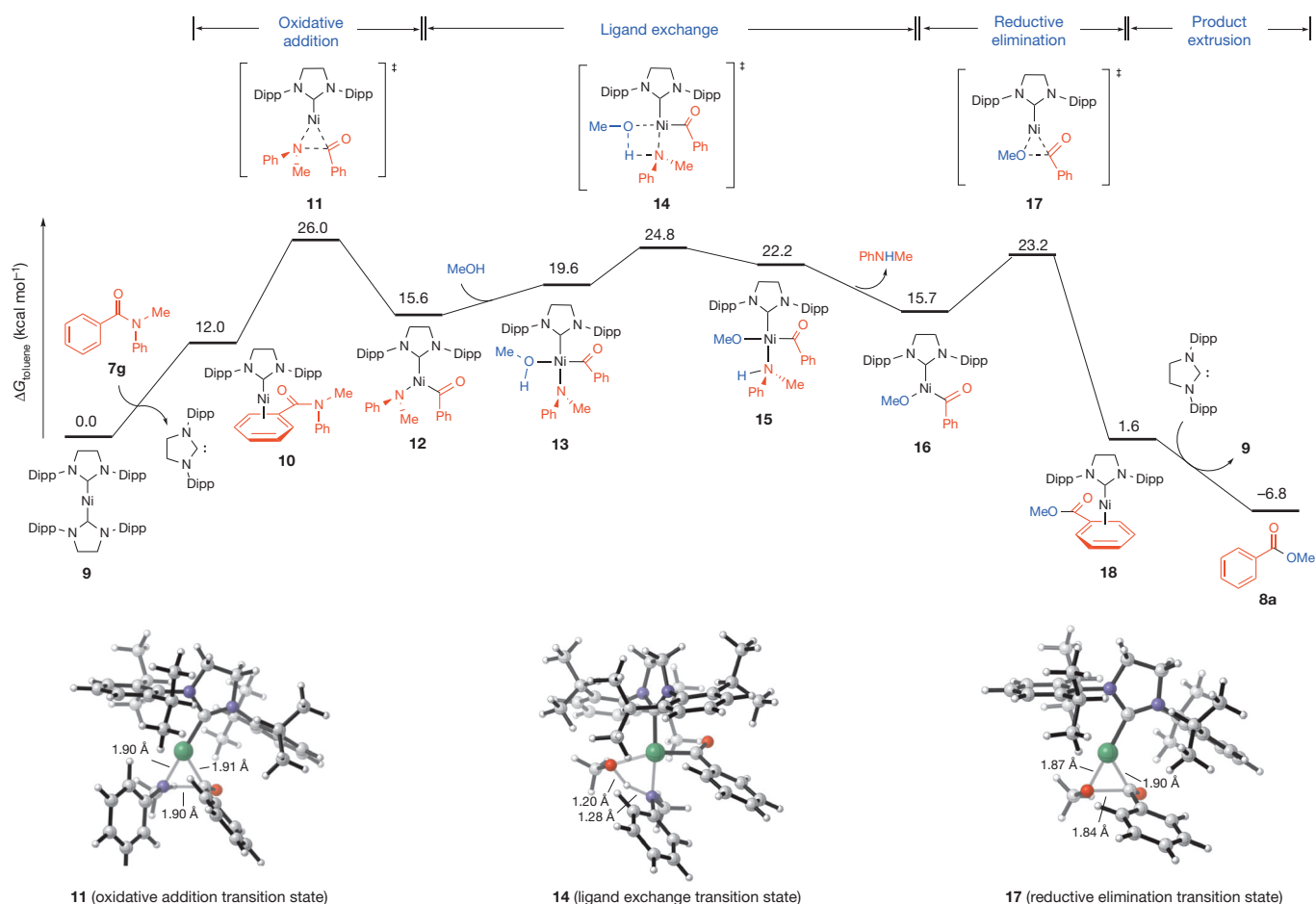


Figure 4 | Computational study of catalytic cycle. DFT methods were used to calculate the full catalytic cycle for the amide-to-ester conversion (assuming a temperature of 298 K). We propose that the reaction occurs by oxidative

addition, ligand exchange, and reductive elimination. Key transition state structures (**11**, **14**, and **17**) are shown at the bottom. Dipp, 2,6-diisopropylphenyl.

gave a quantitative yield of product (entry 7), and further optimization showed that even with only 1.2 equivalents of methanol and a temperature of 80 °C, product formation occurred smoothly (entry 8) to give complete conversion to **8a**. Importantly, no reaction takes place if either the precatalyst or the ligand are omitted, whereas the use of alternative *N*-heterocyclic carbene or phosphine ligands typically leads to lower yields or no reaction. We conclude that nickel catalysis is indeed operative in the amide activation/esterification process.

Having determined the optimal reaction conditions, we examined the scope of the transformation with regard to the amide substrate (Fig. 3a). In addition to the parent benzamide (entry 1), substrates containing the electron-withdrawing trifluoromethyl or fluoride substituents (entries 2 and 3) or the electron-donating methoxy or methyl substituents (entries 4 and 5) were well tolerated. The transformation also proceeded smoothly using *meta*- and *ortho*-methyl-substituted substrates to give the desired esters in excellent yields (entries 6 and 7). Beyond the use of phenyl derivatives, we examined naphthyl and heterocyclic substrates. Naphthyl compounds readily coupled (entries 8 and 9), as did furan, quinoline, and isoquinoline substrates (entries 10–12, respectively). However, amides derived from alkyl carboxylic acids did not undergo the nickel-catalysed esterification under our reaction conditions. This attribute provides opportunities to realize selective amide C–N bond cleavages in more complex substrates (see below).

A variety of *N*-substituents were also surveyed, as shown in Fig. 3a. In addition to the longer *N*-butyl (Bu) and the branched *N*-*iso*-propyl alkyl chains (entries 13 and 14, respectively), we found that a cyclic amide derived from indoline was tolerated by the methodology (entry 15). Lastly, protected *N*-alkyl benzamides were tested. Although use of the *N*-*p*-toluenesulfonyl (Ts) derivative gave the corresponding ester in modest yield (entry 16), the corresponding *N*-*tert*-butoxycarbonyl (Boc) substrate more efficiently underwent conversion to ester **8a** (entry 17). The analogous *N*-benzyl, *N*-*tert*-butoxycarbonyl (*N*-Bn,Boc) substrate was also evaluated and gave the desired ester in 89% yield (entry 18). These results show that the methodology is not restricted to anilide substrates, as long as the overall reaction energetics are thermodynamically favourable (see Supplementary Information for energetics involving the *N*-Boc,Me substrate). Moreover, secondary benzamides can be used strategically as sub-

strates for esterification, following a straightforward activation step (Boc-protection).

Using amide **7g** as the substrate, we evaluated the scope of the methodology with respect to the alcohol nucleophile (Fig. 3b). As shown, synthetically useful yields of product were obtained using only 1.2 equivalents of the alcohol, even when complex and hindered alcohols were used. Cyclohexanol, *t*-butanol, and 1-adamantol coupled smoothly to give the corresponding esters (entries 19–21, respectively); *tert*-butyl esters can readily be hydrolysed to carboxylic acids under acidic conditions. Similarly, we found that cyclopropyl carbinol and an oxetane-derived alcohol could be used in the esterification reaction (entries 22 and 23, respectively). The use of the hindered secondary alcohol (–)-menthol was also tested and the desired ester was obtained in 88% yield (entry 24). Furthermore, we found that Boc-L-prolinol was tolerated in the methodology (entry 25), in addition to an indole-containing alcohol (entry 26), which further demonstrates the promise our methodology holds for reactions of heterocyclic substrates. As shown in entries 27 and 28, a complex sugar-containing alcohol bearing two acetals and an estrone-derived steroidal alcohol, respectively, also underwent the desired esterification reaction.

Although nickel-catalysed aryl and acyl C–O bond activation processes have been previously studied computationally^{24–28}, no analogous studies involving C–N bond activation have been reported. Thus, to shed light on the mechanism of the facile amide-to-ester conversion, the catalytic cycle was computed using DFT calculations. Figure 4 provides the free energy profile using amide substrate **7g**. The [Ni(SIPr)₂] complex, **9**, is believed to be the resting state of the catalytic cycle. Dissociation of one carbene ligand from complex **9** provides a coordination site for amide **7g**. Following coordination to give intermediate **10**, oxidative addition occurs via transition state **11**. This key event cleaves the amide C–N bond and produces acyl nickel species **12**. The next step of the catalytic cycle is ligand exchange, which proceeds by coordination of methanol to give intermediate **13**. Subsequent ligand exchange via transition state **14** facilitates the deprotonation of methanol, giving nickel complex **15**. Dissociation of *N*-Me-aniline produces acyl nickel species **16**, which in turn, undergoes reductive elimination via transition state **17** to deliver the ester-coordinated complex **18**. Finally, the ester product **8a** is released to regenerate catalyst **9**. The rate-determining step in the catalytic cycle is the oxidative addition (transition state **11**) with an

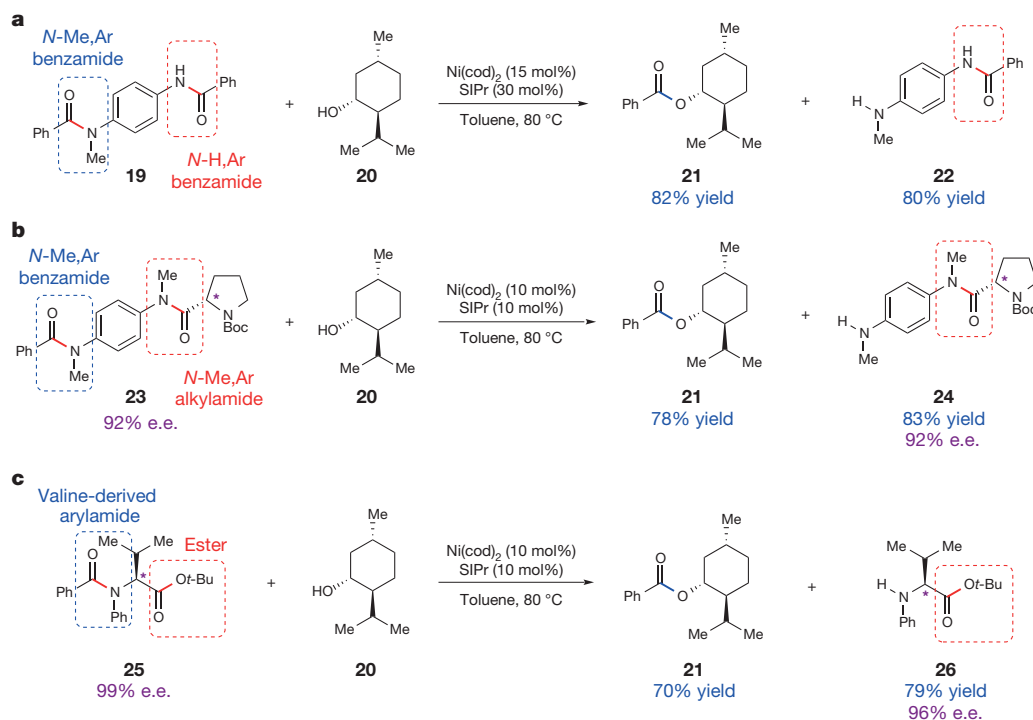


Figure 5 | Selective amide-bond cleavage processes. **a**, Cleavage of tertiary over secondary amide using menthol (1.2 equiv.). **b**, Cleavage of benzamide over an alkyl proline-derived amide using menthol (1.2 equiv.). **c**, Cleavage of valine-derived amide in the presence of an ester using menthol (1.2 equiv.). e.e., enantiomeric excess.

overall barrier of $26.0 \text{ kcal mol}^{-1}$ relative to the resting state **9**. The overall reaction is thermodynamically favoured by $-6.8 \text{ kcal mol}^{-1}$. Because decarbonylation of acyl nickel species have been observed^{29,30}, we also calculated the kinetic barrier for decarbonylation events (see Supplementary Information). Consistent with experiments, decarbonylation pathways from acyl nickel species **12** or **16** were found to be less favourable than the product formation pathways.

As highlighted by the experiments shown in Fig. 5, the nickel-catalysed conversion of amides to esters can be used to achieve selective and mild amide-bond cleavages. First, we performed the esterification of bis(amide) substrate **19** using (–)-menthol (Fig. 5a). Although both amides are *N*-arylated benzamides, only the tertiary amide was cleaved to give ester **21**, while also releasing aminoamide **22**. Second, bis(amide) **23**, which possesses two tertiary amides, was studied in the nickel-catalysed esterification reaction (Fig. 5b). In this case, the tertiary *L*-proline-derived alkyl amide was not disturbed, while the tertiary benzamide underwent cleavage to give ester **21** and aminoamide **24** in good yields. Lastly, we prepared *L*-valine derivative **25**, which also bears an ester (Fig. 5c). Upon exposure of **25** to 1.2 equivalents of (–)-menthol and the nickel-catalysed conditions, ester **21** and aminoester **26** were obtained in 70% and 79% yields, respectively. We believe that the ester functionality withstands the reaction conditions because it is not attached to an arene, analogous to the lack of reactivity seen in our attempts to esterify amides derived from alkyl carboxylic acids (for example, **23**). Compounds **24** and **26** were obtained in high enantiomeric excess, highlighting the mild nature of the reaction conditions, which avoid any substantial epimerization of the α stereocentres.

We have presented an efficient way to convert amides to esters. The methodology circumvents the classic problem of amides being poorly reactive functional groups by using nickel catalysis to achieve the previously unknown catalytic activation of amide C–N bonds. DFT calculations support a catalytic cycle that involves a rate-determining oxidative addition step, followed by ligand exchange and reductive elimination. The methodology is broad in scope, particularly with respect to the alcohol nucleophiles, and proceeds under exceptionally mild reaction conditions using just 1.2 equivalents of the alcohol nucleophile. Moreover, selective amide-bond cleavage is achieved in the presence of other functional groups, including less reactive amides and esters, without the epimerization of α stereocentres. We envision that this methodology will lead to advances such as the catalytic esterification of primary amides, additional *N,N*-disubstituted amides, amides derived from alkyl or vinyl carboxylic acids, and perhaps even polyamide substrates bearing multiple stereocentres. This study should enable the further use of amides as valuable building blocks for the construction of C–heteroatom or C–C bonds using non-precious-metal catalysis.

Received 20 December 2014; accepted 20 May 2015.

Published online 22 July 2015.

- Greenberg, A., Breneman, C. M. & Liebman, J. F. (eds) *The Amide Linkage: Structural Significance in Chemistry, Biochemistry, and Materials Science* (Wiley, 2003).
- Pauling, L., Corey, R. B. & Branson, H. R. The structure of proteins: two hydrogen-bonded helical configurations of the polypeptide chain. *Proc. Natl Acad. Sci. USA* **37**, 205–211 (1951).
- Brix, K. & Stöcker, W. (eds) *Proteases: Structure and Function* (Springer, 2013).
- Corey, E. J. & Cheng, X.-M. *The Logic of Chemical Synthesis* (Wiley, 1995).
- Hudlicky, T. & Reed, J. W. *The Way of Synthesis: Evolution of Design and Methods for Natural Products* (Wiley, 2007).
- Van Vranken, D. L. & Weiss, G. A. *Introduction to Bioorganic Chemistry and Chemical Biology* (Garland Science, 2013).
- Spletstoser, J. T., White, J. M., Tunoori, A. R. & Georg, G. I. Mild and selective hydrozirconation of amides to aldehydes using $\text{Cp}_2\text{Zr}(\text{H})\text{Cl}$: scope and mechanistic insight. *J. Am. Chem. Soc.* **129**, 3408–3419 (2007).
- Nahm, S. & Weinreb, S. M. *N*-methoxy-*N*-methylamides as effective acylating agents. *Tetrahedron Lett.* **22**, 3815–3818 (1981).
- Blangetti, M., Rosso, H., Prandi, C., Deagostino, A. & Venturello, P. Suzuki–Miyaura cross-coupling in acylation reactions, scope and recent developments. *Molecules* **18**, 1188–1213 (2013).

- Tatamidani, H., Kakiuchi, F. & Chatani, N. A new ketone synthesis by palladium-catalyzed cross-coupling reactions of esters with organoboron compounds. *Org. Lett.* **6**, 3597–3599 (2004).
- Dineen, T. A., Zajac, M. A. & Myers, A. G. Efficient transamidation of primary carboxamides by in situ activation with *N,N*-dialkylformamide dimethyl acetals. *J. Am. Chem. Soc.* **128**, 16406–16409 (2006).
- Stephenson, N. A., Zhu, J., Gellman, S. H. & Stahl, S. S. Catalytic transamidation reactions compatible with tertiary amide metathesis under ambient conditions. *J. Am. Chem. Soc.* **131**, 10003–10008 (2009).
- Keck, G. E., McLaws, M. D. & Wager, T. T. A direct and mild conversion of tertiary aryl amides to methyl esters using trimethyloxonium tetrafluoroborate: a very useful complement to directed metalation reactions. *Tetrahedron* **56**, 9875–9883 (2000).
- Nishimoto, S.-i., Izukawa, T. & Kagiya, T. Photo-induced ring-opening reactions of 1-(2-naphthoyl)aziridine in various solvents. *Bull. Chem. Soc. Jpn* **55**, 1484–1488 (1982).
- White, E. H. The chemistry of *N*-alkyl-*N*-nitrosoamides. II. A new method for the deamination of aliphatic amines. *J. Am. Chem. Soc.* **77**, 6011–6014 (1955).
- Guthrie, J. P., Pike, D. C. & Lee, Y.-C. Equilibrium constants and heats of formation of methyl esters and *N,N*-dimethyl amides of substituted benzoic acids. *Can. J. Chem.* **70**, 1671–1683 (1992).
- Tasker, S. Z., Standley, E. A. & Jamison, T. F. Recent advances in homogeneous nickel catalysis. *Nature* **509**, 299–309 (2014).
- Mesganaw, T. & Garg, N. K. Ni- and Fe-catalyzed cross-coupling reactions of phenol derivatives. *Org. Process Res. Dev.* **17**, 29–39 (2013).
- Rosen, B. M. et al. Nickel-catalyzed cross-couplings involving carbon–oxygen bonds. *Chem. Rev.* **111**, 1346–1416 (2011).
- Blakey, S. B. & MacMillan, D. W. C. The first Suzuki cross-couplings of aryltrimethylammonium salts. *J. Am. Chem. Soc.* **125**, 6046–6047 (2003).
- Zhang, X.-Q. & Wang, Z.-X. Nickel-catalyzed cross-coupling of aryltrimethylammonium triflates and amines. *Org. Biomol. Chem.* **12**, 1448–1453 (2014).
- Tobisu, M., Nakamura, K. & Chatani, N. Nickel-catalyzed reductive and borylative cleavage of aromatic carbon–nitrogen bonds in *N*-aryl amides and carbamates. *J. Am. Chem. Soc.* **136**, 5587–5590 (2014).
- Shiba, T., Kurahashi, T. & Matsubara, S. Nickel-catalyzed decarbonylative alkylation of phthalimides with trimethylsilyl-substituted alkynes. *J. Am. Chem. Soc.* **135**, 13636–13639 (2013).
- Quasdorf, K. W. et al. Suzuki–Miyaura cross-coupling of aryl carbamates and sulfamates: experimental and computational studies. *J. Am. Chem. Soc.* **133**, 6352–6363 (2011).
- Mesganaw, T. et al. Nickel-catalyzed amination of aryl carbamates and sequential site-selective cross-couplings. *Chem. Sci.* **2**, 1766–1771 (2011).
- Hong, X., Liang, Y. & Houk, K. N. Mechanisms and origins of switchable chemoselectivity of Ni-catalyzed C(aryl)–O and C(acyl)–O activation of aryl esters with phosphine ligands. *J. Am. Chem. Soc.* **136**, 2017–2025 (2014).
- Lu, Q., Yu, H. & Fu, Y. Mechanistic study of chemoselectivity in Ni-catalyzed coupling reactions between azoles and aryl carboxylates. *J. Am. Chem. Soc.* **136**, 8252–8260 (2014).
- Xu, H. et al. Key mechanistic features of Ni-catalyzed C–H/C–O biaryl coupling of azoles and naphthalene-2-yl pivalates. *J. Am. Chem. Soc.* **136**, 14834–14844 (2014).
- Yamamoto, T., Ishizu, J., Kohara, T., Komiya, S. & Yamamoto, A. Oxidative addition of aryl carboxylates to nickel(0) complexes involving cleavage of the acyl–oxygen bond. *J. Am. Chem. Soc.* **102**, 3758–3764 (1980).
- Amaike, K., Muto, K., Yamaguchi, J. & Itami, N. Decarbonylative C–H coupling of azoles and aryl esters: unprecedented nickel catalysis and application to the synthesis of muscoride A. *J. Am. Chem. Soc.* **134**, 13573–13576 (2012).

Supplementary Information is available in the online version of the paper.

Acknowledgements We are grateful to Boehringer Ingelheim, DuPont, Bristol-Myers Squibb, the Camille and Henry Dreyfus Foundation, the A. P. Sloan Foundation, the S. T. Li Foundation, the University of California, Los Angeles (UCLA), and the NIH-NIGMS (grant number GM036700 to K.N.H.) for financial support. We are grateful to the NIH (grant number F31 GM101951-02 to N.F.F.N.), the NSF (grant number DGE-1144087 to E.L.B.), the Foote Family (L.H., T.K.S. and X.H.), and the ACS Division of Organic Chemistry (L.H.) for fellowship support. Computations were performed with resources made available by the Extreme Science and Engineering Discovery Environment (XSEDE), which is supported by the NSF (grant number OCI-1053575), as well as the UCLA Institute of Digital Research and Education (IDRE). This work was also supported by shared instrumentation grants from the NSF (grant number CHE-1048804) and the National Center for Research Resources (grant number S10RR025631).

Author Contributions L.H., N.F.F.N., T.K.S., and E.L.B. designed and performed the experiments and analysed the experimental data; X.H., Y.-F.Y., and P.L. designed the computational studies and performed the analysis; K.N.H. and N.K.G. conceived and directed the investigations, and prepared the manuscript with contributions from all authors; all authors contributed to discussions.

Author Information Reprints and permissions information is available at www.nature.com/reprints. The authors declare no competing financial interests. Readers are welcome to comment on the online version of the paper. Correspondence and requests for materials should be addressed to K.N.H. (hok@chem.ucla.edu) and N.K.G. (neilgarg@chem.ucla.edu).

Erosion of organic carbon in the Arctic as a geological carbon dioxide sink

Robert G. Hilton¹, Valier Galy², Jérôme Gaillardet³, Mathieu Dellinger³, Charlotte Bryant⁴, Matt O'Regan⁵, Darren R. Gröcke⁶, Helen Coxall⁵, Julien Bouchez³ & Damien Calmels⁷

Soils of the northern high latitudes store carbon over millennial timescales (thousands of years) and contain approximately double the carbon stock of the atmosphere^{1–3}. Warming and associated permafrost thaw can expose soil organic carbon and result in mineralization and carbon dioxide (CO₂) release^{4–6}. However, some of this soil organic carbon may be eroded and transferred to rivers^{7–9}. If it escapes degradation during river transport and is buried in marine sediments, then it can contribute to a longer-term (more than ten thousand years), geological CO₂ sink^{8–10}. Despite this recognition, the erosional flux and fate of particulate organic carbon (POC) in large rivers at high latitudes remains poorly constrained. Here, we quantify the source of POC in the Mackenzie River, the main sediment supplier to the Arctic Ocean^{11,12}, and assess its flux and fate. We combine measurements of radiocarbon, stable carbon isotopes and element ratios to correct for rock-derived POC^{10,13,14}. Our samples reveal that the eroded biospheric POC has resided in the basin for millennia, with a mean radiocarbon age of $5,800 \pm 800$ years, much older than the POC in large tropical rivers^{13,14}. From the measured biospheric POC content and variability in annual sediment yield¹⁵, we calculate a biospheric POC flux of $2.2^{+1.3}_{-0.9}$ teragrams of carbon per year from the Mackenzie River, which is three times the CO₂ drawdown by silicate weathering in this basin¹⁶. Offshore, we find evidence for efficient terrestrial organic carbon burial over the Holocene period, suggesting that erosion of organic carbon-rich, high-latitude soils may result in an important geological CO₂ sink.

Photosynthesis and the production of organic carbon by the terrestrial biosphere (OC_{biosphere}) is a major pathway of atmospheric CO₂ drawdown. Over millennial timescales, some OC_{biosphere} escapes oxidation and contributes to a transient CO₂ sink in soil^{2,3,17}. Longer-term CO₂ drawdown can be achieved if OC_{biosphere} is eroded, transferred by rivers and buried in sedimentary basins^{9,10,18,19}. Burial of OC_{biosphere} represents a major geological CO₂ sink (and source of oxygen, O₂) alongside the chemical weathering of silicate minerals by carbonic acid, coupled to carbonate precipitation^{16,19}. These fluxes negate CO₂ emissions from the solid Earth²⁰ and from oxidation of rock-derived OC²¹, contributing to the long-term regulation of global climate^{19,20}. Physical erosion is thought to play an important part in this OC_{biosphere} transfer because it controls the rate of biospheric particulate organic carbon (POC_{biosphere}) export by rivers^{22,23} and influences sediment accumulation and the efficiency of OC burial^{10,18,24}.

In the northern high latitudes, large amounts of OC_{biosphere} are stored in soil^{1,2}. The upper three metres of soil in the region of northern circumpolar permafrost are estimated to contain $1,035 \pm 150$ petagrams of carbon (PgC), approximately double the CO₂ content of the pre-industrial atmosphere^{2,17}. Many of these soils accumulated during the retreat of large continental ice sheets following the Last Glacial Maximum, with a peak expansion between 12,000 and 8,000

calibrated years before present (BP)²⁵, where 'present' is 1950, and the OC_{biosphere} can be thousands of years old⁸. This vast carbon reservoir is located in a region sensitive to environmental change over glacial–interglacial timescales²⁵ and to warming over the coming century³. Much focus has been placed on its potential to become a CO₂ source^{3–6,8}. However, geological CO₂ drawdown by POC_{biosphere} erosion at high latitudes has remained poorly constrained⁹.

Here we sample POC carried by the major rivers in the Mackenzie basin and investigate its fate using an offshore sediment core extending over the Holocene (Extended Data Fig. 1). The Mackenzie River is the largest source of sediment to the Arctic Ocean^{11,12,15} and erosion of mountainous topography in the basin results in a high sediment discharge, similar to the combined total of 16 Eurasian rivers draining to the Arctic Ocean^{11,15}. We collected river depth profiles to characterize

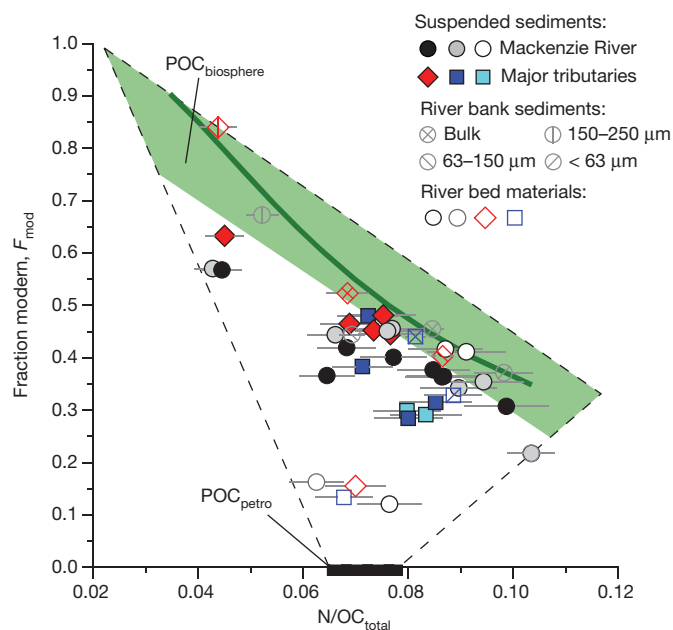


Figure 1 | Source of POC in the Mackenzie River basin. Radiocarbon activity of POC (F_{mod}) versus the nitrogen to organic carbon ratio (N/OC_{total}) of suspended sediments from the Mackenzie River (circles) at the delta (black), at Tsiigehtchic (grey) and at Norman Wells (white) and from its major tributaries the Liard (diamond), the Peel (dark blue square) and the Arctic Red (light blue square). River depth profiles collected in 2010 and 2011 suspended load (filled symbols), river bed materials (open symbols) and sieved bank samples (collected in 2009, sizes shown on figure) are shown with analytical errors (2 standard deviations, s.d.) as grey lines if larger than the data points. The dashed line shows the compositions expected by mixing rock-derived POC_{petro} (black rectangle) and POC_{biosphere} (green shading). The solid green line is the trend from a peat core in western Canada²⁷.

¹Department of Geography, Durham University, South Road, Durham DH1 3LE, UK. ²Department of Marine Chemistry and Geochemistry, Woods Hole Oceanographic Institution, 266 Woods Hole Road, Woods Hole, Massachusetts 02543-1050, USA. ³Institut de Physique du Globe de Paris, Sorbonne Paris Cité, Université Paris Diderot, UMR 7154 CNRS, F-75005 Paris, France. ⁴NERC Radiocarbon Facility, East Kilbride G75 0QF, UK. ⁵Department of Geological Sciences, Stockholm University, Stockholm, SE-10691, Sweden. ⁶Department of Earth Sciences, Durham University, South Road, Durham DH1 3LE, UK. ⁷Université Paris-Sud, Laboratoire GEOPS, UMR 8148-CNRS, Orsay, F-91405, France.

POC across the range of grain sizes carried by large rivers^{13,14,26} at the main conduit for sediment export to the Arctic Ocean in the Mackenzie delta, at key points on the Mackenzie River and from its major tributaries (Extended Data Fig. 1). To investigate temporal variability of POC composition, river depth profiles were collected shortly after ice break-up at the high/rising stage (June 2011) and during the falling stage (September 2010), while river surface and bank samples were collected in June 2009.

To correct for rock-derived, 'petrogenic' POC ($\text{POC}_{\text{petro}}$), likely to be important in the Mackenzie basin^{7,26}, we combine measurements of radiocarbon (^{14}C , reported as the 'fraction modern', F_{mod}), total OC content ($[\text{OC}_{\text{total}}]$), stable isotopes of OC ($\delta^{13}\text{C}_{\text{org}}$), the nitrogen to OC ratio ($\text{N}/\text{OC}_{\text{total}}$) and the aluminium to OC ratio ($\text{Al}/\text{OC}_{\text{total}}$), all of which allow us to assess the age and concentration of $\text{POC}_{\text{biosphere}}$ (see Methods)^{7,10,13,14,22,23}. Published ^{14}C ages of surface samples from the Mackenzie River^{4,7} ($n = 5$) vary between 6,010 yr and 10,000 yr but the ^{14}C depletion caused by $\text{POC}_{\text{petro}}$ versus aged $\text{POC}_{\text{biosphere}}$ has not been assessed. We also examine the hydrodynamic behaviour of POC, using the aluminium-to-silicon ratio (Al/Si) ratio as a proxy of sediment grain size and mineral composition²⁶.

We find that river POC is depleted in ^{14}C throughout the Mackenzie basin (Extended Data Table 1). F_{mod} values range between 0.28 (^{14}C age $10,106 \pm 42$ yr) and 0.63 (^{14}C age $3,675 \pm 36$ yr) in the suspended load ($n = 27$) and between 0.12 (^{14}C age $17,002 \pm 84$ yr) and 0.16 (^{14}C age $14,601 \pm 64$ yr) in the river bed materials ($n = 4$). To investigate the cause of this ^{14}C depletion, we examine the $\text{N}/\text{OC}_{\text{total}}$ ratio. Degradation of organic matter in soils can increase the relative N abundance^{6,27}, differentiating degraded $\text{POC}_{\text{biosphere}}$ (high $\text{N}/\text{OC}_{\text{total}}$) from young, fresh $\text{POC}_{\text{biosphere}}$ (low $\text{N}/\text{OC}_{\text{total}}$). Suspended load samples display a negative relationship between $\text{N}/\text{OC}_{\text{total}}$ and F_{mod} (Fig. 1), similar to measurements from a peat core in the Mackenzie basin²⁷ away from permafrost. There, $\text{N}/\text{OC}_{\text{total}}$ ratios increased with ^{14}C age (1,250–10,200 yr) and soil depth (0–3 m). In contrast, river bed materials have lower F_{mod} values and a relatively restricted range of $\text{N}/\text{OC}_{\text{total}}$ values and are distinct from suspended load (Fig. 1). A dominance of $\text{POC}_{\text{petro}}$ in bed materials^{10,14} with a $\text{N}/\text{OC}_{\text{total}}$ ratio of about 0.07 can explain their composition.

Together, the F_{mod} and $\text{N}/\text{OC}_{\text{total}}$ values suggest that POC in the Mackenzie River is a mixture of $\text{POC}_{\text{petro}}$ and $\text{POC}_{\text{biosphere}}$, itself varying in ^{14}C age from 'modern' to about 8,000 yr old (Fig. 1). The $\delta^{13}\text{C}_{\text{org}}$ values and $\text{Al}/\text{OC}_{\text{total}}$ ratios support this inference (Extended Data Fig. 2). Using an endmember mixing analysis^{10,13} we quantify $\text{POC}_{\text{petro}}$ content of sediments (Methods) and find that suspended

load at the Mackenzie River delta is dominated by $\text{POC}_{\text{biosphere}}$ ($\sim 70\%$ – 90% of the total POC). Having corrected for $\text{POC}_{\text{petro}}$, we investigate the source of $\text{POC}_{\text{biosphere}}$ by estimating its average ^{14}C age. This varies from $3,030 \pm 150$ yr to $7,900 \pm 400$ yr (Extended Data Fig. 3) with an average ^{14}C age of $\text{POC}_{\text{biosphere}} = 5,800 \pm 800$ yr (± 2 standard errors, s.e.) in suspended sediments of the Mackenzie River delta. These values are older than estimates of $\text{POC}_{\text{biosphere}}$ age from the Amazon River (1,120–2,750 yr)¹⁴ and Ganges River (1,600–2,960 yr)¹³. The ages reflect mixing of young, fresh $\text{POC}_{\text{biosphere}}$ (present in each of these large river basins) with an older $\text{POC}_{\text{biosphere}}$ in the Mackenzie basin (Fig. 1), likely to consist of peat soils that expanded between 9,000 yr and 8,000 yr (^{14}C age)²⁵. $\text{POC}_{\text{biosphere}}$ can be eroded by slumping and landsliding on river banks, across deep soil profiles^{4,7}. Sections of the landscape that have discontinuous permafrost and those undergoing permafrost degradation²⁸ may be important sources of aged $\text{POC}_{\text{biosphere}}$, in addition to river banks, which are undercut during peak water discharge following ice break-up¹⁵. Our samples suggest that erosion and fluvial transfer of millennial-aged $\text{POC}_{\text{biosphere}}$ is extensive in the Mackenzie basin.

Once in the river, $\text{POC}_{\text{biosphere}}$ is sorted with river depth, revealed by the Al/Si ratio (Fig. 2b) a proxy for grain size²⁶. In bed materials with low Al/Si , $\text{POC}_{\text{petro}}$ dominates (Fig. 1) and leads to low F_{mod} values (Fig. 2c). Just above the river bed, during the two sampling campaigns, coarse suspended sediments (low Al/Si) hosted the youngest, least degraded $\text{POC}_{\text{biosphere}}$ (low N/C), leading to a large contrast in ^{14}C age from the bed materials. Towards the river surface, older, more degraded $\text{POC}_{\text{biosphere}}$ appears to become more dominant, and is transported with fine sediment and clays (high Al/Si)²⁶. The large contribution of degraded, very old $\text{POC}_{\text{biosphere}}$ ($>5,000$ yr) in the Mackenzie River contrasts with large tropical rivers where organic matter turnover in terrestrial ecosystems is more rapid (Fig. 2c)^{13,14}.

To assess how erosion in the Mackenzie River may lead to long-term CO_2 drawdown, we estimate $\text{POC}_{\text{biosphere}}$ discharge. River depth profiles collected at the high and falling stages suggest that the $[\text{OC}_{\text{total}}]$ of the suspended sediment load did not vary systematically with sediment grain size (Extended Data Fig. 4). Future work should seek to assess temporal variability in POC content and composition. Our data suggest that changes in grain size with water discharge (Fig. 2b) could be important in setting the variability of $\text{POC}_{\text{biosphere}}$ age carried by the river (Fig. 2c). The $[\text{OC}_{\text{total}}]$ values at the Mackenzie delta were $1.6 \pm 0.5\%$ ($n = 8$, $\pm 1\sigma$), which were similar to the mean measured in the Mackenzie delta in June–July 1987 of 1.4 ± 0.2 ($n = 10$)¹². Although our sample set is modest in size, it helps us to better constrain

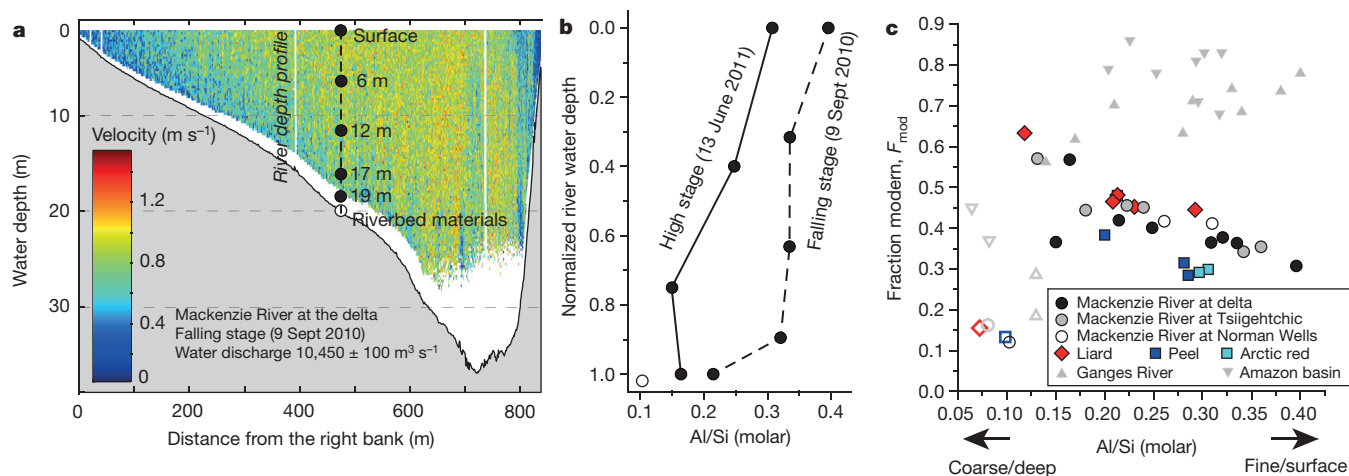


Figure 2 | Transport of POC in the Mackenzie River. **a**, River depth profile collection from the Mackenzie River delta during the falling stage, with Acoustic Doppler Current Profiler data used to determine channel geometry, water velocity and water discharge. **b**, Aluminium to silicon ratio (Al/Si), a proxy for sediment grain size²⁶, with water depth normalized to maximum

depth. Coarser materials are carried throughout the profile during the high stage. **c**, Radiocarbon activity of POC (F_{mod}) versus Al/Si for the Mackenzie basin (this study, symbols as in Fig. 1), Amazon River¹⁴, and Ganges River^{10,13}. River suspended load (filled symbols) and river bed materials (open symbols) are distinguished. Analytical errors (2 s.d.) are smaller than the data points.

the range of POC contents in the suspended load of the Mackenzie River. In addition, our endmember mixing analysis allows us to provide the first estimates of $[OC_{\text{biosphere}}]$, which varies between $0.7 \pm 0.1\%$ and $2.4 \pm 0.2\%$.

To estimate $POC_{\text{biosphere}}$ discharge, we use the most complete data set of annual sediment discharge to the Mackenzie delta (1974–1994)¹⁵, which ranged from 81 teragrams per year ($Tg\ yr^{-1}$) to $224\ Tg\ yr^{-1}$. A Monte Carlo approach is used to account for the modest sample size by using the full measured variability in both $[OC_{\text{biosphere}}]$ and annual sediment discharge (Methods). We estimate $POC_{\text{biosphere}}$ discharge to be $2.2^{+1.3}_{-0.9}$ teragrams of carbon per year ($Tg\ C\ yr^{-1}$), which is sustainable over 1,000 to 10,000 years, depleting the soil carbon stock by $\sim 0.006\%$ per year (Methods). We estimate the POC_{petro} discharge to be $0.4^{+0.1}_{-0.1}\ Tg\ C\ yr^{-1}$. These estimates do not account for ice-covered conditions, when $<10\%$ of the annual sediment discharge is conveyed¹². Nevertheless, our estimate of $POC_{\text{biosphere}}$ discharge is greater than the combined POC discharge of around $1.9\ Tg\ C\ yr^{-1}$ by the major Eurasian Arctic rivers (Ob, Yenisei, Lena, Indigirka and Koyma)^{11,28} which cover approximately 8.6 million square kilometres. According to the available measurements, the Mackenzie River dominates the input of $POC_{\text{biosphere}}$ to the Arctic Ocean.

The mobilization of millennial-aged $POC_{\text{biosphere}}$ from soils at high latitudes has been viewed as a short-term source to the atmosphere if decomposition releases greenhouse gases (CH_4 and CO_2)^{2–6,8}. However, if $POC_{\text{biosphere}}$ escapes oxidation during river transport and is buried offshore, erosion acts as a long-term CO_2 sink^{10,18,20,23}. Offshore, aged $POC_{\text{biosphere}}$ from the Mackenzie River (Fig. 1) can explain the ^{14}C depletion and $\delta^{13}C$ of bulk organic matter, and old ^{14}C ages of terrestrial plant wax compounds (up to 20,000 yr) in surface sediments of the Beaufort Sea^{7,29,30}. We provide new evidence that terrestrial POC is buried efficiently offshore and accumulates in sediments over 10,000 years. Benthic foraminifera ^{14}C ages in a borehole located at the head of the Mackenzie trough (MTW01) indicate that 21 m of sediment have accumulated since $9,183^{+125}_{-156}$ calibrated years BP, suggesting a high sedimentation rate during the Holocene of 2.7 ± 0.1 m per thousand years (Extended Data Table 2, Methods). These marine sediments have $[OC_{\text{total}}]$ values similar to those measured in the Mackenzie River in both the $<63\ \mu m$ (1.5% to 1.7%) and $>63\ \mu m$ (1.1% to 1.4%) size fractions (Fig. 3). Their N/OC_{total} and $\delta^{13}C_{\text{org}}$ values suggest that they are dominated by terrestrial POC with minor marine OC addition (Extended Data Fig. 5). We use the change in OC_{total}/Al ratios offshore to estimate OC burial efficiencies to have been $65 \pm 27\%$ or more over the Holocene at this site (Methods). Rapid sediment accumulation and low temperature are likely to promote high POC burial efficiency^{18,23,29}. Also, the fluvial transport dynamics of $POC_{\text{biosphere}}$ may promote burial (Fig. 2c). The oldest, most-degraded $POC_{\text{biosphere}}$ is transported with clays²⁶, whose association with organic matter may enhance burial efficiency¹⁸, while the youngest, least-degraded $POC_{\text{biosphere}}$ is carried near the river bed at the highest sediment concentrations. Our findings suggest that erosion and riverine transfer at high latitudes can lead to the long-term preservation of terrestrial POC in marine sediments (Fig. 3).

Erosion of high latitude soils and riverine export of $POC_{\text{biosphere}}$ may represent an important geological CO_2 sink. Our estimate of the modern day $POC_{\text{biosphere}}$ discharge of $2.2^{+1.3}_{-0.9}\ Tg\ C\ yr^{-1}$ in the Mackenzie River may be refined by additional temporal sampling. However, it is three times the modern rates of CO_2 drawdown by weathering of silicate minerals by carbonic acid in the Mackenzie River¹⁶, at around $0.7\ Tg\ C\ yr^{-1}$. Preservation of POC offshore (Fig. 3) suggests that the erosion of high-latitude soils, riverine $POC_{\text{biosphere}}$ transport and export to the ocean acts as the largest geological CO_2 sink operating in the Mackenzie basin. We note that these longer-term fluxes are lower than estimates of greenhouse gas emissions from high-latitude soils in permafrost zones, owing to projected warming over the coming century^{3,5,6,31}. While these fluxes remain uncertain, recent work³¹ has proposed emissions of around $1\text{--}2\ Pg\ C\ yr^{-1}$ which equate to a yield of

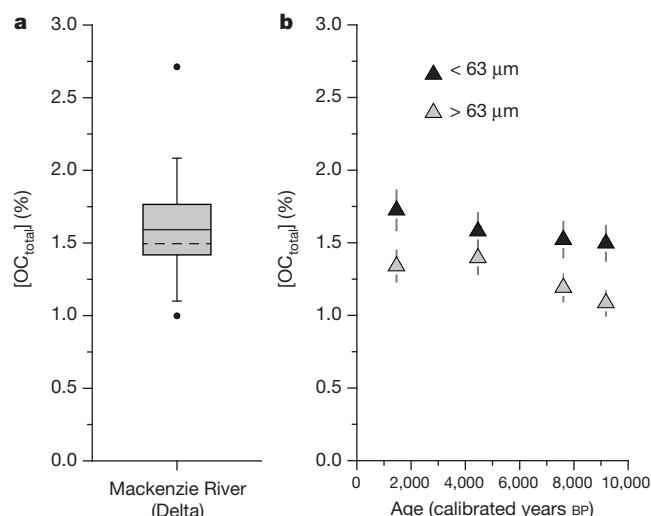


Figure 3 | Fate of particulate organic carbon offshore. **a**, Percentage organic carbon concentration of suspended sediments in the Mackenzie River delta ($n = 8$) where solid line and grey box show the mean \pm s.e., whiskers show \pm s.d. and the circles indicate the minimum and maximum values. **b**, Percentage $[OC]_{\text{total}}$ in sediments $<63\ \mu m$ and $>63\ \mu m$ from core MTW01 in the Mackenzie trough (Extended Data Fig. 1) for depths dated by the ^{14}C activity of mixed benthic foraminifera (Methods), where whiskers show the analytical error if larger than the data point size.

~ 70 tonnes of carbon per square kilometre per year ($t\ C\ km^{-2}\ yr^{-1}$) over 17.8×10^8 square kilometres of soils in permafrost zones. This estimate of accelerated release of CO_2 due to anthropogenic warming³¹ is more rapid than the natural geological drawdown fluxes, of which we estimate a value for $POC_{\text{biosphere}}$ of $2\text{--}5\ t\ C\ km^{-2}\ yr^{-1}$ for the Mackenzie basin (Methods). Over longer time periods, we postulate that this geological CO_2 sink may be sensitive to climate conditions in the Arctic. The carbon transfer can operate when high latitudes host substantial $POC_{\text{biosphere}}$ stocks in soil, and when rivers can erode and transfer sediments to the Arctic Ocean. Over the last million years, the $POC_{\text{biosphere}}$ transfer is likely to have been enhanced during interglacials²⁵ (Fig. 3), whereas during glacial conditions, lower soil $POC_{\text{biosphere}}$ stocks and extensive ice-sheet coverage suggest that $POC_{\text{biosphere}}$ erosion may have been suppressed. We propose that erosion of terrestrial $POC_{\text{biosphere}}$ by large rivers draining the Arctic could be important in long-term CO_2 drawdown^{19,20}, coupling the carbon cycle to climatic conditions at high latitudes.

Online Content Methods, along with any additional Extended Data display items and Source Data, are available in the online version of the paper; references unique to these sections appear only in the online paper.

Received 28 August 2014; accepted 3 June 2015.

- Gorham, E. Northern peatlands: Role in the carbon cycle and probable responses to climatic warming. *Ecol. Appl.* **1**, 182–195 (1991).
- Hugelius, G. *et al.* Estimated stocks of circumpolar permafrost carbon with quantified uncertainty ranges and identified data gaps. *Biogeosciences* **11**, 6573–6593 (2014).
- Schuur, E. A. G. *et al.* Vulnerability of permafrost carbon to climate change: Implications for the global carbon cycle. *Bioscience* **58**, 701–714 (2008).
- Guo, L., Ping, C.-L. & Macdonald, R. W. Mobilization pathways of organic carbon from permafrost to arctic rivers in a changing climate. *Geophys. Res. Lett.* **34**, L13603 (2007).
- MacDougall, A. H., Avis, C. A. & Weaver, A. L. Significant contribution to climate warming from the permafrost carbon feedback. *Nature Geosci.* **5**, 719–721 (2012).
- Schädel, C. *et al.* Circumpolar assessment of permafrost C quality and its vulnerability over time using long-term incubation data. *Glob. Change Biol.* **20**, 641–652 (2014).
- Goñi, M. A., Yunker, M. B., Macdonald, R. W. & Eglinton, T. I. The supply and preservation of ancient and modern components of organic carbon in the Canadian Beaufort Shelf of the Arctic Ocean. *Mar. Chem.* **93**, 53–73 (2005).
- Vonk, J. E. *et al.* Activation of old carbon by erosion of coastal and subsea permafrost in Arctic Siberia. *Nature* **489**, 137–140 (2012).

9. Vonk, J. E. & Gustafsson, O. Permafrost-carbon complexities. *Nature Geosci.* **6**, 675–676 (2013).
10. Galy, V. *et al.* Efficient organic carbon burial in the Bengal fan sustained by the Himalayan erosional system. *Nature* **450**, 407–410 (2007).
11. Stein, R. & Macdonald, R. W. *The Organic Carbon Cycle in the Arctic Ocean* (Springer, 2004).
12. Macdonald, R. W. *et al.* A sediment and organic carbon budget for the Canadian Beaufort Shelf. *Mar. Geol.* **144**, 255–273 (1998).
13. Galy, V. & Eglinton, T. I. Protracted storage of biospheric carbon in the Ganges-Brahmaputra basin. *Nature Geosci.* **4**, 843–847 (2011).
14. Bouchez, J. *et al.* Source, transport and fluxes of Amazon River particulate organic carbon: insights from river sediment depth-profiles. *Geochim. Cosmochim. Acta* **133**, 280–298 (2014).
15. Carson, M. A., Jasper, J. N. & Conly, F. M. Magnitude and sources of sediment input to the Mackenzie Delta, Northwest Territories, 1974–94. *Arctic* **51**, 116–124 (1998).
16. Gaillardet, J., Dupré, B., Louvat, P. & Allegre, C. A. Global silicate weathering and CO₂ consumption rates deduced from the chemistry of large rivers. *Chem. Geol.* **159**, 3–30 (1999).
17. Sundquist, E. T. & Visser, K. in *Treatise on Geochemistry* (ed. Schlesinger, W. H.), Vol. 8 *Biogeochemistry* 425–472 (Elsevier-Pergamon, 2004).
18. Blair, N. E. & Aller, R. C. The fate of terrestrial organic carbon in the marine environment. *Annu. Rev. Mar. Sci.* **4**, 17.1–17.23 (2012).
19. Hayes, J. M., Strauss, H. & Kaufman, A. J. The abundance of ¹³C in marine organic matter and isotopic fractionation in the global biogeochemical cycle of carbon during the past 800 Ma. *Chem. Geol.* **161**, 103–125 (1999).
20. Berner, R. A. Atmospheric CO₂ levels over Phanerozoic time. *Science* **249**, 1382–1386 (1990).
21. Hilton, R. G., Gaillardet, J., Calmels, D. & Birk, J. L. Geological respiration of a mountain belt revealed by the trace element rhenium. *Earth Planet. Sci. Lett.* **403**, 27–36 (2014).
22. Hilton, R. G. *et al.* Climatic and geomorphic controls on the erosion of terrestrial biomass from subtropical mountain forest. *Glob. Biogeochem. Cycles* **26**, <http://dx.doi.org/10.1029/2012GB004314> (2012).
23. Galy, V., Peucker-Ehrenbrink, B. & Eglinton, T. Global carbon export from the terrestrial biosphere controlled by erosion. *Nature* **521**, 204–207 (2015).
24. Burdige, D. J. Burial of terrestrial organic matter in marine sediments: a re-assessment. *Glob. Biogeochem. Cycles* **19**, GB4011 (2005).
25. MacDonald, G. M. *et al.* Rapid development of the circumarctic peatland complex and atmospheric CH₄ and CO₂ variations. *Science* **314**, 285–288 (2006).
26. Dellinger, M. *et al.* Lithium isotopes in large rivers reveal the cannibalistic nature of modern continental weathering and erosion. *Earth Planet. Sci. Lett.* **401**, 359–372 (2014).
27. Kuhry, P. & Vitt, D. H. Fossil carbon/nitrogen ratios as a measure of peat decomposition. *Ecology* **77**, 271–275 (1996).
28. Feng, X. *et al.* Differential mobilization of terrestrial carbon pools in Eurasian Arctic river basins. *Proc. Natl Acad. Sci. USA* **110**, 14168–14173 (2013).
29. Goñi, M. A. *et al.* Distribution and sources of organic matter in surface marine sediments across the North American Arctic margin. *J. Geophys. Res.* **118**, 4017–4035 (2013).
30. Drenzek, N. J., Montluçon, D. B., Yunker, M. B., Macdonald, R. W. & Eglinton, T. I. Constraints on the origin of sedimentary organic carbon in the Beaufort Sea from coupled molecular ¹³C and ¹⁴C measurements. *Mar. Chem.* **103**, 146–162 (2007).
31. Schuur, E. A. G. *et al.* Climate change and the permafrost carbon feedback. *Nature* **520**, 171–179 (2015).

Acknowledgements Radiocarbon measurements were funded by the Natural Environment Research Council (NERC), UK (Allocation 1611.0312) to R.G.H. and C.B. Fieldwork was funded by CNRS (OXYMORE and CANNIBALT) to J.G. and R.G.H., the Woods Hole Oceanographic Institution Arctic Research Initiative to V.G. and an Early Career Research Grant by the British Society for Geomorphology to R.G.H. V.G. was supported by the US National Science Foundation (OCE-0928582) and H.C. by a Royal Society University Fellowship. The research was carried out under Scientific Research Licence No. 14802 issued by the Aurora Research Centre, who we thank for logistical support (in particular D. Ross and J. Gareis). We also thank I. Peters for preparation of offshore borehole samples, C. Johnson, X. Philippon and M. Bollard for analytical assistance, E. Tipper and K. Hilton for field assistance and discussions and D. Ofukany, G. Lennie, R. Wedel and R. Pilling of Environment Canada for loan of equipment.

Author Contributions R.G.H., V.G. and J.G. conceived the study and R.G.H., J.B., D.C., V.G. and M.D. designed the fieldwork and collected the river samples. M.O. and H.C. collected sediment and carbonate data from the offshore borehole. R.G.H., V.G., M.D., C.B. and D.G. processed the samples and carried out the geochemical analyses. R.G.H. wrote the manuscript with input from all co-authors.

Author Information Reprints and permissions information is available at www.nature.com/reprints. The authors declare no competing financial interests. Readers are welcome to comment on the online version of the paper. Correspondence and requests for materials should be addressed to R.G.H. (r.g.hilton@durham.ac.uk).

METHODS

River sample collection and preparation. River depth-profiles from September 2010 and June 2011 (Extended Data Table 1) were used to collect the full range of erosion products and POC in large river systems, taking advantage of the hydrodynamic sorting of particles^{10,13,14,26}. At each sampling site (Fig. 1), channel depth, water velocity and instantaneous water discharge were measured by two or more transects with an Acoustic Doppler Current Profiler (ADCP Rio Grande 600 kHz) before each depth profile was collected at a single point (± 10 m) in the middle of the channel. On the boat, each sample (~ 7 –8 litres) was evacuated into a clean bucket and stored in sterilized plastic bags and the procedure was repeated depending upon the total water depth. Each bag was weighed to determine the sampled volume, then the entire sample was filtered within 24 h using pre-cleaned Teflon filter units through 90 mm diameter 0.2 μ m PES (polyethersulfone) filters^{13,26}. Suspended sediment was immediately rinsed from the filter using filtered river water into clean amber-glass vials and kept cool. River bed materials were collected at the base of the depth transects from the boat, using a metal bucket as a dredge, and were decanted to a sterile bag. Riverbank deposits (June 2009) were collected from fresh deposits close to the channel (Extended Data Table 3) and sieved at 250 μ m, 150 μ m and 63 μ m to investigate the sorting of POC³². All sediments were freeze-dried upon return to laboratories within two weeks, weighed and homogenized in an agate grinder.

Offshore borehole sample preparation. Marine sediment samples containing benthic foraminifera were obtained from the upper 22 m Holocene sequence of an 85.1-m MTW01 borehole³³ located at 69° 20' 53" N, 137° 59' 13" in 45-m water depth in the Mackenzie trough (Extended Data Fig. 1). Drilled by the Geological Survey of Canada in 1984, the core is currently archived at the GSC-Atlantic core repository. To isolate foraminifera, sediment samples were disaggregated over a sieve with <38 μ m mesh using deionized water. On the basis of microfossil counts, four samples were selected with sufficient specimens for radiocarbon dating.

Geochemical analyses. For the river-suspended sediments and core samples for organic carbon analyses, inorganic carbon was removed using a HCl fumigation technique to avoid the loss of a component of POC that is known to occur during a HCl leach³⁴. A method adapted to ensure full removal of detrital dolomite was used³⁵. In summary, samples were placed in an evacuated desiccator containing about 50 ml 12 N HCl in an oven at between 60 °C and 65 °C for 60–72 h. Samples were then transferred to another vacuum desiccator charged with indicating silica gel, pumped down again and dried to remove HCl fumes. River sediment samples were analysed for organic carbon concentration [OC_{total}] on acidified aliquots and percentage nitrogen concentration [N] on non-acidified aliquots by combustion at 1,020 °C in O_2 using a Costech elemental analyser in Durham. For river depth profile samples, acidified aliquots were prepared to graphite at the NERC Radiocarbon Facility of 1–2 mg C for each sample and standard and ^{14}C was measured by Accelerator Mass Spectrometry at the Scottish Universities Environmental Research Centre and reported as the fraction modern F_{mod} by standard protocol³⁶. Process standards (96H humin) and background materials (bituminous coal) were taken through all stages of sample preparation and ^{14}C analysis and were within 2 σ uncertainty of expected values. Stable isotopes of POC ($\delta^{13}C_{org}$) were measured by dual-inlet isotope ratio mass spectrometer (IRMS) on an aliquot of the same CO_2 . These measurements were consistent with $\delta^{13}C_{org}$ measurements made by an elemental analyser IRMS, normalized to measured standard values ($n = 7$) spanning >30% and long-term analytical precision of 0.2‰. Riverbank samples from 2009 were analysed by similar procedures at the National Ocean Sciences Accelerator Mass Spectrometry Facility (NOSAMS) at Woods Hole Oceanographic Institution.

Mixed benthic foraminifera samples chosen from the MTW01 core were analysed at NOSAMS for ^{14}C analyses. Samples were rinsed and no pre-treatments were used. The samples were directly hydrolysed with strong acid (H_3PO_4) to convert the carbon in the sample to CO_2 . Calibration of the ^{14}C dates was performed using CALIB (version 7.1)³⁷. All ^{14}C dates were normalized to a $\delta^{13}C$ of -25 ‰ versus VPDB (<http://intcal.qub.ac.uk/calib/>). Foraminifera dates were calibrated using the MARINE13 data set³⁸, with a reservoir age correction (ΔR) of 335 ± 85 yr (Extended Data Table 2). The ΔR value is based on a recent reanalysis of ages from 24 living molluscs collected before 1956 from the northwestern Canadian Arctic Archipelago³⁹. This calibration set does not include specimens from the Beaufort Sea and as such provides only a best available estimate for ΔR in the Mackenzie trough.

Endmember mixing model. The F_{mod} , N/OC_{total} (Fig. 1), $\delta^{13}C_{org}$ values and Al/OC_{total} values (Extended Data Fig. 2) are consistent with a mixing of POC_{petro} and $POC_{biosphere}$ dominating the bulk geochemical composition of river POC. Autochthonous sources are not an important component based on those measured values, which is consistent with the turbid nature of the Mackenzie River (mean suspended sediment concentration of ~ 300 –400 mg per litre), meaning

that like other turbid river systems (for example, the Ganges–Brahmaputra) light penetration is minimal. A mixture of POC_{petro} and $POC_{biosphere}$ can be described by the governing equations^{10,13,32},

$$f_{biosphere} + f_{petro} = 1 \quad (1)$$

$$f_{biosphere} \times \theta_{biosphere} + f_{petro} \theta_{petro} = \theta_{sample} \quad (2)$$

where $f_{biosphere}$ and f_{petro} are the fractions of POC derived from biospheric and petrogenic sources, respectively. θ_{sample} is the measured composition (for example, F_{mod}) of a river POC sample, and $\theta_{biosphere}$ and θ_{petro} are the compositions of biospheric and petrogenic sources. To quantify the f_{petro} in each sample we use the aluminium (Al) to OC_{total} concentration ratio in river sediments. At each locality, a linear trend between F_{mod} and Al/OC_{total} (Extended Data Fig. 2b) can be explained by a mixture of an Al-rich, OC-poor material (rock fragments containing POC_{petro}) with Al-poor, OC-rich material (soils and vegetation debris as $POC_{biosphere}$). Taking advantage of the fact that the POC_{petro} has $F_{mod} \approx 0$ (unmeasurable above the background ^{14}C content), the intercept at $F_{mod} = 0$ gives an estimate of the Al/OC_{total} values and associated uncertainty of the sedimentary rock endmember. To estimate the average concentration of OC_{petro} of bedrocks in each basin, we use the Al concentration of river bed materials as a proxy for the Al concentration in the bedrocks²⁶ and the Al/OC_{total} value at $F_{mod} \approx 0$. Following previous work in large rivers, we then assume that the OC_{petro} is well mixed in the water column and has a relatively constant [OC_{petro}] value^{10,13,14}. This method may overestimate f_{petro} if OC_{petro} has been more extensively oxidized in fine-grained weathering products carried in the suspended load²¹. f_{petro} is quantified using [OC_{petro}] and measured [OC_{total}].

The mixing analysis returns a [OC_{petro}] = $0.12 \pm 0.03\%$ ($\pm 2\sigma$) in the Liard River and Mackenzie River at Tsiigehtchic, higher values in the Peel River [OC_{petro}] = $0.63 \pm 0.30\%$, with the Mackenzie River at the delta having an intermediate value of [OC_{petro}] = $0.29 \pm 0.05\%$. This is consistent with the known presence of POC_{petro} -bearing sedimentary rocks in the Mackenzie River basin and high OC_{total} contents of bedrocks in the upper Peel River basin and Mackenzie mountains³⁹. To quantify the average ^{14}C age of $POC_{biosphere}$ in each sample, equations (1) and (2) can be solved for $\theta_{biosphere}$ using the f_{petro} value and assumed $F_{mod} = 0$ of POC_{petro} . The uncertainty mainly derives from that on f_{petro} and [OC_{total}] and has been propagated through the calculations.

To test whether the mixing of $POC_{biosphere}$ and POC_{petro} can describe the composition of the suspended load samples, we predict the $\delta^{13}C_{org}$ measurements that were not used in the mixing analysis. The calculated f_{petro} values and end-member values of -26.2 ± 0.5 ‰ for $POC_{biosphere}$ and -28.6 ± 0.5 ‰ for POC_{petro} were used, informed by measurements of bedrocks⁴⁰ and vegetation and soil in the basin⁴¹. The mixing model (equation (2)) can robustly predict the $\delta^{13}C_{org}$ differences between the Peel and Liard rivers, and between suspended load and bed material $\delta^{13}C_{org}$ values (Extended Data Fig. 2c), supporting a mixing control on the variables.

Mackenzie River POC discharge. To quantify the discharge of POC we need to account for the variability in suspended sediment discharge and the variability in the $POC_{biosphere}$ and POC_{petro} content of sediments in the basin. We use the longest, most complete quantification of sediment flux by the Mackenzie River from 1974–1994 (ref. 15), which has an annual average 127 ± 40 Tg yr⁻¹ ($\pm 1\sigma$). Annual sediment yield varied from 81 Tg yr⁻¹ to 224 Tg yr⁻¹. Although the POC samples were not collected at the same time period, our measurements of [OC_{total}] at the delta (mean $1.6 \pm 0.5\%$; $n = 8$, $\pm 1\sigma$) do not vary systematically between the falling and high stage (Extended Data Fig. 4) and are consistent with available data from samples¹² collected in 1987 (1.4 ± 0.2 , $n = 10$).

While future work should aim to constrain the variability in POC composition further, these observations suggest that temporal variability may be less important than the potential variability in [OC_{total}] with depth at a given time, where we find [OC_{total}] values can range from 1.0% to 2.7%. We use our measured range of [$OC_{biosphere}$] and [OC_{petro}] values and the full range of annual sediment yields¹⁵ to quantify $POC_{biosphere}$ and POC_{petro} discharge and the associated uncertainty using a Monte Carlo approach. Over 100,000 simulations, we use a 'flat' probability for the range of values for both variables (that is, equal probability of all measured values). This allows us to fully explore the range of estimates given the available measurements. Future work seeking to expand the number of [$OC_{biosphere}$] measurements to assess its flux-weighted mean and variability, while assessing temporal variability in more detail, will allow POC discharge estimates and their uncertainty to be refined. $POC_{biosphere}$ ($2.2^{+1.3}_{-0.9}$ Tg C yr⁻¹) and POC_{petro} ($0.4^{+0.1}_{-0.1}$ Tg C yr⁻¹) discharges are reported as the median (50%) ± 1 s.d. Over the sediment source areas of the Mackenzie (downstream of the Great Slave Lake¹⁵) of 774,200 km², these equate to yields of $POC_{biosphere} = 2.9^{+1.7}_{-1.1}$ t C km⁻² yr⁻¹ and $POC_{petro} = 0.6^{+0.2}_{-0.2}$ t C km⁻² yr⁻¹.

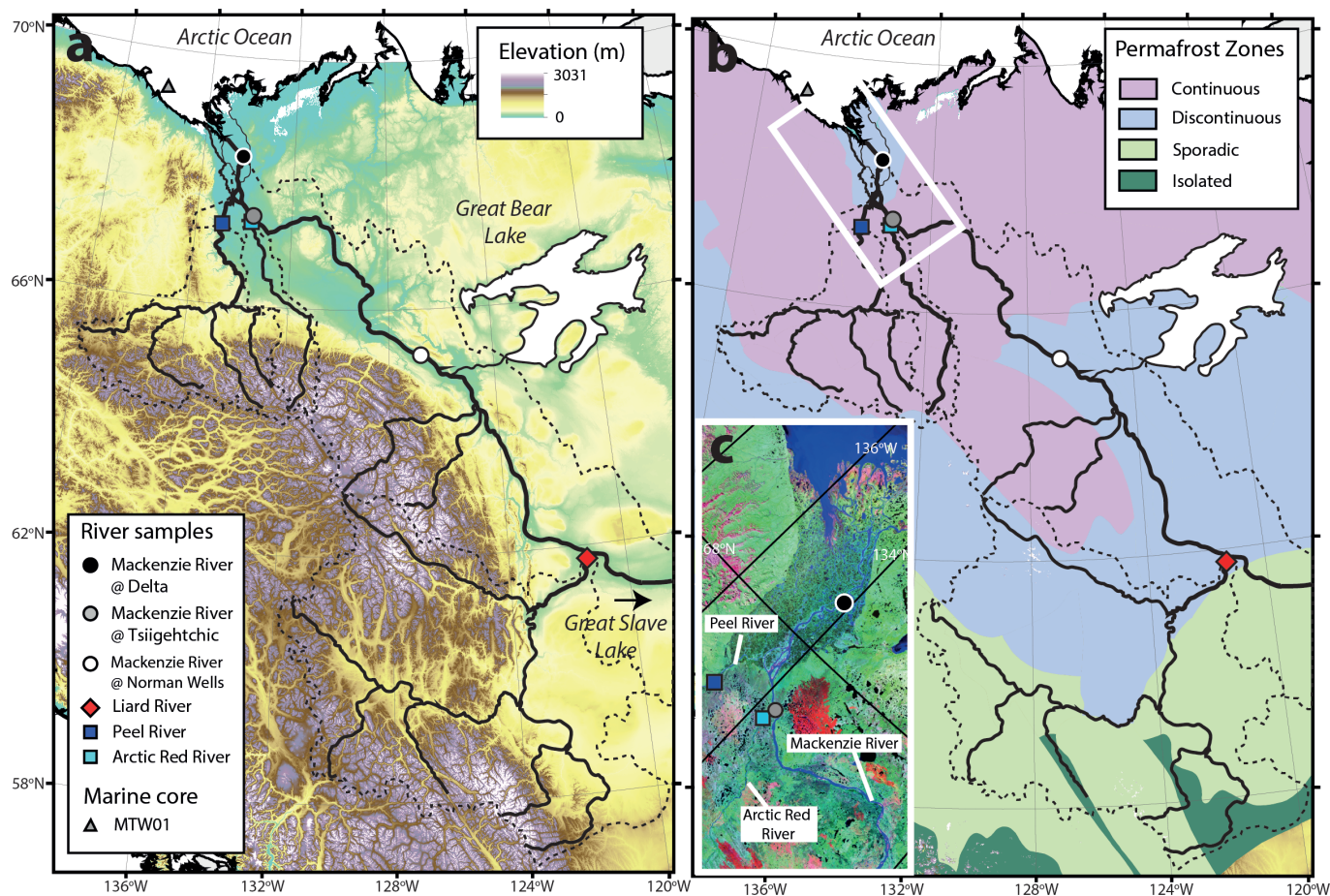
The total POC discharge is slightly higher than a previous estimate (2.1 Tg C yr^{-1})¹² based on measurements of POC content made in 1987 because: (1) we account for higher $\text{POC}_{\text{biosphere}}$ concentrations which may occur in water-logged $\text{POC}_{\text{biosphere}}$ near the river bed (Fig. 2c, Extended Data Fig. 4); and (2) we account for the potential for very high annual sediment discharge¹⁵. Based on estimates of soil carbon stock in the Mackenzie basin² of $\sim 50 \times 10^3 \text{ t C km}^{-2}$ and the upstream sediment source area (downstream of the Great Slave Lake, $774,200 \text{ km}^2$), the present rate of $\text{POC}_{\text{biosphere}}$ export represents a depletion of the soil carbon stock by $\sim 0.006\%$ per year, which is sustainable over 1,000 to 10,000 years.

OC burial efficiency in MTW01. To estimate the burial efficiency of terrestrial POC at the MTW01 site, we normalize the measured $[\text{OC}_{\text{total}}]$ concentrations (Fig. 3) by Al concentration; Al is an immobile inorganic element hosted by major mineral phases. The $\text{OC}_{\text{total}}/\text{Al}$ normalization allows the effects of dilution to be distinguished from net OC gain (increased ratio) or OC loss (decreased ratio). The mean $\text{OC}_{\text{total}}/\text{Al}$ of the MTW01 samples was $0.17 \pm 0.02 \text{ g C per g Al}$ ($n = 4, \pm 2 \text{ s.e.}$). This is lower than the mean $\text{OC}_{\text{total}}/\text{Al}$ of the suspended load samples from the Mackenzie River delta of $0.26 \pm 0.10 \text{ g C per g Al}$ ($n = 8, \pm 2 \text{ s.e.}$). The decrease in the ratio offshore may suggest a higher relative proportion of $\text{POC}_{\text{petro}}$ (Extended Data Fig. 2b); however, this is not consistent with the less negative $\delta^{13}\text{C}_{\text{org}}$ values (Extended Data Fig. 5). The decrease can therefore be interpreted in terms of OC loss, with the ratio of core to river samples being $0.17 \pm 0.02/0.26 \pm 0.10$.

Assuming that all the change in $\text{OC}_{\text{total}}/\text{Al}$ is driven by OC loss, and taking into account the measurement variability in these values, we estimate that $65 \pm 27\%$ of the OC has been preserved. However, we note that the $\text{OC}_{\text{total}}/\text{Al}$ ratios in the core are not statistically different from the river suspended load samples (one-way ANOVA, $P > 0.1$) which suggests that the OC burial efficiency could be higher (that is, 100%). In addition, if we use the $\text{OC}_{\text{total}}/\text{Al}$ of finer river sediments carried near the channel surface—which may be more easily conveyed offshore—of $0.20 \pm 0.04 \text{ g g}^{-1}$ ($n = 4, \pm 2 \text{ s.e.}$), we calculate burial efficiency to be $85 \pm 20\%$.

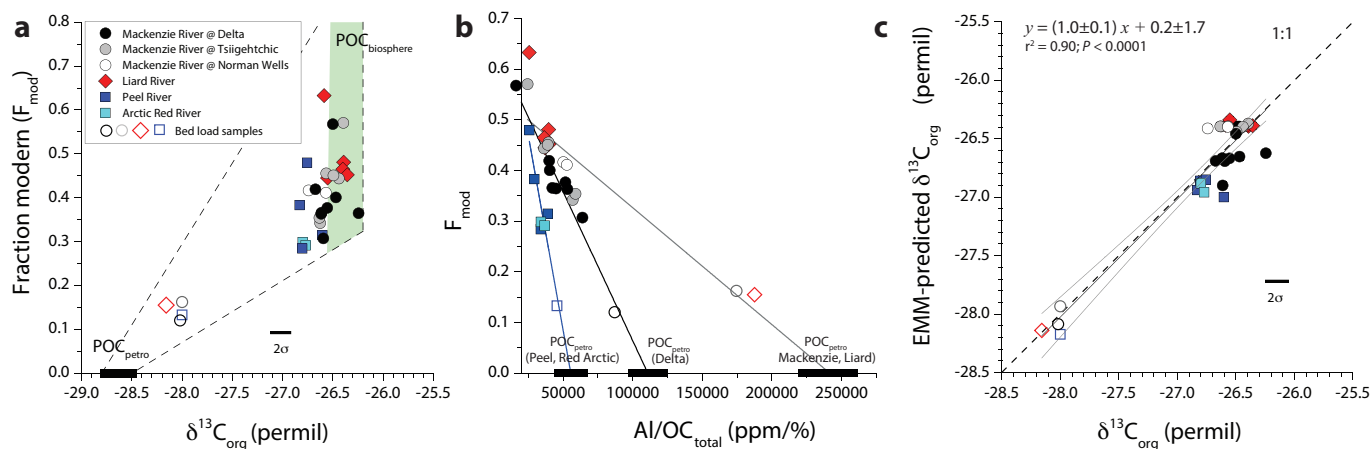
Future work should seek to better constrain these burial efficiencies with additional terrestrial and marine samples. Nevertheless, despite the remaining uncertainty, these high burial efficiencies¹⁸ are consistent with the high sedimentation rate and low temperature setting. The long-term burial of POC delivered to sites deeper in the Beaufort Sea²⁹ still remains to be assessed to provide a complete picture of source-to-sink carbon transfers.

32. Hilton, R. G., Galy, A., Hovius, N., Horng, M. J. & Chen, H. The isotopic composition of particulate organic carbon in mountain rivers of Taiwan. *Geochim. Cosmochim. Acta* **74**, 3164–3181 (2010).
33. Moran, K., Hill, P. R. & Blasco, S. M. Interpretation of piezocene penetrometer profiles in sediment from the Mackenzie Trough, Canadian Beaufort Sea. *J. Sedim. Petrol.* **59**, 88–97 (1989).
34. Komada, T., Anderson, M. R. & Dorfmeier, C. L. Carbonate removal from coastal sediments for the determination of organic carbon and its isotopic signatures, ^{13}C and ^{14}C : comparison of fumigation and direct acidification by hydrochloric acid. *Limnol. Oceanogr.* **6**, 254–262 (2008).
35. Whiteside, J. H. *et al.* Pangean great lake paleoecology on the cusp of the end-Triassic extinction. *Palaeogeogr. Palaeoclimatol. Palaeoecol.* **301**, 1–17 (2011).
36. Stuiver, M. & Polach, H. A. Discussion: Reporting of ^{14}C data. *Radiocarbon* **19**, 55–63 (1977).
37. Stuiver, M. & Reimer, P. J. Extended ^{14}C database and revised CALIB radiocarbon calibration program. *Radiocarbon* **35**, 215–230 (1993).
38. Reimer, P. J. *et al.* IntCal09 and Marine09 radiocarbon age calibration curves, 0–50,000 years cal BP. *Radiocarbon* **51**, 1111–1150 (2009).
39. Coulthard, R. D., Furze, M. F. A., Pienkowski, A. J., Nixon, F. C. & England, J. H. New marine ΔR values for Arctic Canada. *Quat. Geochronol.* **5**, 419–434 (2010).
40. Johnston, D. T., Macdonald, F. A., Gill, B. C., Hoffman, P. F. & Schrag, D. P. Uncovering the Neoproterozoic carbon cycle. *Nature* **483**, 320–323 (2012).
41. Bird, M., Santruckova, H., Lloyd, J. & Lawson, E. The isotopic composition of soil organic carbon on a north-south transect in western Canada. *Eur. J. Soil Sci.* **53**, 393–403 (2002).
42. Brown, J. *et al.* *Circum-Arctic Map of Permafrost and Ground Ice Conditions* <http://nsidc.org/data/ggd318> (National Snow and Ice Data Center/World Data Center for Glaciology, 1998).



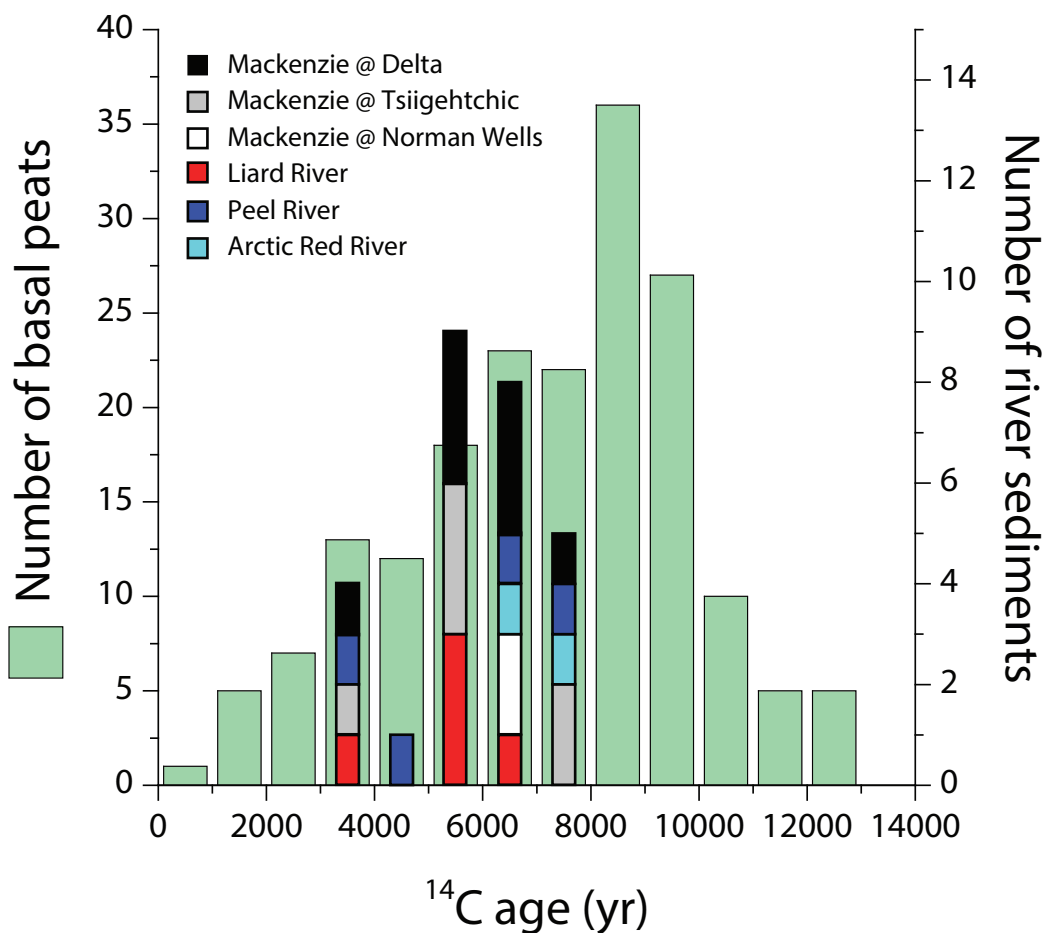
Extended Data Figure 1 | The location of river depth profiles collected from the Mackenzie River. Three locations along the Mackenzie River were sampled (circles) at the delta (black), Tsiigehtchic (grey) and Norman Wells (white) in addition to the major tributaries, the Liard River (red diamond), Arctic Red River (light blue square) and Peel River (dark blue square). The location of the sediment core MTW01 from the Mackenzie trough is shown (triangle). **a**, Major river channels (black lines) overlain on digital

elevation model GMTED 15 arcsec with upstream sediment source catchment areas delineated by flow accumulation and flow direction outputs from the digital elevation model (dotted lines). The Great Slave Lake is indicated upstream of the Liard confluence and acts as an effective sediment trap in the basin¹⁵. **b**, Permafrost zone coverage in the upstream areas of the basin⁴². White rectangle shows the sample locations near the Mackenzie delta displayed in **c**, overlain on LANDSAT imagery.



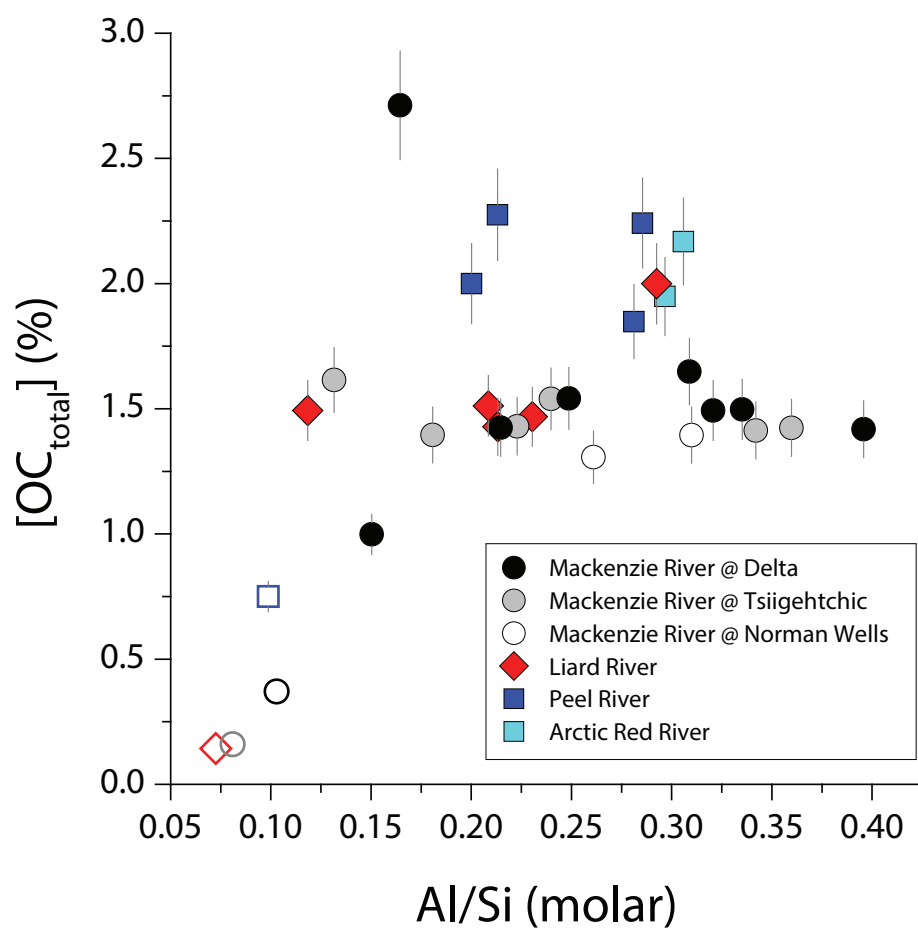
Extended Data Figure 2 | Source of particulate organic carbon in the Mackenzie River basin. **a**, Radiocarbon content (reported as F_{mod}) as a function of the stable isotope ratio of organic carbon ($\delta^{13}\text{C}_{\text{org}}$) of river sediments for the Mackenzie River (circles) and its major tributaries (diamonds and squares) for suspended load samples from river depth profiles (filled symbols) and river bed materials (open symbols). Dashed lines and shaded regions show hypothetical compositions produced by mixing rock-derived $\text{POC}_{\text{petro}}$ ⁴⁰ and $\text{POC}_{\text{biosphere}}$ ⁴¹. **b**, F_{mod} as a function of $\text{Al}/\text{OC}_{\text{total}}$. High $\text{Al}/\text{OC}_{\text{total}}$ and low F_{mod} correspond to the petrogenic source of POC ($\text{POC}_{\text{petro}}$). Linear trends are shown for the Peel and Arctic Red rivers (blue, $y = (-1.5 \pm 0.3 \times 10^{-6})x + (0.85 \pm 0.11)$, $r^2 = 0.85$, $P < 0.02$), the Mackenzie River at delta (black, $y = (-5.9 \pm 0.5 \times 10^{-6})x + (0.65 \pm 0.03)$, $r^2 = 0.95$,

$P < 0.001$), and the Mackenzie and Liard rivers (grey, $y = (-2.3 \pm 0.3 \times 10^{-6})x + (0.56 \pm 0.03)$, $r^2 = 0.82$, $P < 0.001$). The intercepts at $F_{\text{mod}} = 0$ for $\text{POC}_{\text{petro}}$ are given with uncertainty (± 1 s.d.) and are different for each sub-basin, reflecting the distribution of organic carbon-rich rocks in the Mackenzie mountains⁴⁰. **c**, Measured $\delta^{13}\text{C}_{\text{org}}$ versus those predicted by the endmember mixing model (EMM-predicted) (equations (1) and (2); Methods). The good agreement between measured and predicted values within the uncertainty on the measurements suggests that mixing of $\text{POC}_{\text{petro}}$ and $\text{POC}_{\text{biosphere}}$ can explain the first-order variability in $\delta^{13}\text{C}_{\text{org}}$ values between catchments and between suspended load and river bed materials.

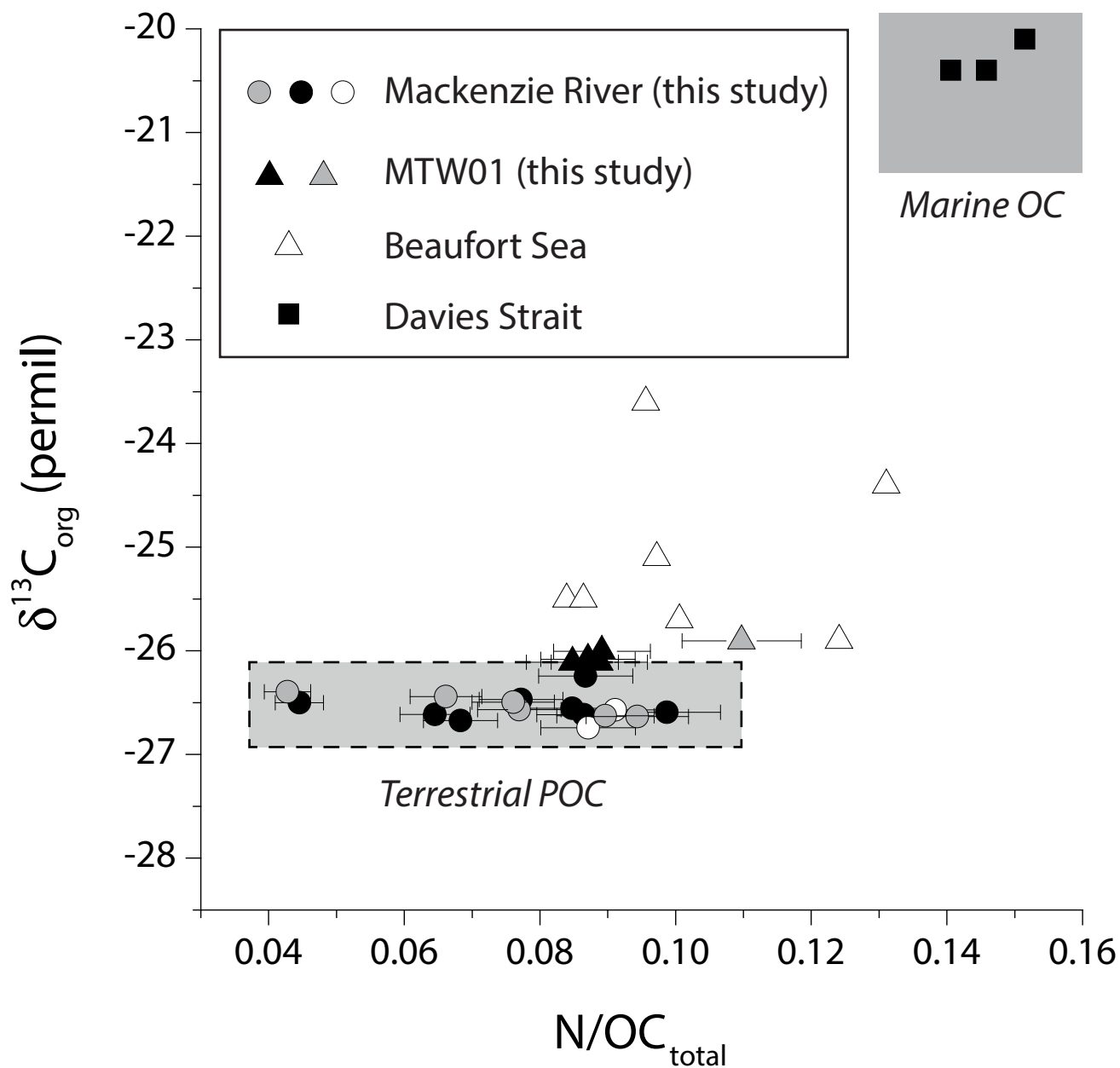


Extended Data Figure 3 | Radiocarbon age of biospheric particulate organic carbon in the Mackenzie River derived from the mixing analysis. The number of $\text{POC}_{\text{biosphere}}$ measurements of a given range of ^{14}C ages is shown for

each sampling location as a narrow rectangle. The distribution of published basal peat sample ^{14}C ages for the Mackenzie River basin²⁵ is shown as wide rectangles.



Extended Data Figure 4 | River particulate organic carbon in the Mackenzie basin. Organic carbon concentration as a function of Al/Si, which is a function of grain size in the Mackenzie River basin²⁶. Analytical errors (2 s.d.) are shown as grey lines if larger than the point size.



Extended Data Figure 5 | Stable isotope composition and nitrogen to organic carbon ratio of terrestrial and marine sediments. Suspended sediments from the Mackenzie River (circles) at the delta (black), Tsiigehtchic (grey) and Norman Wells (white) are shown. Marine sediment samples from the MTW01 sediment core (this study, triangles, black <63 μm ,

grey >63 μm) are shown with published surface sediment samples from the Beaufort Sea (white triangles) and Davis Strait (black squares)^{7,29}. The terrestrial POC field shows an indicative range of values measured in the Mackenzie River. The marine OC field shows values expected for Arctic Ocean marine OC. Analytical errors (2 s.d.) are shown as grey lines if larger than the point size.

Extended Data Table 1 | River suspended sediment and bed material samples from the Mackenzie basin in 2009–2011

Sample ID	River	Location	Date	Lat.	Long.	Type ^a	Depth (m)	SSC ^b (mg/L)	Al (ppm)	Al/Si ^c (molar)	[OC _{total}] (%)	$\delta^{13}\text{C}_{\text{org}}$ (permil)	N/OC _{total}	F _{mod} ^d	Publication Code
CAN10_28	Mackenzie	Delta	09/09/2010	68.4092	134.0805	SL	19	513	56947	0.21	1.42 ± 0.11	-26.7	0.068 ± 0.005	0.419 ± 0.002	SUERC-43077
CAN10_29	Mackenzie	Delta	09/09/2010	68.4092	134.0805	SL	17	275	77165	0.32	1.49 ± 0.12	-26.6	0.085 ± 0.007	0.377 ± 0.002	SUERC-43078
CAN10_31	Mackenzie	Delta	09/09/2010	68.4092	134.0805	SL	6	251	79441	0.34	1.50 ± 0.12	-26.6	0.086 ± 0.007	0.363 ± 0.002	SUERC-43079
CAN10_32	Mackenzie	Delta	09/09/2010	68.4092	134.0805	SL	0	162	90608	0.40	1.42 ± 0.11	-26.6	0.099 ± 0.008	0.307 ± 0.002	SUERC-43080
CAN11_87	Mackenzie	Delta	13/06/2011	68.4092	134.0805	SL	20	848	43833	0.16	2.71 ± 0.22	-26.5	0.045 ± 0.004	0.568 ± 0.003	SUERC-43100
CAN11_88	Mackenzie	Delta	13/06/2011	68.4092	134.0805	SL	15	850	42155	0.15	1.00 ± 0.08	-26.6	0.065 ± 0.005	0.366 ± 0.002	SUERC-43101
CAN11_89	Mackenzie	Delta	13/06/2011	68.4092	134.0805	SL	8	240	62214	0.25	1.54 ± 0.12	-26.5	0.077 ± 0.006	0.401 ± 0.002	SUERC-43102
CAN11_90	Mackenzie	Delta	13/06/2011	68.4092	134.0805	SL	0	119	74070	0.31	1.65 ± 0.13	-26.2	0.087 ± 0.007	0.365 ± 0.002	SUERC-43103
CAN10_38	Mackenzie	Delta	09/09/2010	68.4092	134.0805	BM	Thalweg	-	32258	0.10	0.37 ± 0.03	-28.0	0.076 ± 0.006	0.120 ± 0.001	SUERC-46907
CAN09_55	Mackenzie	Tsiigehtchic	23/07/2009	67.4530	133.7405	SL	0	-	-	-	1.50 ± 0.03	-26.6	0.104 ± 0.004	0.217 ± 0.001	OS-78930
CAN10_16	Mackenzie	Tsiigehtchic	07/09/2010	67.4530	133.7405	BM	Thalweg	-	27913	0.08	0.16 ± 0.01	-28.0	0.063 ± 0.005	0.162 ± 0.001	SUERC-46902
CAN10_10	Mackenzie	Tsiigehtchic	07/09/2010	67.4530	133.7405	SL	23	255	80393	0.34	1.41 ± 0.11	-26.6	0.090 ± 0.007	0.342 ± 0.002	SUERC-43071
CAN10_15	Mackenzie	Tsiigehtchic	07/09/2010	67.4530	133.7405	SL	0	231	83833	0.36	1.42 ± 0.11	-26.6	0.094 ± 0.008	0.354 ± 0.002	SUERC-43072
CAN11_65	Mackenzie	Tsiigehtchic	11/06/2011	67.4530	133.7405	SL	13	941	39509	0.13	1.62 ± 0.13	-26.4	0.043 ± 0.003	0.570 ± 0.003	SUERC-43091
CAN11_66	Mackenzie	Tsiigehtchic	11/06/2011	67.4530	133.7405	SL	10	445	50607	0.18	1.40 ± 0.11	-26.4	0.066 ± 0.005	0.444 ± 0.002	SUERC-43092
CAN11_67	Mackenzie	Tsiigehtchic	11/06/2011	67.4530	133.7405	SL	5	322	56614	0.22	1.43 ± 0.11	-26.6	0.077 ± 0.006	0.456 ± 0.002	SUERC-43093
CAN11_68	Mackenzie	Tsiigehtchic	11/06/2011	67.4530	133.7405	SL	0	291	59948	0.24	1.54 ± 0.12	-26.5	0.076 ± 0.006	0.451 ± 0.002	SUERC-43097
CAN10_39	Mackenzie	Norman Wells	10/09/2010	65.2650	126.7594	SL	3.15	168	65521	0.26	1.31 ± 0.10	-26.7	0.087 ± 0.007	0.417 ± 0.002	SUERC-43082
CAN10_40	Mackenzie	Norman Wells	10/09/2010	67.4530	126.7594	SL	0	136	73513	0.31	1.39 ± 0.11	-26.6	0.091 ± 0.007	0.411 ± 0.002	SUERC-43083
CAN10_50	Liard	Fort Simpson	13/09/2010	61.8234	121.2976	BM	Thalweg	-	26796	0.07	0.14 ± 0.01	-28.2	0.070 ± 0.006	0.155 ± 0.001	SUERC-46906
CAN10_46	Liard	Fort Simpson	13/09/2010	61.8234	121.2976	SL	4.8	492	38265	0.12	1.49 ± 0.12	-26.6	0.045 ± 0.004	0.633 ± 0.003	SUERC-43086
CAN10_49	Liard	Fort Simpson	13/09/2010	61.8234	121.2976	SL	0	79	73830	0.29	2.00 ± 0.16	-26.6	0.077 ± 0.006	0.445 ± 0.002	SUERC-43087
CAN11_03	Liard	Fort Simpson	04/06/2011	61.8234	121.2976	SL	6.5	490	56524	0.21	1.43 ± 0.11	-26.4	0.075 ± 0.006	0.481 ± 0.002	SUERC-43088
CAN11_05	Liard	Fort Simpson	04/06/2011	61.8234	121.2976	SL	3.5	542	55058	0.21	1.51 ± 0.12	-26.4	0.069 ± 0.006	0.465 ± 0.002	SUERC-43089
CAN11_07	Liard	Fort Simpson	04/06/2011	61.8234	121.2976	SL	0	438	58509	0.23	1.47 ± 0.12	-26.4	0.073 ± 0.006	0.452 ± 0.002	SUERC-43090
CAN10_07	Peel	Fort McPherson	07/09/2010	67.3313	134.8656	BM	Thalweg	-	34205	0.10	0.75 ± 0.06	-28.0	0.068 ± 0.005	0.133 ± 0.001	SUERC-46905
CAN10_03	Peel	Fort McPherson	07/09/2010	67.3313	134.8656	SL	8.5	250	58694	0.20	2.00 ± 0.16	-26.8	0.071 ± 0.006	0.383 ± 0.002	SUERC-43069
CAN10_06	Peel	Fort McPherson	07/09/2010	67.3313	134.8656	SL	0	101	76053	0.29	2.24 ± 0.18	-26.8	0.080 ± 0.006	0.284 ± 0.002	SUERC-43070
CAN11_77	Peel	Fort McPherson	11/06/2011	67.3313	134.8656	SL	6	325	58519	0.21	2.27 ± 0.18	-26.8	0.072 ± 0.006	0.480 ± 0.002	SUERC-43098
CAN11_79	Peel	Fort McPherson	11/06/2011	67.3313	134.8656	SL	0	146	72153	0.28	1.85 ± 0.15	-26.6	0.085 ± 0.007	0.315 ± 0.002	SUERC-43099
CAN10_17	Arctic Red	Tsiigehtchic	07/09/2010	67.4394	133.7529	SL	6	123	73830	0.31	2.17 ± 0.17	-26.8	0.080 ± 0.006	0.299 ± 0.002	SUERC-43073
CAN10_19	Arctic Red	Tsiigehtchic	07/09/2010	67.4394	133.7529	SL	0	123	71608	0.30	1.95 ± 0.16	-26.8	0.083 ± 0.007	0.291 ± 0.002	SUERC-43076

^aRiver sample type: SL, suspended load; BM, bed material, collected at the thalweg (deepest part of the river channel cross-section).^bSSC, suspended sediment concentration.^cAluminium to silicon ratio²⁶.^dF_{mod} from radiocarbon activity.

Extended Data Table 2 | Sediment samples from the offshore core MTW01

Interval	Depth (m)	Dated material	¹⁴ C Age (yrs)	$\delta^{13}\text{C}_{\text{foram}}$ (permil)	¹⁴ C Age $\delta^{13}\text{C}$ normalised (yrs) ^a	ΔR (yr) ^b	Calibrated age (cal. yrs BP) ^c	plus σ	minus σ	Publication code #	Date Reported	Grain size fraction	[OC _{total}] (%) ^d		$\delta^{13}\text{C}_{\text{org}}$ (permil)	N/OC _{total}	Al (ppm)
1A	0-0.2	Mixed Benthic Foraminifera	1860 ±25	-1.4	2244±89	335±85	1461	1548	1353	OS-103002	21/05/2013	>63µm	1.34	± 0.11	-25.7	-	-
												<63µm	1.72	± 0.14	-26.1	0.09 ± 0.01	89010
6B	7.62-8.12	Mixed Benthic Foraminifera	4280 ±20	-1.6	4661±87	335±85	4462	4590	4333	OS-103185	24/05/2013	>63µm	1.40	± 0.11	-25.8	-	-
												<63µm	1.58	± 0.13	-26.1	0.08 ± 0.01	89127
12B	16.92-17.42	Mixed Benthic Foraminifera	7080 ±35	-0.9	7472±92	335±85	7612	7689	7517	OS-95351	22/05/2012	>63µm	1.19	± 0.10	-25.9	0.11 ± 0.01	80960
												<63µm	1.52	± 0.12	-26.0	0.09 ± 0.01	87687
15B	20.73-21.09	Mixed Benthic Foraminifera	8490 ±70	-0.9	8882±110	335±85	9183	9308	9027	OS-95606	04/06/2012	>63µm	1.09	± 0.09	-25.9	-	-
												<63µm	1.50	± 0.12	-26.1	0.09 ± 0.01	-

^aSee Methods.^bReservoir age (see Methods).^cCalibrated age in calibrated years before present, based on MARINE13 data set in CALIB v7.1 (Methods).^dOrganic carbon concentration for the sediment samples.

Extended Data Table 3 | River bank samples from the Mackenzie River in 2009

Sample ID	Grain size fraction	River	Location	Date	Lat.	Long.	Type	[OC _{total}] (%)			$\delta^{13}\text{C}_{\text{org}}$ (permil)	N/OC _{total}			F _{mod}			Publication Code
CAN09-54	150-250 μm	Mackenzie	Tsiigehtchie	23/07/2009	67.45384	133.70741	Flood dep.	2.02	\pm	0.11	-26.7	0.052	\pm	0.003	0.672	\pm	0.003	OS-78930
CAN09-54	63-150 μm	Mackenzie	Tsiigehtchie	23/07/2009	67.45384	133.70741	Flood dep.	1.01	\pm	0.03	-27.0	0.069	\pm	0.002	0.444	\pm	0.002	OS-78929
CAN09-54	<63 μm	Mackenzie	Tsiigehtchie	23/07/2009	67.45384	133.70741	Flood dep.	1.06	\pm	0.05	-27.0	0.098	\pm	0.005	0.371	\pm	0.001	OS-78928
CAN09-54	Bulk	Mackenzie	Tsiigehtchie	23/07/2009	67.45384	133.70741	Flood dep.	0.99	\pm	0.00	-26.9	0.085	\pm	0.002	0.455	\pm	0.002	OS-78927
CAN09-12	150-250 μm	Liard	Fort Simpson	16/07/2009	61.84457	121.31625	Flood dep.	17.47	\pm	1.24	-26.6	0.044	\pm	0.003	0.839	\pm	0.003	OS-79575
CAN09-12	63-150 μm	Liard	Fort Simpson	16/07/2009	61.84457	121.31625	Flood dep.	0.84	\pm	0.01	-26.6	0.087	\pm	0.001	0.403	\pm	0.002	OS-79574
CAN09-12	<63 μm	Liard	Fort Simpson	16/07/2009	61.84457	121.31625	Flood dep.	0.66	\pm	0.02	-26.6	0.132	\pm	0.006	0.364	\pm	0.002	OS-79573
CAN09-12	Bulk	Liard	Fort Simpson	16/07/2009	61.84457	121.31625	Flood dep.	1.04	\pm	0.06	-26.7	0.069	\pm	0.004	0.523	\pm	0.002	OS-79576
CAN09-42	<63 μm	Peel	Fort McPherson	22/07/2009	67.33189	134.86912	Flood dep.	1.63	\pm	0.10	-27.1	0.089	\pm	0.005	0.328	\pm	0.002	OS-78922
CAN09-42	Bulk	Peel	Fort McPherson	22/07/2009	67.33189	134.86912	Flood dep.	2.01	\pm	0.04	-27.1	0.082	\pm	0.002	0.440	\pm	0.002	OS-78921

Viral-genetic tracing of the input–output organization of a central noradrenaline circuit

Lindsay A. Schwarz^{1*}, Kazunari Miyamichi^{1,2*}, Xiaojing J. Gao¹, Kevin T. Beier^{1,3}, Brandon Weissbourd¹, Katherine E. DeLoach¹, Jing Ren¹, Sandy Ibanes⁴, Robert C. Malenka³, Eric J. Kremer^{4,5} & Liqun Luo¹

Deciphering how neural circuits are anatomically organized with regard to input and output is instrumental in understanding how the brain processes information. For example, locus coeruleus noradrenaline (also known as norepinephrine) (LC-NE) neurons receive input from and send output to broad regions of the brain and spinal cord, and regulate diverse functions including arousal, attention, mood and sensory gating^{1–8}. However, it is unclear how LC-NE neurons divide up their brain-wide projection patterns and whether different LC-NE neurons receive differential input. Here we developed a set of viral-genetic tools to quantitatively analyse the input–output relationship of neural circuits, and applied these tools to dissect the LC-NE circuit in mice. Rabies-virus-based input mapping indicated that LC-NE neurons receive convergent synaptic input from many regions previously identified as sending axons to the locus coeruleus, as well as from newly identified presynaptic partners, including cerebellar Purkinje cells. The ‘tracing the relationship between input and output’ method (or TRIO method) enables trans-synaptic input tracing from specific subsets of neurons based on their projection and cell type. We found that LC-NE neurons projecting to diverse output regions receive mostly similar input. Projection-based viral labelling revealed that LC-NE neurons projecting to one output region also project to all brain regions we examined. Thus, the LC-NE circuit overall integrates information from, and broadcasts to, many brain regions, consistent with its primary role in regulating brain states. At the same time, we uncovered several levels of specificity in certain LC-NE sub-circuits. These tools for mapping output architecture and input–output relationship are applicable to other neuronal circuits and organisms. More broadly, our viral-genetic approaches provide an efficient intersectional means to target neuronal populations based on cell type and projection pattern.

Figure 1a, b illustrates two extreme connectivity models for input–output relationships of projection neurons. At one extreme, neurons from each input A region connect to a subtype of B neurons that send output to a unique C region (Fig. 1a); this model segregates information into discrete pathways. At the other extreme, B neurons are homogeneous in receiving input from all A regions and sending output to all C regions with a common probability distribution (Fig. 1b); this model allows an overall indiscriminate integration and broadcast of information. The input–output relationship for most neural circuits is not known (Supplementary Note 1).

To determine the input–output organization of neural circuits, we have developed a method we have termed TRIO (for tracing the relationship between input and output) and cell-type-specific TRIO (cTRIO). TRIO identifies neurons in A regions that synapse onto B neurons projecting to a specific C region. A→B connections are determined by rabies-virus-mediated retrograde trans-synaptic tracing⁹, which relies on monosynaptic spread of EnvA-pseudotyped,

glycoprotein deleted and GFP-expressing rabies viruses (RVdG hereafter) from starter cells in the B region. Starter cells express rabies glycoprotein (G) and the TVA receptor for EnvA fused with mCherry (TC)^{10,11}, which allow RVdG infection and complementation, enabling trans-synaptic spread to presynaptic neurons in A regions. In TRIO (Fig. 1c), expression of TVA–mCherry fusion and rabies glycoprotein depends on Cre/loxP-mediated recombination from adeno-associated viruses (AAVs) injected in region B. Cre is delivered at a specific C region by canine adenovirus type 2 (CAV hereafter) that efficiently transduces axon terminals^{12,13}. Thus, TRIO does not distinguish between different cell types within region B. In cTRIO (Fig. 1d), TRIO is performed in transgenic mice in which Cre recombinase is expressed in a specific cell type in the B region. Expression of the TVA–mCherry fusion and rabies glycoprotein delivered in the B region depends on Flp/FRT-based recombination and Flp recombinase from CAV-FLEX^{loxP}-Flp, which is injected at a specific C region. Thus, only B neurons that express Cre and project to a specific C region can become starter cells for RVdG-mediated trans-synaptic tracing.

As a proof-of-principle, we applied TRIO and cTRIO to the mouse motor cortex (Fig. 1e). In TRIO experiments, we injected CAV-Cre in contralateral motor cortex and AAV-FLEX^{loxP}-TC/G into motor cortex of wild-type mice; this resulted in starter cells in motor cortex layers 2/3 (L2/3), L5, (Fig. 1f, left; arrowheads) and L6. In cTRIO experiments, we injected CAV-FLEX^{loxP}-Flp in contralateral motor cortex or medulla of retinol binding protein 4 (*Rbp4*)-Cre mice to target intracortical- or subcortical-projecting L5 neurons, respectively, and AAV-FLEX^{FRT}-TC/G into motor cortex; this resulted in starter cells that were restricted to motor cortex L5 (Fig. 1f, middle and right), as predicted by the *Rbp4*-Cre expression pattern¹⁴. For comparison, we also performed trans-synaptic tracing in motor cortex of *Rbp4*-Cre mice, where starter cells were not selected based on output projections. A large majority of the GFP⁺ input neurons to the motor cortex were from the cortex or thalamus (Fig. 1f, bottom). Interestingly, contralateral-motor-cortex-projecting L5 neurons received proportionally more input from the cortex, whereas medulla-projecting L5 neurons received more input from the thalamus. Almost all other inputs came from the globus pallidus, a recently identified direct input to the cortex¹⁵ (Fig. 1g; Supplementary Table 1). Control experiments indicated that rabies-mediated labelling of most local and all long-range input neurons were dependent on CAV-Cre for TRIO, and CAV-FLEX^{loxP}-Flp and *Rbp4*-Cre for cTRIO (Extended Data Fig. 1). These experiments demonstrated that cTRIO can restrict starter cells to a more specific population than TRIO, and suggested that subcortical- and callosal-projecting L5 neurons receive differential thalamic versus cortical input. TRIO also identified presynaptic partners of callosal- or striatal-projecting motor cortex neurons in rat (Extended Data Fig. 2).

As the precision of TRIO/cTRIO analysis is defined by CAV-mediated transduction from axons and presynaptic terminals, we

¹Howard Hughes Medical Institute and Department of Biology, Stanford University, Stanford, California 94305, USA. ²Department of Applied Biological Chemistry, Graduate School of Agricultural and Life Sciences, The University of Tokyo, Tokyo 113-8657, Japan. ³Nancy Pritzker Laboratory, Department of Psychiatry and Behavioral Sciences, Stanford University School of Medicine, Stanford, California 94305, USA. ⁴Institut de Génétique Moléculaire de Montpellier, CNRS 5535, 34293 Montpellier, France. ⁵Université de Montpellier, 34000 Montpellier, France.

*These authors contributed equally to this work.

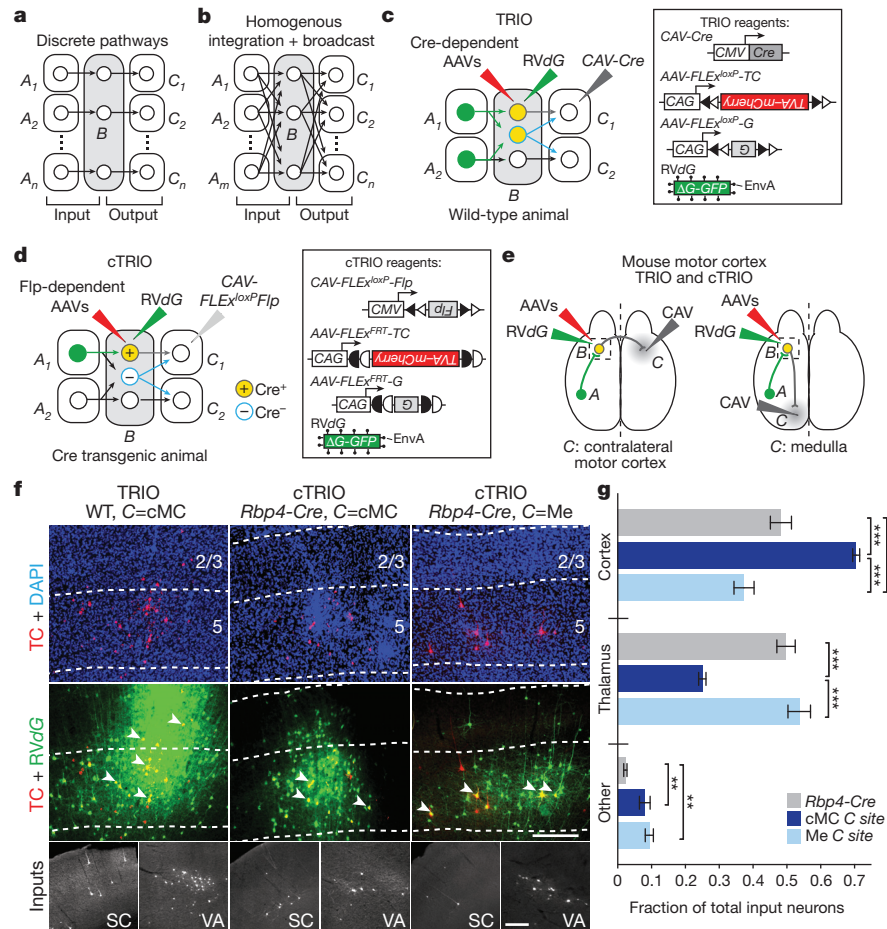


Figure 1 | Strategy and proof-of-principle of TRIO and cTRIO.

a, b, Schematic of two extreme connection patterns of region *B* neurons with inputs from *A* regions and outputs to *C* regions. **c, d**, Strategies for trans-synaptic input tracing from *B* neurons based on their outputs. TRIO (**c**) does not distinguish between region *B* cell types projecting to the selected *C* region (two different cell types are outlined in grey and blue). cTRIO (**d**) avoids labelling promiscuous projections from Cre⁺ cells (blue). Open and filled triangles, incompatible *loxP* sites; open and filled half circles, incompatible *FRT* sites. **e**, Schematic of TRIO and cTRIO in mouse motor cortex. CAV was injected into contralateral motor cortex or medulla along with AAVs expressing Cre- or Flp-dependent TVA-mCherry (TC)/rabies glycoprotein (G) into motor cortex, followed by RVdG. Experiments were performed in wild-type (TRIO) or *Rbp4-Cre* (cTRIO) mice. **f**, Example coronal sections of motor cortex starter cells in TRIO and cTRIO. cMC, contralateral motor cortex; Me, medulla. Cortical layers are separated by dotted lines based on the DAPI (4',6-diamidino-2-phenylindole) stain (blue). Starter cells (yellow, a subset

indicated by arrowheads) can be distinguished from input cells labelled only with GFP from RVdG (green). TC⁺ cells in motor cortex spanned layers 2/3 and 5 for TRIO (left), but were restricted to L5 with cTRIO. Bottom inset, example images of input neurons from the somatosensory cortex (SC) and ventral anterior thalamus (VA), derived from larger composites (see Methods). **g**, Average fraction of total input neurons in *Rbp4-Cre*-based input tracing and cTRIO of motor cortex L5 pyramidal neurons. Values represent the average fraction of input in each category ($n = 4$ animals for *Rbp4-Cre* input tracing and contralateral motor cortex cTRIO; $n = 3$ animals for medulla cTRIO). Two-way ANOVA determined that inputs to *Rbp4-Cre*⁺ motor cortex starter cells generated by input tracing or cTRIO ($C = cMC$ or $C = Me$) are significantly different in brain regions from which they receive input (interaction $P < 0.0001$). One-way ANOVA and post hoc Tukey's multiple comparison tested the significance within each input region. Error bars, s.e.m. *** $P < 0.001$; ** $P < 0.01$; Scale bars, 250 μ m (**f**, middle row), 100 μ m (**f**, bottom row).

characterized its spread by injecting CAV-Cre and retrobeads into the *Ail4* Cre-reporter mice¹⁶ in the piriform cortex at varied distances from the mitral cell axon layer and quantifying labelled mitral cells. We found that CAV spread mostly within 200 μ m from the injection site and could also infect axons in passage (Extended Data Fig. 3; Supplementary Note 2). CAV tropism was examined by injecting CAV-Cre into five diverse brain regions of *Ail4* mice. Neurons known to project to these brain regions, some of which are >1 cm away from the injection sites, were efficiently labelled (Extended Data Fig. 4). Thus, CAV can infect axons and terminals of diverse neuronal types across long distances.

We next applied our viral-genetic tools to the noradrenaline neurons in the locus coeruleus, a small bilateral nucleus in the brainstem (~1,500 noradrenaline neurons per locus coeruleus) that collectively project axons throughout the brain¹⁻⁴. It is unclear whether different LC-NE neurons receive differential input, how LC-NE neurons divide

up their brain-wide projection patterns¹⁷, and what their input-output relationships are. We first identified synaptic inputs received by these neurons using RVdG-mediated retrograde trans-synaptic tracing in dopamine β -hydroxylase (*Dbh*)-Cre mice (Fig. 2a), where Cre-dependent TVA-mCherry fusion and rabies glycoprotein expression was restricted to LC-NE neurons that express the noradrenaline biosynthetic enzyme *Dbh* (Fig. 2b). Control experiments validated that Cre recombination occurred almost exclusively in locus coeruleus neurons expressing tyrosine hydroxylase (TH), another LC-NE neuron marker, and that long-range trans-synaptic tracing depended on *Dbh*-Cre and AAV-delivered rabies glycoprotein (Extended Data Fig. 5).

We counted all input neurons to LC-NE starter cells from the anterior forebrain to posterior medulla (Fig. 2c-h) except in coronal sections immediately surrounding the locus coeruleus, as non-specific viral labelling of neurons can occur locally at the AAV/RVdG injection site (Extended Data Fig. 5c-f). We assigned each input

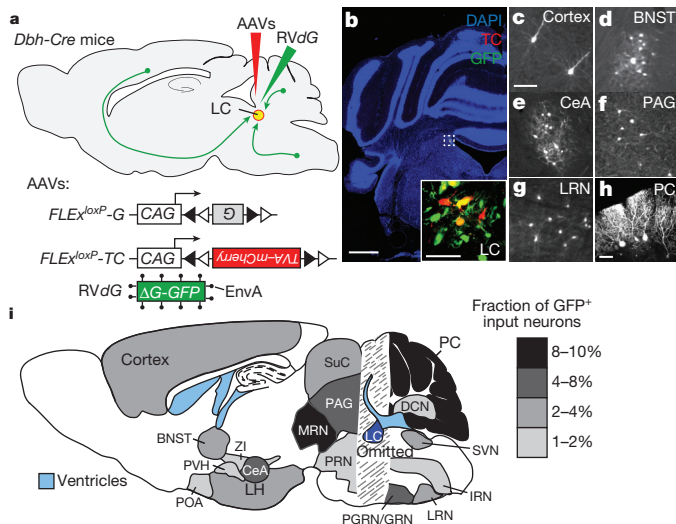


Figure 2 | Presynaptic input to LC-NE neurons revealed by rabies-mediated trans-synaptic tracing. **a**, Strategy for trans-synaptic tracing of input to LC-NE neurons. **b**, Coronal section of a mouse brain at the locus coeruleus (dotted square) stained with DAPI (blue). A region within the square is magnified in the inset. LC-NE starter cells (yellow) can be distinguished from cells receiving only TC from AAV (red) or only GFP from RVdG (green) at the injection site. **c–g**, Coronal sections showing representative input neurons in diverse brain regions. **h**, Sagittal section of the cerebellum showing trans-synaptically labelled Purkinje cells. Images in **b–h** were derived from larger composites. **i**, Schematic summary of brain regions that provide the largest average fractional inputs to LC-NE neurons ($n = 9$ animals). Scale bars, 1 mm (**b**), 50 μ m (**b**, inset; **c–h**). BNST, bed nucleus of the stria terminalis; CeA, central amygdala; DCN, deep cerebellar nuclei; IRN, intermediate reticular nucleus; LC, locus coeruleus; LH, lateral hypothalamus; LRN, lateral reticular nucleus; MRN, midbrain reticular nucleus; PAG, periaqueductal grey; PC, Purkinje cells; PGRN/GRN, paragigantocellular/gigantocellular nucleus; POA, preoptic area; PRN, pontine reticular nucleus; PVH, paraventricular hypothalamic nucleus; SuC, superior colliculus; SVN, spinal vestibular nucleus; ZI, zona incerta.

neuron to one of 111 brain regions according to the Allen Brain Atlas (<http://mouse.brain-map.org/static/atlas>) to categorize brain regions ipsi- or contralateral to the injected locus coeruleus (Supplementary Table 2). Regions that contributed more than 1% of total input from nine *Dbh-Cre* tracing brains are summarized in Fig. 2i. Although most brain regions we identified as presynaptic to LC-NE neurons are consistent with previous retrograde tracing studies^{6–8}, our experiment validated that these neurons directly synapse onto LC-NE neurons rather than just projecting axons to the locus coeruleus. We also found that deep cerebellar nuclei and cerebellar Purkinje cells contributed a notable fraction of direct synaptic input to LC-NE neurons (Fig. 2h, i), which (to our knowledge) has not been previously reported. Labelled Purkinje cells were enriched in the ipsilateral medial zones throughout the cerebellum, at distances up to 2.5 mm away from the locus coeruleus (Extended Data Fig. 6a). Consistent with a direct connection between Purkinje cells and LC-NE neurons, we found that an inhibitory postsynaptic marker, gephyrin, was present in TH⁺ LC-NE dendrites apposing GABAergic Purkinje cell axons (Extended Data Fig. 6b, c).

We next applied TRIO and cTRIO to test if populations of LC-NE neurons, defined by their output targets, received distinct input. We selected five diverse brain regions known to receive LC-NE projections: the olfactory bulb, auditory cortex, hippocampus, cerebellum and medulla (Fig. 3a). CAV-*Cre* injection into these regions in *Ai14* mice confirmed labelling of noradrenaline neurons throughout the locus coeruleus (Extended Data Fig. 7a). We did not observe significant differences in the spatial distribution along the anterior–posterior or medial–lateral axes for LC-NE neurons that projected to these brain regions. However, forebrain-projecting LC-NE neurons were

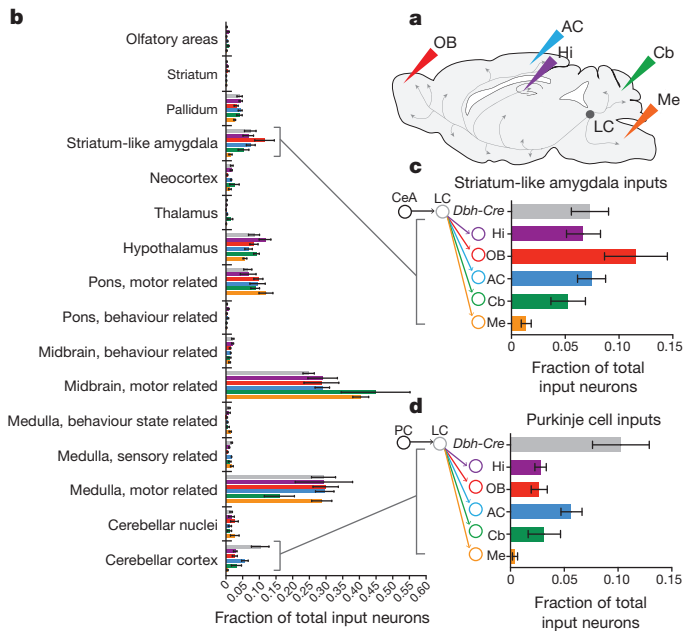


Figure 3 | Input–output relationship of LC-NE neurons revealed by TRIO and cTRIO. **a**, Schematic of CAV injections into locus coeruleus output regions for TRIO and cTRIO. AC, auditory cortex; Cb, cerebellum; Hi, hippocampus; Me, medulla; OB, olfactory bulb. **b–d**, Average fractional inputs in *Dbh-Cre*-based input tracing (grey, $n = 9$ animals), TRIO (Hi, purple; OB, red; AC, blue; $n = 4$ animals each), and cTRIO (Cb, green; Me, orange; $n = 4$ animals each). Input neurons were grouped into 16 broader categories. Magnified insets highlight the average fraction of input from striatum-like amygdala (>98% from the central amygdala) (**c**) or from Purkinje cells (**d**) to LC-NE neurons that project to the 5 output regions or in *Dbh-Cre*-based input tracing. Error bars, s.e.m.

more dorsally biased compared to the hindbrain-projecting ones (Extended Data Fig. 7b–f), consistent with a previous observation in the rat¹⁸. We applied TRIO to olfactory bulb, auditory cortex and hippocampus, and cTRIO to cerebellum and medulla, as locus coeruleus projections to the former group predominately came from TH⁺ neurons, whereas the latter group contained TH[−] neurons (Extended Data Fig. 7a). Control experiments indicated that the labelling of input neurons depended on CAV-*Cre* in the case of TRIO (Extended Data Fig. 5c, e), and on both *Dbh-Cre* and CAV-*FLEX^{loxP}-Flp* in the case of cTRIO (Extended Data Fig. 8).

We analysed inputs for the TRIO and cTRIO experiments analogous to *Dbh-Cre*-based input tracing (Supplementary Table 2). We observed that LC-NE neurons received inputs from all input regions regardless of their diverse output, with a grossly similar proportional distribution (Fig. 3b). These data suggest that the LC-NE circuit is largely indiscriminate with respect to its input–output relationship. However, region-by-region one-way ANOVA (Supplementary Table 3, top) rejected the overall null hypothesis that input distribution is independent of output conditions (combined $P = 0.002$), indicating that the input–output relationships were not entirely homogeneous. Of the individual input that exhibited the smallest P values (Supplementary Table 3, bottom), LC-NE neurons projecting to the medulla received less input from the central amygdala (Fig. 3c). In addition, the fraction of Purkinje cell inputs in *Dbh-Cre* based tracing was higher than any of the TRIO/cTRIO conditions (Fig. 3d), suggesting that Purkinje cells contribute input to an LC-NE population that do not project axons extensively to any of the output sites we examined.

The largely indiscriminate input–output relationship revealed by TRIO can in principle be accounted for by input convergence (Fig. 1b, left), output divergence (Fig. 1b, right), or both. A simulation analysis of the two sparsest input tracing samples (Supplementary Table 2) suggested that individual LC-NE neurons must receive input

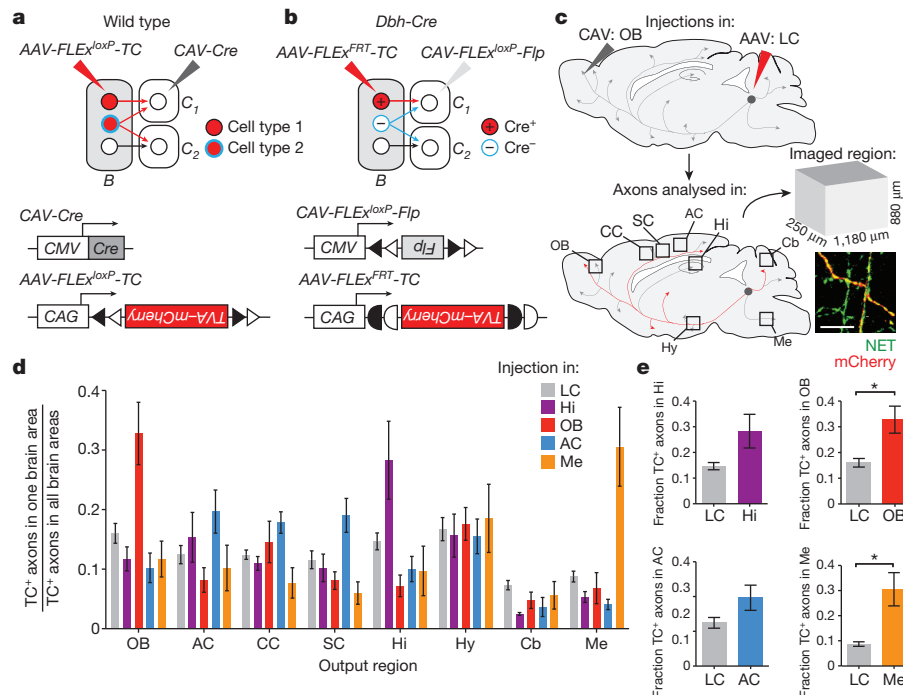


Figure 4 | Broad output divergence of LC-NE neurons revealed by projection-based viral-genetic labelling. **a**, In this strategy, neurons in region B projecting to the C region where CAV-Cre is delivered are labelled, including their collaterals to other output regions (for example, blue neurons to C₂). **b**, In this strategy, only Cre⁺ neurons in region B projecting to the C region where CAV-FLEX^{loxP}-Flp is delivered are labelled. **c**, Schematic for data in (d). In this example, CAV was injected in the olfactory bulb and TC was injected in the locus coeruleus. TC⁺ LC-NE axons were imaged in the designated brain regions. All TC⁺ axons were co-stained with anti-noradrenaline transporter (NET; inset), confirming their noradrenergic identity. **d**, Average normalized fraction of TC⁺ LC-NE axons in each brain region when CAV was injected into four output sites, or Cre-dependent TC was injected directly into the locus

coeruleus of *Dbh-Cre* mice (colour code on top right). LC: *n* = 4 animals (*Dbh-Cre*); Hi: *n* = 4 animals (*Dbh-Cre*); AC: *n* = 4 animals (2 wild-type, 2 *Dbh-Cre*); OB: *n* = 5 animals (3 wild-type, 2 *Dbh-Cre*); Me: *n* = 4 animals (*Dbh-Cre*). The average number of LC-NE neurons labelled in each condition was: 855 ± 102 (mean ± s.e.m., in locus coeruleus, *n* = 4 animals); 235 ± 35 (Hi, *n* = 4 animals); 80 ± 31 (OB, *n* = 5 animals); 114 ± 31 (AC, *n* = 4 animals); 202 ± 63 (Me, *n* = 4 animals). **e**, Comparison of the fraction of TC⁺ axons at CAV injection sites between projection-based and direct locus coeruleus labelling methods. Unpaired two-tail *t*-tests. **P* < 0.05. Error bars, s.e.m. Scale bar, 10 μm. Abbreviations: AC, auditory cortex; Cb, cerebellum; CC, cingulate cortex; Hi, hippocampus; Hy, hypothalamus; LC, locus coeruleus; Me, medulla; OB, olfactory bulb; SC, somatosensory cortex.

from more than 15 or 9 brain regions, respectively (Extended Data Fig. 9). This is most likely a lower bound as rabies tracing efficiency is far from 100%. However, such extensive integration is not entirely homogenous (Supplementary Table 4). Thus, individual LC-NE neurons integrate inputs from many regions, yet exhibit heterogeneity with respect to brain regions from which they receive input.

We next explored the output architecture of LC-NE neurons (Fig. 1a, b, right). Previous dual-retrograde-tracer experiments indicated that individual LC-NE neurons could project to two brain regions far apart^{19–21}, but did not examine collateralization between more than two output regions in a given experiment. We devised a general method for tracing output divergence of specific neuronal populations based on their projection to one output site (Fig. 4a, b). We found that populations of LC-NE neurons projecting to the olfactory bulb, auditory cortex, hippocampus or medulla also projected to all seven additional brain regions analysed (Fig. 4c, d and Extended Data Fig. 10). Thus, the output of LC-NE neuronal populations is highly divergent, resembling the broadcast model (Fig. 1b, right) much more than the discrete output model (Fig. 1a, right). We nevertheless found a general trend of increased axon density in the output region where labelling was initiated compared to labelling initiated from the locus coeruleus, with the bias from olfactory bulb- or medulla-initiated labelling reaching statistical significance (Fig. 4e). This suggests that LC-NE neurons projecting to the olfactory bulb or medulla contain populations with biased output to these regions, consistent with the observation that LC-NE neurons projecting to these regions have a biased distribution along the dorsoventral axis in the locus coeruleus (Extended Data Fig. 7a).

Our study provides the first whole-brain quantitative analysis of synaptic input onto LC-NE neurons (Figs 2i and 3b–d and Supplementary Table 2). Although the total input encompasses brain regions that control cognitive, autonomic, endocrine and somatic motor activities²², LC-NE neurons receive abundant input from motor-related nuclei in the midbrain, pons, medulla and cerebellum (Fig. 3b). Our viral-genetic tools also revealed a highly extensive output divergence (Fig. 4d). Together with input convergence, this probably explains the largely indiscriminate input–output relationship of LC-NE neurons (Fig. 3b). This property fits well with a primary function of the LC-NE neurons in regulating states of the entire brain during sleep/wake cycles and arousal^{3,23–25}.

Despite the overall integrative nature, however, our data also revealed specificity in the input–output relationship of LC-NE sub-circuits. Medulla-projecting LC-NE neurons receive disproportionately smaller input from the central amygdala than LC-NE neurons projecting to other regions (Fig. 3b, c). Input from the central amygdala to the locus coeruleus is an important component for initiating stress response²⁶. Our observation implies that modulation of medulla by LC-NE neurons is preferentially immune to this type of stress input. Although our output studies demonstrated the broad projection pattern of LC-NE neurons, they also highlighted specificities both in regard to biased cell body distribution within the locus coeruleus (Extended Data Fig. 7f) and biased projections (Fig. 4e). The existence of such input–output specificity, along with differential distribution of adrenergic receptors in target neuronal populations⁴, enables the LC-NE circuit to selectively modulate specific targets.

The viral-genetic tools we described here can be applied to other circuits in the mammalian brain, such as motor cortex (Fig. 1 and Extended Data Fig. 2). TRIO and particularly cTRIO have extended previous projection-selective targeting methods^{27–29} for analysing complex circuits in the central nervous system. Furthermore, intersecting projection and cell type using *CAV-FLEX^{loxP}-Flp* and numerous Cre transgenic mice can refine genetic access to specific populations of neurons to record and functionally manipulate their activity³⁰.

Online Content Methods, along with any additional Extended Data display items and Source Data, are available in the online version of the paper; references unique to these sections appear only in the online paper.

Received 20 August 2014; accepted 1 June 2015.

Published online 1 July 2015.

- Dahlström, A. & Fuxe, K. Evidence for the existence of monoamine containing neurons in the central nervous system. I. Demonstration of monoamines in the cell bodies of brain stem neurons. *Acta Physiol. Scand.* **232** (Suppl.) 1–55 (1964).
- Swanson, L. W. & Hartman, B. K. The central adrenergic system. An immunofluorescence study of the location of cell bodies and their efferent connections in the rat utilizing dopamine-beta-hydroxylase as a marker. *J. Comp. Neurol.* **163**, 467–505 (1975).
- Sara, S. J. & Bouret, S. Orienting and reorienting: the locus coeruleus mediates cognition through arousal. *Neuron* **76**, 130–141 (2012).
- Szabadi, E. Functional neuroanatomy of the central noradrenergic system. *J. Psychopharmacol.* **27**, 659–693 (2013).
- Robertson, S. D., Plummer, N. W., de Marchena, J. & Jensen, P. Developmental origins of central norepinephrine neuron diversity. *Nature Neurosci.* **16**, 1016–1023 (2013).
- Cedarbaum, J. M. & Aghajanian, G. K. Afferent projections to the rat locus coeruleus as determined by a retrograde tracing technique. *J. Comp. Neurol.* **178**, 1–16 (1978).
- Aston-Jones, G. *et al.* Afferent regulation of locus coeruleus neurons: anatomy, physiology and pharmacology. *Prog. Brain Res.* **88**, 47–75 (1991).
- Luppi, P. H., Aston-Jones, G., Akaoka, H., Chouvet, G. & Jouvet, M. Afferent projections to the rat locus coeruleus demonstrated by retrograde and anterograde tracing with cholera-toxin B subunit and *Phaseolus vulgaris* leucoagglutinin. *Neuroscience* **65**, 119–160 (1995).
- Wickersham, I. R. *et al.* Monosynaptic restriction of transsynaptic tracing from single, genetically targeted neurons. *Neuron* **53**, 639–647 (2007).
- Miyamichi, K. *et al.* Dissecting local circuits: parvalbumin interneurons underlie broad feedback control of olfactory bulb output. *Neuron* **80**, 1232–1245 (2013).
- Watabe-Uchida, M., Zhu, L., Ogawa, S. K., Vamanrao, A. & Uchida, N. Whole-brain mapping of direct inputs to midbrain dopamine neurons. *Neuron* **74**, 858–873 (2012).
- Soudais, C., Laplace-Builhe, C., Kissa, K. & Kremer, E. J. Preferential transduction of neurons by canine adenovirus vectors and their efficient retrograde transport *in vivo*. *FASEB J.* **15**, 2283–2285 (2001).
- Salinas, S. *et al.* CAR-associated vesicular transport of an adenovirus in motor neuron axons. *PLoS Pathog.* **5**, e1000442 (2009).
- Gerfen, C. R., Paletzki, R. & Heintz, N. GENSAT BAC Cre-recombinase driver lines to study the functional organization of cerebral cortical and basal ganglia circuits. *Neuron* **80**, 1368–1383 (2013).
- Saunders, A. *et al.* A direct GABAergic output from the basal ganglia to frontal cortex. *Nature* **521**, 85–89 (2015).
- Madisen, L. *et al.* A robust and high-throughput Cre reporting and characterization system for the whole mouse brain. *Nature Neurosci.* **13**, 133–140 (2010).
- Chandler, D. J., Gao, W. J. & Waterhouse, B. D. Heterogeneous organization of the locus coeruleus projections to prefrontal and motor cortices. *Proc. Natl Acad. Sci. USA* **111**, 6816–6821 (2014).
- Mason, S. T. & Fibiger, H. C. Regional topography within noradrenergic locus coeruleus as revealed by retrograde transport of horseradish peroxidase. *J. Comp. Neurol.* **187**, 703–724 (1979).
- Room, P., Postema, F. & Korf, J. Divergent axon collaterals of rat locus coeruleus neurons: demonstration by a fluorescent double labeling technique. *Brain Res.* **221**, 219–230 (1981).
- Nagai, T., Satoh, K., Imamoto, K. & Maeda, T. Divergent projections of catecholamine neurons of the locus coeruleus as revealed by fluorescent retrograde double labeling technique. *Neurosci. Lett.* **23**, 117–123 (1981).
- Steindler, D. A. Locus coeruleus neurons have axons that branch to the forebrain and cerebellum. *Brain Res.* **223**, 367–373 (1981).
- Swanson, L. W. *Brain Architecture: Understanding the Basic Plan* (Oxford Univ. Press, 2011).
- Aston-Jones, G. & Bloom, F. E. Activity of norepinephrine-containing locus coeruleus neurons in behaving rats anticipates fluctuations in the sleep-waking cycle. *J. Neurosci.* **1**, 876–886 (1981).
- Gompf, H. S. *et al.* Locus coeruleus and anterior cingulate cortex sustain wakefulness in a novel environment. *J. Neurosci.* **30**, 14543–14551 (2010).
- Carter, M. E. *et al.* Tuning arousal with optogenetic modulation of locus coeruleus neurons. *Nature Neurosci.* **13**, 1526–1533 (2010).
- Van Bockstaele, E. J., Colago, E. E. & Valentino, R. J. Corticotropin-releasing factor-containing axon terminals synapse onto catecholamine dendrites and may presynaptically modulate other afferents in the rostral pole of the nucleus locus coeruleus in the rat brain. *J. Comp. Neurol.* **364**, 523–534 (1996).
- Stepien, A. E., Tripodi, M. & Arber, S. Monosynaptic rabies virus reveals premotor network organization and synaptic specificity of cholinergic partition cells. *Neuron* **68**, 456–472 (2010).
- Pivetta, C., Esposito, M. S., Sigrist, M. & Arber, S. Motor-circuit communication matrix from spinal cord to brainstem neurons revealed by developmental origin. *Cell* **156**, 537–548 (2014).
- Kinoshita, M. *et al.* Genetic dissection of the circuit for hand dexterity in primates. *Nature* **487**, 235–238 (2012).
- Luo, L., Callaway, E. M. & Svoboda, K. Genetic dissection of neural circuits. *Neuron* **57**, 634–660 (2008).

Supplementary Information is available in the online version of the paper.

Acknowledgements We thank N. Makki for initiating the locus coeruleus project, Stanford and UNC Viral Cores for producing AAVs, K. Touhara for support, D. Berns for suggesting the TRIO acronym, and members of the Luo laboratory, L. de Lecea and S. Hestrin for critiques. L.A.S. is supported by a Ruth L. Kirschstein National Service Research Award from NIMH, X.J.G. is supported by a Stanford Bio-X Enlight Foundation Interdisciplinary Fellowship, B.W. is supported by a Stanford Graduate Fellowship and an NSF Graduate Research Fellowship, E.J.K. is supported by EU FP7 BrainVector (no. 286071), K.M. was a Research Specialist and L.L. is an investigator of HHMI. This work is supported by an HHMI Collaborative Innovation Award.

Author Contributions L.A.S. performed all the experiments on locus coeruleus input, output and TRIO analysis, as well as motor cortex TRIO experiments and analysis. K.M. designed the TRIO and cTRIO methods, made all the constructs, performed proof-of-principle experiments for TRIO along with B.W. and performed rat TRIO and mitral cell experiments. X.J.G. performed statistical analysis together with L.A.S. K.T.B. participated in testing TRIO and cTRIO conditions and is co-supervised by R.C.M. and L.L. K.E.D. and J.R. provided technical support. S.I. and E.J.K. produced *CAV-FLEX^{loxP}-Flp*. L.L. supervised the project and wrote the paper together with L.A.S., with contributions from all authors, in particular K.M. and X.J.G.

Author Information Reprints and permissions information is available at www.nature.com/reprints. The authors declare no competing financial interests. Readers are welcome to comment on the online version of the paper. Correspondence and requests for materials should be addressed to L.L. (lluo@stanford.edu).

METHODS

Animals. *Dbh-Cre* mice³¹ and *Rbp4-Cre* transgenic mice¹⁴ were obtained from the Mutant Mouse Regional Resource Center. Purkinje cell protein 2 (*Pcp2*)-*Cre*³² and the *ROSA26*^{Ail14} *Cre*-dependent tdTomato reporter (*Ail14*)¹⁶ were obtained from the Jackson Laboratories. Mice were housed on a 12-h light/dark cycle with food and water *ad libitum*. Transgenic mice were of a mixed genetic background, and there was a similar distribution of male and female mice included in all experiments. Wister Rats were purchased from Japan SLC (Hamamatsu, Japan). All rats used for experiments were female. All procedures for mice followed animal care guidelines approved by Stanford University's Administrative Panel on Laboratory Animal Care (APLAC). All rat experiments were performed in accordance with the animal care and use committee guidelines of the University of Tokyo.

DNA constructs. *CAG-FLEX^{loxP}-G* and *CAG-FLEX^{loxP}-TC* (same as *CAG-FLEX-TC*)⁸ have been described previously¹⁰. *CAG-FLEX^{FRT}-G* and *CAG-FLEX^{FRT}-TC* were constructed using standard molecular cloning methods with enzymes from New England Biolabs (Ipswich, USA). The custom DNA fragment (389 base pairs) shown below was synthesized by DNA 2.0 (Menlo Park, USA). This DNA fragment contained restriction enzyme sites and two heterospecific pairs of *FRT* (shown by the underline) and *FRT5* (shown by bold italic) in the following order: 5'-NotI-MluI-KpnI-FRT-*FRT5*-SalI-AscI-FRT(complementary)-*FRT5*(complementary)-HindIII-SpeI-NotI, with the sequence as follows: 5'-GCGGCCGACGCGTACGTGGTACCGAAGTTCCTATTCCGAAGTTCCTATTCTCTAGAAAGTATAGGAATTCATCAAATAGGAAGACCAATGCTTCACCATCGACCCGAAATTCGAAGCATCACCATCGACAGAAGTTCCTATTCCGAAGTTCCTATTTCTTCAAAAGGTATAGGAAGTTCGTCGACAATTGGCGCGCCGAAGTTCCTATACTTTCTAGAGAATAGGAAGTTCGGAATAGGAAGTTCGTTGGGATTCTTCCTATTTTGATCCAAGCATCACCATCGACCCCTAGTCCAGATCTCACCATCGACCCGAAGTTCCTATACCTTTTGAAGATAGGAAGTTCGGAATAGGAAGTTCGAAGCTTAATTACTAGTGGCGCGC.

This DNA fragment was cloned into the modified *pBluescript II SK* vector that contains only a NotI recognition sequence in the cloning site. We serially inserted into this *pBluescript* the following DNA fragments by using the unique restriction sites. (1) HindIII/SpeI fragment containing the *WPRE* and human growth hormone polyA signal obtained from *pAAV-TRE-HTG* (Addgene number 27437)³³. (2) MluI/KpnI fragment containing the *CAG* promoter. To make this fragment, we sub-cloned PstI-XmaI flanked *CAG* promoter from *pCA-T-int-G* (Addgene number 36887)³⁴ into a modified *pBluescript II SK* vector that only contains MluI-PstI-XmaI-KpnI recognition sequence in the cloning site. (3) AscI/SalI fragment containing coding sequence of *G* or *TC* cassette, obtained from *pAAV-CAG-FLEX^{loxP}-G* (Addgene number 48333) or *pAAV-CAG-FLEX^{loxP}-TC* (Addgene number 48332)¹⁰. The assembled cassettes were sub-cloned into *pAAV-MCS* (AAV helper free system, Stratagene, catalogue number 240071-12) using the NotI sites. Flp-dependent mCherry expression from *CAG-FLEX^{FRT}-TC* was confirmed by transient transfection into cultured HEK293 cells by using a Flp-expressing plasmid (data not shown). To generate *CAV-FLEX^{loxP}-Flp*, we first constructed the *CAV* targeting vector *pCAV-FLEX^{loxP}-Flp*. AscI-SalI flanking *Flp* coding sequence was PCR amplified by using *pBT340* (Addgene number 52549) as a template and sub-cloned into SalI-AscI site of a precursor of *pAAV-CAG-FLEX^{loxP}-TC*⁸ (ref. 10) that does not contain *WPRE*-polyA signal. XmaI-NotI fragment containing *FLEX^{loxP}-Flp* was then subcloned into KpnI-NotI site of pCL20c lentivirus vector³⁵ by using blunt-end ligation. EcoRI-SpeI fragment containing *FLEX^{loxP}-Flp* was then subcloned into EcoRI-EcoRV site of *pTCAV-12vk* (description available upon request to E.J.K.) by using one-sided (SpeI site) blunt-end ligation, resulting in *pCAV-FLEX^{loxP}-Flp*.

Virus preparations. All viral procedures followed the Biosafety Guidelines approved by the Stanford University Administrative Panel on Laboratory Animal Care (A-PLAC), Administrative Panel of Biosafety (APB), and equivalent committees of the University of Tokyo. Recombinant AAV vectors (serotype 5 for TVA receptor fused with mCherry and serotype 8 for rabies glycoprotein) were produced in the Stanford University or University of North Carolina Viral Core. The AAV titre was estimated to be 2.6 and 1.3×10^{12} viral particles per ml for *CAG-FLEX^{FRT}-TC* and *CAG-FLEX^{FRT}-G*, based on quantitative PCR analysis. RVdG was prepared as previously described³⁶. The pseudotyped RVdG titer was estimated to be $\sim 5 \times 10^5$ infectious particles per ml based on serial dilutions of the virus stock followed by infection of the 293-TVA800 cell line. The recombinant *CAV-Cre* and *CAV-FLEX^{loxP}-Flp* were generated, expanded and purified by previously described methods³⁷. The final titre of *CAV-Cre* and *CAV-FLEX^{loxP}-Flp* were 2.5×10^{12} and 5×10^{12} viral particles per ml, respectively. All handling of *CAV* and rabies virus followed procedures approved by Stanford University's Administrative Panel on Biosafety (APB) for biosafety level 2, and the equivalent committees of the University of Tokyo (P2/P2A).

Locus coeruleus trans-synaptic input tracing. Experiments in Fig. 2 were performed in *Dbh-Cre* mice at 8–12 weeks of age following procedure as described

previously^{10,38}. Mice were anaesthetized with 65 mg per kg ketamine and 13 mg per kg xylazine (Vedco/Lloyd Laboratories) via intraperitoneal injection. Then $\sim 0.5 \mu\text{l}$ of a 1:1 mixture of AAV8 *CAG-FLEX^{loxP}-G* and AAV5 *CAG-FLEX^{loxP}-TC* were injected into the left locus coeruleus of the mouse using stereotaxic equipment (Kopf). The coordinates were 0.8 mm lateral from midline, 0.8 mm posterior from lambda, and 3.2 mm ventral from the surface of the brain. Two weeks later, 0.3–0.5 μl RVdG was injected into the same area of the locus coeruleus using the procedure described above. After recovery, mice were housed in a biosafety level 2 (BSL2) facility for 4 days before euthanasia.

Assessment of locus coeruleus terminal infectivity by CAV-Cre. Experiments in Extended Data Figs 4 and 7 were performed in *Ail14* mice 6–8 weeks of age. Mice were anaesthetized and injected, as described above, with 0.25–0.5 μl *CAV-Cre* plus 0.02 μl green retrobeads (Lumofluor, USA) into predicted LC output sites: olfactory bulb (OB), auditory cortex (AC), hippocampus (Hi), medulla (Me), or cerebellum (Cb). The coordinates used for *CAV-Cre* injection sites are listed as measurements from bregma for OB, AC and Hi, and from lambda for Me and Cb. Ventral measurements are from the surface of the brain. OB: 0.75 mm lateral, 4.0 mm anterior, 1 mm ventral; AC: 4.2 mm lateral, 2.5 mm posterior, 0.8 mm ventral; Hi: 1.5 mm lateral, 2 mm posterior, 1.5 mm ventral; Me: 0.75 mm lateral, 3.3 mm posterior, 3.5 mm ventral; Cb: 2.0 mm lateral, 3.0 mm posterior, 1.5 mm ventral. After recovery, mice were housed in a BSL2 facility for 5–7 days before euthanasia.

Locus coeruleus projection-based viral labelling. Experiments in Fig. 4 and Extended Data Fig. 10 were performed in wild-type or *Dbh-Cre* mice 8–12 weeks of age. Mice were anaesthetized and injected with $\sim 0.25 \mu\text{l}$ AAV5-expressing TC (*CAG-FLEX^{loxP}-TC* for wild-type mice or *CAG-FLEX^{FRT}-TC* for *Dbh-Cre* mice) into the left locus coeruleus as described above. Mice were also injected with $\sim 0.5 \mu\text{l}$ *CAV-Cre* (wild-type mice) or *CAV-FLEX^{loxP}-Flp* (*Dbh-Cre* mice) at locus coeruleus output sites in the ipsilateral hemisphere (OB, AC, Hi, Me; coordinates listed above). After recovery, mice were housed in a BSL2 facility for 3–4 weeks before euthanasia.

Locus coeruleus TRIO and cTRIO. Experiments shown in Fig. 3 were performed in wild-type (TRIO) or *Dbh-Cre* (cTRIO) mice at 8–12 weeks of age. For TRIO, mice were anaesthetized and injected with $\sim 0.5 \mu\text{l}$ of a 1:1 mixture of AAV8 *CAG-FLEX^{loxP}-G* and AAV5 *CAG-FLEX^{loxP}-TC* into the left locus coeruleus, and also injected with $\sim 0.5 \mu\text{l}$ *CAV-Cre* into ipsilateral OB, Hi, or AC using coordinates described above. For cTRIO, mice were anaesthetized and injected with $\sim 0.5 \mu\text{l}$ of a 1:1 mixture of AAV8 *CAG-FLEX^{FRT}-G* and AAV5 *CAG-FLEX^{FRT}-TC* into the left locus coeruleus, and also injected with $\sim 0.5 \mu\text{l}$ *CAV-FLEX^{loxP}-Flp* into either ipsilateral Cb or Me using coordinates described above. After recovery, mice were housed in a BSL2 facility. Two weeks later, 0.3–0.5 μl RVdG was injected into the locus coeruleus using the procedure described above. After recovery, mice were housed in a BSL2 facility for 4 days before euthanasia.

Motor cortex TRIO and cTRIO. Experiments in Fig. 1 were performed in wild-type (TRIO) or *Rbp4-Cre* (cTRIO) mice at 8–12 weeks of age. For TRIO, mice were anaesthetized and injected with $\sim 0.5 \mu\text{l}$ of a 1:1 mixture of AAV8 *CAG-FLEX^{loxP}-G* and AAV5 *CAG-FLEX^{loxP}-TC* into the left motor cortex (MC), and also injected with $\sim 0.5 \mu\text{l}$ *CAV-Cre* into contralateral MC (cMC) using the following coordinates from bregma: 1.5 mm lateral, 1.5 mm anterior, 0.8 mm ventral from the surface of the brain. For cTRIO, *Rbp4-Cre* mice were anaesthetized and injected with $\sim 0.5 \mu\text{l}$ of a 1:1 mixture of AAV8 *CAG-FLEX^{FRT}-G* and AAV5 *CAG-FLEX^{FRT}-TC* into the left motor cortex, and also injected with $\sim 0.5 \mu\text{l}$ *CAV-FLEX^{loxP}-Flp* into the coordinates described above (for cMC), or the following coordinates for medulla (from lambda): 1 mm lateral, 3 mm posterior, 4 mm ventral from the surface of the brain. After recovery, mice were housed in a BSL2 facility. Two weeks later, 0.3–0.5 μl RVdG was injected into motor cortex. After recovery, mice were housed in a BSL2 facility for 4 days before euthanasia.

Rat motor cortex TRIO. For TRIO experiments in rat (Extended Data Fig. 2), $\sim 0.4 \mu\text{l}$ of a 1:1 mixture of AAV2 *CAG-FLEX^{loxP}-G* and AAV2 *CAG-FLEX^{loxP}-TC* was injected into the brain of ~ 5 -week-old Wister rat using stereotaxic equipment (Narishige, Japan). During surgery, animals were anaesthetized with 65 mg per kg ketamine and 13 mg per kg xylazine. For motor cortex injections, the needle was placed 2.5 mm anterior and 2.3 mm lateral from the bregma, and 0.9 mm ventral from the brain surface. $\sim 0.5 \mu\text{l}$ *CAV-Cre* was injected subsequently into either the ipsilateral striatum (1.0 mm posterior and 4.0 mm lateral from the bregma, and 4.0 mm ventral from the brain surface) or the contralateral motor cortex. After recovery, animals were housed in a BSL2 room. Two weeks later, 0.3 μl RVdG was injected into the AAV injection site under anaesthesia. After recovery, animals were housed in a BSL2 room for 4 days before euthanasia.

Control TRIOs. Control experiments (Extended Data Figs 1, 2, 5 and 8) were performed using conditions described above for locus coeruleus and motor cortex experiments.

Characterizing CAV-Cre spread in the piriform cortex. To test the extent of local spread of *CAV-Cre* in the injection site (Extended Data Fig. 3), $\sim 0.3 \mu\text{l}$ *CAV-Cre* plus $\sim 0.025 \mu\text{l}$ green retrobeads (Lumofluor, USA) were injected into

the anterior piriform cortex or surrounding areas of adult mice heterozygous for the *Ail4* Cre reporter. During surgery, animals were anaesthetized with 65 mg per kg ketamine and 13 mg per kg xylazine. The stereotactic coordinates were anterior 1.7 mm from the bregma; lateral 1.7–2.8 mm from the midline; ventral 2.5–4.0 mm from the surface of the brain. One week after the injection, animals were perfused and brain tissue was processed and sectioned as described in the histology and imaging section. Then, 60- μ m coronal sections through the olfactory bulb until the end of anterior piriform cortex (APC) were collected. The needle location was visualized by the presence of concentrated retrobeads. The distance between the needle tip and the nearest layer 1a of anterior piriform cortex or lateral olfactory tract was measured. In the main and accessory olfactory bulb, the number of tdTomato⁺ cells was counted either in every section (when total number of labelling was less than ~1,000 cells) or in every other section (when total the number of labelling was greater than ~1,000 cells).

Histology and imaging. For all tracing analyses and CAV-Cre infectivity analyses (Figs 1–4 and Extended Data Figs 1–5, 6a, 7, 8 and 10), animals were perfused transcardially with phosphate-buffered saline (PBS) followed by 4% paraformaldehyde (PFA) in PBS. Brains were dissected, post-fixed in 4% PFA for 24 h, and placed in 30% sucrose in PBS for 24–48 h. After embedding in Optimum Cutting Temperature (OCT, Tissue Tek), samples were stored at -80°C until sectioning. For Figs 1–3 and Extended Data Figs 1–6a, and 8, consecutive 60- μ m coronal sections were collected onto Superfrost Plus slides, washed 2×20 min with PBS, and stained with DAPI (1:10,000 of 5 mg ml⁻¹, Sigma-Aldrich), which was included in the last PBS wash. Slides were coverslipped with Fluorogel (Electron Microscopy Sciences). Samples were imaged using a Leica Ariol slide scanner with the SL200 slide loader. Briefly, the scanner first imaged slides using a 1.25 \times objective and the ‘TissueFind’ function to generate composite brightfield images of the entire slide. Then, the scanner automatically detected individual tissue sections from these brightfield images (~15–20 coronal tissue sections per slide), and performed automated tiled imaging of each tissue section on the slide in two channels (DAPI and Spectrum Green filters) using a 5 \times objective. Each tile was approximately 1.2 mm by 1.2 mm, and included ~20- μ m overlap between tiles. Leica Ariol software automatically stitched together individual tiles during image collection to generate a composite SCN file of the entire slide. For analysis of locus coeruleus output (Fig. 4 and Extended Data Fig. 10), every 50- μ m sagittal section within the brain regions designated for analysis were collected sequentially into PBS. Sections were washed 2×10 min in PBS and blocked for 2–3 h at room temperature (RT) in 10% normal donkey serum (NDS) in PBS with 0.3% Triton-X100 (PBST). Primary antibodies (mouse anti-noradrenaline transporter (NET), PhosphoSolutions, 1447-NET, 1:10,000; rat anti-mCherry, M11217, Invitrogen, 1:2,000) were diluted in 5% NDS in PBST and incubated for four nights at 4°C . After 3×10 min washes in PBST, secondary antibodies were applied for 2–3 h at room temperature (donkey anti-mouse, Alexa-488, and donkey anti-rat Cy3, Jackson ImmunoResearch), followed by 3×10 min washes in PBST. Sections were additionally stained with DAPI. For immunostaining of locus coeruleus neuron cell bodies (Extended Data Figs 5 and 7), 50- μ m coronal sections through the locus coeruleus were collected into PBS. Sections were washed, immunostained, and mounted as described above, using a primary antibody for tyrosine hydroxylase (rabbit anti-tyrosine hydroxylase (TH), Millipore, AB152, 1:2,000). All images were processed using NIH ImageJ software. For gephyrin immunostaining (Extended Data Fig. 6), fresh tissue was processed and 14- μ m horizontal sections were collected through the locus coeruleus following ‘Method B’ in a previously published protocol³⁹. Sections were immunostained with primary antibodies for gephyrin (mouse anti-gephyrin, Synaptic Systems, 147011, 1:700), and tyrosine hydroxylase (Millipore, 1:2,000). Representative images in Fig. 1f (top and middle) and Extended Data Figs 1, 4, 5c, d, 6b, c (left), 7a, c, 8a, b (bottom) and Extended Data Fig. 10a were obtained on a Zeiss epifluorescence microscope with a Nikon CCD camera. Representative images in Figs 2b (inset), 4c (inset), Extended Data Figs 5a, 6b (right), c (middle and right), and 7a (inset) were obtained on a Zeiss LSM 780 confocal microscope. Representative images in Figs 1f (bottom), 2b–h, and Extended Data Fig. 6a were obtained on a Leica Ariol slide scanner with the SL200 slide loader. Representative images in Extended Data Figs 2 and 3 were obtained by cooled CCD camera (ORCA-R2, Hamamatsu Photonics) connected with a upright fluorescent microscope (4 \times or 10 \times objective, BX53, Olympus).

Data analysis for trans-synaptic tracing and TRIO. Because each brain differed in total numbers of input neurons, we normalized neuronal number in each region by the total number of input neurons counted in the same brain. For trans-synaptic tracing and TRIO/cTRIO analyses (Figs 1–3, and Supplementary Tables 1 and 2), GFP⁺ input neurons were manually counted from every 60- μ m section through the entire brain, except near the starter cell location (motor cortex or locus coeruleus), as specified in Extended Data Figs 1 and 5. GFP⁺ input neurons were assigned to specific brain regions based on classifications of the

Allen Brain Atlas (<http://mouse.brain-map.org/static/atlas>), using anatomical landmarks in the sections visualized by DAPI counterstaining and autofluorescence of the tissue itself. In a small minority of cases, assignment of input neurons to specific brain nuclei may be approximate if GFP⁺ cell bodies were located on borders between regions, or when anatomical markers were lacking between directly adjacent regions (such as hypoglossal nucleus/nucleus prepositus or lateral reticular nucleus/gigantocellular reticular nucleus). However, quantitative analyses of input tracing results (Figs 1–3) were performed on anatomical classifications (specified by the Allen Brain Atlas) that were at least one hierarchical level broader than the discrete brain regions in which GFP⁺ cells were originally assigned to. For instance, the fraction of GFP⁺ cells designated to ‘paraventricular hypothalamic nucleus’ and ‘lateral hypothalamic nucleus’ were grouped into a broader category of ‘hypothalamus’. In almost all cases where individual GFP⁺ cells were difficult to classify, their location was within brain regions that belonged to the same broad group. Also, some brain regions partially overlapped with the region excluded from analysis, such as motor and somatosensory cortex for the motor cortex tracing/cTRIO analyses (Fig. 1g, Supplementary Table 1), and the dorsal raphe, periaqueductal grey, and pontine reticular nucleus for the locus coeruleus tracing/TRIO/cTRIO analyses (Figs 2i, 3b, and Supplementary Table 2). Therefore, the inputs reported for these regions are likely under-representations of their contribution to motor cortex or locus coeruleus input. We did not adjust for the possibility of double-counting cells in any of our quantifications, which likely results in slight over-estimates, with the amount of over-estimation depending on the size of the cell in each region quantified. Nearly all starter cells were TH⁺ for TRIO experiments with the CAV injection site being hippocampus ($98.6\% \pm 0.8\%$, $n = 4$ animals), olfactory bulb ($96.0\% \pm 2.7\%$, $n = 4$ animals), or auditory cortex ($98.8\% \pm 1.2\%$, $n = 4$ animals), consistent with our observation that cells at the locus coeruleus projecting to these target areas are predominantly noradrenaline neurons (Extended Data Fig. 7a). All starter cells were confirmed to be TH⁺ in cTRIO experiments with the CAV injection site in Cb (100%, $n = 4$ animals) or Me (100%, $n = 4$ animals).

Data analysis for locus coeruleus output. For locus coeruleus output quantification (Fig. 4 and Extended Data Fig. 10), images were taken from 5 consecutive sections in each of the 8 brain regions (OB, AC, CC, SC, Hi, Hy, Cb, Me) on a Zeiss epifluorescence microscope with a 10 \times objective. We attempted to image from identical volumes within each brain region between samples, based on pre-determined coordinates for these regions and the section number, as sections were collected sequentially and kept in order. The field of view for each image was located based solely on DAPI staining so the experimenter was blind to the level of TC⁺ locus coeruleus axons before imaging. An image was also taken of the noradrenaline transporter (NET) immunostaining in the same field of view to confirm that all TC⁺ axons were also NET⁺. For analysis, the TC channels for each image were made binary in ImageJ, after performing background subtraction and thresholding to a value $\sim 4\times$ greater than mean background intensity. The pixel densities of these binary images were measured and averaged (5 images per brain region) to determine the fraction of TC⁺ axons resulting from LC-NE neurons in each brain region, as a fraction of the total TC⁺ axons quantified from all of the imaged regions in that brain.

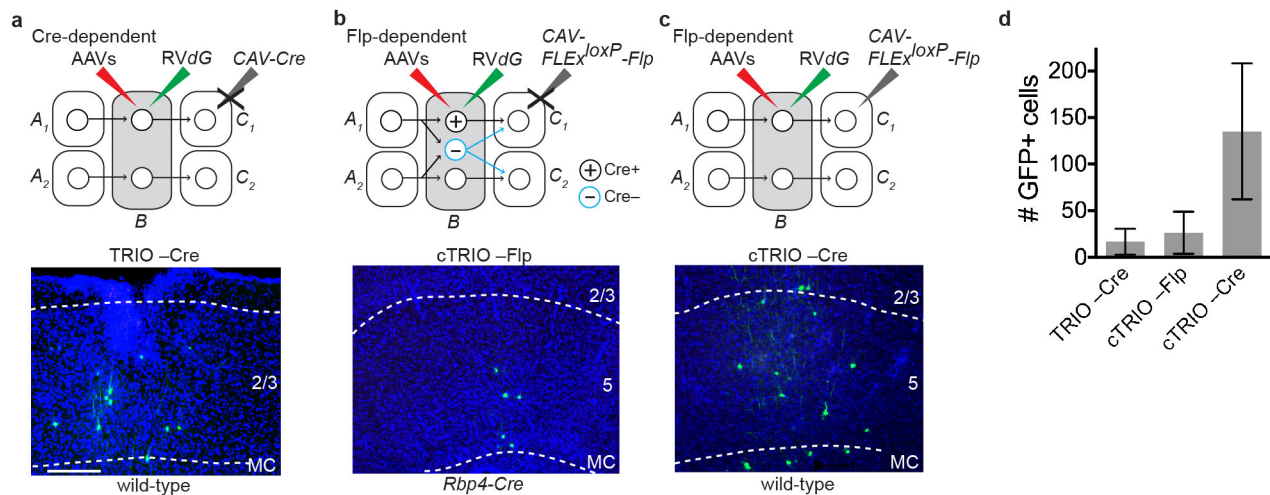
Analysis of spatial distribution in the locus coeruleus. To assess the distribution of discrete LC-NE neurons within the locus coeruleus dependent on their output (Extended Data Fig. 7), 50- μ m coronal sections were collected in order through the locus coeruleus of experimental mice and processed as described above in the histology and imaging section. The experimenter was blind to the location of the output injection site when imaging and quantifying locus coeruleus sections. The outlines of the digital model were manually drawn using TH immunostaining of LC-NE cell bodies as a guide. A cross (+) marks the approximate centre of each locus coeruleus section following the procedure below. (1) measure the maximal height (H_{max}) of the locus coeruleus (based on the shape of TH immunostaining); (2) measure the maximum width (W_{max}) of the locus coeruleus at the $0.5 H_{\text{max}}$ height level; (3) place a cross at the $0.5 W_{\text{max}}$ position. This cross was used to align each locus coeruleus image with its corresponding digital locus coeruleus section, before designating the location of the tdTomato⁺ LC-NE cell bodies with coloured dots on the digital section. Before quantifying experimental sections, two independent sets of TH-immunostained locus coeruleus sections were found to fit within the boundaries of the digital model using this method of alignment. The distribution of tdTomato⁺ LC-NE dots from each digital section were counted and assigned to dorsal/ventral and medial/lateral sub-regions using horizontal and vertical lines drawn through the centre cross of each digital section, respectively (Extended Data Fig. 7).

Input simulation. We simulated the number of input areas for the two sparsest *Dbh-Cre* tracing samples with Matlab. For each starter cell, when assuming it receives inputs from n areas, we randomly sampled n areas from the 111 input areas without replacement, weighted by the total counts of cells in each area derived from all the *Dbh-Cre* brains. The simulated input areas to the 4 (sparsest

sample) or 22 (second sparsest sample) starter cells were then consolidated to generate the final number of input areas. Ten thousand rounds of simulations were performed for each n between 11 and 30 (sparsest sample) or 3 and 22 (second sparsest sample).

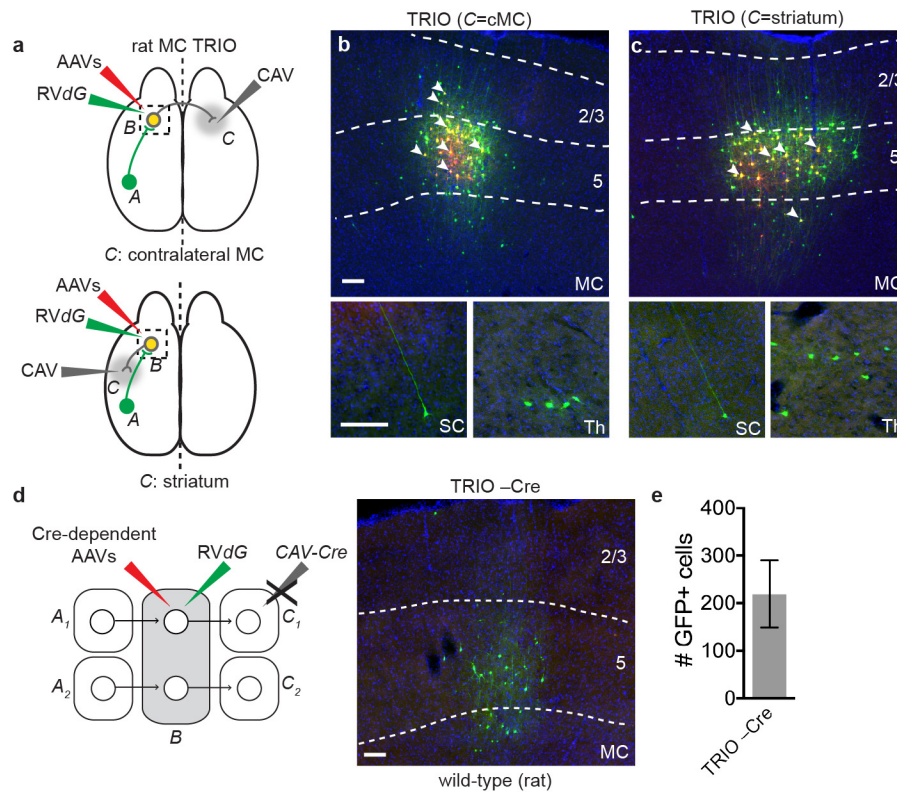
Statistical methods. No statistical methods were used to predetermine sample size. Animals were excluded from certain experiments using the following pre-established criteria. For all trans-synaptic tracing, TRIO, and cTRIO experiments in motor cortex and locus coeruleus, samples were excluded if less than 50 GFP⁺ neurons were observed in the brain outside of the area designated as local background. For projection-based viral-genetic labelling, samples were excluded if less than 10 LC-NE neurons were observed to be TC⁺. No method of randomization was used in any of the experiments. For ANOVA analyses, the variances were similar as determined by Brown–Forsythe test.

31. Gong, S. *et al.* Targeting Cre recombinase to specific neuron populations with bacterial artificial chromosome constructs. *J. Neurosci.* **27**, 9817–9823 (2007).
32. Zhang, X. M. *et al.* Highly restricted expression of Cre recombinase in cerebellar Purkinje cells. *Genesis* **40**, 45–51 (2004).
33. Miyamichi, K. *et al.* Cortical representations of olfactory input by trans-synaptic tracing. *Nature* **472**, 191–196 (2011).
34. Tasic, B. *et al.* Site-specific integrase-mediated transgenesis in mice via pronuclear injection. *Proc. Natl Acad. Sci. USA* **108**, 7902–7907 (2011).
35. Hanawa, H. *et al.* Efficient gene transfer into rhesus repopulating hematopoietic stem cells using a simian immunodeficiency virus-based lentiviral vector system. *Blood* **103**, 4062–4069 (2004).
36. Osakada, F. & Callaway, E. M. Design and generation of recombinant rabies virus vectors. *Nature Protocols* **8**, 1583–1601 (2013).
37. Kremer, E. J., Boutin, S., Chillon, M. & Danos, O. Canine adenovirus vectors: an alternative for adenovirus-mediated gene transfer. *J. Virol.* **74**, 505–512 (2000).
38. Weissbourd, B. *et al.* Presynaptic partners of dorsal raphe serotonergic and GABAergic neurons. *Neuron* **83**, 645–662 (2014).
39. Schneider Gasser, E. M. *et al.* Immunofluorescence in brain sections: simultaneous detection of presynaptic and postsynaptic proteins in identified neurons. *Nature Protocols* **1**, 1887–1897 (2006).



Extended Data Figure 1 | Controls for TRIO and cTRIO at the motor cortex. **a–c**, Negative control experiments omitting CAV-Cre for TRIO (**a**), and omitting CAV-FLEX^{loxP}-Flp (**b**) or the *Rbp4-Cre* transgene (**c**) for cTRIO showed only local non-specific infection of RVdG. This background labelling is likely due to Cre- or Flp-independent leaky expression of a small amount of TVA-mCherry (TC), too low for mCherry to be detected but still capable of permitting infection by EnvA-pseudotyped RVdG due to the high sensitivity of TVA¹⁰. **d**, Quantification for three controls ($n = 4, 4, 7$ animals, respectively).

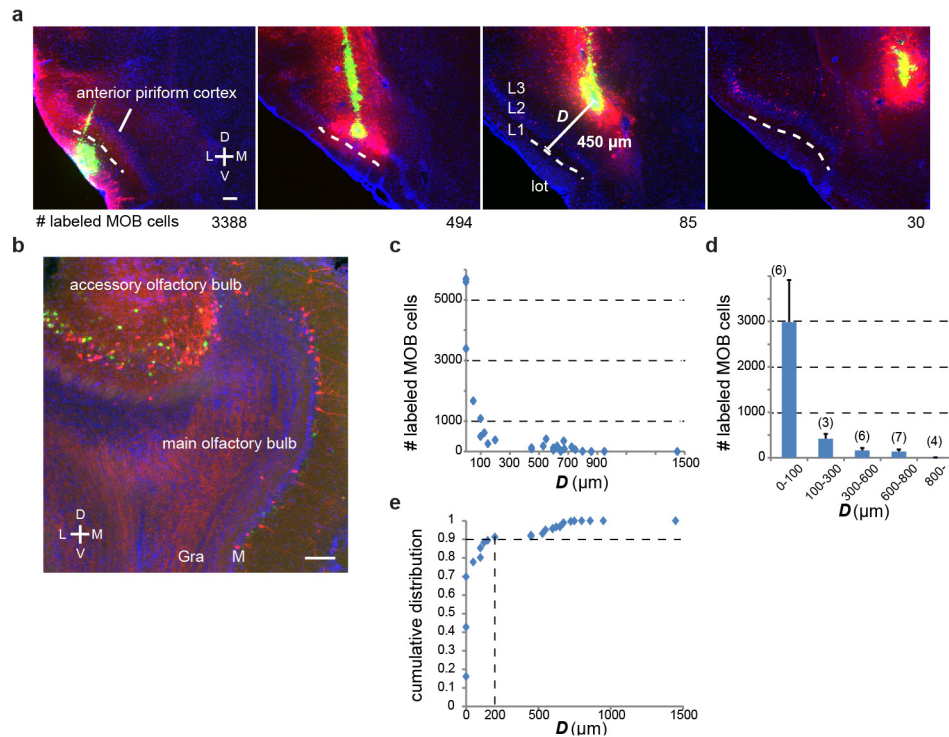
By comparison, 672 GFP⁺ neurons were counted in the same region for an experimental brain that has the lowest starter cells among the 11 brains whose data were used for quantitative analysis of motor cortex TRIO input tracing. These background cells were restricted within ~500 μm of the injection site. Because of these observations, GFP⁺ cells on sections within ~600 μm of the injection site were excluded from the input analysis in Fig. 1g. Scale bar, 100 μm . Error bars, s.e.m.



Extended Data Figure 2 | TRIO applied to rat primary motor cortex.

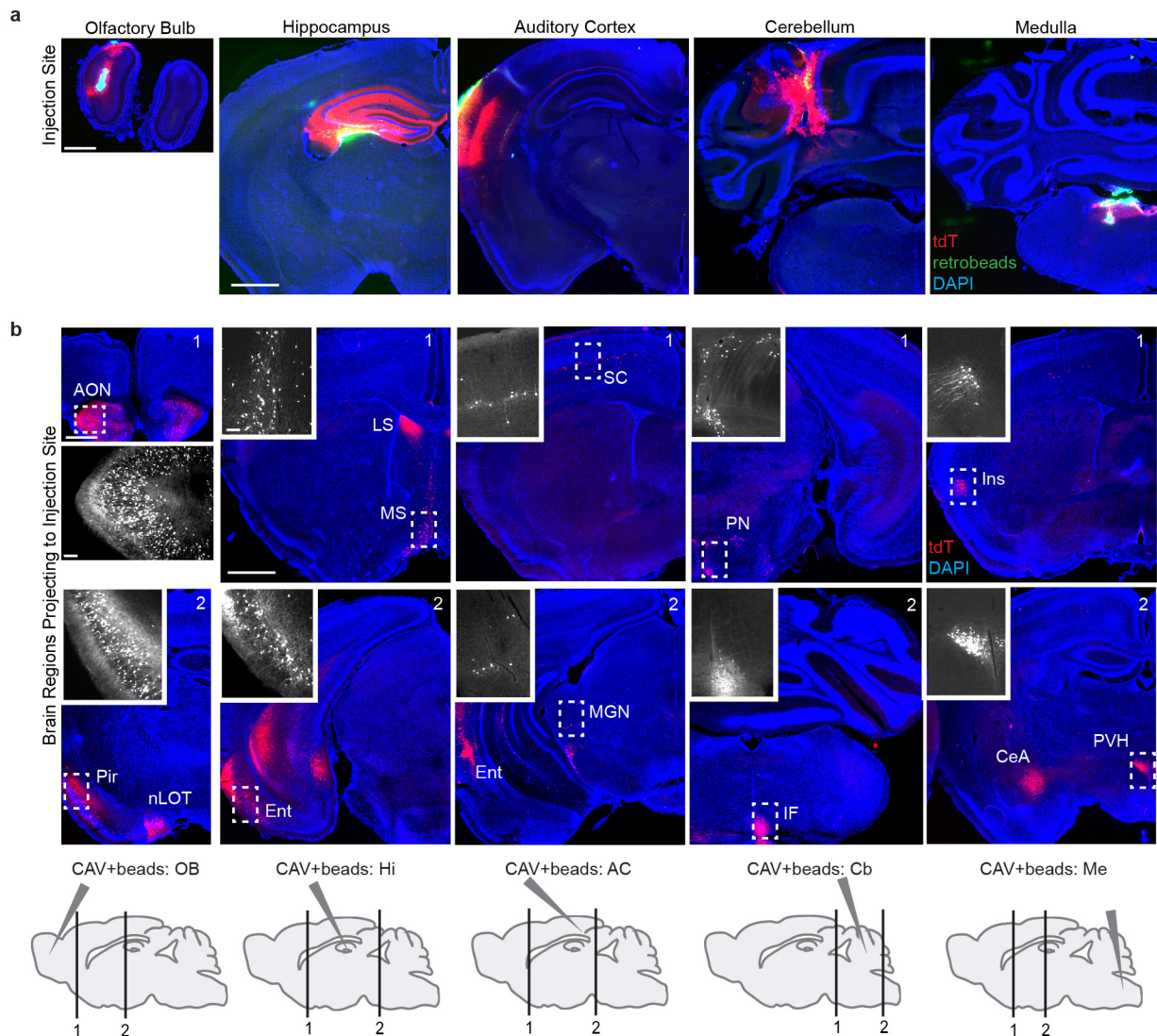
a, Schematic of injection sites used for TRIO in rat motor cortex (see Fig. 1c for details of the viruses). Two different C regions were tested: striatum or contralateral motor cortex (cMC). **b**, **c**, Coronal section of rat motor cortex stained with DAPI (blue). Starter pyramidal neurons projecting to contralateral motor cortex (**b**) or striatum (**c**) (yellow, a subset indicated by arrowheads) can be distinguished from neurons receiving CAV-Cre and AAV-FLEX^{loxP}-TC (red) or GFP from RVdG (green). Bottom insets, coronal sections showing representative presynaptic GFP⁺ cells in somatosensory cortex (SC) or

thalamus (Th). These data indicate that callosal-projecting neurons and striatum-projecting neurons in rat motor cortex both receive direct synaptic input from somatosensory cortex and thalamus ($n = 2$ animals for cMC C region; $n = 3$ animals for striatum C region). **d**, **e**, Omitting CAV-Cre for TRIO in the rat also resulted in local non-specific infection of RVdG. On average ~200 cells were observed ($n = 4$ animals) within 800 μ m from the injection site in these control experiments. By comparison, 1,392 GFP⁺ neurons were counted in the same region of a TRIO sample that has the lowest starter cells among the 5 brains analysed. Scale bars, 100 μ m. Error bars, s.e.m.



Extended Data Figure 3 | Evaluation of *CAV-Cre* spread by using the OB→APC projection. **a**, Four representative 60-μm coronal sections of the *CAV-Cre* injection site in the anterior piriform cortex (APC) of four *Ail4* Cre-reporter mice. Red, tdTomato; green, retrobeads; blue, DAPI. The location of the injection site was readily visualized by concentrated retrobeads. D, dorsal; L, lateral; M, medial; V, ventral. In each mouse, we determined the minimal distance (D) between the injection site and layer 1a of the piriform cortex, where mitral cell axons terminate, or lateral olfactory tract, where mitral cell axon bundles are present. Dashed lines represent the boundary between layer 1a and layer 1b. For each sample, we counted the number of tdTomato-labelled mitral cells (numbers below each image) from serial olfactory bulb (OB) sections. **b**, An example 60-μm coronal section of the OB. Both tdTomato and retrobeads signals were found to be mostly restricted to the mitral cell

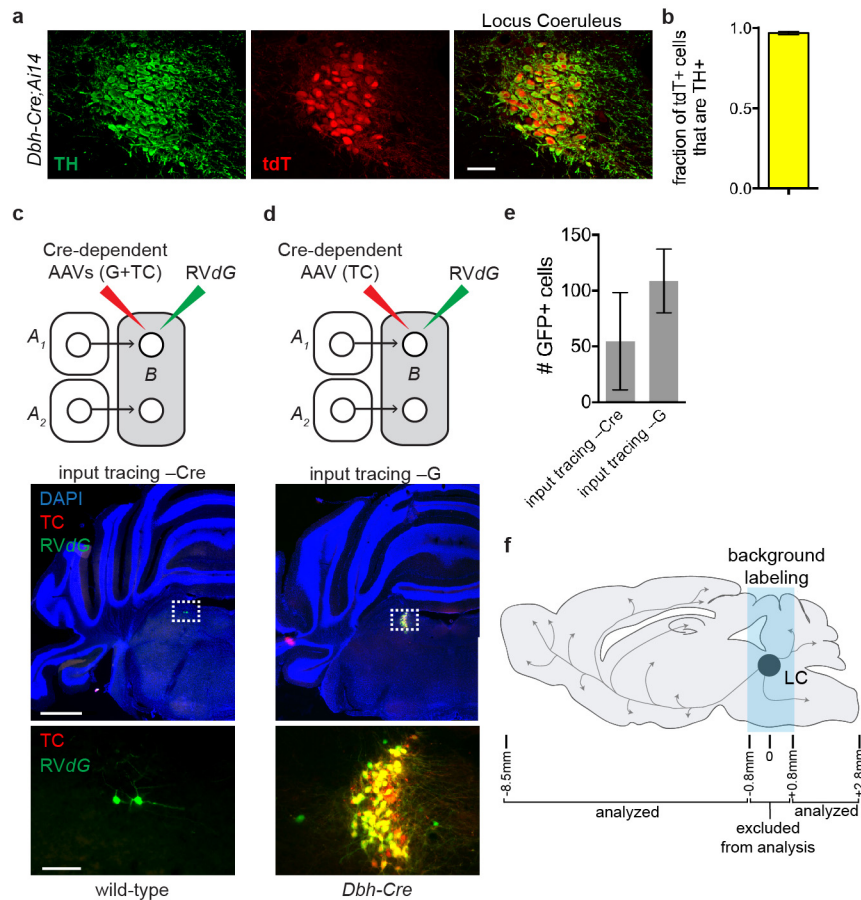
layer (M) of the main olfactory bulb (MOB) and accessory olfactory bulb (AOB) with minor labelling in the granule cell layer (Gra). As AOB mitral cells do not form synapses in the APC, this observation indicates that *CAV-Cre* can infect axons-in-passage. **c**, Distribution of D among 26 injections (x axis) and relationship between D and the numbers of labelled cells in the MOB (y axis). **d**, Histogram based on **c**. Dense labelling (over 1,000) was obtained only when $D < 100$ μm. *CAV-Cre* injections with $D > 800$ μm rarely labelled the OB (2.8 ± 1.9 cells per bulb, $n = 4$ animals). **e**, Cumulative distribution plot of MOB cell counts. A sample of the ninth smallest D ($D = 200$ μm) reached 90% of the labelling (indicated by vertical dotted line) detected in all 26 samples, suggesting that given our sample distribution, ~90% of axonal transduction occurred within 200 μm from the *CAV-Cre* injection site. Scale bars, s.e.m.



Extended Data Figure 4 | Evaluation of retrograde infection by CAV-Cre.

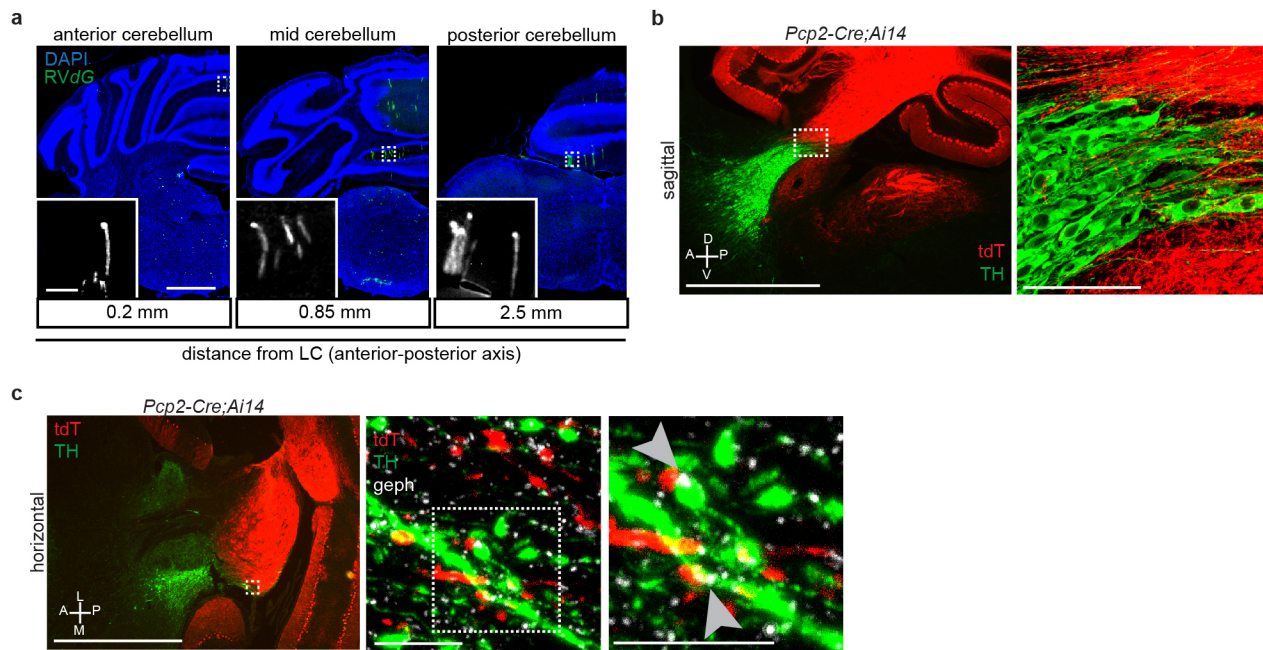
a, Representative coronal sections of the injection sites where CAV-Cre plus retrobeads were delivered into the olfactory bulb, dorsal hippocampus, auditory cortex, cerebellum or medulla of the *Ail4* Cre-reporter mice (see Methods for coordinates). Red, tdTomato; green, retrobeads; blue, DAPI. tdTomato labelling was densest at the injection site, and corresponded with the presence of retrobeads. We did not observe dense tdTomato or retrobeads labelling in other brain regions adjacent to the injection site unless these sites sent direct projections to the injection site, indicating that for our experiments, CAV-Cre was efficiently and specifically delivered to the targeted brain regions. $n = 4$ animals per injection site. **b**, Representative coronal sections of brain regions that contained tdTomato⁺ labelling of specific cell populations known to project to CAV-Cre injection sites. The following is a partial list: neurons

projecting to olfactory bulb (first column): ipsi- and contralateral anterior olfactory nucleus (AON), piriform cortex (Pir), nucleus of the lateral olfactory tract (nLOT), but not contralateral olfactory bulb; to dorsal hippocampus (second column): lateral and medial septum (LS, MS) and entorhinal cortex (Ent); to auditory cortex (third column): somatosensory cortex (SC), entorhinal cortex (Ent), and medial geniculate nucleus (MGN); to cerebellum (fourth column): contralateral pontine nuclei (PN) and inferior olive (IF); to medulla (fifth column): insular cortex (Ins), central amygdala (CeA), and paraventricular hypothalamic nucleus (PVH). Coronal images are composites generated from overlapping tiled images. Insets show high magnification images of boxed regions. Bottom, sagittal schematic of the CAV-Cre injection sites (**a**) and the approximate location of the two representative coronal sections above. Scale bars, 1 mm; inset, 100 μ m.



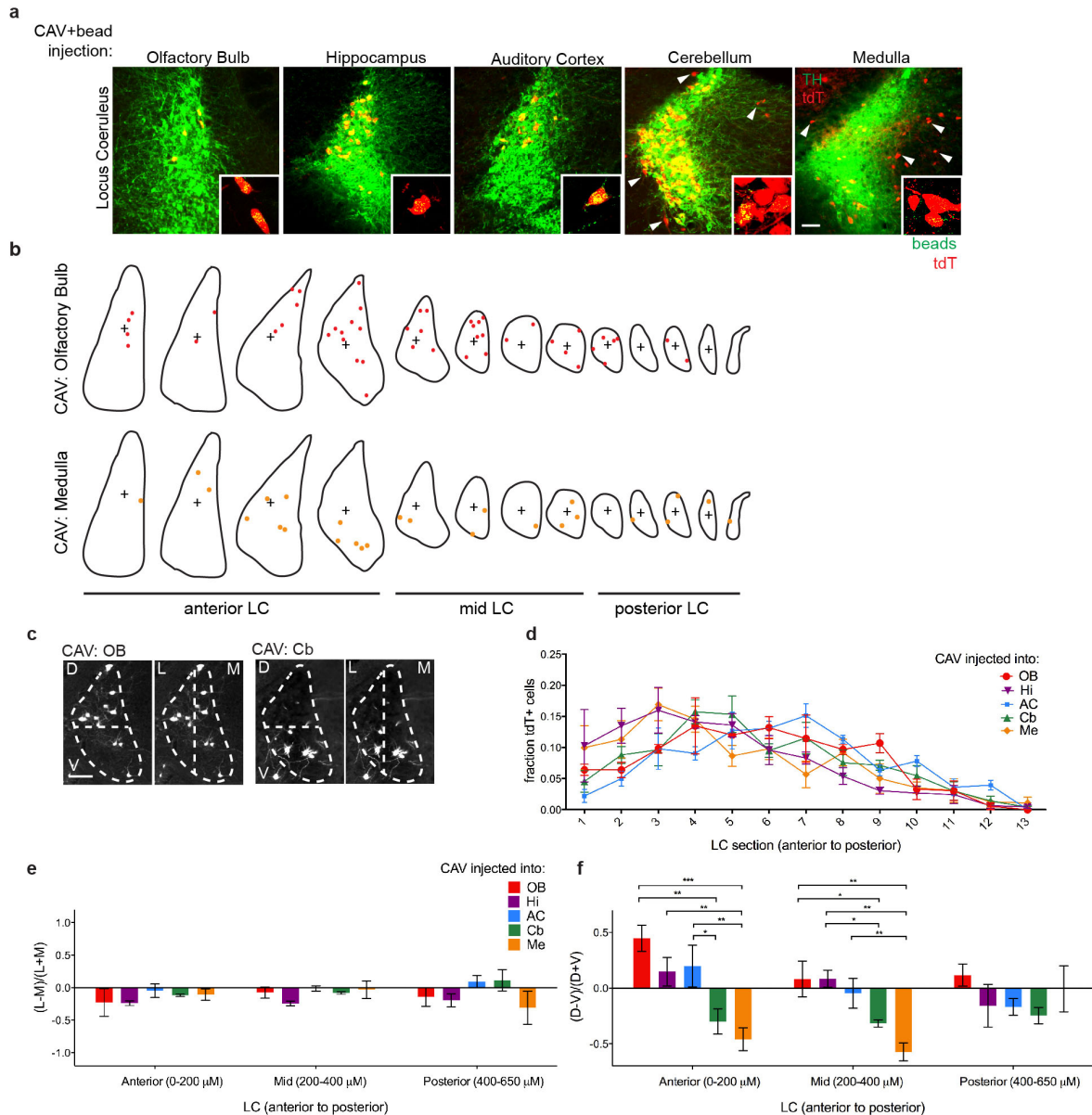
Extended Data Figure 5 | Controls for *Dbh-Cre*-based trans-synaptic tracing and TRIO analysis in locus coeruleus. **a**, A Representative coronal section of the locus coeruleus from a mouse heterozygous for *Dbh-Cre* and *Ai14* Cre-reporter transgenes. Sections were labelled with an antibody against tyrosine hydroxylase (TH), an enzyme in the biosynthetic pathway for noradrenaline (green), while cells expressing Cre recombinase are visible by expression of tdTomato (red). **b**, Quantification of the number of tdTomato⁺ neurons in the locus coeruleus that were also labelled by TH antibody ($n = 3$ animals). Every 50- μ m section through the locus coeruleus was collected for quantification. Qualitatively, all TH⁺ cells expressed tdTomato; however, we cannot determine quantitatively because we could not accurately count TH⁺ cells due to dense process staining. **c**, Top, schematic for negative control where AAVs that express Cre-dependent TVA-mCherry fusion (TC) and rabies glycoprotein (G) were injected into the locus coeruleus of wild-type mice, followed by injection of RVdG. Middle, coronal section of the locus coeruleus stained with DAPI (blue) shows a small number of GFP⁺ neurons at the injection site. The dotted rectangle highlights GFP⁺ neurons magnified in the bottom panel. **d**, Top, in this negative control, *Dbh-Cre* mice received Cre-dependent TVA-mCherry fusion (without rabies glycoprotein) via AAV

injection into the locus coeruleus, followed by RVdG. Middle, a coronal section of the locus coeruleus stained with DAPI (blue) shows infection of Cre⁺ locus coeruleus neurons with TC (red) or TC and RVdG (yellow) at the injection site. The dotted rectangle highlights infected locus coeruleus neurons magnified in the bottom panel. Most green cells are also red. No GFP⁺ cells were observed outside the region immediately adjacent to the injection site, indicating that trans-synaptic tracing depends on rabies glycoprotein. **e**, Quantification of the number of GFP⁺ cells (**c**), or GFP⁺ cells that did not colocalize with TC (**d**), that were observed in the experiments described in (**c**, $n = 8$ animals) and (**d**, $n = 6$ animals). By comparison, 1,381 GFP⁺ neurons were counted in the same region for an experimental brain that has the median number of starter cells among the 9 brains. For explanation of background labelling, see Extended Data Fig. 1a–c. In either case, no GFP⁺ neurons were visible >800 μ m away from the injection site. **f**, Schematic of brain regions quantified for presynaptic GFP⁺ neurons. Regions approximately 800 μ m anterior and posterior to the centre of the locus coeruleus were excluded from analysis due to local background labelling from TVA-mCherry fusion and GFP. Scale bars, 50 μ m (**a**), 1 mm (**c**, **d**, middle panels), 100 μ m (**c**, **d**, bottom panels). Error bars, s.e.m.



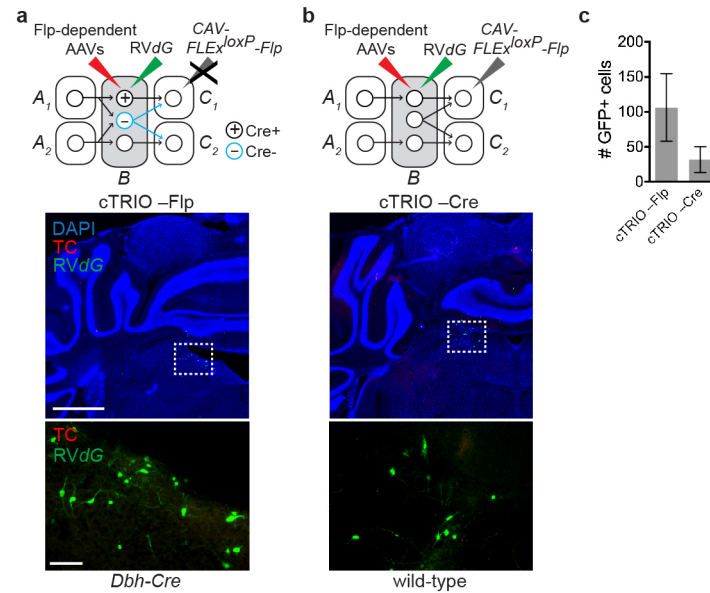
Extended Data Figure 6 | Purkinje cell axons contact noradrenergic processes in the locus coeruleus. **a**, Coronal sections counterstained with DAPI (blue) showing representative GFP⁺ Purkinje cells (green) from *Dbh-Cre* trans-synaptic tracing experiments described in Fig. 2. Labelled Purkinje cells span the anterior–posterior axis, but are enriched in the medial portion of the ipsilateral cerebellum. **b**, Sagittal section through the locus coeruleus of mice heterozygous for the transgenes *Pcp2-Cre* and *Ai14*, in which tdTomato (tdT) expression was restricted to cerebellar Purkinje cells and their processes (red). Sections were labelled with DAPI (blue) and anti-TH antibody (green) to label LC-NE neurons. The right panel is a maximum-projection confocal stack taken with a 40× objective of the boxed region in the left panel. Purkinje cell axons are intermingled with TH⁺ locus coeruleus neurons and their processes. **c**, Left, Representative image of a horizontal section collected through the locus coeruleus of a mouse heterozygous for the transgenes

Pcp2-Cre and *Ai14*. Sections were stained with anti-TH antibody (green) to label LC-NE neurons and their processes, and anti-gephyrin (geph) antibody (white) to label inhibitory post-synaptic densities. Middle, maximum-projection confocal stack taken with a 40× objective of the dashed box of the left panel showing the overlap between tdTomato⁺ Purkinje cell axons and TH⁺ LC processes. Right, high magnification of the dashed box of the middle panel, showing that several of these contact points also contained gephyrin⁺ puncta (arrowheads) within green processes apposing the red processes, consistent with GABAergic Purkinje cell axons forming synapses onto dendrites of TH⁺ LC-NE neurons. Images in **a** were derived from larger composite images generated by a Leica Ariol Slide Scanner. A, anterior; D, dorsal; L, lateral; M, medial; P, posterior; V, ventral. Scale bars, 1 mm (**a**; **b** and **c**, left), 100 μm (**a**, inset; **b**, right), 10 μm (**c**, middle and right).



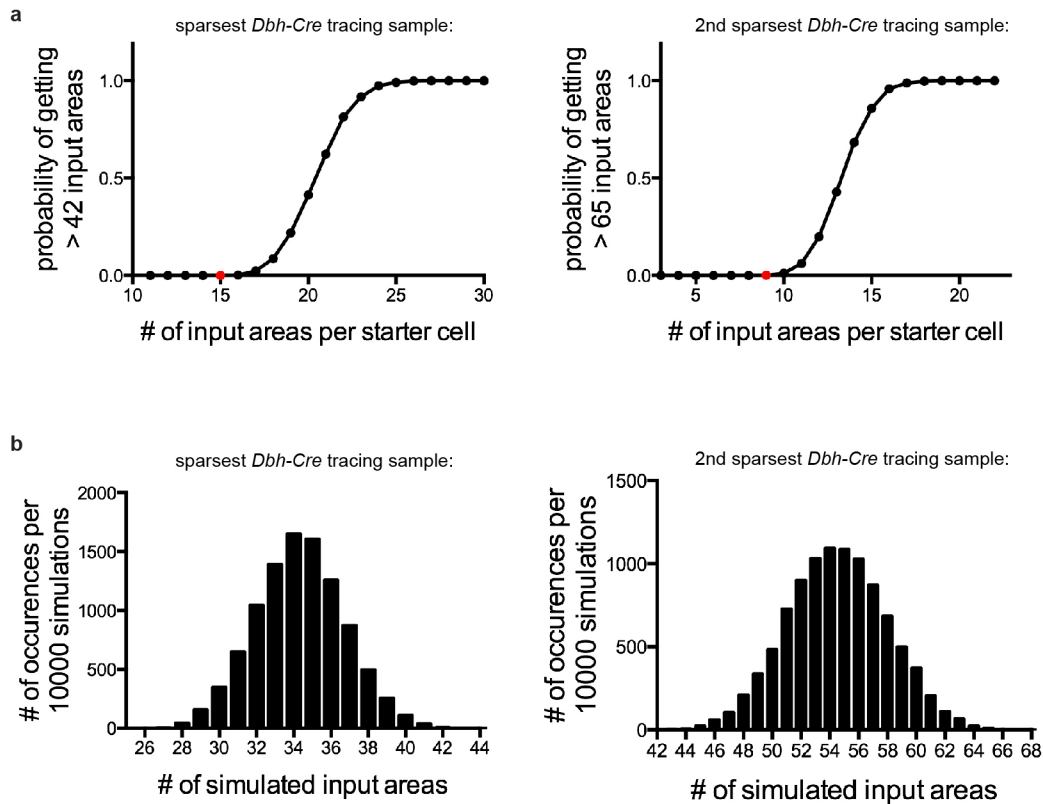
Extended Data Figure 7 | Spatial distribution of LC-NE neurons projecting to distinct output brain regions. **a**, Representative images of individual LC-NE neurons labelled within the locus coeruleus by injection of CAV-Cre at specific output sites (see Extended Data Fig. 4a) in *Ai14* Cre-reporter mice. Coronal sections through the locus coeruleus were collected in order and stained with anti-TH antibody (pseudocoloured in green). All tdTomato (tdT)⁺ neurons within the locus coeruleus were also TH⁺, and many of these cells also contained retrobeads (green in inset). Injection of CAV-Cre into the olfactory bulb, hippocampus or auditory cortex resulted in high tdTomato expression in NE⁺ neurons within the locus coeruleus, whereas tdTomato labelling was almost completely absent in adjacent brain regions, indicating that regions next to the locus coeruleus contribute minimal projections to these output sites. However, CAV-Cre injected into the cerebellum or medulla labelled NE⁺ locus coeruleus neurons as well as adjacent, NE⁻ cell populations (a subset of which are highlighted by arrowheads). **b**, The locations of tdTomato⁺ LC-NE neurons from sequential 50- μ m coronal sections collected through the entire locus coeruleus were transferred to corresponding sections of a digital locus coeruleus model and are represented by coloured dots (see Methods). **c**, Schematic of the dorsal/ventral and medial/lateral classifications used with tdTomato⁺ LC-NE neurons occurring from CAV-Cre injections into the olfactory bulb (left) or cerebellum (right) of *Ai14* mice. These classifications were made by drawing horizontal and vertical lines through the cross (b) designating the middle of each locus coeruleus section. **d**, Quantification of the fraction of tdTomato⁺ LC-NE cells in each locus coeruleus section along the anterior-posterior axis of the locus coeruleus. No significant differences were

observed for the anterior-posterior distribution of tdTomato⁺ LC-NE neurons projecting to different output sites. **e**, Quantification of the medial-lateral distribution of LC-NE neurons projecting to different output sites. LC-NE neurons showed no bias in the medial versus lateral portion of the locus coeruleus, regardless of where they sent projections. **f**, Quantification of the dorsal-ventral distribution of tdTomato⁺ LC-NE neurons projecting to different output sites. Although no bias was observed in the posterior locus coeruleus, significant differences were observed in the anterior and mid-LC. Specifically, LC-NE neurons projecting to the forebrain showed a dorsal bias for tdTomato⁺ cell labelling within the anterior locus coeruleus, whereas LC-NE neurons projecting to the cerebellum and medulla were located in more ventral portions of the anterior- and mid-LC. $n = 4$ animals per CAV injection site. Data in **d** was analysed with one-way ANOVA. Data in **e**, **f** were analysed by first performing two-way ANOVA, which did not uncover any significance in the medial/lateral bias of tdTomato⁺ LC-NE neurons. Two-way ANOVA determined that (1) the location of the CAV injection site contributes to the dorsal/ventral bias of tdTomato⁺ LC-NE neurons within the locus coeruleus ($P < 0.0001$), (2) there is interaction between the CAV injection site and the location (anterior, mid, posterior) of tdTomato⁺ NE neurons within the locus coeruleus ($P = 0.0389$), and (3) the locus coeruleus subdivisions themselves did not significantly contribute to the variance observed in tdTomato⁺ LC-NE neurons. One-way ANOVA and post hoc Tukey's multiple comparison were then performed to test the significance of dorsal/ventral bias in each locus coeruleus region based on CAV injection sites. Scale bars, 50 μ m. Error bars represent s.e.m. * $P < 0.05$; ** $P < 0.01$, *** $P < 0.001$.



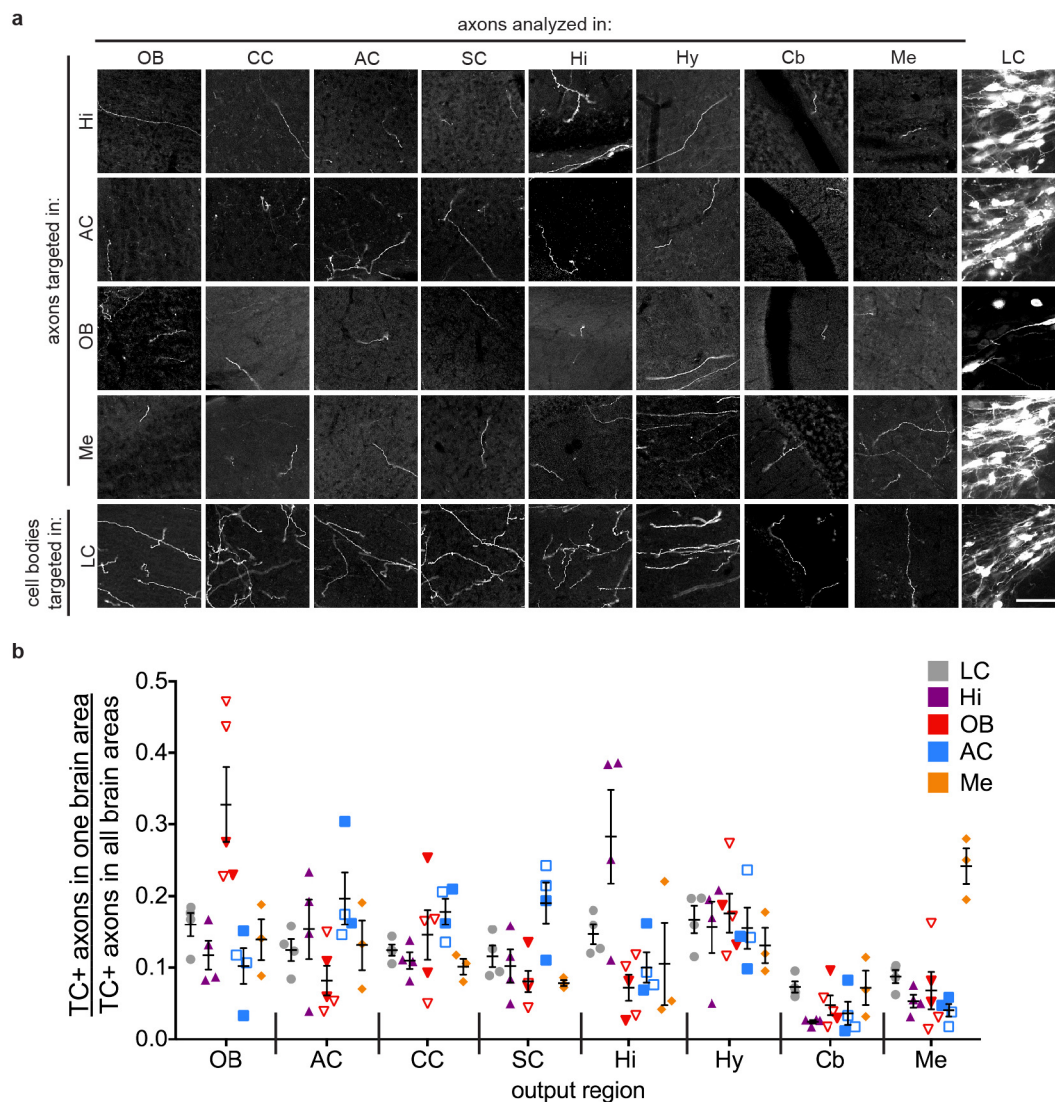
Extended Data Figure 8 | Controls for locus coeruleus cTRIO. **a**, Top, schematic for negative controls where AAVs expressing Flp-dependent TVA-mCherry fusion and rabies glycoprotein were injected into the locus coeruleus of *Dbh-Cre* mice, followed by RVdG injection into the locus coeruleus, but the CAV-FLEX^{loxP}-Flp injection was omitted. Middle, coronal section of the locus coeruleus stained with DAPI (blue) shows a small number of GFP⁺ neurons at the injection site. The dotted rectangle highlights GFP⁺ neurons magnified in the lower panel. **b**, Top, schematic for negative control where CAV-FLEX^{loxP}-Flp was injected into the olfactory bulb and AAVs expressing Flp-dependent TVA-mCherry fusion and rabies glycoprotein were injected

into the locus coeruleus of wild-type mice, followed by RVdG injection; hence there was no Cre to mediate Flp expression in locus coeruleus cells. Middle, coronal section of the locus coeruleus stained with DAPI (blue) shows a small number of GFP⁺ neurons at the injection site. The dotted rectangle highlights GFP⁺ neurons magnified in the lower panel. **c**, Quantification of GFP⁺ background labelling in the locus coeruleus ($n = 4$ and 8 animals). This labelling is likely caused by leaky TVA expression as discussed in Extended Data Fig. 1. In none of these control experiments did we observe GFP⁺ or TC⁺ neurons >800 μm away from the injection site. Scale bars, 1 mm (middle panels), 100 μm (lower panels). Error bars represent s.e.m.



Extended Data Figure 9 | Simulation of input convergence in *Dbh-Cre* tracing experiments. In the sparsest *Dbh-Cre* trans-synaptic tracing brain, 4 starter cells received input from 43 distinct input regions (309 input neurons, see Supplementary Table 2, sample number 8). In the second sparsest sample, 22 starter cells received input from 66 distinct input regions (756 input neurons; see Supplementary Table 2, sample number 9). **a**, The relation between the number of input regions for each LC-NE starter cell and the probability of observing >42 (left) or >65 (right) input regions in simulation, assuming that each starter cell receives input from a given region with the same probability. As the number of input regions per starter cell increases, the probability of observing inputs from >42 or >65 regions also increases. Based on a threshold

of P value <0.001, these simulations suggest that, to account for the total number of observed input areas in each brain sample, there must be individual LC-NE neurons that receive input from more than 15 regions for the sparsest sample (red dot, left) or more than 9 regions for second sparsest sample (red dot, right). **b**, Detailed view of the distribution of simulation results corresponding to the red dots in **a**. Assuming that each cell receives input from 15 (left) or 9 (right) distinct regions, only 5 (left) or 6 (right) out of 10,000 simulations label >42 (left) or >65 (right) input regions. Note that if the assumption that each starter cell receives input from the same number of regions does not apply, then there must be at least one cell receiving input from more regions than the number specified in the simulation.



Extended Data Figure 10 | Representative images and distribution of individual samples for projection-based viral-genetic labelling experiments.

a, Representative images from sagittal sections of TC⁺ LC-NE axons in 8 brain regions indicated at the top of each column (the last column shows cell bodies for LC-NE neurons) resulting from CAV injections at four projection sites indicated on the left (top four rows), or *AAV-FLEX^{loxP}-TC* injection at the locus coeruleus of *Dbh-Cre* animals (bottom row). All TC⁺ processes were confirmed to contain noradrenaline transporter (NET, an NE neuron marker) by anti-NET immunostaining (not shown; see Fig. 4 inset). **b**, The normalized fraction of TC⁺ LC-NE axons for individual experiments for five conditions are colour coded on the top right. Filled symbols represent experiments where *Dbh-Cre*

mice were used along with *CAV-FLEX^{loxP}-Flp*; open symbols represent experiments where wild-type mice were used along with *CAV-Cre*. The distribution of individual samples with regards to the fraction of TC⁺ axons observed at output sites was similar between wild-type and *Dbh-Cre* mice. Collectively, the samples for each condition were averaged to quantify the normalized fraction of TC⁺ LC-NE axons in each brain region as reported in Fig. 4d. Scale bar, 50 μ m. Error bars represent s.e.m. Abbreviations: AC, auditory cortex; CC, cingulate cortex; Cb, cerebellum; Hi, hippocampus; Hy, hypothalamus; LC, locus coeruleus; Me, medulla; OB, olfactory bulb; SC, somatosensory cortex.

Genetic diversity and evolutionary dynamics of Ebola virus in Sierra Leone

Yi-Gang Tong^{1*}, Wei-Feng Shi^{2*}, Di Liu^{3*}, Jun Qian^{5*}, Long Liang^{1*}, Xiao-Chen Bo^{4*}, Jun Liu^{6*}, Hong-Guang Ren^{1*}, Hang Fan^{1*}, Ming Ni^{4*}, Yang Sun^{5*}, Yuan Jin¹, Yue Teng¹, Zhen Li⁴, David Kargbo⁷, Foday Daffae⁷, Alex Kanu⁸, Cheng-Chao Chen⁹, Zhi-Heng Lan⁹, Hui Jiang⁹, Yang Luo¹⁰, Hui-Jun Lu⁵, Xiao-Guang Zhang⁶, Fan Yang¹¹, Yi Hu¹, Yu-Xi Cao⁶, Yong-Qiang Deng¹, Hao-Xiang Su¹¹, Yu Sun¹, Wen-Sen Liu⁵, Zhuang Wang¹, Cheng-Yu Wang⁵, Zhao-Yang Bu⁵, Zhen-Dong Guo⁵, Liu-Bo Zhang¹², Wei-Min Nie¹³, Chang-Qing Bai¹⁴, Chun-Hua Sun¹, Xiao-Ping An¹, Pei-Song Xu⁴, Xiang-Li-Lan Zhang¹, Yong Huang¹, Zhi-Qiang Mi¹, Dong Yu¹, Hong-Wu Yao¹, Yong Feng¹⁵, Zhi-Ping Xia⁵, Xue-Xing Zheng⁵, Song-Tao Yang⁵, Bing Lu¹, Jia-Fu Jiang¹, Brima Kargbo⁷, Fu-Chu He¹⁶, George F. Gao^{3,6,17}, Wu-Chun Cao¹ & The China Mobile Laboratory Testing Team in Sierra Leone†

A novel Ebola virus (EBOV) first identified in March 2014 has infected more than 25,000 people in West Africa, resulting in more than 10,000 deaths^{1,2}. Preliminary analyses of genome sequences of 81 EBOV collected from March to June 2014 from Guinea and Sierra Leone suggest that the 2014 EBOV originated from an independent transmission event from its natural reservoir³ followed by sustained human-to-human infections⁴. It has been reported that the EBOV genome variation might have an effect on the efficacy of sequence-based virus detection and candidate therapeutics^{5,6}. However, only limited viral information has been available since July 2014, when the outbreak entered a rapid growth phase⁷. Here we describe 175 full-length EBOV genome sequences from five severely stricken districts in Sierra Leone from 28 September to 11 November 2014. We found that the 2014 EBOV has become more phylogenetically and genetically diverse from July to November 2014, characterized by the emergence of multiple novel lineages. The substitution rate for the 2014 EBOV was estimated to be 1.23×10^{-3} substitutions per site per year (95% highest posterior density interval, 1.04×10^{-3} to 1.41×10^{-3} substitutions per site per year), approximating to that observed between previous EBOV outbreaks. The sharp increase in genetic diversity of the 2014 EBOV warrants extensive EBOV surveillance in Sierra Leone, Guinea and Liberia to better understand the viral evolution and transmission dynamics of the ongoing outbreak. These data will facilitate the international efforts to develop vaccines and therapeutics.

A large-scale Ebola viral disease (EVD) outbreak has been ongoing in Western Africa for nearly a year, with more than 23,000 reported cases¹. Previous findings have shown that the causative agent is a novel Ebola virus (EBOV)². Among the three West African countries with widespread and intense EBOV transmission, Sierra Leone reported the largest number of confirmed cases, approximately 58% of the total confirmed EBOV infection cases. To help Sierra Leone fight against EVD, the Chinese government dispatched the China Mobile Laboratory Testing Team (CMLTT) in September upon request of the Sierra Leone government. The CMLTT, equipped with medical experts who specialize in laboratory testing, epidemiology, and running a holding and treatment centre, has kept working at the Sierra Leone-China Friendship Hospital at Jui Town (represented as a red

star in Fig. 1a) of Western Area, approximately 30 km southeast of Freetown, the capital city of Sierra Leone. All the activities of the CMLTT were coordinated by the Emergency Operations Center jointly established by the Ministry of Health and Sanitation of Sierra Leone and the World Health Organization (WHO).

To fight against this novel EBOV, Gire and colleagues systematically analysed 81 EBOV genomes from Guinea ($n = 3$)² and Sierra Leone ($n = 78$)⁴ collected from the early stage of the 2014 EBOV outbreak, revealing the origin, transmission, and rapid accumulation of genetic variation of the 2014 EBOV. However, only a few additional full-length EBOV genome sequences were published since July 2014, when the outbreak entered a rapid growth phase driven by sustained human-to-human transmission⁴. From 28 September to 11 November 2014, a total of 823 samples were tested to be EBOV-positive using reverse transcription-PCR (RT-PCR) by the CMLTT, among which 175 full-length genomes were successfully sequenced with each from an individual EVD patient (Fig. 1a and Supplementary Table 1). These 175 samples were obtained from five severely stricken districts in Sierra Leone, including 47 from Western Urban, 67 from Western Rural, 47 from Port Loko, 5 from Kambia, and 9 from Bombali (Fig. 1a). In detail, approximately one fifth of the EBOV-positive samples for each region were sequenced, 19.5% for Western Urban, 21.2% for Western Rural, 22.1% for Port Loko, and 16.1% for Kambia. Regarding Bombali, 9 out of 17 (52.9%) strains were sequenced. Therefore, our sequenced genomes were roughly proportional to the prevalence in different regions.

Phylogenetic analysis of all available full-length EBOV genome sequences from Sierra Leone ($n = 253$) and Guinea ($n = 3$) from 2014 was performed using MrBayes⁸ in which the three Guinean strains were designated as root^{4,9}. Our phylogenetic analysis showed that the 2014 EBOV increased in diversity at least through October after its initial introduction into Sierra Leone (Fig. 1b and Extended Data Fig. 1). Apart from the previously described lineages SL1 and SL2⁴, the SL3 lineage has evolved into two major lineages, SL3.1 and SL3.2 in June in eastern Sierra Leone, both of which were then transmitted to western Sierra Leone. The majority of the EBOV collected from late September to mid-November fell into lineage SL3.2, with a few belonging to lineage SL3.1. However, none of them belonged to lineages SL1 and SL2. In particular, the EBOV sequenced by us could

¹State Key Laboratory of Pathogen and Biosecurity, Beijing 100071, China. ²Institute of Pathogen Biology, Taishan Medical College, Taian 271000, China. ³Institute of Microbiology, Chinese Academy of Sciences, Beijing 100101, China. ⁴Beijing Key Laboratory of New Molecular Diagnostics Technology, Beijing 100850, China. ⁵Key Laboratory of Jilin Province for Zoonosis Prevention and Control, Changchun 130122, China. ⁶Institute for Viral Disease Control and Prevention, Chinese Center for Disease Control and Prevention, Beijing 102206, China. ⁷Sierra Leone Ministry of Health and Sanitation, Freetown, Sierra Leone. ⁸Sierra Leone-China Friendship Hospital, Freetown, Sierra Leone. ⁹BGI-Shenzhen, Shenzhen 518083, China. ¹⁰Wellcome Trust Sanger Institute, Cambridge CB10 1SA, UK.

¹¹Chinese Academy of Medical Sciences & Peking Union Medical College, Beijing 100730, China. ¹²Institute of Environmental Health and Related Product Safety, Chinese Center for Disease Control and Prevention, Beijing 100021, China. ¹³The No. 302 Hospital, Beijing 100039, China. ¹⁴The No. 307 Hospital, Beijing 100071, China. ¹⁵Department of international cooperation, National Health and Family Planning Commission, Beijing 100044, China. ¹⁶State Key Laboratory of Proteomics, Beijing 102206, China. ¹⁷Chinese Center for Disease Control and Prevention, Beijing 102206, China.

*These authors contributed equally to this work.

†Lists of participants and their affiliations appear at the end of the paper

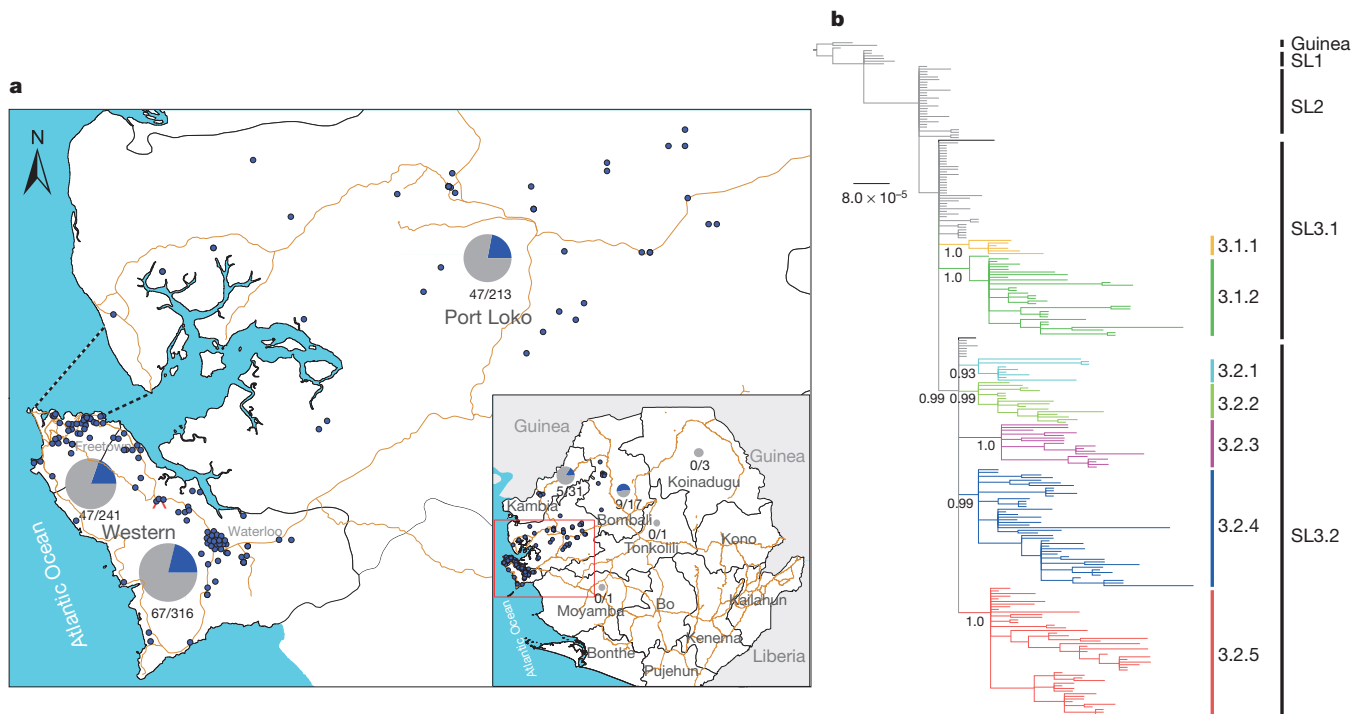


Figure 1 | Geographical distribution and phylogenetic analysis of the 2014 EBOV from Sierra Leone. **a**, Geographical distribution of the 823 EBOV positive samples and the 175 newly sequenced genomes (represented as blue dots). In the panel, main roads and waterways are shown as yellow lines and

black dash lines, respectively. **b**, A Bayesian phylogenetic tree of the 2014 EBOV. The 175 newly sequenced viruses in this study are shown in colours, and others are shown in grey. The seven novel lineages designated in the present are highlighted. Posterior support for major nodes is shown.

be classified into seven novel independent sublineages based on the phylogenetic topology, two sublineages belonging to SL3.1 (SL3.1.1 and SL3.1.2) and five belonging to SL3.2 (SL3.2.1 to SL3.2.5) (Fig. 1b). Phylogenetic tree constructed using the maximum likelihood method showed a similar topology (Extended Data Fig. 2). Therefore, the 2014 EBOV has become highly diverse in its first year along with its spread in Sierra Leone.

To explore the spatiotemporal relationships of the EBOV in western Sierra Leone, we performed a phylogeographic analysis using BEAST¹⁰ (Fig. 2 and Extended Data Fig. 3). In this analysis, only 22 out of the 78 sequences previously published by Gire *et al.* (ref. 4) were included in our analysis to reduce the computation load. To this end, we selected representative sequences from the previously described lineages GIN, SL1, SL2 and SL3, ensuring that there is at least one sequence for every sampling date. From a time point of view, all of the novel sublineages probably emerged before August (Fig. 2). In addition, multiple lineages were co-circulating in a single town/district. All of the seven sublineages were identified in Waterloo, indicating the highest phylogenetic diversity in this region. Viruses from Freetown belonged to six of the seven sublineages, with sublineage 3.2.3 undetected. Five novel sublineages have also been found in Maforki Chiefdom of Port Loko.

The spatiotemporal linkage of our sequenced EBOV genomes is further shown in Fig. 3a. First, viruses from Freetown and Waterloo, the capital and the traffic hub, are estimated to be spatiotemporally related, as also observed in sublineages 3.1.1, 3.1.2 and 3.2.4 (Fig. 2), indicating that frequent transmission events might have occurred between the two regions. Second, this network reveals that viral transmission events have also occurred between the three major sites (Freetown, Waterloo and Maforki Chiefdom) and their surrounding regions. Third, our results also suggest spatiotemporal connections of EBOV between Waterloo and Port Loko, Kambia, and Bombali, respectively, as exemplified in sublineages 3.2.1 and 3.2.5 (Fig. 2). Based on the higher transmission rates of Waterloo, Freetown and Maforki Chiefdom, intensive EBOV surveillance in

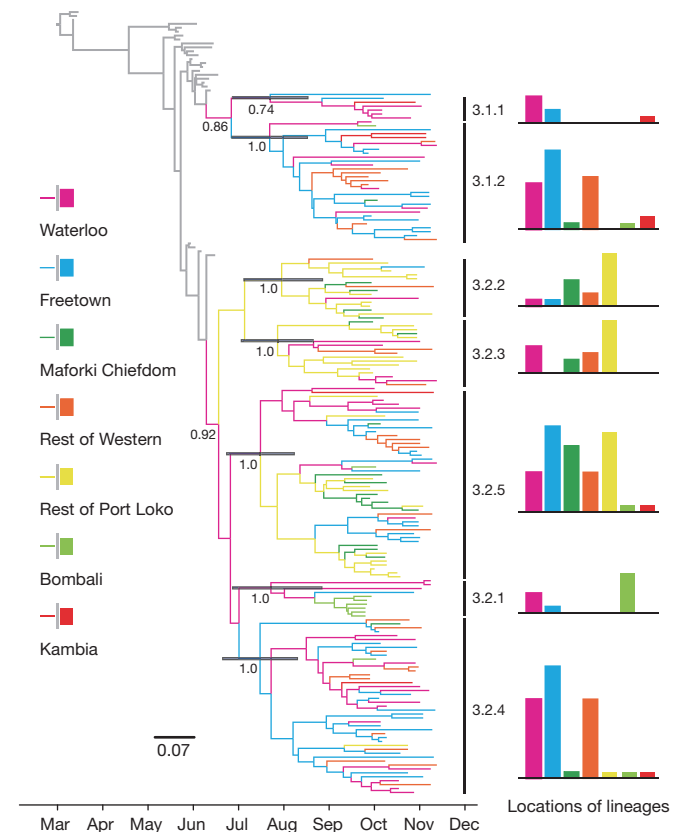


Figure 2 | Phylogeographic reconstruction of the 2014 EBOV using BEAST. In the left panel, the novel 175 EBOV genome sequences were coloured by geographic regions. The transition of different colours represents a potential transmission event. In the right panel, the number of sequences from different geographic regions in each lineage is summarized.

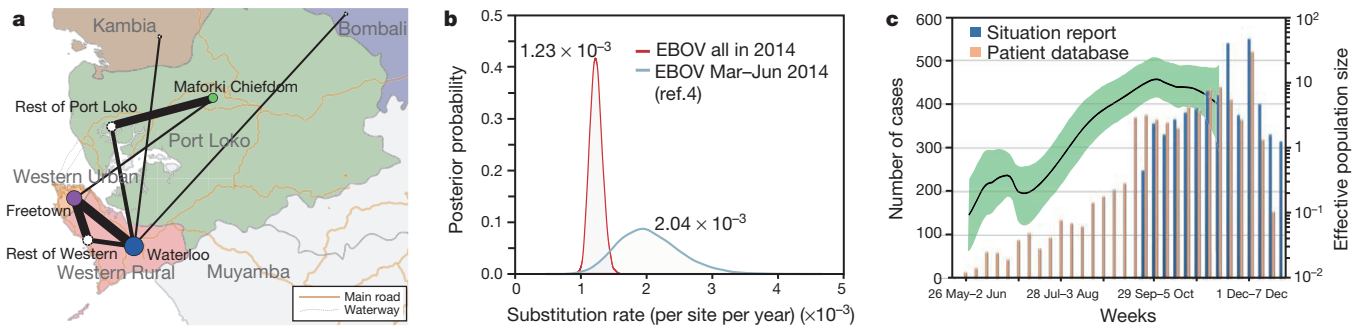


Figure 3 | Reconstructed phylogeographic linkage, substitution rate, and effective population size of the 2014 EBOV in western Sierra Leone from September to November 2014. **a**, The phylogeographic linkage constructed using BEAST. Thickness of lines represents the relative transmission rate between two regions. The size of each node is proportional to the sum of the relative rates of the region with Bayes factor >3 . **b**, Substitution rates of the

2014 EBOV. The red line represents the substitution rate estimated using all the 2014 EBOV samples. Estimations of Gire and colleagues were repeated by us and shown as the blue line. **c**, Gaussian Markov random field Bayesian skyline reconstruction of the 2014 EBOV. Bar chart, adapted from the World Health Organization website, shows the numbers of confirmed cases of EBOV infection and patients. Smooth black line shows the effective population size.

the three regions should be helpful for the prevention and control of the EVD outbreak in Western Sierra Leone.

The substitution rate for all of the 2014 EBOV was estimated using BEAST to be 1.23×10^{-3} substitutions per site per year (95%

highest posterior density interval, 1.04×10^{-3} to 1.41×10^{-3} substitutions per site per year) (Fig. 3b). Our estimate was similar to those between previous EBOV outbreaks, approximately 1.00×10^{-3} substitutions per site per year^{4,11–14}. This suggests that, over a longer

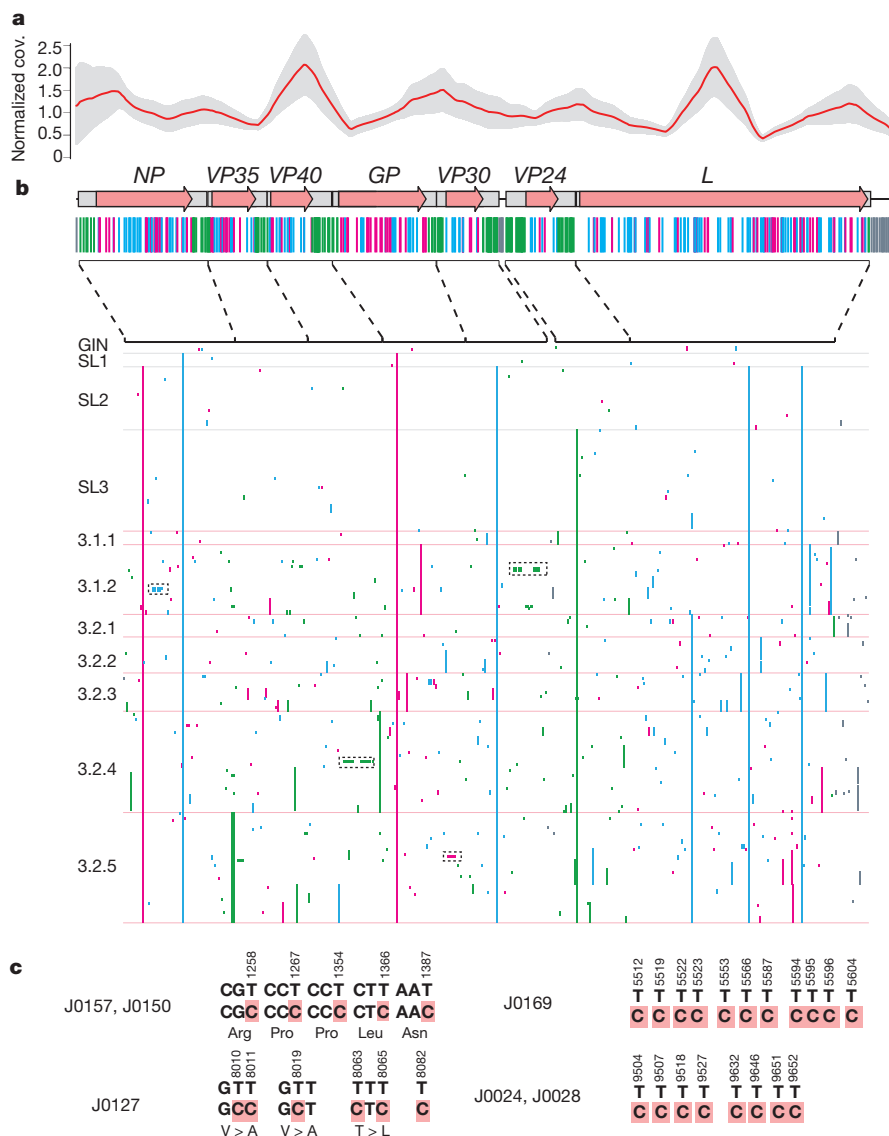


Figure 4 | Genomic variations of the 2014 EBOV. **a**, Sequence depth across sequenced genomes. The x axis represents the virus genome structure, and the y axis represents the normalized average depth. One unit equals approximately 1,400 coverage per site. The mean depth is shown using the red line and the standard deviation is shown in shade. **b**, Substitutions of the 2014 EBOV. Only positions with substitutions are shown. Different lineages are separated by lines. Different types of substitutions are indicated using different colours: cyan for synonymous (S), magenta for non-synonymous (NS), green for un-translated regions (UTR), and grey for intergenic regions (IG). **c**, All the serial T $>$ C substitutions are found within a range less than 150 bp. Substitutions within coding regions are shown in codons.

time interval, EBOV is still undergoing evolution at a relatively constant rate.

The estimated population size of the 2014 EBOV from Sierra Leone steadily increased from July to early October, and then entered a plateau period (Fig. 3c). This therefore implies that the effective population size of the 2014 EBOV became stable in October, which was also broadly consistent with the weekly change of numbers of confirmed EBOV infection cases and EVD patients in Sierra Leone (Fig. 3c)¹. The doubling time estimated using BEAST was 22.1 days (95% confidence interval, 18.9–25.59 days), which was comparable to that calculated using the epidemiological data from Sierra Leone, with the mean value of 18.9 days.

We then investigated the molecular characterization of the novel EBOV genome. Raw reads of each genome were mapped to the reference genome (KJ660346.2). The average normalized coverage was approximately 1,400-fold (Fig. 4a). 341 single nucleotide polymorphisms (SNPs) have been previously identified between the 2014 outbreak EBOV and previous EBOV⁴, and 440 SNPs were identified in our sequenced genomes. The substitutions in the 175 newly sequenced EBOV genomes were summarized among different lineages (Fig. 4b and Supplementary Table 2). Approximately a quarter of the identified substitutions were non-synonymous, and half of them were synonymous (Extended Data Fig. 5). Some of the SNPs were lineage-specific and could be used as markers to distinguish different lineages (Fig. 4b and Supplementary Table 2). For example, substitutions A7148G and A17445G were only found in sublineage 3.1.2, whereas sublineage 3.2.4 possessed a specific T5849C substitution. The T > C substitutions that occurred in the 3' UTR region of NP gene (at genome positions 3008 and 3011) were specific to sublineage 3.2.5. In particular, the T > C substitution at position 14019 occurred in all sequences of lineage 3.2, which was first described in this study. Moreover, seven previously reported substitutions (at positions 800, 1849, 6283, 8928, 10218, 15963, 17142)⁴ were always present in the novel lineages from June to November 2014 and became the dominant allele in the population, suggesting that they have been fixed. These substitutions included two non-synonymous substitutions (C800T in the NP gene and C6283T in the GP gene), four synonymous substitutions, and one in the non-coding regions.

Interestingly, we observed several serial T > C substitutions in six newly sequenced EBOV genomes, which occurred within a genome region of 150 base pairs in length (Fig. 4c and Extended Data Fig. 4). The serial T > C substitutions were further confirmed by Sanger sequencing after PCR amplification (Extended Data Table 1). Such serial substitutions were found in four different regions of six strains belonging to three different lineages, two of which were in coding regions and the other two were in non-coding regions. However, the emergence mechanism of such serial T > C substitutions and their potential biological functions warrant further investigation.

In summary, our findings highlighted the increasing genetic diversity and transmission dynamics of the 2014 EBOV, with an evolutionary rate estimated to be similar to that between previous EBOV outbreaks. This information provided an insight into the viral evolution and transmission dynamics, which would facilitate the prevention and control of EBOV in Sierra Leone and would also guide research on vaccines and therapeutic targets.

Online Content Methods, along with any additional Extended Data display items and Source Data, are available in the online version of the paper; references unique to these sections appear only in the online paper.

Received 30 January; accepted 23 April 2015.

Published online 13 May 2015.

1. World Health Organization. Ebola response roadmap - Situation report. <http://www.who.int/csr/disease/ebola/situation-reports/en> (accessed 1 April 2015).

- Baize, S. *et al.* Emergence of Zaire Ebola virus disease in Guinea. *N. Engl. J. Med.* **371**, 1418–1425 (2014).
- Leroy, E. M. *et al.* Fruit bats as reservoirs of Ebola virus. *Nature* **438**, 575–576 (2005).
- Gire, S. K. *et al.* Genomic surveillance elucidates Ebola virus origin and transmission during the 2014 outbreak. *Science* **345**, 1369–1372 (2014).
- Kugelman, J. R. *et al.* Evaluation of the potential impact of Ebola virus genomic drift on the efficacy of sequence-based candidate therapeutics. *MBio* **6**, e02227–14 (2015).
- Feldmann, H. *et al.* Ebola virus: from discovery to vaccine. *Nature Rev. Immunol.* **3**, 677–685 (2003).
- WHO Ebola Response Team. Ebola virus disease in West Africa—the first 9 months of the epidemic and forward projections. *N. Engl. J. Med.* **371**, 1481–1495 (2014).
- Huelsenbeck, J. P. & Ronquist, F. MRBAYES: Bayesian inference of phylogenetic trees. *Bioinformatics* **17**, 754–755 (2001).
- Dudas, G., Rambaut, A. Phylogenetic analysis of Guinea 2014 EBOV Ebolavirus outbreak. *PLoS Curr.* <http://dx.doi.org/10.1371/currents.outbreaks.84eef5ce43ec9dc0bf0670f7b8b417d> (2014).
- Drummond, A. J. & Rambaut, A. BEAST: Bayesian evolutionary analysis by sampling trees. *BMC Evol. Biol.* **7**, 214 (2007).
- Jenkins, G. M. *et al.* Rates of molecular evolution in RNA viruses: a quantitative phylogenetic analysis. *J. Mol. Evol.* **54**, 156–165 (2002).
- Calvignac-Spencer, S. *et al.* Clock rooting further demonstrates that Guinea 2014 EBOV is a member of the Zaire lineage. *PLoS Curr.* <http://dx.doi.org/10.1371/currents.outbreaks.c0e035c86d721668a6ad73537f6fe86> (2014).
- Carroll, S. A. *et al.* Molecular evolution of viruses of the family *Filoviridae* based on 97 whole-genome sequences. *J. Virol.* **87**, 2608–2616 (2013).
- Li, Y. H. & Chen, S. P. Evolutionary history of Ebola virus. *Epidemiol. Infect.* **142**, 1138–1145 (2014).

Supplementary Information is available in the online version of the paper.

Acknowledgements We thank P. Lemey and S. Ho for technical assistance. This work is partially supported by the special project of Ebola virus research from the President Foundation of Chinese Academy of Sciences. It was also supported by grants from the China Mega-Project on Infectious Disease Prevention (nos 2013ZX10004202-002, 2013ZX10004605), China Mega-Project on Major Drug Development (no. 2013ZX09304101) and the National Hi-Tech Research and Development (863) Program of China (nos 2014AA021402, 2014AA021501). We thank the government of Sierra Leone, the Sierra Leone Ministry of Health and Sanitation and the Chinese National Health and Family Planning Commission. We also thank the medical workers and volunteers in Sierra Leone. G.F.G. is a leading principal investigator of Innovative Research Group of the National Natural Science Foundation of China, NSFC (grant no. 81321063).

Author Contributions The manuscript was written by Y.-G.T., W.-F.S., D.L., G.F.G. and W.-C.C. Samples were collected by J.Q., D.K., F.D., A.K., B.K., Y.S., H.-J.L., X.-G.Z., F.Y., Y.H., Y.-X.C., Y.-Q.D., H.-X.S., Y.S., W.-S.L., Z.W., C.-Y.W., Z.-Y.B., Z.-D.G., L.-B.Z., W.-M.N., C.-Q.B., C.-H.S., Y.F., Z.-P.X., X.-X.Z., S.-T.Y. and B.L. Experiment and data analysis were performed by Y.-G.T., W.-F.S., D.L., H.F., M.N., H.-G.R., J.L., Y.J., Y.T., Z.L., C.-C.C., Z.-H.L., H.-J., Y.L., X.-P.A., P.-S.X., X.-L.-L.Z., Y.H., Z.-Q.M., D.Y., H.-W.Y., J.-F.J., X.-C.B., L.L., F.-C.H. and W.-C.C. The study was designed by B.K., X.-C.B., L.L., J.Q., F.-C.H., G.F.G. and W.-C.C.

Author Information The 175 newly sequenced genomes have been submitted to GenBank. The accession numbers are provided in Supplementary Table 1. Reprints and permissions information is available at www.nature.com/reprints. The authors declare no competing financial interests. Readers are welcome to comment on the online version of the paper. Correspondence and requests for materials should be addressed to W.-C.C. (caowc@bmi.ac.cn), G.F.G. (gaof@im.ac.cn) or F.-C.H. (hefc@nic.bmi.ac.cn).

The China Mobile Laboratory Testing Team in Sierra Leone

Yi-Gang Tong¹, Jun Qian², Yang Sun², Hui-Jun Lu², Xiao-Guang Zhang³, Fan Yang⁴, Yi Hu¹, Yu-Xi Cao³, Yong-Qiang Deng¹, Hao-Xiang Su⁴, Yu Sun¹, Wen-Sen Liu², Zhuang Wang¹, Cheng-Yu Wang², Zhao-Yang Bu², Zhen-Dong Guo², Liu-Bo Zhang⁵, Wei-Min Nie⁶, Chang-Qing Bai⁷, Chun-Hua Sun¹, Yong Feng⁸, Jia-Fu Jiang¹ & George F. Gao^{3,9,10}

¹State Key Laboratory of Pathogen and Biosecurity, Beijing 100071, China. ²Key Laboratory of Jilin Province for Zoonosis Prevention and Control, Changchun 130122, China. ³Institute for Viral Disease Control and Prevention, Chinese Center for Disease Control and Prevention, Beijing 102206, China. ⁴Chinese Academy of Medical Sciences & Peking Union Medical College, Beijing 100730, China. ⁵Institute of Environmental Health and Related Product Safety, Chinese Center for Disease Control and Prevention, Beijing 100021, China. ⁶The No. 302 Hospital, Beijing 100039, China. ⁷The No. 307 Hospital, Beijing 100071, China. ⁸Department of international cooperation, National Health and Family Planning Commission, Beijing 100044, China. ⁹Institute of Microbiology, Chinese Academy of Sciences, Beijing 100101, China. ¹⁰Chinese Center for Disease Control and Prevention, Beijing 102206, China.

METHODS

Ethics statement. This work was conducted as part of the surveillance and public health response to contain the EVD outbreak in Sierra Leone. Blood samples from suspected individuals and oropharyngeal swab samples from corpses were collected for EVD testing and outbreak surveillance with a waiver to provide a written informed consent during the EVD outbreak under the agreement between the Sierra Leone government and Chinese government. The activities were coordinated by the Emergency Operations Centre in the charge of Sierra Leone Ministry of Health and Sanitation and WHO. All the information regarding individual persons has been anonymized in the report.

Genome sequencing and assembly. RNA samples extracted from whole blood from 175 EVD patients were reverse transcribed to cDNA. PCR amplifications were performed with EBOV-specific primer pairs with overlaps. Amplicons from one patient were pooled for library preparation. Next generation sequencing (NGS) was performed using the BGISEQ-100 (Ion Proton) platform. All the sequenced reads were filtered to remove the low quality and short reads. The genome sequences of the viruses were assembled by mapping the filtered reads to the 2014 EBOV consensus sequence using Roche 454 Newbler version 2.9 (Roche), and the mutation site was manually checked with original sequencing data.

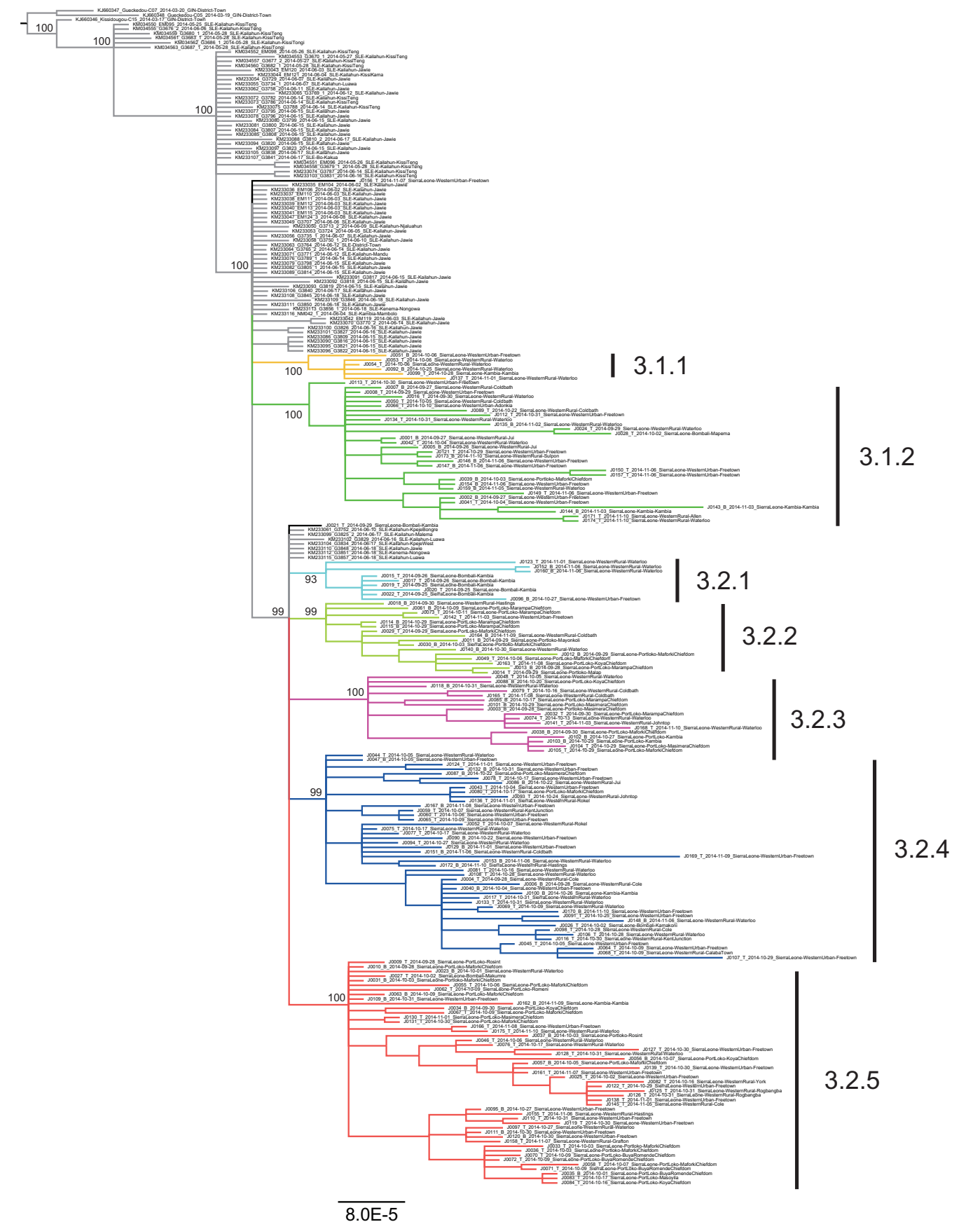
Phylogenetic and phylogeographic reconstruction. All previously published EBOV genome sequences and our newly released 175 sequences were aligned using MAFFT v7.058¹⁵. Phylogenetic analyses were performed using MrBayes⁸ v3.2 (10 million generations) and RAxML v8.1.6 (1000 bootstrap replicates), with the GTR model of nucleotide substitution and γ -distributed rates among sites. Phylogeographic reconstruction of the 2014 EBOV was estimated using BEAST v1.8.0¹⁰, with a continuous time Markov Chain (CTMC) over discrete sampling locations. The 175 newly sequenced samples in this paper were grouped into 7 regions (Waterloo, Freetown, Rest of Western, Maforki Chiefdom, Rest of Port Loko, Bombali and Kambia). Bayesian Markov chain Monte Carlo analysis was run for 100 million steps, 10% of which were removed as burn-in and sampled

every 10,000 steps. Bayes factor tests were performed to provide statistical support for potential transmission routes between different geographic locations using SPREAD v1.0.6¹⁶. Bayes factors for rates were derived from a Bayesian stochastic search variable selection procedure. The phylogeographic linkage was constructed by routes with Bayes factor values >3 .

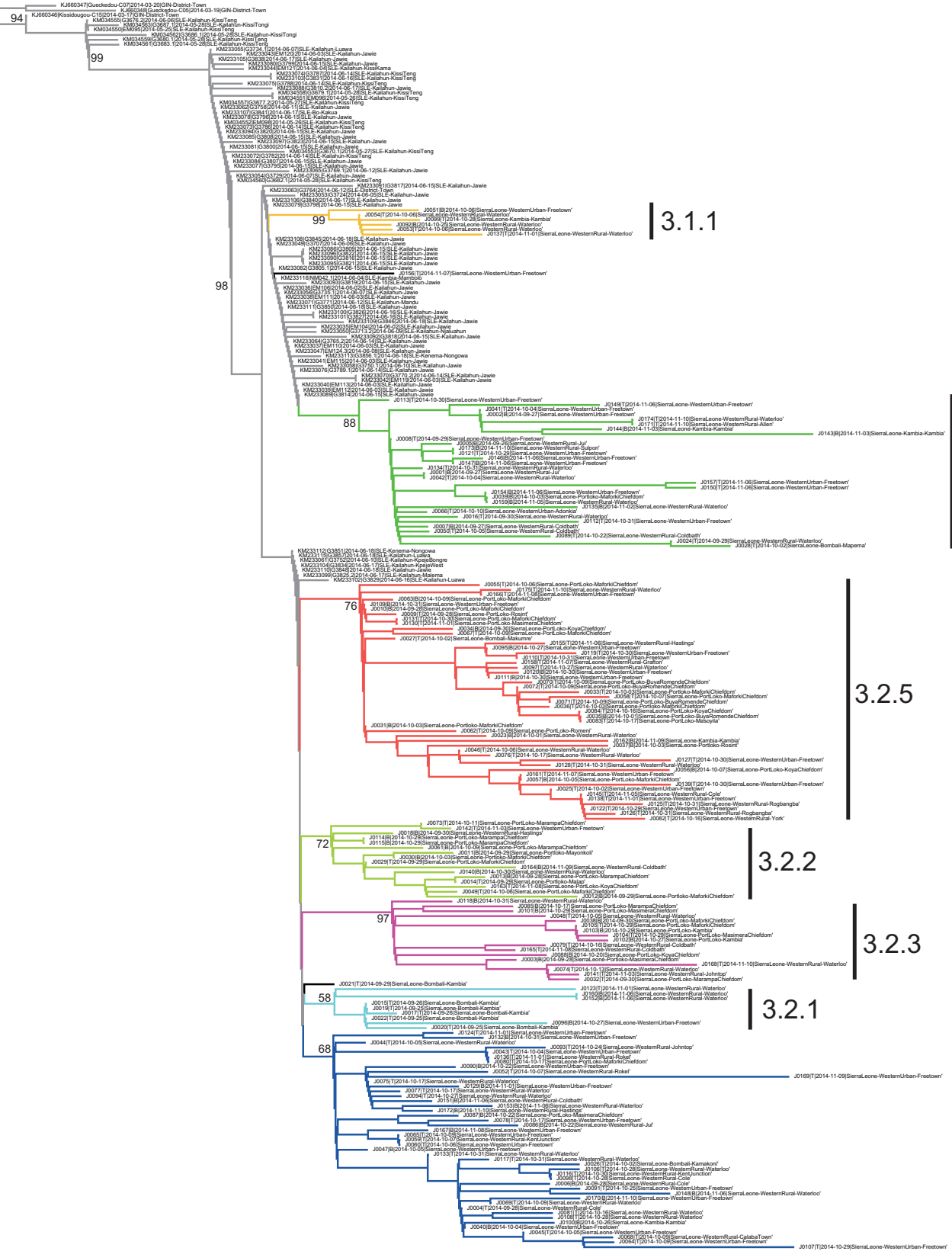
Substitution rates and population dynamics. The substitution rates were estimated using Bayesian Markov chain Monte Carlo (MCMC) as implemented in BEAST v1.8.0. In this analysis, two data sets were compiled, with one including all the 2014 EBOV sequences and the other including sequences from September to November, 2014. We performed two independent runs for 100 million generations, sampling every 10,000 steps. In addition, to accurately estimate the substitution rate, we repeated this analysis using a previously described data set using the same parameters. Population dynamics of the 2014 EBOV in Sierra Leone was estimated using a flexible non-parametric Bayesian skyride model¹⁷ incorporated in BEAST v1.8.0, with the HKY+ Γ model and a strict molecular clock.

Molecular characterizations of the 2014 EBOV. SNPs were called directly from the sequence alignment using the CLC Genomic Workbench v7.5.1, GeneiousR8 and Newbler v2.9. The earliest strain of EBOV 2014, H.sapiens-wt/GIN/2014/Makona-Kissidougou-C15 (GenBank accession number KJ660346.2) was used as the reference genome. The synonymous substitutions, non-synonymous substitutions, and substitutions in non-coding regions were marked with coloured dots.

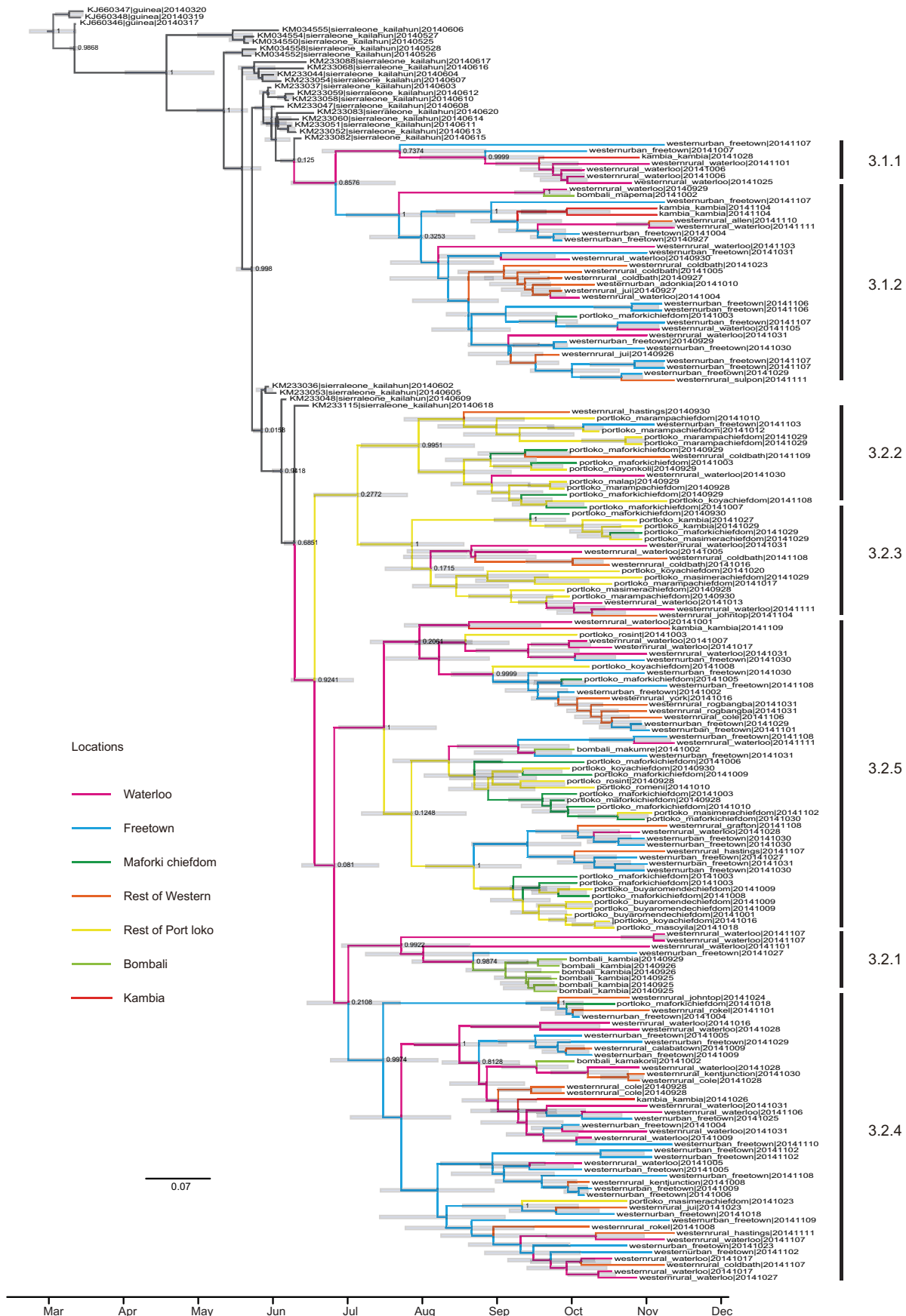
15. Katoh, K. & Standley, D. M. MAFFT multiple sequence alignment software version 7: improvements in performance and usability. *Mol. Biol. Evol.* **30**, 772–780 (2013).
16. Bielejec, F. *et al.* SPREAD: spatial phylogenetic reconstruction of evolutionary dynamics. *Bioinformatics* **27**, 2910–2912 (2011).
17. Minin, V.N. *et al.* Smooth skyride through a rough skyline: Bayesian coalescent-based inference of population dynamics. *Mol. Biol. Evol.* **25**, 1459–1471 (2008).



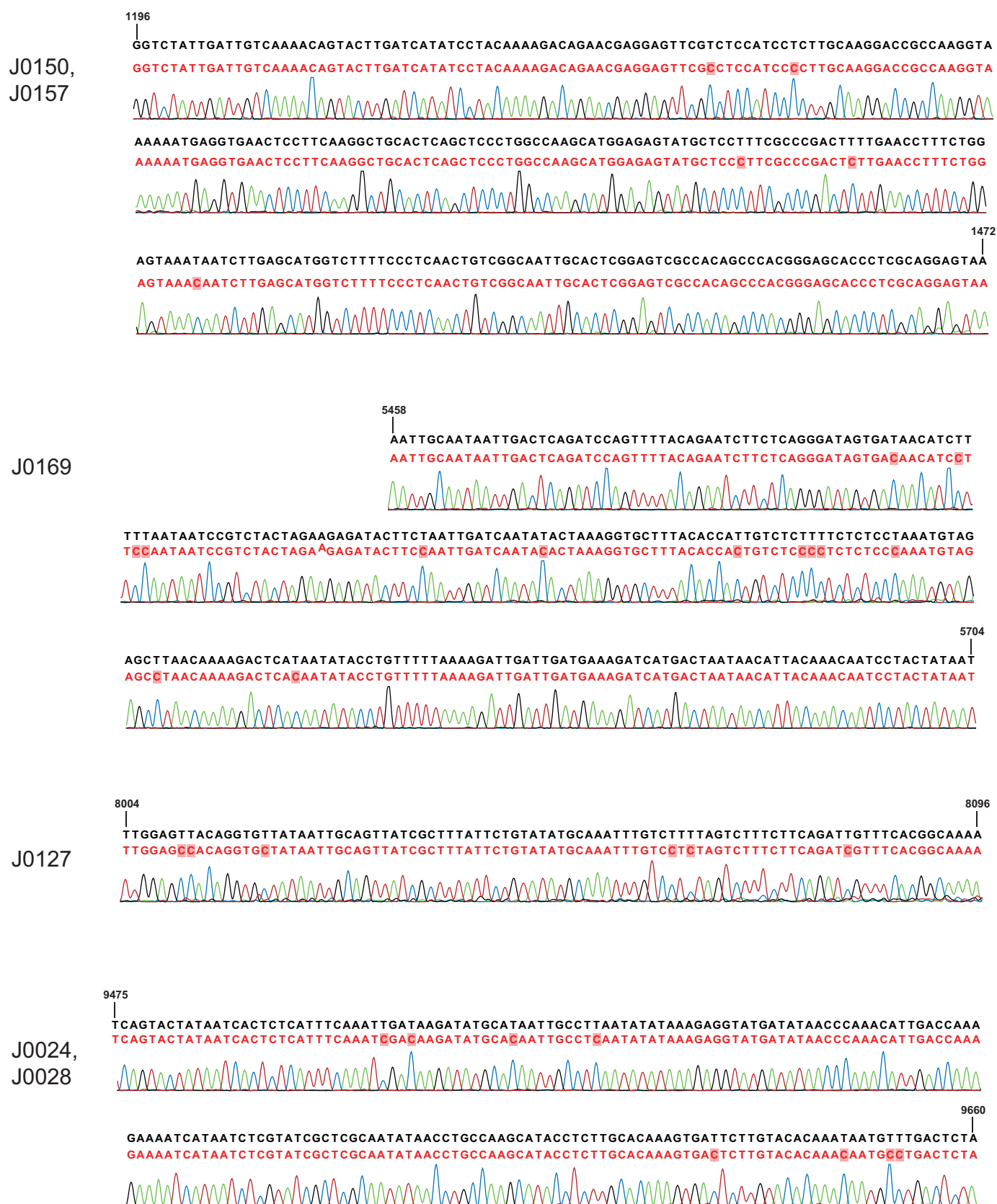
Extended Data Figure 1 | Phylogenetic tree of the 2014 EBOV inferred using MrBayes. The seven novel sublineages are highlighted using different colours. Previously described EBOV sequences are shown in grey. Posterior probability for each lineage is shown.



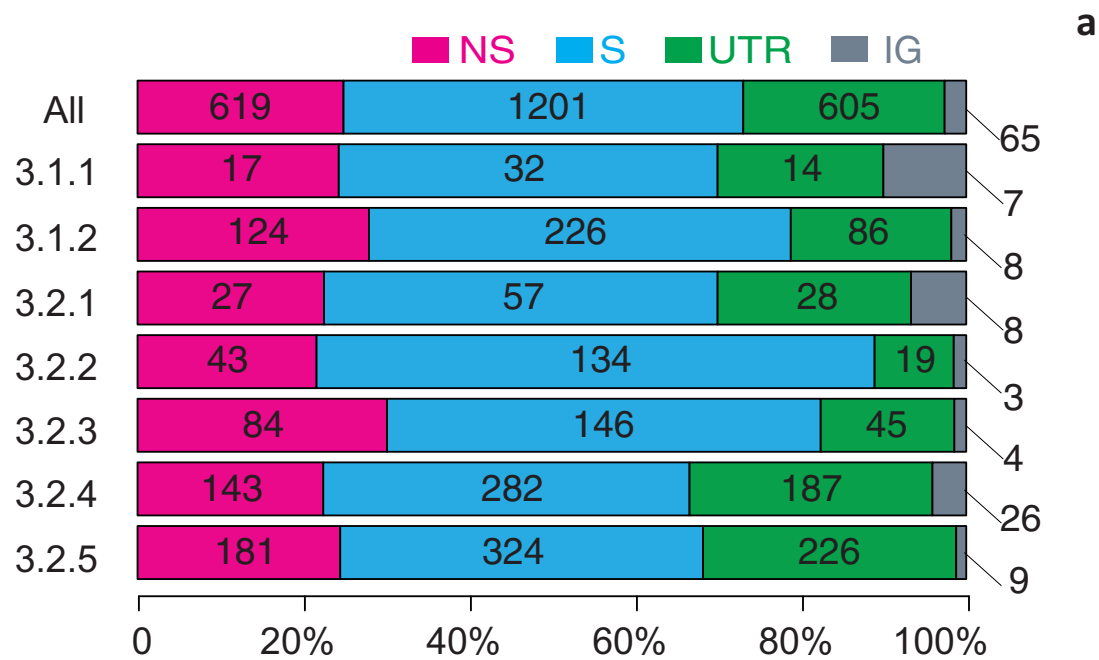
Extended Data Figure 2 | Maximum likelihood tree of 2014 EBOV constructed using RAXML.



Extended Data Figure 3 | Phylogeographic inference of the 2014 EBOV using BEAST. Previously described EBOV sequences are shown in grey. Posterior probability for each lineage is shown.



Extended Data Figure 4 | Original sequencing results of the serial T > C substitutions using the Sanger method. All of the four regions including serial T > C substitutions were sequenced using the Sanger method with the primers provided in Extended Data Table 1.



b

Gene-specific dN/dS

Gene	dN/dS	95% HPD
NP	0.4069	(0.2429, 0.6324)
VP35	0.4497	(0.2409, 0.7548)
VP40	0.2339	(0.0839, 0.5029)
GP	0.6065	(0.3828, 0.9047)
VP30	0.2359	(0.0938, 0.4782)
VP24	0.1114	(0.0064, 0.4907)
L	0.2463	(0.1777, 0.3308)

c

Lineage-specific dN/dS

Lineage	dN/dS	95% HPD
3.1.1	0.5847	(0.2096, 1.2562)
3.1.2	0.2769	(0.1593, 0.4415)
3.2.1	0.4242	(0.1822, 0.8202)
3.2.2	0.2087	(0.1003, 0.3762)
3.2.3	0.3869	(0.2179, 0.6263)
3.2.4	0.2879	(0.1837, 0.4255)
3.2.5	0.3414	(0.2301, 0.4839)

Extended Data Figure 5 | Synonymous and non-synonymous substitutions of the 2014 EBOV. **a**, Distribution of synonymous and non-synonymous substitutions in different lineages. The numbers of substitutions are labelled within bars. NS, non-synonymous; S, synonymous; UTR, UTR region; IG, intergenic. **b**, Gene-specific global dN/dS estimates. The dN/dS and 95% highest posterior density interval were calculated using HyPhy. **c**, Lineage-specific global dN/dS estimates.

Extended Data Table 1 | Primers designed for the confirmation of the serial T > C substitutions

Sample ID	Target region	Primer
J0150 & J0157	1139-1474	GGACATGATGCCAACGATGC(+) ATTTACTCCTGCGAGGGTGC(-)
J0169	5434-5731	GTCTTCCAGCTGTGGTTGAGA(+) AAGATTGACATTTGAATCACCGT(-)
J0127	7967-8200	TGGTGGACAGGATGGAGACA(+) GGCTATGTTTGAAGCTCCAGTG(-)
J0024 & J0028	9401-9783	CCTTCTACTTGATCACAATACTCCG(+) CCTCCTCCACAACCTGAAGCA(-)

Temporal and spatial analysis of the 2014–2015 Ebola virus outbreak in West Africa

Miles W. Carroll^{1,2,3}, David A. Matthews^{4*}, Julian A. Hiscox^{5*}, Michael J. Elmore^{1*}, Georgios Pollakis^{5*}, Andrew Rambaut^{6,7,8*}, Roger Hewson^{1,2,9}, Isabel García-Dorival⁵, Joseph Akoi Bore^{2,10,11}, Raymond Koundouno^{2,10,11}, Saïd Abdellati^{2,12}, Babak Afrough^{1,2}, John Aiyepada^{2,13}, Patience Akhilomen^{2,13}, Danny Asogun^{2,13}, Barry Atkinson^{1,2}, Marlis Badusche^{2,14,15}, Amadou Bah^{2,16}, Simon Bate^{1,2}, Jan Baumann^{2,14}, Dirk Becker^{2,15,17}, Beate Becker-Ziaja^{2,14,15}, Anne Bocquin^{2,18,19}, Benny Borremans^{2,20}, Andrew Bosworth^{1,2,5}, Jan Peter Boettcher^{2,21}, Angela Cannas^{2,22}, Fabrizio Carletti^{2,22}, Concetta Castilletti^{2,22}, Simon Clark^{1,2}, Francesca Colavita^{2,22}, Sandra Diederich^{2,15,23}, Adomeh Donatus^{2,13}, Sophie Duraffour^{2,14,24}, Deborah Ehichioya^{2,14,25}, Heinz Ellerbrok^{2,21}, Maria Dolores Fernandez-García^{2,26}, Alexandra Fizez^{2,18,27}, Erna Fleischmann^{2,15,28}, Sophie Gryseels^{2,20}, Antje Hermelink^{2,21}, Julia Hinzmann^{2,21}, Ute Hopf-Guevara^{2,21}, Yemisi Ighodalo^{2,13}, Lisa Jameson^{1,2}, Anne Kelterbaum^{2,15,17}, Zoltan Kis^{2,29}, Stefan Kloth^{2,21}, Claudia Kohl^{2,21}, Miša Korva^{2,30}, Annette Kraus^{2,31}, Eeva Kuisma^{1,2}, Andreas Kurth^{2,21}, Britta Liedigk^{2,14,15}, Christopher H. Logue^{1,2}, Anja Lütke^{2,15,32}, Piet Maes^{2,24}, James McCowen^{1,2}, Stéphane Mély^{2,18,19}, Marc Mertens^{2,15,23}, Silvia Meschi^{2,22}, Benjamin Meyer^{2,15,33}, Janine Michel^{2,21}, Peter Molkenthin^{2,15,28}, César Muñoz-Fontela^{2,15,32}, Doreen Muth^{2,15,33}, Edmund N. C. Newman^{1,2}, Didier Ngabo^{1,2}, Lisa Oestereich^{2,14,15}, Jennifer Okosun^{2,13}, Thomas Olorok^{2,13}, Racheal Omiunu^{2,13}, Emmanuel Omomoh^{2,13}, Elisa Pallasch^{2,14,15}, Bernadett Pályi^{2,29}, Jasmine Portmann^{2,34}, Thomas Pottage^{1,2}, Catherine Pratt^{1,2}, Simone Priesnitz^{2,35}, Serena Quartu^{2,22}, Julie Rappe^{2,36}, Johanna Repits^{2,37}, Martin Richter^{2,21}, Martin Rudolf^{2,14,15}, Andreas Sachse^{2,21}, Kristina Maria Schmidt^{2,21}, Gordian Schudt^{2,15,17}, Thomas Strecker^{2,15,17}, Ruth Thom^{1,2}, Stephen Thomas^{1,2}, Ekaete Tobin^{2,13}, Howard Tolley^{1,2}, Jochen Trautner^{2,38}, Tine Vermoesen^{2,12}, Inês Vitoriano^{1,2}, Matthias Wagner^{2,15,28}, Svenja Wolff^{2,15,17}, Constanze Yue^{2,21}, Maria Rosaria Capobianchi^{2,22}, Birte Kretschmer³⁹, Yper Hall¹, John G. Kenny⁴⁰, Natasha Y. Rickett⁵, Gytis Dudas⁶, Cordelia E. M. Coltart⁴¹, Romy Kerber^{2,14,15}, Damien Steer⁴², Callum Wright⁴³, Francis Senyah¹, Sakoba Keita⁴⁴, Patrick Drury⁴⁵, Boubacar Diallo⁴⁶, Hilde de Clerck⁴⁷, Michel Van Herp⁴⁷, Armand Sprecher⁴⁷, Alexis Traore⁴⁸, Mandiou Diakite⁴⁹, Mandy Kader Konde⁵⁰, Lamine Koivogui¹¹, N'Faly Magassouba¹⁰, Tatjana Avšič-Županc^{2,30}, Andreas Nitsche^{2,21}, Marc Strasser^{2,34}, Giuseppe Ippolito^{2,22}, Stephan Becker^{2,15,17}, Kilian Stoecker^{2,15,28}, Martin Gabriel^{2,14,15}, Hervé Raoul^{2,19}, Antonino Di Caro^{2,22}, Roman Wölfel^{2,15,28}, Pierre Formenty⁴⁵ & Stephan Günther^{2,14,15*}

West Africa is currently witnessing the most extensive Ebola virus (EBOV) outbreak so far recorded^{1–3}. Until now, there have been 27,013 reported cases and 11,134 deaths. The origin of the virus is thought to have been a zoonotic transmission from a bat to a two-year-old boy in December 2013 (ref. 2). From this index case the virus was spread by human-to-human contact throughout Guinea, Sierra Leone and Liberia. However, the origin of the particular virus in each country and time of transmission is not known and currently relies on epidemiological analysis, which may be unreliable owing to the difficulties of obtaining patient information. Here we trace the genetic evolution of EBOV in the current outbreak that has resulted in multiple lineages. Deep sequencing of 179 patient samples processed by the European Mobile Laboratory, the first diagnostics unit to be deployed to the epicentre of the outbreak in Guinea, reveals an epidemiological and evolutionary

history of the epidemic from March 2014 to January 2015. Analysis of EBOV genome evolution has also benefited from a similar sequencing effort of patient samples from Sierra Leone. Our results confirm that the EBOV from Guinea moved into Sierra Leone, most likely in April or early May. The viruses of the Guinea/Sierra Leone lineage mixed around June/July 2014. Viral sequences covering August, September and October 2014 indicate that this lineage evolved independently within Guinea. These data can be used in conjunction with epidemiological information to test retrospectively the effectiveness of control measures, and provides an unprecedented window into the evolution of an ongoing viral haemorrhagic fever outbreak.

We used a deep sequencing approach to gain insight into the evolution of Ebola virus (EBOV) in Guinea from the ongoing West African outbreak. This was an approach based on analysis pipelines developed

¹Public Health England, Porton Down, Wiltshire SP4 0JG, UK. ²The European Mobile Laboratory Consortium, Bernhard-Nocht-Institute for Tropical Medicine, D-20359 Hamburg, Germany. ³University of Southampton, South General Hospital, Southampton SO16 6YD, UK. ⁴Department of Cellular and Molecular Medicine, School of Medical Sciences, University of Bristol, Bristol BS8 1TD, UK. ⁵Institute of Infection and Global Health, University of Liverpool, Liverpool L69 2BE, UK. ⁶Institute of Evolutionary Biology, University of Edinburgh, Edinburgh EH9 2FL, UK. ⁷Fogarty International Center, National Institutes of Health, Bethesda, Maryland 20892, USA. ⁸Centre for Immunology, Infection and Evolution, University of Edinburgh, Edinburgh EH9 2FL, UK. ⁹London School of Hygiene and Tropical Medicine, Keppel Street, London WC1E 7HT, UK. ¹⁰Université Gamal Abdel Nasser de Conakry, Laboratoire des Fièvres Hémorragiques en Guinée, Conakry, Guinea. ¹¹Institut National de Santé Publique, Conakry, Guinea. ¹²Institute of Tropical Medicine, B-2000 Antwerp, Belgium. ¹³Institute of Lassa Fever Research and Control, Irrua Specialist Teaching Hospital, Irrua, Edo State, Nigeria. ¹⁴Bernhard Nocht Institute for Tropical Medicine, D-20359 Hamburg, Germany. ¹⁵German Centre for Infection Research (DZIF), 38124 Braunschweig, Germany. ¹⁶Swiss Tropical and Public Health Institute, University of Basel, CH-4002 Basel, Switzerland. ¹⁷Institute of Virology, Philipps University Marburg, 35043 Marburg, Germany. ¹⁸National Reference Center for Viral Hemorrhagic Fevers, 69365 Lyon, France. ¹⁹Laboratoire P4 Inserm-Jean Mérioux, US003 Inserm, 69365 Lyon, France. ²⁰Department of Biology, University of Antwerp, B-2020 Antwerp, Belgium. ²¹Robert Koch Institute, 13353 Berlin, Germany. ²²National Institute for Infectious Diseases (INMI) Lazzaro Spallanzani, 00149 Rome, Italy. ²³Friedrich Loeffler Institute, Federal Research Institute for Animal Health, 17493 Greifswald, Insel Riems, Germany. ²⁴KU Leuven Rega Institute, B-3000 Leuven, Belgium. ²⁵Reedeemer's University, Osun State, Nigeria. ²⁶Centro Nacional de Microbiología, Instituto de Salud Carlos III, 28029 Madrid, Spain. ²⁷Unité de Biologie des Infections Virales Emergentes, Institut Pasteur, 69365 Lyon, France. ²⁸Bundeswehr Institute of Microbiology, 80937 Munich, Germany. ²⁹National Center for Epidemiology, National Biosafety Laboratory, H-1097 Budapest, Hungary. ³⁰Institute of Microbiology and Immunology, Faculty of Medicine, University of Ljubljana, SI-1000 Ljubljana, Slovenia. ³¹Public Health Agency of Sweden, 171 82 Solna, Sweden. ³²Heinrich Pette Institute – Leibniz Institute for Experimental Virology, 20251 Hamburg, Germany. ³³Institute of Virology, University of Bonn, 53127 Bonn, Germany. ³⁴Federal Office for Civil Protection, Spiez Laboratory, CH-3700 Spiez, Switzerland. ³⁵Bundeswehr Hospital, 22049 Hamburg, Germany. ³⁶Institute of Virology and Immunology, CH-3147 Mittelhäusern, Switzerland. ³⁷Janssen-Cilag, SE-192 07 Sollentuna, Sweden. ³⁸Thünen Institute, D-22767 Hamburg, Germany. ³⁹Eurice - European Research and Project Office GmbH, 10115 Berlin, Germany. ⁴⁰Centre for Genomic Research, Institute of Integrative Biology, University of Liverpool, Liverpool L69 7ZB, UK. ⁴¹Department of Infection and Population Health, University College London, London WC1E 6JB, UK. ⁴²Research IT, University of Bristol, Bristol BS8 1HH, UK. ⁴³Advanced Computing Research Centre, University of Bristol, Bristol BS8 1HH, UK. ⁴⁴Ministry of Health Guinea, Conakry, Guinea. ⁴⁵World Health Organization, 1211 Geneva 27, Switzerland. ⁴⁶World Health Organization, Conakry, Guinea. ⁴⁷Médecins Sans Frontières, B-1050 Brussels, Belgium. ⁴⁸Section Prévention et Lutte contre la Maladie à la Direction Préfectorale de la Santé de Guéckédou, Guéckédou, Guinea. ⁴⁹Université Gamal Abdel Nasser de Conakry, CHU Donka, Conakry, Guinea. ⁵⁰Health and Sustainable Development Foundation, Conakry, Guinea.

*These authors contributed equally to this work.

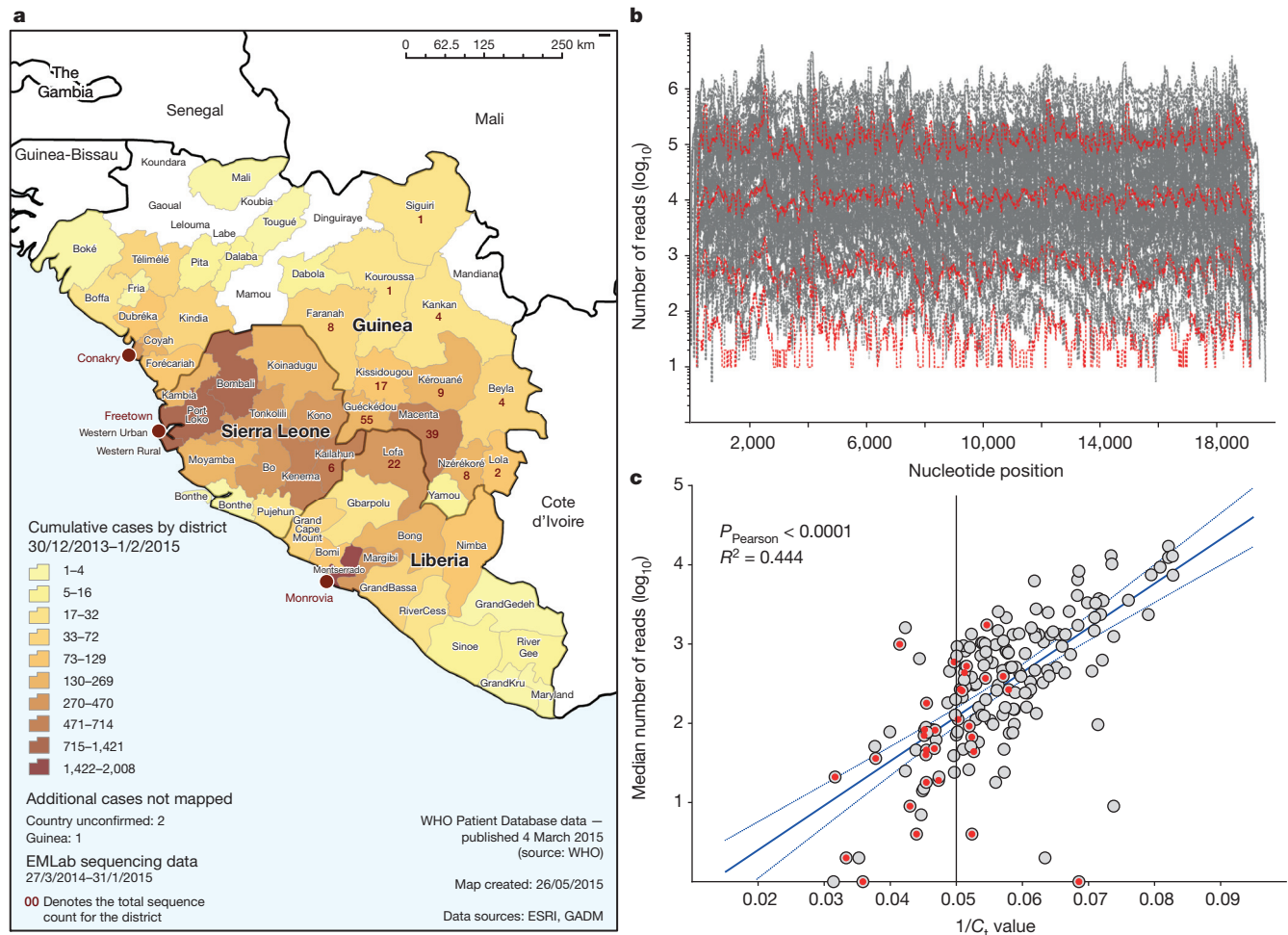


Figure 1 | Geographical location, sequence read depth, and read depth vs C_t value of patient samples. **a**, Geographical location of patient samples. The origin of the sequenced samples (one sample per patient) from Guinea, Sierra Leone, and Liberia processed by EMLab Guéckédou are plotted as numbers of cases by district. EMLab data are overlaid on an Ebola outbreak distribution map where cumulative cases are plotted as a heat map (low (yellow) to high (brown)) of confirmed cases from March 2014 to January 2015. Case data sourced from World Health Organization (WHO) Ebola response situation reports (<http://apps.who.int/ebola/en/ebola-situation-reports>); Geographic Information Systems (GIS) data sourced from Environmental Systems Research Institute (ESRI) and Database of Global Administrative Areas

for a guinea-pig model of EBOV infection and Hendra virus infection of human and bat cells^{4,5}. Here we use this approach to derive consensus EBOV genomes from individual patient samples that can be used to study viral genome evolution during the course of the outbreak. Viral genomes were derived primarily from blood samples that had been taken from patients in Guinea and sent to the European Mobile Laboratory (EMLab), deployed by the World Health Organisation within the Médecins Sans Frontières Ebola Treatment Centre Guéckédou in March 2014 to aid the diagnostic effort. With the permission of Guinean authorities a biobank of samples was assembled which had known provenance of EBOV infection. Linked to each sample were the following data: patient location (to district level), sample collection date, disease onset and outcome. The collection dates were a median of 4 days after the date of onset of symptoms. Baseline data was cleaned, formatted and imported into the Geographic Information System, ESRI ArcGIS. Statistical tools were used to generate tabular output and to join the numeric case data with the district level boundaries of Guinea, Liberia and Sierra Leone (district geometries freely available from <http://www.gadm.org/>) (Fig. 1a).

(GADM; <http://www.gadm.org/>). **b**, Sequence depth per nucleotide position. The number of reads for each nucleotide position was plotted across the full length of the virus genome for each of the 179 virus isolates we analysed. In red is shown the uniformity of the depth across individual genomes, although the median number of reads per nucleotide position had a variation spanning over four log₁₀ units. **c**, Linear regression of the log₁₀ median sequence depth of each virus isolate versus the C_t value of the viral load as determined by qRT-PCR. Red dots indicate samples from patients who went on to survive EBOV infection and grey shaded dots are from patients who records suggest died from EBOV infection.

The viral genome sequence was derived from RNA sequencing analysis of the patient samples with no pre-amplification of the viral genome. In general we selected a range of samples from both males and females of different ages and a fair representation of sequences for each month (Extended Data Fig. 1), and with C_t values less than 20 for EBOV RNA. In this selected patient cohort, with a relatively high viral load, there was approximately 80% mortality. The read depth mapping to the EBOV genome varied between samples and regions in the genome (Fig. 1b) and in general the number of sequence reads obtained for each genome correlated with the amount of viral load as determined by quantitative reverse-transcription PCR (qRT-PCR) (Fig. 1c).

Phylogenetic analysis revealed the dynamic nature of the epidemic and molecular change in the viral sequence (Fig. 2a). Several distinct lineages were identified, with an initial lineage A (Figs 2a, 3 and Extended Data Fig. 2) linked to early Guinean cases dating from March 2014 including the three original viruses published by Baize *et al.*². A second lineage, B, emerged in May and June and comprises all the sequences from Gire *et al.*⁶ and the remainder of those described

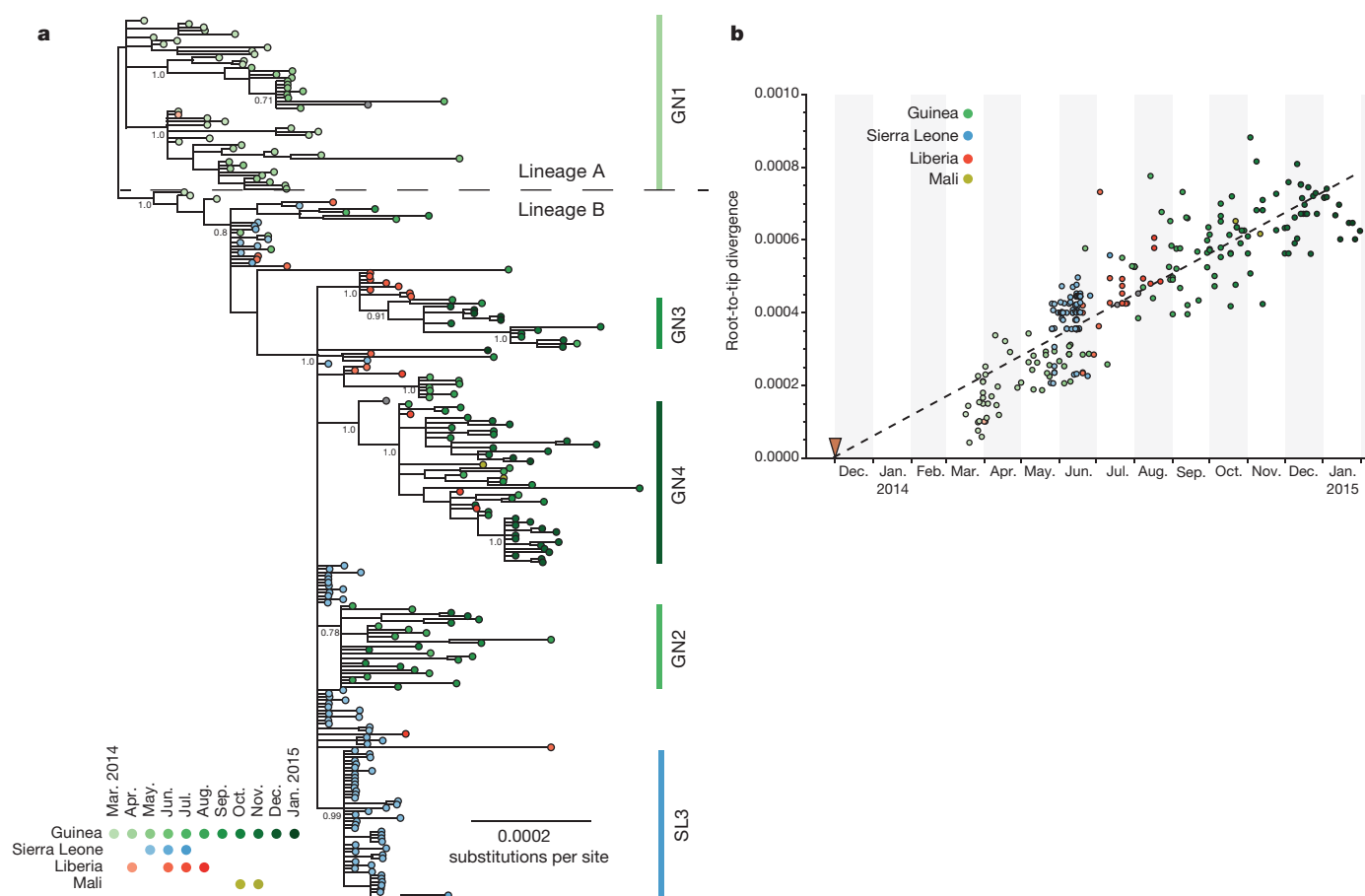


Figure 2 | Phylogenetic relatedness and nucleotide sequence divergence of EBOV isolates from the 2013–2015 outbreak. **a**, Phylogenetic relatedness of EBOV isolates. Phylogenetic tree inferred using MrBayes¹¹ for full-length EBOV genomes sequenced from 179 patient samples obtained between March 2014 and January 2015. Displayed is the majority consensus of 10,000 trees sampled from the posterior distribution with mean branch lengths. Posterior support is shown for selected key nodes. Twenty-two samples originated in Liberia and were collected between March and August 2014 and six samples

from Sierra Leone were obtained in June and July 2014. In our analysis we also included published sequences, including the three early Guinean sequences² and 78 sequences described by Gire *et al.*⁶. A number of lineages predominantly circulating in Guinea are denoted as GN1–4 along with a uniquely Sierra Leone lineage (SL3) recognised in Gire *et al.*⁶. **b**, EBOV nucleotide sequence divergence from root of the phylogeny in Fig. 2a plotted against time of collection of each virus. The date of the first documented case near Meliandou in eastern Guinea is indicated by the red triangle.

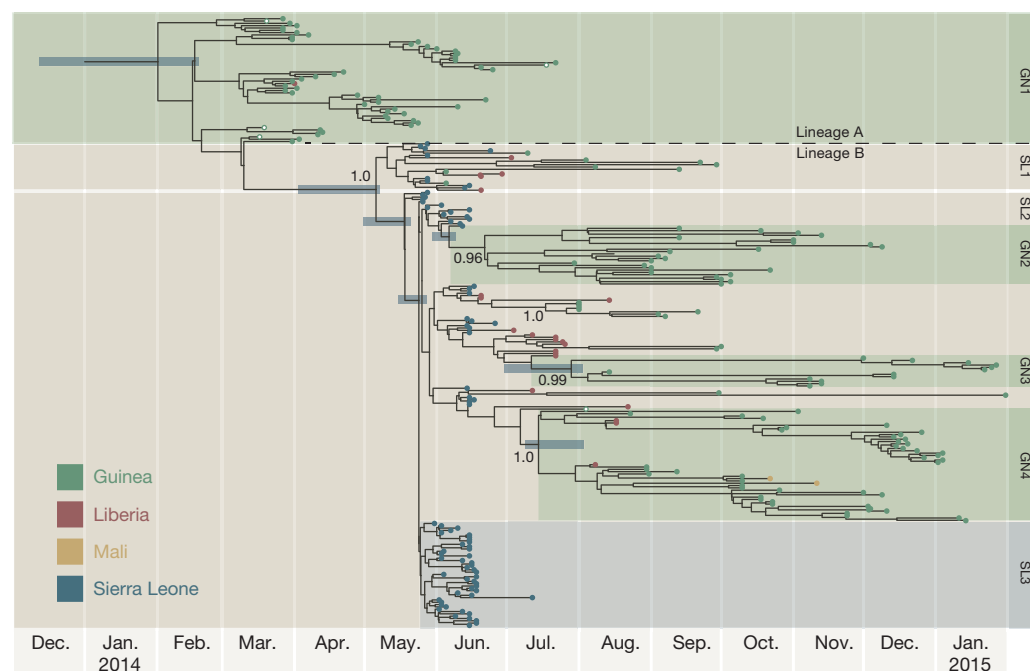


Figure 3 | A time-scaled phylogenetic tree of 262 EBOV genomes from Guinea, Sierra Leone, Liberia and Mali. Shown is a maximum clade credibility tree constructed from 10,000 trees sampled from the posterior distribution with mean node ages. Clades described in Gire *et al.*⁶ are identified here (SL1, SL2 and SL3) as well as a number of lineages predominantly circulating in Guinea and posterior probability support is given for these. For certain key node ages, 95% credible intervals are shown by horizontal bars.

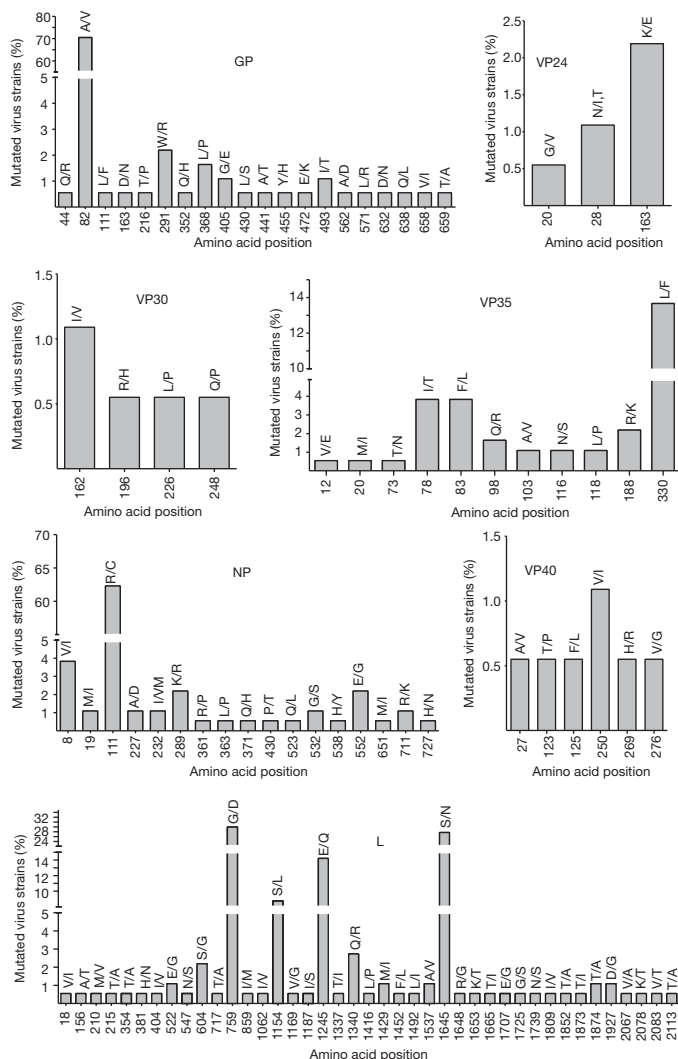


Figure 4 | Position of non-synonymous amino acid variations in the 179 genomes analysed in this study compared to a reference sequence taken from March 2014 (KJ660346.2). Shown is the frequency of all amino acid positions that had variability and the substitution that occurred with the first single letter position indicating the reference sequence and the second position showing the variation. The percentage frequency in the 179 genomes is shown on the y axis. GP, glycoprotein; NP, nucleoprotein; L, RNA polymerase; VP, viral protein.

here. As the epidemic expanded, lineage A remained confined in Guinea from March to June 2014, except for one sequence from 18 July 2014. A single Liberian sequence from March 2014 grouped within this lineage. No further EBOV genomes that we sequenced from samples taken after July 2014 belonged to lineage A. This clade was likely to have been associated with the original outbreak in Guinea and was almost successfully contained in May 2014 by the interventions of the multi-agency response. Two clusters of Sierra Leone viruses described by Gire *et al.*⁶ (denoted by the authors as clusters SL1 and SL2), both of which contain later viruses from Guinea and Liberia, suggest continued spread across the border during this time. Early cases in SL1 and SL2 were both associated with a single funeral⁶, so it is possible that this event may have reignited the epidemic. Thereafter, lineage B spread into Guinea, Liberia and Sierra Leone. This lineage is associated with the large epidemics in these three countries and persisted into 2015. The spatiotemporal spread of these viruses based on the phylogenetic analysis presented in Figs 2a and 3 was summarized (Extended Data Fig. 3) and indicated how the virus may have spread between the neighbouring countries. There was no

evidence from the data that increases or decreases in mortality were associated with any particular virus cluster (Extended Data Fig. 4).

The Bayesian time-scaled phylogenetic analysis estimated an average rate of evolution over the genome of 1.42×10^{-3} substitutions per site per year with 95% credible intervals of 1.22×10^{-3} and 1.62×10^{-3} . Details of the model assumptions are given in the Methods section. This rate is lower than that initially described for the West African outbreak by Gire *et al.*⁶ but still higher than the long-term, between-outbreak rate of 0.8×10^{-3} estimated using viruses back to the 1976 Yambuku outbreak⁶. This apparent drop in rate of evolution between these two studies is consistent with the explanation provided by Gire *et al.*⁶ that the short sampling interval (March to June) provided insufficient time for the action of purifying selection. However, the much longer sampling interval in the present study may simply be providing a more precise estimate of the rate. It should be noted, however, that the between-outbreak rate will exclusively reflect transmission and evolution that has occurred in the non-human reservoir species, so may not be directly comparable to the rate within a human outbreak. We observed no evidence of a change in evolutionary rate over the course of the epidemic with the accumulation of genetic change having a linear relationship with time (Fig. 2b), confirming that the apparent decline in rate between the two studies is an observational phenomenon⁷ rather than a change in the virus.

The estimate of the date of the most recent common ancestor of the sampled viruses is mid-January 2014 (95% credible intervals 12 December 2013, 18 February 2014). Although this is an estimate of first transmission event that resulted in more than one lineage in our sample, this provides an upper bound on the date of emergence of the virus into the human population. This date estimate is consistent with the epidemiological tracing of the first suspected cases to December 2013².

Given the error-prone nature of EBOV genome replication we examined the potential amino acid variation in EBOV proteins from the start of our sample collection in March 2014 to January 2015. The location of amino acid changes on EBOV proteins and their relative representation in the 179 assembled genomes were compared to an isolate identified in March 2014 (ref. 2) (Fig. 4). While there is amino acid variation in all of the genomes sampled, there were very few changes in viral protein 30 (VP30), viral protein 40 (VP40) and viral protein 24 (VP24), and these changes are only in less than ~2% of the genomes sampled. However, a single amino acid substitution in VP24 is associated with adaptation to a new host^{4,8}, and this may be due to interactions with host-cell proteins^{9,10}. While some of the variation may be attributed to a purely random molecular clock pattern, in GP, VP35, NP and L there are some amino acid variations that are present in over ~15% of the genomes sampled. For example, in GP there is an A to V substitution in ~70.5% of the genomes sampled compared to the reference genome. Implications of the mutations within GP in relation to immune escape of therapeutics and vaccines will need to be assessed in pseudotype neutralization assays using EBOV monoclonal antibodies and serum from people who have been vaccinated.

Online Content Methods, along with any additional Extended Data display items and Source Data, are available in the online version of the paper; references unique to these sections appear only in the online paper.

Received 9 April; accepted 1 June 2015.

Published online 17 June; corrected online 5 August 2015 (see full-text HTML version for details).

- Schieffelin, J. S. *et al.* Clinical illness and outcomes in patients with Ebola in Sierra Leone. *N. Engl. J. Med.* **371**, 2092–2100 (2014).
- Baize, S. *et al.* Emergence of Zaire Ebola virus disease in Guinea. *N. Engl. J. Med.* **371**, 1418–1425 (2014).
- Gatherer, D. The unprecedented scale of the West African Ebola virus disease outbreak is due to environmental and sociological factors, not special attributes of the currently circulating strain of the virus. *Evid. Based Med.* **20**, 28 (2015).

4. Dowall, S. D. *et al.* Elucidating variations in the nucleotide sequence of Ebola virus associated with increasing pathogenicity. *Genome Biol.* **15**, 540 (2014).
5. Wynne, J. W. *et al.* Proteomics informed by transcriptomics reveals Hendra virus sensitizes bat cells to TRAIL-mediated apoptosis. *Genome Biol.* **15**, 532 (2014).
6. Gire, S. K. *et al.* Genomic surveillance elucidates Ebola virus origin and transmission during the 2014 outbreak. *Science* **345**, 1369–1372 (2014).
7. Ho, S. Y., Phillips, M. J., Cooper, A. & Drummond, A. J. Time dependency of molecular rate estimates and systematic overestimation of recent divergence times. *Mol. Biol. Evol.* **22**, 1561–1568 (2005).
8. Mateo, M. *et al.* VP24 is a molecular determinant of Ebola virus virulence in guinea pigs. *J. Infect. Dis.* **204** (Suppl 3), S1011–S1020 (2011).
9. García-Dorival, I. *et al.* Elucidation of the Ebola virus VP24 cellular interactome and disruption of virus biology through targeted inhibition of host-cell protein function. *J. Proteome Res.* **13**, 5120–5135 (2014).
10. Basler, C. F. & Amarasinghe, G. K. Evasion of interferon responses by Ebola and Marburg viruses. *J. Interferon Cytokine Res.* **29**, 511–520 (2009).
11. Ronquist, F. *et al.* MrBayes 3.2: efficient Bayesian phylogenetic inference and model choice across a large model space. *Syst. Biol.* **61**, 539–542 (2012).

Supplementary Information is available in the online version of the paper.

Acknowledgements The authors would like to acknowledge that the EMLab response and the subsequent EBOV genome sequencing study would not have been possible without the extensive support from the many different agencies and organisations working in the West African EBOV disease outbreak region. EMLab worked with WHO, MSF and the Guinean authorities to tackle the outbreak in the Guéckédou area where the samples from this study were collected. We thank those who helped make this possible and the Guinean authorities for their decision to release the diagnostic samples to EMLab for shipment to Europe to undergo further analysis, including sequencing. We acknowledge Air France, Brussels Airlines and Virgin Airlines for transporting EMLab personnel and equipment in and out of West Africa during the outbreak period; World Courier for shipping our EBOV-positive samples out of Guinea to Europe; and the logistics support units and pilots and drivers of WHO/United Nations in West Africa for transporting our people and equipment throughout the region, and especially the drivers who made the 28 h round trip journey from Conakry to enable the EMLab unit to be established and resupplied in Guéckédou. We appreciate the work of the numerous European Embassies operating in West Africa who provided emergency support to our personnel at times of need. We thank M. Bull, J. Lewis, P. Payne and S. Leach from the Microbial Risk Assessment and Behavioural Science Team, Emergency Response Department, Public Health England; J. Tree from Public Health

England for help with GenBank submission; and S. Price and I. Stewart for helping with the running of our software on BlueCrystal, University of Bristol. We thank the people of West Africa for their gratitude and optimism, and for their positive attitude to our presence that we encountered on the daily journey to the Ebola Treatment Centre in Guéckédou. We acknowledge the efforts of the late Dr Lamine Ouendeno, who was one of the first healthcare workers to die during the current EBVD outbreak. We also thank Isabel and Maurice Ouendeno for providing us with food and shelter whilst delivering our Ebola response duties. This work was carried out in the context of the project EVIDENT (Ebola virus disease: correlates of protection, determinants of outcome, and clinical management) that received funding from the European Union's Horizon 2020 research and innovation programme under grant agreement No 666100 and in the context of service contract IFS/2011/272-372 funded by Directorate-General for International Cooperation and Development. The EMLab is a technical partner in the WHO Emerging and Dangerous Pathogens Laboratory Network (EDPLN), and the Global Outbreak Alert and Response Network (GOARN) and the deployments in West Africa have been coordinated and supported by the GOARN Operational Support Team at WHO/HQ.

Author Contributions M.W.C., S.G., J.A.H., D.A.M and N.M. designed the study. J.A.H., D.A.M., M.J.E., A.R., G.P., S.G. and M.W.C. wrote the manuscript. D.A.M., J.A.H., M.J.E., A.R., G.P., M.W.C., S.G., Y.H. and I.G.D. analysed the data. All other authors were involved either in sample collection, processing and/or logistical support and strategic oversight for the work.

Author Information The 179 consensus genome sequences described in this study have been assigned the GenBank accession numbers KR817067–KR817245. Further information is provided in Supplementary Table 1. Reprints and permissions information is available at www.nature.com/reprints. The authors declare no competing financial interests. Readers are welcome to comment on the online version of the paper. Correspondence and requests for materials should be addressed to M.W.C. (miles.carroll@phe.gov.uk).



This work is licensed under a Creative Commons Attribution-NonCommercial-ShareAlike 3.0 Unported licence. The images or other third party material in this article are included in the article's Creative Commons licence, unless indicated otherwise in the credit line; if the material is not included under the Creative Commons licence, users will need to obtain permission from the licence holder to reproduce the material. To view a copy of this licence, visit <http://creativecommons.org/licenses/by-nc-sa/3.0>

METHODS

No statistical methods were used to predetermine sample size. There was no randomization or blinding in selection of samples for sequencing.

Ethics statement. The National Committee of Ethics in Medical Research of Guinea approved the use of diagnostic leftover samples and corresponding patient data for this study (permit no. 11/CNERS/14). As the samples had been collected as part of the public health response to contain the outbreak in Guinea, informed consent was not obtained from patients.

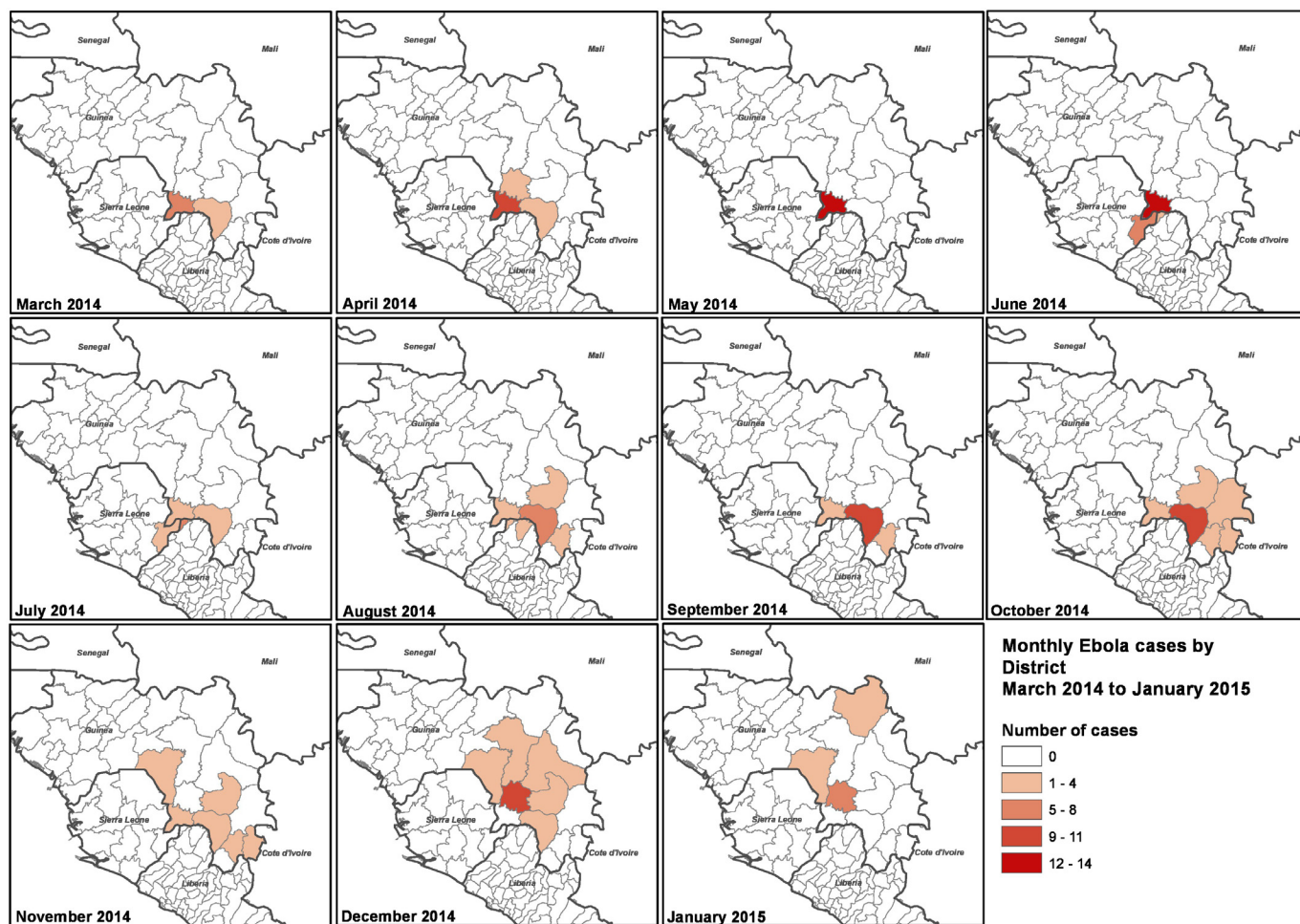
Genome sequencing and consensus building. Viral genome sequence was derived from the RNA extracted for diagnostic purposes from blood samples in the field with no pre-amplification of the viral genome. These samples were processed by the EMLab and are detailed in Supplementary Table 1, which indicates sample name, geographical location, date of onset of symptoms, date sample was collected, and the C_t value of EBOV RNA at the date of test. The clinical status is also indicated as well as malaria co-infection where known. Extracted RNA was DNase treated with Turbo DNase (Ambion) using the rigorous protocol. RNA sequencing libraries were prepared from the resultant RNA using the Epicentre ScriptSeq v2 RNA-Seq Library Preparation Kit. Following 10–15 cycles of amplification, libraries were purified using AMPure XP beads. Each library was quantified using Qubit and the size distribution assessed using the Agilent 2100 Bioanalyzer. These final libraries were pooled in equimolar amounts using the Qubit and Bioanalyzer data with 9–10 libraries per pool. The quantity and quality of the pool was assessed by Bioanalyzer and subsequently by qPCR using the Illumina Library Quantification Kit from Kapa on a Roche Light Cycler LC480II according to manufacturer's instructions. Each pool of libraries was sequenced on one lane of a HiSeq2500 at 2×125 -bp paired-end sequencing with v4 chemistry.

The trimmed fastq files were first aligned to a copy of the human genome using Bowtie2 (ref. 12) and the unaligned reads were then mapped with Bowtie2 to a list of 3731 known viral genomes excluding EBOV genomes. The reads that were still unmapped were then aligned to the EBOV genome—either the prototype strain isolated in Zaire in 1976 (AF086833.2) or a strain isolated during the current outbreak (KJ660348.2). For this step we again used Bowtie2 and the resultant alignment files were filtered with samtools to remove unmapped reads and reads with a mapping quality score below 11, followed by filtering with markdup to remove PCR duplicates. The resultant BAM file was then analysed by Quasirecomb¹³ to generate a phred-weighted table of nucleotide frequencies which were parsed with a custom perl script to generate a consensus genome in fasta format. This consensus genome was then used as a reference genome to which we remapped the sequence reads which did not map to the human genome or other

viruses in order to generate a second consensus. In this way we were able to manually determine if the reference genome used by Bowtie2 influenced the process of calling a consensus genome. In addition, we used FreeBayes to independently call and identify SNPs and indels. The pipeline is entirely open source and implemented in the Galaxy environment¹⁴, a Galaxy compatible workflow, novel scripts and XML wrappers needed for implementation in Galaxy are freely available and included in Supplementary Data File 1. Sequence alignment maps were manually inspected and curated over regions with consistent low coverage (for example, at the 5' ends).

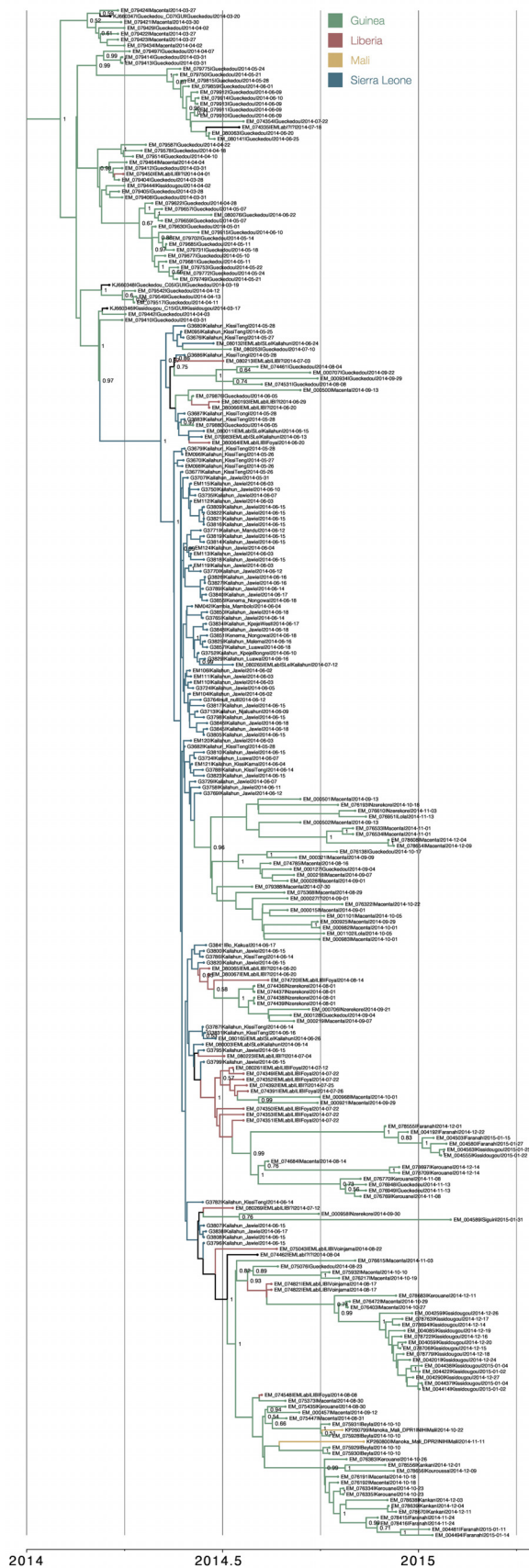
Phylogenetic analysis. Phylogenetic analysis comprised the 179 EBOV genomes from this study, 78 genomes from Sierra Leone⁶, three sequences from Guinea² and two sampled from Mali¹⁵. The genomes were partitioned into four sets of sites—1st, 2nd and 3rd codon positions of the protein-coding regions and the non-coding intergenic regions—with each partition being assigned a generalized time reversible substitution model¹⁶, gamma distributed rate heterogeneity¹⁷ and a relative rate of evolution. This model was used to construct a Bayesian nucleotide divergence tree (Fig. 2) using MrBayes¹¹ and a time-scaled phylogenetic analysis (Fig. 3) using BEAST¹⁸ with a log-normal distributed relaxed molecular clock¹⁹, and the 'Skygrid' non-parametric coalescent tree prior²⁰. The alignments and control files for both analyses are available in Supplementary Data Files 2 and 3 and provide documentation of all model parameters.

12. Langmead, B. & Salzberg, S. L. Fast gapped-read alignment with Bowtie 2. *Nature Methods* **9**, 357–359 (2012).
13. Topfer, A. *et al.* Probabilistic inference of viral quasispecies subject to recombination. *J. Comput. Biol.* **20**, 113–123 (2013).
14. Goecks, J., Nekrutenko, A., Taylor, J. & Galaxy, T. Galaxy: a comprehensive approach for supporting accessible, reproducible, and transparent computational research in the life sciences. *Genome Biol.* **11**, R86 (2010).
15. Hoenen, T. *et al.* Mutation rate and genotype variation of Ebola virus from Mali case sequences. *Science*, (2015).
16. Tavaré, S. Some Probabilistic and Statistical Problems in the Analysis of DNA Sequences in *Lectures on Mathematics in the Life Sciences* Vol. 17 (ed. Muir, R. M.) *Some Mathematical Questions in Biology: DNA Sequence Analysis* (American Mathematical Society, 1986).
17. Yang, Z. Maximum likelihood phylogenetic estimation from DNA sequences with variable rates over sites: approximate methods. *J. Mol. Evol.* **39**, 306–314 (1994).
18. Drummond, A. J., Suchard, M. A., Xie, D. & Rambaut, A. Bayesian phylogenetics with BEAUti and the BEAST 1.7. *Mol. Biol. Evol.* **29**, 1969–1973 (2012).
19. Drummond, A. J., Ho, S. Y., Phillips, M. J. & Rambaut, A. Relaxed phylogenetics and dating with confidence. *PLoS Biol.* **4**, e88 (2006).
20. Gill, M. S. *et al.* Improving Bayesian population dynamics inference: a coalescent-based model for multiple loci. *Mol. Biol. Evol.* **30**, 713–724 (2013).

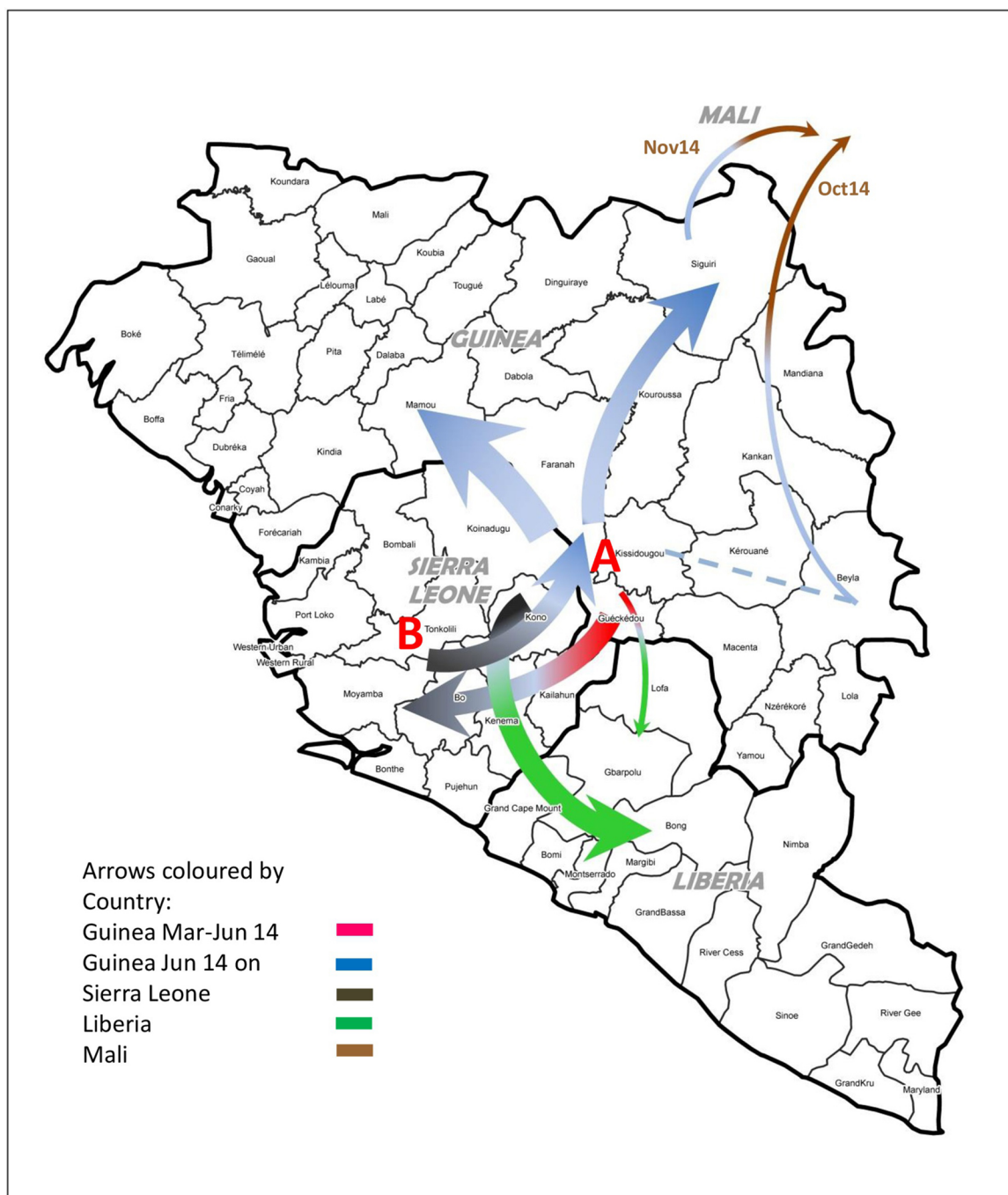


Extended Data Figure 1 | Spatial and temporal location of patient samples. Geographical locations of sequenced samples are plotted by district as panels for each month of collection (March 2014–January 2015). In brief, the number of samples obtained for each month was as follows: March 2014, 11;

April 2014, 14; May 2014, 14; June 2014, 22; July 2014, 16; August 2014, 19; September 2014, 18; October 2014, 21; November 2014, 11; December 2014, 22; January 2015, 11. Total number of samples sequenced, 179.

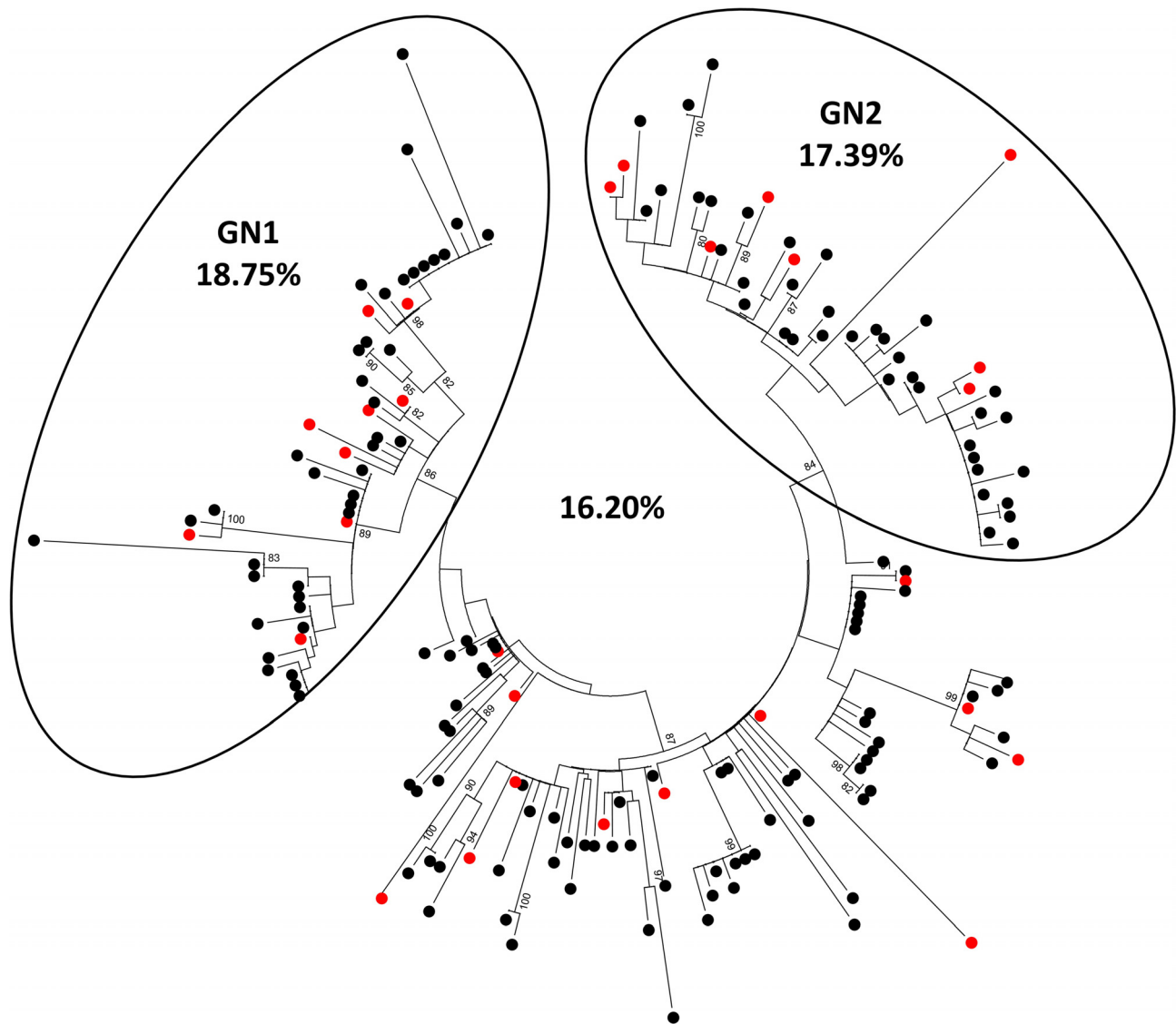


Extended Data Figure 2 | Enlarged view of phylogenetic tree presented in Fig. 3. Posterior support shown where >0.5 .



Extended Data Figure 3 | Temporal spread of EBOV based on phylogenetic analyses in Figs 2a and 3. Colour scheme is as follows: Guinea is red/blue (1st half/2nd half of 2014, respectively), Sierra Leone is grey-black, Liberia is green, Mali is brown. Lineage A (A) is associated with the initial focus of the outbreak (Guéckédou, Macenta and Kissidougou) in March 2014, expanded around this area and then declined around July 2014. From lineage A a second lineage (B)

emerged in May/June 2014 and expanded into Sierra Leone (end of May 2014) and Liberia (small arrow). Lineage B continued to spread into Sierra Leone, Liberia, and further into Guinea (beyond the original focus into most districts of Guinea). EBOV disease entered Mali from Guinea via two separate routes (from the Beyla district (possibly originally from Kissidougou) in October 2014 and from the Siguiri district in November 2014).



Extended Data Figure 4 | Survival rate amongst individuals with known EBOV sequences. The total survival rate for the 179 sequenced virus isolates included in this study is presented, as is the survival rate for two sub-lineages, GN1 and GN2, as defined by phylogenetic inference in Figs 2a and 3. The

sequences available for GN1 were collected during the period of March–July 2014 and the sequences available for GN2 were collected during the period of August 2014–January 2015. Red dots indicate survivors.

Distinct lineages of Ebola virus in Guinea during the 2014 West African epidemic

Etienne Simon-Loriere^{1,2*}, Ousmane Faye^{3*}, Oumar Faye^{3*}, Lamine Koivogui⁴, Nfaly Magassouba⁵, Sakoba Keita⁶, Jean-Michel Thiberge⁷, Laure Diancourt⁷, Christiane Bouchier⁸, Matthias Vandenberghe⁷, Valérie Caro⁷, Gamou Fall³, Jan P. Buchmann⁹, Christan B. Matranga¹⁰, Pardis C. Sabeti^{10,11}, Jean-Claude Manuguerra⁷, Edward C. Holmes^{9§} & Amadou A. Sall^{3§}

An epidemic of Ebola virus disease of unprecedented scale has been ongoing for more than a year in West Africa. As of 29 April 2015, there have been 26,277 reported total cases (of which 14,895 have been laboratory confirmed) resulting in 10,899 deaths¹. The source of the outbreak was traced to the prefecture of Guéckédou in the forested region of southeastern Guinea^{2,3}. The virus later spread to the capital, Conakry, and to the neighbouring countries of Sierra Leone, Liberia, Nigeria, Senegal and Mali¹. In March 2014, when the first cases were detected in Conakry, the Institut Pasteur of Dakar, Senegal, deployed a mobile laboratory in Donka hospital to provide diagnostic services to the greater Conakry urban area and other regions of Guinea. Through this process we sampled 85 Ebola viruses (EBOV) from patients infected from July to November 2014, and report their full genome sequences here. Phylogenetic analysis reveals the sustained transmission of three distinct viral lineages co-circulating in Guinea, including the urban setting of Conakry and its surroundings. One lineage is unique to Guinea and closely related to the earliest sampled viruses of the epidemic. A second lineage contains viruses probably reintroduced from neighbouring Sierra Leone on multiple occasions, while a third lineage later spread from Guinea to Mali. Each lineage is defined by multiple mutations, including non-synonymous changes in the virion protein 35 (VP35), glycoprotein (GP) and RNA-dependent RNA polymerase (L) proteins. The viral GP is characterized by a glycosylation site modification and mutations in the mucin-like domain that could modify the outer shape of the virion. These data illustrate the ongoing ability of EBOV to develop lineage-specific and potentially phenotypically important variation.

We combined our 85 Guinean EBOV sequences (Extended Data Table 1) with 110 publicly available 2014 EBOV genome sequences sampled from Guinea, Mali and Sierra Leone, producing a total data set of 195 sequences. Phylogenetic analysis reveals greater genetic diversity than previously described, with the presence of three distinct lineages, in contrast to the relatively limited variation documented early in the Sierra Leone outbreak⁴ (Fig. 1). The first lineage (denoted GUI-1) represents a cluster of sequences only found in Guinea, although from all urban and rural regions sampled in this country, and that is most closely related to the earliest viruses sampled in March 2014 (ref. 2). This lineage co-circulated in the greater Conakry region with viruses of the remaining two lineages described below. Notably, GUI-1 is characterized by multiple non-synonymous mutations in the nucleoprotein (NP), VP35 and GP such that it may also be phenotypically distinct, although this will require future experimental verification (Fig. 2a).

These data also reveal that EBOV sequences from the two documented introductions into Mali (October and November 2014) belong to another larger cluster of Guinean viruses, denoted here as GUI-2. This phylogenetically distinct lineage is most closely related to the second cluster of Sierra Leone sequences (SLE-2), and could represent either a reintroduction from Sierra Leone or the continued diffusion in Guinea of strains related to those initially introduced to Sierra Leone. Finally, a third cluster of viruses (SLE-GUI-3) is found in Conakry, Forécariah, Dalaba and to a limited extent in Coyah (Fig. 2b), with multiple sequences falling within the third cluster⁴ of Sierra Leonean sequences. Such a phylogenetic structure suggests that there have been multiple migrations of EBOV into Guinea from Sierra Leone (although viral traffic from Guinea to Sierra Leone may also have occurred on occasion). An example of such cross-border virus traffic is a documented case that initiated a transmission chain in June 2014 in Conakry⁵, as well as transmission chains in Dalaba (260 km from Conakry), each of which is directly linked to different travellers from Sierra Leone. Although the numbers are small, the decreasing proportion of these sequences (matching the third cluster of Sierra Leone sequences) along the road from the Sierra Leonean border towards Conakry via Forécariah, and deeper inland in Coyah, might reflect the major transmission route of these viruses (Fig. 2b).

The area constituted by the urban setting of Conakry and the neighbouring prefectures harbours extensive EBOV genetic diversity, characterized by multiple co-circulating viral lineages. For example, all three lineages defined above (GUI-1 to SLE-GUI-3) co-circulated in Conakry during September and October 2014 (Figs 1 and 2c). Although early concerns associated with the presence of Ebola virus disease in high population density settings such as Conakry did not result in increased viral transmission, the capital city of Guinea nevertheless represents an important regional travel hub and highlights the challenge of controlling Ebola virus disease in and near large urban centres. In addition, although it is clear that a number of the EBOV strains circulating in Guinea are also present in neighbouring Sierra Leone (lineage SLE-GUI-3), reflecting the continued mobility of individuals between these localities during the peak of the epidemic and in the face of outbreak control measures, Guinea is also characterized by a number of independently evolving viral lineages, such that the epidemics in these countries have generated localized genetic diversity. Despite case reports reaching very low values in Conakry at several points during the summer of 2014, the recurrent transmission of the three distinct lineages in this locality is another indication of the challenges of controlling Ebola virus disease in large urban centres with highly mobile populations.

¹Institut Pasteur, Functional Genetics of Infectious Diseases Unit, 75724 Paris Cedex 15, France. ²CNRS URA3012, Paris 75015, France. ³Institut Pasteur de Dakar, Arbovirus and Viral Hemorrhagic Fever Unit, BP 220, Dakar, Senegal. ⁴Institut National de Santé Publique de Guinée, Conakry, Guinea. ⁵Projet de fièvres hémorragiques de Guinée, Université Gamal Abdel Nasser, BP 1147, Conakry, Guinea. ⁶Ministry of Health, BP 585 Conakry, Guinea. ⁷Institut Pasteur, Unité Environnement et Risques Infectieux, Cellule d'Intervention Biologique d'Urgence, 75724 Paris Cedex 15, France. ⁸Institut Pasteur, Genomic platform, 75724 Paris Cedex 15, France. ⁹Marie Bashir Institute for Infectious Diseases and Biosecurity, Charles Perkins Centre, School of Biological Sciences and Sydney Medical School, The University of Sydney, Sydney, New South Wales 2006, Australia. ¹⁰Broad Institute, 75 Ames Street, Cambridge, Massachusetts 02142, USA. ¹¹FAS Center for Systems Biology, Department of Organismic and Evolutionary Biology, Harvard University, 52 Oxford Street, Cambridge, Massachusetts 02138, USA.

*These authors contributed equally to this work.

§These authors jointly supervised this work.

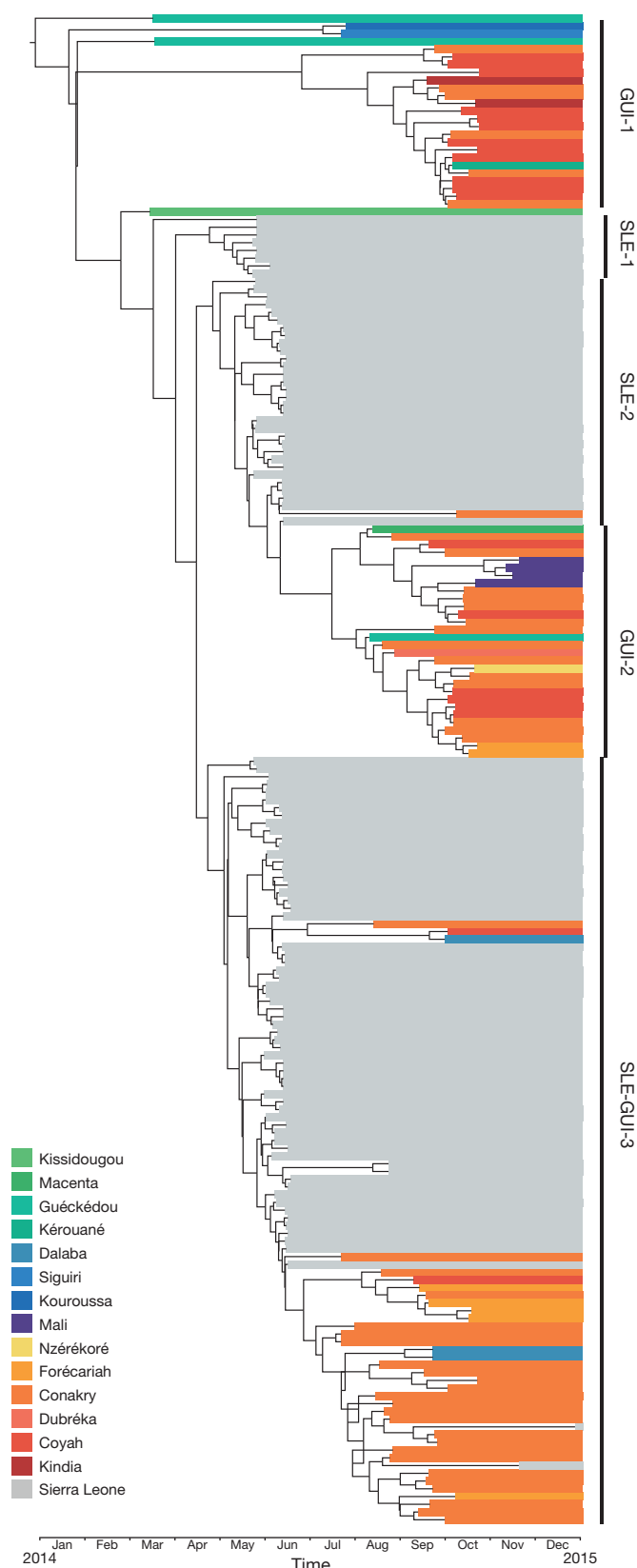


Figure 1 | Maximum clade credibility (MCC) phylogenetic tree of the 195 EBOV isolates from West Africa. Tip times are scaled to the date of sampling (with a timescale shown on the *x* axis), and colour-coded according to the geographic location of sampling (at the district level for Guinea, and country level for Sierra Leone and Mali).

A total of 207 single nucleotide polymorphisms (SNPs) (51 non-synonymous, including 24 novel, 88 synonymous and 68 inter-genic), have been fixed in individual patients within the sample of viruses analysed here. In contrast to the situation early in Sierra Leone, the viruses sampled from Guinea harbour numerous non-synonymous mutations which define lineages (Fig. 2a). Notably in GP, in which mutations could affect the efficacy of vaccines or antibody treatments, a C7025T (Pro→Ser) substitution in part defines GUI-1, and belongs to the heavily glycosylated mucin-like domain. Although *O*-glycosylation does involve the attachment of *N*-acetylglucosamine (GlcNAc) to a serine (and/or threonine) residue, the sialylation pattern of this disordered domain appears to vary with the cellular environment. Two mutations (A6357G (Asn→Asp), in GP1 domain II and G7476A (Gly→Asp) in GP1 carboxy terminus) co-occur in a later branch of this cluster, whereas C7256T (His→Tyr), again in the mucin-like domain, is observed in another branch. We also observed one change in a glycosylation site (A6726G (Thr→Ala)) in a sub-cluster of sequences in SLE-GUI-3. Surprisingly, a mutation in the highly conserved interferon inhibitory domain of VP35 (C4116T) introduces a phenylalanine, characteristic of Sudan EBOV, but never previously observed in EBOV-Zaire. Another mutation in VP35, G3151A (Arg→Lys), lies in the sequence targeted by AVI-7539, a phosphorodiamidate morpholino oligomer (PMO)-based therapeutic candidate⁶. Studies of the phenotypic consequences of such mutations on viral components directly interacting with the host immune response could provide key insights into their epidemic potential, and also inform the therapeutic options currently considered for deployment^{7,8}.

There has been some debate over the rate at which EBOV has evolved during the West African outbreak of EBOV, and what this may mean for the adaptive capacity of the virus, including changes in virulence⁹. Our estimates of the rate of nucleotide substitution for the combined Guinea and Mali and Sierra Leone data set under both strict and relaxed molecular clocks and using a variety of demographic and substitution models fall within the range of those obtained previously for EBOV^{4,9–11}, with mean rates of between 0.87×10^{-3} to 0.91×10^{-3} nucleotide substitutions per site per year (range of credible intervals of 0.68×10^{-3} to 1.1×10^{-3} substitutions per site per year) (Extended Data Fig. 2). Essentially identical rates were observed when studying the Guinean viruses in isolation. However, these rates are lower than those observed during the early spread of the virus in Sierra Leone⁴. It is therefore possible that the rate estimate provided by ref. 4 represents a random fluctuation due to limited genetic variation within sequences from Sierra Leone sampled over a relatively short time-period, and/or has been elevated by the presence of transient deleterious mutations that have yet to be removed by purifying selection, as suggested by those authors⁴. Indeed, evolutionary rates in RNA viruses are known to have a strongly time-dependent quality, such that they are expected to be higher in the short-term than the long-term¹². In addition, it is possible that differences in rate estimates in part reflect minor differences in substitution model parameters, the duration of intra-host virus evolution, as well as local epidemiological variation. More generally, it is difficult to translate relatively small differences in estimates of substitution rate, such as those obtained for EBOV in West Africa, into predictions on the future evolution of such key phenotypic traits as virulence, as the latter are more dependent on the nature of the selection pressures acting on the virus as well as the complex relationship between virulence and transmissibility. The data presented here indicates EBOV is able to generate and fix nucleotide and amino acid variation within co-circulating viral lineages on the time-scale of individual outbreaks, including the presence of country-specific lineages, and which may ultimately produce variants with important fitness differences.

Continued genomic surveillance is a strong complement to sometimes difficult local epidemiological investigations. We believe that the deployment of additional next-generation sequencing facilities in the

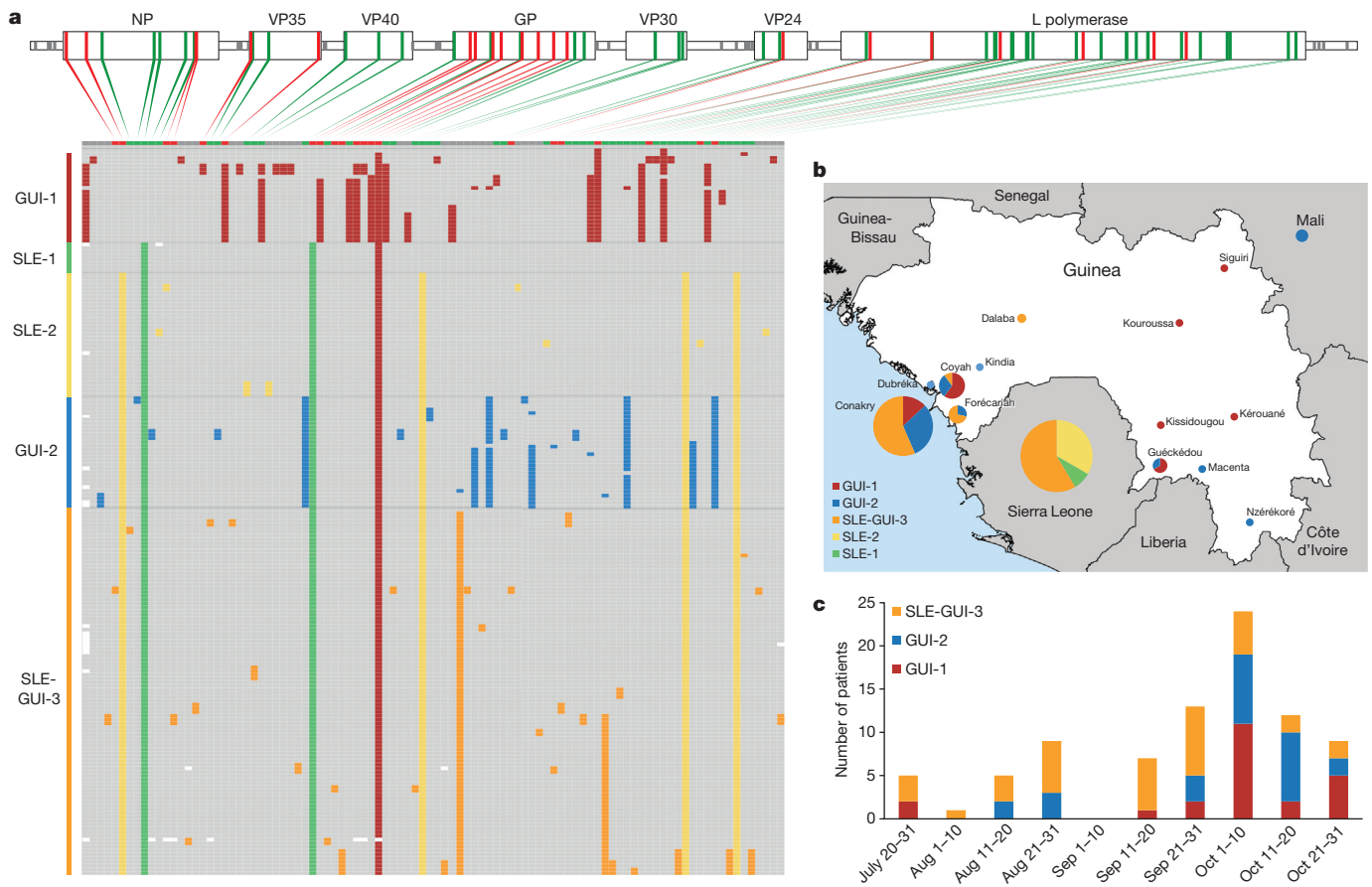


Figure 2 | Patterns of mutation accumulation during the 2014 epidemic. **a**, Mutations found in at least two separate sequences, showing one patient per row. Grey blocks indicate identity with the Kissidougou Guinean sequence (GenBank accession KJ660346). The top row shows the type of mutation (dark

West African surveillance network, thereby avoiding the logistical and regulatory¹³ hurdles associated with long-distance sample transportation, will positively contribute to the control of the current epidemic and help limit future outbreaks.

Online Content Methods, along with any additional Extended Data display items and Source Data, are available in the online version of the paper; references unique to these sections appear only in the online paper.

Received 15 April; accepted 5 June 2015.

Published online 24 June 2015.

1. The World Health Organization <http://www.who.int/csr/don/archive/disease/ebola/en/> (2014).
2. Baize, S. *et al.* Emergence of Zaire Ebola virus disease in Guinea. *N. Engl. J. Med.* **371**, 1418–1425 (2014).
3. Mari Saéz, A. *et al.* Investigating the zoonotic origin of the West African Ebola epidemic. *EMBO Mol. Med.* **7**, 17–23 (2015).
4. Gire, S. K. *et al.* Genomic surveillance elucidates Ebola virus origin and transmission during the 2014 outbreak. *Science* **345**, 1369–1372 (2014).
5. Faye, O. *et al.* Chains of transmission and control of Ebola virus disease in Conakry, Guinea, in 2014: an observational study. *Lancet Infect. Dis.* **15**, 320–326 (2015).
6. Warren, T. K. *et al.* Advanced antisense therapies for postexposure protection against lethal filovirus infections. *Nature Med.* **16**, 991–994 (2010).
7. Kugelman, J. R. *et al.* Evaluation of the potential impact of Ebola virus genomic drift on the efficacy of sequence-based candidate therapeutics. *MBio* **6** (2015).
8. Sayburn, A. WHO gives go ahead for experimental treatments to be used in Ebola outbreak. *Br. Med. J.* **349**, g5161 (2014).
9. Hoenen, T. *et al.* Mutation rate and genotype variation of Ebola virus from Mali case sequences. *Science* **348**, 117–119 (2015).
10. Duchêne, S., Holmes, E. C. & Ho, S. Y. Analyses of evolutionary dynamics in viruses are hindered by a time-dependent bias in rate estimates. *Proc. R. Soc. B* **281**, 20140732 (2014).
11. Biek, R., Walsh, P. D., Leroy, E. M. & Real, L. A. Recent common ancestry of Ebola Zaire virus found in a bat reservoir. *PLoS Pathog.* **2**, e90 (2006).

grey, intergenic; green, synonymous; red, non-synonymous), with the genomic location indicated above. Cluster assignment is shown at the left. **b**, The geographic distribution of EBOV variants, coloured by clusters. **c**, Number of Ebola virus disease patients sequenced per ten days, coloured by cluster.

12. Carroll, S. A. *et al.* Molecular evolution of viruses of the family Filoviridae based on 97 whole-genome sequences. *J. Virol.* **87**, 2608–2616 (2013).
13. Devaux, C. A. The hidden face of academic researches on classified highly pathogenic microorganisms. *Infect. Genet. Evol.* **29**, 26–34 (2015).

Acknowledgements This study was supported by the Pasteur Ebola Task Force (PETF) and has also received funding from the French government's Investissement d'Avenir programme, Laboratoire d'Excellence 'Integrative Biology of Emerging Infectious Diseases' (grant number ANR-10-LABX-62-IBEID) and Institut Pasteur de Dakar. We are grateful to all members of the PETF for their support, and in particular F. Rey and K. Victor. High-throughput sequencing was performed on the Genomics Platform of Institut Pasteur, member of 'France Génomique' consortium (ANR10-INBS-09-08). We thank L. Ma for technical assistance and Institut Pasteur Clinical Research Department for their help with ethical approval procedures. E.C.H. is supported by an NHMRC Australia fellowship.

Author Contributions E.S.-L., E.C.H. and A.A.S. designed the experiments. Ous.F., Our.F., L.K., N.M., S.K., G.F. and A.A.S. collected samples and epidemiological data. C.B.M. and P.C.S. provided protocols for sample processing and sequencing. E.S.-L., J.-M.T., L.D., C.B., M.V., V.C. and J.-C.M. performed the deep sequencing. E.S.-L., E.C.H. and J.P.B. analysed the genomic sequence data. E.S.-L. and E.C.H. wrote the manuscript with contributions from all authors.

Author Information Sequences have been deposited in GenBank, under accession numbers KR534507–KR534591. Reprints and permissions information is available at www.nature.com/reprints. The authors declare no competing financial interests. Readers are welcome to comment on the online version of the paper. Correspondence and requests for materials should be addressed to E.S.-L. (etienne.simon-loriere@pasteur.fr), E.C.H. (edward.holmes@sydney.edu.au) or A.A.S. (asall@pasteur.sn).

This work is licensed under a Creative Commons Attribution-NonCommercial-ShareAlike 3.0 Unported licence. The images or other third party material in this article are included in the article's Creative Commons licence, unless indicated otherwise in the credit line; if the material is not included under the Creative Commons licence, users will need to obtain permission from the licence holder to reproduce the material. To view a copy of this licence, visit <http://creativecommons.org/licenses/by-nc-sa/3.0>

METHODS

Ethics statement. This study has been evaluated and approved by the ethics committee of Guinea (ref: 35/CNERS/15), the Ebola research committee and the Institutional Review Board at Institut Pasteur. The Office of the Guinean Ethics and Scientific Review Committee granted a waiver to provide written consent to sequence and make publicly available viral sequences obtained from patient and contact samples collected during the Ebola virus disease outbreak in Guinea.

Sample collection and processing. Samples were collected from suspected Ebola cases hospitalized at an Ebola treatment centre in Conakry (Donka hospital) or from other regions of Guinea. EBOV detection was tested by quantitative RT-PCR using a Taqman assay with 5-FAM and 3-TAMRA probes on a portable Smart-Cycler TD. Each sample was run three times on three separate assays.

Carrier RNA and host ribosomal RNA depletion. Carrier RNA and host ribosomal RNA was depleted from RNA samples as described in ref. 14, using the NEBNext rRNA Depletion Kit (New England Biolabs).

cDNA synthesis, Nextera library construction and Illumina sequencing of EBOV samples. RNA from selective depletion was used for cDNA synthesis and Illumina library preparation as described previously^{4,14}. Each individual sample was indexed with a unique dual barcode and libraries were pooled equally and sequenced on a HiSeq2500 (101-base-pair (bp) paired-end reads; Illumina) platform.

Demultiplexing of raw Illumina sequencing reads. Illumina Analysis Pipeline version 1.8 was used for image analysis, base calling, error estimation and demultiplexing.

Mapping of full-length EBOV genomes. Sequencing read pairs were obtained, from which low-quality bases and remaining adaptor/barcode sequences were removed. Reads were mapped to a 2014 EBOV genome (GenBank accession number: KM233070) using the CLC Genomics Assembly Cell v4.2 implemented in Galaxy^{15–17}. All genomes generated here were annotated and manually inspected for accuracy, such as the presence of intact open reading frames, using Geneious v8 (ref. 18). Multiple sequence alignments across all EBOV from the 2014–2015 outbreak were generated by first aligning amino acid sequences using MUSCLE¹⁹, and then aligning the nucleotide sequence based on the amino acid alignment.

Screening for recombinant sequences. To screen for potential recombination in the 2014–2015 EBOV sequences we used the RDP, GENECONV, MAXCHI, CHIMAERA, 3SEQ, BOOTSCAN and SISCAN methods as implemented in the RDP4 (ref. 20) software package with default settings. No recombinant sequences were identified, nor was there any evidence for phylogenetic incongruence among the sequences analysed here.

Phylogenetic tree inference. Phylogenetic trees on our total data set of 195 sequences, 18,959 bp alignment length, were estimated using the maximum likelihood (ML) procedure in RAxML v8, employing the GTR- Γ model of nucleotide substitution. Fifty instances were run to obtain the best tree, and statistical support for each node was calculated using the standard bootstrapping algorithm with 500 pseudoreplicates (Extended Data Fig. 1). A topologically equivalent ML tree was obtained using the GTR+ Γ model available in PhyML²¹.

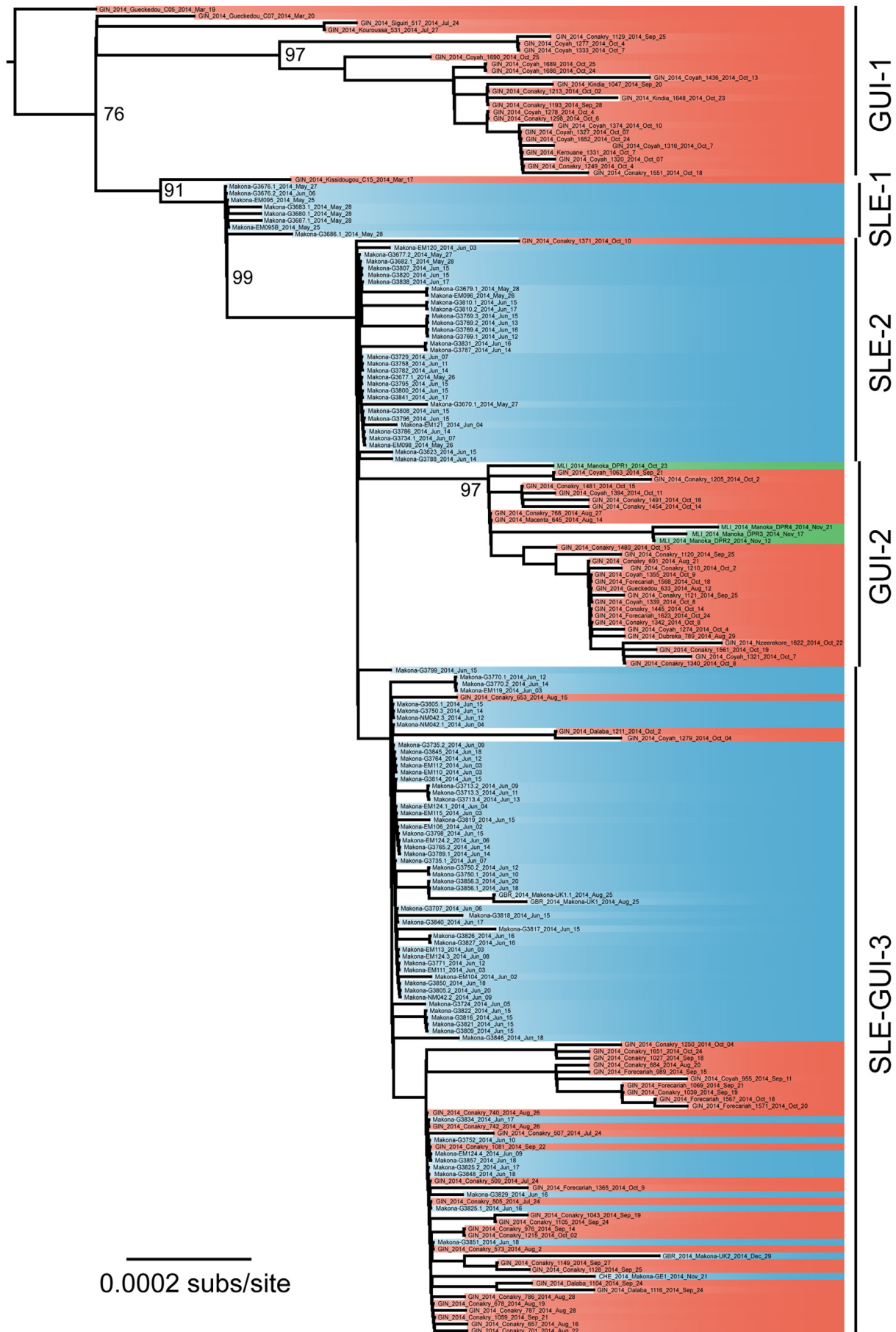
Analysis of evolutionary rates. We employed the Bayesian Markov Chain Monte Carlo (MCMC) method in BEAST v1.8 (ref. 22) to estimate the rate of EBOV

evolution (nucleotide substitution) during the 2014–2015 epidemic. The date (day) for each individual sample was based on the time of diagnostic testing. Importantly, very similar estimates were obtained using a variety of substitution, coalescent and molecular clock models, namely (i) the HKY- Γ and GTR- Γ nucleotide substitution models (with four categories of the gamma distribution of among-site rate variation, Γ), (ii) constant population size, Bayesian SkyGrid, and exponential population tree priors, and (iii) strict and relaxed (uncorrelated lognormal) molecular clocks (Extended Data Fig. 2). In all cases the MCMC was run until convergence was (easily) achieved (Extended Data Fig. 2). A broadly similar substitution rate (0.99×10^{-3} substitutions per site per year), and relatively strong temporal structure (correlation coefficient = 0.87, R^2 = 0.76), was obtained using a regression of root-to-tip genetic distance in the ML (PhyML) tree against sampling date using the Path-O-Gen program (<http://tree.bio.ed.ac.uk/software/pathogen/>). The posterior distribution of trees obtained from the BEAST analysis was also used to obtain the maximum clade credibility (MCC) tree for these sequences. For simplicity, we used the results of the HKY+ Γ , constant population size, strict molecular clock analysis to create the MCC tree as this had the narrowest distribution (Extended Data Fig. 2). Prior to inference of the MCC tree, 10% of the runs were removed as burn-in.

Glycoprotein RNA editing. The RNA editing site of the GP gene consists of 7 U residues; co-transcriptional stuttering can result in transcripts with more or less A residues. The resulting frameshifts allow for the expression of distinct glycoproteins called sGP (7 A), GP (predominantly 8 A), and ssGP (predominantly 6 A). Deep sequencing revealed 8 U at ~1% and 7 U at ~99%, values similar to those described in ref. 4.

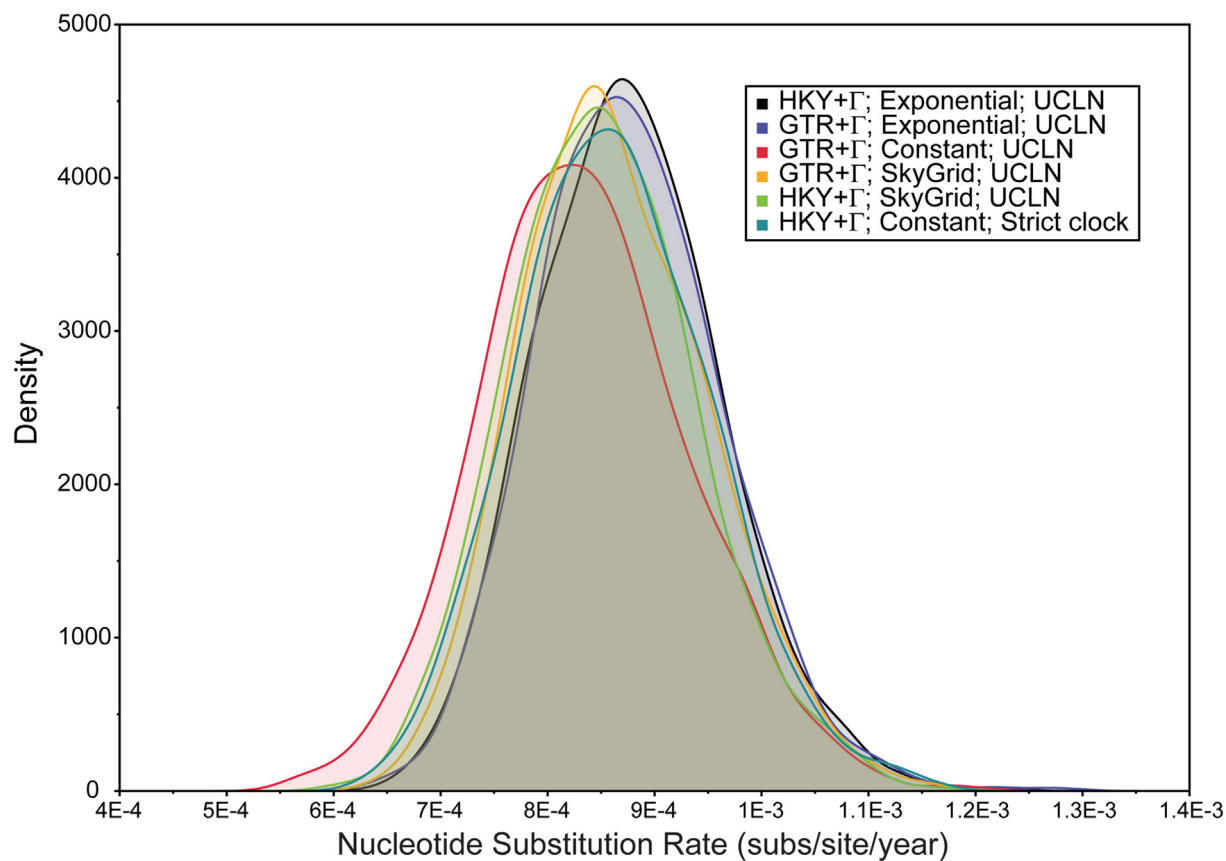
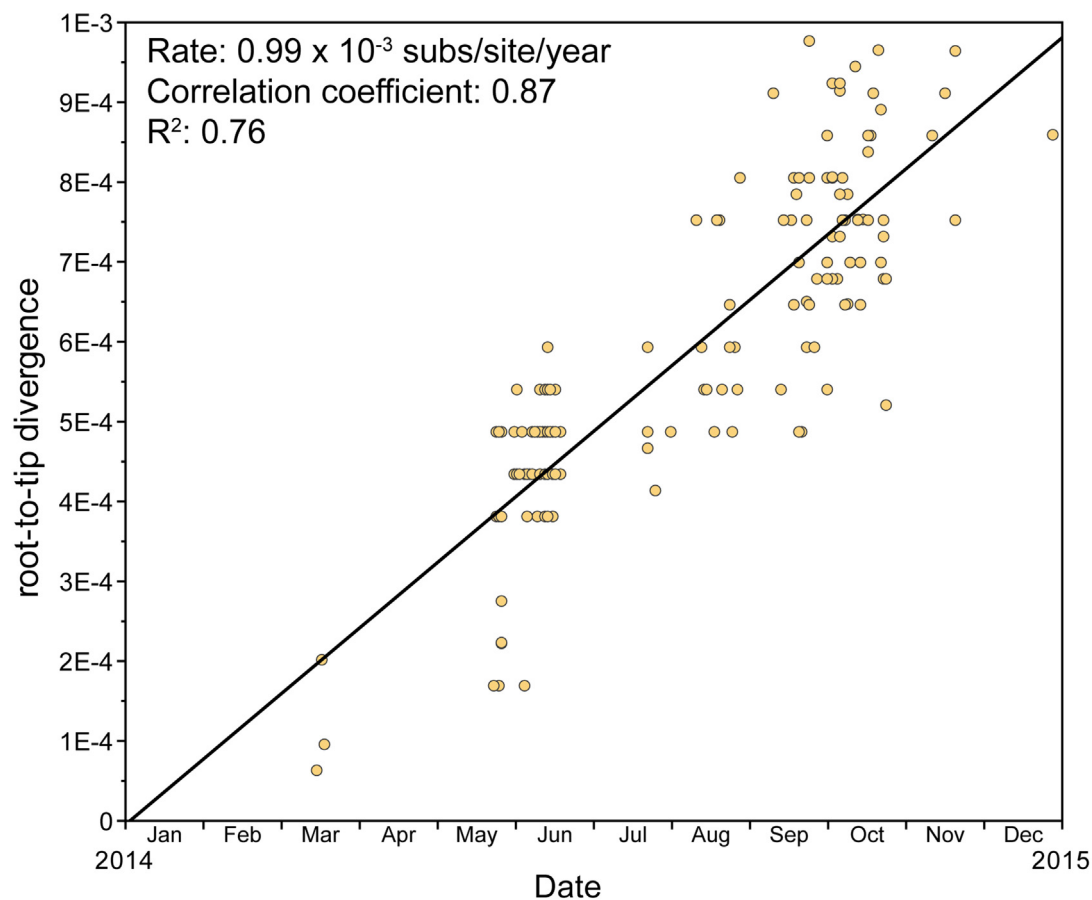
Data reporting. No statistical methods were used to predetermine sample size. The experiments were not randomized. The investigators were not blinded to allocation during experiments and outcome assessment.

14. Matranga, C. B. *et al.* Enhanced methods for unbiased deep sequencing of Lassa and Ebola RNA viruses from clinical and biological samples. *Genome Biol.* **15**, 519 (2014).
15. Blankenberg, D. *et al.* Galaxy: a web-based genome analysis tool for experimentalists. *Curr. Protocols Mol. Biol.*, (2010).
16. Giardine, B. *et al.* Galaxy: a platform for interactive large-scale genome analysis. *Genome Res.* **15**, 1451–1455 (2005).
17. Goecks, J., Nekrutenko, A. & Taylor, J. Galaxy: a comprehensive approach for supporting accessible, reproducible, and transparent computational research in the life sciences. *Genome Biol.* **11**, R86 (2010).
18. Kearse, M. *et al.* Geneious Basic: an integrated and extendable desktop software platform for the organization and analysis of sequence data. *Bioinformatics* **28**, 1647–1649 (2012).
19. Edgar, R. C. MUSCLE: multiple sequence alignment with high accuracy and high throughput. *Nucleic Acids Res.* **32**, 1792–1797 (2004).
20. Martin, D. P. *et al.* RDP3: a flexible and fast computer program for analyzing recombination. *Bioinformatics* **26**, 2462–2463 (2010).
21. Guindon, S. *et al.* New algorithms and methods to estimate maximum-likelihood phylogenies: assessing the performance of PhyML 3.0. *Syst. Biol.* **59**, 307–321 (2010).
22. Drummond, A. J., Suchard, M. A., Xie, D. & Rambaut, A. Bayesian phylogenetics with BEAUti and the BEAST 1.7. *Mol. Biol. Evol.* **29**, 1969–1973 (2012).



Extended Data Figure 1 | Maximum likelihood phylogenetic tree of EBOV from the 2014–2015 outbreak in West Africa. Published sequences from Sierra Leone are shown in blue, those from Mali in green, and those from Guinea in red. All horizontal branch lengths are scaled to the number of nucleotide substitutions per site. Bootstrap values are shown for key nodes.

The tree is rooted according to the topology seen in the MCC tree (Fig. 1) under the assumption of a molecular clock, although the observation of three main lineages of EBOV in Guinea is robust to rooting position (including rooting on the oldest sequences from March 2014).

a**b**

Extended Data Figure 2 | Substitution rates and temporal signal.

a, Posterior distribution of nucleotide substitution rates ($\times 10^{-4}$ substitutions per site per year) in the 195 sequence EBOV data set and using a range of substitution (HKY+ Γ and GTR+ Γ), demographic (constant population size,

exponential population growth, Bayesian SkyGrid), and molecular clock (strict, relaxed lognormal (UCLN)) models. Note the extensive overlap among estimates under a range of models. **b**, Root-to-tip regression of genetic distance against day of sampling for the 195 sequence EBOV data set.

Extended Data Table 1 | Guinean EBOV samples sequenced in this study

Virus	Sampling date	Virus	Sampling date
Conakry-505	24 July 2014	Conakry-1213	02 October 2014
Conakry-509	24 July 2014	Conakry-1215	02 October 2014
Siguiriri-517	24 July 2014	Conakry-1249	04 October 2014
Conakry-507	24 July 2014	Coyah-1274	04 October 2014
Kouroussa-531	27 July 2014	Coyah-1277	04 October 2014
Conakry-573	02 August 2014	Coyah-1278	04 October 2014
Gueckedou-633	12 August 2014	Conakry-1250	04 October 2014
Macenta-645	14 August 2014	Coyah-1279	04 October 2014
Conakry-653	15 August 2014	Conakry-1298	06 October 2014
Conakry-657	16 August 2014	Coyah-1316	07 October 2014
Conakry-678	19 August 2014	Coyah-1321	07 October 2014
Conakry-684	20 August 2014	Kerouane-1331	07 October 2014
Conakry-691	21 August 2014	Coyah-1333	07 October 2014
Conakry-701	22 August 2014	Coyah-1320	07 October 2014
Conakry-740	26 August 2014	Coyah-1327	07 October 2014
Conakry-742	26 August 2014	Coyah-1339	08 October 2014
Conakry-768	27 August 2014	Conakry-1340	08 October 2014
Conakry-786	28 August 2014	Conakry-1342	08 October 2014
Conakry-787	28 August 2014	Coyah-1355	09 October 2014
Dubreka-789	29 August 2014	Forecariah-1365	09 October 2014
Coyah-955	11 September 2014	Conakry-1371	10 October 2014
Conakry-976	14 September 2014	Coyah-1374	10 October 2014
Forecariah-989	15 September 2014	Coyah-1394	11 October 2014
Conakry-1027	18 September 2014	Coyah-1436	13 October 2014
Conakry-1043	19 September 2014	Conakry-1445	14 October 2014
Conakry-1039	19 September 2014	Conakry-1454	14 October 2014
Kindia-1047	20 September 2014	Conakry-1480	15 October 2014
Conakry-1059	21 September 2014	Conakry-1481	15 October 2014
Coyah-1063	21 September 2014	Conakry-1491	16 October 2014
Forecariah-1069	21 September 2014	Conakry-1551	18 October 2014
Conakry-1081	22 September 2014	Forecariah-1567	18 October 2014
Dalaba-1104	24 September 2014	Forecariah-1568	18 October 2014
Dalaba-1116	24 September 2014	Conakry-1561	19 October 2014
Conakry-1105	24 September 2014	Forecariah-1571	20 October 2014
Conakry-1120	25 September 2014	Nzeerekore-1622	22 October 2014
Conakry-1121	25 September 2014	Kindia-1648	23 October 2014
Conakry-1128	25 September 2014	Forecariah-1623	24 October 2014
Conakry-1129	25 September 2014	Conakry-1651	24 October 2014
Conakry-1149	27 September 2014	Coyah-1652	24 October 2014
Conakry-1193	28 September 2014	Coyah-1686	24 October 2014
Conakry-1205	02 October 2014	Coyah-1689	25 October 2014
Conakry-1210	02 October 2014	Coyah-1690	25 October 2014
Dalaba-1211	02 October 2014		

Cyanate as an energy source for nitrifiers

Marton Palatinszky¹, Craig Herbold¹, Nico Jehmlich², Mario Pogoda¹, Ping Han¹, Martin von Bergen^{2,3,4}, Ilias Lagkouvardos^{1†}, Søren M. Karst⁴, Alexander Galushko^{1‡}, Hanna Koch¹, David Berry¹, Holger Daims¹ & Michael Wagner¹

Ammonia- and nitrite-oxidizing microorganisms are collectively responsible for the aerobic oxidation of ammonia via nitrite to nitrate and have essential roles in the global biogeochemical nitrogen cycle. The physiology of nitrifiers has been intensively studied, and urea and ammonia are the only recognized energy sources that promote the aerobic growth of ammonia-oxidizing bacteria and archaea. Here we report the aerobic growth of a pure culture of the ammonia-oxidizing thaumarchaeote *Nitrososphaera gargensis*¹ using cyanate as the sole source of energy and reductant; to our knowledge, the first organism known to do so. Cyanate, a potentially important source of reduced nitrogen in aquatic and terrestrial ecosystems², is converted to ammonium and carbon dioxide in *Nitrososphaera gargensis* by a cyanase enzyme that is induced upon addition of this compound. Within the cyanase gene family, this cyanase is a member of a distinct clade also containing cyanases of nitrite-oxidizing bacteria of the genus *Nitrospira*. We demonstrate by co-culture experiments that these nitrite oxidizers supply cyanase-lacking ammonia oxidizers with ammonium from cyanate, which is fully nitrified by this microbial consortium through reciprocal feeding. By screening a comprehensive set of more than 3,000 publically available metagenomes from environmental samples, we reveal that cyanase-encoding genes clustering with the cyanases of these nitrifiers are widespread in the environment. Our results demonstrate an unexpected metabolic versatility of nitrifying microorganisms, and suggest a previously unrecognized importance of cyanate in cycling of nitrogen compounds in the environment.

Cyanate is a small molecule containing carbon, nitrogen, and oxygen atoms. It is formed spontaneously within cells from urea and carbamoyl phosphate^{3,4}, but also occurs in the environment where it may be produced from the chemical/physicochemical decomposition of urea or cyanide^{5,6}. Until recently, environmental cyanate concentrations were difficult to obtain, as the available analytical methods were inadequate for sub-micromolar detection. Furthermore, cyanate is not chemically stable and decomposes relatively slowly to ammonium and carbon dioxide (CO₂). The decomposition rate is linearly related to the concentration of cyanate and thus the compound is reasonably stable at low concentrations (Extended Data Fig. 1). A more sensitive chromatographic method for the detection of cyanate in aquatic samples was recently developed and revealed nanomolar-range cyanate concentrations in seawater⁶. These cyanate levels are in the same order of magnitude as ammonium concentrations typically found in oligotrophic marine environments⁷. Consistently, cyanate has been postulated to serve as a nitrogen source for the growth of certain marine cyanobacteria under nitrogen limitation^{2,8}. For assimilation of cyanate, these phototrophic bacteria convert it to ammonium and CO₂ with the enzyme cyanase (also known as cyanate lyase and cyanate hydratase). Cyanases are also found in a variety of other bacteria and archaea, where they have been reported to play a role in nitrogen assimilation or detoxification as cyanate chemically modifies proteins through carbamylation^{9,10}. However, to our knowledge, no microorganism has been described that can grow using cyanate as a source of energy and reductant.

Nitrifying microorganisms are generally considered to be highly specialized chemolithoautotrophs that oxidize either ammonia or nitrite to generate energy and reductant for growth, and use CO₂ as a carbon source. Over the past few decades, however, this perception has been challenged by several studies^{11–13}. For example, it was reported that uncultured thaumarchaeota closely related to the ammonia oxidizer *Nitrososphaera gargensis* thrive in wastewater treatment plants using unknown sources of energy and reductant other than ammonium or urea¹⁴, and that nitrite oxidizers of the genus *Nitrospira* can derive energy for growth by aerobic hydrogen oxidation¹⁵. Furthermore, the growth of some thaumarchaeotal ammonia oxidizers is stimulated by the addition of organic compounds¹⁶, while others may be obligate mixotrophs¹⁷. However, aerobic growth of ammonia-oxidizing microorganisms has thus far only been demonstrated in the presence of urea or ammonium.

Recently, we sequenced the genome of *N. gargensis* enriched from a thermal spring sample¹. Unexpectedly, a gene encoding a putative cyanase was detected close to the gene of a putative cyanate/nitrite/formate transporter¹⁸. In contrast, all other sequenced genomes of archaeal or bacterial ammonia oxidizers, including its closest relative *Nitrososphaera viennensis*¹⁹, do not contain a cyanase-encoding gene. As *N. gargensis* shares most central metabolic pathways with other thaumarchaeotes, it is very unlikely that it requires cyanase for detoxification of internally produced cyanate. We therefore hypothesized that *N. gargensis* may instead use cyanate as a source of energy and reductant for growth. Prior to testing our hypothesis, we obtained a pure culture of *N. gargensis* by repeated serial dilutions over a period of 16 months (see Supplementary Information). The pure culture of *N. gargensis* grew well in the presence of 2 mM ammonium and growth was not inhibited by addition of 0.5 mM cyanate. After a short period of growth in the presence of both ammonium and cyanate, the biomass of *N. gargensis* was transferred to a medium in which cyanate was the sole source of energy, reductant and nitrogen. In this medium, *N. gargensis* stoichiometrically converted cyanate via ammonium to nitrite (Fig. 1a), and cyanate degradation was the rate-limiting step of the overall process (Extended Data Fig. 1). A much slower conversion of cyanate to ammonium, reflecting chemical decay, was observed in control experiments with equal amounts of dead biomass of *N. gargensis* (Fig. 1b). Notably, growth of *N. gargensis* in the medium containing only cyanate as an energy source was demonstrated by total protein measurements (Fig. 1c) and by a quantitative polymerase chain reaction (qPCR) assay targeting its 16S rRNA gene (Extended Data Fig. 2). During growth on 0.5 mM cyanate, *N. gargensis* showed, according to total protein measurements, a mean generation time of 136.3 h (±11.4 (s.d.)), which is slightly higher than the mean generation time observed during growth on 0.5 mM ammonium, which was determined to be 113.4 h (±6.1). This difference might reflect the toxicity of cyanate, despite the presence of a cyanase, or the additional energy demand for the synthesis of cyanase during growth. Proteomic analyses revealed that on first exposure of *N. gargensis* to 0.5 mM cyanate for 48 h, cyanase was the most strongly induced protein

¹Department of Microbiology and Ecosystem Science, Division of Microbial Ecology, University of Vienna, Althanstrasse 14, 1090 Vienna, Austria. ²Department of Proteomics, Helmholtz Centre for Environmental Research - UFZ, Permoserstr. 15, 04318 Leipzig, Germany. ³Department of Metabolomics, Helmholtz Centre for Environmental Research - UFZ, Permoserstr. 15, 04318 Leipzig, Germany. ⁴Department of Chemistry and Bioscience, The Faculty of Engineering and Science, Aalborg University, Fredrik Bajers Vej 7, 9220 Aalborg, Denmark. [†]Present addresses: ZIEL Research Center for Nutrition and Food Sciences, Technische Universität München, Gregor-Mendel-Str. 2, 85354 Freising, Germany (I.L.); Agrophysical Research Institute, 14 Grazhdanskiy pr., 195220 Saint Petersburg, Russia (A.G.).

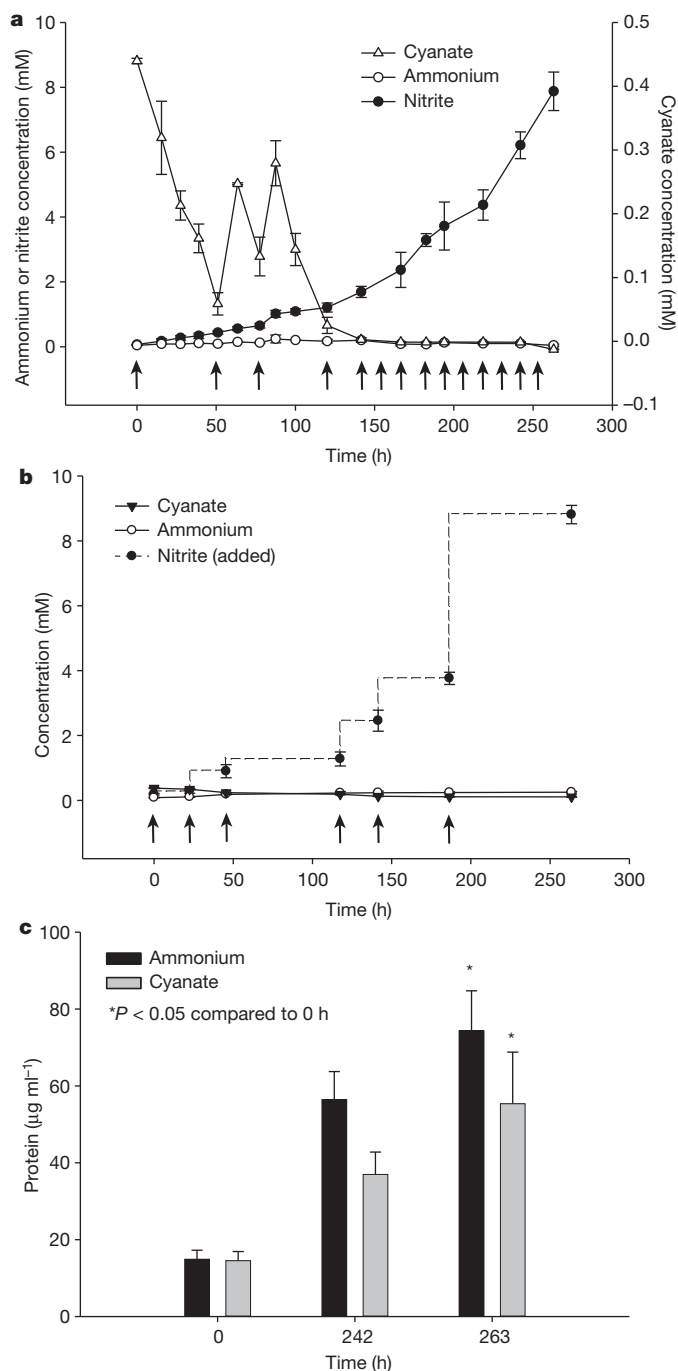


Figure 1 | *N. gargensis* grows on cyanate. **a**, Concentration changes of cyanate, ammonium, and nitrite during the growth of *N. gargensis* in a mineral medium containing 0.5 mM cyanate as the sole source of energy and reductant. Arrows indicate additions of 0.5 mM cyanate. **b**, Control experiment with an identical amount of dead biomass of *N. gargensis*. Nitrite was added at different time points, as indicated by the arrows, to mimic the conditions in the experiment with living biomass. All experiments shown in panels **a** and **b** were performed in four replicates and the chemical measurements were done in three technical replicates (averaged). Data points are mean values of four biological replicates, error bars show s.d. **c**, Total protein concentration of *N. gargensis* during growth on cyanate. For comparison, the respective protein concentration of *N. gargensis* after growth in medium with 0.5 mM ammonium is presented. Protein concentration increased 4.99-fold during growth on ammonium and 3.81-fold during growth on cyanate over 263 h. Significance was calculated by paired *t*-test, * $P < 0.05$ compared to 0 h. Columns show mean values of four biological replicates; error bars show s.d. Biomass increase was independently confirmed by qPCR (Extended Data Fig. 2).

(Extended Data Fig. 3; 32-fold change; mean from triplicates), confirming its key role in growth on cyanate. However, the putative cyanate/nitrite/formate transporter encoded in the same genomic region was not detected, despite the fact that a protocol optimized for extraction of membrane proteins was applied (see 'Proteomic analysis' section of Methods). This is probably due to the fact that cyanate diffuses through biological membranes at millimolar concentrations²⁰. Interestingly, cyanate conversion was also observed in *N. gargensis* cultures without a previous period of growth in the presence of ammonium and cyanate. Furthermore, conversion of cyanate to nitrite by *N. gargensis* could also be detected at a tenfold lower concentration of the compound (0.05 mM) (Extended Data Fig. 4).

While *N. gargensis* is the only ammonia-oxidizing microorganism with a sequenced genome in which a cyanase-encoding gene is present (which was probably acquired from a *Nitrospira* strain via lateral gene transfer¹⁸), all nitrite oxidizers for which a genome sequence is available contain a gene annotated as cyanase (Extended Data Table 1). To test whether these genes are functional, we performed experiments with a pure culture of the nitrite oxidizer *Nitrospira moscoviensis*, which possesses a cyanase closely related to that of *N. gargensis*. After 96 h of incubation in the presence of around 1 mM cyanate, *N. moscoviensis* degraded significantly more cyanate, causing ammonium release from cells, than did a negative control that included an identical amount of dead biomass of this strain, demonstrating that *N. moscoviensis* is capable of cyanate degradation (Extended Data Fig. 5). In a separate experiment, addition of 1 mM cyanate only decreased nitrite oxidation rates slightly in *N. moscoviensis*, while higher concentrations showed a stronger effect (Extended Data Fig. 6). The presence of a cyanase in the genomes of all nitrite oxidizers might reflect that these nitrifiers make more cyanate as a side product of their metabolism than ammonia-oxidizing microorganisms. Cyanate is produced from both carbamoyl phosphate metabolism and urea formation, and while the enzymatic repertoire involved in these processes is highly similar between ammonia oxidizers and nitrite oxidizers, many members of the latter group (but also some thaumarchaeotes) do not contain enzymes for degradation of internally produced urea (Extended Data Table 1). In addition, it is possible that nitrite-oxidizers continuously import cyanate from the environment, as some of their transporters for uptake of environmental nitrite are also capable of transporting cyanate²¹. In both scenarios the presence of a cyanase enzyme is beneficial for nitrite oxidizers because it allows them to detoxify cyanate, and the formed ammonium is not only available for assimilation but after secretion (Extended Data Fig. 5) might also serve as a source of energy and reductant for ammonia oxidizers, which typically grow in close vicinity to nitrite oxidizers^{22,23}. The subsequent activity of the ammonia oxidizers leads to the formation of nitrite, which can then be consumed by the nitrite oxidizers (Fig. 2a). This reciprocal feeding pattern would enable nitrite oxidizers as well as ammonia oxidizers without a cyanase to collectively convert cyanate for energy and reductant generation. We tested this hypothesis by establishing a co-culture of the ammonia-oxidizing bacterium *Nitrosomonas nitrosa* Nm90 (ref. 24), which has no cyanase activity but is not inhibited in its activity by 1 mM cyanate (Extended Data Fig. 7), with the cyanase-encoding nitrite oxidizer *N. moscoviensis*. Consistent with the reciprocal feeding hypothesis, the co-culture stoichiometrically converted cyanate to nitrate (Fig. 2c and Extended Data Fig. 8), and fluorescence *in situ* hybridization with specific 16S rRNA-targeted probes revealed that dense clusters containing both nitrifiers had formed (Fig. 2b). Conversion rates of cyanate to nitrate were accelerated by addition of ammonium at the start of the experiment, allowing consortium members to gain energy and reductant before interspecies cyanate degradation was fully established (Fig. 2d). In contrast, no nitrate formation was observed in abiotic control experiments using the same medium (Extended Data Fig. 9).

The cyanases found in *N. gargensis* and members of the genus *Nitrospira* form a deep-branching clade to the exclusion of other

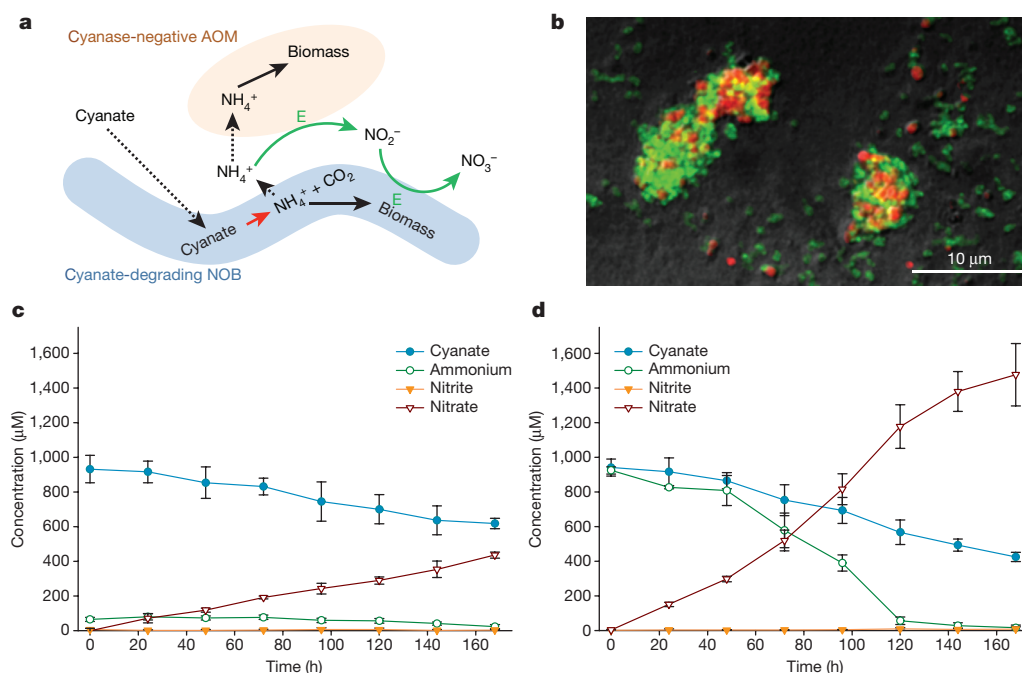


Figure 2 | Reciprocal feeding between ammonia and nitrite oxidizers during cyanate conversion. **a**, Schematic illustration of the interaction between cyanate-degrading nitrite-oxidizing bacteria (NOB) and cyanase-negative ammonia-oxidizing microorganisms (AOM). Solid arrows represent conversions of compounds; dashed arrows represent the uptake or release of compounds. Green arrows represent conversions used for energy (E) and reductant generation. Red arrow shows the conversion of cyanate by the cyanase. **b**, Co-aggregation of *Nitrosomonas nitrosa* (red) and *N. moscoviensis* (green) in the co-culture experiment shown in panel **d** after 168 h, as revealed

by fluorescence *in situ* hybridization. **c**, **d**, Concentration changes of cyanate, ammonium, nitrite, and nitrate during the growth of the cyanase-negative ammonia-oxidizing bacterium *N. nitrosa* and the cyanase-positive nitrite oxidizer *N. moscoviensis* in a mineral medium containing 1 mM cyanate (**c**) or 1 mM cyanate and 1 mM ammonium (**d**). Error bars show s.d. of three technical replicates. For each experiment, three biological replicates were performed (one replicate is displayed in panels **c** and **d**, all replicates including mass balances are shown in Extended Data Fig. 8). Note that *N. nitrosa* did not grow equally well in all replicates.

cultured organisms¹⁸. We searched a collection of 3,000 metagenomic data sets available from the Integrated Microbial Genomics (IMG) system²⁵ and identified 225 additional metagenomic cyanase genes (fragments) that are related to the cyanases of these known nitrifiers (Fig. 3). These findings show that this novel cyanase gene family is

widespread in the environment. Most of these cyanases were located on very small contigs, preventing an independent phylogenetic classification of the organisms carrying these genes. The metagenomic cyanase fragments most closely related to *N. gargensis* (47–55% amino acid similarity) were retrieved from three different peat and

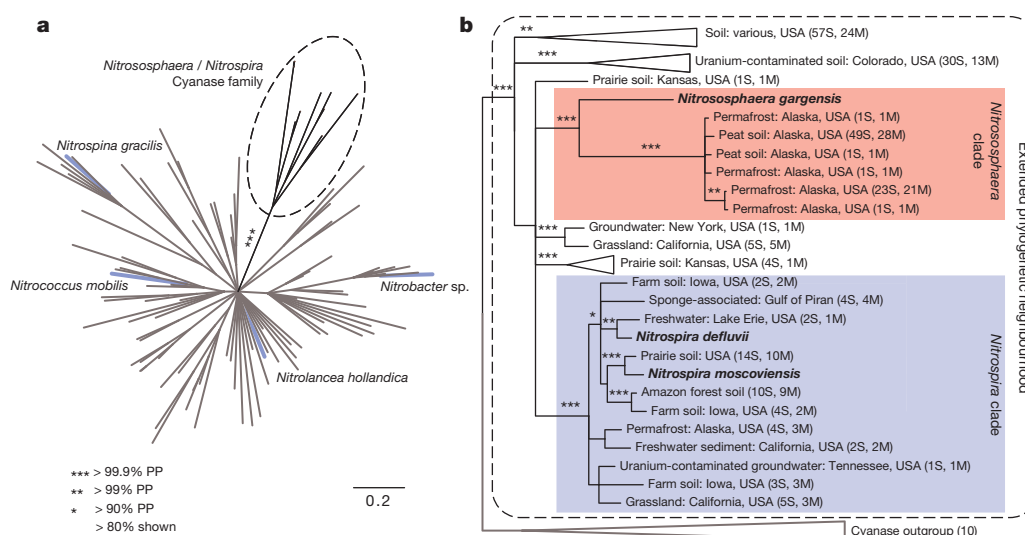


Figure 3 | Nitrososphaera gargensis and Nitrospira cyanases form a distinct family containing sequences from various metagenomes. **a**, Bayesian 80% consensus amino acid tree with alignment uncertainty calculated with BALI-phy²⁸. For clarity, posterior support is shown only for the branch separating this cyanase family from other cyanases. Cyanases from nitrite-oxidizing bacteria are indicated by blue branches. PP, posterior probability. **b**, Bayesian 80% consensus amino acid tree of the *Nitrososphaera/Nitrospira*

cyanase family that contains separate well-supported *Nitrososphaera*-related (red) and *Nitrospira*-related (blue) clades. Metagenomic cyanase sequences that showed more than 99% amino acid similarity were clustered using Usearch²⁹. Beside each metagenomic sequence, the total number of clustered sequences (S) and the number of metagenomic data sets (M) from which they were retrieved is displayed. Scale indicates the number of substitutions per site.

permafrost soils in Alaska, while the sequences most closely affiliated with *Nitrospira* cyanases (67–80% amino acid similarity) were mostly found in temperate forest and agricultural soil from lower latitudes as well as in lakes, freshwater sediment and groundwater, matching the known distribution of *Nitrospira* in a broad range of different ecosystems²⁶ (Fig. 3b).

Our findings show that an archaeal ammonia oxidizer can grow on cyanate, utilizing it as the sole source of energy, reductant, and nitrogen. Furthermore, nitrite oxidizers of the genus *Nitrospira* (and probably all nitrite oxidizers) can convert cyanate to ammonium and are capable of fully nitrifying it through a newly discovered type of reciprocal feeding with cyanase-negative ammonia oxidizers. This metabolic capability potentially provides them with a selective advantage in environments where cyanate is present, in particular if ammonium concentrations are low, and thus may be an important facet of the ecology of nitrifiers. Cyanate forms spontaneously by isomerization of urea in aqueous solution. The high concentration of urea in many ecosystems (ranging from polar seawater and sea ice²⁷ to the huge areas of urea-fertilized soils in global agriculture) combined with the wide distribution of nitrifier-related cyanase genes underscores the potential environmental ubiquity of this unique physiology.

Online Content Methods, along with any additional Extended Data display items and Source Data, are available in the online version of the paper; references unique to these sections appear only in the online paper.

Received 19 December 2014; accepted 24 June 2015.

Published online 29 July 2015.

- Hatzenpichler, R. et al. A moderately thermophilic ammonia-oxidizing crenarchaeote from a hot spring. *Proc. Natl Acad. Sci. USA* **105**, 2134–2139 (2008).
- Kamennaya, N. A. & Post, A. F. Distribution and expression of the cyanate acquisition potential among cyanobacterial populations in oligotrophic marine waters. *Limnol. Oceanogr.* **58**, 1959–1971 (2013).
- Qian, M., Eaton, J. W. & Wolff, S. P. Cyanate-mediated inhibition of neutrophil myeloperoxidase activity. *Biochem. J.* **326**, 159–166 (1997).
- Purcareau, C. et al. *Aquifex aeolicus* aspartate transcarbamoylase, an enzyme specialized for the efficient utilization of unstable carbamoyl phosphate at elevated temperature. *J. Biol. Chem.* **278**, 52924–52934 (2003).
- Ubalua, A. O. Cyanogenic glycosides and the fate of cyanide in soil. *Aust. J. Crop. Sci.* **4**, 223–237 (2010).
- Widner, B., Mulholland, M. R. & Mopper, K. Chromatographic determination of nanomolar cyanate concentrations in estuarine and sea waters by precolumn fluorescence derivatization. *Anal. Chem.* **85**, 6661–6666 (2013).
- Rees, A. P., Woodward, E. M. S. & Joint, I. Concentrations and uptake of nitrate and ammonium in the Atlantic Ocean between 60 degrees N and 50 degrees S. *Deep Sea Res.* **53**, 1649–1665 (2006).
- Rocap, G. et al. Genome divergence in two *Prochlorococcus* ecotypes reflects oceanic niche differentiation. *Nature* **424**, 1042–1047 (2003).
- Luque-Almagro, V. M. et al. Characterization of the *Pseudomonas pseudoalcaligenes* CECT5344 cyanase, an enzyme that is not essential for cyanide assimilation. *Appl. Environ. Microbiol.* **74**, 6280–6288 (2008).
- Kamennaya, N. A., Chernihovsky, M. & Post, A. F. The cyanate utilization capacity of marine unicellular Cyanobacteria. *Limnol. Oceanogr.* **53**, 2485–2494 (2008).
- Bock, E. Growth of nitroreducer in the presence of organic matter. II. Chemotrophic growth of *Nitrobacter agilis*. *Arch. Microbiol.* **108**, 305–312 (1976).
- Bock, E., Schmidt, I., Stüven, R. & Zart, D. Nitrogen loss caused by denitrifying *Nitrosomonas* cells using ammonium or hydrogen as electron-donors and nitrite as electron-acceptor. *Arch. Microbiol.* **163**, 16–20 (1995).
- Hommes, N. G., Sayavedra-Soto, L. A. & Arp, D. J. Chemolithoautotrophic growth of *Nitrosomonas europaea* on fructose. *J. Bacteriol.* **185**, 6809–6814 (2003).
- Musmann, M. et al. Thaumarchaeotes abundant in refinery nitrifying sludges express *amoA* but are not obligate autotrophic ammonia oxidizers. *Proc. Natl Acad. Sci. USA* **108**, 16771–16776 (2011).
- Koch, H. et al. Growth of nitrite-oxidizing bacteria by aerobic hydrogen oxidation. *Science* **345**, 1052–1054 (2014).
- Tourna, M. et al. *Nitrososphaera viennensis*, an ammonia oxidizing archaeon from soil. *Proc. Natl Acad. Sci. USA* **108**, 8420–8425 (2011).
- Qin, W. et al. Marine ammonia-oxidizing archaeal isolates display obligate mixotrophy and wide ecotypic variation. *Proc. Natl Acad. Sci. USA* **111**, 12504–12509 (2014).
- Spang, A. et al. The genome of the ammonia-oxidizing *Candidatus Nitrososphaera gargensis*: insights into metabolic versatility and environmental adaptations. *Environ. Microbiol.* **14**, 3122–3145 (2012).
- Stieglmeier, M. et al. *Nitrososphaera viennensis* gen. nov., sp. nov., an aerobic and mesophilic, ammonia-oxidizing archaeon from soil and a member of the archaeal phylum Thaumarchaeota. *Int. J. Syst. Evol. Microbiol.* **64**, 2738–2752 (2014).
- Maeda, S. & Omata, T. Nitrite transport activity of the ABC-type cyanate transporter of the cyanobacterium *Synechococcus elongatus*. *J. Bacteriol.* **191**, 3265–3272 (2009).
- Muñoz-Centeno, M. C., Paneque, A. & Cejudo, F. J. Cyanate is transported by the nitrate permease in *Azotobacter chroococcum*. *FEMS Microbiol. Lett.* **137**, 91–94 (1996).
- Schramm, A., de Beer, D., van den Heuvel, J. C., Ottengraf, S. & Amann, R. Microscale distribution of populations and activities of *Nitrososphaera* and *Nitrospira* spp. along a macroscale gradient in a nitrifying bioreactor: Quantification by in situ hybridization and the use of microarrays. *Appl. Environ. Microbiol.* **65**, 3690–3696 (1999).
- Maixner, F. et al. Nitrite concentration influences the population structure of *Nitrospira*-like bacteria. *Environ. Microbiol.* **8**, 1487–1495 (2006).
- Koops, H. P., Bottcher, B., Moller, U. C., Pommereningroser, A. & Stehr, G. Classification of eight new species of ammonia-oxidizing bacteria: *Nitrosomonas communis* sp. nov., *Nitrosomonas ureae* sp. nov., *Nitrosomonas aestuarii* sp. nov., *Nitrosomonas marina* sp. nov., *Nitrosomonas nitrosa* sp. nov., *Nitrosomonas eutropha* sp. nov., *Nitrosomonas oligotropha* sp. nov. and *Nitrosomonas halophila* sp. nov. *J. Gen. Microbiol.* **137**, 1689–1699 (1991).
- Markowitz, V. M. et al. IMG 4 version of the integrated microbial genomes comparative analysis system. *Nucleic Acids Res.* **42**, D560–D567 (2014).
- Daims, H., Nielsen, J. L., Nielsen, P. H., Schleifer, K. H. & Wagner, M. In situ characterization of *Nitrospira*-like nitrite oxidizing bacteria active in wastewater treatment plants. *Appl. Environ. Microbiol.* **67**, 5273–5284 (2001).
- Alonso-Sáez, L. et al. Role for urea in nitrification by polar marine Archaea. *Proc. Natl Acad. Sci. USA* **109**, 17989–17994 (2012).
- Suchard, M. A. & Redelings, B. D. BAli-Phy: simultaneous Bayesian inference of alignment and phylogeny. *Bioinformatics* **22**, 2047–2048 (2006).
- Edgar, R. C. Search and clustering orders of magnitude faster than BLAST. *Bioinformatics* **26**, 2460–2461 (2010).

Supplementary Information is available in the online version of the paper.

Acknowledgements We thank E. Lebedeva for efforts in purifying *N. gargensis*, M. Mooshammer for help with cyanate analytics, K. Eismann and B. Scheer for help with the proteomic analysis, and M. Schmid for performing the FISH experiment. A. Pommerening-Röser is acknowledged for providing the *Nitrosomonas nitrosa* Nm90 strain. M.Pa., M.Po., A.G., P.H., and M.W. were supported by the European Research Council Advanced Grant project NITRICARE 294343 (to M.W.). H.D., H.K., and D.B. were supported by the Austrian Science Fund (FWF, grants P25231-B21 and P26127-B20). We are grateful for use of the analytical facilities of the Centre for Chemical Microscopy (ProVIS) at the Helmholtz Centre for Environmental Research, which is supported by European Regional Development Funds (EFRE–Europe funds Saxony) and the Helmholtz Association. M.vB. was partially funded by the Collaborative Research Centre AquaDivi of the German Research Foundation.

Author Contributions M.Pa., P.H. and A.G. performed experiments with *N. gargensis*; C.H. and I.L. carried out analysis of metagenomic data sets and proteomics data; N.J. and M.vB. performed proteomics measurements and data analysis; M.Po. and H.K. performed all experiments with *N. moscoviensis*; H.K. carried out genomic analysis of ammonia- and nitrite-oxidizing organisms; S.M.K. contributed to metagenomic data analysis; D.B. performed cyanate decomposition modelling; M.W., H.D., and M.Pa. designed the study and analysed data. M.W. wrote the paper. All authors discussed the results and commented the manuscript.

Author Information Reprints and permissions information is available at www.nature.com/reprints. The authors declare no competing financial interests. Readers are welcome to comment on the online version of the paper. Correspondence and requests for materials should be addressed to M.W. (wagner@microbial-ecology.net).

METHODS

Purification and standard cultivation of *Nitrososphaera gargensis*. A pure culture of the ammonia-oxidizing archaeon *Nitrososphaera gargensis*¹ was obtained through a series of antibiotics treatments (50 mg l⁻¹ kanamycin; 50 mg l⁻¹ penicillin-G; 100 mg l⁻¹ streptomycin; 100 mg l⁻¹ carbenicillin; 50 mg l⁻¹ ampicillin; 20 mg l⁻¹ erythromycin; 20 mg l⁻¹ doxycycline) and repeated serial dilutions in the ammonia-oxidizer medium described below. Purity of the culture was confirmed by phase contrast microscopy and by using a specific catalysed reported deposition–fluorescence *in situ* hybridization (CARD–FISH) assay¹, as well as by PCR targeting the 16S rRNA gene, using various universal eubacterial and archaeal primer combinations (27f 5′-AGAGTTTGATYMTGGCTCAG-3′; Arch21f 5′-TTCCGGTTGATCCYCCGGA-3′; 907f 5′-AAACTCAAAGAATTGACGG-3′; 909r 5′-CCGTCWATTCMTTGTAGT-3′; 1390r 5′-GACGGCGGTGTGTACAA-3′; 1492r 5′-GGYTACCTTGTACGACTT-3′) on DNA extracted by three different DNA isolation methods (bead-beating with phenol:chloroform extraction; MoBio UltraClean Soil DNA kit; FastDNA SPIN Kit for Soil). Any PCR product obtained was cloned and sequenced, retrieving only *N. gargensis* 16S rRNA gene sequences. In addition, no growth was observed if the *N. gargensis* culture was inoculated into various rich media such as lysogeny broth, nutrient agar and tryptic soy agar. Subsequently, *N. gargensis* was grown at 46 °C in a modified ammonia-oxidizing archaea (AOA) medium³⁰ containing (per litre): 50 mg KH₂PO₄; 75 mg KCl; 50 mg MgSO₄ × 7H₂O; 584 mg NaCl; 4 g CaCO₃ (mostly undissolved, acting as a solid buffering system and growth surface); 1 ml of specific trace element solution (AOA-TES); and 1 ml of selenium-wolfram solution (SWS)³¹. The composition of TES and SWS is described below. Both solutions were added to the autoclaved medium by sterile filtration using 0.2 µm pore-size cellulose acetate filters (Thermo Scientific). The pH of the medium was around 8.4 after autoclaving and was kept around 8.2 during growth of *N. gargensis* by the CaCO₃ buffering system. AOA-TES contained (per litre): 34.4 mg MnSO₄ × 1H₂O; 50 mg H₃BO₃; 70 mg ZnCl₂; 72.6 mg Na₂MoO₄ × 2H₂O; 20 mg CuCl₂ × 2H₂O; 24 mg NiCl₂ × 6H₂O; 80 mg CoCl₂ × 6H₂O; 1 g FeSO₄ × 7H₂O. All salts except the FeSO₄ × 7H₂O were dissolved in 997.5 ml Milli-Q water and 2.5 ml of 37% (smoking) HCl was added before dissolving the FeSO₄ × 7H₂O salt. SWS contained (per litre): 0.5 g NaOH; 3 mg Na₂SeO₃ × 5H₂O; 4 mg Na₂WO₄ × 2H₂O. After completing the medium, ammonium chloride (from an autoclaved 0.2 M stock solution) or potassium cyanate (filter sterilized, Sigma Aldrich) was added to the medium based on the experimental setups. All cultures were grown in the dark in screw-cap Schott bottles (Schott AG) at 46 °C without shaking.

Growth of *N. gargensis* on 0.5 mM cyanate. Cultures were induced with 0.5 mM (final concentration) potassium cyanate (KOCN) and 0.5 mM NH₄Cl 2 days before the experiment. After 48 h, cyanase-induced cultures were harvested by centrifugation (10,000g for 30 min at room temperature), washed in AOA medium, centrifuged again, and inoculated into 20 ml fresh AOA medium in 50 ml CELLSTAR plastic suspension culture flasks (Greiner Bio-One), containing no ammonium but 0.5 mM KOCN final concentration. Biomass protein concentrations used for inoculation were 14.51 ± 2.3 µg ml⁻¹. Cultures were incubated without shaking at 46 °C in the dark, for 11 days (264 h). All incubations were done in four replicates. Samples for chemical, protein and qPCR analysis were taken every 12 h for the first 4 days, with daily sampling thereafter. After the experiment, the cells were harvested and washed as described above and then transferred into 20 ml of fresh AOA medium without ammonium and autoclaved. After cooling to room temperature, 20 µl TES, 20 µl SWS, and 0.5 mM of filter sterilized KOCN was added, and the dead biomass was incubated for 46 °C in the dark for 264 h. To mimic the production of nitrite in these control experiments with dead biomass, NaNO₂ was added at each sampling time point, according to the respective levels of nitrite in the biotic experiments at the next time point, resulting in a nitrite concentration, which is always at least as high as in the biotic parallels. In both experiments (either living or dead biomass) the pH stayed constant around 8.2 ± 0.3 during the incubation time.

Growth of *N. gargensis* on 0.05 mM cyanate. Cultures were induced with 0.05 mM (final concentration) potassium cyanate (KOCN) and 0.5 mM NH₄Cl 2 days before the experiment. After 48 h, cyanase-induced cultures were harvested by centrifugation (10,000g for 30 min, room temperature), washed in AOA medium, centrifuged again, and inoculated into 20 ml fresh AOA medium in 50 ml CELLSTAR plastic suspension culture flasks (Greiner Bio-One), containing no ammonium but 0.05 mM KOCN final concentration. Cultures were incubated without shaking at 46 °C in the dark for 264 h. In parallel, abiotic controls were started with similar parameters, without biomass. All incubations were done in 4 replicates. Samples for chemical analysis were taken at 7 time points during the 11 days. In both experiments (either biotic or abiotic) the pH stayed constant around 8.2 ± 0.3 during the incubation time.

Cultivation of *N. moscoviensis*. The nitrite-oxidizing bacterium *Nitrospira moscoviensis* was pre-grown in mineral nitrite-oxidizing bacteria (NOB) medium³²

containing (per litre): 1,000 ml distilled water; 10 mg CaCO₃; 500 mg NaCl; 50 mg MgSO₄ × 7H₂O; 150 mg KH₂PO₄, as well as 1 ml filter-sterilized NOB-specific trace elements solution (NOB-TES) added after autoclaving. The pH was initially adjusted to 8.6 which changed during autoclaving to 7.6. NOB-TES contained (per litre): 34.4 mg MnSO₄ × 1H₂O; 50 mg H₃BO₃; 70 mg ZnCl₂; 72.6 mg Na₂MoO₄ × 2H₂O; 20 mg CuCl₂ × 2H₂O; 24 mg NiCl₂ × 6H₂O; 80 mg CoCl₂ × 6H₂O; 1 g FeSO₄ × 7H₂O. All salts, except FeSO₄ × 7H₂O were dissolved in 997.5 ml distilled water and 2.5 ml of 37% (smoking) HCl was added before dissolving the FeSO₄ × 7H₂O salt. After autoclaving, 1 mM (final concentration) of filter-sterilized NaNO₂ (if not stated otherwise) was added to the medium. All cultures were grown in the dark without shaking at 37 °C. If all nitrite was consumed, it was re-added to a final concentration of 1 mM.

Cyanate degradation by *N. moscoviensis*. Nitrite-oxidizing cultures of *N. moscoviensis* were supplied with 0.5 mM (final concentration) KOCN and incubated for 48 h at 37 °C to induce the expression of cyanase. Biomass was harvested (8,500 rpm for 15 min at room temperature) and washed twice with fresh NOB medium without nitrite. Cells were then transferred into 50 ml NOB medium, which either contained 1 mM NaNO₂ or 1 mM KOCN. Biomass concentrations were inferred from total protein concentrations, which were 27.6 ± 3.9 µg ml⁻¹ as measured by the Pierce BCA Protein Assay Kit (Thermo Scientific). Abiotic experiments were performed by adding 1 mM KOCN to the NOB medium in the absence of nitrite. Dead biomass controls were performed by treating similar amounts of *N. moscoviensis* biomass fixed with paraformaldehyde (4%) as described above. The dead biomass was incubated in nitrite-free NOB medium containing 1 mM KOCN. All incubations were amended by filter-sterilized 1.5 mM NaHCO₃ (final concentration). All incubations were performed in 250 ml Schott bottles closed by rubber stoppers without shaking at 37 °C in the dark for 96 h. All experiments were performed in triplicate.

In order to evaluate the effect of increasing cyanate concentrations on nitrite oxidation by *N. moscoviensis*, biomass was harvested (9,300g for 15 min at room temperature) and washed twice with fresh NOB medium without nitrite. Cells were then transferred into 100 ml NOB medium. Incubations were performed with 1 mM NaNO₂ and 0 mM, 1 mM, 2 mM, 3 mM, 4 mM, or 5 mM of KOCN. As an abiotic control, medium containing 5 mM KOCN and 1 mM NaNO₂ was incubated without addition of biomass. All incubations were performed in 250 ml Schott bottles closed by rubber stoppers without shaking at 37 °C in the dark for 60 h. All experiments were performed in duplicate.

Response of *Nitrosomonas nitrosa* Nm90 to cyanate. The ammonia-oxidizing bacterium *N. nitrosa* Nm90 (strain collection of the University of Hamburg, Germany) was grown in AOA medium amended with 10 mM NH₄Cl at 37 °C. Biomass was harvested (8,500 rpm for 15 min at room temperature) and washed twice with fresh AOA medium without ammonium. Cells were inoculated into 25 ml batches of AOA medium containing either 1 mM KOCN alone, 1 mM NH₄Cl and 1 mM KOCN, or 10 mM NH₄Cl and 1 mM KOCN. Cultures were incubated in 50 ml CELLSTAR plastic suspension culture flasks (Greiner Bio-One) at 37 °C in the dark and shaken at 150 rpm.

Co-culture experiments with *N. nitrosa* Nm90 and *N. moscoviensis*. Nitrite-oxidizing cultures of *N. moscoviensis* were supplied with 0.5 mM (final concentration) KOCN and incubated for 48 h to induce the expression of cyanase. Biomass was harvested (8,500 rpm for 15 min at room temperature) and washed twice with fresh AOA medium without nitrite. *N. nitrosa* Nm90 was grown in AOA medium supplied with 10 mM NH₄Cl. Biomass was harvested (8,500 rpm for 15 min at room temperature) and washed twice with fresh AOA medium without ammonium. Biomass concentrations were measured separately for *N. moscoviensis* and *N. nitrosa* Nm90, inferred from total protein concentrations which were 446.5 µg ml⁻¹ and 164 µg ml⁻¹ respectively in 50 ml final volumes for each culture-stock, measured by the Pierce BCA Protein Assay kit (Thermo Scientific). All biomass were combined and diluted up to 1 litre serving as a master-mix, which was aliquoted to 100 ml batches for the experimental setups resulting in a starting protein concentration 20 times less than in the separate stocks measured. Subsequently, either 1 mM KOCN, 1 mM KOCN and 1 mM NH₄Cl, or only 1 mM NH₄Cl was added to the experiments (final concentrations). In addition, abiotic experiments were performed by adding either 1 mM KOCN or 1 mM KOCN and 1 mM NH₄Cl to 100 ml AOA medium. All incubations were amended by filter-sterilized 1.5 mM NaHCO₃ (final concentration). All experiments were done in 250 ml Schott bottles closed by rubber stoppers, incubated without shaking at 37 °C in the dark for 168 h. All experiments were performed in triplicate.

Chemical analysis. Nitrite levels were measured by photometry with the sulfanilamide *N*-(1-naphthyl)ethylenediamine dihydrochloride (NED) reagent method³³. Ammonium levels were measured photometrically as described previously³⁴. Cyanate was measured fluorometrically after derivatization with 2-aminobenzoic acid to quinazoline-2,4-dione³⁵, with the modification using fluorescence readout (excitation, 312 nm; emission, 370 nm). All photometric and fluorometric reads were performed with an Infinite 200 Pro spectrophotometer (Tecan Group AG).

qPCR quantification of *N. gargensis*. A qPCR assay was developed using the newly designed *N. gargensis* 16S rRNA gene-specific primers NG1052 5'-TAGTT GCTACCTCTGTTC-3' and NG1436R 5'-ACCTTGTTACGACTTCTC-3'. The qPCR reactions were run with three technical replicates in a Bio-Rad C1000-CFX96 Real-Time PCR system, using the Bio-Rad iQ SYBR Green Supermix kit (Bio-Rad).

Fluorescence *in situ* hybridization. Prior to FISH, calcium carbonate-containing formaldehyde-fixed samples were treated with 0.1 M HCl for 3 min. After the calcium carbonate dissolved, the cells were centrifuged (3 min, 10,000g) and the supernatant discarded. The pellet was resuspended in 50 µl EtOH and PBS (50:50) and the cell suspension was spotted on slides. The FISH procedure was performed according to the standard protocol with 16S rRNA-targeted probes Ntspa712 (specific for the phylum *Nitrospira*²⁶) and Nso1225 (specific for β -proteobacterial ammonia-oxidizing bacteria³⁶). Images were acquired with a Leica SP8 confocal laser scanning microscope (Leica).

Total protein quantification. Protein concentrations were measured using the Pierce BCA protein assay kit (Thermo Scientific).

Replication of physiological experiments. The number of replications are detailed in the subsections for each specific experiment, and were mostly determined by the amount of biomass available for the different nitrifier cultures. In all experiments, a minimum of three biological replications were used, with the exception of one auxiliary experiment: decelerating effect of increasing cyanate concentrations on nitrite oxidation by *N. moscoviensis* (Extended Data Fig. 6). No statistical methods were used to predetermine sample size.

Proteomic analysis. Concentrated *N. gargensis* biomass was inoculated in 140 ml modified AOA medium (amended with 1 mM ammonium final concentration, no cyanate) in three replicates. After a pre-incubation for 24 h, 40-ml samples were taken for proteomic analysis (time point 1) and the remaining cultures were amended with 0.5 mM KOCN and 0.1 mM NH₄Cl (final concentrations) and further incubated. Cultures were regularly fed afterwards with 0.5 mM KOCN (final concentration), keeping the concentration between 0.1 mM and 0.6 mM based on residual KOCN levels calculated from the produced nitrite levels, measured every 12 h. Forty-eight hours after switching to cyanate feeding, 40-ml samples were taken again for proteomic analyses. Cells in the samples from the two different time points were harvested by centrifugation (9,000g, 30 min, 4 °C) and stored at -80 °C.

The harvested cell pellets were dissolved in 500 µl urea:thiourea buffer (8 M urea; 2 M thiourea) and sonicated, using a UP50H homogenizer (Hielscher Ultrasonic Technology), twice on ice for 1 min (amplitude 0.7; power 70%). The samples were then ultracentrifuged (100,000g, 1 h, 4 °C), and the supernatant was transferred into a fresh reaction tube. Pellets were dissolved in 200 µl preparation buffer (100 mM tris-HCl; pH 7.5; 300 mM NaCl; 1% digitonin) and incubated overnight at 16 °C with 1,200 rpm shaking. After centrifugation (12,000g, 10 min, 4 °C), the supernatant was combined with the supernatant of the previous preparation step. This combined lysate was precipitated with acetone (5× volume, ice-cold) by incubation for 1 h at -20 °C, centrifuged (12,000g, 15 min), and the protein pellet was air-dried. Protein concentrations of all extracts were determined photometrically using a Bradford assay (Bio-Rad Laboratories). SDS-PAGE preparation, reduction, alkylation, and proteolytic digestion by trypsin with subsequent C18-purification were performed as described previously³⁷. Mass spectrometry was performed by a Orbitrap Fusion mass spectrometer (Thermo Fisher Scientific) coupled to a TriVersa NanoMate (Advion, Ltd). Five microlitres of the peptide lysates were separated with a Dionex Ultimate 3000 nano-LC system (Dionex/Thermo Fisher Scientific).

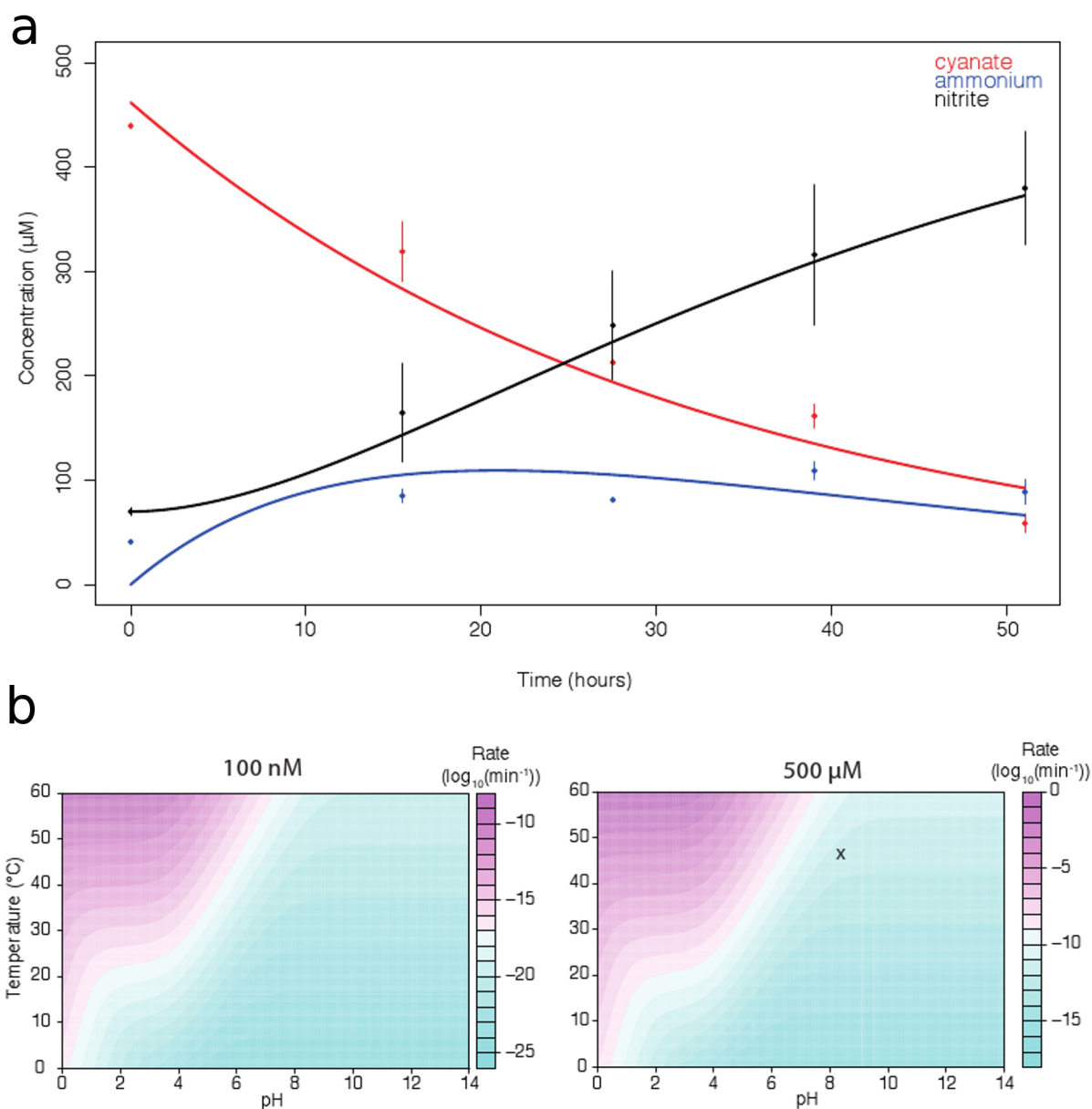
Mass spectrometry (MS) raw files were processed using Proteome Discoverer (version 1.4, Thermo Scientific). MS spectra were searched against a *N. gargensis* database (Uniprot/Swiss-Prot, containing 3,786 unreviewed sequence entries) and a common Repository of Adventitious Proteins (cRAP) database using the Sequest HT algorithm. Enzyme specificity was selected as trypsin with up to two missed cleavages allowed using 10 ppm peptide ion tolerance and 0.1 Da MS/MS tolerances. Oxidation (methionine) and carbamylation (lysine and arginine) were selected as variable modifications, and carbamidomethylation (cysteine) as a static modification. Only peptides with a false discovery rate (FDR) greater than 1% calculated by Percolator³⁸ and a peptide rank equal to 1 were considered as identified.

Modelling biotic and abiotic cyanate degradation kinetics. For cyanate utilization experiments with *N. gargensis*, the chemical reaction kinetics for the species cyanate, ammonia, and nitrite were modelled as two consecutive first-order reactions. Reaction rates were then estimated using ordinary least squares optimization for a system of nonlinear equations³⁹, as implemented by the nlsystemfit algorithm in the package systemfit⁴⁰ in R⁴¹. For calculation of the abiotic degradation of cyanate and isocyanic acid (formed by cyanate in aqueous solution) as a function of temperature and pH, established reactions and values from the literature were used. Degradation was modelled as three first-order reactions: (1) hydronium-ion-catalysed hydrolysis of isocyanic acid; (2) direct hydrolysis of isocyanic acid; and (3) direct hydrolysis of

cyanate, as described previously⁴². Published values were used for rate constants and their temperature dependence⁴². A value of 3.7 was used for the acid dissociation constant for isocyanic acid (reported to range from 3.29 to 3.92), which has no detectable temperature dependence in the range of 0 °C to 80 °C⁴³.

Phylogenetics of cyanase genes in published metagenomes. Amino acid sequences for all members of the newly discovered 'Cyanase Family' (2,425 entries) were downloaded from UniProt⁴⁴ and all predicted amino acid sequences annotated as cyanase, cyanate hydratase or cyanate lyase were downloaded from the Joint Genome Institute IMG Expert Review (IMG/ER) (3,028 sequences) and IMG with Microbiome Samples Expert Review (IMG/MER) (5,476 sequences) databases²⁵ on 8 August 2014. Cyanase sequences from IMG were filtered according to inferred distance (<1.25 replacements per position) and bit scores (>56) from UniProt references using alignment/distance calculation in Mafft⁴⁵ and blastp⁴⁶ (word_size 2, BLOSUM45), respectively. In addition, the predicted amino acid sequence of the *N. gargensis* cyanase was used as a query in a tblastn search against publicly available metagenomes of the IMG/M database. Hits were filtered by *E*-value (*E*-values <10⁻¹⁰), at least 50% length coverage of the query sequence, and assignment to the cyanase superfamily (*E*-value <10⁻¹⁰) of the Conserved Domain Database (CDD)⁴⁷. All putative cyanase sequences were filtered for length (100 residues) and clustered at 99% identity using USEARCH²⁹. The resulting 3,340 cyanase sequences were aligned in Mafft to produce a distance matrix and clustered into 100 sequence clusters using the hclust(method = "complete") and cutree(k = 100) commands in R⁴¹. Clusters were examined manually and three singleton sequences that aligned poorly were discarded. Cyanase from *N. gargensis* and *N. moscoviensis* were added into the data set. Alignment and phylogeny for the set of 99 representative cyanase genes was calculated using BALI-Phy²⁸ with an initial alignment randomization and the number of iterations in each run set to 1,100 with a burnin of 600. Posterior tree pools from three independent runs were combined to assess bipartition support. The 225 environmental cyanase sequences identified in a *Nitrososphaera*/*Nitrospira* clade were clustered into 61 representative sequences using USEARCH at 99% minimum identity. Alignment and phylogenetic reconstruction for these representative sequences and ten broadly sampled outgroup cyanases was carried out in BALI-Phy (randomize alignment, iterations set to 1,100, burnin of 600). Posterior tree pools from four independent runs were combined to generate an 80% posterior probability (PP) consensus tree to assess bipartition support.

30. Lebedeva, E. V. *et al.* Enrichment and genome sequence of the group I.1a ammonia-oxidizing Archaeon "Ca. Nitrosotenuis uzonensis" representing a clade globally distributed in thermal habitats. *PLoS ONE* **8**, e80835 (2013).
31. Widdel, F. Anaerobier Abbau von Fettsäuren und Benzoesäure durch neu isolierte Arten Sulfat-reduzierender Bakterien. *Dissertation, Universität Göttingen* (1980).
32. Ehrich, S., Behrens, D., Lebedeva, E., Ludwig, W. & Bock, E. A new obligately chemolithoautotrophic, nitrite-oxidizing bacterium, *Nitrospira moscoviensis* sp. nov. and its phylogenetic relationship. *Arch. Microbiol.* **164**, 16–23 (1995).
33. Strickland, J. D. H. & Parsons, T. R. *A Practical Handbook of Seawater Analysis*. (Fisheries Research Board of Canada, 1972).
34. Kandeler, E. & Gerber, H. Short-term assay of soil urease activity using colorimetric determination of ammonium. *Biol. Fertil. Soils* **6**, 68–72 (1988).
35. Guilloton, M. & Karst, F. A spectrophotometric determination of cyanate using reaction with 2-aminobenzoic acid. *Anal. Biochem.* **149**, 291–295 (1985).
36. Mobarry, B. K., Wagner, M., Urbain, V., Rittmann, B. E. & Stahl, D. A. Phylogenetic probes for analyzing abundance and spatial organization of nitrifying bacteria. *Appl. Environ. Microbiol.* **62**, 2156–2162 (1996).
37. Schiffmann, C. L. *et al.* Proteome profile and proteogenomics of the organohalide-respiring bacterium *Dehalococcoides mccartyi* strain CBDB1 grown on hexachlorobenzene as electron acceptor. *J. Proteomics* **98**, 59–64 (2014).
38. Käll, L., Canterbury, J. D., Weston, J., Noble, W. S. & MacCoss, M. J. Semi-supervised learning for peptide identification from shotgun proteomics datasets. *Nature Methods* **4**, 923–925 (2007).
39. Gallant, R. *Nonlinear Equation Estimation* 610 (John Wiley and Sons, 1987).
40. Henningsen, A. & Hamann, J. D. systemfit: A package for estimating systems of simultaneous equations in R. *J. Stat. Softw.* **23**, 1–40 (2007).
41. Team, R. D. C. R. A language and environment for statistical computing. *Proc. Natl Acad. Sci. USA* <http://www.R-project.org/> (2011).
42. DeMartini, N., Murzin, D. Y., Forssen, M. & Hupa, M. Kinetics of cyanate decomposition in alkaline solutions of high ionic strength: The catalytic effect of bicarbonate. *Ind. Eng. Chem. Res.* **43**, 4815–4821 (2004).
43. Taillades, J. *et al.* A pH-dependent cyanate reactivity model: application to preparative N-carbamoylation of amino acids. *J. Chem. Soc. Perkin. T.* **2**, 1247–1254 (2001).
44. UniProt Consortium. Activities at the Universal Protein Resource (UniProt). *Nucleic Acids Res.* **42**, D191–D198 (2014).
45. Katoh, K. & Standley, D. M. MAFFT multiple sequence alignment software version 7: improvements in performance and usability. *Mol. Biol. Evol.* **30**, 772–780 (2013).
46. Altschul, S. F., Gish, W., Miller, W., Myers, E. W. & Lipman, D. J. Basic Local Alignment Search Tool. *J. Mol. Biol.* **215**, 403–410 (1990).
47. Marchler-Bauer, A. *et al.* CDD: conserved domains and protein three-dimensional structure. *Nucleic Acids Res.* **41**, D348–D352 (2013).

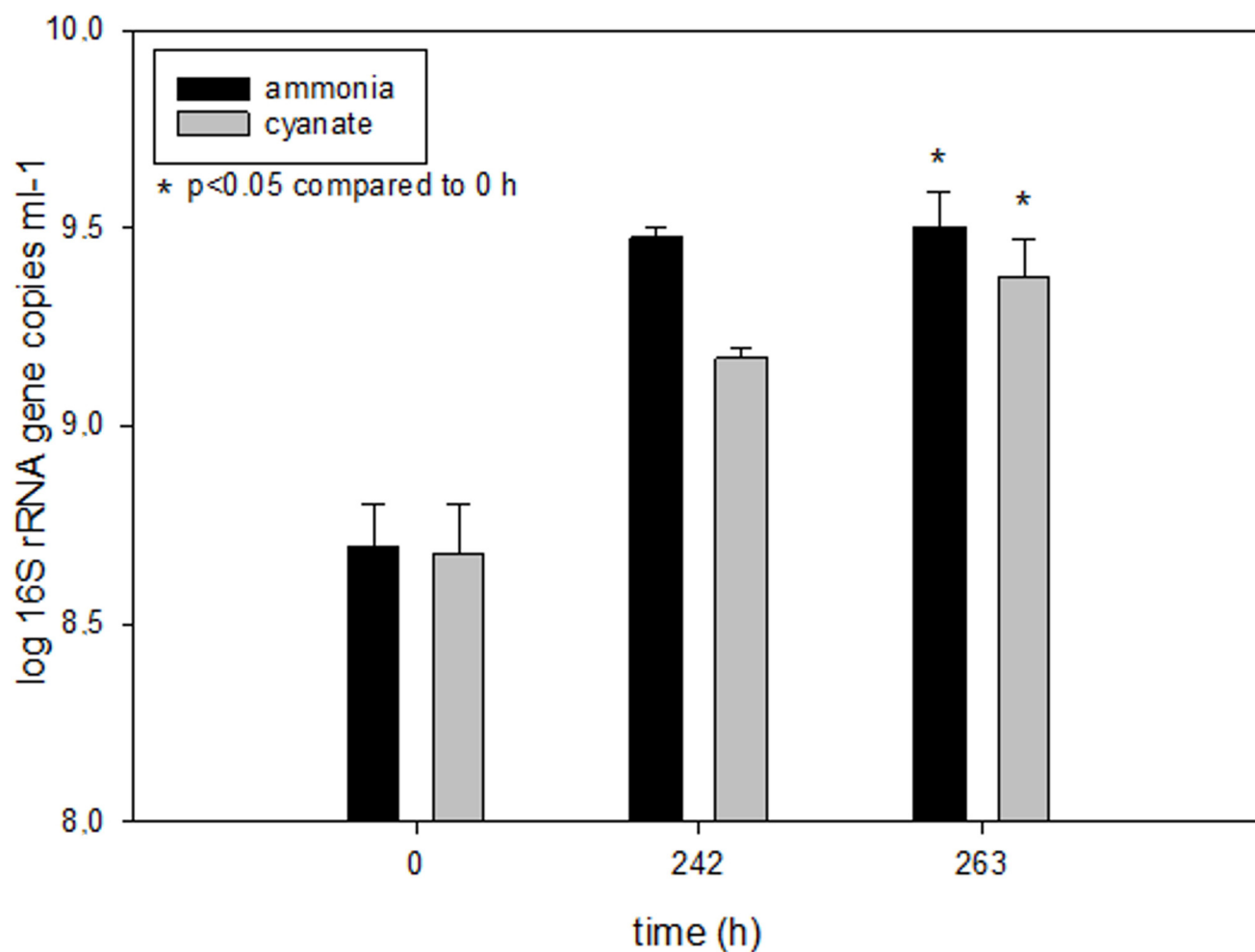


Extended Data Figure 1 | Biotic and abiotic cyanate degradation kinetics.

a, Degradation of 500 μM cyanate and utilization of ammonium by *N. gargensis* modelled as two consecutive first order reactions (cyanate–ammonium–nitrite). Measured data are shown as dots and error bars (mean \pm s.e.m.) and model predictions with estimated rate parameters are shown as solid lines. Estimated rate constants were $k_{\text{cyanate–ammonium}} = 4.872 \times 10^{-4} \text{ min}^{-1}$ and $k_{\text{ammonium–nitrite}} = 1.064 \times 10^{-3} \text{ min}^{-1}$. The abiotic hydrolysis of 500 μM cyanate in this medium was measured to be much slower than enzymatic degradation ($k_{\text{cyanate–hydrolysis}} = 8.71 \times 10^{-5} \text{ min}^{-1}$). **b**, The abiotic

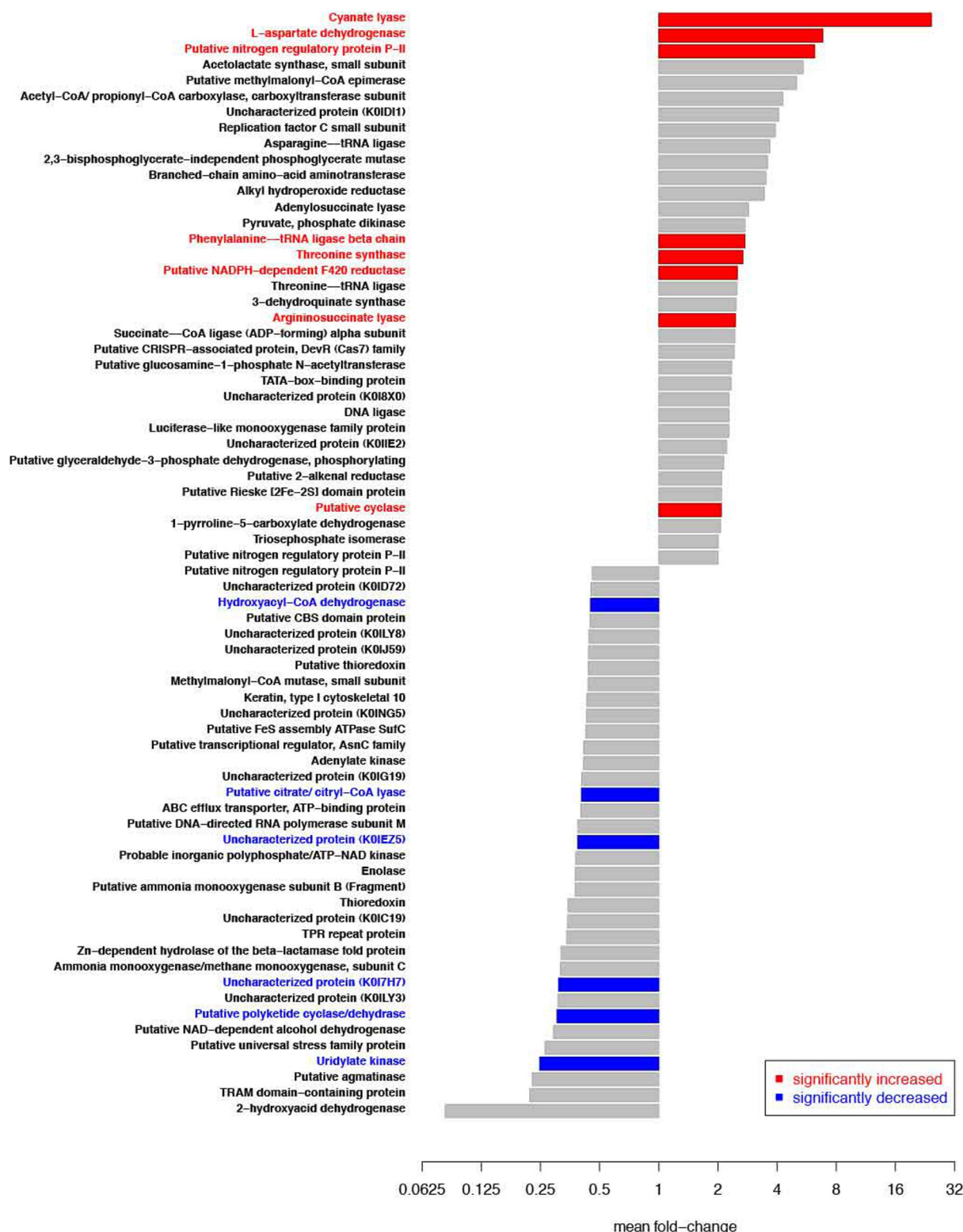
degradation of low (100 nM; left) and high (500 μM ; right) concentrations of isocyanic acid/cyanate across a range of temperatures and pH.

Degradation was modelled using a well-established model of three first-order reactions: (1) hydronium-ion-catalysed hydrolysis of isocyanic acid ($k_1 = e^{25.97} \times e^{-7201.29/T}$); (2) direct hydrolysis of isocyanic acid ($k_2 = e^{72.30} \times e^{-21646.66/T}$); and (3) direct hydrolysis of cyanate⁴² ($k_3 = e^{22.23} \times e^{-8725/T}$). The log-transformed degradation rates are shown (as min^{-1}). The conditions that were used to test cyanate degradation by *N. gargensis* are marked with a cross.



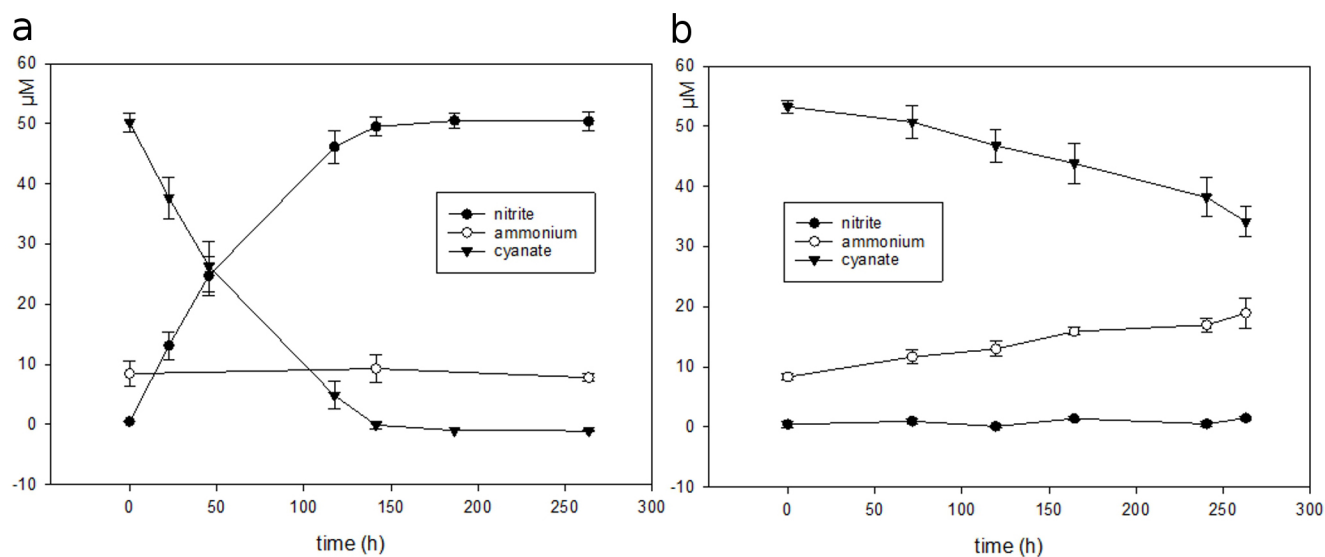
Extended Data Figure 2 | *Nitrososphaera gargensis* grows on cyanate. 16S rRNA gene copy numbers of *N. gargensis* as determined by qPCR at three different time points during the experiment shown in Fig. 1. For comparison, the respective gene copy numbers after growth in medium with 0.5 mM

ammonium are displayed. The gene copy numbers increased 6.49-fold during growth on ammonium and 4.98-fold during growth on cyanate over 263 h. Columns show means, error bars show s.d. of four biological replicates. Significance was calculated by a paired *t*-test.



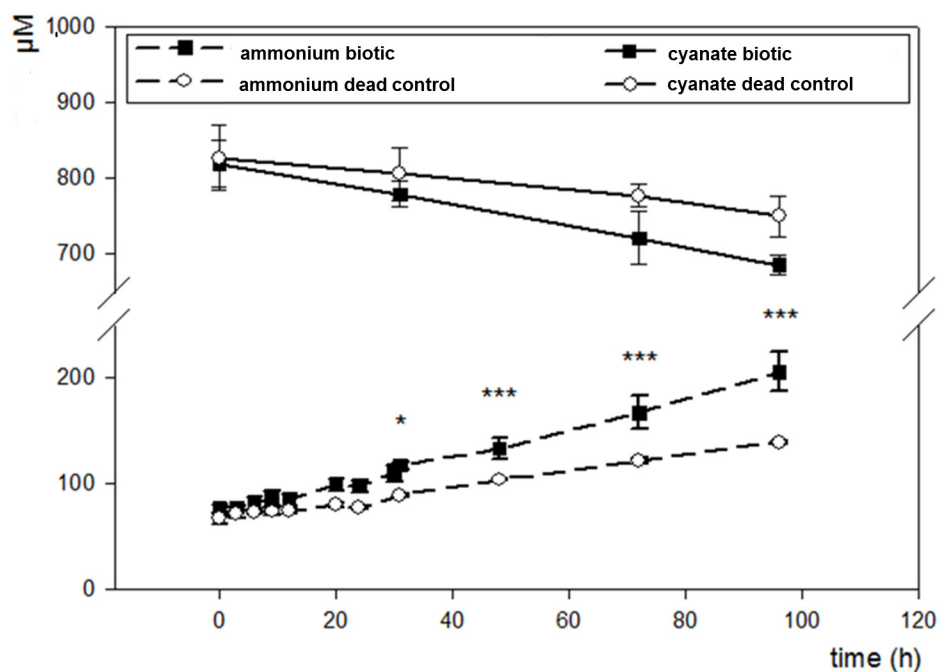
Extended Data Figure 3 | Cyanase increase upon exposure of *N. gargensis* to cyanate. Fold-increase and -decrease of the 35 most affected proteins after 48 h exposure of *N. gargensis* to 0.5 mM cyanate (in comparison to $t = 0$ of *N. gargensis* biomass that had not been exposed to cyanate). Experiments were performed in three biological replicates. Proteins with a significant difference in expression are colour coded. Significance of difference was calculated by a one-sample t -test on log-fold induction, with the Benjamini-Hochberg false

discovery rate set to 0.05 (P value cutoff 0.00878). For the proteomic analyses, 10 μ g protein and 500 ng peptide lysate per sample was used. Protein abundances within a sample were normalized by dividing the peak area for a given protein by the median peak area for all detected proteins. Note that during growth on cyanate, *N. gargensis* experiences much lower concentrations of ammonium than during growth on ammonium in batch culture, which probably influences the expression patterns of some of the listed proteins.



Extended Data Figure 4 | Conversion of 0.05 mM cyanate by *N. gargensis*.
a, Concentration changes of cyanate, ammonium, and nitrite caused by *N. gargensis* in a mineral medium containing 0.05 mM cyanate as the only source of energy and reductant. **b**, Abiotic control experiment. All experiments

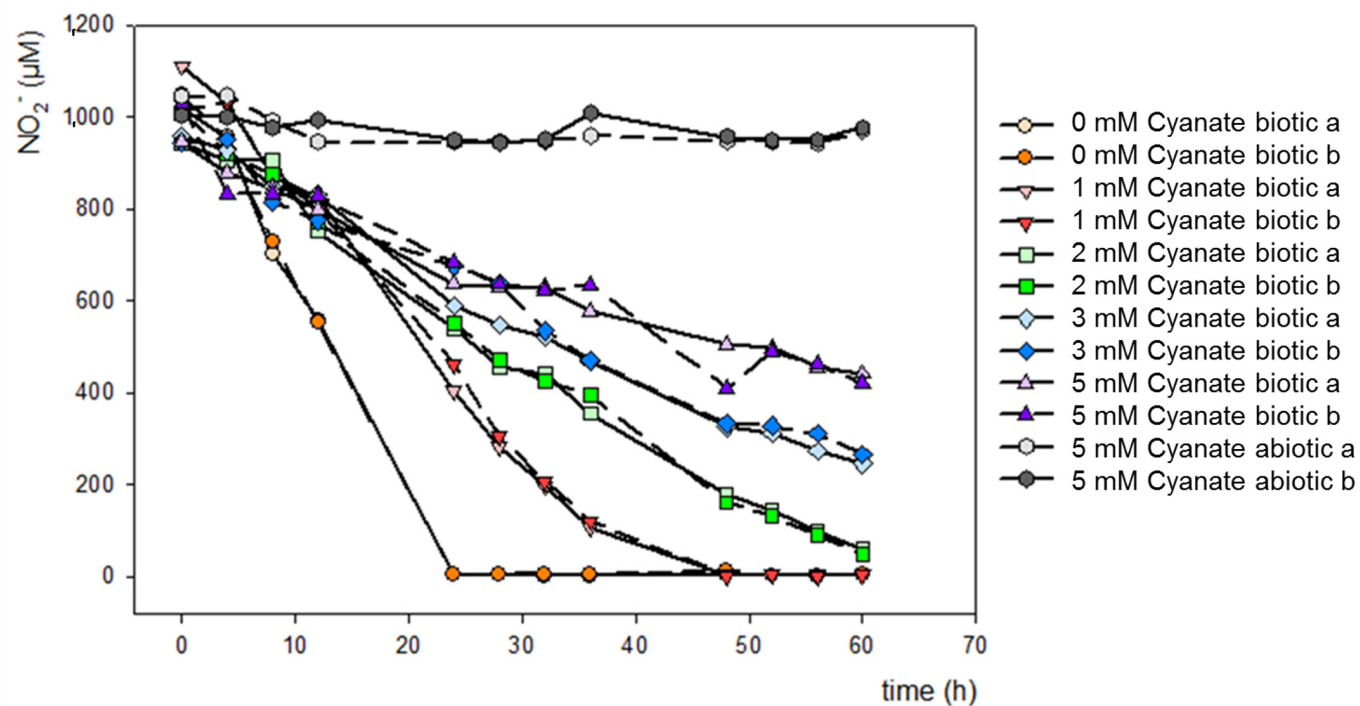
were performed in four biological replicates and the chemical measurements were done in three technical replicates (averaged). Data points are mean values of four biological replicates, error bars show s.d.



Extended Data Figure 5 | *Nitrospira moscoviensis* has a functional cyanase.

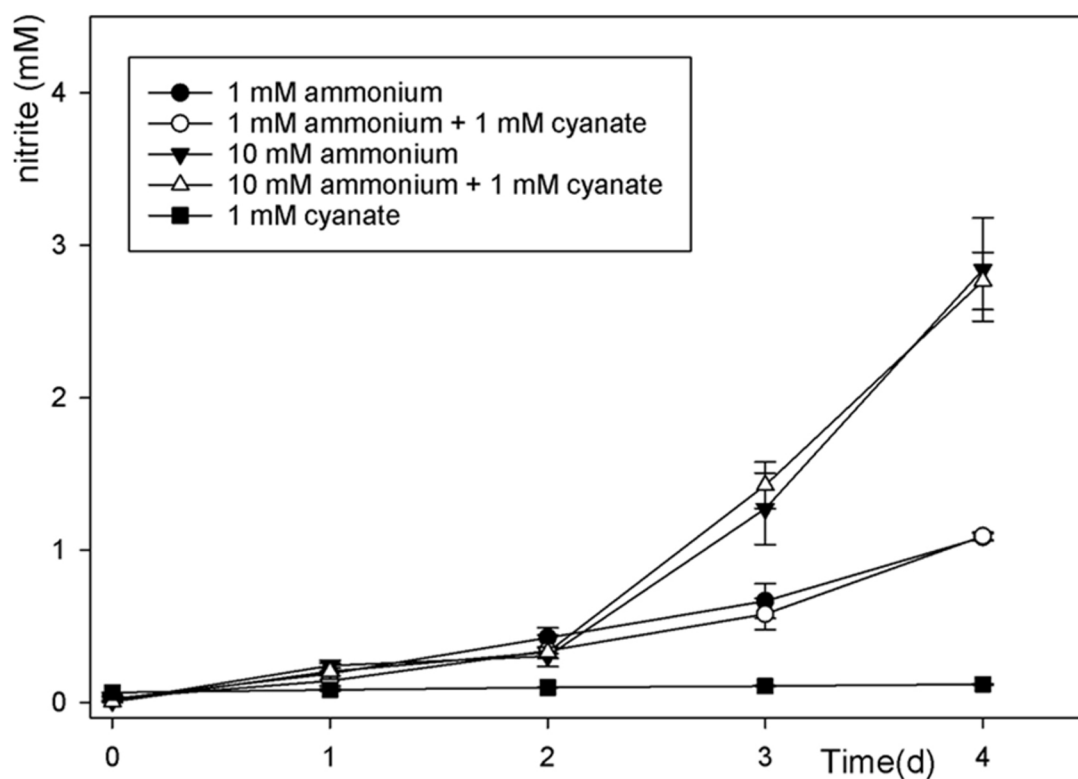
Concentration changes of cyanate and ammonium during incubation of *N. moscoviensis* ($27.6 \pm 3.9 \mu\text{g ml}^{-1}$ protein) in a mineral medium containing cyanate, but no nitrite. Results from a control experiment with identical amounts of dead biomass of *N. moscoviensis* are also displayed. All experiments were performed in triplicate and the chemical measurements from each

replicate were done in three replicates. Data points are mean values, error bars show s.d. Asterisks indicate statistical significance between *N. moscoviensis* and dead biomass, * $P < 0.05$, *** $P < 0.001$. Significance was assessed by two-way analysis of variance (ANOVA) including Tukey's honest significant difference (HSD) test.



Extended Data Figure 6 | Decelerating effect of increased cyanate concentrations on nitrite oxidation by *N. moscoviensis*. Biomass was incubated for 60 h in medium containing 1 mM nitrite and cyanate

concentrations ranging from 0 mM to 5 mM, and nitrite oxidation was monitored. Incubations were performed in duplicates.



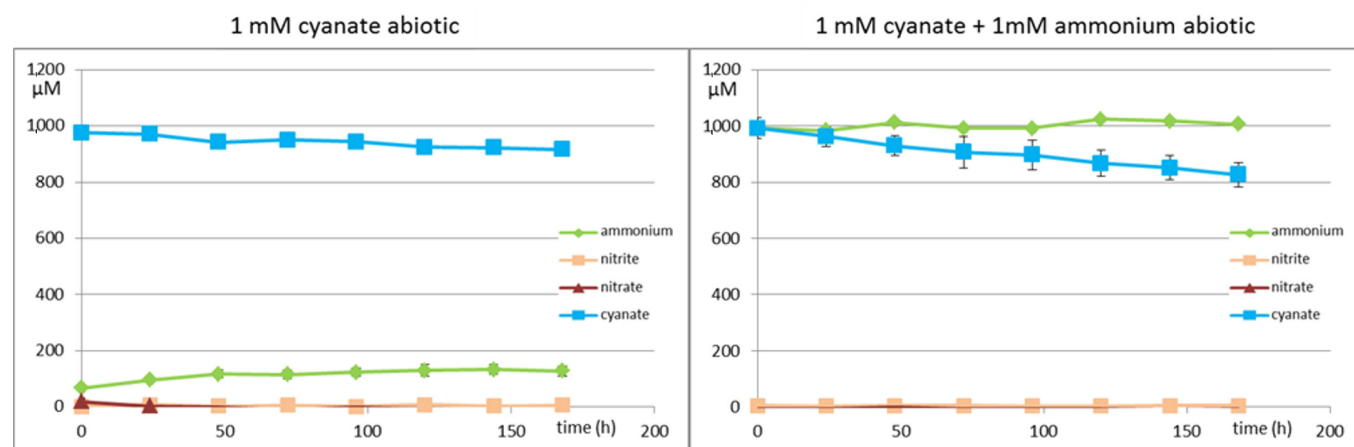
Extended Data Figure 7 | *Nitrosomonas nitrosa* Nm90 has no cyanase activity and is not inhibited by 1 mM cyanate. Concentration of nitrite during incubation of *N. nitrosa* in a mineral medium containing: 1 mM ammonium (filled circles); 1 mM cyanate (filled squares); 1 mM cyanate and 1 mM

ammonium (open circles); 10 mM ammonium (filled triangles); and 1 mM cyanate and 10 mM ammonium (open triangles). All experiments were performed in three biological replicates, data points are mean values, error bars show s.d.

Extended Data Figure 8 | Reciprocal feeding of ammonia and nitrite

oxidizers during cyanate conversion. As activities differed between biological replicates (as often observed for nitrifying strains that are very sensitive to rubber stoppers, contaminants on glass material, etc.), data are displayed for each replicate individually. Concentrations of cyanate, ammonium, nitrite, and nitrate are displayed as bar (left) and line charts (right) during the growth of

the cyanase-negative ammonium-oxidizing bacterium *Nitrosomonas nitrosa* Nm90 and the cyanase-positive nitrite oxidizer *N. moscoviensis* in a mineral medium containing 1 mM cyanate (**a–c**) or 1 mM cyanate and 1 mM ammonium (**d–f**). Data points are mean values, error bars show s.d. of three technical replicates.



Extended Data Figure 9 | Abiotic controls for the reciprocal-feeding experiment. See also Fig. 2 and Extended Data Fig. 8. Concentration changes of cyanate, ammonium, nitrite, and nitrate during 168 h of incubation under similar conditions to the biotic experiments: mineral medium containing 1 mM cyanate (left) or 1 mM cyanate and 1 mM ammonium (right). The rate of

cyanate decay is much slower than in biotic setups (see Extended Data Fig. 8). Cyanate decay in the presence of ammonium led to formation of a product other than ammonium (possibly carbamylate). No nitrite or nitrate was formed abiotically. Data points are mean values, error bars show s.d. of three technical replicates.

Extended Data Table 1 | Presence of cyanase, nitrite/nitrate transporters and enzymes related to urea metabolism in ammonia- and nitrite-oxidizing microorganisms with fully a sequenced genome.

Organism	Cyanase	Nitrite/nitrate transporter			Urea metabolism		
		FNT family *	NNP Family †	ABC transporter ‡	Urea transporter §	Urea production	Urea degradation ¶
Ammonia oxidizing archaea							
<i>Nitrososphaera gargensis</i>	+	+	-	+	+	+	+
<i>Nitrososphaera viennensis</i> EN76	-	-	-	+	+	+	+
<i>Ca. Nitrososphaera evergladensis</i> SR1	-	-	-	+	+	+	+
<i>Nitrosopumilus maritimus</i> SCM1	-	-	-	+	-	+	-
<i>Nitrosopumilus</i> sp. AR	-	-	-	+	+	+	+
<i>Nitrosopumilus</i> sp. SJ	-	-	-	+	-	+	-
<i>Ca. Nitrosopumilus koreensis</i> AR1	-	-	-	+	-	+	-
<i>Ca. Nitrosopumilus salaria</i> BD31	-	-	-	+	-	+	-
<i>Ca. Nitrosopumilus</i> sp. AR2	-	-	-	-	+	+	+
<i>Ca. Nitrosoarchaeum koreensis</i> MY1	-	-	-	+	-	+	-
<i>Ca. Nitrosoarchaeum limnia</i> BG20	-	-	-	+	-	+	-
<i>Ca. Nitrosoarchaeum limnia</i> SFB1	-	-	-	+	-	+	-
<i>Ca. Nitrosotenuis uzonensis</i> N4	-	-	-	+	-	+	-
<i>Cenarchaeum symbiosum</i> A	-	-	-	+	+	+	+
Ammonia oxidizing bacteria							
<i>Nitrosococcus halophilus</i> Nc4	-	+	-	-	-	-	-
<i>Nitrosococcus oceani</i> AFC27	-	+	-	-	+	+	+
<i>Nitrosococcus oceani</i> ATCC 19707	-	+	-	-	+	+	+
<i>Nitrosococcus watsonii</i> C-113	-	+	-	-	+	+	+
<i>Nitrosomonas europaea</i> ATCC 19718	-	+	-	+	+	+	-
<i>Nitrosomonas eutropha</i> C91	-	+	-	+	-	+	-
<i>Nitrosomonas</i> sp. AL212	-	+	-	-	+	+	+
<i>Nitrosomonas</i> sp. ls79A3	-	+	-	-	-	+	+
<i>Nitrospira multiformis</i> ATCC 25196	-	+	-	-	+	-	+
Nitrite oxidizing bacteria							
<i>Nitrospira moscoviensis</i>	+	+	+	+	+	+	+
<i>Ca. Nitrospira defluvii</i>	+	+	+	-	-	+	-
<i>Nitrobacter</i> sp. Nb-311A	+	+	+	+	-	+	-
<i>Nitrobacter winogradskyi</i> Nb-255	+	+	+	+	-	+	-
<i>Nitrobacter hamburgensis</i> X14	+	+	+	+	-	+	-
<i>Nitrococcus mobilis</i> Nb-231	+	+	+	-	-	+	-
<i>Nitrolancea hollandica</i>	+	+	+	-	+	+	-
<i>Nitrospina gracilis</i>	+	+	-	-	-	+	-

*Formate-nitrite transporter family: encoded by *focA/nirC*, has been postulated to transport cyanate¹⁸.

†Nitrate/nitrite transporter family: encoded by *nark*, might also transport cyanate due to its chemical similarity to nitrite.

‡ABC transporter of nitrate/sulfonate/bicarbonate: this transporter family has been shown to transport cyanate as well²⁰.

§Urea transporter: ABC transporter, or urea channel.

||Urea produced internally by the enzymes agmatine amidinohydrolase or arginine amidinohydrolase.

¶Urea consumed internally by the enzymes urease or urea carboxylase and allophanate hydrolase.

A hemi-fission intermediate links two mechanistically distinct stages of membrane fission

Juha-Pekka Mattila^{1*}, Anna V. Shnyrova^{2*}, Anna C. Sundborger³, Eva Rodriguez Hortelano², Marc Fuhrmans⁴, Sylvia Neumann⁵, Marcus Müller⁴, Jenny E. Hinshaw³, Sandra L. Schmid¹ & Vadim A. Frolov^{2,6}

Fusion and fission drive all vesicular transport. Although topologically opposite, these reactions pass through the same hemi-fusion/fission intermediate^{1,2}, characterized by a 'stalk' in which only the outer membrane monolayers of the two compartments have merged to form a localized non-bilayer connection¹⁻³. Formation of the hemi-fission intermediate requires energy input from proteins catalysing membrane remodelling; however, the relationship between protein conformational rearrangements and hemi-fusion/fission remains obscure. Here we analysed how the GTPase cycle of human dynamin 1, the prototypical membrane fission catalyst⁴⁻⁶, is directly coupled to membrane remodelling. We used intramolecular chemical crosslinking to stabilize dynamin in its GDP·AlF₄⁻-bound transition state. In the absence of GTP this conformer produced stable hemi-fission, but failed to progress to complete fission, even in the presence of GTP. Further analysis revealed that the pleckstrin homology domain (PHD) locked in its membrane-inserted state facilitated hemi-fission. A second mode of dynamin activity, fuelled by GTP hydrolysis, couples dynamin disassembly with cooperative diminishing of the PHD wedging, thus destabilizing the hemi-fission intermediate to complete fission. Molecular simulations corroborate the bimodal character of dynamin action and indicate radial and axial forces as dominant, although not independent, drivers of hemi-fission and fission transformations, respectively. Mirrored in the fusion reaction^{7,8}, the force bimodality might constitute a general paradigm for leakage-free membrane remodelling.

Membrane fission and fusion both involve a pivotal stage, in which lipids rapidly rearrange into a new topology under extreme protein-driven stress^{2,3}. It is generally accepted that lipid rearrangements proceed in distinct steps, involving the formation of transient highly curved non-bilayer intermediate(s)^{9,10}. How conformational changes of the protein machinery orchestrate this orderly remodelling of lipids remains unknown. This knowledge gap is highlighted in dynamin, the founding member of a superfamily of large GTPases implicated in membrane fission and fusion events⁴⁻⁶. Self-assembly of dynamin into helical structures around the necks of deeply invaginated clathrin-coated pits and the consequent stimulated GTPase activity drive conformational changes that underpin its role in catalysing membrane fission and the release of clathrin-coated vesicles^{4,6}. Crystallographic studies have provided multiple insights into the nature of these GTPase-driven conformational changes. The amino- and carboxy-terminal helices of dynamin's GTPase (G) domain, together with the C-terminal helix from the GTPase effector domain (GED), form a three-helix bundle, termed the 'bundle signalling element' (BSE) (Extended Data Fig. 1a). Crystal structures of a minimal G domain-BSE dynamin construct bound to either GMPPCP or the nucleotide transition-state analogue GDP·AlF₄⁻ revealed two distinct conformations corresponding to a ~70° swing of the BSE relative to the

G domain core (Fig. 1a, inset)^{11,12}. Thus, akin to a lever arm in motor proteins¹³, it was proposed that BSE movements transmit and amplify transition-state-dependent conformational changes in the G domain to affect intra- and/or intermolecular conformational changes required for fission¹². Observed only in the context of a minimal dynamin construct^{11,12}, whether the dramatic nucleotide-dependent movement of the BSE occurs in the full-length protein and how it is transmitted to the membrane-interacting PHD and further on to lipids are unknown.

To gain insight into the functional consequences of this nucleotide-dependent conformational change, we used molecular engineering to access and control BSE motility in full-length wild-type dynamin 1 (WT-Dyn1). To this end, we introduced Cys at position 11 into a functional reactive-Cys-less (RCL) derivative of WT-Dyn1 (ref. 14) for site-specific labelling with a thiol-reactive BODIPY derivative and replaced Tyr at position 125 with Trp to yield CW-Dyn1 (Fig. 1a, inset). This mutant and its BODIPY conjugate retained near normal basal and assembly-stimulated GTPase activities (Extended Data Fig. 1b, c). To detect BSE movements we used photo-induced electron transfer (PET)¹⁵, which results in the quenching of the BODIPY label in the BSE (Fig. 1a) by the Trp residue in the G domain only if the two moieties reside within a radius of 10 Å (Fig. 1a, inset)¹⁶. When bound to lipid nanotubes (Fig. 1b), the magnitude of PET-induced quenching of BODIPY varies in a nucleotide-dependent manner, becoming progressively higher along the transition from the GTP-bound state (stabilized by GMPPCP) to the GDP·PI transition state (stabilized by GDP·AlF₄⁻). This behaviour is consistent with the GTP-dependent BSE movement predicted by structural analyses (Fig. 1a)^{11,12}, which further suggest that the BSE pivots around a Pro residue (P294) connecting the C-terminal helix of the G domain to the core^{12,17,18}. Consistent with this, mutation of P294 reduces BSE motility and impairs both the GTPase and fission activities of dynamin (Extended Data Fig. 2). Together, these data confirm that the BSE in full-length dynamin undergoes GTP-dependent conformational changes consistent with a rotation around P294 away from the G domain core.

We next applied site-specific crosslinking between the G domain and the BSE to stabilize the 'transition-state' conformer. Trp 125 in CW-Dyn1 was replaced with Cys to produce CC-Dyn1. Using a series of variable-length thiol-specific homo-bifunctional methanethiosulfonate (MTS) reagents, we identified MTS-4-MTS, which has a theoretical crosslinking span of 7.8 Å, as the shortest reagent able to yield ~100% crosslinking efficiency of CC-Dyn1, as evidenced by a gel shift to a faster migrating species (Fig. 1c). This is in good agreement with the distance separating the two Cys residues in the transition state (Fig. 1a). Hereafter, we refer to the crosslinked species as CxC-Dyn1.

In solution, CxC-Dyn1 exhibited enhanced GTPase activity and self-assembled into rings, similar to GDP·AlF₄⁻-bound WT-Dyn1 (Extended Data Fig. 3a, b), verifying that crosslinking stabilizes the

¹Department of Cell Biology, UT Southwestern Medical Center, Dallas, Texas 75201, USA. ²Biophysics Unit (CSIC, UPV/EHU) and Department of Biochemistry and Molecular Biology, University of The Basque Country, 48940 Leioa, Spain. ³Laboratory of Cell and Molecular Biology, National Institute of Diabetes and Digestive and Kidney Diseases, NIH, Bethesda, Maryland 20892, USA. ⁴Institute for Theoretical Physics, Georg-August University, 37077 Göttingen, Germany. ⁵Department of Cell Biology, The Scripps Research Institute, La Jolla, California 92037, USA. ⁶IKERBASQUE, Basque Foundation of Science, 48011 Bilbao, Spain.

*These authors contributed equally to this work.

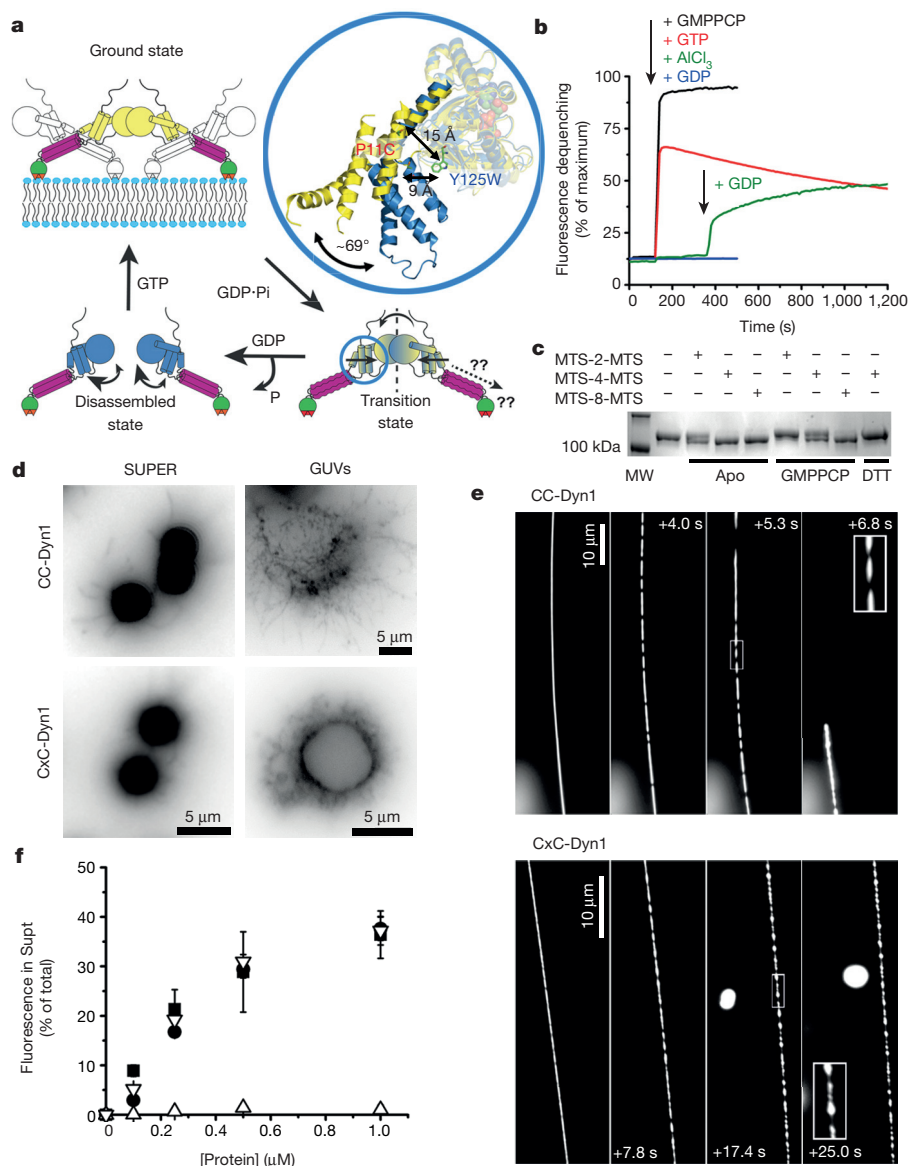


Figure 1 | Stabilization of the transition-state conformer of dynamin.

a, Cartoon illustrating the mobility of BSE during dynamin's GTPase cycle. Blue, apo (no nucleotide)/GDP-bound; yellow, GMPPCP-bound; yellow/blue, GDP·AlF₄⁻-bound transition-state. Inset shows BSE conformation in the crystal structures of GMPPCP-bound (yellow; Protein Data Bank (PDB) accession 3ZYC) and GDP·AlF₄⁻-bound (blue; PDB accession 2X2E) G-domain–BSE fusion protein. **b**, Loss of PET-dependent quenching of BODIPY fluorescence after addition of GMPPCP, GTP, or GDP either alone or in the presence of AlCl₃ and NaF (that is, GDP·AlF₄⁻). The decline in fluorescence signal in the presence of GTP reflects its hydrolysis. **c**, SDS–polyacrylamide gel electrophoresis (SDS–PAGE) of CC-Dyn1 ± crosslinker. The faster migrating CxC-Dyn1 is stabilized in the transition state. MW,

BSE at or near its transition-state conformation. CxC-Dyn1 retains the ability of WT-Dyn1 to produce high membrane curvature from flat lipid templates (Fig. 1d and Extended Data Fig. 4). Furthermore, like CC-Dyn1 (and WT-Dyn1)¹⁹, CxC-Dyn1 rapidly assembles on and constricts tubular membrane templates (Fig. 1e). However, unlike CC-Dyn1, CxC-Dyn1 failed to produce membrane fission either in the presence (Fig. 1e, f and Supplementary Videos 1 and 2) or absence (Fig. 1d and data not shown) of GTP. Reversal of the crosslink with dithiothreitol (DTT) led to full recovery of fission activity (Fig. 1f), indicating that inhibition was due to disruption of dynamin's conformational changes and not to chemical modification of the cysteine residues.

molecular weight. **d**, Representative images showing membrane tubulation of SUPER templates (≥5 independent experiments) or GUVs (3 independent experiments) by CC- and CxC-Dyn1 in the absence of nucleotides. Images are inverted for clarity. **e**, Constriction (seen as dark patches) and fission activity of CC- and CxC-Dyn1 on fluorescently labelled membrane tethers incubated in the presence of 1 mM GTP (see Supplementary Videos 1 and 2; representative data from 3 independent experiments). **f**, Fission activity assessed by vesicle release into the supernatant (Supt) from SUPER templates of WT-Dyn1 (filled squares) CC-Dyn1 (filled circles) and CxC-Dyn1 (open upward-pointing triangles), and CxC-Dyn1 treated with DTT (open downward-pointing triangles) (average ± s.d., *n* = 3).

To determine at which stage fission is disrupted, we analysed the membrane activity of CxC-Dyn1 by measuring protein-induced changes of the ionic conductance of the lumen of thin lipid nanotubes pulled from a planar reservoir membrane^{20,21}. In the presence of GTP, CC-Dyn1 behaved like WT-Dyn1 (ref. 21): it caused a decrease in conductance due to nanotube constriction, followed (in 3 out of 3 cases) by an acute drop in conductivity to zero, indicating complete closure of the tube lumen (Fig. 2a), which for WT-Dyn1 correlated with membrane fission²¹. In contrast, CxC-Dyn1 failed to trigger lumen closure in the presence of GTP in 11 out of 11 cases, although it retained the ability to constrict and lower nanotube conductance (Fig. 2a). In the absence of nucleotide (apo) or with GMPPCP

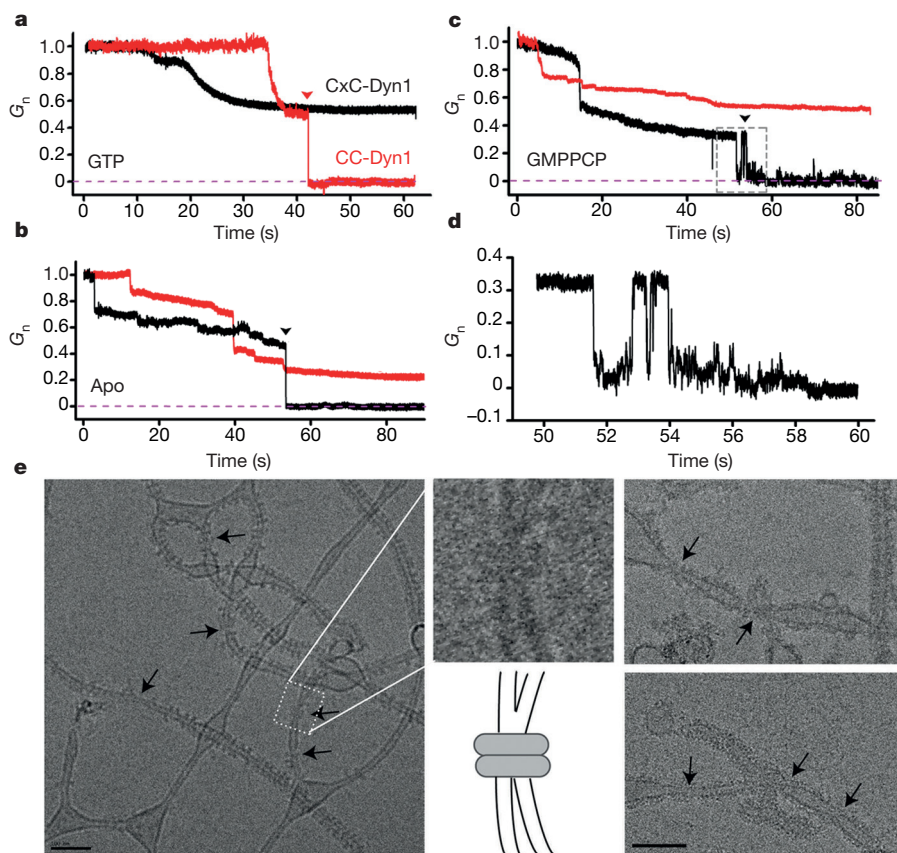


Figure 2 | CxC-Dyn1 produces stable hemi-fission. **a–d**, Representative traces of nanotube conductance changes in the presence of CC-Dyn1 (red traces) or CxC-Dyn1 (black traces) obtained in the presence (**a**) or absence (**b**) of GTP, or in the presence of GMPPCP (**c**, **d**). **d**, Expanded timescale of the flickering hemi-fission phenotype, boxed in **c**. G_n indicates conductance normalized to

the nanotube conductance before protein addition. **e**, Cryo-EM images (representative examples from 4 independent experiments) of membrane tubulation by CxC-Dyn1 in the presence of GMPPCP. Arrows indicate putative hemi-fission events detected by the loss of a defined inner leaflet of the bilayer occurring at sites of super-constriction (see inset). Scale bars, 100 nm.

(Fig. 2b, c), CC-Dyn1, like WT-Dyn1, produced stationary constriction but no lumen closure in 10 out of 10 cases and 3 out of 5 cases, respectively.

Surprisingly, CxC-Dyn1 in either the apo (Fig. 2b; 10 out of 12 cases) or GMPPCP-bound state (Fig. 2c; 8 out of 9 cases) produced complete closure of the tube lumen. These observations contrasted with the lack of scission of membrane tethers constricted by CxC-Dyn1 (Fig. 1d, e). The lumen closure could also correspond to hemi-fission, a state characterized by self-merger of the inner monolayer of the nanotube membrane without rupture of the outer one^{20,21}. In support of this interpretation, we observed the occurrence of long-lived (up to seconds; Fig. 2d) flickering events that indicate reversible formation of a hemi-fission intermediate, both in the absence of nucleotide (3 out of 10 closure events) and in the presence of GMPPCP (Fig. 2c, d; 2 out of 8 closure events). Flickering events were also occasionally detected with WT-Dyn1, but these were highly transient (milliseconds) intermediates²¹.

Cryo-electron microscopy (cryo-EM) analyses provided additional evidence for the formation of hemi-fission intermediates. Upon close examination of individual liposomes tubulated by CxC-Dyn1, we observed frequent examples of highly constricted tube segments in which the inner luminal diameter of the tube was no longer discernable (Fig. 2e, arrows, insert). Such putative hemi-fission events were observed about five times more frequently in tubules decorated by CxC-Dyn1 (3.87 ± 1.7 per μm protein-coated tubes) as compared to CC-Dyn1 (0.86 ± 1.3 per μm protein-coated tubes). As the inner diameter can no longer be resolved at these putative sites of hemi-fission (Fig. 2e, inset), we measured their outer diameter (32 ± 4.83 nm) and found that they were even narrower than those previously measured

for the super-constricted tubes formed by Dyn1(K44A) in the presence of GTP (37 nm) (ref. 22). Given that the latter had an inner luminal diameter of 4 nm (ref. 22), these data further support our conclusion that CxC-Dyn1 stabilizes a hemi-fission intermediate. Interestingly, long-ordered protein lattices were not observed at these sites, suggesting that the hemi-fission transformation is predominantly driven by small protein oligomers²¹.

The ability of CxC-Dyn1 to generate hemi-fission in the absence of nucleotide suggests that conformational changes in the BSE are somehow transmitted through the stalk to the PHD (Fig. 1a) to alter dynamin–membrane interactions and enhance its ability to remodel membranes (Fig. 3a). To test this we measured the nature of dynamin–membrane interactions using fluorescence resonance energy transfer (FRET) between Trp residues in the PHD and dansyl lipids in the target membranes²³. CxC-Dyn1 exhibited a nearly 20% increase in the dansyl fluorescence emission upon Trp excitation compared to either WT- or CC-Dyn1 (Fig. 3b and Extended Data Fig. 5a), suggesting increased membrane penetration of the PHD in the transition state. Consistent with this interpretation, membrane binding of CxC-Dyn1 also displayed a decreased sensitivity to salt extraction (Fig. 3c), indicative of increased hydrophobic versus electrostatic interactions with the membrane²³. Together these data provide direct evidence for the enhanced ‘membrane wedging’ activity of transition-state dynamin (Fig. 3b, insets).

The hemi-fission activity of CxC-Dyn1 in the apo state contrasts with its inability to produce either hemi-fission or complete fission in the presence of GTP (Fig. 2a–d). To understand this paradoxical effect of GTP on CxC-Dyn1, we further examined the nature of the membrane constriction of membrane nanotubes produced by CxC-Dyn1.

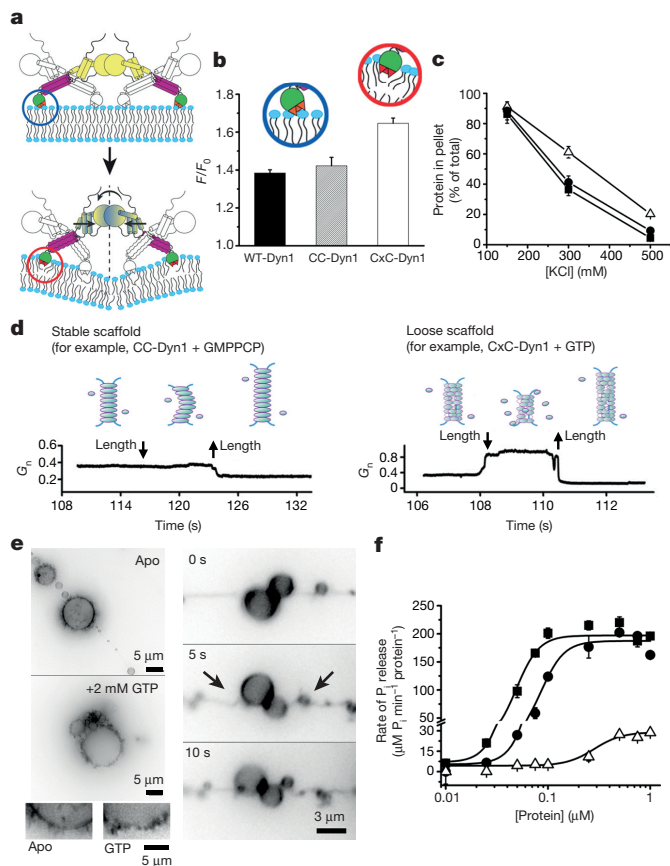


Figure 3 | Cx-C-Dyn1 displays enhanced membrane wedging activity and altered scaffolding properties. **a**, Cartoon illustrating transmission of transition-state BSE conformational information through the stalk to the PHD. **b**, FRET between PHD Trp residues and dansyl lipids measuring the relative membrane insertion of CC- and Cx-C-Dyn1 (average \pm s.d., $n = 3$) (see Extended Data Fig. 5 for complete spectra). F_0 and F correspond to fluorescence intensities of dansyl-labelled liposomes in the absence and presence of FRET donors, respectively. **c**, Hydrophobic character of membrane insertion of WT-Dyn1 (filled squares), CC-Dyn1 (filled circles) and Cx-C-Dyn1 (open upward-pointing triangles) measured by resistance to salt extraction (average \pm s.d., $n = 3$). **d**, Differential behaviour of nanotubes to vertical displacement of the patch-pipette depending on the nature/persistence of the protein scaffold. Long scaffolds formed by WT- or CC-Dyn1 in the presence of GMPPCP prevent retraction of the nanotube into the reservoir when shortened, and hence there is no change in tube conductance (left). Short/flexible scaffolds formed by Cx-C-Dyn1 in the presence of GTP allow free movement of membranes back into the reservoir, with concomitant increase in conductance (right). **e**, Addition of GTP to GUVs previously tubulated by preassembled Cx-C-Dyn1 (3 independent experiments) promotes tubule retraction towards the vesicle membrane. The tubules remain constricted during retraction (see Supplementary Video 3). Images are inverted for clarity. **f**, Concentration dependence and cooperativity of the assembly-stimulated GTPase activity of WT-Dyn1 (filled squares), CC-Dyn1 (filled circles) and Cx-C-Dyn1 (open upward-pointing triangles) measured on 100 nm L - α -phosphatidylinositol-4,5-bisphosphate (PIP₂)-containing liposomes by quantifying the release of inorganic phosphate (P_i) (average \pm s.d., $n = 3$).

The nanotube conductance characterizing stationary constriction produced by Cx-C-Dyn1 in the presence of GTP ($G_n = 0.22 \pm 0.1$) was comparable to that produced by CC-Dyn1 ($G_n = 0.27 \pm 0.05$) in the absence of nucleotide (Fig. 2a, b). Such tight membrane constriction is traditionally associated with polymerization of a rigid helical scaffold that, as with CC-Dyn1, prevents retraction of the underlying constricted nanotube to the reservoir, and the accompanying increase in the tube conductance²¹ (Fig. 3d, left). In contrast, the length of the nanotube constricted by Cx-C-Dyn1 could be freely decreased in the presence of GTP, seen as an increase in conductance (Fig. 3d, right).

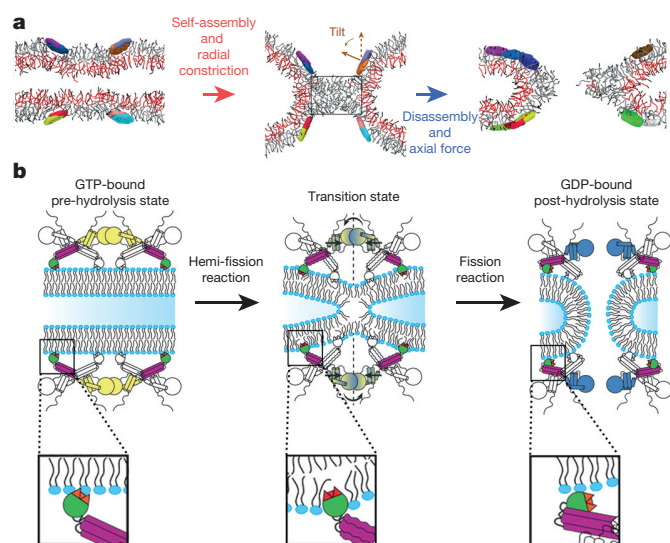


Figure 4 | The two stages of dynamin-catalysed membrane fission.

a, Coarse-grained simulations revealed formation of a stable hemi-fission intermediate (wormlike lipid micelle, middle panel) separating the two different stages of membrane fission. Axial cross-sections of representative snapshots from the simulation runs are shown. Localized radial constriction of a membrane tube by a two-protein-mimetic ring system (effective radius 5–6 nm, inter-ring distance ~ 10 nm) triggered hemi-fission (red arrow). The tilt characterizes the local membrane orientation imposed by the disks²⁶ (see Extended Data Fig. 6a for the ring description). The micelle intermediate remained stable under simulation conditions (see Extended Data Fig. 7) unless a moderate axial force was applied to cause its rupture, thus completing the fission reaction (blue arrow). The rectangular box indicates the dimensions of the wormlike micelle (~ 9 nm \times 5.5 nm). **b**, Model of distinct dynamin activities and conformational changes mediating the two stages of dynamin-catalysed membrane fission that are required to form the metastable hemi-fission intermediate and then to drive full fission (see Extended Data Fig. 8).

This ‘weakening’ of the dynamin scaffold by GTP can be associated with GTP-driven depolymerization and/or loosening of the scaffold^{14,20}. Indeed, addition of GTP to tubes produced by Cx-C-Dyn1 from giant unilamellar vesicles (GUVs) or supported bilayers with excess membrane reservoir (SUPER) templates caused their partial retraction, while they remained constricted (Fig. 3e and Supplementary Video 3). Moreover, the GTPase activity of membrane-bound Cx-C-Dyn1 (Fig. 3f) is significantly reduced relative to WT- or CC-Dyn1, but its membrane binding is unaffected. Importantly, Cx-C-Dyn1 is no longer released from membranes during GTP hydrolysis (Extended Data Fig. 5b, c). Together, these data suggest that although GTP induces depolymerization, the impaired hydrolysis and enhanced membrane interactions of Cx-C-Dyn1 prevent its release from lipid templates in the presence of GTP. The resulting loosened scaffolds retain their curvature activity but fail to produce hemi-fission, corroborating the notion that formation of this fission intermediate requires a critical degree of dynamin oligomerization, for example, a single rung of two-start helix^{21,22}.

To test the generality of our findings that localized membrane constriction by a short membrane-inserting scaffold yields stable hemi-fission but not complete fission, we applied coarse-grained computer simulations previously used to analyse membrane fusion^{24,25}, and more recently dynamin-mediated membrane fission²⁶. The main stages of dynamin-driven fission were remarkably well reproduced in these simulations by modelling simple constriction of a cylindrical lipid bilayer using a system of amphiphilic disks arranged in rings²⁶ (Extended Data Figs 6 and 7). Intriguingly, ring constriction could not bring the simulations past the hemi-fission state²⁶. To obtain mechanistic insights into this disruption of the fission reaction, we further analysed the structure and stability of the hemi-fission

intermediate using similar simulation modelling. Closely imitating the localized constriction of the membrane nanotube by CxC-Dyn1 (Fig. 4a and Extended Data Fig. 6a, b), we induced self-mergers of the inner monolayer of the tube that further developed into an extended wormlike micelle structure (Fig. 4a and Extended Data Fig. 6b). The micelle geometry was reproducible in different simulation runs (length (L) = 9.0 ± 0.9 nm, standard deviation (s.d.); $n = 8$; four independent simulation runs). These micelles remained stable throughout the observation period even under application of moderate membrane tension (see Methods). Relaxation of the geometric constraints imposed by the ring system (ring 'disassembly'²⁶) caused shortening of the micelle (to $L = 5.2 \pm 0.6$ s.d.; $n = 10$) without rupture (Extended Data Figs 6 and 7), demonstrating that the hemifission intermediate does not spontaneously rupture even in the absence of the protein support. Hence, as for membrane fusion²⁵, completion of the fission reaction requires additional energy input to overcome the intrinsic lipid resistance and the stabilizing effect of the protein scaffold.

This energy input apparently comes from GTP hydrolysis. Importantly, the connection between the G domains and PHD, mediated by BSE and disrupted in CxC-Dyn1, is required to deliver energy to the hemi-fission intermediate. It is unlikely that this GTP hydrolysis-driven conformational change causes additional membrane constriction because progression of the GTP cycle past the transition state diminishes the curvature activity of dynamin²⁰ and structural studies clearly associate membrane super-constriction with the pre-transition-state dynamin conformer²². Interestingly, in computer simulations, application of moderate (~ 0.6 dyn cm⁻¹) membrane tension²⁷ in combination with ring disassembly produced immediate rupture of the hemi-fission intermediate. The combination of tenfold weaker tension and a gradual increase of the separation between rings (for example, due to abrupt loosening of the scaffold²⁸) also mediated the transition from hemi-fission to complete fission (Extended Data Fig. 7). Although the mechanics of this transition require further investigation, our data suggest that they differ from radial constriction and probably involve production of an axial force in coordination with disassembly of the dynamin scaffold.

These findings demonstrate that dynamin implements different strategies while mediating sequential topological transitions of inner and outer membrane monolayers for fission (Fig. 4b and Extended Data Fig. 8). This bimodality, which is probably embedded in the molecular design of the proteins that catalyse fission and fusion, may constitute a fundamental feature required to coordinate the sequential, two-step, remodelling of membrane monolayers required for non-leaky formation of hemi-fusion/fission intermediates and subsequent fusion/fission. It is tempting to speculate that the current controversies regarding mechanistic models of dynamin^{4–6} are related to the previously unappreciated bimodal nature of the fission process. That is, the different models may reflect sequential modes of dynamin action required for formation and rupture of hemi-fission.

Online Content Methods, along with any additional Extended Data display items and Source Data, are available in the online version of the paper; references unique to these sections appear only in the online paper.

Received 11 January; accepted 5 May 2015.

Published online 29 June 2015.

- Chernomordik, L. V. & Kozlov, M. M. Mechanics of membrane fusion. *Nature Struct. Mol. Biol.* **15**, 675–683 (2008).
- Kozlov, M. M., McMahon, H. T. & Chernomordik, L. V. Protein-driven membrane stresses in fusion and fission. *Trends Biochem. Sci.* **35**, 699–706 (2010).
- Frolov, V. A. & Zimmerberg, J. Cooperative elastic stresses, the hydrophobic effect, and lipid tilt in membrane remodeling. *FEBS Lett.* **584**, 1824–1829 (2010).
- Schmid, S. L. & Frolov, V. A. Dynamin: functional design of a membrane fission catalyst. *Annu. Rev. Cell Dev. Biol.* **27**, 79–105 (2011).
- Ferguson, S. M. & De Camilli, P. Dynamin, a membrane-remodelling GTPase. *Nature Rev. Mol. Cell Biol.* **13**, 75–88 (2012).
- Morlot, S. & Roux, A. Mechanics of dynamin-mediated membrane fission. *Annu. Rev. Biophys.* **42**, 629–649 (2013).

- Cohen, F. S. & Melikyan, G. B. The energetics of membrane fusion from binding, through hemifusion, pore formation, and pore enlargement. *J. Membr. Biol.* **199**, 1–14 (2004).
- Lee, J. Y. & Schick, M. Calculation of free energy barriers to the fusion of small vesicles. *Biophys. J.* **94**, 1699–1706 (2008).
- Kozlovsky, Y. & Kozlov, M. M. Membrane fission: model for intermediate structures. *Biophys. J.* **85**, 85–96 (2003).
- Frolov, V. A., Escalada, A., Akimov, S. A. & Shnyrova, A. V. Geometry of membrane fission. *Chem. Phys. Lipids* **185**, 129–140 (2015).
- Chappie, J. S., Acharya, S., Leonard, M., Schmid, S. L. & Dyda, F. G. Domain dimerization controls dynamin's assembly-stimulated GTPase activity. *Nature* **465**, 435–440 (2010).
- Chappie, J. S. *et al.* A pseudoatomic model of the dynamin polymer identifies a hydrolysis-dependent powerstroke. *Cell* **147**, 209–222 (2011).
- Gennerich, A. & Vale, R. D. Walking the walk: how kinesin and dynein coordinate their steps. *Curr. Opin. Cell Biol.* **21**, 59–67 (2009).
- Ramachandran, R. & Schmid, S. L. Real-time detection reveals that effectors couple dynamin's GTP-dependent conformational changes to the membrane. *EMBO J.* **27**, 27–37 (2008).
- Doose, S., Neuweiler, H. & Sauer, M. Fluorescence quenching by photoinduced electron transfer: a reporter for conformational dynamics of macromolecules. *ChemPhysChem* **10**, 1389–1398 (2009).
- Mansoor, S. E., Dewitt, M. A. & Farrens, D. L. Distance mapping in proteins using fluorescence spectroscopy: the tryptophan-induced quenching (TriQ) method. *Biochemistry* **49**, 9722–9731 (2010).
- Faelber, K. *et al.* Crystal structure of nucleotide-free dynamin. *Nature* **477**, 556–560 (2011).
- Ford, M. G., Jenni, S. & Nunnari, J. The crystal structure of dynamin. *Nature* **477**, 561–566 (2011).
- Pucadyil, T. J. & Schmid, S. L. Real-time visualization of dynamin-catalyzed membrane fission and vesicle release. *Cell* **135**, 1263–1275 (2008).
- Bashkurov, P. V. *et al.* GTPase cycle of dynamin is coupled to membrane squeeze and release, leading to spontaneous fission. *Cell* **135**, 1276–1286 (2008).
- Shnyrova, A. V. *et al.* Geometric catalysis of membrane fission driven by flexible dynamin rings. *Science* **339**, 1433–1436 (2013).
- Sundborger, A. C. *et al.* A dynamin mutant defines a superconstricted prefission state. *Cell Rep.* **8**, 734–742 (2014).
- Mehrotra, N., Nichols, J. & Ramachandran, R. Alternate pleckstrin homology domain orientations regulate dynamin-catalyzed membrane fission. *Mol. Biol. Cell* **25**, 879–890 (2014).
- Grafmüller, A., Shillcock, J. & Lipowsky, R. Pathway of membrane fusion with two tension-dependent energy barriers. *Phys. Rev. Lett.* **98**, 218101 (2007).
- Risselada, H. J., Bubnis, G. & Grubmüller, H. Expansion of the fusion stalk and its implication for biological membrane fusion. *Proc. Natl Acad. Sci. USA* **111**, 11043–11048 (2014).
- Fuhrmans, M. & Müller, M. Coarse-grained simulation of dynamin-mediated fission. *Soft Matter* **11**, 1464–1480 (2015).
- Morlot, S. *et al.* Membrane shape at the edge of the dynamin helix sets location and duration of the fission reaction. *Cell* **151**, 619–629 (2012).
- Stowell, M. H., Marks, B., Wigge, P. & McMahon, H. T. Nucleotide-dependent conformational changes in dynamin: evidence for a mechanochemical molecular spring. *Nature Cell Biol.* **1**, 27–32 (1999).

Supplementary Information is available in the online version of the paper.

Acknowledgements We thank J. Chappie for helpful discussions, A. Mohanakrishnan and D. Reed for technical assistance. S.L.S. was supported by National Institutes of Health grant R01-GM42455 and the Welch Foundation Grant I-1823. V.A.F. was supported by grants from the Spanish Ministry of Economy and Competitiveness BFU2012-34885, the Basque Government Program Etorik IE12-332 and European FEDER funds. J.E.H. was supported by the National Institute of Diabetes and Digestive and Kidney Diseases Intramural Research Program. M.F. and M.M. were supported by the Volkswagen foundation and the DFG-CRC803 “Functionality controlled by organization in and between membranes” (B03). Simulations were performed at the Jülich Supercomputing Center and the North-German Supercomputer Alliance Hannover/Berlin. J.-P.M. was supported by a postdoctoral research grant from the Academy of Finland.

Author Contributions J.-P.M. and S.L.S. initiated the project. J.-P.M. designed and generated the CC- and CXC-Dyn1 mutants and performed all of the FRET and PET analysis, as well as their biochemical and functional characterization on liposomes and SUPER templates. A.V.S., E.R.H. and V.A.F. performed the nanotube conductance and GUV experiments. S.N. characterized the P294 mutants. A.C.S. and J.E.H. performed the cryo-EM and negative-stain EM analyses. M.F. and M.M. performed the molecular simulations. All authors discussed and interpreted the experimental data and the results of molecular simulation. S.L.S. and V.A.F. coordinated the project and wrote the manuscript, with considerable contributions from all co-authors who also approved the final version.

Author Information Reprints and permissions information is available at www.nature.com/reprints. The authors declare no competing financial interests. Readers are welcome to comment on the online version of the paper. Correspondence and requests for materials should be addressed to S.L.S. (sandra.schmid@utsouthwestern.edu), J.E.H. (jennyh@helix.nih.gov) or V.A.F. (vadim.frolov@ehu.eus).

METHODS

Protein expression and purification. Sf9 insect cells were transiently transfected with complementary DNAs encoding wild-type human dynamin 1 or indicated mutants subcloned in pEx-6 vector (EMD Millipore) for protein production. Proteins were purified by affinity chromatography using glutathione *S*-transferase (GST)-tagged Amphiphysin-II SH3 domain as an affinity ligand as described previously²⁸. Purified proteins were dialysed overnight in 20 mM HEPES (pH 7.5), 150 mM KCl, 1 mM EDTA, 1 mM DTT and 10% (v/v) glycerol, aliquoted, flash-frozen in liquid N₂, and stored at -80 °C. Protein concentrations were determined by absorbance at 280 nm using a molar absorptivity coefficient of 59,820 M⁻¹ cm⁻¹ for Dyn1^{RCL}(P11C/Y125W) and Dyn1^{RCL}(P11C/Y125W/P294A), 54,445 M⁻¹ cm⁻¹ for Dyn1^{RCL}(P11C/Y125C), and 56,185 M⁻¹ cm⁻¹ for other dynamin-1 proteins.

Protein labelling. The Cys residues at positions 11 in Dyn1^{RCL}(P11C/Y125W), Dyn1^{RCL}(P11C/Y125W/P294A), and 752 in Dyn1^{RCL}(T752C) were selectively labelled in the absence of reducing agent using tenfold molar excess of the thiol-reactive iodoacetamide derivative of BODIPY-Fl (Life Technologies). After 30 min incubation at room temperature, DTT was added to 5 mM to quench the reaction. The solution was extensively dialysed against buffer containing 20 mM HEPES (pH 7.5), 150 mM KCl, 1 mM EDTA and 1 mM DTT to separate unreacted dye molecules. After high-speed ultracentrifugation (100,000g) to discard any precipitated protein, the efficiency of labelling was determined using a molar absorptivity coefficient of 76,000 M⁻¹ cm⁻¹ at 502 nm for BODIPY.

Protein crosslinking. MTS-based homobifunctional crosslinking reagents were obtained from Toronto Research Chemicals. Unless otherwise indicated, crosslinking of Dyn1^{RCL}(P11C/Y125C) was carried out at room temperature for 15–30 min with 50 μM MTS reagents. The theoretical spanning distance of MTS reagents was derived from ref. 29. For visualization of the crosslinked proteins, all unreacted Cys residues were blocked by 10 mM *N*-ethylmaleimide prior to addition of 6× SDS sample buffer. Samples were subsequently resolved on a 7.5% polyacrylamide gel followed by Coomassie staining. For reversal of crosslinking samples were incubated for 30 min on ice with 20 mM DTT.

Preparation of liposomes, lipid nanotubes and SUPER templates. 1,2-Dioleoyl-*sn*-glycero-3-phosphocholine (DOPC), 1,2-dioleoyl-*sn*-glycero-3-phospho-(1'-*rac*-glycerol) (DOPG), 1,2-dioleoyl-*sn*-glycero-3-phosphoethanolamine (DOPE), 1,2-dioleoyl-*sn*-glycero-3-phospho-L-serine (DOPS), 1- α -phosphatidylinositol-4,5-bisphosphate (PIP₂), 1,2-dioleoyl-*sn*-glycero-3-phosphoethanolamine-*N*-lissaminerhodamine B sulfonyl (RhPE), 1,2-dioleoyl-*sn*-glycero-3-phosphoethanolamine-*N*-(5-dimethylamino-1-naphthalenesulfonyl) (dansyl-PE), and C24:1 β -D-galactosylceramide (GalCer) were purchased from Avanti Polar Lipids. Cholesterol was from Sigma-Aldrich. Appropriate amounts of lipid stock solutions were mixed in a glass tube to obtain the desired compositions. The solvent was removed under a gentle stream of nitrogen and the lipid residue was subsequently maintained under a reduced pressure for 1–2 h. The dry lipid film was hydrated for 30 min at room temperature in Milli-Q H₂O (for preparation of SUPER templates) or 20 mM HEPES (pH 7.5), 150 mM KCl and subjected to three freeze-thaw cycles. The resulting suspensions of multilamellar vesicles were extruded through polycarbonate membranes of varying pore diameters to yield unilamellar liposomes of desired size. Lipid nanotubes composed of DOPC:DOPS:PIP₂:GalCer (40:15:5:40) were generated using a bath sonicator according to procedures described previously³⁰. Supported bilayers with excess membrane reservoir (SUPER) templates were prepared as previously reported^{19,31}, with minor modifications. Briefly, a 20 μl aliquot of an aqueous suspension (5% w/w) of 2.5-μm-diameter silica microspheres (Corpuscular) was added to a NaCl-containing solution of 100 nm liposomes (DOPC:DOPG:DOPE:DOPS:PIP₂:RhPE = 19:40:20:15:5:1) for a total volume of 100 μl (with final lipid and NaCl concentrations of 200 μM and 300 mM, respectively) in a 1.5 ml low-adhesion polypropylene centrifuge tube (USA Scientific). This mixture was incubated for 30 min at room temperature with intermittent mixing. The templates were subsequently washed four times with 1 ml of Milli-Q H₂O by a low-speed spin (260g) for 2 min in a swinging-bucket rotor at room temperature, leaving behind after each wash a 100 μl volume for resuspension of the pelleted templates.

GTPase assay. Basal and assembly-stimulated GTP hydrolysis rates of wild-type and mutant dynamins were measured using a Malachite Green-based colorimetric assay that detects the inorganic phosphate released during the time course of the reaction³⁰. Briefly, indicated concentrations of proteins were incubated at 37 °C in the absence (basal) or presence of (assembly-stimulated) 100 nm liposomes prepared with DOPC:DOPS:PIP₂ = 80:15:5 (total lipid concentration = 150 μM) in a buffer containing 20 mM HEPES (pH 7.5), 150 mM KCl, 1 mM MgCl₂ and 1 mM GTP (Jena Bioscience). Twenty-microlitre aliquots were drawn from the reaction mixtures at several time-points and transferred to wells of a 96-well microplate containing 5 μl 0.5 M EDTA, thereby quenching the hydrolysis reaction.

One-hundred and fifty microlitres of Malachite Green stock solution was added to each well and the absorbance at 650 nm was measured using a microplate reader. Free phosphate was determined from the absorbance values using a standard curve. The initial rates of GTP hydrolysis were calculated from the linear phase of the time course.

Preparation of giant unilamellar vesicles. Giant unilamellar vesicles (GUVs) were formed by spontaneous swelling of lipid films deposited on 40 μm silica beads. Briefly, DOPC:DOPE:DOPS:Chol:PIP₂:RhPE 28:24:15:30:2:1 mixture in chloroform (0.05 mg total lipid) was dried in a vacuum for 1 h. Then the mixture was rehydrated by adding 10 μl of 1 mM HEPES buffer, pH 7.0. After vigorous mixing, the multilamellar lipid solution was doped with 40 μm plain silica beads and deposited on a Teflon film as 4–5 drops of ~2 μl and then vacuum-dried for 30 min. The beads covered by lipid film were picked from the Teflon film by a thin glass pipette, pre-hydrated for 5 min under H₂O saturated N₂ atmosphere, and then added from the top to a vertically placed plastic pipette tip filled with 5 μl of a pH-buffered sucrose solution. GUVs formed spontaneously on the bead surface upon 10 min of gentle hydration at 60 °C. Then the lower end of the tip was briefly immersed into a homemade observation chamber filled with 1 ml of buffer (150 mM KCl, 10 mM HEPES, 1 mM EDTA, 2 mM MgCl₂), thus transferring the beads with the attached and detached GUVs into the chamber. The 0.13–0.16-mm-thick cover glass of the chamber was pretreated with bovine serum albumin (BSA) solution (0.1 g l⁻¹, 5 min at room temperature) to inhibit lipid attachment to the glass surface. GUVs were further monitored by fluorescence microscopy, as described later.

Preparation of lipid nanotubes for the ionic conductance measurements. Bilayer lipid membranes (BLMs) were formed from the same lipid composition as GUVs on a gilded copper grid (mesh 200, Agar Scientific) pretreated with the same lipid mixture (10 g l⁻¹ total lipid) dissolved in decane:octane (1:1 v/v): a small drop of the mixture was deposited across the grid and the solvents were then evaporated under argon stream. The grid was mounted on the bottom of an observation chamber that was subsequently filled with the buffer containing 150 mM KCl, 10 mM HEPES, 1 mM EDTA, 2 mM MgCl₂. Finally, a small amount of lipid mixture in squalane (20–30 g l⁻¹, total lipid) was 'painted over' the grid using a thin brush. Lipid bilayers formed spontaneously on each mesh covered by a thick film deposited by the brush. The excess lipid material, expelled to the periphery of the mesh, formed a toroidal meniscus maintaining the lateral tension of the lipid bilayer.

Lipid membrane nanotubes were pulled from the parent BLM using a nano-positioning system based upon high-resolution NanoPZ actuators (Newport Corporation) and calibrated piezo-micromanipulator (Newport; 30 mm travel). Fire-polished borosilicate patch-pipettes (tip diameter of ~1 mm) were used for pulling. The tube formation and manipulation were performed as described earlier^{20,21}. Proteins were delivered with a second micropipette, back-filled with a 7 mM solution of the CC- or Cx-C-Dyn1 solution in 150 mM KCl, 20 mM HEPES, 1 mM EDTA and 2 mM MgCl₂. For experiments conducted in the presence of nucleotide, the nucleotides were added in equal concentration both to the observation chamber and the protein delivery pipette.

Fission assay. The efficiency of wild-type and mutant dynamins to catalyse the release of membrane vesicles from RhPE-labelled SUPER templates was analysed by means of a sedimentation assay, as described elsewhere^{19,31}. In brief, an aliquot of template suspension was added without mixing to a final volume of 100 μl of 20 mM HEPES (pH 7.5), 150 mM KCl, with 1 mM MgCl₂, 1 mM GTP, and indicated protein concentrations. The samples were left undisturbed for 30 min at room temperature, the templates subsequently pelleted at 260g for 2 min and the supernatants mixed with Triton X-100 to dissolve released vesicles. Total membrane fluorescence of templates was determined in a separate reaction by adding equal amount of templates to Triton X-100 before pelleting. The fluorescence intensity of the supernatants was read on 96-well plates using a plate reader (Bio-Tek Instruments) with excitation and emission monochromators set at 530/25 and 590/25 nm, respectively.

Sedimentation assay. Self-assembly of wild-type and mutant dynamins and their GTP hydrolysis-triggered disassembly were assessed by sedimentation after high-speed centrifugation. Two identical sets of samples were prepared by incubating dynamin (1 μM) for 30 min with or without 400 nm DOPS liposomes (total lipid concentration = 300 μM) in 20 mM HEPES, (pH 7.5), 150 mM KCl, 1 mM MgCl₂ in a final volume of 30 μl at room temperature. One millimolar GTP or GMPPCP was added to one set of samples and both sets were transferred to a 37 °C water bath for 5 min. Mixtures were then spun at 20,800g for 20 min in a microfuge refrigerated at 4 °C to obtain supernatant (S) and pellet (P) fractions. The pellet fraction containing liposomes and assembled protein was resuspended in 30 μl of the same buffer to obtain equal volumes of S and P fractions. Samples were subsequently resolved on a 7.5% polyacrylamide gel and visualized by Coomassie staining to evaluate protein levels. Dynamin self-assembly on

100 nm DOPC:DOPS:PIP₂ = 80:15:5 liposomes in the absence of GTP was quantified using an identical approach.

Fluorescence spectroscopy. All fluorescence measurements were carried out with 0.1 μ M BODIPY-labelled Dyn1^{RCL}(P11C/Y125W) or Dyn1^{RCL}(P11C/Y125W/P294A) in buffer containing 20 mM HEPES (pH 7.5), 150 mM KCl and 1 mM MgCl₂ using a Fluorolog-3 photon-counting steady-state spectrofluorometer (Horiba Jobin Yvon) equipped with double excitation and emission monochromators, a cooled PMT housing, and a 450 W xenon lamp. Samples (2.4 ml final volume) were prepared in 10 mm path length quartz cuvettes held at 25 °C and continuously stirred with a magnetic stir bar during data acquisition. Where indicated, dynamin was incubated with PIP₂-containing lipid nanotubes (1:300 molar ratio of protein to lipid) for 10 min to induce self-assembly. In PET experiments BODIPY was excited at 490 nm (2.5 nm bandpass) and emission was monitored at 510 nm (2.5 nm bandpass) with fluorescence intensity values recorded at 10 s intervals (5 s signal integration). Nucleotides or AlCl₃ (1 mM final concentration) were added to the cuvette at indicated time-points. For experiments involving GDP·AlF₄⁻, 10 mM NaF was added to the buffer before data collection was initiated. Concentration-matched sample of BODIPY conjugated to Dyn1^{RCL}(T752C) was used to establish the level of BODIPY emission intensity corresponding to complete loss of PET-induced quenching.

FRET between PH domain tryptophans and dansyl-PE-containing 400 nm liposomes (DOPS:dansyl-PE = 90:10) was used to investigate membrane interaction of dynamin proteins, as described elsewhere²³. Briefly, 2.4 ml samples composed of either 0.1 μ M protein (donor only) or 5 μ M lipid (acceptor only) were excited at 280 nm (2 nm bandpass) and their emission spectra recorded between 315 and 550 nm (4 nm bandpass). Increase in dansyl fluorescence due to FRET was monitored at 515 nm in samples containing both donor and acceptor after a 20 min incubation. Data in Fig. 3 are presented as F/F_0 , where F_0 corresponds to fluorescence intensity of dansyl-labelled liposomes in the absence of FRET donors, and F is the intensity measured.

Fluorescence microscopy. Fluorescence imaging of RhPE-labelled SUPER templates was performed in BSA-coated Nunc Lab-Tek chambered microscope slides (Thermo Scientific) using a Nikon Eclipse Ti (Nikon instruments) inverted microscope equipped with a $\times 100$, 1.45-NA oil-immersion objective and ORCA-Flash 4.0 CMOS camera (Hamamatsu). An aliquot of template suspension was added to 200 μ l 20 mM HEPES (pH 7.5), 150 mM KCl, 1 mM MgCl₂ in the presence or absence of indicated nucleotides (1 mM final concentration) and allowed to settle to the bottom of the chamber. For curvature generation (tubulation) experiments, 0.5 μ M dynamin was added to the observation chamber before templates, and imaging was performed after 10–15 min incubation at room temperature. Membrane tethers were generated by rolling 20 μ m silica beads over the surface of the SUPER templates through tilting of the observation chamber³¹.

The GUVs were monitored using an Olympus IX-70 inverted microscope ($\times 150$, 1.45-NA objective) equipped with an Andor iXon+ camera (Andor Technology). A halogen lamp was used as the excitation source, ensuring minimal photobleaching. 550/590 nm excitation/emission wavelengths were used. All images were collected and processed using the ImageJ μ Manager open source software³².

Electron microscopy. For negative-stain EM, samples (1–3 μ M dynamin and 200 μ M DOPS liposomes incubated in the presence or absence of 1 mM GTP or GMPPCP for 30 min at room temperature) were absorbed onto carbon-coated 400 mesh Cu/Rh grids (Ted Pella), stained with 2% uranyl acetate, and imaged in a Tecnai 12 (FEI) transmission electron microscope at 120 kV using a 2×2 Gatan CCD camera. For cryo-EM, a 3.5 μ l sample (prepared as described earlier) was placed on a plasma-cleaned (Fishione) Quantifoil holey carbon EM grid (SPI Supplies), blotted with filter paper, and flash-frozen in liquid ethane using a Leica EM GP (Leica Microsystems). The grids were subsequently stored in liquid nitrogen. The vitrified samples were imaged at liquid nitrogen temperature on a Tecnai 20 FEG electron microscope (FEI) operating at 200 kV and images were collected with a 4×4 CCD camera.

Measurement of ionic conductance through lipid nanotubes. The equivalent electrical circuit for nanotubes pulled from planar BLMs has been described previously²⁰. The nanotube conductance was measured at 50–100 mV holding potential using an Axopatch 200B (Molecular Devices) amplifier. The signal was digitized using a PC-44 acquisition board (Signallogic) as described previously²⁰. The current was acquired at voltage-clamp mode of the amplifier, collected using the acquisition board and processed offline using Origin software (OriginLab). The measured conductance of the nanotube in the presence of the protein was normalized to the conductance level measured for the nanotube just before protein addition.

Molecular simulations. The simulation method³³ and the model parameters³⁴ used were as previously described^{26,33,34}. The simulations were conducted using a molecular dynamics scheme with a dissipative particle dynamics thermostat^{33,35,36}.

The simulations were performed in an ensemble that allows the length of the simulation box along the axis of the lipid cylinder to dynamically vary during the simulations to keep the tension in that direction constant.

For modelling lipids, our simulations used a coarse-grained, solvent-free lipid model^{26,33,37} in which the lipids are represented as linear chains composed of two polar head-group particles and eight hydrophilic tail particles. The particles are connected by a harmonic bond potential and a soft bond-angle potential, while the non-bonded interactions are based on a third-order weighted-density functional of the particle densities. This model was shown to successfully reproduce the elastic and dynamic properties of lipid bilayers^{33,38} as well as lipid phase behaviour and topological transitions^{33,34}.

The cylindrical tubes of lipid bilayers were assembled by using estimates for the number of lipids in the inner and outer monolayer based on their radii. These configurations were then relaxed by simulating the system in an ensemble that allowed the cylinder length to dynamically vary, keeping the tension along the cylinder axis at zero, resulting in a radius of 6.2 nm and an inside-to-outside lipid ratio of 126:205. The cylinders used in our simulations had a length of 38.8 nm at zero axial tension and consisted of 7,200 lipids.

To explicitly test the effects of the insertion of the PH domains of the dynamin complex, we modelled the PH domains as amphiphilic hexagonal disks consisting of one layer of polar particles connected to one layer of hydrophilic particles. Each layer had three particles per edge and an edge length of 1.3 nm, and the two layers had a separation of 0.6 nm. The particles in each peptide disk were held together by a network of stiff, elastic bonds²⁶.

To constrict the lipid cylinder, we arranged the peptide disks into the ring system described previously²⁶. Twelve disks were restrained at positions equally distributed on a ring forming a belt around the cylindrical lipid bilayer (Extended Data Fig. 6a). Only the disks' centres of mass were restrained, while the orientations of the disks could freely change in response to interactions with the lipids. To represent one 'rung' of the dynamin spiral formed by the protein dimers⁸, we used pairs of such rings separated by $\Delta x \approx 0.45$ nm. This distance was smaller than the disk size so the disks from the juxtaposed rings overlapped while preserving their independent mobility (Extended Data Fig. 6a). This way the disk pair created a flexible membrane-interacting surface imitating the adaptive membrane wedging by a pair of PH domains of dynamin dimers. The radius of one of the two juxtaposed rings was slightly smaller ($\Delta r = 0.45$ – 0.9 nm) so that the disk pair exerted a direct influence on the orientation of the membrane at the location of the peptides, thus stimulating formation of an hourglass-shaped lipid morphology²⁶. Two of the juxtaposed ring pairs situated 9 nm apart (separation between the inner rings corresponding to ~ 10 nm separation between the mid-points of the ring pairs) constituted the ring system used in simulations (Extended Data Fig. 6a).

In simulations with restrained disks, the ring radii and the separation between the rings were fixed and the position of the disks on the rings were tied to their respective anchor points with a harmonic potential²⁶. In the experiments with gradually changing separation between the rings, we fixed the position of one ring pair and slowly moved the other pair away along the axis of the membrane cylinder. In other simulations, we effectively 'disassemble' the rings by omitting the positional restraints and allowing the disks to move freely along the membrane surface after the stable hemi-fission intermediate has formed.

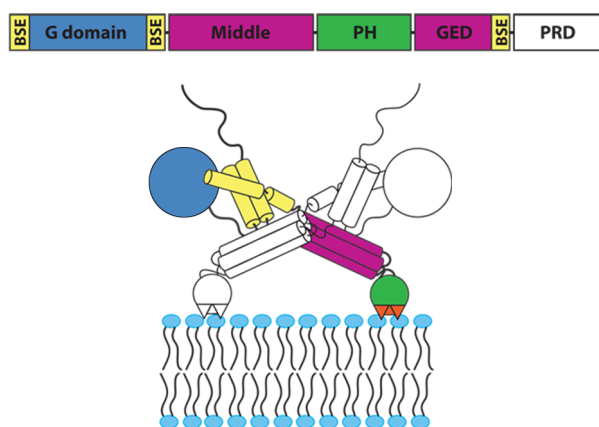
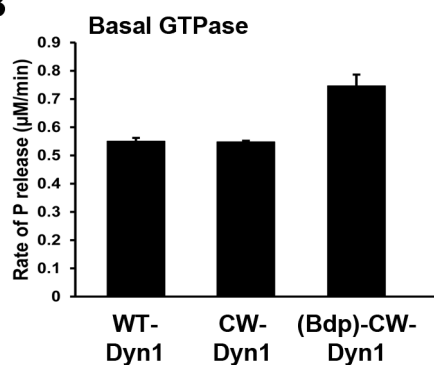
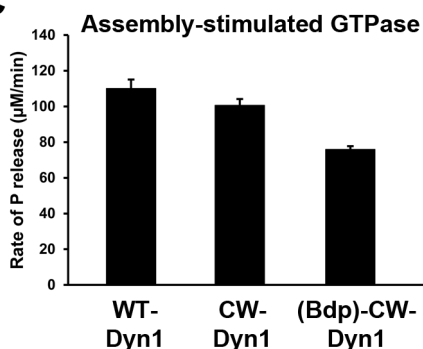
A more detailed description of the peptide model and the simulation setup can be found elsewhere²⁶.

Stability and rupture of the hemi-fission intermediate. The time unit in our simulations, obtained from the self-diffusion coefficient for lipid at room temperature³⁴, was $\tau = 2$ ns. The characteristic time for a local relaxation process in the cylindrical bilayer system described can be estimated as $\sim 100\tau$ (ref. 26). The total lifetime of the wormlike micelle obtained in the restrained system (9 nm ring separation) under zero tension was $30,200\tau$ (four independent simulations). Disassembly of the rings did not produce rupture of the micelle ($5,900\tau$). To probe the stability of this unrestrained system we applied small axial tension. The system remained stable for $18,200\tau$ under 0.06 dyn cm⁻¹ tension (Extended Data Fig. 7; three independent simulations) and for $15,800\tau$ under 0.12 dyn cm⁻¹ tension (two independent simulations), indicating that moderate membrane tensions are not sufficient to make the hemi-fission intermediate unstable. From the lifetime of the hemi-fission state, the lower boundary for the barrier separating hemi-fission from fission can be estimated to be on the order of $\sim 10 k_B T$ (where k_B is the Boltzmann constant and T is ambient temperature); however, the exact pathway(s) of the membrane transformations leading to complete fission and the corresponding free energy profiles require further investigation.

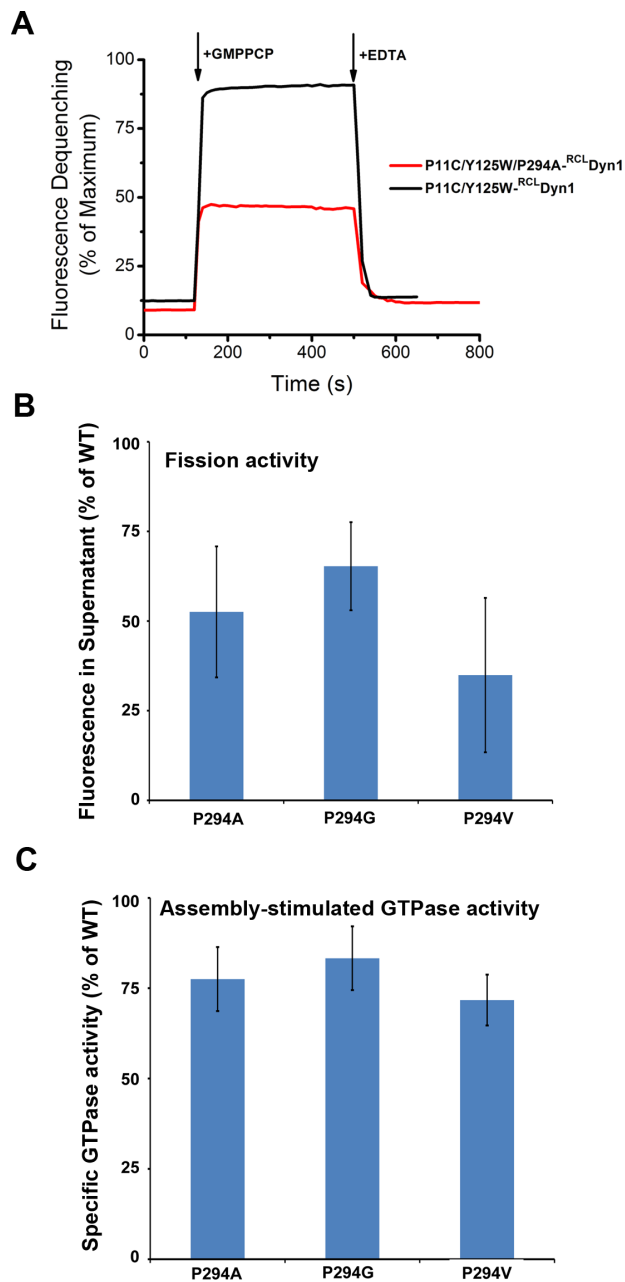
To induce rupture of the pre-formed hemi-fission intermediate we applied an axial tension of 0.6 dyn cm⁻¹, typical for the planar bilayer systems used in the experiments. This tension produces immediate (lifetime $< 100\tau$, five independent simulations) rupture in the unrestrained systems and also destabilized the

restrained systems, although much less efficiently (lifetime of $3,400 \pm 1,400\tau$, s.d.; three independent simulations). To augment the effect of tension we add an additional axial force-factor by slowly (~ 0.03 nm per τ) increasing the separation distance between the two double rings. This ring movement augmented the tension effect so that immediate rupture ($< 100\tau$; three independent simulations) was produced under 0.06 dyn cm^{-1} tension. The pathways of the hemi-fission rupture explored here are summarized in Extended Data Fig. 7.

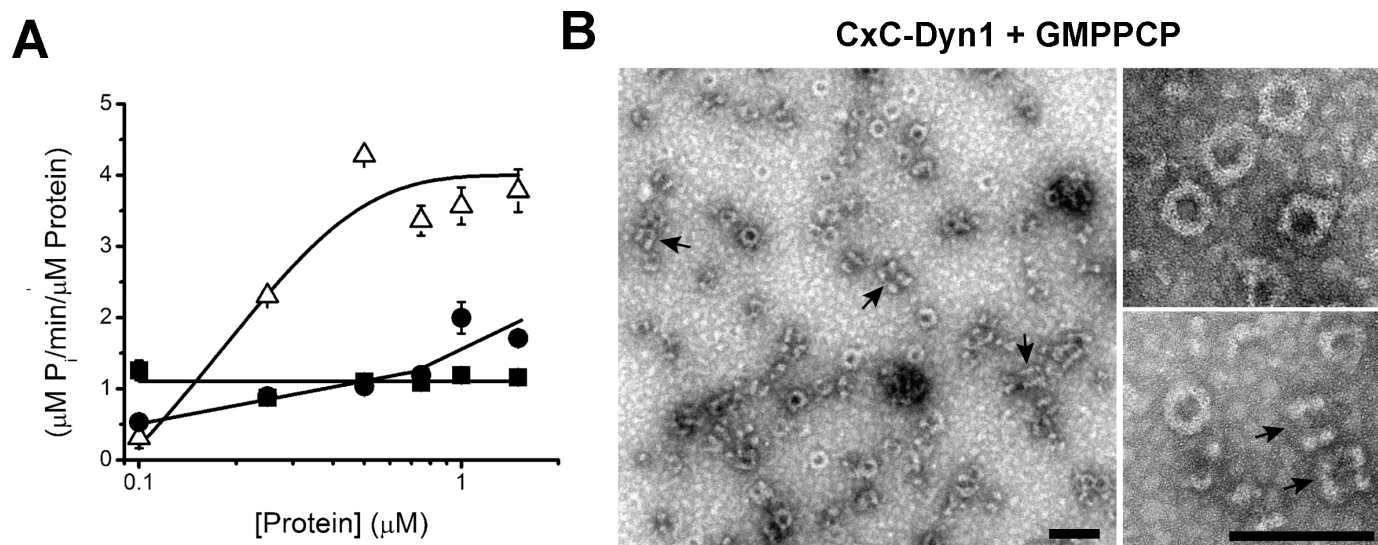
29. Loo, T. W. & Clarke, D. M. Determining the dimensions of the drug-binding domain of human P-glycoprotein using thiol cross-linking compounds as molecular rulers. *J. Biol. Chem.* **276**, 36877–36880 (2001).
30. Leonard, M., Song, B. D., Ramachandran, R. & Schmid, S. L. Robust colorimetric assays for dynamin's basal and stimulated GTPase activities. *Methods Enzymol.* **404**, 490–503 (2005).
31. Neumann, S., Pucadyil, T. J. & Schmid, S. L. Analyzing membrane remodeling and fission using supported bilayers with excess membrane reservoir. *Nature Protocols* **8**, 213–222 (2013).
32. Edelstein, A., Amodaj, N., Hoover, K., Vale, R. & Stuurman, N. Computer control of microscopes using microManager. *Curr. Protoc. Mol. Biol.* Chapter 14, Unit 14.20 (2010).
33. Hömberg, M. & Müller, M. Main phase transition in lipid bilayers: phase coexistence and line tension in a soft, solvent-free, coarse-grained model. *J. Chem. Phys.* **132**, 155104 (2010).
34. Fuhrmans, M. & Müller, M. Mechanisms of vesicle spreading on surfaces: coarse-grained simulations. *Langmuir* **29**, 4335–4349 (2013).
35. Español, P. & Warren, P. Statistical mechanics of dissipative particle dynamics. *EPL* **30**, 191 (1995).
36. Trofimov, S. Y., Nies, E. L. & Michels, M. A. Constant-pressure simulations with dissipative particle dynamics. *J. Chem. Phys.* **123**, 144102 (2005).
37. Daoulas, K. C. & Müller, M. Comparison of simulations of lipid membranes with membranes of block copolymers. *Adv. Polym. Sci.* **224**, 197–233 (2010).
38. Hömberg, M. & Müller, M. The role of inertia and coarse-graining on the transverse modes of lipid bilayers. *EPL* **97**, 68010 (2012).
39. Carr, J. F. & Hinshaw, J. E. Dynamin assembles into spirals under physiological salt conditions upon addition of GDP and gamma phosphate analogues. *J. Biol. Chem.* **272**, 28030–28035 (1997).

A**B****C**

Extended Data Figure 1 | Domain structure and biochemical characterization of dynamin constructs. **a**, Domain structure of dynamin and cartoon illustrating that the GTPase domain (G domain, blue) connects through the bundle signalling element (BSE), composed of the N- and C-terminal helices of the G domain and the C-terminal helix from GED (yellow) to the stalk formed by the middle domain and GED (magenta). The pleckstrin homology domain (PHD, green) interacts with membrane lipids. **b**, **c**, Basal (**b**) and assembly-stimulated (**c**) rates of GTP hydrolysis for 0.5 μM WT-Dyn1 and CW-Dyn1 before and after BODIPY conjugation. Data are shown as average ± s.d., $n = 3$.

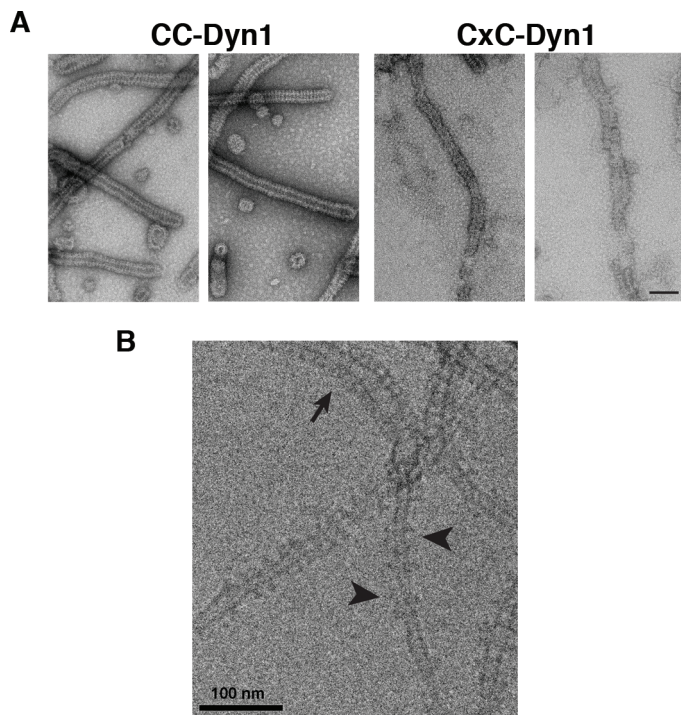


Extended Data Figure 2 | Role of P294 in BSE conformational dynamics.
a, Changes in emission intensity of BODIPY-labelled CW-Dyn1 and CW-Dyn1(P294A) due to loss of PET after addition of 1 mM GMPPCP. Although the BSE partially opens upon addition of GMPPCP, its movements are constrained relative to wild type by the mutation of P294. **b**, Assembly-stimulated GTPase activity of 0.5 μ M P294A, P294G and P294V Dyn1 measured on 100 nm liposomes relative to WT-Dyn1. The mutants show near wild-type activity, indicating their ability to self-assemble onto and tubulate liposomes (data shown as average \pm s.d., $n = 4$). **c**, Fission activity of 0.5 μ M P294A, P294G and P294V Dyn1 relative to WT-Dyn1 measured as the percentage of total membrane released from SUPER templates during 30 min incubation in the presence of GTP (data shown as average \pm s.d., $n = 3$). Substitution of P294 with the more rigid valine residue has a greater effect on fission activity.

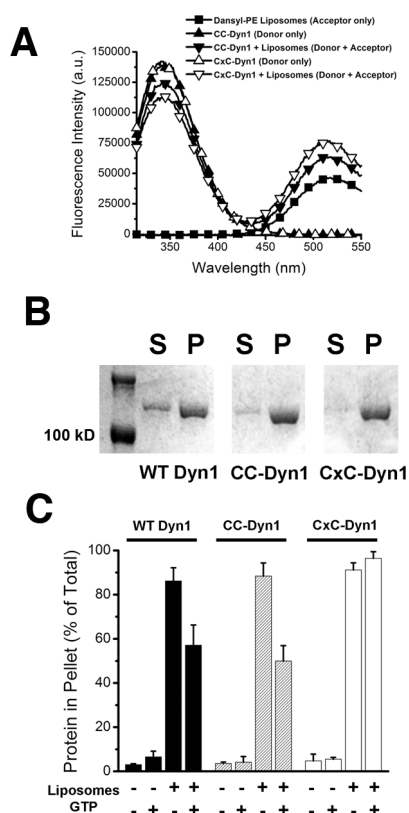


Extended Data Figure 3 | Characterization of CxC-Dyn1. **a**, Concentration dependence of the specific GTPase hydrolysis rates of WT-Dyn1 (filled squares), CC-Dyn1 (filled circles) and CxC-Dyn1 (open triangles) measured in solution at 1 mM GTP (data shown as average \pm s.d., $n = 3$). **b**, EM micrographs (representative images from four independently prepared samples) showing CxC-Dyn1 assembled into rings and short spirals (arrows) in

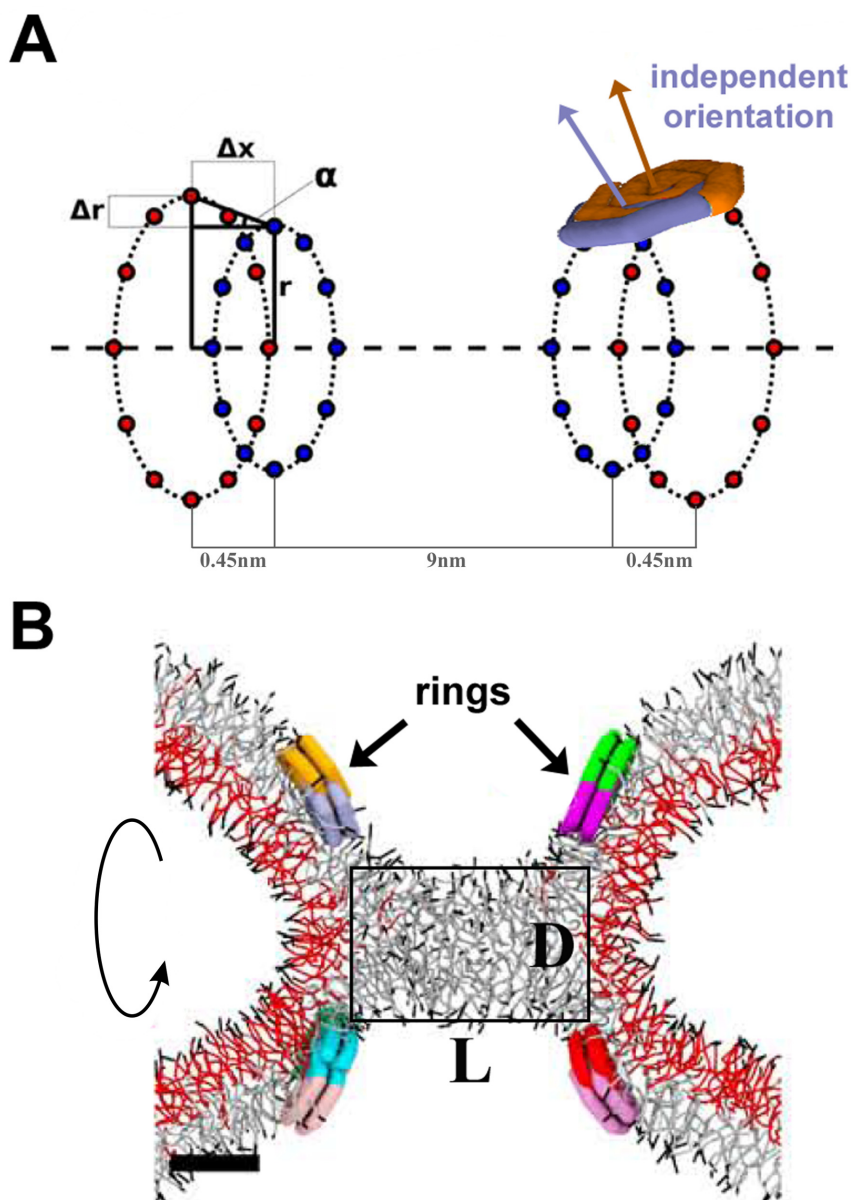
the presence of GMPPCP visualized by negative stain. Insets: top view, rings; side view, short spirals (arrows). These rings are reminiscent of those previously observed with WT-Dyn1 only in the presence of transition state nucleotide analogues (for example, $\text{GDP} \cdot \text{AlF}_4^-$)³⁹. Unlike CxC-Dyn1, CC-Dyn1 remained unassembled in the presence of GMPPCP (data not shown). Scale bars, 100 nm.



Extended Data Figure 4 | Negative-stain and cryo-EM images of CC- and CxC-Dyn1 assembled onto PS liposomes in the absence of nucleotides. **a, b,** Negative-stain (**a**) and cryo-EM (**b**) images are shown. Note the disordered nature of CxC-Dyn1 spirals relative to CC-Dyn1 structures seen via negative stain in **a**. Scale bars, 100 nm. **b,** Arrow points to relatively ordered CxC-Dyn1 assemblies, while arrowheads point to sparse dynamin assemblies appearing as single or double rings.

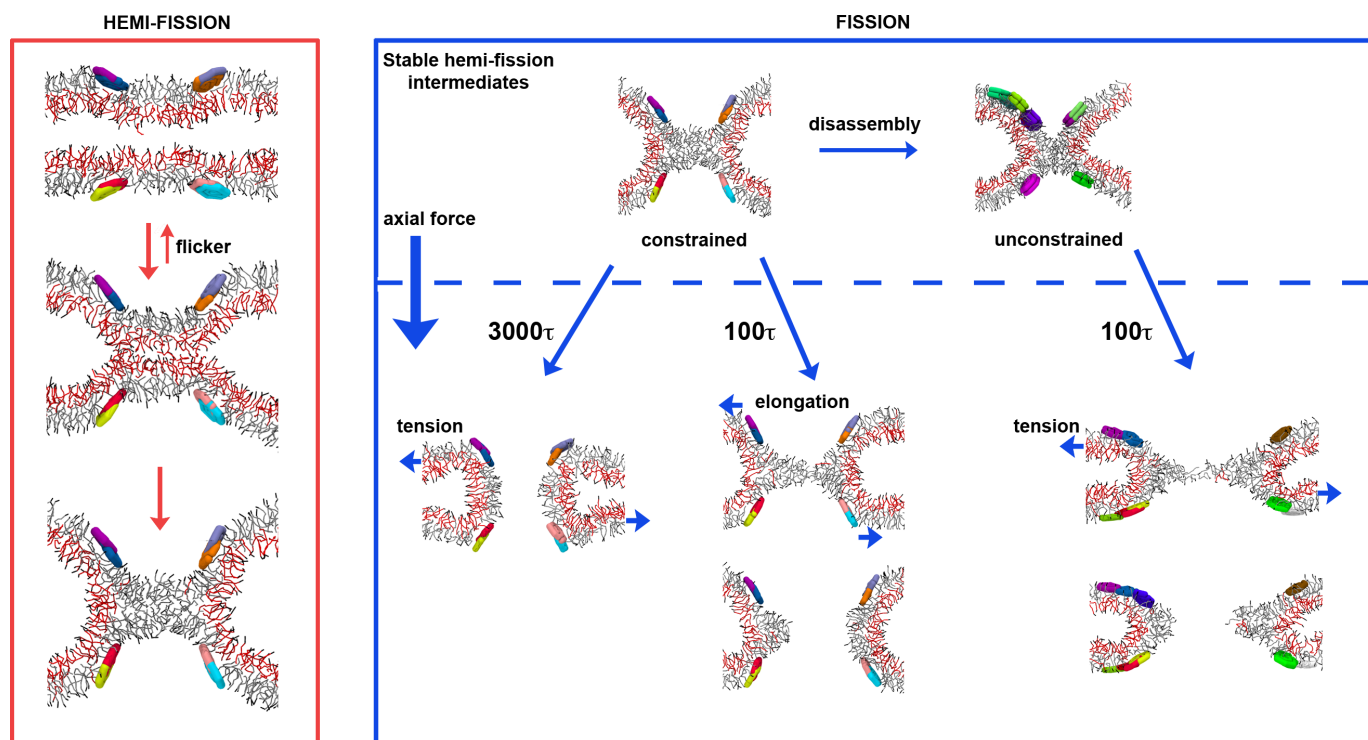


Extended Data Figure 5 | Altered membrane interactions of the CxC-Dyn1 transition-state conformer. **a**, Fluorescence emission spectra of 0.1 μM CC-Dyn1 or CxC-Dyn1 (donor) as well as dansyl-PE (acceptor)-containing liposomes (5 μM total lipid; 90 mol% PS, 10 mol% dansyl-PE) upon excitation at 280 nm. FRET between the PH domain Trp residues and dansyl is evident in the donor plus acceptor samples as a decrease in donor and an increase in acceptor emission. **b**, Self-assembly of the indicated proteins (1 μM) on liposomes identical to those used in the GTPase assay (300 μM total lipid; Fig. 3f) examined by sedimentation followed by SDS-PAGE analysis of the supernatant (S) and pellet (P) fractions. **c**, Percentages of proteins pelleted after incubation with or without 400 nm PS liposomes (1 μM protein, 300 μM total lipid) and 1 mM GTP, as indicated, was quantified by sedimentation followed by SDS-PAGE and densitometric analyses of the protein levels in supernatant and pellet fractions (data shown are average \pm s.d., $n = 3$).



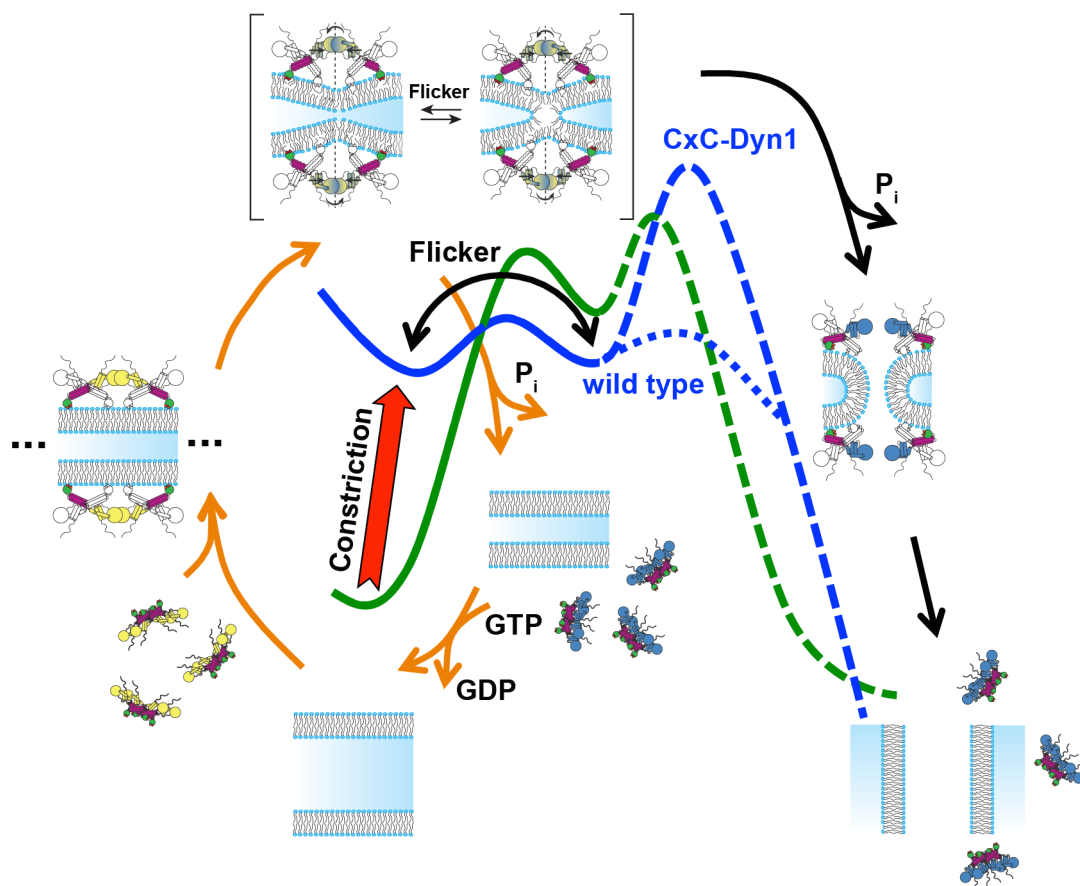
Extended Data Figure 6 | Coarse-grained approach to modelling localized membrane constriction by Cx-C-Dyn1. **a**, Schematic representation of the geometry of the ring system used to produce local constriction of a prototype membrane tube. Two pairs of rings are shown, each formed by two closely juxtaposed rings (separated by a small distance Δx). The inner ring in each pair has the radius r and the outer ring has a slightly larger radius $r + \Delta r$ so that the ring pair promotes creation of an hourglass membrane shape. The PHDs of dynamin are represented as amphiphilic disks evenly distributed over the rings

with the centre of mass of each disk being restrained to a position on the ring (marked by blue and orange points). Two overlapping disks (purple and brown) attached to the right juxtaposed ring pair are shown. The orientations of the disks are not fixed, so the normal to the disk surface (purple and brown arrows) can have an arbitrary direction. **b**, Axial cross-section of a stable hemifission intermediate, the cylindrical micelle, created by the ring system shown in **a**. The rectangular box indicates the dimensions of the cylindrical micelles (the diameter D and the length L).



Extended Data Figure 7 | Molecular simulations of the hemi-fission and fission transformations. The red box shows a representative sequence of simulation snapshots (axial cross-sections) demonstrating the formation of the stable hemi-fission intermediate²⁶. Radial constriction of a membrane tube resulted in reversible closure of the tube lumen, that is, flicker²⁶, followed by formation of a stable cylindrical micelle structure. The blue box summarizes the simulation runs exploring the stability of the hemi-fission intermediate and its

rupture. The top part shows stable structures corresponding to the constrained intermediate (left, taken at zero tension) and the unconstrained intermediate (right, taken at 0.06 dyn cm⁻¹ tension). The bottom part shows the rupture of the intermediates by 0.6 dyn cm⁻¹ tension (left and right) or by elongation of the ring system at 0.06 dyn cm⁻¹ tension (middle). The characteristic times for the rupture are indicated near the corresponding blue arrows.



Extended Data Figure 8 | Dynamin-catalysed membrane fission occurs in two mechanistically distinct stages through a hemi-fission intermediate. Model overlaying the distinct dynamin activities and conformational changes onto the two energy barriers (green curve) that must be overcome, first to catalyse formation of the metastable hemi-fission intermediate and subsequently to drive full fission. When trapped in the transition state and in the absence of GTP, CxC-Dyn1 can drive the formation of a metastable and

flickering hemi-fission state (solid blue curve) through the assembly of small scaffolds and enhanced wedging activity of the PHD. However, without subsequent GTPase-driven conformational changes required to loosen the scaffold, generate axial force and retract the PHD, as occurs for WT-Dyn1 (dotted blue line), the membrane-bound CxC-Dyn1 creates an insurmountable barrier to fission (dashed blue line).

CDA directs metabolism of epigenetic nucleosides revealing a therapeutic window in cancer

Melania Zauri¹, Georgina Berridge², Marie-Laëtitia Thézénas², Kathryn M. Pugh^{2,3}, Robert Goldin⁴, Benedikt M. Kessler² & Skirmantas Kriaucionis¹

Cells require nucleotides to support DNA replication and repair damaged DNA. In addition to *de novo* synthesis, cells recycle nucleotides from the DNA of dying cells or from cellular material ingested through the diet. Salvaged nucleosides come with the complication that they can contain epigenetic modifications. Because epigenetic inheritance of DNA methylation mainly relies on copying of the modification pattern from parental strands^{1–3}, random incorporation of pre-modified bases during replication could have profound implications for epigenome fidelity and yield adverse cellular phenotypes. Although the salvage mechanism of 5-methyl-2′-deoxycytidine (5mdC) has been investigated before^{4–6}, it remains unknown how cells deal with the recently identified oxidized forms of 5mdC: 5-hydroxymethyl-2′-deoxycytidine (5hmdC), 5-formyl-2′-deoxycytidine (5fdC) and 5-carboxyl-2′-deoxycytidine (5cadC)^{7–10}. Here we show that enzymes of the nucleotide salvage pathway display substrate selectivity, effectively protecting newly synthesized DNA from the incorporation of epigenetically modified forms of cytosine. Thus, cell lines and animals can tolerate high doses of these modified cytidines without any deleterious effects on physiology. Notably, by screening cancer cell lines for growth defects after exposure to 5hmdC, we unexpectedly identify a subset of cell lines in which 5hmdC or 5fdC administration leads to cell lethality. Using genomic approaches, we show that the susceptible cell lines overexpress cytidine deaminase (CDA). CDA converts 5hmdC and 5fdC into variants of uridine that are incorporated into DNA, resulting in accumulation of DNA damage, and ultimately, cell death. Our observations extend current knowledge of the nucleotide salvage pathway by revealing the metabolism of oxidized epigenetic bases, and suggest a new therapeutic option for cancers, such as pancreatic cancer, that have CDA overexpression and are resistant to treatment with other cytidine analogues¹¹.

Modified cytidines can enter deoxynucleotide pools, because salvage and nutrient uptake pathways can recover nucleosides, rather than simpler degradation products such as uric acid in the salvage of purines¹². Previous biochemical work has suggested that 5mdC is not incorporated in the DNA, but is salvaged as thymidine^{4–6}. Salvage of oxidized 5-methylcytosine variants has not been previously characterized. We rationalized that, if nucleosides are recovered in unphosphorylated forms (through import) or monophosphate forms (through intracellular hydrolysis), the barrier restricting their incorporation into the DNA may lie in the nucleotide salvage enzymes or DNA polymerases. Providing cells with a final substrate for DNA polymerases, in the form of deoxynucleoside triphosphate, would allow decoupling of DNA synthesis from salvage enzyme activity. Therefore, we transfected two human cancer cell lines—MDA-MB-231 and H1299—with 5-hydroxymethyl-2′-deoxycytidine triphosphate (5hmdCTP), isolated DNA and analysed the base composition by a high-performance liquid chromatography–ultraviolet (HPLC–UV) method, using a set of nucleoside standards for calibration

(Fig. 1a). After 5hmdCTP transfection, two additional nucleosides were observed in the hydrolysed DNA that correspond to 5hmdC and 5hmdU (Fig. 1b, c and Extended Data Fig. 1b). This indicates that DNA polymerases can incorporate 5hmdC into DNA, and also demonstrates strong deaminase activity acting on either the nucleotide or the incorporated base, resulting in the presence of 5-hydroxymethyluracil (5hmUra) in the DNA. The capacity for DNA polymerases to use 5hmdCTP was also evident in an *in vitro* replication assay¹³ (Fig. 1d), demonstrating that human DNA polymerases are not selective against the incorporation of 5hmdC into DNA. Therefore, if salvage pathways can convert pre-existing sources of 5hmdC into their nucleotide triphosphate forms, this could result in their incorporation into cellular DNA and potentially lead to deleterious effects on the epigenome.

The final triphosphate form of cytidine in a cell is produced by sequential phosphorylation by three classes of cytidine kinases. First, deoxycytidine kinase (DCK) produces a monophosphate, which is then converted into a diphosphate by cytidine monophosphate kinases (CMPK1 and CMPK2), and subsequently converted into a triphosphate by the family of nucleoside diphosphate kinases¹⁴. Because nucleoside diphosphate kinases phosphorylate both purine and pyrimidine nucleosides¹⁵, and CMPK2 is found in the mitochondria¹⁶, we directed our efforts towards examining the substrate selectivity of DCK and CMPK1. Recombinant DCK was able to transfer the phosphate from ATP[γ -³²P] to 5mdC, 5hmdC and 5fdC, but not to 5cadC (Fig. 1e and Extended Data Fig. 1d), while CMPK1 phosphorylated only unmodified cytidine monophosphate (Fig. 1e). In agreement with previous work on 5mdC (ref. 4), we can conclude that the inability of CMPK1 to create diphosphates of modified nucleotides provides the main barrier to the formation of respective dCTPs, limiting their availability for DNA polymerases, which can instead accept modified dCTPs.

Given this inherent selectivity of the nucleotide salvage pathway kinase CMPK1 for unmodified cytidine, we proposed that the introduction of abundant biologically modified cytidine variants would have little adverse effect on the physiology of a cell, unless they significantly impaired nucleotide metabolism. First, we determined that biological cytidine variants retain 70–100% of their original form after incubation in water and cell culture media for 10 days at 37 °C, while 80% of the synthetic variant 5-aza-2′-deoxycytidine (5azadC) decomposed by day 2 in agreement with previous observations¹⁷ (Extended Data Fig. 2a–c). Next, a panel of 19 human cell lines was selected, sampling various tissue origins and p53 mutation statuses¹⁸ (Extended Data Fig. 2d). When cell growth media was supplemented with 10 μ M 5hmdC or dC, most of the cell lines continued to proliferate at a normal rate. However, two cell lines (HOP-92 and MDA-MB-231) unexpectedly ceased to proliferate in the presence of 5hmdC (Fig. 2a). We found that 10 μ M 5hmdC was lethal and 1 μ M 5hmdC caused mild growth inhibition (Fig. 2b). Interestingly, 5fdC was more potent at 1 and 10 μ M doses in the MDA-MB-231 cell line, but showed the same cell line selectivity as 5hmdC (Fig. 2b).

¹Ludwig Cancer Research, Nuffield Department of Medicine, University of Oxford, Oxford OX3 7DQ, UK. ²Target Discovery Institute, Nuffield Department of Medicine, University of Oxford, Oxford OX3 7FZ, UK. ³Structural Genomics Consortium, Nuffield Department of Medicine, University of Oxford, Oxford OX3 7DQ, UK. ⁴Centre for Pathology, Imperial College, London W2 1NY, UK.

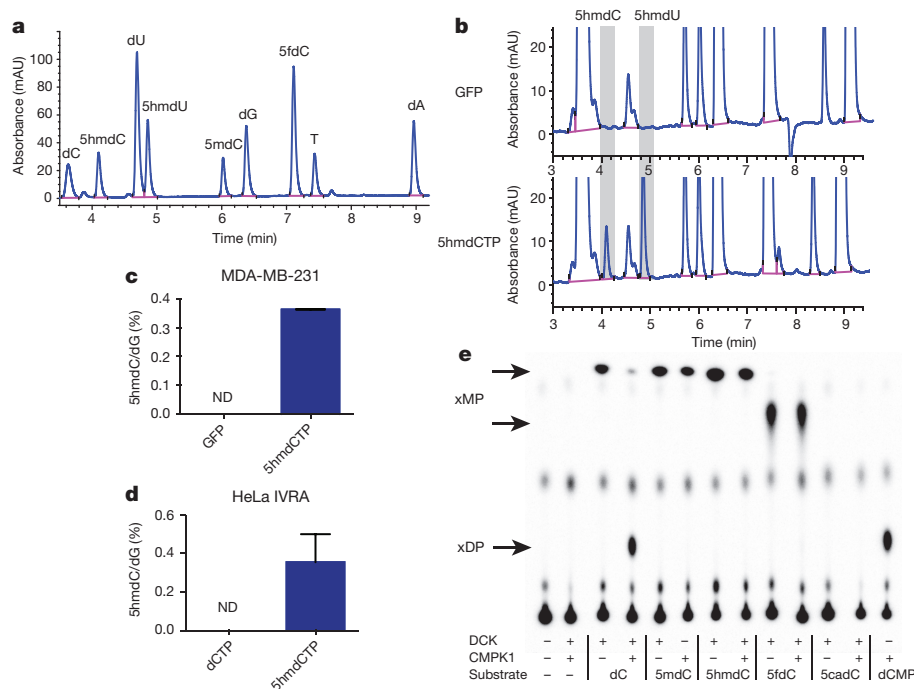


Figure 1 | DNA polymerase and nucleoside kinase activities on modified nucleosides.
a, HPLC–UV (260 nm) chromatogram of nucleosides mixed in equimolar amounts.
b, HPLC–UV examination of nucleosides derived from DNA extracted from MDA-MB-231 cells nucleoparated with 5hmdCTP. **c**, The abundance of 5hmdC relative to dG in nucleoparated MDA-MB-231 ($n = 3$). **d**, 5hmdCTP incorporation assessed by *in vitro* replication assay (IVRA) performed in HeLa cells, measured by HPLC–UV ($n = 5$). Error bars in **c** and **d** denote s.d.; ND, not detected **e**, Thin-layer chromatography (TLC) separation of reaction products of DCK and CMPK1 kinases, which were supplied with different modified cytidine substrates. xDP, cytidine diphosphates; xMP, cytidine monophosphates.

Genetic alterations or gene expression differences could modify the response of a cell line to biologically modified cytidine variants. By comparing the existing gene expression profiles of the cell lines (NCI60 and CCLE projects^{19,20}) that we established as sensitive to modified cytidine variants to two randomly chosen resistant ones, we identified 1,380 differentially expressed genes ($P < 0.01$, >2 -fold change). Notably, by focusing on differentially expressed genes known to be involved in nucleoside metabolism, we identified cytidine deaminase (CDA) overexpression in the 5hmdC-sensitive cell types, which had the ninth lowest P value of all the genes (Fig. 2c and Supplementary Table 1). None of the other known genes involved, either in nucleoside

transport or cytidine recycling, were differentially expressed (Fig. 2c). To identify other cell lines with CDA overexpression, we ranked the 21 available cell lines according to their *CDA* messenger RNA levels (Fig. 2d). SN12C and Capan-2 cell lines had the highest expression levels of *CDA*, and this was confirmed at the protein level by western blot (Fig. 2e). Examination of 5hmC and 5fdC tolerance revealed that a 10 μ M dose substantially inhibited the growth of both cell lines, suggesting that the expression level of *CDA* is predictive of cytotoxicity for these epigenetic cytidine variants (Fig. 2e).

To determine whether CDA overexpression is necessary for selective cytotoxicity, we manipulated CDA levels in the identified cell lines.

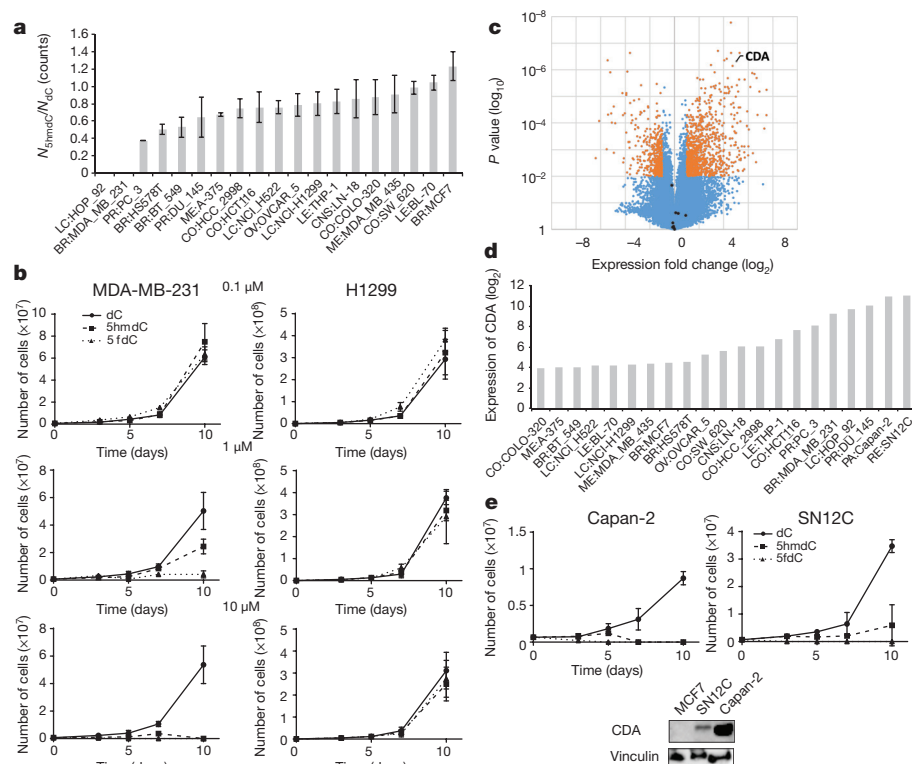


Figure 2 | Identification of CDA overexpression as a primary determinant for cytotoxic action of natural cytidine variants. **a**, Ratio of live cells after 10 days of treatment with 5hmdC versus dC ($n = 3$). **b**, Growth curves of MDA-MB-231 and H1299 cell lines treated with three different concentrations of dC, 5hmdC and 5fdC over a period of 10 days ($n = 3$). **c**, Volcano plot illustrating analysis of gene expression of MDA-MB-231 and HOP-92 versus MCF-7 and MDA-MB-435 cell lines. Shown in orange are the genes that are significantly different between the groups ($P < 0.01$; >2 -fold change). Dots in black show nucleoside transporters (SLC29A1, SLC29A2, SLC29A3, SLC29A4, SLC28A1, SLC28A2 and SLC28A3) and kinases (DCK and CMPK1). **d**, CDA expression levels from NCI60 and CCLE global gene expression data sets for different cancer cell lines. **e**, Western blot confirming CDA overexpression in SN12C and Capan-2 cell lines. Growth curves of Capan-2 and SN12C after treatment with $10\ \mu\text{M}$ 5hmdC, 5fdC and dC ($n = 3$). Error bars denote s.d.

Cell lines (MDA-MB-231 and SN12C) with stable short hairpin RNA (shRNA) knockdown of CDA were able to survive 10 μ M 5hmdC (Fig. 3a and Extended Data Fig. 2e). Furthermore, stable overexpression of CDA in normally 5hmdC-resistant cell lines (H1299 and MCF-7) induced substantial growth inhibition (Fig. 3b and Extended Data Fig. 2f). These experiments clearly established that CDA overexpression is predictive, necessary and sufficient for cytotoxic activity. *In vitro* measurements of recombinant CDA protein activity were performed with various cytidine variants. First, we determined that CDA deaminates 5mdC, 5hmdC and 5fdC, but not 5cadC, creating thymidine and respective variants of uridine (Extended Data Fig. 2g, h). Second, reaction kinetic data fitted well with a pseudo zero-order kinetics model ($R^2 > 0.9$) revealing that, after deoxycytidine, the second best substrate (that is, with the second highest turnover number (k_{cat})) for CDA is 5fdC (Fig. 3c, d and Extended Data Fig. 2h). This was unexpected, because the catalytic activity does not follow a simple relationship with the dimensions of the 5' modification as it does in the case of AID and APOBEC enzymes²¹. Molecular docking of cytidine variants to the CDA structure²² suggested that 5fdC docks to the catalytic site with nearly 180° rotation when compared to unmodified cytidine, retaining the amino group position close to the active site containing Zn^{2+} (Extended Data Fig. 3a). By contrast, 5hmdC docks in the active site by displacing the amino group, which provides a potential explanation for the lower catalytic turnover observed (Extended Data Fig. 3a).

The deamination of dC and 5mdC results in dU and T, which are the normal precursors for thymidine triphosphate synthesis. Conversely, deamination of 5hmdC and 5fdC produces 5hmdU and 5fdU, respectively, which are not canonical nucleosides. When phosphorylated and incorporated into DNA, 5hmdU and 5fdU are toxic to

the cells (Extended Data Fig. 3b) as they are recognized as damaged bases and trigger extensive uracil glycosylase activity resulting in DNA breaks²³. Therefore, we asked whether the uptake of 5hmdC in CDA-overexpressing cells leads to its conversion into 5hmdU and to its incorporation into DNA, potentially explaining cell-type-specific lethality. First, we determined activities of thymidine kinase and thymidylate kinase on 5hmdU and 5fdU. In contrast to the inability of CMPK1 to act on equivalent cytidine variants, thymidine kinase and thymidylate kinase phosphorylated both uridine variants (Fig. 3e). Notably, the corresponding triphosphates are not substrates nor potent inhibitors of dUTPase, a robust enzyme that removes dUTP from cells (Extended Data Fig. 3c). Finally, analysis of the genomic DNA composition of 5hmdC- and 5fdC-treated MDA-MB-231 cells identified 5hmUra and 5fUra, but no detectable change in 5-hydroxymethylcytosine (5hmCyt) or 5-formylcytosine (5fdCyt) levels in the DNA (Fig. 3f, Extended Data Figs 3d, e and 4a–c). Overall, in all the cell lines examined, a linear correlation was observed between CDA expression and the amount of 5hmUra in the DNA after treatment with 5hmdC (Extended Data Fig. 4d). Signs of extensive DNA damage were detected by phosphorylated H2AX (γ H2AX) staining in 5hmdC-treated CDA-overexpressing cells (MDA-MB-231). By contrast, a cell line expressing low CDA levels (H1299) had no obvious γ H2AX staining (Fig. 3g and Extended Data Fig. 5c, d). Also, increased numbers of cells in S and G2 phases of the cell cycle were observed in CDA-overexpressing cell lines, consistent with cell cycle arrest triggered by a DNA damage response (Extended Data Fig. 5a). We did not observe deviations in the dNTP pools of treated cells, indicating that the cell death is likely to be caused by extensive base excision by SMUG1 DNA glycosylase, which recognizes 5hmUra and 5fUra triggering repair and DNA double-stranded breaks (Extended Data Fig. 6). Together, these

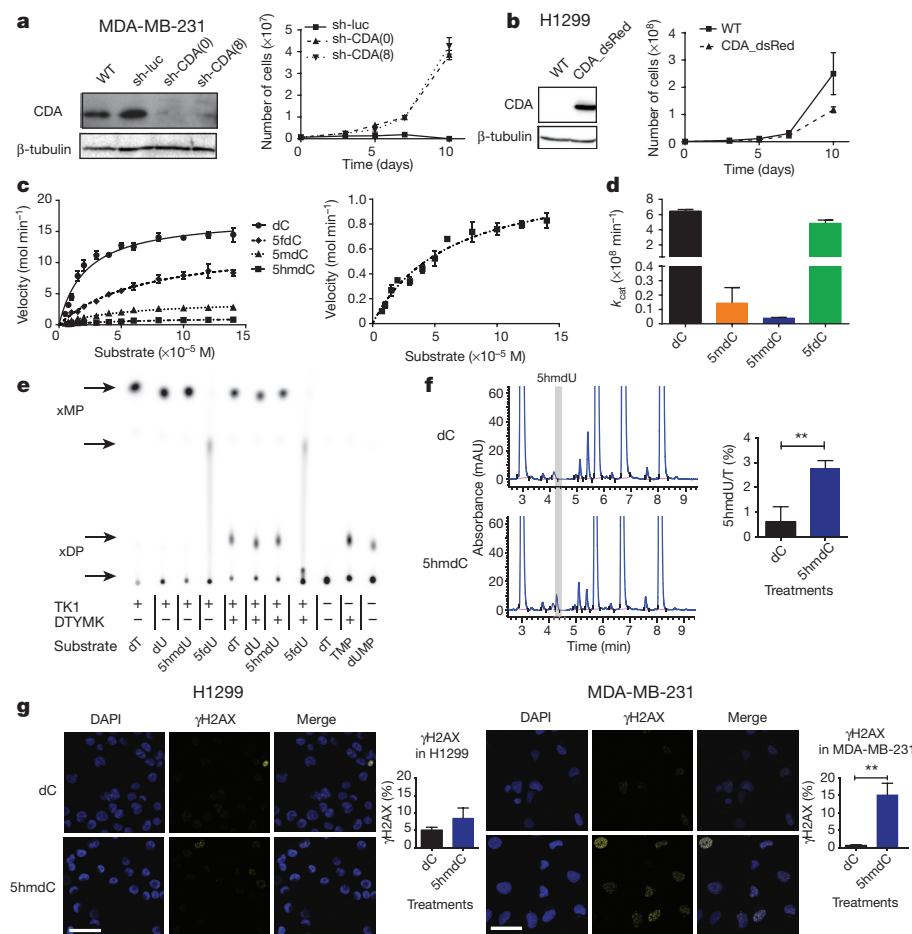


Figure 3 | Molecular mechanism of CDA-dependent cytotoxicity of cytidine variants.

a, Western blot showing knockdown of CDA by shRNA (using sh-CDA) in the MDA-MB-231 cell line. Right panel illustrates growth curves of derived stable cell lines after treatment with 10 μ M 5hmdC ($n = 3$). (0) and (8) indicate two different shRNA constructs used for the experiments, and sh-luc denotes a non-targeting control shRNA that targets luciferase. WT, wild type. **b**, Western blot showing overexpression of CDA after lentiviral transduction of H1299 cells with a construct overexpressing CDA (CDA_dsRed). Right panel shows the growth curve after treatment with 10 μ M 5hmdC ($n = 3$). **c**, CDA activity fitted to the Michaelis-Menten model. Right panel shows a zoomed-in curve, when 5hmdC was used as a substrate. **d**, k_{cat} values of CDA supplied with cytidine variants. **e**, TLC separation of reaction products of thymidine kinase 1 (TK1) and thymidylate kinase (DTYMK), which were exposed to different modified uridine substrates. xDP indicates diphosphates; xMP, monophosphates. **f**, HPLC-UV chromatogram of nucleosides from DNA of MDA-MB-231 cells treated with 10 μ M 5hmdC or dC for 3 days. Right panel shows the abundance of 5hmdU relative to T ($n = 3$, t -test, $**P = 0.0057$). **g**, γ H2AX immunofluorescence in MDA-MB-231 and H1299 cell lines at day 3 after treatment with 10 μ M 5hmdC or dC. Scale bars, 50 μ m. Below are quantifications of cells showing positive signals ($n = 3$, t -test, $P = 0.0017$). DAPI, 4',6'-diamidino-2-phenylindole. All error bars denote s.d.

observations demonstrate that CDA deaminates 5hmdC and 5fdC, creating 5hmdU and 5fdU, respectively, which are incorporated into the DNA, leading to cell cycle arrest and eventually death.

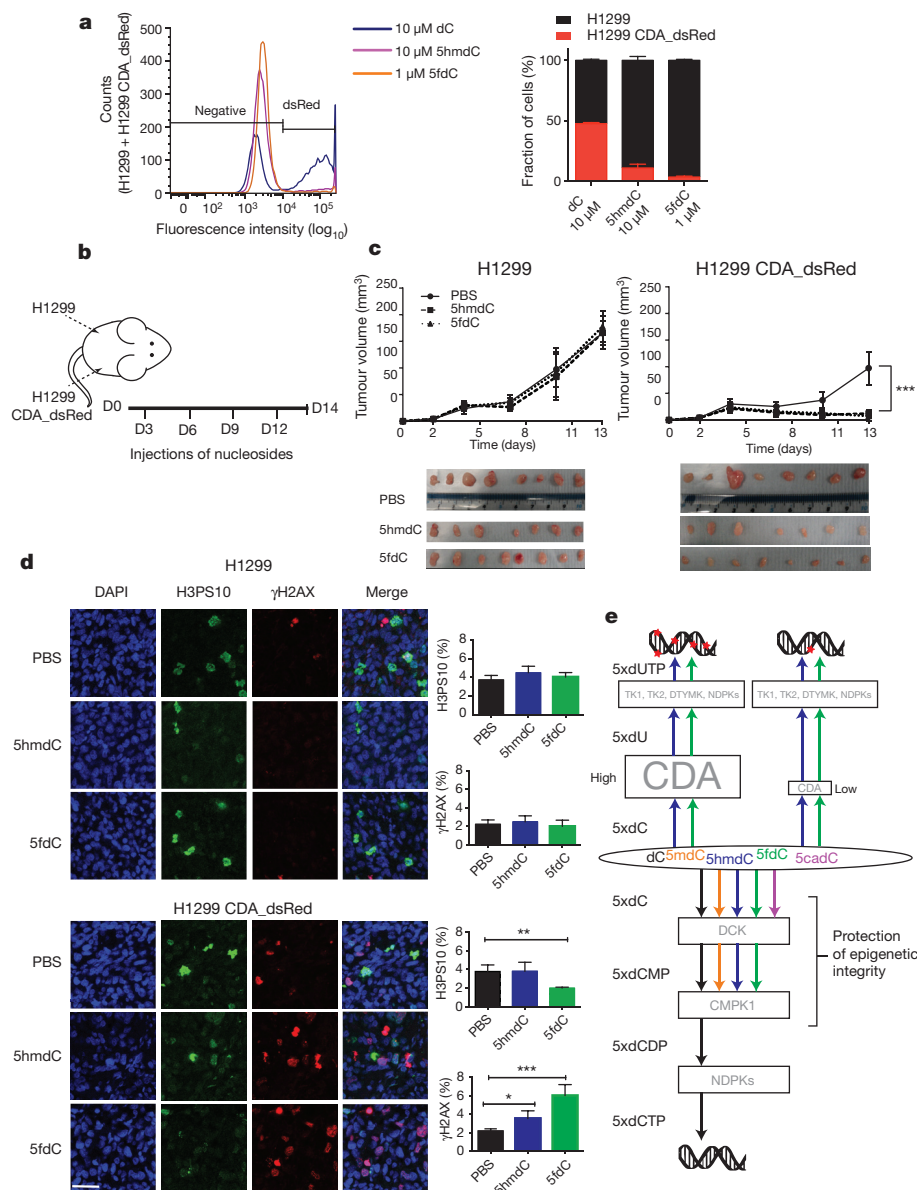
CDA overexpression has been linked to resistance to cytidine analogues—such as gemcitabine, cytosine arabinoside or 5-azacytidine—that are currently used in cancer treatment, presenting a major obstacle to their use^{11,24–26}. Our observations about biological nucleoside variants demonstrate an opposite effect: CDA overexpression sensitizes cells to otherwise non-toxic 5hmdC and 5fdC. Because cancers originating in the pancreas²⁷, stomach, testis and vagina have upregulated CDA expression²⁸ (Extended Data Fig. 7a, b), we postulated that the administration of 5hmdC and 5fdC could have a selective activity against these tumour cells. We first tested whether cytotoxic activity is cell autonomous for CDA-overexpressing H1299 cells in the presence of wild-type (CDA-low) H1299 cells. Both 5hmdC and 5fdC were able to eliminate CDA-overexpressing cells selectively, suggesting that secreted CDA or 5hmdU is insufficient for cytotoxicity (Fig. 4a). Tolerance to and the stability of 5hmdC and 5fdC *in vivo* was determined in immunocompromized BALB/cOlaHsd-Foxn1^{nu/nu} mice after they received a range of doses (12.5 to 100 mg kg⁻¹) of 5hmdC and 5fdC by intraperitoneal injection. Half an hour after injection, we were able to detect 5hmdC and 5fdC in the bloodstream, and to

quantify 5hmdC using RapidFire mass spectrometry (Extended Data Fig. 7c, d). We observed no adverse effects on behaviour, injection site, weight or histology in the panel of tissues studied, even though some tissues (kidney and intestine) express CDA (Extended Data Fig. 7e–h, data not shown). To determine whether cytidine variants have an effect on tumour growth in proliferating cells, we subcutaneously injected H1299 wild-type and CDA-overexpressing cells into each side of an animal, which was later treated with 5hmdC or 5fdC (Fig. 4b). Xenografts with CDA overexpression grew slightly slower (reaching 64% of wild-type tumour volume), and the volume of the tumour was further reduced twofold in animals treated with 5hmdC or 5fdC (Fig. 4c). CDA-overexpressing tumours showed a twofold decrease in the number of proliferating cells and a threefold increase in the number of cells with DNA damage in 5fdC-injected animals, but smaller differences in animals that were injected with 5hmdC (Fig. 4d). Similar CDA-dependent effects on tumour volume and proliferation were observed when SN12C wild-type and SN12C CDA knockdown cells were used in the xenograft assay (Extended Data Fig. 8).

Here, we have characterized the metabolism of newly discovered biologically modified nucleosides, leading to a model in which the selectivity of CMPK1 prevents random incorporation of modified cytosines (Fig. 4e). Notably, we have discovered that 5hmdC and

Figure 4 *In vivo* evaluation of cytidine variants and the proposed model of epigenetic nucleoside variants in the nucleoside recycling pathway.

a, Wild-type and CDA-overexpressing H1299 cells were mixed at equal ratios and exposed to the indicated variants of cytidine. Representative histogram (left) and quantification of the results (right) are shown ($n = 3$, 10,000 events recorded). Lower concentrations of 5fdC were used to demonstrate higher cytotoxic potency. **b**, Schematic illustration of xenograft establishment and treatment with nucleoside variants. D, days. **c**, Volume of tumours, calculated by assuming that tumours were spheres with their diameters measured using Vernier calipers ($n = 8$ in 5fdC and $n = 7$ in 5hmdC experiments, two-way analysis of variance (ANOVA) with repeated measures Holm–Sidak correction, $P < 0.0001$). Dissected tumours are illustrated below. **d**, Evaluation of proliferation (immunofluorescence, H3PS10) and DNA damage (immunofluorescence, γ H2AX) in dissected tumour samples. Scale bar, 50 μ m ($n = 4$, one-way ANOVA, H3PS10: $**P = 0.0057$, γ H2AX: $*P = 0.0491$ (5hmdC versus PBS), $***P = 0.0001$ (5fdC versus PBS)). Error bars denote s.d. **e**, Model of metabolism of epigenetic nucleoside variants.



5fdC, but not 5cadC, are deaminated by CDA at different rates, resulting in the formation of cytotoxic 5hmdU and 5fdU. Our data on oxidized epigenetic bases are similar to the proposed mechanism of 5mdC salvage, in which CMPK1 is rate-limiting in the production of the diphosphate, whereas 5mdC deamination produces a normal T (refs 4–6). We did not observe any adverse effects during the administration of 5hmdC and 5fdC in mice, presumably because the cytotoxic threshold is only reached in highly proliferating and CDA-overexpressing cells, in which there is substantial incorporation of nucleoside variants in the DNA, reflected by the CDA-dependent regression of xenografts. Together with recent publications demonstrating the importance of and therapeutic opportunities targeting MTH1, which surveys damaged nucleosides^{29,30}, our data extend the current understanding of the metabolism of biological cytidine variants and provide a novel avenue for cancer therapy.

Online Content Methods, along with any additional Extended Data display items and Source Data, are available in the online version of the paper; references unique to these sections appear only in the online paper.

Received 10 November 2014; accepted 24 June 2015.

Published online 22 July 2015.

- Riggs, A. D. X inactivation, differentiation, and DNA methylation. *Cytogenet. Cell Genet.* **14**, 9–25 (1975).
- Wigler, M., Levy, D. & Peruchio, M. The somatic replication of DNA methylation. *Cell* **24**, 33–40 (1981).
- Gruenbaum, Y., Cedar, H. & Razin, A. Substrate and sequence specificity of a eukaryotic DNA methylase. *Nature* **295**, 620–622 (1982).
- Vilpo, J. A. & Vilpo, L. M. Nucleoside monophosphate kinase may be the key enzyme preventing salvage of DNA 5-methylcytosine. *Mutat. Res.* **286**, 217–220 (1993).
- Jekunen, A., Puukka, M. & Vilpo, J. Exclusion of exogenous 5-methyl-2'-deoxycytidine from DNA in human leukemic cells. A study with [2-(¹⁴C)]- and [methyl-¹⁴C]5-methyl-2'-deoxycytidine. *Biochem. Pharmacol.* **32**, 1165–1168 (1983).
- Jekunen, A. & Vilpo, J. A. 5-Methyl-2'-deoxycytidine. Metabolism and effects on cell lethality studied with human leukemic cells *in vitro*. *Mol. Pharmacol.* **25**, 431–435 (1984).
- Kriaucionis, S. & Heintz, N. The nuclear DNA base 5-hydroxymethylcytosine is present in Purkinje neurons and the brain. *Science* **324**, 929–930 (2009).
- Tahiliani, M. *et al.* Conversion of 5-methylcytosine to 5-hydroxymethylcytosine in mammalian DNA by MLL partner TET1. *Science* **324**, 930–935 (2009).
- Ito, S. *et al.* Tet proteins can convert 5-methylcytosine to 5-formylcytosine and 5-carboxylcytosine. *Science* **333**, 1300–1303 (2011).
- Pfaffeneder, T. *et al.* The discovery of 5-formylcytosine in embryonic stem cell DNA. *Angew. Chem.* **50**, 7008–7012 (2011).
- Frese, K. K. *et al.* nab-Paclitaxel potentiates gemcitabine activity by reducing cytidine deaminase levels in a mouse model of pancreatic cancer. *Cancer Discov.* **2**, 260–269 (2012).
- Löffler, M., Fairbanks, L. D., Zameitat, E., Marinaki, A. M. & Simmonds, H. A. Pyrimidine pathways in health and disease. *Trends Mol. Med.* **11**, 430–437 (2005).
- Hershey, H. V., Stieber, J. F. & Mueller, G. C. DNA synthesis in isolated HeLa nuclei. A system for continuation of replication *in vivo*. *Eur. J. Biochem.* **34**, 383–394 (1973).
- Arner, E. S. & Eriksson, S. Mammalian deoxyribonucleoside kinases. *Pharmacol. Ther.* **67**, 155–186 (1995).
- Boissan, M. *et al.* The mammalian Nm23/NDPK family: from metastasis control to cilia movement. *Mol. Cell. Biochem.* **329**, 51–62 (2009).
- Xu, Y., Johansson, M. & Karlsson, A. Human UMP-CMP kinase 2, a novel nucleoside monophosphate kinase localized in mitochondria. *J. Biol. Chem.* **283**, 1563–1571 (2008).
- Lin, K. T., Momparler, R. L. & Rivard, G. E. High-performance liquid chromatographic analysis of chemical stability of 5-aza-2'-deoxycytidine. *J. Pharm. Sci.* **70**, 1228–1232 (1981).
- Petitjean, A. *et al.* Impact of mutant p53 functional properties on TP53 mutation patterns and tumor phenotype: lessons from recent developments in the IARC TP53 database. *Hum. Mutat.* **28**, 622–629 (2007).
- Ross, D. T. *et al.* Systematic variation in gene expression patterns in human cancer cell lines. *Nature Genet.* **24**, 227–235 (2000).
- Barretina, J. *et al.* The Cancer Cell Line Encyclopedia enables predictive modelling of anticancer drug sensitivity. *Nature* **483**, 603–607 (2012).
- Nabel, C. S. *et al.* AID/APOBEC deaminases disfavor modified cytosines implicated in DNA demethylation. *Nature Chem. Biol.* **8**, 751–758 (2012).
- Chung, S. J., Fromme, J. C. & Verdine, G. L. Structure of human cytidine deaminase bound to a potent inhibitor. *J. Med. Chem.* **48**, 658–660 (2005).
- Boorstein, R. J., Chiu, L. N. & Teebor, G. W. A mammalian cell line deficient in activity of the DNA repair enzyme 5-hydroxymethyluracil-DNA glycosylase is resistant to the toxic effects of the thymidine analog 5-hydroxymethyl-2'-deoxyuridine. *Mol. Cell. Biol.* **12**, 5536–5540 (1992).
- Weizman, N. *et al.* Macrophages mediate gemcitabine resistance of pancreatic adenocarcinoma by upregulating cytidine deaminase. *Oncogene* **33**, 3812–3819 (2013).
- Eliopoulos, N., Cournoyer, D. & Momparler, R. L. Drug resistance to 5-aza-2'-deoxycytidine, 2',2'-difluorodeoxycytidine, and cytosine arabinoside conferred by retroviral-mediated transfer of human cytidine deaminase cDNA into murine cells. *Cancer Chemother. Pharmacol.* **42**, 373–378 (1998).
- Qin, T. *et al.* Mechanisms of resistance to decitabine in the myelodysplastic syndrome. *PLoS ONE* **6**, e23372 (2011).
- Pei, H. *et al.* FKBP51 affects cancer cell response to chemotherapy by negatively regulating Akt. *Cancer Cell* **16**, 259–266 (2009).
- Shin, G. *et al.* GENT: gene expression database of normal and tumor tissues. *Cancer Inform.* **10**, 149–157 (2011).
- Gad, H. *et al.* MTH1 inhibition eradicates cancer by preventing sanitation of the dNTP pool. *Nature* **508**, 215–221 (2014).
- Huber, K. V. *et al.* Stereospecific targeting of MTH1 by (S)-crizotinib as an anticancer strategy. *Nature* **508**, 222–227 (2014).

Supplementary Information is available in the online version of the paper.

Acknowledgements We acknowledge Ludwig Cancer Research and BBSRC for funding; R. Klose, T. Milne, G. Bond, M. Muers and members of the Kriaucionis laboratory for the discussions and critical reading of the manuscript. M. Shipman for his technical assistance in image acquisition and analysis; I. Ratnayaka and R. Lisle for assistance with histology; S. Laird and J. Tanner for help with animal experiments; X. Lu, S. Lunardi and G. Bond for providing cell lines; P. Filippakopoulos for advice on molecular docking. B.M.K. was supported by the John Fell Fund 133/075 (BMK) and the Wellcome Trust 097813/Z/11/Z.

Author Contributions M.Z. performed all experiments, with the following exceptions: mass spectrometry was done by G.B., M.-L.T., K.M.P. and B.M.K.; gene expression analysis was done by S.K.; analysis of tissue pathology was done by R.G. S.K. conceived the study, S.K. and M.Z. designed experiments and wrote the manuscript.

Author Information Reprints and permissions information is available at www.nature.com/reprints. The authors declare no competing financial interests. Readers are welcome to comment on the online version of the paper. Correspondence and requests for materials should be addressed to S.K. (skirmantas.kriaucionis@ludwig.ox.ac.uk).

METHODS

Purification of DCK, CMPK1, CDA, TMPK and DUT. Human DCK with a carboxy-terminal 6×His tag was cloned in pET28a(+) and expressed in *Escherichia coli* BL21 RIPL (Life Technologies) for 4 h at 37 °C following induction with 1 mM isopropyl β-D-1-thiogalactopyranoside (IPTG) in LB. The bacterial pellet was resuspended in 50 mM sodium phosphate, pH 8, 300 mM NaCl and protease inhibitors (Complete EDTA-free, Roche). The protein was bound to a Hi-TRAP HP 5 ml column (GE Healthcare) and eluted with a linear gradient of 0–500 mM imidazole in the lysis buffer, supplemented with 10% glycerol. The fractions were assessed by electrophoresis and ones containing the protein were pooled, concentrated with Amicon 3-kDa centrifugal filter units (Millipore) and separated on a HiPrep 16/60 Sephacryl S-200 gel filtration column (GE Healthcare). The protein was again concentrated using Amicon columns, supplemented with final 10 mM dithiothreitol (DTT) and 40% of glycerol, snap-frozen and stored in aliquots at –80 °C. Human CMPK1 was tagged at the C terminus with 6×His and purified using a similar workflow to DCK with the following exceptions: the lysis buffer was 50 mM Tris, pH 7.5, 10 mM NaCl and protease inhibitors (Complete Mini, Roche); after the gel-filtration step the protein was bound to an anion exchange column HiTrap Q HP 5 ml (GE Healthcare) and eluted with a 20-column-volumes linear gradient of 0–1 M NaCl. The salt was removed by dialysis in 50 mM Tris, pH 8, the protein concentrated and 10 mM DTT added to the final preparation, before storage in 40% glycerol at –80 °C. C-terminal 6×His-tagged CDA was purified in a similar workflow to CMPK1 with the following modifications: the protein was expressed for 19 h at 37 °C; the lysis buffer was 50 mM Tris, pH 7.5, 1 mM DTT, 1 mM EDTA and protease inhibitors (Complete Mini, Roche); following HiTRAP purification, 6×His tag was cleaved by thrombin (Sigma); cleaved tag and uncleaved protein was removed by separation using a HiTRAP HP 5 ml column and collection of the flow-through. Subsequently, the protein was purified using gel filtration as indicated above and stored in aliquots at –80 °C. Protein purity was assessed by electrophoresis and CDA was additionally identified by mass spectrometry. Human TMPK1 with a C-terminal 6×His tag was cloned in pET28a(+) and expressed in *E. coli* BL21 RIPL (Life Technologies) for 4 h at 37 °C following induction with 1 mM IPTG in LB. The bacterial pellet was resuspended in 50 mM sodium phosphate, pH 7, 300 mM NaCl and protease inhibitors (Complete EDTA-free, Roche) and lysed with a French press (EmulsiFlex C5, Avestin) at ~100 MPa equipped with a recirculating cooler (F250, Julabo) set at 4 °C. The protein was bound to a Hi-TRAP HP 5 ml column (GE Healthcare) and eluted with a linear gradient of 0–500 mM imidazole in the lysis buffer, supplemented with 10% glycerol. The fractions were assessed by electrophoresis and ones containing the protein were pooled, concentrated with Amicon 3 kDa centrifugal filter units (Millipore), supplemented with 40% of glycerol, snap frozen in aliquots and stored at –80 °C. Human DUT with a C-terminal 6×His tag was cloned in pET28a(+) and expressed in *E. coli* BL21 RIPL (Life Technologies) for 4 h at 37 °C following induction with 0.2 mM IPTG in LB. The bacterial pellet was resuspended in 20 mM sodium phosphate pH 7.3, 150 mM NaCl, 1% Triton X-100 and protease inhibitors (Complete EDTA-free, Roche) and lysed with a French press (EmulsiFlex C5, Avestin) at ~100 MPa equipped with a recirculating cooler (F250, Julabo) set at 4 °C. The protein was bound to a Hi-TRAP HP 5 ml column (GE Healthcare) and eluted with a linear gradient of 0–500 mM imidazole in the lysis buffer, supplemented with 10% glycerol. The fractions were assessed by electrophoresis and ones containing the protein were pooled, concentrated with Amicon 3 kDa centrifugal filter units (Millipore), supplemented with 40% of glycerol, snap frozen and stored in aliquots at –80 °C. Thymidine kinase was purchased and the purity assessed by SDS–PAGE (8180-TK-050, R&D Systems).

Nucleoside stability. Nucleosides were obtained from the following sources: 5hmdC (PY-7588, Berry & Associates), 5fdC (PY-7589, Berry & Associates), 5cadC (PY-7593, Berry & Associates), 5azadC (A3656, Sigma Aldrich), ATP solution (Thermo Fisher), [γ - 32 P]ATP (Perkin Elmer), dC (Sigma Aldrich, D3897), dCMP (Sigma Aldrich, D7625), 5hmdCTP (Bioline, BIO-39046). 100 μ M solutions of 5hmdC, 5fdC and 5azadC were prepared in HPLC-grade water (Thermo Fisher) or in DMEM (Lonza). The solutions were incubated at 37 °C for 10 days. A sample was taken every 24 h and subjected to HPLC–UV analysis.

Enzyme assays. The substrate selectivity of DCK and CMPK1 kinases were measured by 32 P transfer and detection using 1D or 2D TLC. 1 μ g of DCK was incubated in 100 mM Tris, pH 7.5, 100 mM KCl, 10 mM MgCl₂, 1 mM [γ - 32 P]ATP and 200 μ M of the respective nucleoside in a 50 μ l reaction volume at 37 °C for 2 h. 1 μ l of products was separated via 2D TLC on glass-backed AVICEL cellulose plates (Analtech) as described³¹. CMPK1 was assayed through a coupled assay with DCK following the conditions described previously³² with 1 μ g DCK, 1 μ g CMPK1 and 1 mM substrate. Thymidine kinase (8180-TK-050, R&D Systems) and TMPK1 were assayed through a coupled assay with 1 μ g thymidine kinase, 1 μ g TMPK1 and 1 mM substrate in 50 mM Tris, pH 7.4,

50 mM KCl, 5 mM MgCl₂, 1 mM ATP and 2.5 μ Ci [γ - 32 P]ATP at 37 °C. 1D TLC was performed using glass-backed TLC sheets (PEI cellulose F, Millipore) as described previously³². The plates were exposed to a storage phosphor screen (GE Healthcare), which was scanned using PhosphorImager (Biorad) and images analysed with ImageLab software (Biorad). CDA kinetic activity data was collected as described³³ by monitoring the absorbance at 260 nm with a spectrophotometer (SpectraMax M2, Molecular devices) using 45 ng of enzyme (500 ng for 5hmdC) and the data fitted according to pseudo zero order Michaelis–Menten enzyme kinetic model by Prism software (GraphPad). 1 μ g DUT was assayed in 50 mM Tris, pH 7.5, 4 mM MgCl₂, 1 mM DTT, 0.1 mg ml^{–1} BSA with 5 μ M of substrate in 40 μ l reaction volume for 10 min at 37 °C. The generated pyrophosphate was detected with a bioluminescent coupled assay (PPLight inorganic pyrophosphate assay LT07-500, Lonza). The plate was then read in a GloMax instrument (Promega).

Molecular docking. A tetramer was generated with CDA structure 1MQ0 (ref. 22) and subject to DockPrep in Chimera 1.8 (<http://www.cgl.ucsf.edu/chimera>). Substrates were dC (ZINC18286013)³⁴, 5hmdC (ZINC77300654)³⁴ and 5fdC (CSID:10291642) (<http://www.chemspider.com>) downloaded as .mol files and subjected to .mol2 files conversion in Chimera. Docking was subsequently performed with SwissDock (<http://www.swissdock.ch/docking>)³⁵. The model with the lowest Δ G of ligand was then visualized and analysed with Chimera.

In vitro replication assay. The assay was carried out following protocols for nuclear extract and cytoplasmic fraction preparation and for the replication assay^{13,36}. The reaction contained 0.3 mM of each canonical nucleotide, except dCTP which was substituted by 5hmdCTP. The reaction was stopped with the addition of 0.1 M EDTA final. DNA was extracted with phenol and chloroform, treated with RNase A/T1 (Thermo Fisher) and free nucleotides removed with a Mini Quick Spin DNA column (Roche) before HPLC assay.

DNA glycosylase assay. The single stranded DNA oligonucleotide substrates (5'-FAM CATAAAGTGXAAAGCCTGGA, in which X denotes uracil, 5hmdUra or 5fUra) were purchased from AtdBio and their complementary strand from IDT (all HPLC purified). Recombinant human SMUG1 (NEB) was incubated with annealed oligonucleotides as described before³⁷. The reaction products were resolved on a 15% denaturing polyacrylamide TBE–urea gel (Invitrogen) and quantified using ChemoDoc (BioRad) with blot detection protocol for Alexa 488.

Quantification of nucleosides by HPLC. Genomic DNA was extracted with Gene Jet Genomic DNA extraction Kit (Thermo Fisher) or TRI Reagent (Sigma Aldrich), incubated with RNase A/T1 (Thermo Fisher) in buffer 2 (NEB), phenol/chloroform extracted and precipitated with ethanol. 1–10 μ g of DNA was hydrolysed as described before⁷. Nucleosides were resolved with an Agilent UHPLC 1290 instrument fitted with Eclipse Plus C18 RRHD 1.8 μ m, 2.1 \times 150 mm column and detected with Agilent 1290 DAD fitted with a Max-Light 60 mm cell. Buffer A was 100 mM ammonium acetate, pH 6.5; buffer B was 40% acetonitrile, and the flow rate 0.4 ml min^{–1}. The gradient was between 1.8–100% of 40% acetonitrile with the following steps: 1–2 min, 100% A; 2–16 min 98.2% A, 1.8% B; 16–18 min 70% A, 30% B; 18–20 min 50% A, 50% B; 20–21.5 min 25% A, 75% B; 21.5–24.5 min 100% B.

Quantification of nucleotides by HPLC. MDA-MB-231 and H1299 cells were treated with 10 μ M dC, 10 μ M 5hmdC and 1 μ M 5fdC. Metabolites were extracted at day 3 as described before³⁸. In brief, cells were washed in PBS and scraped on ice. The pellet was washed again in cold PBS and extraction was done with 50 μ l of ice-cold 50% ACN per mg of pellet. The samples were vortexed and incubated on ice for 10 min. Insoluble material was pelleted at 20,000g for 10 min and supernatants were dried using a SpeedVac (Thermo Scientific). Metabolites were dissolved in 30 μ l of buffer A and 20 μ l was used for chromatography. HPLC was performed as described³⁸ with some minor modifications as listed below. Nucleotides were resolved with an Agilent UHPLC 1290 instrument fitted with Eclipse Plus C18 RRHD 1.8 μ m, 2.1 \times 150 mm column and detected with Agilent 1290 DAD fitted with a Max-Light 60 mm cell at 254, 260 and 280 nm. Buffer A consisted of 100 mM KH₂PO₄ (60221, Sigma) with 8 mM tetrabutylammoniumbisulfate (98479, Sigma) set at pH 5.5. Buffer B consisted of buffer A with 25% methanol. After 8 min at 0% buffer B, the gradient started with a linear increase of buffer B to 35% in 19 min, followed by a linear increase from 35% to 38% buffer B in 5 min and from 38% to 100% buffer B in 22 min. After an 8-min hold at 100% buffer B, the gradient was reversed from 100% to 0% buffer B in 2 min, followed by a hold at 0% buffer B for 2 min. The column temperature was set at 30 °C and the flow rate was 0.4 ml min^{–1}. The compounds were identified by comparing their retention times and their UV spectra with those of known standards, which were purchased from Sigma-Aldrich. The integrated area was used to quantify the relative abundance of nucleotides by normalizing each peak area to the ADP area as an indication of loaded amount.

Cell culture and transfections. Cell lines were routinely tested for mycoplasma contamination using Lonza Mycoalert kit. Cell proliferation assays were done by seeding cells in p60 plates or in a T25 flask with appropriate concentrations of

5hmdC, 5fdC or dC in the growth media. The cells were passaged, counted and the media was replaced every 2 days. Before counting, 1 volume of Trypan blue solution (Lonza) was added to an aliquot of single cell suspension. The live cells were counted by TC-20 Cell Counter (Bio-Rad). NTPs were introduced by nucleofection. One million MDA-MB-231 cells were nucleofected with 50 mM 5hmdC in a 100- μ l volume using an Amaxa nucleofector kit (Lonza), following the manufacturer's instructions. After transfection, cells were seeded in a 6-well plate, 24 h later washed twice with PBS, and 48 h later DNA extracted for HPLC analysis.

Production of stable cell lines. Stable cell lines were generated via lentiviral infection using a standard protocol³⁹ with second generation packaging plasmids (pCMV-VSVG, pCMV-dR8.9, a gift from B. Amati). CDA knockdown was achieved by infecting MDA-MB-231 and SN12C cell lines with pLKO.1 vectors containing five different shRNA constructs (SHCLND-NM_001785, Sigma-Aldrich) and a control pLKO.1 containing shRNA silencing luciferase (a gift from X. Lu). Infected cells were selected by incubation with 1.5 μ g ml⁻¹ puromycin (Sigma) for 60 h. Two cell lines with the lowest CDA mRNA levels (shRNA TRCN0000051290 and TRCN0000051288, designated (0) and (8), respectively) were further assessed by immunoblotting and used for experiments. Lentivirus for CDA overexpression was generated with pLenti-puro (39481, Addgene, I.-M. Shih laboratory) expressing dsRed-IRES-CDA. H1299 and MCF-7 were infected as above. Infected cells were selected with puromycin at 2 μ g ml⁻¹ for 60 h.

Immunoblotting, FACS and immunofluorescence. For western blot analysis, 10⁶ cells were lysed with RIPA buffer (20 mM HEPES at pH 7.5, 300 mM NaCl, 5 mM EDTA, 10% glycerol, 1% Triton X-100, supplemented with protease inhibitors (Complete EDTA-free, Roche)) and sonicated. Cleared lysates were electrophoresed and immunoblotted with the following primary antibodies: anti-CDA (Sigma, SAB1300717 1:250), anti-actin (Abcam, ab185058 1:75000). Chemiluminescent detection, after incubation of the membranes with appropriate secondary antibodies, was done through a CCD camera using the ChemiDoc System (Bio-Rad) with Image Lab software (Bio-Rad, version 4.0). For FACS analysis, 5 \times 10⁵ cells were trypsinized, washed in PBS and fixed in 70% ethanol for 1 h on ice. The pelleted cells were resuspended in 250 μ l of staining solution (50 μ g ml⁻¹ propidium iodide (P4864, Sigma), 0.1 mg ml⁻¹ RNaseA and 0.05% Triton X-100) and incubated at 37 °C for 40 min. Controls were used for G1 (serum starvation overnight) and G2 (0.1 μ g μ l⁻¹ nocodazole overnight). Fluorescence of 10,000 cells was recorded with a FACS Canto flow cytometer (BD Biosciences) and analysed using FlowJo software (Version 7.6.5, TreeStar). For immunofluorescence, cells were grown on coverslips and fixed with 4% paraformaldehyde for 20 min at room temperature. Cells were washed twice in PBS and permeabilized for 10 min in 0.2% Triton X-100. After two washes in PBS, cells were blocked for 1 h in 3% BSA (Sigma Aldrich), dissolved in PBS and incubated with γ H2A.X antibody (Millipore, 05-636, 1:500) overnight at 4 °C in a humidified chamber. Cells were then washed three times in PBS and incubated with anti-mouse secondary antibody conjugated with Alexa546 (1:400, Life Technologies) and DAPI (Sigma Aldrich). Coverslips were then washed three times in PBS and mounted with mounting media (Vectashield). Tiled pictures were automatically taken with a Zeiss 710 microscope with a 20 \times lens. The amount of nuclear fluorescence was quantified using ImageJ.

Gene expression analysis and public data sets. Data sets used in the study: Gene Expression Omnibus (GEO) accessions GSE36139 (GPL15308)²⁰ and GSE32474 (GPL570)⁴⁰. Gene expression analysis comparing was done on the data from the NCI-60 panel¹⁹ as follows. Affy HG-U133 Plus 2.0 microarray data was downloaded from CellMiner database (<http://discover.nci.nih.gov/cellminer/loadDownload.do>) and cell files were extracted for triplicate experiments done on BR:MCF7, ME:MDA_MB_435, BR:MDA_MB_231 and LC:HOP_92 cell lines. Data was then imported into ArrayStar v11 (DNASTar) and signal normalization and intensity correction was done using RMA Quantile method. Experiment was designed by grouping BR:MCF7, ME:MDA_MB_435 cell lines into 'resistant' group and BR:MDA_MB_231 and LC:HOP_92 cell lines into 'sensitive' group. Differential expression between the groups was determined using the Student's *t*-test with Benjamini-Hochberg multiple testing correction. Genes were called as differentially expressed when *P* < 0.01 and fold change > 2. The full data set is included in Supplementary Table 1. To derive CDA expression values in tumours, GPL15308 (ref. 20) and GPL570 (ref. 40) were analysed directly on the NCBI portal with GEO2R. *P* values were adjusted with Benjamini-Hochberg correction.

Toxicology and dose determination in animal experiments. Animal work was done after approval by the UK Home Office and University of Oxford Local Ethical review. Three 5–7-week-old BALB/cOlaHsd-Foxn1^{nu/nu} (Harlan) mice per dose were injected (intraperitoneally) with 25, 50 and 100 mg kg⁻¹ of 5hmdC and 12.5, 25, 50 and 100 mg kg⁻¹ of 5fdC. Animals were monitored for any deviations from normal behaviour. At 30 min post-injection, a few drops of blood were collected through tail vein bleeding using Microvette CB300 (Sarstedt) to assess the amounts of the compounds in the bloodstream.

RapidFire mass spectrometry analysis of serum samples. Serum was isolated by centrifugation of Microvettes according to the recommendations of the manufacturer (Sarstedt). The samples were brought up to 200 μ l with water and three volumes of methanol, and 150 μ l of chloroform was added. After intense vortexing, 450 μ l of water was added, samples were vortexed again and centrifuged at 14,000g for 1 min. The aqueous phase containing the soluble molecules was collected and dried in a Speedvac (Thermo Scientific). The dried pellets were then resuspended in 10 μ l water, then 3 μ l diluted further into 50 μ l of water to load on a RapidFire 360 high throughput sample delivery system coupled to a 6530 quadrupole time-of-flight (QTOF) mass spectrometer (Agilent). The samples were aspirated by vacuum at -40 bar for 400 ms into a 10- μ l sample loop and loaded onto a graphitized carbon solid phase extraction cartridge running buffer 5 mM ammonium formate at a flow of 1.5 ml min⁻¹. The matrix components not retained on the cartridge were diverted to waste for 4,500 ms, and the retained components eluted with 95% acetonitrile 5 mM ammonium formate for 4,500 ms at a flow of 1 ml min⁻¹. The SPE was then re-equilibrated for 4,500 ms with 5 mM ammonium formate. Data were collected in positive electrospray ionisation (ESI) mode using a 2 Gb data configuration, gas temperature 300 °C, drying gas 8 l min⁻¹, nebuliser gas ~240 MPa, Vcap 3,500 V and fragmentor voltage 175 V. The amount of nucleoside was measured against a standard curve produced by dissolving known amounts of 5hmdC and 5fdC in serum and processed as indicated above. Data were analysed using an Agilent Mass Hunter Qualitative (vB.06) and Quantitative (vB.05) analysis software. Standard curve analysis was determined by using a quadratic curve fit algorithm for each nucleoside with an *R*² > 0.98 in all instances.

Nucleoside analysis by mass spectrometry (HPLC-QTOF). Samples were dried in a speed-vac and re-suspended in 10 μ l of water. For the analysis by HPLC-QTOF mass spectrometry, a 1290 Infinity UHPLC was fitted with a BEH C18 XP Column, (130 Å, 1.7 μ m, 2.1 mm \times 150 mm; Waters) and coupled to a 6560 Ion mobility QTOF LC/MS mass spectrometer (Agilent Technologies) equipped with a Jetstream ESI-AJS source. The data were acquired in QTOF mode using positive electrospray ionisation (ESI+). Two reference ions, *m/z* 121.0508 and 922.0097 were used as internal standards. The Dual AJS ESI settings were as follows: gas temperature: 150 °C, the drying gas: 5 l min⁻¹, nebulizer 240 MPa, sheath gas temperature 360 °C, sheath gas flow 12 l min⁻¹, Vcap 4,000 V and nozzle voltage 300 V. The fragmentor of the mass spectrometer TOF was set to 275 V.

The gradient used to elute the nucleosides started by a 1-min isocratic gradient composed with 99.5% buffer A (10 mM ammonium acetate, pH 6) and 0.5% buffer B (composed of 40% CH₃CN) with a flow rate of 0.350 ml min⁻¹ and was followed by the subsequent steps: 1–2 min, 98.2% A; 2–16 min 80% A; 16–18 min 50% A; 18–20 min 25% A; 20.20–21.5 min 0% A; 21.5–22.5 min 100% B; 22.5–24.5 min 99.5% B. The gradient was followed by a 5 min post time to re-equilibrate the column.

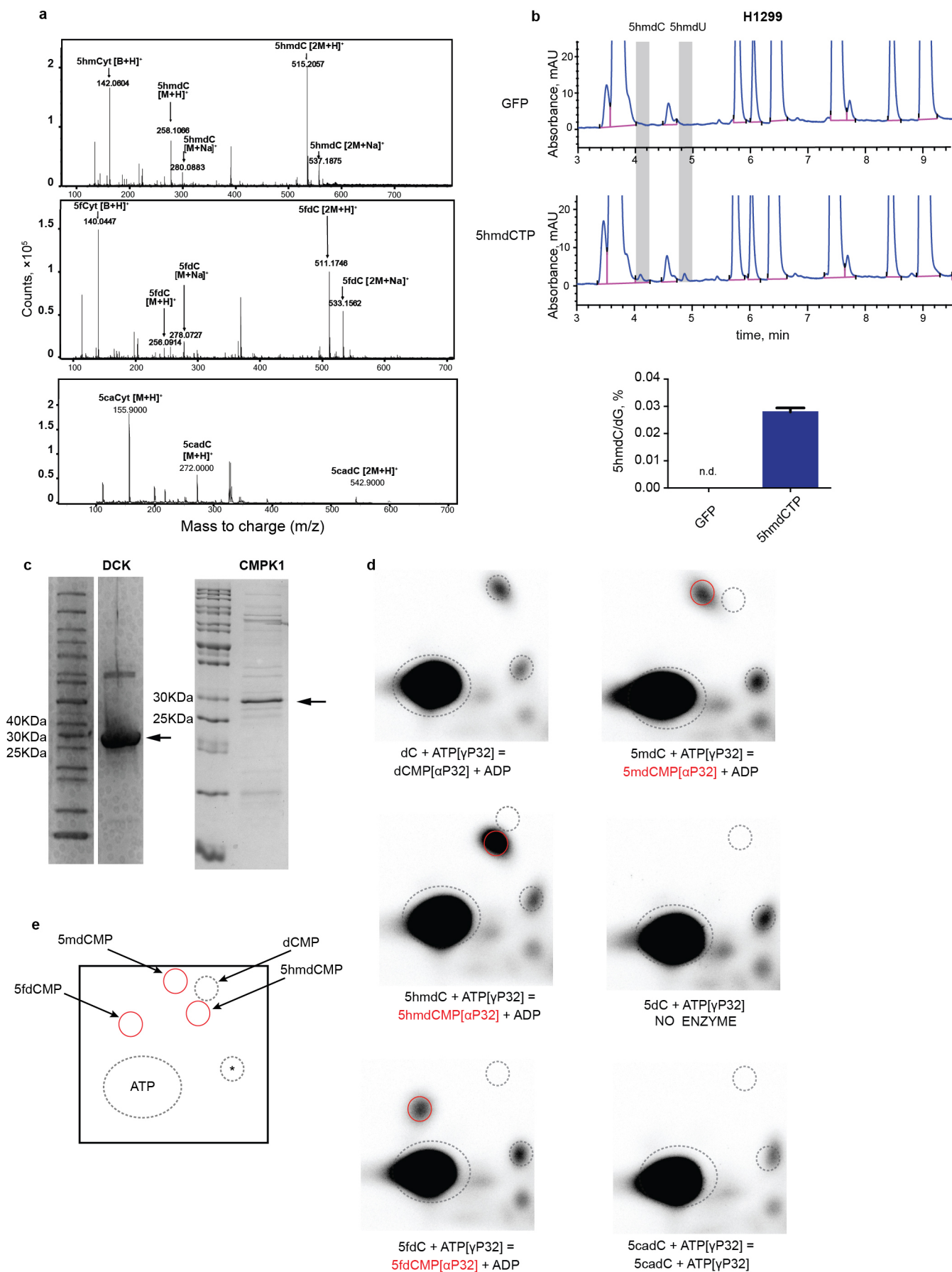
The raw mass spectrometry data was analysed using the MassHunter Qual Software package (Agilent Technologies, version B7.0), and the masses/retention times used for the characterization of nucleosides and their adducts are summarized in Supplementary Table 2. For the identification of compounds, raw mass spectrometry data were processed using the molecular feature extraction function in the MassHunter software, followed by metabolite searching through mass/isotope matching using the PCDL software (version B.07.00 build 7024.0) and the METLIN database (<https://metlin.scripps.edu/index.php>). For each nucleoside, precursor ions corresponding to the M+H, M+Na, M+K, 2M and base only species were extracted, and the most intense ion species observed for each nucleoside was used for quantification. Identities of peaks eluting at 4.5 and 5.1 min (Figs 1b and 3f) are shown in Extended Data Figs 9 and 10.

Subcutaneous xenografts. Animal work was done after approval by the UK Home Office and University of Oxford Local Ethical review. Power calculations suggested 9–6 animals per group if we were to observe a significant 50% difference in tumour size with power of 90% and s.d. between 40 and 30%. One million cells in a 50% suspension of MatriGel (200 μ l) were injected into 5–7-week-old BALB/cOlaHsd-Foxn1^{nu/nu} (Harlan) mice, 8 animals per group in each flank following the scheme: SN12C/H1299 left, SN12C shCDA8/H1299 dsRedCDA right. When the tumours reached palpable size, 8 mice were assigned randomly to each treatment group: PBS, 100 mg kg⁻¹ of 5hmdC and 100 mg kg⁻¹ 5fdC. The compounds were administered every 72 h (four doses in total). Tumour size was measured every 3 days by Vernier caliper and the animal cohort euthanized when the cumulative tumour diameter in the first animal reached 12 mm. The experimenter was unaware of the cell line genotypes during the measurements. Tumour volume was calculated assuming that the tumours were spheres with the following formula: $4/3\pi (D/2)^3$, in which *D* represents the diameter of the tumour.

Histology. Organs and tumours were collected and immediately fixed in 10% formalin for 48 h. They were then embedded in wax and 4- μ m thick sections cut. All sections were stained with H&E. Tumours were additionally stained with a Masson's Trichrome Stain Kit (Sigma Aldrich) according to the manufacturer instructions.

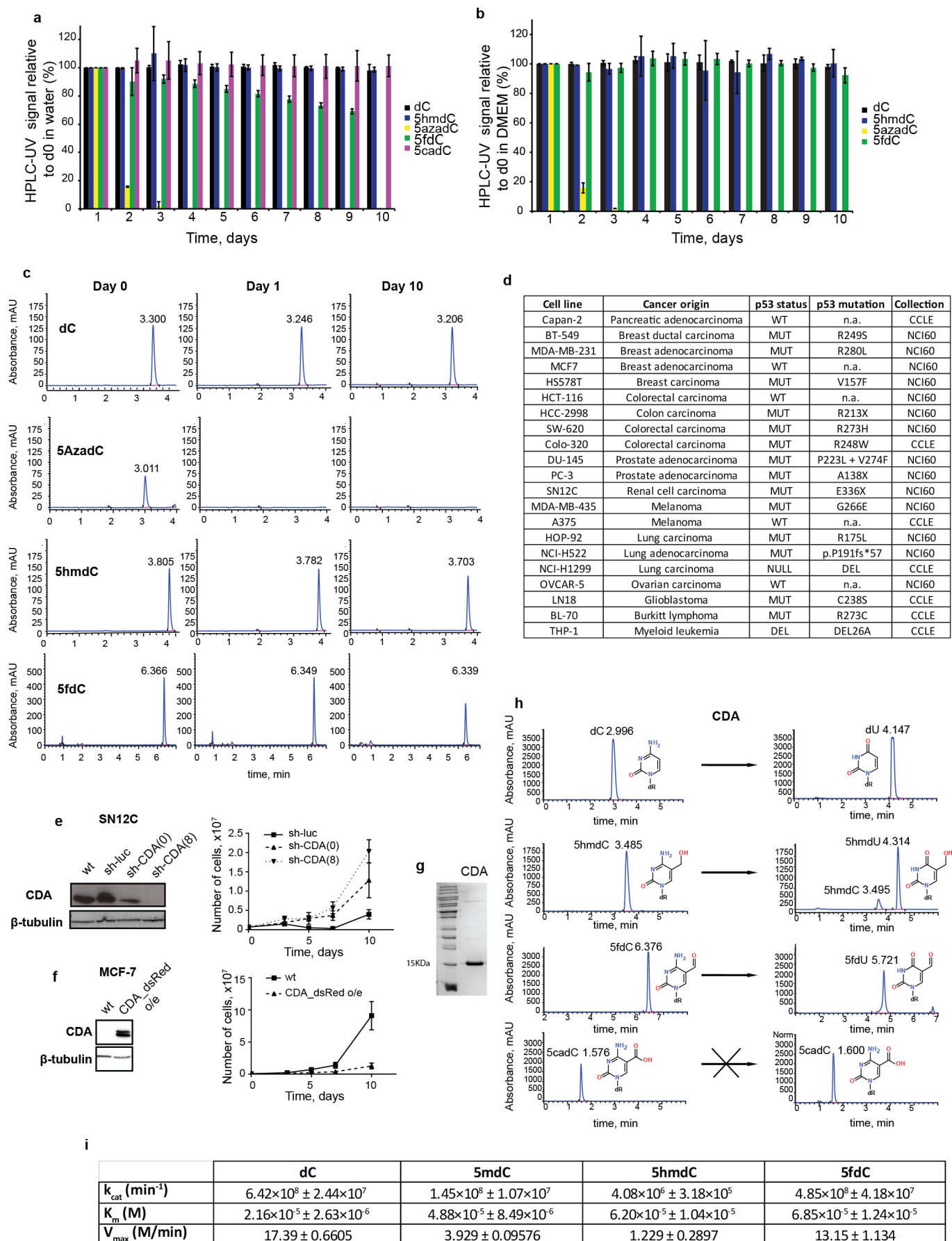
Immunofluorescence of tissues and tumours. The 4- μ m thick sections were subjected to antigen retrieval with a pressure cooker in Tris buffer, pH 9 (10 mM Tris base, 0.05% Tween 20). They were then blocked in 3% BSA in PBS for 30 min and incubated overnight in a humidified chamber at 4 °C with the following antibodies: γ H2A.X (Millipore, 05-636, 1:200) and PH3 (Millipore, 06-570, 1:200) or β -catenin (BD Transduction Laboratories, 610153, 1:250) and CDA (Sigma Aldrich, SAB1300717, 1:100). The slides were then washed vigorously three times in PBS and incubated for 1 h at room temperature with an appropriate secondary antibody, Alexa546 and Alexa488 conjugated (1:400, Life Technologies) and DAPI (Sigma Aldrich). Coverslips were then washed three times in PBS and mounted with mounting media (Vectashield). Images were acquired with a Zeiss 710 confocal microscope with a \times 20 objective. For quantification of DNA damage and proliferation in tumours, tiled images with Z stacks were acquired to cover the entire central section of the tumour. Image J was used to quantify the immunofluorescence signal.

31. Ramsahoye, B. H. Nearest-neighbor analysis. *Methods Mol. Biol.* **200**, 9–15 (2002).
32. Van Rompay, A. R., Johansson, M. & Karlsson, A. Phosphorylation of deoxycytidine analog monophosphates by UMP-CMP kinase: molecular characterization of the human enzyme. *Mol. Pharmacol.* **56**, 562–569 (1999).
33. Vincenzetti, S., Cambi, A., Neuhaud, J., Garattini, E. & Vita, A. Recombinant human cytidine deaminase: expression, purification, and characterization. *Protein Expr. Purif.* **8**, 247–253 (1996).
35. Irwin, J. J., Sterling, T., Mysinger, M. M., Bolstad, E. S. & Coleman, R. G. ZINC: a free tool to discover chemistry for biology. *J. Chem. Inf. Model.* **52**, 1757–1768 (2012).
35. Grosdidier, A., Zoete, V. & Michielin, O. SwissDock, a protein-small molecule docking web service based on EADock DSS. *Nucleic Acids Res.* **39**, W270–W277 (2011).
36. Planck, S. R. & Mueller, G. C. DNA chain growth in isolated HeLa nuclei. *Biochemistry* **16**, 2778–2782 (1977).
37. Kemmerich, K., Dingler, F. A., Rada, C. & Neuberger, M. S. Germline ablation of SMUG1 DNA glycosylase causes loss of 5-hydroxymethyluracil- and UNG-backup uracil-excision activities and increases cancer predisposition of *Ung^{-/-}Msh2^{-/-}* mice. *Nucleic Acids Res.* **40**, 6016–6025 (2012).
38. Dietmair, S., Timmins, N. E., Gray, P. P., Nielsen, L. K. & Kromer, J. O. Towards quantitative metabolomics of mammalian cells: development of a metabolite extraction protocol. *Anal. Biochem.* **404**, 155–164 (2010).
39. MacKenzie, C. J. & Shioda, T. COS-1 cells as packaging host for production of lentiviruses. *Curr. Protocols Cell Biol.* **Chapter 26**, Unit-26.27 (2011).
40. Pfister, T. D. *et al.* Topoisomerase I levels in the NCI-60 cancer cell line panel determined by validated ELISA and microarray analysis and correlation with indenoisoquinoline sensitivity. *Mol. Cancer Ther.* **8**, 1878–1884 (2009).



Extended Data Figure 1 | DNA polymerase and nucleoside kinase activities on modified nucleosides. **a**, Mass spectrometry confirmation of 5hmdC, 5fdC and 5cadC in the purchased nucleosides. **b**, HPLC–UV chromatogram of nucleosides from DNA extracted from H1299 cells transfected with 5hmdCTP. The abundance of 5hmdC relative to dG is illustrated in the right panel ($n = 3$). n.d., not detected. Error bars denote s.d. **c**, Coomassie-stained SDS–PAGE gel of recombinant purified DCK and CMPK1 enzymes used in the study.

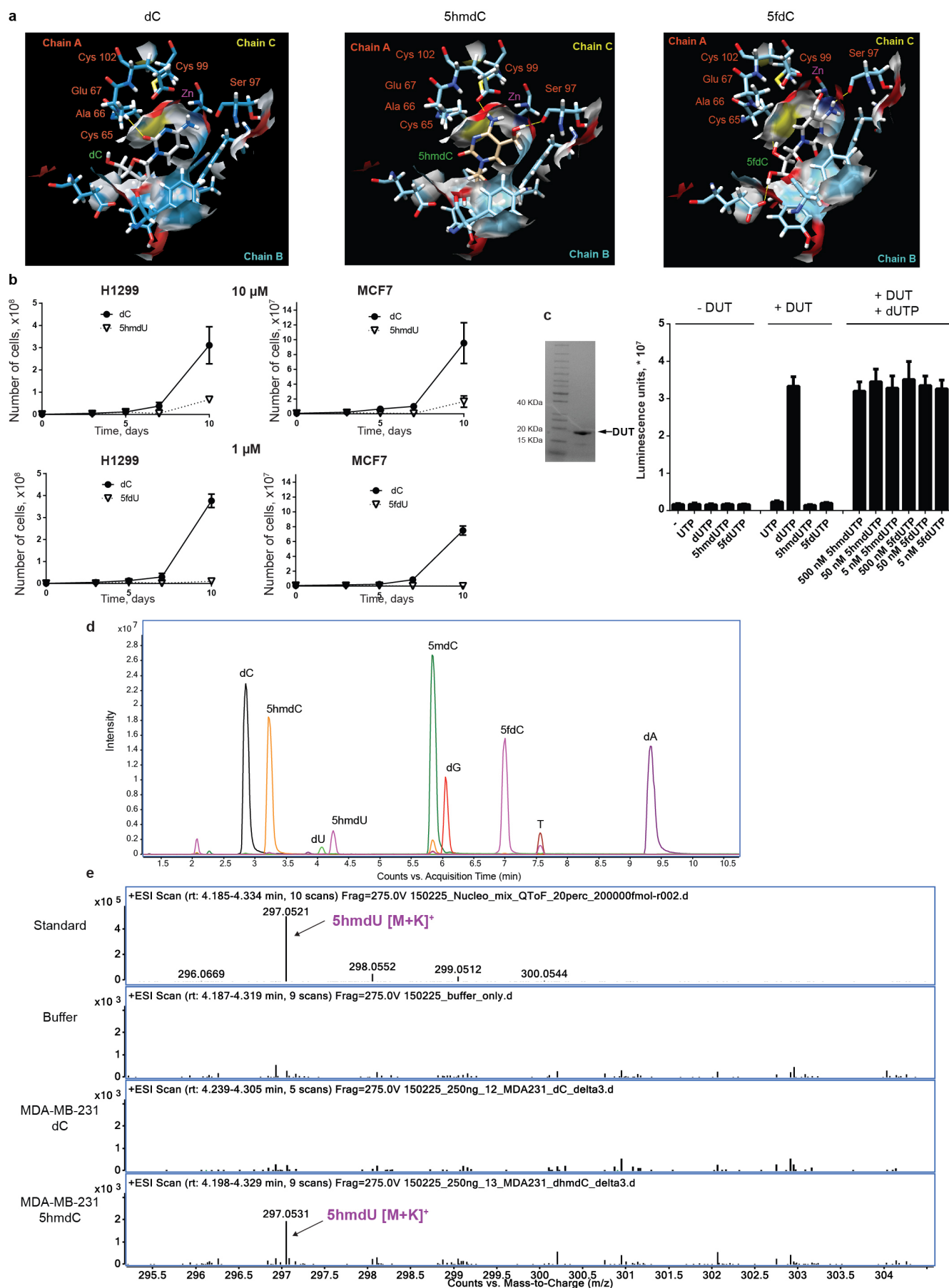
d, Two-dimensional TLC images of DCK reaction products. Dotted lines indicate reference points, which aid in tracking the migration localization of the nucleosides. The monophosphate in each reaction is circled in red (representative picture, $n = 3$). **e**, Schematic map of nucleoside migration on two-dimensional TLC plate (asterisk indicates a background spot coming from ATP and used as a reference point)



Extended Data Figure 2 | Stability of the nucleosides and CDA activity.

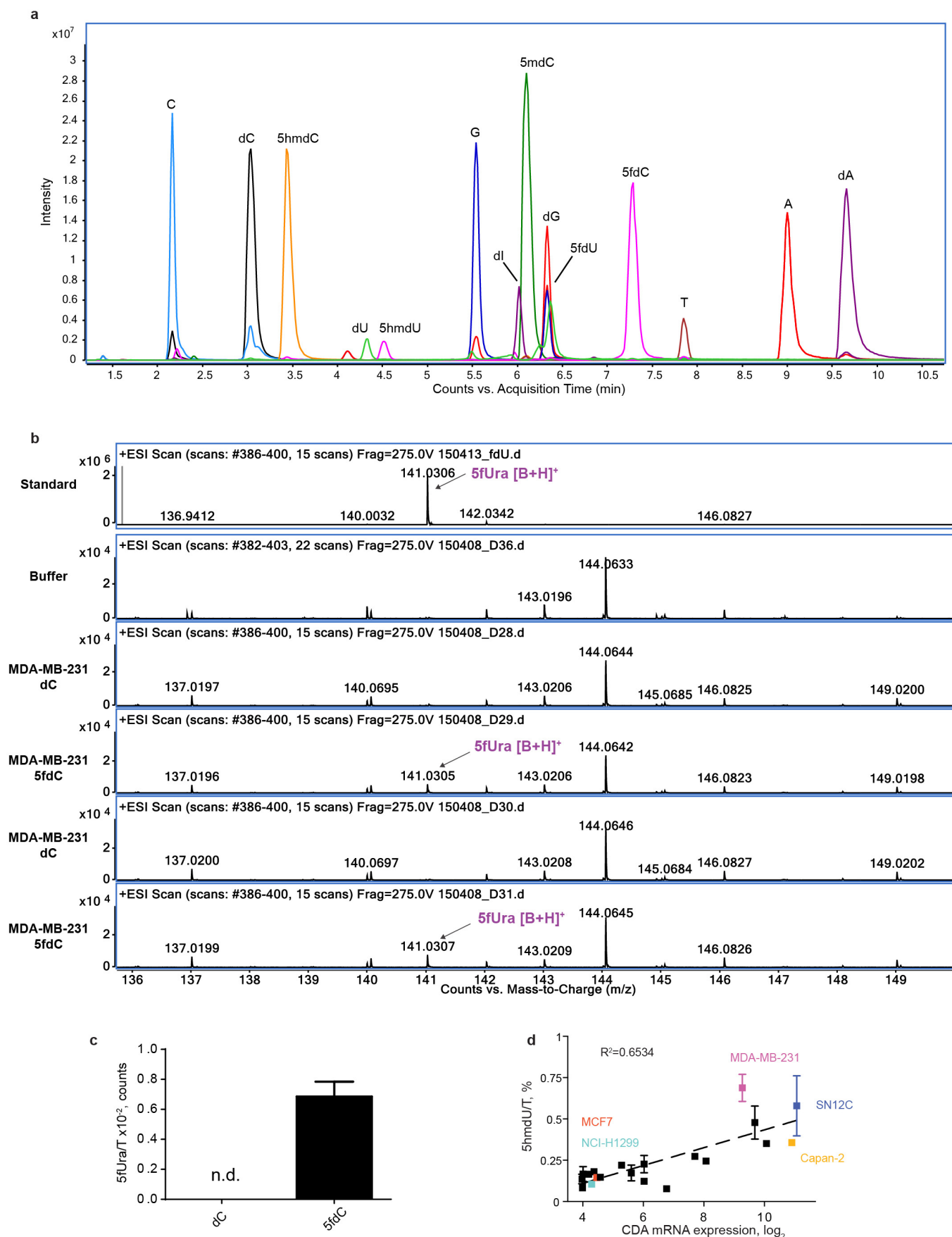
a, b, Quantification of nucleosides by HPLC–UV during 10 days of incubation in water (**a**) and DMEM (**b**) at 37 °C ($n = 3$). **c**, Representative HPLC–UV chromatograms at days 0, 2 and 10 with retention times indicated above each peak. **d**, Cell lines used in the study and their characteristics. **e**, Western blot showing knockdown of CDA by shRNA in the SN12C cell line. Right panel illustrates the growth of the cell line during treatment with 10 μ M 5hmdC ($n = 3$). **f**, Western blot showing expression of CDA in wild-type and

lentivirally transduced MCF7 cell line. Growth curve after treatment with 10 μ M 5hmdC is shown on the right ($n = 3$). **g**, Coomassie-stained SDS–PAGE gel of recombinant purified CDA enzyme used in this study. **h**, HPLC–UV chromatograms showing the retention times and identity of substrates and CDA-catalysed products. **i**, List of K_m , k_{cat} and v_{max} values of catalytic activity of CDA catalysing the deamination of cytidine variants. All error bars denote s.d.



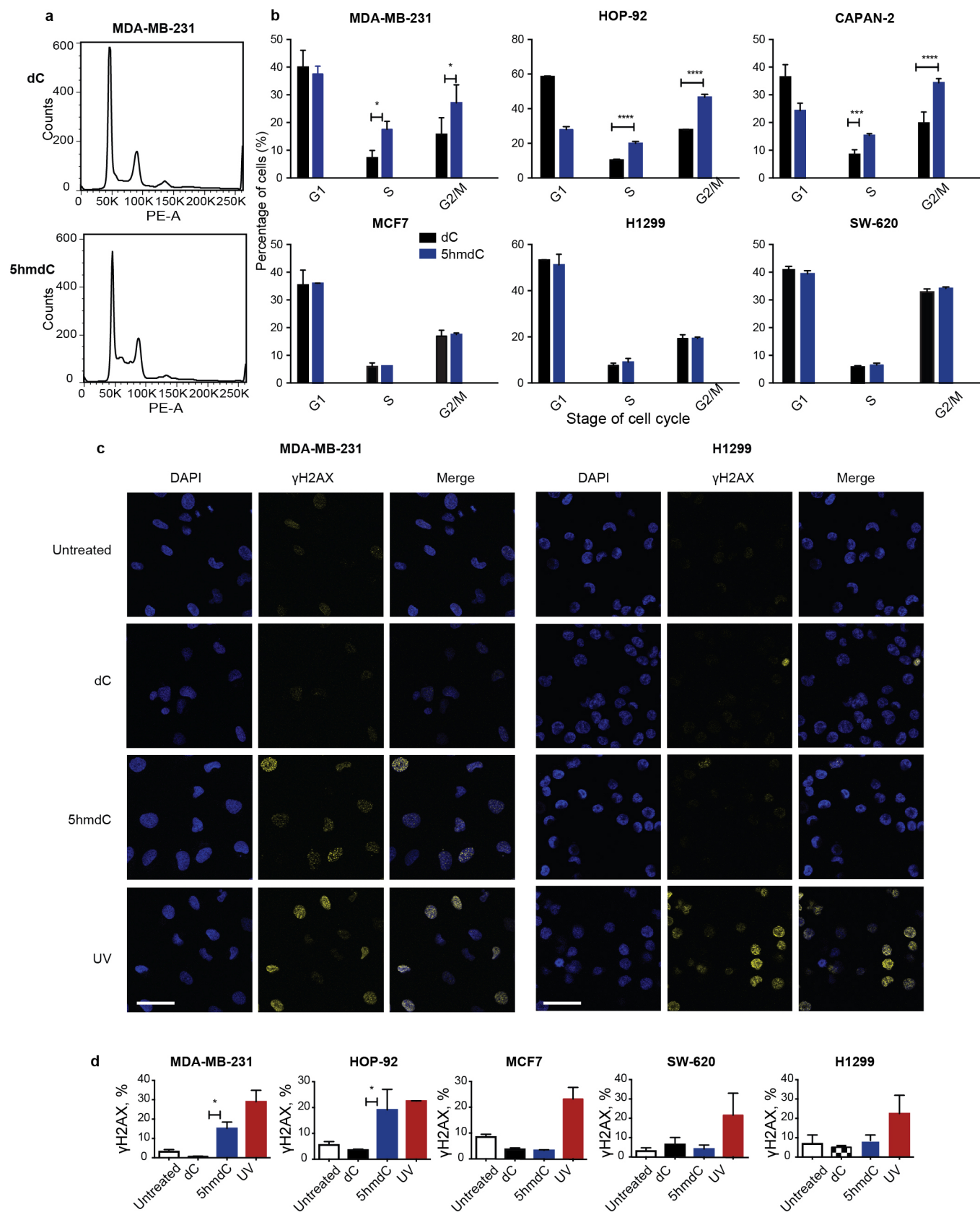
Extended Data Figure 3 | Mechanism of CDA catalysed deamination of epigenetic nucleosides, their cytotoxicity and dUTPase activity. **a**, Molecular docking of dC, 5hmdC and 5fdC on the CDA active site (Protein Data Bank (PDB) accession 1MQ0). The detailed view of the catalytic pocket is shown with the modified nucleoside in the centre. Chains A, B and C indicate units of the tetramer, which CDA forms to deaminate four nucleosides. Thin yellow lines show compatible distances for the formation of hydrogen bonds. **b**, Growth curves of H1299 and MCF7 cell lines treated with 10 and 1 μ M of dC, 5hmdU and 5fdU over a period of 10 days ($n = 3$). **c**, Coomassie-stained gel

demonstrating recombinant purified DUT (molecular mass, 18 kDa) and *in vitro* measurements of dUTPase activity using non-canonical uridine triphosphates ($n = 3$). **d**, Extracted ion chromatogram of nucleoside standards analysed by HPLC–QTOF mass spectrometry. Each nucleoside intensity was measured using the merged m/z values of the $[M+H]^+$, $[M+Na]^+$, $[M+H]^+$, $[2M+H]^+$ and $[base+H]^+$ and a symmetric single m/z expansion of ± 0.02 . **e**, The most prominent ion of 5hmdU was identified in 5hmdC-treated MDA-MB-231 cells. All error bars denote s.d.



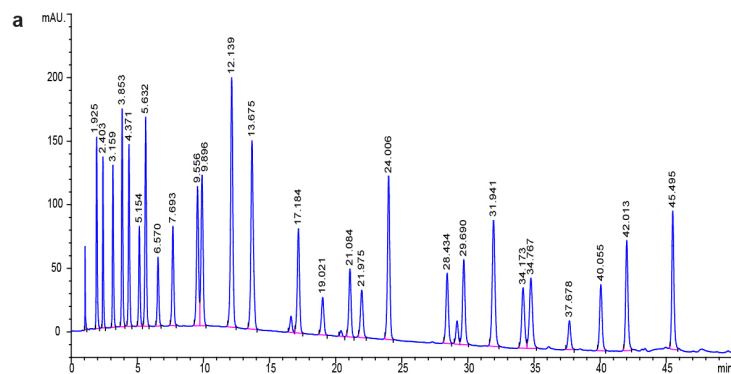
Extended Data Figure 4 | Mass spectrometry identification of 5fUra and ultraviolet quantification of 5hmdU in the DNA. **a**, Extracted ion chromatogram of nucleoside standards with 5fdU analysed by HPLC–QTOF mass spectrometry (as in Extended Data Fig. 3d). **b**, Weak, but consistent signal of 5fUra is identified in DNA of 5fdC-treated MDA-MB-231 cells, but not dC-treated cells or buffer alone. Two representative examples are shown.

c, Relative quantification of 5fUra signal from three biological mass spectrometry replicates. **d**, Relationship between measured 5hmdU/T in the DNA of cell lines treated with 10 μ M 5hmdC for 3 days and CDA expression levels. The cell lines used in this study are in coloured font ($n = 3$). All error bars denote s.d.



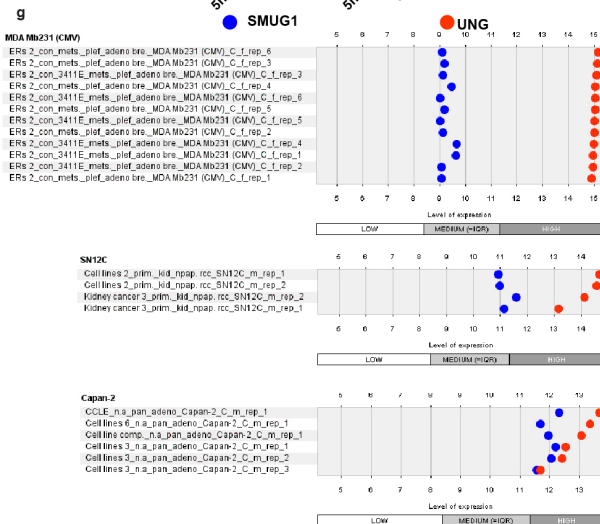
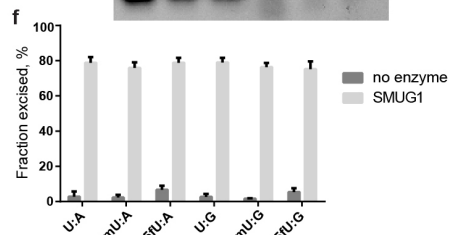
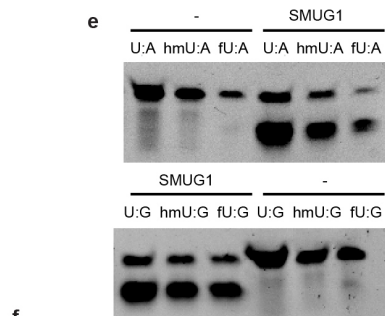
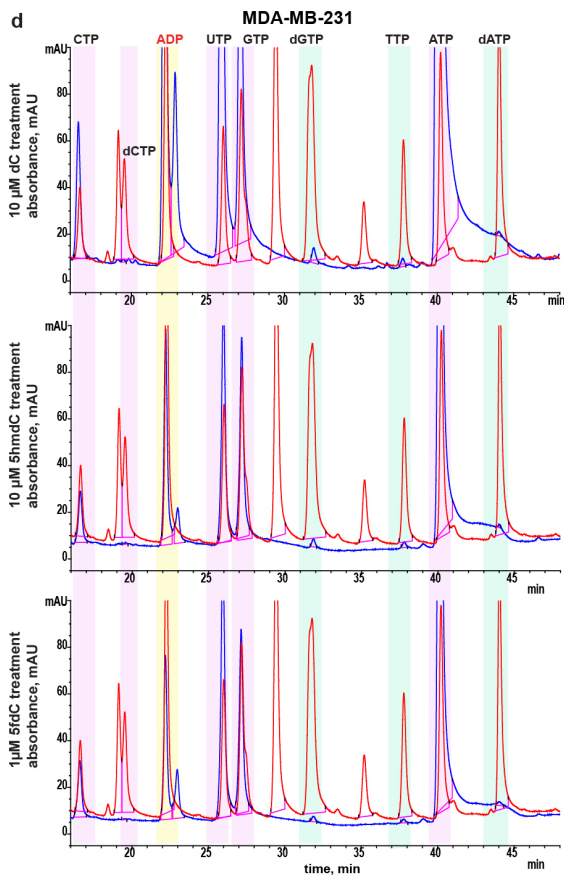
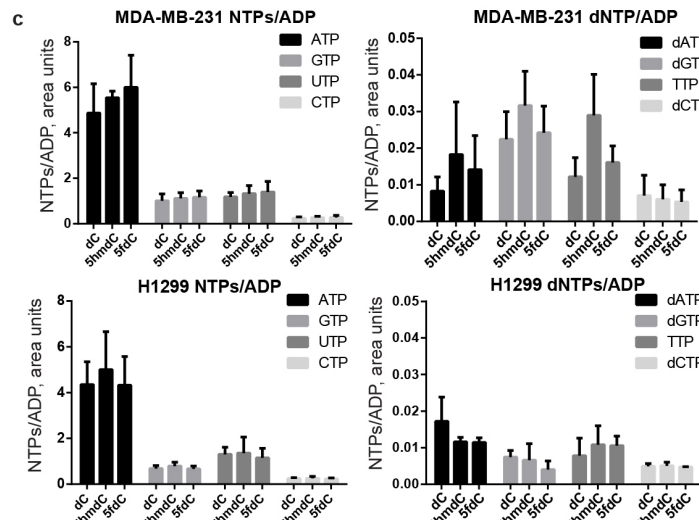
Extended Data Figure 5 | Effect of 5hmdC administration on the cell cycle and DNA damage. **a, b**, Propidium iodide FACS assay of the cell cycle. Shown are two representative plots of MDA-MB-231 cells at day 3 of treatment with dC and 5hmdC (10 μ M) (**a**) and quantification for all the cell lines analysed ($n = 3$) (**b**). Two-way ANOVA: $P = 0.0027$ (S: 5hmdC versus dC MDA-MB-231), $P = 0.0149$ (G2-M: 5hmdC versus dC MDA-MB-231). HOP-92 $P < 0.0001$, $P = 0.0005$ (S: 5hmdC versus dC Capan-2), $P < 0.0001$

(G2-M: 5hmdC versus dC Capan-2) ($n = 3$; 10,000 events acquired). **c**, γ H2AX immunofluorescence in MDA-MB-231 and H1299 cell lines at day 3 after treatment with 10 μ M 5hmdC or dC. Scale bar, 50 μ m. **d**, Fraction of cells showing a γ H2AX signal above background ($n = 3$). ANOVA with Sidak correction for multiple comparisons: $P = 0.0208$ (5hmdC versus dC MDA-MB-231), $P = 0.0135$ (5hmdC versus dC HOP-92). Error bars denote s.d.



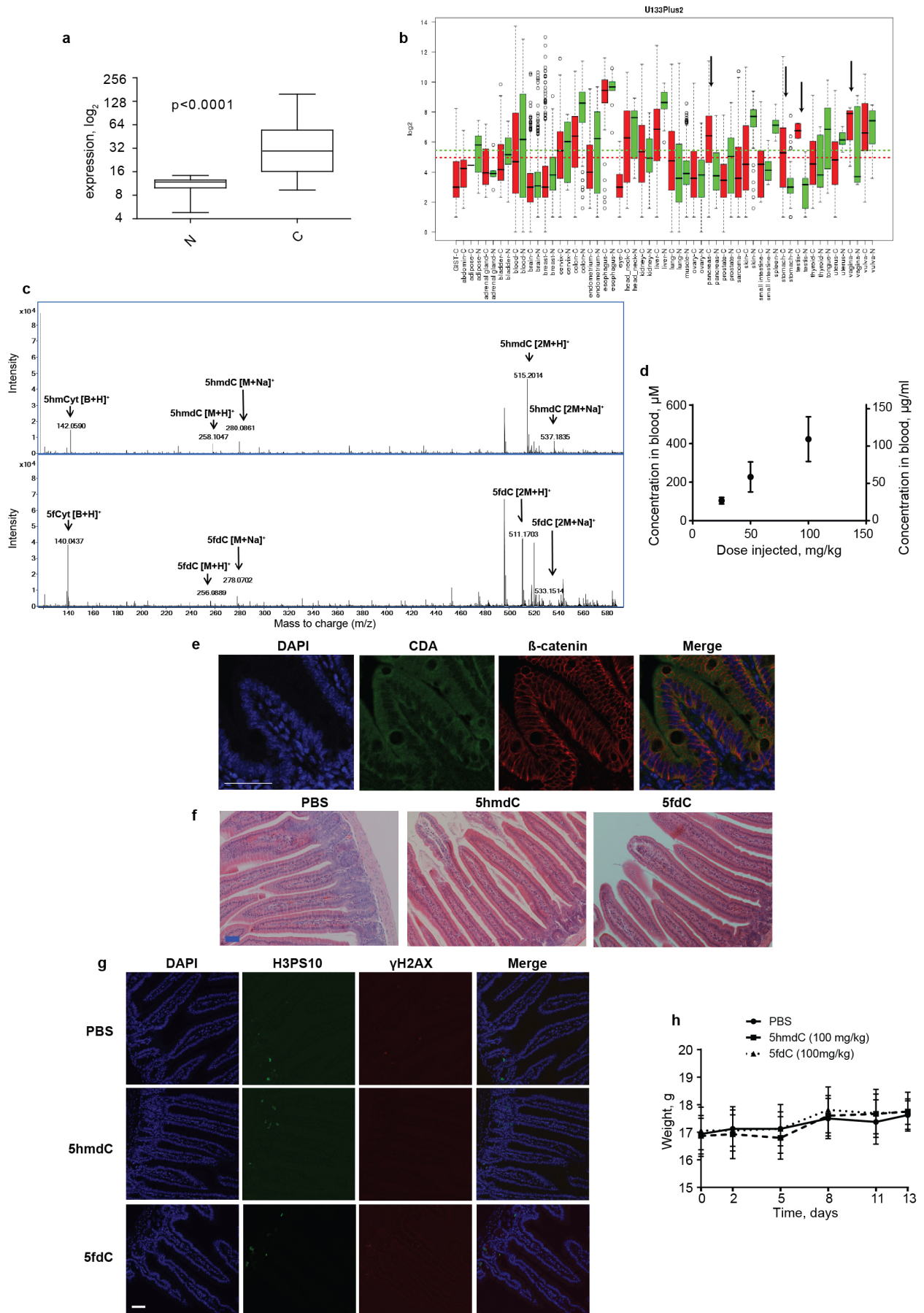
b

Elution time	Nucleotide
1.925	CMP
2.403	dCMP
3.159	UMP
3.853	GMP
4.371	dUMP
5.154	CDP
5.632	dGMP
6.57	dCDP
7.693	TMP
9.556	AMP
9.896	UDP
12.139	GDP
13.675	dAMP
17.184	dGDP
19.021	CTP
21.084	TDP
21.975	dCTP
24.006	ADP
28.434	UTP
29.69	GTP
31.941	dUTP
34.173	5hmdUTP
34.767	dGTP
37.678	5fdUTP
40.055	TTP
42.013	ATP
45.495	dATP



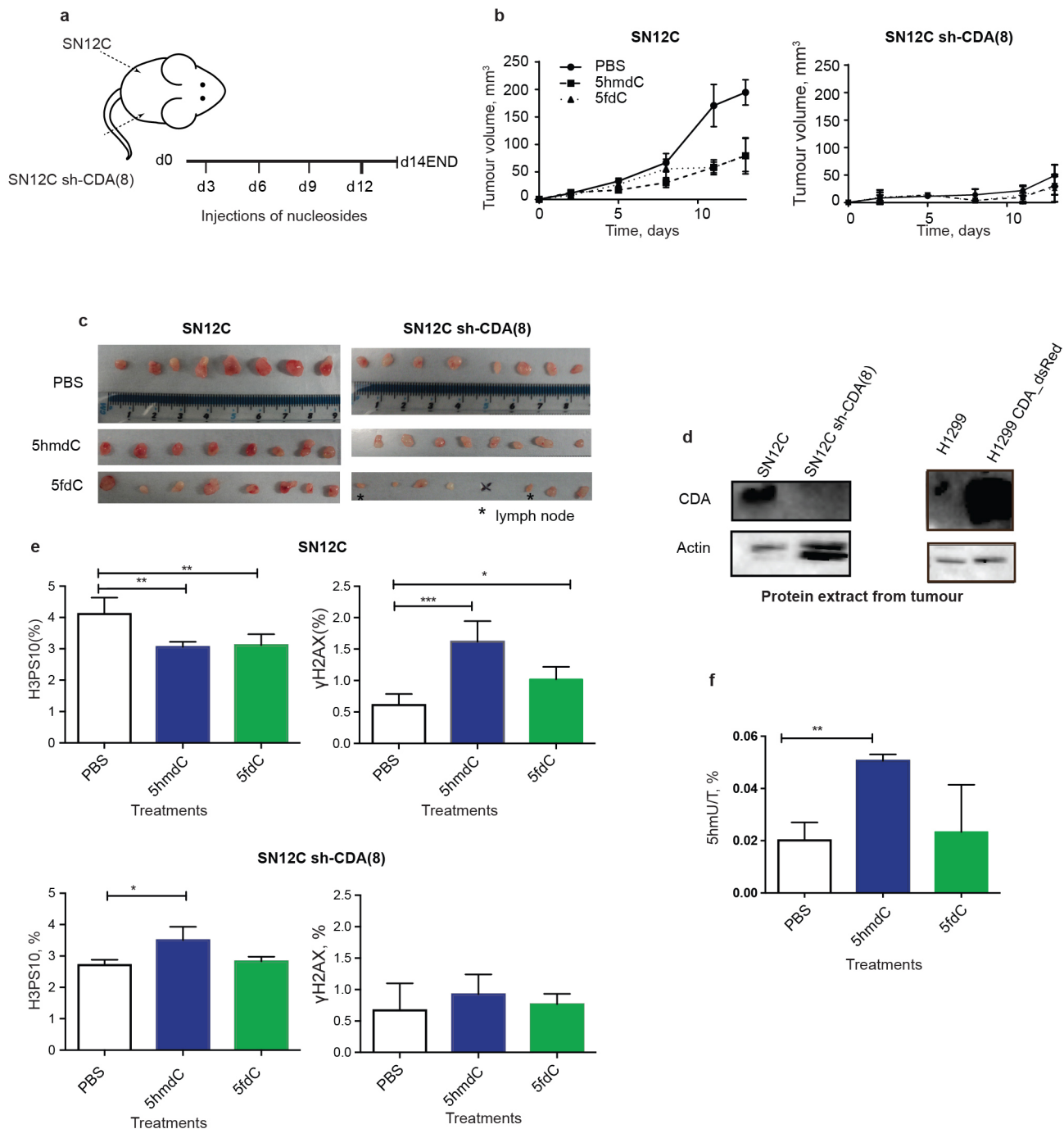
Extended Data Figure 6 | Quantification of intracellular nucleotides by ion-pair HPLC and SMUG1 glycosylase activity. **a**, Illustrative chromatogram of all standards indicated in **b** mixed together. **b**, Retention times of nucleotides were determined by analysing each standard separately and are indicated in the table. **c**, An average relative abundance of NTP and dNTP levels in cells treated with dC, 5hmdC and 5fdC ($n = 3$). **d**, Representative chromatograms of

indicated experiments (blue) overlaid with standards separated on the same run (red). **e**, Typical image of denaturing PAGE electrophoresis of DNA incubated with SMUG1 and cleaved with APE1. **f**, Quantification of the DNA oligonucleotides with excised bases. **g**, Expression of SMUG1 and uracil DNA glycosylase (UNG) in MDA_MB_231, SN12C and Capan-2 cell lines (Genevestigator). Error bars denote s.d.



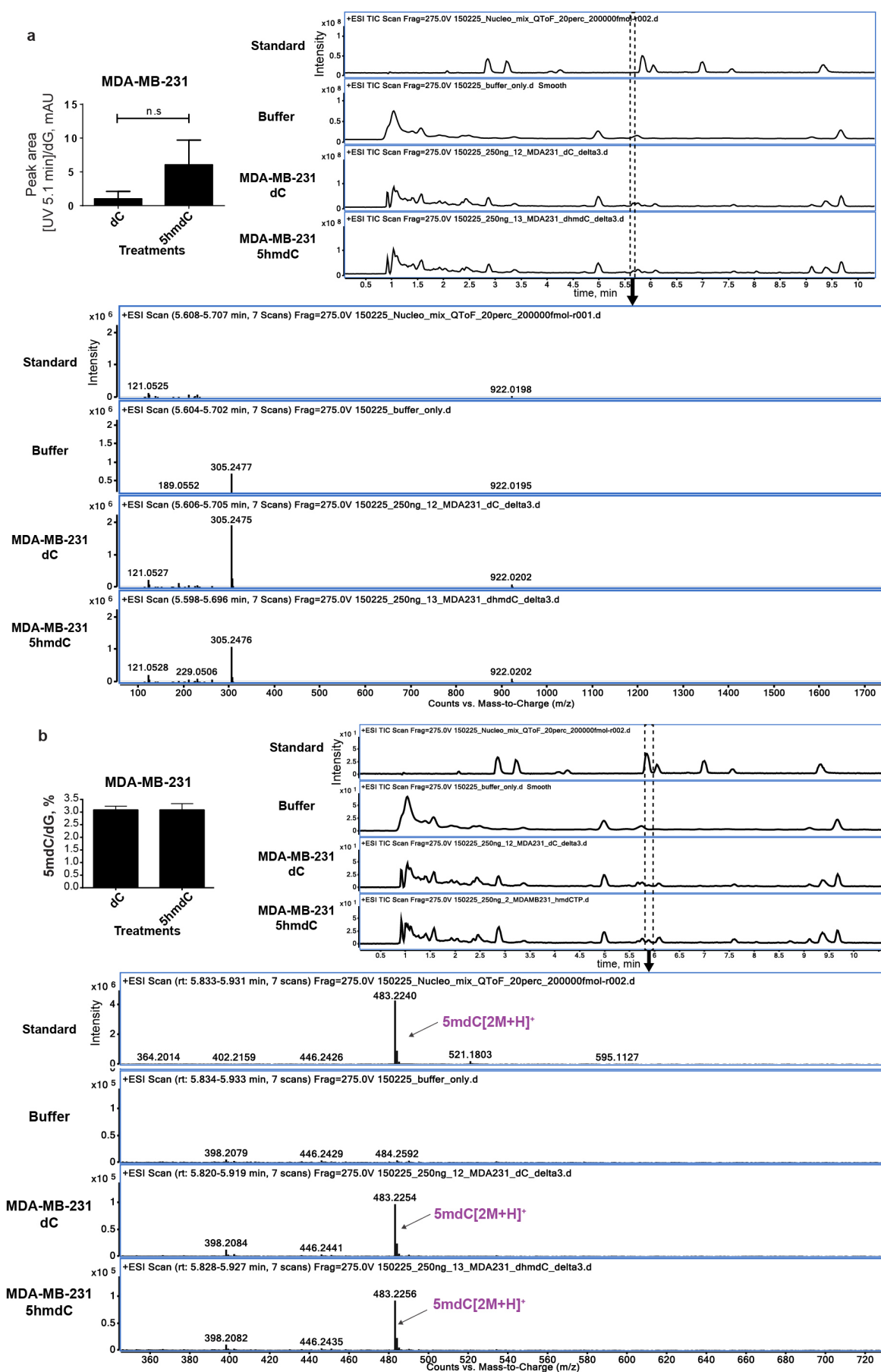
Extended Data Figure 7 | CDA expression in human cancer and normal tissues, and toxicity evaluation of 5hmdC and 5fdC in mice. **a**, CDA overexpression in pancreatic cancer (*t*-test, $P < 0.0001$). **b**, CDA expression across a panel of cancer (red) versus normal (green) tissues (GENT database). Arrows indicate cancer types with an evident difference between normal (N) and cancerous tissues (C). **c**, 5hmdC and 5fdC detection in the blood (mass spectrometry) of intraperitoneally injected mice at 30 min after injection. **d**, Label-free mass spectrometry quantification of 5hmdC in the blood of animals injected with doses of 25, 50 and 100 mg kg⁻¹ ($n = 3$ (100 mg ml⁻¹) and $n = 4$ (25 and 50 mg ml⁻¹)). Error bars denote s.e.m.

e, Immunohistochemistry showing CDA expression in the intestine. **f**, Haematoxylin and eosin staining of the intestine of mice injected with PBS and 100 mg kg⁻¹ of 5hmdC and 5fdC. Tissue was removed 5 days after the injection. **g**, Immunofluorescence evaluation of proliferation (H3PS10) and DNA damage (γ H2AX) in the intestine of mice treated with PBS and 100 mg kg⁻¹ of 5hmdC and 5fdC 5 days after treatment. In parallel, the protocol was done on testis of irradiated mice, where positive signals for γ H2AX were observed (data not shown). Scale bars, 50 μ m (**e–g**). **h**, Weight of the mice plotted over the treatment period ($n = 16$ per group).



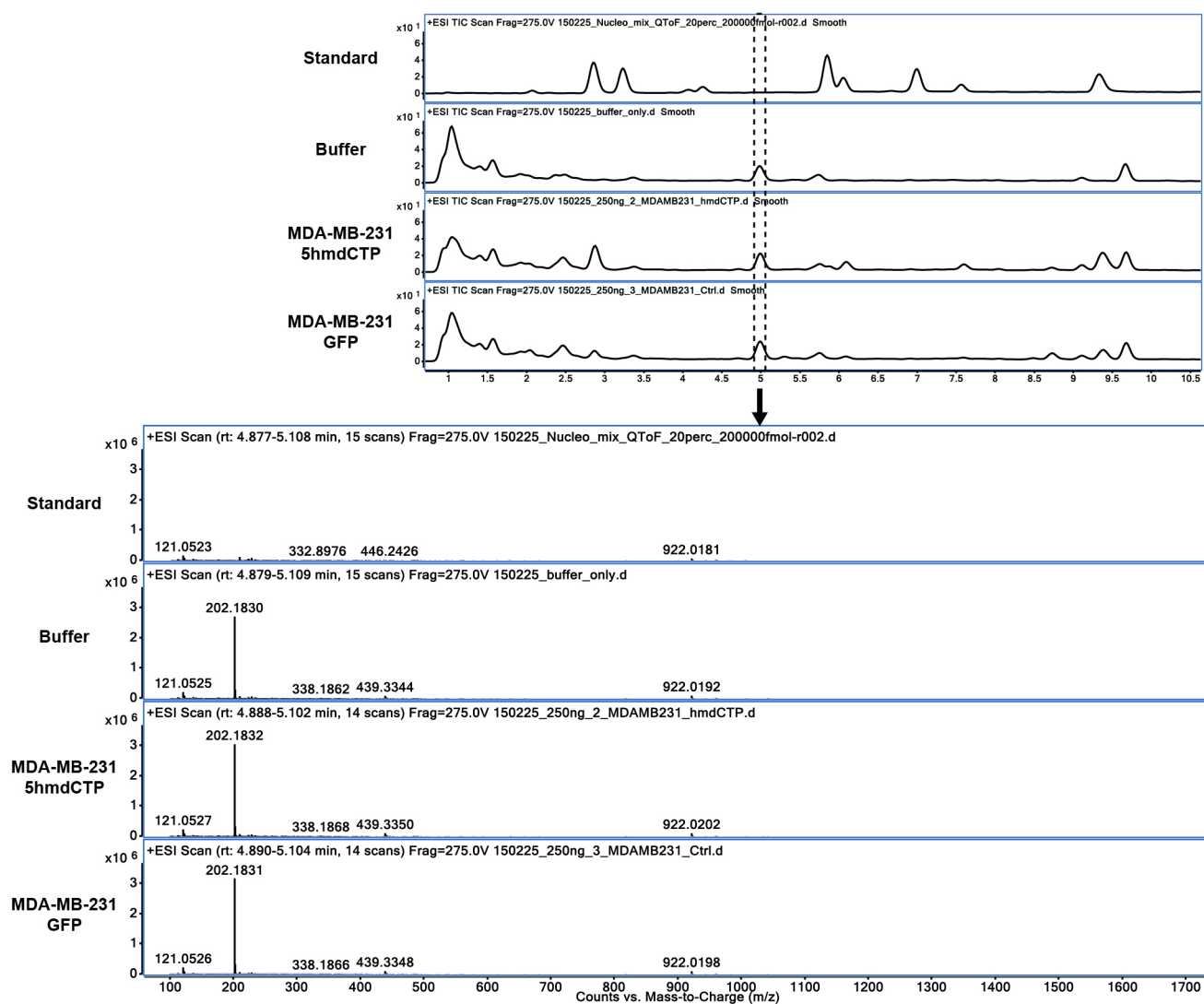
Extended Data Figure 8 | Evaluation of wild-type SN12C cell line and CDA knockdown in a mouse xenograft model. **a**, Schematic illustration of xenograft establishment and treatment with nucleoside variants. **b**, Tumour diameter was measured by Vernier caliper and volume calculated by assuming that tumours were spheres (*n* = 8, two-way ANOVA with repeated measures and Holm–Sidak correction, *P* < 0.0001). **c**, Photos of the dissected tumours (asterisks indicate dissected lymph nodes found after histological analysis). **d**, Western blot showing CDA expression in tumours extracted from

mice. **e**, Quantification of proliferation (H3PS10) and DNA damage (γH2AX) using confocal microscopy and ImageJ of the central section of the tumour. Scale bar, 50 μm (*n* = 4, one-way ANOVA, SN12C H3PS10: *P* = 0.0033 (PBS versus 5hm dC), *P* = 0.0046 (PBS versus 5fdC); γH2AX: *P* = 0.0003 (PBS versus 5hm dC), *P* = 0.0436 (PBS versus 5fdC); SN12CshCDA_8: *P* = 0.0130 (PBS versus 5hm dC)). **f**, 5hmU quantified from a HPLC-UV chromatogram of nucleosides from DNA extracted from tumours of mice treated with 5hm dC and PBS (*n* = 4, one-way ANOVA *P* = 0.0041). Error bars denote s.d.



Extended Data Figure 9 | Identification and quantification of compounds' resulting peaks in HPLC-UV. **a**, The abundance of molecule eluting at 5.1 min (5.7 min on the HPLC-QTOF) is not significantly different between dC- and 5hmdC-treated samples. It is a common component of DNA

hydrolysis buffer. **b**, 5-methylcytosine in the DNA does not change after treatment with 5hmdC. Identity of 5mdC in the samples was confirmed by HPLC-QTOF mass spectrometry.



Extended Data Figure 10 | Identification and quantification of compounds' resulting peaks in HPLC-UV. Compound eluting at 4.5 min (5.0 min on the HPLC-QTOF) is an abundant component of DNA hydrolysis buffer, generating a m/z of 202.18.

Protein synthesis by ribosomes with tethered subunits

Cédric Orelle^{1†*}, Erik D. Carlson^{2,3*}, Teresa Szal¹, Tanja Florin¹, Michael C. Jewett^{2,3} & Alexander S. Mankin¹

The ribosome is a ribonucleoprotein machine responsible for protein synthesis. In all kingdoms of life it is composed of two subunits, each built on its own ribosomal RNA (rRNA) scaffold. The independent but coordinated functions of the subunits, including their ability to associate at initiation, rotate during elongation, and dissociate after protein release, are an established model of protein synthesis. Furthermore, the bipartite nature of the ribosome is presumed to be essential for biogenesis, since dedicated assembly factors keep immature ribosomal subunits apart and prevent them from translation initiation¹. Free exchange of the subunits limits the development of specialized orthogonal genetic systems that could be evolved for novel functions without interfering with native translation. Here we show that ribosomes with tethered and thus inseparable subunits (termed Ribo-T) are capable of successfully carrying out protein synthesis. By engineering a hybrid rRNA composed of both small and large subunit rRNA sequences, we produced a functional ribosome in which the subunits are covalently linked into a single entity by short RNA linkers. Notably, Ribo-T was not only functional *in vitro*, but was also able to support the growth of *Escherichia coli* cells even in the absence of wild-type ribosomes. We used Ribo-T to create the first fully orthogonal ribosome–messenger RNA system, and demonstrate its evolvability by selecting otherwise dominantly lethal rRNA mutations in the peptidyl transferase centre that facilitate the translation of a problematic protein sequence. Ribo-T can be used for exploring poorly understood functions of the ribosome, enabling orthogonal genetic systems, and engineering ribosomes with new functions.

The random exchange of ribosomal subunits between recurrent acts of protein biosynthesis presents an obstacle for making fully orthogonal ribosomes, a task with important implications for fundamental science, bioengineering, and synthetic biology. Previously, it was possible to redirect a subpopulation of the small ribosomal subunits from translating indigenous mRNAs to instead translating a specific mRNA by placing an alternative Shine–Dalgarno sequence in a reporter mRNA and introducing the complementary changes in the anti-Shine–Dalgarno region in 16S rRNA^{2,3}, which enabled selection of mutant 30S subunits with new decoding properties⁴. However, because large subunits freely exchange between native and orthogonal small subunits, creating a fully orthogonal ribosome has been impossible, thereby limiting the engineering of the 50S subunit, including the peptidyl transferase centre (PTC) and the nascent peptide exit tunnel, for specialized new properties.

The orthogonality of the full ribosome could be hypothetically achieved by linking the small and large subunit rRNA into a continuous molecule. A successful chimaeric 16S–23S construct must (1) properly interact with the ribosomal proteins and biogenesis factors for functional ribosome assembly; (2) avoid RNase degradation; and (3) have a linker(s) sufficiently short to ensure subunit *cis*-association, yet long enough for minimal interference with subunit movement required for translation initiation, elongation, and peptide release.

In the native ribosome, the ends of 16S and 23S rRNA are too far apart (>170 Å) to be connected with a nuclease-resistant RNA linker. Therefore, we considered an alternative design in which the 23S rRNA would be ‘grafted’ into the 16S rRNA with the bridges connecting 16S and 23S rRNA sequences located across the rim of the subunits interface. To identify potential linking sites, we connected the native 23S rRNA ends that are proximal to each other, and generated new termini at different locations (Fig. 1a). This circular permutation approach has been successfully exploited *in vitro* previously⁵, and a subsequent pilot study showed that three 23S rRNA circular permutation variants could assemble into a functional subunit *in vivo*⁶. We prepared a comprehensive collection of 91 circularly permuted 23S (CP23S) rRNA mutants with new ends placed at nearly every hairpin (Fig. 1b). The CP23S sequences were introduced in place of the wild-type 23S rRNA gene of the pAM552 plasmid (Fig. 1a, Extended Data Figs 1a and 2), and the resulting constructs were transformed in the *Escherichia coli* SQ171 cells lacking chromosomal rRNA alleles⁷. Twenty-two constructs were able to replace the resident plasmid pCSacB carrying the wild-type rRNA operon (Fig. 1b, Extended Data Fig. 2d, e and Extended Data Table 1). Most of the viable circularly permuted variants had new 23S rRNA ends at the subunit solvent site, including several locations close to the interface rim (Fig. 1c).

One of the viable mutants (CP2861, Fig. 1b) had 23S rRNA ends within the loop of helix 101 (H101), located in the ribosome near the apex loop of the 16S rRNA helix 44 (h44) (Figs 1c and 2c). Because the length of h44 varies among different species, and its terminal loop sequence can tolerate alterations⁸, h44 was a promising site for grafting the CP2861 23S rRNA and generating a hybrid 16S–23S rRNA molecule (Fig. 2a–c). In the chimaeric rRNA, the processing sequences flanking the mature 16S rRNA would remain intact for proper maturation of the 16S rRNA termini, whereas endonuclease processing signals of 23S rRNA would be eliminated, thereby preventing its cleavage from the hybrid molecule.

The RNA linkers must span the 30–40 Å distance between h44 and H101 loops and allow for ~10 Å subunit ratcheting during protein synthesis^{9–12} (Fig. 2c and Extended Data Fig. 3). Being unable to estimate the optimal length of the linkers accurately, we prepared a library of constructs, pRibo-T, in which the length of two tethers—T1 connecting 16S rRNA G1453 with 23S rRNA C2858, and T2 linking 23S C2857 with 16S G1454—varied from 7 to 12 adenine residues (Supplementary Table 2). Notably, plasmid exchange in SQ171 cells yielded several slowly growing colonies, and the pattern of extracted RNA showed a single major RNA species corresponding to the 16S–23S chimaera instead of the individual 16S and 23S bands (Fig. 2d). This result suggested that translation in these cells was carried out exclusively by Ribo-T, and revealed for the first time that the bipartite nature of the ribosome is dispensable for successful protein synthesis and cell viability.

¹Center for Pharmaceutical Biotechnology – m/c 870, University of Illinois at Chicago, 900 South Ashland Avenue, Chicago, Illinois 60607, USA. ²Department of Chemical and Biological Engineering, Northwestern University, 2145 Sheridan Road, Tech E-136, Evanston, Illinois 60208, USA. ³Chemistry of Life Processes Institute, Northwestern University, 2170 Campus Drive, Evanston, Illinois 60208, USA. †Present address: Institut de Biologie et Chimie des Protéines, UMR5086 CNRS/Université Lyon 1, 7 passage du Vercors, 69367 Lyon, France.

*These authors contributed equally to this work.

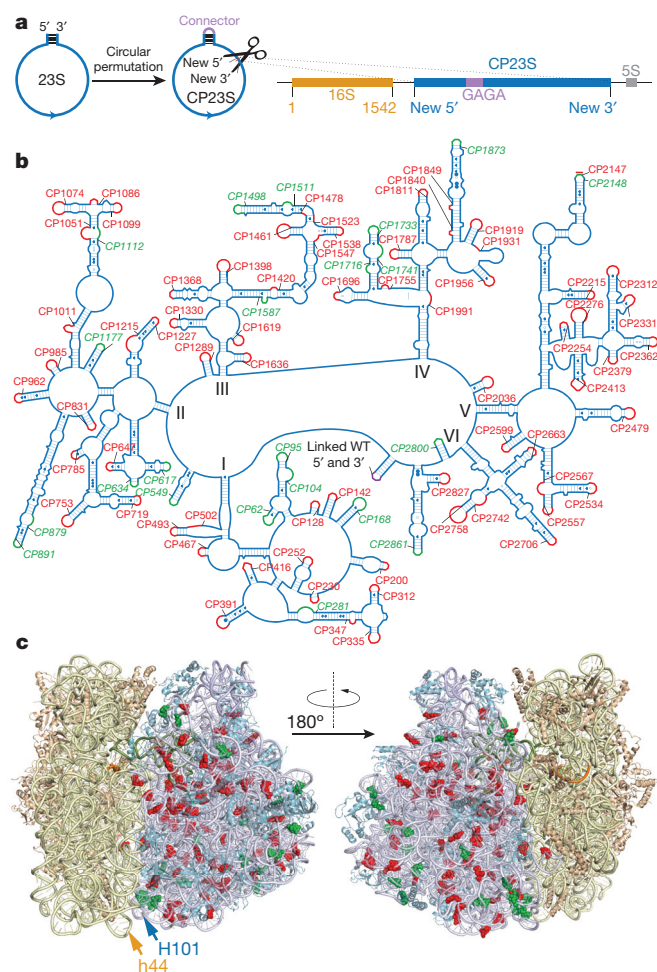


Figure 1 | Global screening of circularly permuted 23S rRNAs identifies variants capable of replacing the natural 23S rRNA in a functional ribosome.

a, The general scheme for constructing the rRNA operon in which the mature 23S rRNA gene sequence is replaced with the circularly permuted gene (CP23S). **b**, Secondary structure diagram of 23S rRNA²⁶ showing circular permutation (CP) constructs tested for their ability to support cell growth in the absence of wild-type ribosomes, named according to the number of the new 5' position in the wild-type (WT) 23S rRNA structure (for example, CP104). Viable circular permutation variants are green and italicized, non-viable variants are red. To assess the viability of CP mutants, two independent attempts to replace wild-type ribosomes with the CP construct were carried out. For all viable CP constructs, the lack of wild-type rRNA genes was confirmed by PCR as shown in the Extended Data Fig. 2, and the identity of the constructs in the resulting clones was verified by sequencing. **c**, The location of the new 5' ends (spheres, viable in green, non-viable in red) of CP variants of the 23S rRNA in the crystallographic structure of the *E. coli* 70S ribosome¹¹ (Protein Data Bank (PDB) accession code 4V9D). The loops of helices h44 and H101 in the small and large subunit rRNA, respectively, used for subsequent experiments, are indicated by arrows.

The linker combinations 8A/9A or 9A/8A (for T1/T2) were found in the six best-growing clones. The first combination showed slightly better behaviour in some subsequent experiments and was chosen for further investigation (pRibo-T plasmid, Extended Data Fig. 1b). The original SQ171/pRibo-T clones, although viable, grew slowly (doubling time 107 ± 3 min compared to 35 ± 1 min for SQ171 cells expressing wild-type ribosomes), exhibited poor recovery from the stationary phase, and low cell density at saturation (Extended Data Fig. 4a). By passaging cells in liquid culture for approximately 100 generations, we isolated faster growing mutants. One such clone, SQ171fg/pRibo-T (for fast growing), exhibited better growth characteristics and shorter doubling time (70 ± 2 min) (Extended Data Fig. 4a). PCR and primer extension analysis showed the lack of

wild-type rDNA and rRNA, respectively, confirming that every ribosome in this strain was assembled with the tethered rRNA (Extended Data Fig. 4b, c). Because the pRibo-T plasmid from the SQ171fg clone was unaltered, we sequenced the entire genome and found a nonsense mutation in the *ybeX* gene encoding a putative $\text{Mg}^{2+}/\text{Co}^{2+}$ transporter, and a missense mutation in the *rpsA* gene encoding ribosomal protein S1 (Extended Data Fig. 4d, e). Either one of these mutations or their combined effect must account for the faster growth of SQ171fg/pRibo-T cells (henceforth called Ribo-T cells).

To establish that protein synthesis in Ribo-T cells was carried out by ribosomes with tethered subunits, we carefully examined the integrity of Ribo-T rRNA. Analysis of Ribo-T preparations in a denaturing gel showed only very faint 16S and 23S-like rRNA bands (marked by asterisks in Extended Data Fig. 5a), possibly reflecting the linker cleavage either in the cell or during Ribo-T isolation. In most of the multiple Ribo-T preparations, these cleavage products accounted for less than 4% of the total Ribo-T rRNA. In some of the preparations, these bands were completely absent (for example, lane 'Ribo-T(1)' in Extended Data Fig. 5a), showing that more than 99% of Ribo-T remained intact. Consistently, primer extension across the T1 and T2 linkers did not show any major stops attesting to the general stability of the oligo(A) connectors (Extended Data Fig. 5d). Protein synthesis rate in Ribo-T cells reached $50.5 \pm 3.5\%$ of that in cells with wild-type ribosomes (Extended Data Fig. 6a) and thus cannot be accounted for by a small fraction of Ribo-T with cleaved tethers. Unequivocal proof of active Ribo-T translation *in vivo* came from analysis of polysomes prepared from Ribo-T cells, in which intact 16S–23S hybrid rRNA (rather than the products of its cleavage) was associated with the heavy polysomal fractions (Fig. 2e). This result provided clear evidence that intact Ribo-T composed of covalently linked subunits is responsible for protein synthesis in the Ribo-T cells. 2D-gel analysis showed that most of the proteins present in SQ171 cells that express wild-type ribosomes are efficiently synthesized in the Ribo-T cells (Extended Data Fig. 6).

We isolated ribosomes with tethered subunits from Ribo-T cells and characterized their composition and properties. The tethered ribosome contains an apparently equimolar amount of 5S rRNA and the full complement of ribosomal proteins in quantities closely matching the composition of wild-type ribosome (Extended Data Fig. 5 b, c). Chemical probing showed that the rRNA hairpins h44 and H101 remain largely unperturbed, while both linkers were highly accessible to chemical modification, indicating that they are solvent-exposed (Extended Data Fig. 7).

Sucrose gradient analysis of Ribo-T showed that at 15 mM Mg^{2+} most of the ribosomal material sedimented as a 70S peak with a minor faster-sedimenting peak, which may represent Ribo-T dimers owing to cross-ribosome subunit association at a high Mg^{2+} concentration (Fig. 3a). At lower Mg^{2+} concentration (1.5 mM), when the native ribosome completely dissociates into subunits, Ribo-T still sediments as a single peak with an apparent sedimentation velocity of 65S (Fig. 3a). The distinctive resistance of Ribo-T to subunit dissociation offers a venue for isolating Ribo-T if it is expressed in cells concomitantly with wild-type ribosomes.

We then tested the activity of Ribo-T in the PURExpress *in vitro* translation system lacking native ribosomes¹³. Ribo-T efficiently synthesized the 18-kilodalton (kDa) dihydrofolate reductase or super folder green fluorescence protein (sfGFP)¹⁴ (Fig. 3b). The rate of Ribo-T-catalysed protein synthesis reaches approximately 45% of that of the wild-type ribosomes (Fig. 3b). To assess which translation step is the most problematic for Ribo-T, progression of Ribo-T through a short synthetic gene¹⁵ was analysed by toe-printing (Fig. 3c). A more pronounced band of the ribosomes at the open reading frame start codon indicated that Ribo-T is impaired in translation initiation at a step subsequent to the start codon recognition. Although the true nature of this effect will require further investigation, it is unlikely to reflect a lower affinity of Ribo-T for initiation factors because higher concentrations of IF1, IF2 and IF3 could not rescue the initiation defect (data not shown).

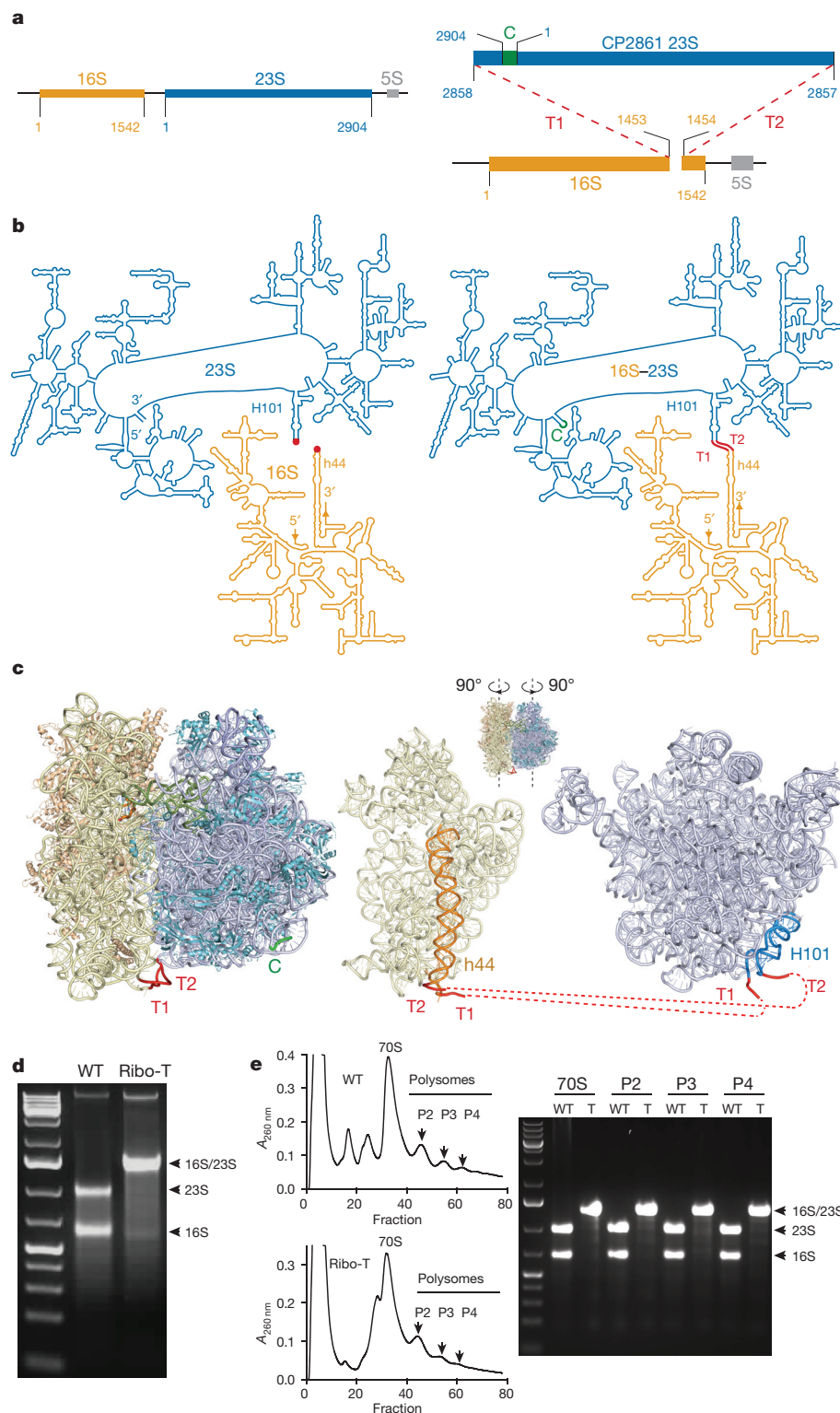


Figure 2 | Ribo-T design. **a**, Wild-type (left) and Ribo-T (right) rRNA genes. In Ribo-T, the circularly permuted 23S rRNA gene, 'closed' at its native ends with a four-nucleotide long connector (C) and 'opened' in the loop of H101, is inserted via short tethers T1 and T2 into the apex loop of h44 in the 16S rRNA gene. The resulting hybrid rRNA gene is transcribed as a single chimaeric 16S-23S rRNA, with its 5' and 3' ends probably processed by the enzymes of 16S rRNA maturation. **b**, Secondary structure of the mature wild-type (left) and Ribo-T (right) rRNAs. The red dots indicate the apex loops of h44 and H101, which in Ribo-T are connected by tethers T1 and T2. The arrows at the 16S rRNA ends and the tethers in the Ribo-T map indicate the direction of transcription of the chimaeric 16S-23S rRNA. **c**, Left, the locations of the T1 and T2 tethers in the three-dimensional model of Ribo-T (based on the structure of *E. coli* ribosome in the unrotated state¹¹; PDB code 4V9D). 16S rRNA is in yellow, 30S proteins are in orange, 23S and 5S rRNA are in blue, 50S proteins are in cyan, P-site-bound tRNA is in olive, mRNA is in orange, connector (C) linking 23S native 5' and 3' ends is in green, and tethers T1 and T2 are in red. Right, the ribosome has been opened up like a book, exposing the subunit interface, with helices h44 (16S) and H101 (23S) highlighted in orange and blue, respectively, and ribosomal proteins removed for clarity. **d**, Agarose gel electrophoresis of total RNA prepared from SQ171 cells expressing wild-type ribosomes or Ribo-T. The gel is representative of five independent biological replicates. **e**, Left, sucrose gradient fractionation of polysomes prepared from cells expressing wild-type ribosomes (top) or Ribo-T (bottom). Peaks corresponding to monosomes (70S), disomes (P2), trisomes (P3) and tetrasomes (P4) are indicated by arrows. Right, the agarose electrophoresis analysis of RNA extracted from the corresponding sucrose gradient peaks, wild-type ribosomes (WT) or Ribo-T (T).

To enable a fully orthogonal ribosome-mRNA system, we next engineered a Ribo-T version (oRibo-T) committed to translation of a particular orthogonal cellular mRNA. The wild-type 16S anti-Shine-Dalgarno region was altered from ACCUCCUUA to AUUGUGGUA (ref. 3) producing a poRibo-T1 construct. When poRibo-T1 was introduced in *E. coli* carrying the *sf-gfp* gene with the Shine-Dalgarno sequence CACCAC cognate to oRibo-T (Extended Data Fig. 1c, pLpp5oGFP), notable sfGFP expression was observed (Extended Data Fig. 8a), demonstrating the activity of oRibo-T.

Ribosomes prepared from poRibo-T1-transformed cells (containing a mixture of wild-type ribosomes and oRibo-T) translated an orthogonal *sf-gfp* gene in a cell-free system (green dotted line in Extended Data Fig. 8b). However, because the orthogonal *sf-gfp* transcript is the only mRNA available during *in vitro* translation and no native mRNA engage wild-type 30S subunits, a fraction of orthogonal sfGFP biosynthesis is accounted for by wild-type ribosomes (pink dotted line in Extended Data Fig. 8b). Therefore, to isolate oRibo-T1 activity *in vitro*, we used the A2058G mutation in the 23S rRNA portion of oRibo-T, which rendered

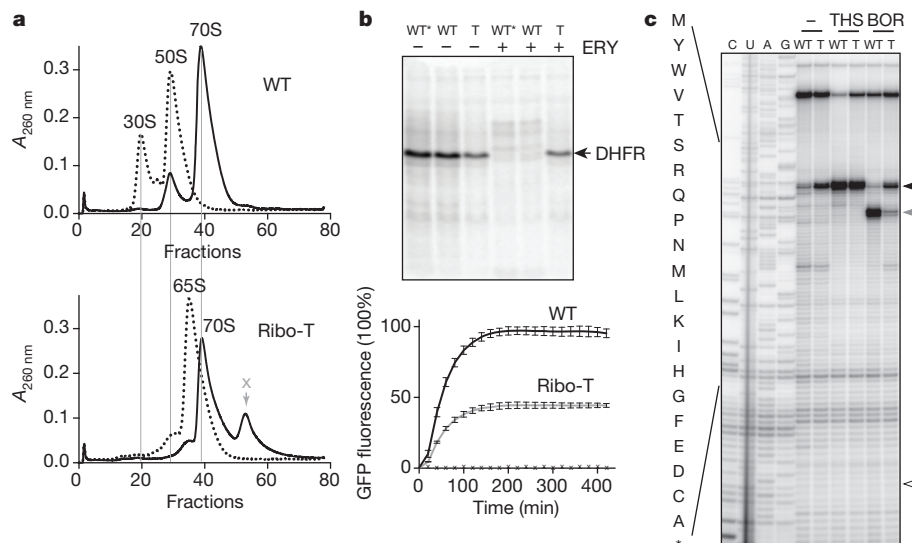


Figure 3 | Functional characterization of Ribo-T. **a**, Sucrose gradient analysis of wild-type ribosomes (top) and Ribo-T (bottom) under 15 mM MgCl_2 (solid line) or 1.5 mM MgCl_2 subunit dissociating conditions (dotted line). The peak marked with grey arrow and 'X' may represent Ribo-T dimers. The result was qualitatively verified in an independent experiment performed at Mg^{2+} concentrations 1.5 mM and 10 mM. **b**, *In vitro* translation of proteins by isolated Ribo-T. Top, SDS-PAGE analysis of the dihydrofolate reductase (DHFR) protein synthesized in the Δ ribosome PURExpress system supplemented with purified wild-type ribosomes or Ribo-T (T); wild-type ribosomes provided with the kit (WT*) were used as a control. The transcription-translation reaction was carried out in the presence of [^{35}S]L-methionine in the absence or presence of 50 μM erythromycin (ERY). The A2058G mutation in Ribo-T renders the Ribo-T-driven translation resistant to the antibiotic. The 'no erythromycin' samples are a representative result of two independent biological experiments. Bottom, time course of sfGFP protein expression in the Δ ribosome PURExpress system supplemented with purified wild-type (black) or Ribo-T (grey) ribosomes. The k_{obs} rates

(385 ± 13 relative fluorescent units (RFU) min^{-1} (mean \pm s.d.) for wild-type, 177 ± 6 RFU min^{-1} for Ribo-T) were determined from the initial slopes. The activity of both ribosomes was fully inhibited by 50 $\mu\text{g ml}^{-1}$ chloramphenicol (time points indicated by x). Each curve is an average of two independent biological replicates, with error bars indicating the s.d. **c**, Toeprinting analysis of translation of a 20-codon synthetic gene *RST1* (ref. 15) by wild-type ribosomes or Ribo-T. The antibiotic thiostrepton (THS), present at 50 μM , arrests the initiating ribosome at the start codon¹⁹ (black arrowhead). The threonyl-tRNA synthetase inhibitor borrelidin (BOR) arrests translation at the fourth codon of *RST1* mRNA (grey arrowhead)¹⁵. The position of a toeprint band that would correspond to the ribosome that has reached the *RST1* stop codon is shown by an open arrowhead. A more pronounced toeprint band at the start codon in the samples lacking thiostrepton indicates that Ribo-T departs from the initiation codon slower than wild-type ribosomes. A weaker borrelidin-specific band observed in the Ribo-T sample suggests that under our experimental conditions, fewer Ribo-T compared to wild-type ribosomes were able to reach the fifth codon, apparently owing to slower initiation.

ribosomes resistant to macrolide and lincosamide antibiotics (for example, clindamycin). The addition of clindamycin to the reaction with wild-type ribosomes completely inhibited expression of the reporter (pink solid line in Extended Data Fig. 8b), whereas marked sfGFP expression was observed in the reaction carrying the oRibo-T preparation (green solid line in Extended Data Fig. 8b). Importantly, the unique conjoined nature of Ribo-T allows for using antibiotic-resistance mutations in any of the ribosomal subunits. We demonstrated this by introducing a G693A mutation in the small subunit moiety of oRibo-T, rendering oRibo-T resistant to pactamycin^{16,17}. Pactamycin (100 μM) completely inhibited the activity of the wild-type ribosomes in the PURExpress translation system, whereas oRibo-T(G693A) remained fully active (Extended Data Fig. 8c). The combination of an orthogonal translation initiation signal with the antibiotic-resistance mutations embedded in oRibo-T allows for exploring unique properties of oRibo-T in a cell-free system even in preparations carrying a substantial fraction of wild-type ribosomes.

During subsequent experiments, we fortuitously isolated a mutant version of the poRibo-T1 plasmid (poRibo-T2) that contained a single mutation in the P_L promoter that improved its transformation properties and was used thereafter (Extended Data Fig. 9).

We next demonstrated the evolvability of oRibo-T by selecting the gain-of-function mutations in the PTC, which could facilitate translation of a problematic protein sequence by the ribosome. The SecM polypeptide presents a classic example of an amino acid sequence for which translation is problematic for the ribosome¹⁸. The expression of the essential SecA secretion ATPase is controlled by programmed ribosome stalling at the Pro166 codon of *secM*. Translation arrest ensues because specific interactions of the SecM nascent chain with

the ribosomal exit tunnel impair the PTC function, preventing the transfer of the 165-amino-acid long peptide to the incoming prolyl-transfer-RNA (Pro-tRNA). Several mutations in the ribosomal exit tunnel (for example, A2058G) have been previously identified as relieving translation arrest possibly by disrupting the interactions between the nascent chain and ribosome, and rRNA residues in the PTC A-site have been proposed to have a key role in the mechanism of ribosome stalling^{18–20}. However, exploring the role of the PTC in the mechanism of the translation arrest has been impossible so far because of the lethal nature of PTC mutations^{21,22}.

We therefore asked whether the PTC A-site mutations can relieve SecM-induced translation arrest. Our interest in testing the use of oRibo-T for manipulating the ribosomal A-site was additionally fuelled by future prospects of engineering ribosomes capable of programmed polymerization of unnatural amino acids and backbone-modified analogues. To search for SecM arrest bypass mutations, we removed the A2058G mutation from poRibo-T2 and prepared a library of plasmids with mutations at two 23S residues, A2451 and C2452. These residues form the amino acid binding pocket in the PTC A-site^{19,23} (Fig. 4b), and their mutations are dominantly lethal in *E. coli*^{21,22}. We also engineered an orthogonal SecM-based reporter, poSML (Fig. 4a and Extended Data Fig. 1d), encoding the SecM arrest sequence fused in frame with *lacZa* gene¹⁸ (Fig. 4a).

Notably, when the C41(DE3) cells capable of α -complementation were transformed first with the poSML reporter and then with the poRibo-T2(A2451N/C2452N) mutant library, some of the colonies gained blue colour on indicator plates (Fig. 4c), demonstrating read-through of the SecM arrest sequence in some of the mutants. Sequencing 15 bluer colonies showed that they all carried a C2451–

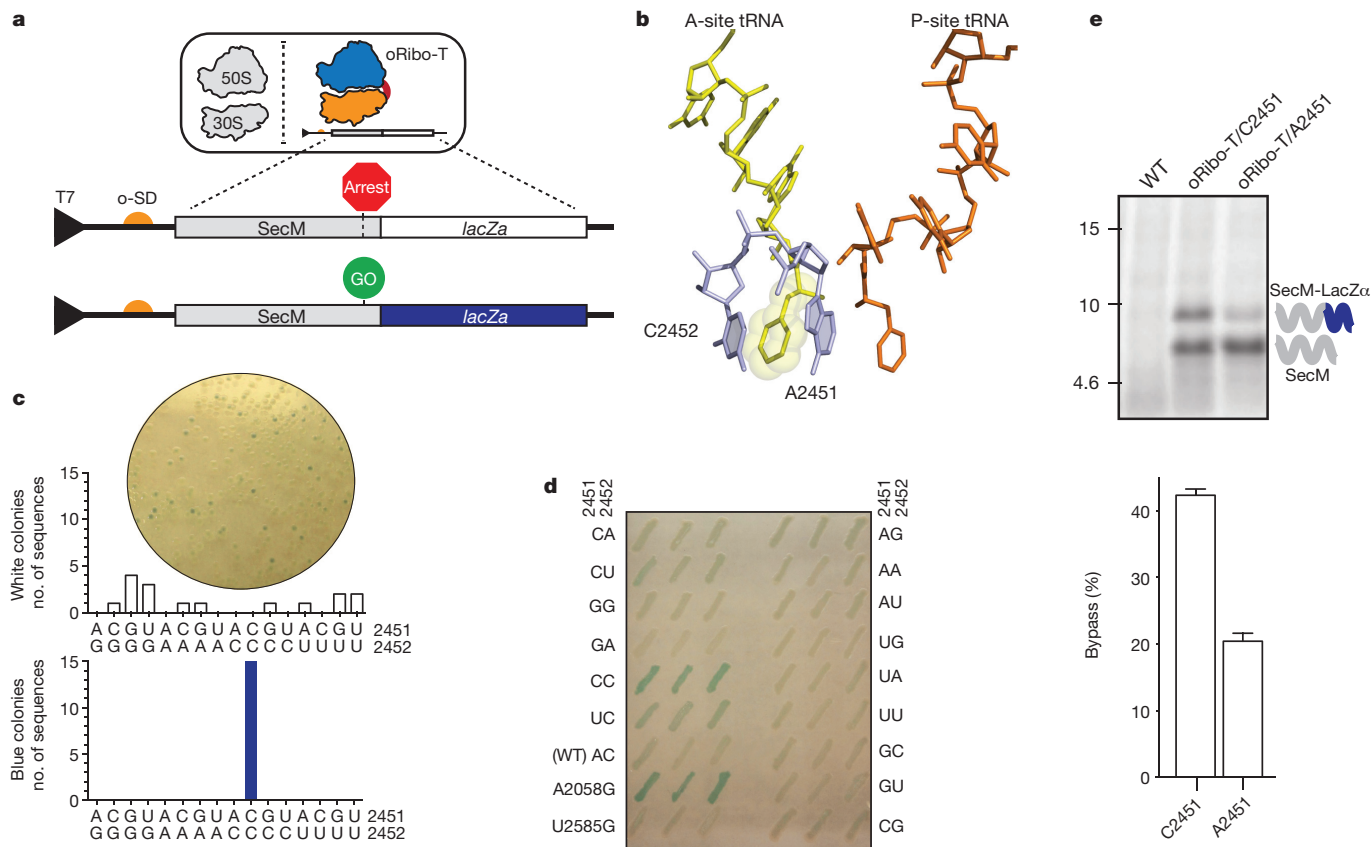


Figure 4 | Evolving Ribo-T to identify gain-of-function PTC mutations that facilitate synthesis of problematic amino acid sequences. **a**, The SecM-LacZ α reporter with an orthogonal Shine–Dalgarno (o-SD) sequence is translated in the cell by oRibo-T. SecM-dependent ribosome stalling prevents expression of the lacZ α gene unless a ribosomal mutation allows for bypass of the SecM arrest site. **b**, The placement of Phe-tRNAs bound in the P-site (orange) and A-site (yellow) of the PTC¹⁰. The conserved 23S rRNA residues A2451 and C2452 (blue) form the amino acid side-chain binding pocket in the A-site. **c**, Top, colonies formed on X-gal/isopropyl β -D-1-thiogalactopyranoside (IPTG) plates by the *E. coli* C41 cells transformed with the secM-lacZ α reporter plasmid and a library of poRibo-T2 plasmids with the PTC mutations at positions 2451 and 2452. Bottom, identity of 2451 and 2452 residues in poRibo-T2 plasmids isolated from randomly picked 16 white colonies and 15 blue colonies. **d**, The *E. coli* C41 cells transformed with the secM-lacZ α reporter and individual poRibo-T2 plasmids with different nucleotide combinations at positions 2451 and 2452. The transformed cells were initially plated on LB agar antibiotic plate without X-gal or IPTG (all colonies pale), and three randomly picked transformants were then streaked on the shown indicator plate containing X-gal and IPTG. The poRibo-T2 mutant with the A2058G mutation, which is known to enhance the bypass

C2452 sequence (the A2451C mutation) in the PTC. By contrast, none of the 16 analysed 'white' colonies had this sequence, and instead exhibited a variety of dinucleotide combinations at positions 2451–2452 (Fig. 4c). We corroborated these results by individually testing all possible 2451–2452 mutants in poSML-transformed C41(DE3) cells. Importantly, all the mutants were viable, confirming that oRibo-T is suitable for expression of dominantly lethal 23S rRNA mutations *in vivo*, indicating a low degree of cross-association of oRibo-T with free wild-type 30S subunits. Consistent with our previous result (Fig. 4c), the A2451C mutation confers the most pronounced blue colour of the transformants, comparable to that seen in cells expressing oRibo-T with the tunnel mutation A2058G (Fig. 4d). The A2451U mutation also increased the blue hue of the cells although to a lesser extent. These results suggested that the A2451C (and A2451U) mutants were not only functional in cellular

of the SecM arrest sequence¹⁸, was used as a positive control. A mutation of another essential PTC nucleotide (U2585G), which has been proposed to be implicated in some translation arrest scenarios²⁷, showed no effect on SecM arrest. The photographs of the agar plates in **c** and **d** have been contrast-enhanced for better colour separation. **e**, The A2451C mutation enhances bypass of the SecM stalling sequence by oRibo-T *in vitro*. The orthogonal construct containing *secM* stalling sequence fused in frame to the truncated *lacZa* gene was translated in the Δ ribosome PURExpress cell-free translation system supplemented with wild-type non-tethered ribosomes or preparations of oRibo-T (A2451 or C2451). The Ribo-T constructs carried the pactamycin-resistance mutation G693A in 16S rRNA, and the reactions were carried out in the presence of pactamycin, which, in addition to the presence of an orthogonal Shine–Dalgarno sequence, ensured that the reporter is translated exclusively by oRibo-T (see the control wild-type lane with no translation products). Numbers on the left indicate the size (kDa) of molecular mass markers. The bar graph at the bottom shows the efficiency of bypass (ratio between the full-size and SecM-arrested translation products). A representative gel of two independent experiments is shown, with error bars indicating the s.d.

protein synthesis but also gained the ability to bypass translation arrest caused by the SecM sequence.

We verified *in vitro* the discovered role of A2451 in the mechanism of SecM translation arrest by testing the translation of the orthogonal *secM-lacZa* gene by isolated oRibo-T with and without the A2451C mutation. To assure oRibo-T activity only, the pactamycin-resistance mutation G693A (refs 16, 17) was introduced into the 16S segment of oRibo-T constructs, and cell-free translation in the PURExpress system was carried out in the presence of pactamycin. Only a small fraction of original oRibo-T was able to bypass the SecM arrest signal and synthesize the full-size hybrid protein (Fig. 4e, lane oRibo-T/A2451). By contrast, the A2451C mutant was able to bypass the SecM arrest site twice as efficiently as the unmodified oRibo-T (Fig. 4e, lane oRibo-T/C2451), confirming that the selected (and otherwise lethal) mutation in the PTC has improved the ability of oRibo-T

to polymerize a polypeptide sequence problematic for wild-type ribosomes. These results provide the first, to our knowledge, direct experimental evidence of a direct involvement of the PTC A-site in the mechanism of nascent peptide-dependent ribosome stalling, and suggest that interactions between the proline moiety of Pro-tRNA and the A-site rRNA residues are crucial for the SecM-induced translation arrest.

By engineering a ribosome with inseparable tethered subunits, and demonstrating its functionality *in vivo* and *in vitro*, we have revised one of the key concepts of molecular biology: that successful expression of the genome requires reversible association and dissociation of the ribosome into individual subunits. Although the ability of translation initiation by 70S ribosome at leaderless mRNAs or via scanning re-initiation has been previously demonstrated^{124,25}, it was surprising that Ribo-T would be active enough to express the entire bacterial genome at a sufficient level for active cell growth and proliferation. This finding in turn made possible a fully orthogonal and evolvable gene expression system in the cell in which an entire specialized ribosome, not just the mRNA-interacting small subunit, is dedicated to the translation of a defined genetic template. As a proof of principle we showed that oRibo-T can be used for studying in cells mutations of functionally crucial rRNA residues that are dominantly lethal, a task that would be difficult or impossible to achieve in any other system. This shows that Ribo-T may find important implications in exploring poorly understood functions of the ribosome in protein synthesis. Furthermore, the opportunity provided by the oRibo-T system to modify the catalytic properties of the protein synthesis machine opens up exciting prospects for engineered ribosomes with principally new properties.

Online Content Methods, along with any additional Extended Data display items and Source Data, are available in the online version of the paper; references unique to these sections appear only in the online paper.

Received 28 January; accepted 26 June 2015.

Published online 29 July 2015.

- Karbstein, K. Quality control mechanisms during ribosome maturation. *Trends Cell Biol.* **23**, 242–250 (2013).
- Hui, A. & de Boer, H. A. Specialized ribosome system: preferential translation of a single mRNA species by a subpopulation of mutated ribosomes in *Escherichia coli*. *Proc. Natl Acad. Sci. USA* **84**, 4762–4766 (1987).
- Rackham, O. & Chin, J. W. A network of orthogonal ribosome-mRNA pairs. *Nature Chem. Biol.* **1**, 159–166 (2005).
- Neumann, H., Wang, K., Davis, L., Garcia-Alai, M. & Chin, J. W. Encoding multiple unnatural amino acids via evolution of a quadruplet-decoding ribosome. *Nature* **464**, 441–444 (2010).
- Erlacher, M. D. *et al.* Chemical engineering of the peptidyl transferase center reveals an important role of the 2'-hydroxyl group of A2451. *Nucleic Acids Res.* **33**, 1618–1627 (2005).
- Kitahara, K. & Suzuki, T. The ordered transcription of RNA domains is not essential for ribosome biogenesis in *Escherichia coli*. *Mol. Cell* **34**, 760–766 (2009).
- Asai, T., Zaporozhets, D., Squires, C. & Squires, C. L. An *Escherichia coli* strain with all chromosomal rRNA operons inactivated: complete exchange of rRNA genes between bacteria. *Proc. Natl Acad. Sci. USA* **96**, 1971–1976 (1999).
- Dorywalska, M. *et al.* Site-specific labeling of the ribosome for single-molecule spectroscopy. *Nucleic Acids Res.* **33**, 182–189 (2005).
- Yusupov, M. M. *et al.* Crystal structure of the ribosome at 5.5 Å resolution. *Science* **292**, 883–896 (2001).
- Voorhees, R. M., Weixlbaumer, A., Loakes, D., Kelley, A. C. & Ramakrishnan, V. Insights into substrate stabilization from snapshots of the peptidyl transferase center of the intact 70S ribosome. *Nature Struct. Mol. Biol.* **16**, 528–533 (2009).
- Dunkle, J. A. *et al.* Structures of the bacterial ribosome in classical and hybrid states of tRNA binding. *Science* **332**, 981–984 (2011).
- Frank, J. & Agrawal, R. K. A ratchet-like inter-subunit reorganization of the ribosome during translocation. *Nature* **406**, 318–322 (2000).
- Shimizu, Y. *et al.* Cell-free translation reconstituted with purified components. *Nature Biotechnol.* **19**, 751–755 (2001).
- Pédélecq, J. D., Cabantous, S., Tran, T., Terwilliger, T. C. & Waldo, G. S. Engineering and characterization of a superfolder green fluorescent protein. *Nature Biotechnol.* **24**, 79–88 (2006).
- Orelle, C. *et al.* Identifying the targets of aminoacyl-tRNA synthetase inhibitors by primer extension inhibition. *Nucleic Acids Res.* **41**, e144 (2013).
- Mankin, A. S. Pactamycin resistance mutations in functional sites of 16S rRNA. *J. Mol. Biol.* **274**, 8–15 (1997).
- Orelle, C. *et al.* Tools for characterizing bacterial protein synthesis inhibitors. *Antimicrob. Agents Chemother.* **57**, 5994–6004 (2013).
- Nakatogawa, H. & Ito, K. The ribosomal exit tunnel functions as a discriminating gate. *Cell* **108**, 629–636 (2002).
- Vázquez-Laslop, N., Ramu, H., Klepacki, D., Ci, K. & Mankin, A. S. The key role of a conserved and modified rRNA residue in the ribosomal response to the nascent peptide. *EMBO J.* **29**, 3108–3117 (2010).
- Bhushan, S. *et al.* SecM-stalled ribosomes adopt an altered geometry at the peptidyl transferase center. *PLoS Biol.* **9**, e1000581 (2011).
- Thompson, J. *et al.* Analysis of mutations at residues A2451 and G2447 of 23S rRNA in the peptidyltransferase active site of the 50S ribosomal subunit. *Proc. Natl Acad. Sci. USA* **98**, 9002–9007 (2001).
- Sato, N. S., Hirabayashi, N., Agmon, I., Yonath, A. & Suzuki, T. Comprehensive genetic selection revealed essential bases in the peptidyl-transferase center. *Proc. Natl Acad. Sci. USA* **103**, 15386–15391 (2006).
- Nissen, P., Hansen, J., Ban, N., Moore, P. B. & Steitz, T. A. The structural basis of ribosome activity in peptide bond synthesis. *Science* **289**, 920–930 (2000).
- Moll, I., Hirokawa, G., Kiel, M. C., Kaji, A. & Blasi, U. Translation initiation with 70S ribosomes: an alternative pathway for leaderless mRNAs. *Nucleic Acids Res.* **32**, 3354–3363 (2004).
- Karamyshev, A. L., Karamysheva, Z. N., Yamami, T., Ito, K. & Nakamura, Y. Transient idling of posttermination ribosomes ready to reinitiate protein synthesis. *Biochimie* **86**, 933–938 (2004).
- Cannone, J. J. *et al.* The Comparative RNA Web (CRW) Site: an online database of comparative sequence and structure information for ribosomal, intron, and other RNAs. *BMC Bioinformatics* **3**, 2 (2002).
- Arenz, S. *et al.* Molecular basis for erythromycin-dependent ribosome stalling during translation of the ErmBL leader peptide. *Nat. Commun.* **5**, 3501 (2014).

Supplementary Information is available in the online version of the paper.

Acknowledgements We thank I. Ntai for mass spectrometry analysis, K. N. Swonger, C. Burghard, E. M. Fulk, V. Raghavan and N. Aleksashin for help with some experiments, K. Ito for providing the sequence of the pNH122 *secM-lacZa* reporter, Y. Polikanov for help in preparing ribosome images, J. Lee for assistance in genome sequence analysis, S. Sothiselvam and J. Marks for discussions and suggestions, and N. Vazquez-Laslop for advice on the project and critical reading of the manuscript. This work was supported by the Defense Advanced Research Projects Agency (N66001-12-C-4211), the National Science Foundation grants MCB-0943393 (to M.C.J.) and MCB-1244455 (to A.S.M.) and the David and Lucille Packard Foundation Fellowship (2011-37152) (to M.C.J.).

Author Contributions M.C.J. and A.S.M. designed the study, analysed results, and wrote the paper. C.O. and E.D.C. designed and performed experiments and analysed data. T.S. and T.F. performed experiments.

Author Information Reprints and permissions information is available at www.nature.com/reprints. The authors declare no competing financial interests. Readers are welcome to comment on the online version of the paper. Correspondence and requests for materials should be addressed to A.S.M. (shura@uic.edu) or M.C.J. (m-jewett@northwestern.edu).

METHODS

No statistical methods were used to predetermine sample size.

Preparation of circularly permuted variants of the 23S rRNA. The A2058G mutation was introduced into the pAM552 plasmid (Extended Data Fig. 1a) by inverse PCR using primers 5'-CCGTCTTGCCGCGGGTAC-3' and 5'-GTGTACCCGCGGCAAGACGGGAAGACCCCGTGAACC-3' (the underlined sequence is complementary to the second primer and the mutation is shown by italicized bold character) followed by re-circularization by Gibson assembly reaction²⁸ (all primers used in this study were synthesized by Integrated DNA Technology). A 23S-A2058G gene with native 5' and 3' ends linked by a GAGA tetra-loop was generated by inverse PCR using primers 5'-GGTTAAGCCTCACGGTTC-3' and 5'-CCGTGAGGCTTAACCGAGAGGTTAAGCGACTAAGCGTAC-3' (GAGA tetra loop in bold) and pAM552-A2058G as template. Purified PCR product (50 ng) was circularized by Gibson assembly reaction for 1 h at 50 °C. The resulting circular 23S rRNA gene was then cloned at its native unique *EagI* restriction site (position 1905 in wild-type 23S rRNA gene) into T7-Flag-4 plasmid (Sigma Aldrich) as follows. The circularized 23S rRNA gene was amplified by inverse PCR using primers 5'-GAGACACAACGTGGCTTTCGGGCCCGTTTACC-3' (added homology to the T7-Flag-4 vector underlined) and Gibson-assembled with the T7-Flag-4 vector amplified with the primers 5'-AAGATCGATCTCGACGAGTG-3' and 5'-GAAAGCCACGTTGTGTCTC-3'. The cloned circularly permuted 23S rRNA gene in the resulting plasmid pCP23S-*EagI* containing a pBR322 origin of replication and KanR selective marker (Extended Data Fig. 2) was fully sequenced.

The pCP23S-*EagI* plasmid was then digested with *EagI* (New England Biolabs) for 1 h at 37 °C, and the circularly permuted 23S rRNA (CP23S) gene was isolated from a SYBRSafe-stained 0.7% agarose gel using a E.Z.N.A. Gel Extraction kit (Omega). The 23S rRNA was circularized by T4 DNA ligase (New England Biolabs) in a 50 µl reaction with 2.5 ng µl⁻¹ DNA for 14 h at 16 °C, followed by heat inactivation at 65 °C for 10 min. The reaction was diluted 1:100 for use as a template in the PCR reactions for generating the circular permutants (Extended Data Fig. 2).

Ninety-one CP23S mutants were designed by introducing new 23S rRNA 5' and 3' ends at most of the apex loops and some internal loops of rRNA helices to assure spatial proximity of the new rRNA termini in the fully assembled 50S ribosomal subunit. Each CP23S rRNA gene was PCR-amplified in a 40 µl reaction using Phusion High Fidelity DNA polymerase (New England Biolabs), with primer pairs shown in Supplementary Table 1, and 4 µl of the 1:100 diluted 23S circular ligation reaction as template. Each primer pair adds to the 5' and 3' ends of the amplified CP23S gene 20-base-pair (bp) of homology to the 23S rRNA processing stem retained in the target vector pAM552-Δ23S-AflII (described below). PCR reactions catalysed by the Phusion High Fidelity DNA polymerase were run under the following conditions: 98 °C, 10 min followed by 25 cycles (98 °C, 30 s; 60 °C, 30 s; 72 °C, 180 s), followed by the final incubation for 15 min at 72 °C. The reaction product was purified using E.Z.N.A. Cycle Pure kit (Omega) and the size of the amplified DNA was confirmed by electrophoresis in a 1% agarose gel. For circular permutations with off target bands (12 in total), the PCR product of the correct size was extracted from the agarose gel.

To minimize PCR errors in generating the vector backbone, which carried 16S and 5S rRNA sequences, and prevent carry-through of the wild-type *rrnB* operon, universal backbone vector pAM552-Δ23S-AflII lacking the 23S rRNA gene and containing added AflII restriction site for cloning of CP23S was prepared. The plasmid pAM552-AflII was constructed from pAM552 by adding AflII restriction sites within the terminal stem of the wild-type 23S rRNA gene by introducing the G2C and C2901G mutations. First, the G2C mutation was introduced by inverse PCR using 5'-phosphorylated primers CTTAAGCGACTAAGCGTACAC and CTCACAACCCGAAGATGTTTC, followed by blunt-end ligation, transformation into *E. coli* POP2136 electrocompetent cells, plating on LB-agar plates supplemented with 50 µg ml⁻¹ carbenicillin, growth overnight at 30 °C, single colony isolation and sequencing. The C2901G mutation was added by the same method using 5'-phosphorylated primers GCCTACAGGTTTCATTAG and TTAA GCCTACAGGTTTCATTAG. The introduced mutations preserved the integrity of the 23S rRNA terminal stem and did not affect growth of SQ171 cells expressing only ribosomes with the pAM552-AflII-encoded rRNA (doubling times 53.9 ± 1.0 min for SQ171 cells transformed with pAM552 and 53.3 ± 2.4 min for SQ171 transformed with pAM552-AflII, as determined from four separate colonies each on Biotek Synergy H1 plate readers in 96-well flat bottom plates (Costar) in 100 µl LB supplemented with 50 µg ml⁻¹ carbenicillin, 37 °C, linear shaking with 2 mm amplitude, at 731 cycles per min). To remove the 23S rRNA gene, pAM552-AflII was digested with AflII (New England Biolabs) for 1 h at 37 °C, the backbone portion of the vector was gel-purified and ligated with T4 DNA ligase (New England Biolabs) overnight at 16 °C. It was then transformed into POP2136 cells,

plated on LB/agar plates supplemented with 50 µg ml⁻¹ carbenicillin, and grown at 30 °C. Plasmids from several colonies were isolated and fully sequenced. The resulting pAM552-Δ23S-AflII plasmid contains the 16S rRNA, 23S processing stems with an added AflII restriction site, 5S rRNA, and β-lactamase resistance gene and ColE1 ori (Extended Data Fig. 2). Vector backbone was prepared by digesting pAM552-Δ23S-AflII with AflII restriction enzyme at 37 °C for 2 h and purification using an E.Z.N.A. Cycle Pure kit.

All the CP23S constructs were assembled in parallel by Gibson assembly reaction (Extended Data Fig. 2) in a 96-well PCR plate. For each CP23S target, 50 ng of AflII-digested purified backbone was added to threefold molar excess of the PCR-amplified and purified CP23S insert. Gibson assembly mix²⁸ (15 µl) was added, the final volumes brought to 48 µl with nuclease-free water, and incubated at 50 °C for 1 h in the PCR machine. No CP23S insert was added to the negative control reaction. To check the efficiency of DNA assembly, 2 µl of selected assembly reactions were transformed into electrocompetent POP2136 cells. After 1 h recovery at 37 °C in SOC media, a quarter of each transformation was plated on LB-agar plates supplemented with 50 µg ml⁻¹ carbenicillin and grown for 20 h at 30 °C. A typical CP23S assembly reaction generated 30–120 POP2136 colonies with the control reaction generating only few colonies.

Testing CP23S rRNA constructs. Transformation of SQ171/pCSacB rubidium chloride-competent cells was carried out in a 96-well plate. Two microlitres of the Gibson Assembly reactions were added to 20 µl competent cells in the pre-chilled plate. After a 45-min incubation in ice/water bath, 45 s at 42 °C and 2 min on ice, 130 µl of SOC medium was added to the wells and the plate was incubated 2 h at 37 °C with shaking at 600 r.p.m. on a microplate shaker. Forty microlitres of medium were then transferred from each well to the wells of another 96-well plate containing 120 µl SOC supplemented with 100 µg ml⁻¹ ampicillin and 0.25% sucrose. The plate was incubated overnight at 37 °C with shaking at 600 r.p.m. A 96-pin replicator was used to spot aliquots of the cultures onto a rectangular LB agar plate containing 100 µg ml⁻¹ ampicillin, 5% sucrose and 1 mg ml⁻¹ erythromycin. The plate was incubated overnight at 37 °C and the appearance of Amp^r/Ery^r transformants was recorded. The completeness of the replacement of the wild-type pCSacB plasmid with the plasmids carrying circularly permuted 23S rRNA gene was verified by PCR using a mixture of three primers: primer 1 (5'-GCAGATTAGCAGTCCTTCA-3') complementary to the 23S rRNA segment 50–69, primer 2 (5'-CGTTGAGCTAACCGGTACTA-3') containing the sequence of the 23S rRNA segment 2863–2882, and primer 3 (5'-GGGTGATGTTTGAGATATTGCT-3') corresponding to the sequence of the 16S/23S intergenic spacer 139–116 bp upstream from the 23S rRNA gene in *rrnB* (Extended Data Fig. 2e). The combination of the primers 1 and 3 produces a 207-bp PCR band if the wild-type *rrn* operon is present; the combination of primers 1 and 2 produces a 112-bp PCR band on the templates with circularly permuted 23S rRNA gene (Extended Data Fig. 2e).

To reduce the number of false-negative CP23S rRNA variants, the experiment was repeated one more time using *de novo* assembled Gibson reactions with the cp23S rRNA constructs that failed to replace pCSacB in the first experiment. Two additional functional CP23S rRNA constructs were recovered from the second attempt. Altogether, 22 CP23S rRNA variants were able to replace pCSacB in the SQ171 cells. CP23S identity was confirmed by plasmid sequencing. Growth rates were analysed on Biotek Synergy H1 plate readers in 96-well flat bottom plates (Costar) in 100 µl LB with 50 µg ml⁻¹ carbenicillin. Doubling times and final A_{600 nm} after 18 h are shown in Extended Data Table 1.

Construction of pRibo-T. To avoid generation of mutations in the 23S rRNA gene during PCR amplification for Gibson assembly, the 23S rRNA gene variant circularly permuted at H101 (corresponding to CP2861 from Fig. 1) was first cloned in the pUC18 vector. For that, the 23S rRNA gene circularly permuted at H101 was PCR-amplified from circularized 23S rRNA gene prepared in the circular permutation study (see above and Extended Data Fig. 2a) by using the high-fidelity AccuPrime Taq polymerase (Life Technologies) and primers containing BamHI restriction sites (shown in bold) 5'-TATTGGATCCGATGCGTTGAGCTAACCGGTA-3' and 5'-TTATGGATCCTGCGCTTACACACCCGGCCTAT-3'. The amplified fragment was cut with BamHI and cloned in dephosphorylated BamHI-cut pUC18 plasmid. A plasmid containing CP2861 23S rRNA (pUC23S) was fully sequenced to verify the lack of mutations in the 23S rRNA gene.

For preparation of pRibo-T (Extended Data Fig. 1b), pAM552-Δ23S-AflII plasmid (see above) served as a recipient for the CP2861 23S rRNA gene. The CP2861 23S rRNA gene was excised from the pUC23S plasmid by BamHI digestion and gel purified. To graft the CP2861 23S rRNA gene into the 16S rRNA gene, the plasmid backbone was prepared by PCR-amplifying the plasmid pAM552-Δ23S-AflII (5 ng in 50 µl reaction) using primers introducing poly-A linkers and sequences corresponding to H101 of 23S rRNA (underlined) and h44 in 16S rRNA (italicized) TTAGTACCGGTTAGCTCAACGCATCG(T)₇₋₁₂CGAAGGTTAAGCTACCTACTTCTTTTGC (reverse primer with tether T1) and TTG

ATAGGCCGGGTGTGTAAGCGCAG(A)₇₋₁₂GGAGGGCGCTTACCCTTTGT (forward primer with tether T2). The PCR reaction, which was catalysed by Phusion High Fidelity DNA polymerase, was carried out under the following conditions: 98 °C for 2 min followed by 30 cycles of (98 °C, 30 s; 62 °C, 30 s; 72 °C, 2 min) followed by 72 °C for 5 min. The resulting 4.6-kilobase (kb) PCR fragment was treated with DpnI for 4 h at 37 °C and purified using Wizard SV Gel and PCR Clean-Up kit (Promega). The PCR-amplified plasmid backbone and the gel-purified CP2861 23S rRNA gene fragment were combined in a Gibson Assembly reaction. Five microlitres of the reaction mixture was transformed into 50 µl electrocompetent POP2136 *E. coli* cells. Cells were plated onto LB/agar plate supplemented with 100 µg ml⁻¹ ampicillin. After 24 h incubation at 30 °C, the colonies appeared. Seventeen colonies were picked, grown in LB/ampicillin at 30 °C, plasmids were isolated and linkers were sequenced using the primers 5'-GAACCTTACCTGGTCTTGACATC-3' (corresponding to the 16S rRNA sequence 976–998) and 5'-ATATCGACGGCGGTGTTG-3' (corresponding to the 23S rRNA sequence 2476–2495) to verify the complexity of the linker library (Supplementary Table 2). All the colonies were then washed off the plate and total plasmid was extracted and used to transform SQ171-competent cells.

Functional replacement of the wild-type ribosome by Ribo-T. SQ171 cells carrying the pCSacB plasmid, which contains the wild-type *rrnB* operon, were transformed with the total pRibo-T preparation isolated from the POP2136 cells. In brief, 250 ng of plasmid preparation were added to 250 µl of rubidium-chloride-competent cells. Cells were incubated for 45 min on ice, 45 s at 42 °C and then 2 min on ice followed by addition of 1 ml SOC medium and incubation at 37 °C for 2 h with shaking. A 150-µl aliquot of the culture was transferred to 1.85 ml SOC supplemented with 100 µg ml⁻¹ ampicillin and 0.25% sucrose (final concentrations) and grown overnight at 37 °C with shaking. Cells were spun down and plated on an LB agar plate containing 100 µg ml⁻¹ ampicillin, 5% sucrose and 1 mg ml⁻¹ erythromycin. Eighty of the colonies that appeared after 48-h incubation of the plate at 37 °C were inoculated in 2 ml LB supplemented with 100 µg ml⁻¹ ampicillin and grown for 48 h. The growth rate of ~30 clones that managed to grow during that period was then assessed in LB/ampicillin medium in the 96-well plate. Plasmids were isolated from six faster growing clones and linkers were sequenced. The linker T1 in five sequenced clones was composed of 9 adenines and linker T2 was composed of 8 adenines, while one clone had the reverse combination. Total RNA was extracted from these clones using RNeasy Mini Kit (Qiagen) and analysed by agarose electrophoresis. The successful replacement of the wild type pCSacB plasmid with the pRibo-T plasmids carrying Ribo-T was verified by PCR using primers 5'-GACAGTTCGGTCCCTATCTG-3' (corresponding to the 23S rRNA sequence 2599–2618) and 5'-TTAAGCCTCACG GTTCATTAG-3' (complementary to the 23S rRNA sequence 2880–2900) and additionally verified by primer extension on the total cellular rRNA as indicated in the Extended Data Fig. 4. The growth of the cells was monitored at 37 °C in 150 µl of LB supplemented with 100 µg ml⁻¹ of ampicillin in the wells of a 96-well plate in the TECAN microplate reader (15 min orbital shaking with a 3-mm amplitude followed by 5 min rest before reading). The doubling time (τ) values estimated from the logarithmic parts of the growth curves are indicated in Extended Data Fig. 4a.

Polysome analysis. The cultures of cells (250 ml) of the SQ171f strain transformed with either pAM552 (wild-type) or pRibo-T8/9 were grown at 37 °C with vigorous shaking. When the optical density reached $A_{600\text{ nm}}$ 0.4–0.7, chloramphenicol solution was added to obtain final concentration of 125 µg ml⁻¹ and, after 5 min, cells were pelleted by centrifugation at 4 °C. Polysomes were prepared following the published protocol²⁹ by freeze-thawing in the lysis buffer (20 mM Tris-HCl, pH 7.5, 15 mM MgCl₂) supplemented with 1 mg ml⁻¹ lysozyme 0.25% sodium deoxycholate and 2 U of RQ1 DNase (Promega). The lysates were centrifuged at 20,000g for 30 min at 4 °C and polysomes-containing supernatants (20 $A_{260\text{ nm}}$ absorbance units) were loaded onto the 12-ml 10–50% sucrose gradient (buffer: 20 mM Tris-HCl, pH 7.5, 10 mM MgCl₂, 100 mM NH₄Cl₂, 2 mM β -mercaptoethanol). Polysomes were resolved by centrifugation in a SW-41 rotor (39,000 r.p.m., 3 h, 4 °C). Gradients were fractionated using BioComp Instrument gradient fractionator and fractions were collected in the wells of a 96-well plate. Appropriate fractions were pooled, ribosomes were ethanol-precipitated and resuspended in 200 µl of buffer containing 300 mM sodium acetate, pH 5.5, 5 mM EDTA, 0.5% SDS. rRNA was isolated by successive extractions with phenol (pH 6.6), phenol/chloroform and chloroform. After ethanol precipitation, RNA was analysed by non-denaturing agarose gel electrophoresis.

Analysis of protein synthesis rate and proteins synthesized in Ribo-T cells. The protein synthesis rate in SQ171f cells expressing either wild-type ribosomes (plasmid pAM552) or Ribo-T (pRibo-T plasmid) was measured by following incorporation of [³⁵S]L-methionine into proteins as described³⁰. Specifically, 0.25 µCi of [³⁵S]L-methionine (specific activity 1,175 Ci mmol⁻¹) (American Radiolabeled Chemicals) was added to 1 ml of exponentially growing cells at

37 °C, and after a 45 s incubation, proteins were precipitated by addition of 1 ml of ice-cold 25% trichloroacetic acid (TCA) containing 2% casamino acids. After incubating for 30 min on ice and then 30 min at 100 °C, samples were passed through G4 glass fibre filters. The filters were washed three times with 3 ml of ice-cold 5% TCA, and once with 3 ml of acetone and air dried, and the amount of retained radioactivity was determined by scintillation counting. Preliminary measurements of the time course of [³⁵S]L-methionine incorporation in the faster-growing SQ171f/pAM552 cells showed that radioactivity curve plateaus after 120 s of incubation of cells with [³⁵S]L-methionine.

Exponential cultures (250 ml) of the SQ171f strain transformed with either pAM552 (A2058G) or pRibo-T8/9 growing in LB medium supplemented with 100 µg ml⁻¹ ampicillin and 50 µg ml⁻¹ spectinomycin were collected by centrifugation and cells were flash-frozen in liquid nitrogen. Protein isolation and two-dimensional gel electrophoresis was performed by Kendrick Labs.

Preparation of Ribo-T and wild-type ribosomes and analysis of their RNA and protein content. Ribosomes were prepared from the exponentially growing cells of the SQ171f strain transformed with either pAM552 (wild-type) or pRibo-T8/9 as described³¹. RNA was phenol extracted, precipitated as previously described and resolved by electrophoresis in a denaturing 6% (acrylamide:bis-acrylamide ratio 1:19, w/w) polyacrylamide gel (for the 5S rRNA analysis) or 4% (acrylamide:bis-acrylamide ratio 1:29, w/w) polyacrylamide gel (for the analysis of large rRNAs).

Ribo-T-associated ribosomal proteins were analysed by mass spectrometry at the Proteomics Center of Excellence, Northwestern University. Ribosomes were precipitated by incubation in 20% trichloroacetic acid at 4 °C overnight and centrifugation at 14,000g for 10 min. Precipitated ribosomes were washed once with cold 10% trichloroacetic acid and twice with acetone. The pellet was air-dried for 10–20 min before resuspension in 20 µl 8 M urea. Proteins were reduced with 10 mM dithiothreitol, and cysteine residues alkylated with 50 mM iodoacetamide in the final volume of 160 µl. Sequencing-grade trypsin (Promega) was added at a 1:50 enzyme:protein ratio, and after overnight digestion at room temperature, the reaction was stopped by addition of formic acid to 1%. After digestion, peptides were desalted using C18 Spin columns (Pierce, 89870) and lyophilized. Amino-reactive tandem mass tag (TMT) reagents (126/127, Thermo Scientific, 90065) were used for peptide labelling. The reagents were dissolved in 41 µl acetonitrile and added to the lyophilized peptides dissolved in 100 µl of 100 mM triethylammonium bicarbonate. After 1 h at room temperature, the reaction was quenched by adding 8 µl of 5% hydroxylamine. After labelling, the two samples under analysis were mixed in 1:1 ratio. Peptides were desalted using C18 ZipTip Pipette Tips (EMD Millipore) and resuspended in 30 µl of solvent A (95% water, 5% acetonitrile, 0.2% formic acid).

Peptides were analysed using nanoelectrospray ionization on an Orbitrap Elite mass spectrometer (Thermo Scientific). Proteome Discoverer (Thermo Scientific) and the Sequest algorithm were used for data analysis. Data were searched against a custom database containing UniProt entries using *E. coli* taxonomy, allowing three missed cleavages, 10 p.p.m. precursor tolerance, and carbamidomethylation of cysteine as a static modification. Variable modifications included oxidation of methionine, TMT of lysine and amino-terminal TMT. For quantification via the reporter ions the intensity of the signal closest to the theoretical m/z , within a ± 10 -p.p.m. window, was recorded. Reporter ion intensities were adjusted based on the overlap of isotopic envelopes of all reporter ions as recommended by the manufacturer. Only peptides with high confidence were used for quantification. Ratios of 126/127 were normalized based on median.

Sucrose gradient analysis of ribosomes and ribosomal subunits. Wild-type 70S ribosomes or Ribo-T isolated from SQ171f cells as described above were diluted approximately 70-fold in high Mg^{2+} buffer (20 mM Tris-HCl, pH 7.5, 100 mM NH₄Cl, 2 mM 2-mercaptoethanol, 15 mM MgCl₂) or low Mg^{2+} buffer (20 mM Tris-HCl, pH 7.5, 100 mM NH₄Cl, 2 mM 2-mercaptoethanol, 1.5 mM MgCl₂). After incubation for 30 min at 4 °C, ribosomes and subunits were resolved in 10–40% 12-ml sucrose gradients prepared with the same buffers. Gradients were centrifuged in the SW41 rotor at 38,000 r.p.m. for 3 h at 4 °C. Ribosome profiles were then analysed using gradient fractionator (BioComp Instrument).

Probing the structure of the Ribo-T tethers. The structure of the tethers was probed by dimethylsulfate (DMS) modification following a published protocol³². In brief, 10 pmol of Ribo-T or wild-type ribosomes were activated by incubation for 5 min at 42 °C in 50 µl of buffer 80 mM HEPES-KOH, pH 7.6, 15 mM MgCl₂, 100 mM NH₄Cl containing 20 U of RiboLock RI RNase inhibitor (Thermo Fisher Scientific). Two microlitres of DMS (SIGMA) diluted 1:10 in ethanol were added (2 µl of ethanol were added to the unmodified controls) and samples were incubated for 10 min at 37 °C. The modification reaction was stopped and rRNA extracted as described³². Primer extensions were carried out using the primers 5'-GACTGCCAGGGCATCCACCG-3' and 5'-AAGGTTAAGCCTCACGG-3' (for tether T1) or 5'-CCCTACGGTTACCTGTTCAG-3' for tether T2.

Additionally, the integrity of the tethers in the Ribo-T preparation was tested by extension of the primers annealing immediately 3' to the tether. Primer 5'-GTACCGTTAGCTCAACGCATC-3' was extended by reverse transcriptase across tether T1 in the presence of dATP, dTTP, dGTP and ddCTP, and primer 5'-CACAAAGTGGTAAAGCGCCCTCT-3' was extended across tether T2 in the presence of dATP, dTTP, dCTP and ddGTP.

Testing Ribo-T activity in cell-free translation system. The DNA template containing the T7 promoter and the *sf-GFP* gene¹⁴ was PCR amplified from a pY71-sfGFP plasmid³³ using primers 5'-TAATACGACTCACTATAGGG-3' and 5'-CTTCCTTTCGGGCTTTGTT-3'. GFP mRNA was prepared by *in vitro* transcription and purified by size-exclusion chromatography on a Sephadex G50 mini-column, phenol extraction and ethanol precipitation. The transcript was translated in the Δ (ribosome, amino acid, tRNA) PURExpress system kit (New England Biolabs). A typical translation reaction was assembled in a total volume of 10 μ l and contained 2 μ l of the kit solution A, 1.2 μ l of factor mixture, 1 μ l amino acid mixture (3 mM each), 1 μ l tRNA (20 μ g ml⁻¹), 0.4 μ l Ribolock RNase inhibitor (40 U μ l⁻¹), 5 μ g (~20 pmol) GFP transcript and 22 pmol of wild-type ribosomes or Ribo-T. Samples were placed in wells of a 384-well black wall/clear flat bottom tissue-culture plate (BD Biosciences) and covered with the lid. Reactions were incubated at 37 °C in a microplate reader (Tecan), and fluorescence values were recorded every 20 min at λ_{exc} = 488 nm and λ_{em} = 520 nm over 7 h. Protein synthesis rates were calculated by linear regression over the time points 0, 40 and 60 min with a R^2 > 0.9 using the trendline function of Excel (Microsoft). Time point 20 min was not taken into consideration because the plate was switched from ice to 37 °C at time 0.

Transcription/translation of the dihydrofolate reductase template supplied with the Δ (ribosome, amino acid, tRNA) PURExpress kit (New England Biolabs) was carried in the presence of [³⁵S]L-methionine (1,175 Ci mmol⁻¹) using manufacturers protocol. A typical 5 μ l reaction, assembled as described above but using 50 ng of the DNA template, was supplemented with 5 μ Ci [³⁵S]L-methionine and 10 pmol of wild-type or Ribo-T ribosomes. When needed, the reactions were supplemented with 50 μ M erythromycin. Reactions were incubated for 2 h at 37 °C, and protein products were analysed by SDS-PAGE in 16.5% Bis-Tris gels (Biorad) using NuPAGE MES/SDS running buffer (Invitrogen). Gels were stained, dried and exposed to a phosphorimager screen overnight. Radioactive bands were visualized by Typhoon phosphorimager (GE Healthcare).

Toeprinting analysis. Toeprinting was performed as previously described^{15,34}. When needed, the threonyl-tRNA synthetase inhibitor borrelidin or the initiation inhibitor thiostrepton were added to the reactions to the final concentrations of 50 μ M.

Construction of the plasmids for testing oRibo-T activity *in vivo*. The backbone plasmid pT7wtK (Extended Data Fig. 1c) was first prepared from the commercial plasmid T7-Flag-4 (Sigma Aldrich) by introducing the following changes. First, the *bla* gene was deleted using inverse PCR with phosphorylated primers 5'-TAAGTGTACAGCAAGTTTACTC-3' and 5'-ACTCTTCCTTTTCAATAT TATTGAAG-3' and Phusion High Fidelity DNA polymerase. Following purification with E.Z.N.A. Cycle Pure kit, DNA was blunt-end ligated for 14 h at 16 °C using T4 DNA ligase, and transformed into electrocompetent DH5 α *E. coli* cells and plated on LB-agar supplemented with 30 μ g ml⁻¹ kanamycin. Next, a BglII-NotI cloning site was introduced using phosphorylated primers 5'-AGATCTGTGCTACGACG GTGCGGCCGCTGAAGATCGATCTCGACG-3' and 5'-GCCTCTATGAAA AAATAACAGATATAGTCTCCCTATAGTGAGTCGTATTAGG-3', with BglII and NotI sites in bold. A sequence 3' of the T7 promoter, termed N15 (underlined), optimized for T7 expression of an orthogonal gene³⁵ was introduced on one of the primers. Purified PCR product was blunt-end ligated with T4 DNA ligase for 14 h at 16 °C, transformed into DH5 α electrocompetent cells and plated on LB-agar supplemented with 30 μ g ml⁻¹ kanamycin. The resulting plasmid pT7wtK contains a T7 promoter, wild-type Shine-Dalgarno sequence, a BglII-NotI cloning site, T1/T2 terminator, pMB1 origin of replication, a *lacI* gene and a kanamycin resistance gene.

To create plasmid pT7wtGFP, primers 5'-GGTGGTAGATCTATGAGCAAA GGTGAAGAAC-3' and 5'-GGTGGTGC GGCCGCGGGCTTTGTTAGCAG-3' were used to PCR amplify the *sf-gfp* gene from pY71-sfGFP³³, adding BglII and NotI restriction sites (bold) at the ends of the *sf-gfp* PCR product. Purified PCR product and plasmid pT7wtK were digested with BglII and NotI (New England Biolabs) for 1 h at 37 °C. The pT7wtK digested vector was treated with alkaline phosphatase CIP (New England Biolabs) for 1 h at 37 °C. Both reactions were purified with E.Z.N.A. Cycle Pure kit. The *sf-gfp* insert was added in threefold molar excess to 50 ng pT7wtK backbone, and ligated with T4 DNA ligase (NEB) for 14 h at 16 °C, transformed into DH5 α electrocompetent cells and plated on LB-agar supplemented with 30 μ g ml⁻¹ kanamycin.

To create pT7oGFP (Extended Data Fig. 1c) containing *sf-gfp*, the translation of which is controlled by an orthogonal Shine-Dalgarno sequence, the wild-type Shine-Dalgarno sequence of pT7wtGFP (AGGAGG) was mutated to an

orthogonal sequence CACCAC (ref. 3) by inverse PCR using phosphorylated primers 5'-ATGAGCAAAGGTGAAGAAC-3' and 5'-AGATCTGTGGTGTGA AAAAATAACAGATATAGTCTC-3'. PCR product purified with E.Z.N.A. Cycle Pure kit was blunt-end ligated with T4 DNA ligase for 14 h at 16 °C, transformed into electrocompetent DH5 α cells and plated on LB-agar supplemented with 30 μ g ml⁻¹ kanamycin.

Finally, the T7 promoter was replaced with the *lpp5* promoter³⁶. To achieve that, inverse PCR was performed using pT7oGFP as template and phosphorylated primers 5'-TATACTTGTGGAATTGTGAGCGGATAACAATTCTATATCTG TTATTTTTC-3' and 5'-ACACAAAGTTTTTATGTGTGTCATATTTTT TTGATAGTGAGTCGTATTAGGATC-3', (the *lpp* promoter is underlined). The *lacO* site (bold) was included to provide for inducible expression in POP2136 strain controlled with IPTG. DNA was purified, blunt-end ligated, transformed into DH5 α cells and plated on LB-agar supplemented with 30 μ g ml⁻¹ kanamycin. The resulting plasmid pLpp5oGFP (Extended Data Fig. 1c) contains a *lpp5* promoter, *lacO* site, orthogonal Shine-Dalgarno sequence, *sf-gfp* gene, T1/T2 terminator, pMB1 origin of replication, a *lacI* gene and a kanamycin-resistance gene.

The anti-Shine-Dalgarno sequence of pRibo-T 16S rRNA was mutated from wild-type (5'-TCACCTCCTTA-3') to an orthogonal sequence (5'-TCATTG TGGTA-3')³ by inverse PCR using phosphorylated primers 5'-CCTTAAGAAG CGTACTTTGTAG-3' and 5'-TACCACAATGATCCAACCGCAGG-3', pRibo-T as template and Phusion High Fidelity DNA polymerase. PCR was run at the following conditions: 98 °C, 3 min followed by 25 cycles (98 °C, 30 s; 55 °C, 30 s; 72 °C, 120 s), followed by final extension 72 °C, 10 min. Correct size band was purified by agarose gel electrophoresis and extracted using the E.Z.N.A. Gel Extraction kit. It was circularized by blunt-end ligation and transformed into POP2136 electrocompetent cells. Cells were plated on LB/agar plates supplemented with 50 μ g ml⁻¹ carbenicillin and grown at 30 °C overnight. Colonies were isolated and poRibo-T was fully sequenced.

Testing activity of oRibo-T *in vivo*. Electrocompetent POP2136 cells were transformed with the following plasmid combinations: (1) pAM552 and pT7wtK (no *gfp* control), (2) pAM552 and pLpp5oGFP, (3) pAM552o and pLpp5oGFP, and (4) poRibo-T1 and pLpp5oGFP. Transformants were plated on LB plates supplemented with 50 μ g ml⁻¹ carbenicillin and 30 μ g ml⁻¹ kanamycin and incubated for 24 h at 30 °C. Wells of a 96-well plate with low evaporation lid (Costar) was filled with 100 μ l of LB media supplemented with 50 μ g ml⁻¹ carbenicillin and 30 μ g ml⁻¹ kanamycin. The wells were inoculated with colonies from each plasmid combination above (six colonies each), and incubated at 30 °C for 14 h with shaking. Clear bottom chimney wells of another 96-well plate (Costar) were filled with 100 μ l of LB media supplemented with 50 μ g ml⁻¹ carbenicillin, 30 μ g ml⁻¹ kanamycin, and 1 mM IPTG. The plate was inoculated with 2 μ l of saturated initial inoculation plate, and incubated with linear shaking (731 cycles per min) for 16 h at 42 °C on a Biotek Synergy H1 plate reader, with continuous monitoring of cell density ($A_{600\text{ nm}}$) and sfGFP fluorescence (excitation 485 and emission 528 with sensitivity setting at 80).

Testing oRibo-T activity in cell-free translation system. Ribosomes (wild-type) or oRibo-T (mixed with wild-type ribosomes) were prepared from SQ171fg cells transformed with pAM552 or poRibo-T1, respectively. An orthogonal *sf-gfp* gene was PCR amplified from the plasmid pT7oGFP using primers 5'-TAATA CGACTCACTATAGGG-3' and 5'-ACTCGTCGAGATCGATCT-3'. The transcription-translation reaction was carried out in Δ (ribosome, amino acid, tRNA) PURExpress system as described above. The 7.5- μ l reactions were supplemented with 18.75 ng DNA template and 7.5 pmol ribosomes, and when needed, clindamycin or pactamycin were added to the reactions to the final concentrations of 50 μ M or 100 μ M, respectively.

For *in vitro* translation of an orthogonal *secM-lacZa* template, it was PCR-amplified from the poSML plasmid using a direct primer 5'-TAATACGACT CACTATAGGG-3' corresponding to the T7 promoter and a reverse primer 5'-TTCCAGTCACGACGTT-3', which allowed preserving 18 codons after the SecM arrest site. mRNA was prepared by *in vitro* transcription and purified. It was then translated in the Δ (ribosome, amino acid, tRNA) PURExpress system assembled in a total volume of 5 μ l and containing 1 μ l of the kit solution A, 0.6 μ l of factor mixture, 0.5 μ l amino acid mixture (3 mM each) lacking methionine, 0.2 μ l of [³⁵S]L-methionine 8.5 μ M (1,175 Ci mmol⁻¹), 0.5 μ l tRNA (20 μ g ml⁻¹), 0.2 μ l Ribolock RNase inhibitor (40 U μ l⁻¹), 100 μ M pactamycin, 10 pmol transcript and 10 pmol of total ribosomes. Translation was carried out for 5 min at 37 °C, followed by addition of 1 μ g of RNase A and incubation for 5 min at 37 °C. Translation products were analysed in 16.5% Tricine SDS-PAGE³⁷. The gel was stained, dried, and exposed to a phosphorimager screen overnight.

Construction of C41(DE3)/ Δ lacZ58(M15). The *AlacZ58*(M15) allele required for alpha complementation was transduced from the *E. coli* strain K1342 (*E. coli* Genetic Stock Center, Yale) into *E. coli* C41(DE3) strain by P1 phage transduction protocol³⁸. Transductants were selected on LB agar supplemented with 10 μ g ml⁻¹

tetracycline. Then colonies were re-streaked on LB-agar plates containing $10 \mu\text{g ml}^{-1}$ tetracycline, $200 \mu\text{M}$ IPTG and $80 \mu\text{g ml}^{-1}$ X-Gal. The replacement of wild-type *lacZ* with the *AlacZ58*(M15) allele was verified by PCR using primers 5'-ACCATGATTACGGATTCACTGG-3' and 5'-CCGTTGCCACACAGATGAA-3' (the sizes of the expected PCR products are 467 bp for wild-type and 374 bp for the mutant).

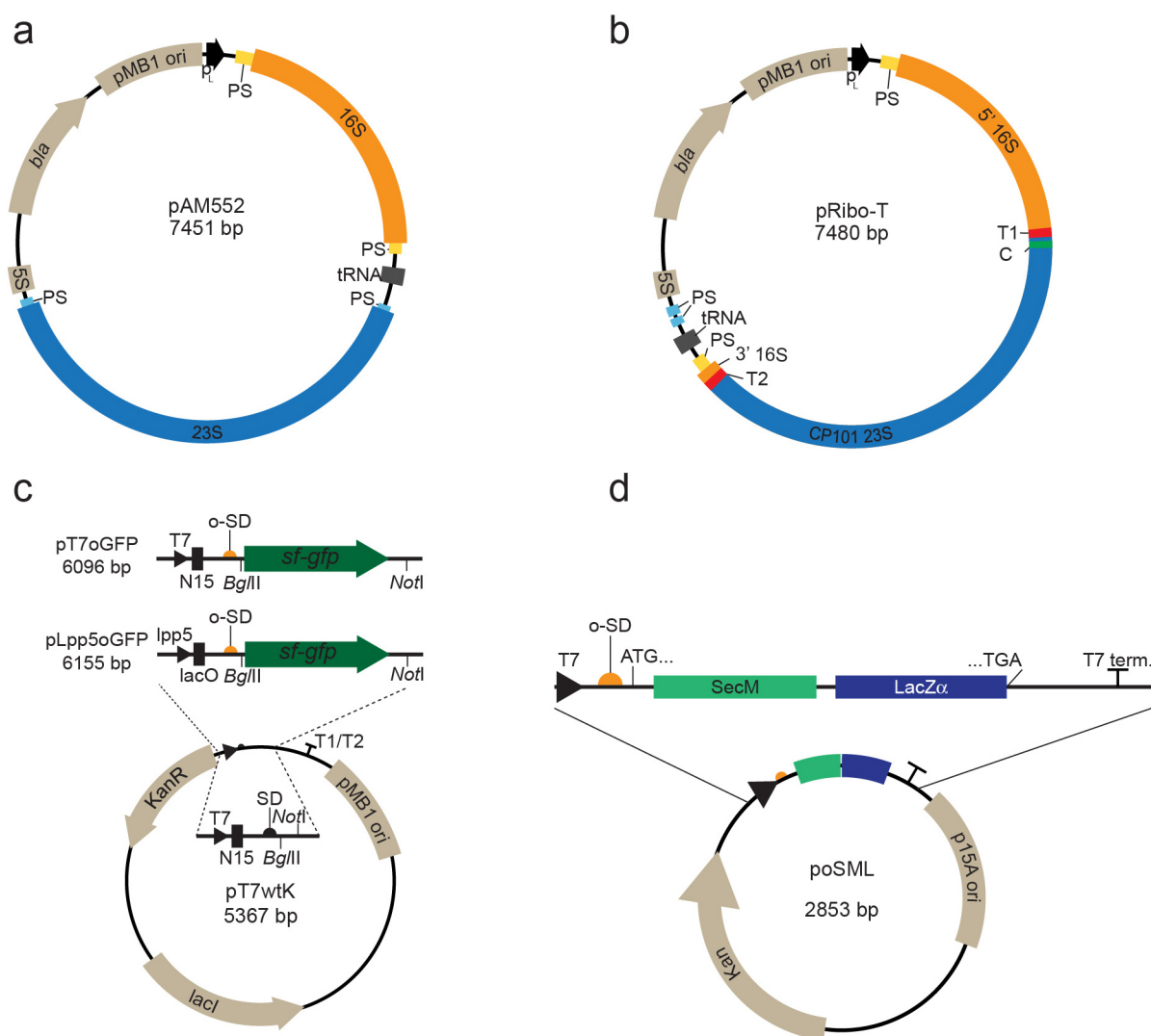
Construction of the orthogonal SecM-lacZa reporter poSML. The backbone of the pACYC177 vector was PCR-amplified using primers 5'-ATCTCATGACCAAATCCCTTAACGTGAGT-3' and 5'-GCGTTAGCTTTTACCCCTGCATCTTGTAG-3'. A 568-bp DNA fragment in which the ends overlapped with the amplified pACYC177 backbone and which contained T7 promoter, the orthogonal Shine-Dalgarno sequence CACCAC³, the *secM*(121–166)-*lacZa* fusion from the plasmid pNH122 (ref. 18), was synthesized by Integrated DNA Technologies. The pACYC177 backbone and the *secM-lacZa* construct were combined using Gibson Assembly and introduced in the C41(DE3)/*AlacZ58*(M15) cells.

Construction of the 2451/2452 mutant poRibo-T library and selecting mutants capable of alleviating SecM-mediated translation arrest. A library of A2451N/C2452N mutants was generated by inverse PCR using plasmid poRibo-T2 as a template, Phusion High Fidelity DNA polymerase, and primers 5'-AGGCTGATACCGCCCAAG-3' and 5'-CTCTTGGGCGGTATCAGCCTNNTATCCCGGAGTACCTTTTATC-3', with added sequence (underlined) used for re-circularization with Gibson assembly. PCR reaction was carried out under the following conditions: 98°C , 3 min followed by 25 cycles (98°C , 30 s; 55°C , 30 s; 72°C , 120 s), followed by final extension 72°C , 10 min. The PCR-amplified DNA band was purified by extraction from the agarose gel with an E.Z.N.A. gel extraction kit, and re-circularized by Gibson assembly for 1 h at 50°C . Two microlitres of the reaction were transformed into electrocompetent POP2136 cells plated on LB plates supplemented with $50 \mu\text{g ml}^{-1}$ carbenicillin and grown for 24 h at 30°C . Individual colonies were picked and sequenced to identify all possible 16 variants of the library.

The C41(DE3)/*AlacZ58*(M15) cells were transformed with the poSML reporter plasmid (Extended Data Fig. 1d) and plated on LB-agar containing $50 \mu\text{g ml}^{-1}$ kanamycin. One of the colonies, which appeared after overnight incubation at 37°C , was inoculated into liquid culture, grown in the presence of $50 \mu\text{g ml}^{-1}$ kanamycin and cells were rendered chemically competent. Cells were transformed with the pooled library of 16 2451/2452 mutants. Transformed cells were plated on LB agar containing $50 \mu\text{g ml}^{-1}$ kanamycin, $100 \mu\text{g ml}^{-1}$ ampicillin, 0.5 mM IPTG, $40 \mu\text{g ml}^{-1}$ X-Gal and 2 mM lacZ inhibitor phenylethyl- β -D-thiogalactopyranoside

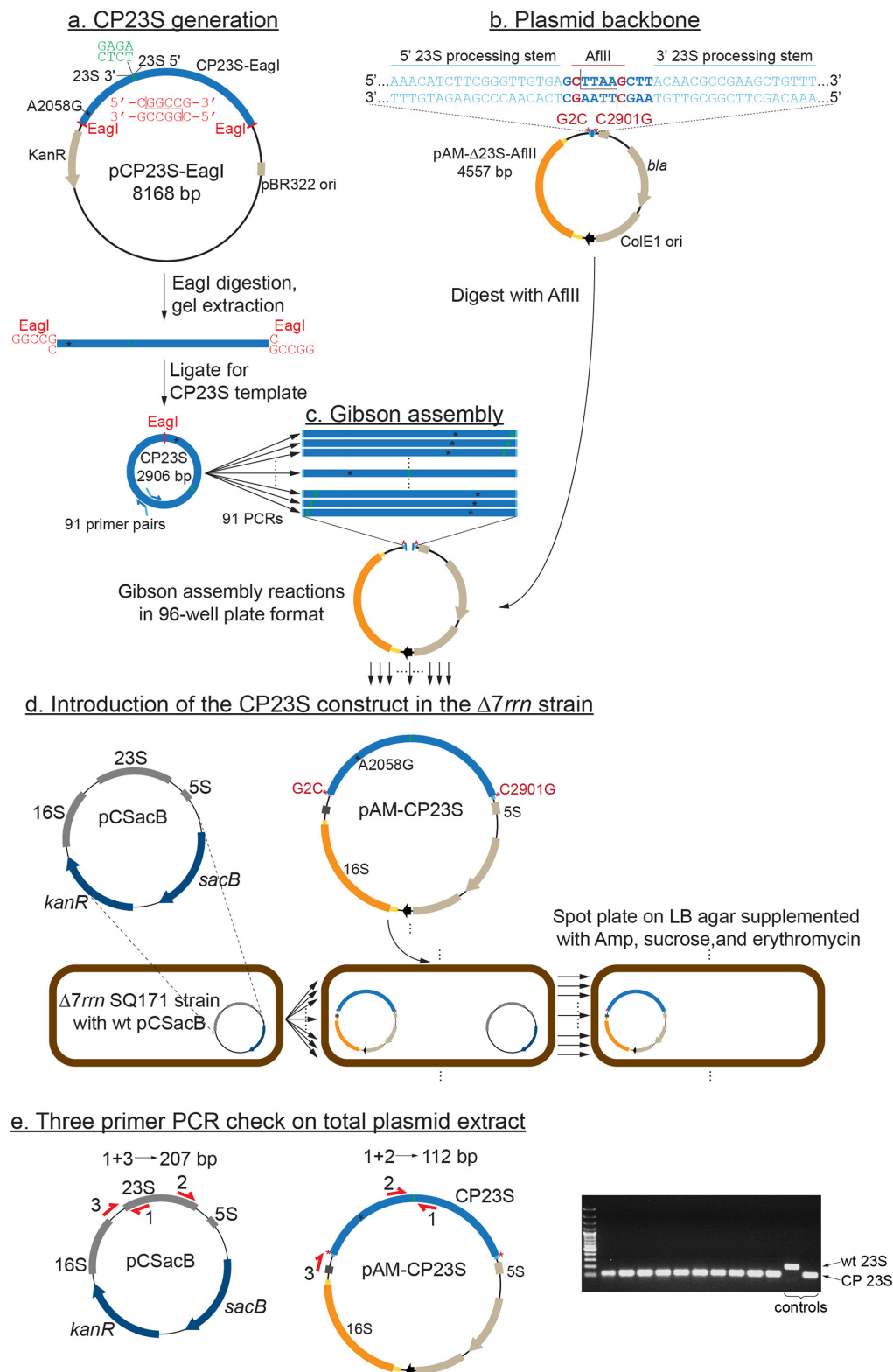
(PETG). Plates were incubated at 37°C for 24 h and photographed. Sixteen white colonies or fifteen blue colonies were inoculated in 5 ml of LB medium supplemented with $100 \mu\text{g ml}^{-1}$ ampicillin and grown overnight. The plasmids were isolated and the identities of nucleotide residues at the position 2451 and 2452 of the 23S rRNA were analysed by sequencing. Alternatively, the poSML-transformed C41(DE3)/*AlacZ58*(M15) cells were transformed with individual plasmids representing all possible 16 variants of the nucleotide combinations at positions 2451 and 2452. The poRibo-T2 plasmid carrying A2058G mutation was used as a control. In addition, the poRibo-T2 plasmid carrying the U2585G mutation was included in the transformation experiment. The transformed cells were plated on LB/agar containing $50 \mu\text{g ml}^{-1}$ kanamycin and $100 \mu\text{g ml}^{-1}$ ampicillin and incubated overnight at 37°C . Three colonies from each transformation were then streaked on LB/agar plates containing $50 \mu\text{g ml}^{-1}$ kanamycin and $100 \mu\text{g ml}^{-1}$ ampicillin and supplemented with 0.5 mM IPTG, $40 \mu\text{g ml}^{-1}$ X-Gal and 2 mM PETG. Plates were incubated at 37°C for 22 h and photographed.

28. Gibson, D. G. *et al.* Enzymatic assembly of DNA molecules up to several hundred kilobases. *Nature Methods* **6**, 343–345 (2009).
29. Fredrick, K., Dunny, G. M. & Noller, H. F. Tagging ribosomal protein S7 allows rapid identification of mutants defective in assembly and function of 30 S subunits. *J. Mol. Biol.* **298**, 379–394 (2000).
30. Kannan, K., Vázquez-Laslop, N. & Mankin, A. S. Selective protein synthesis by ribosomes with a drug-obstructed exit tunnel. *Cell* **151**, 508–520 (2012).
31. Ohashi, H., Shimizu, Y., Ying, B. W. & Ueda, T. Efficient protein selection based on ribosome display system with purified components. *Biochem. Biophys. Res. Commun.* **352**, 270–276 (2007).
32. Merryman, C. & Noller, H. F. in *RNA:Protein Interactions, a Practical Approach* (ed. Smith, C. W. J.) 237–253 (Oxford Univ. Press, 1998).
33. Bundy, B. C. & Swartz, J. R. Site-specific incorporation of p-propargyloxyphenylalanine in a cell-free environment for direct protein-protein click conjugation. *Bioconjug. Chem.* **21**, 255–263 (2010).
34. Vázquez-Laslop, N., Thum, C. & Mankin, A. S. Molecular mechanism of drug-dependent ribosome stalling. *Mol. Cell* **30**, 190–202 (2008).
35. An, W. & Chin, J. W. Synthesis of orthogonal transcription-translation networks. *Proc. Natl Acad. Sci. USA* **106**, 8477–8482 (2009).
36. Inouye, S. & Inouye, M. Up-promoter mutations in the *lpp* gene of *Escherichia coli*. *Nucleic Acids Res.* **13**, 3101–3110 (1985).
37. Schagger, H. & von Jagow, G. Tricine-sodium dodecyl sulfate-polyacrylamide gel electrophoresis for the separation of proteins in the range from 1 to 100 kDa. *Anal. Biochem.* **166**, 368–379 (1987).
38. Thomason, L. C., Costantino, N. & Court, D. L. *E. coli* genome manipulation by P1 transduction. *Curr. Prot. Mol. Biol.* **Chapter 1**, Unit-1 17 (2007).



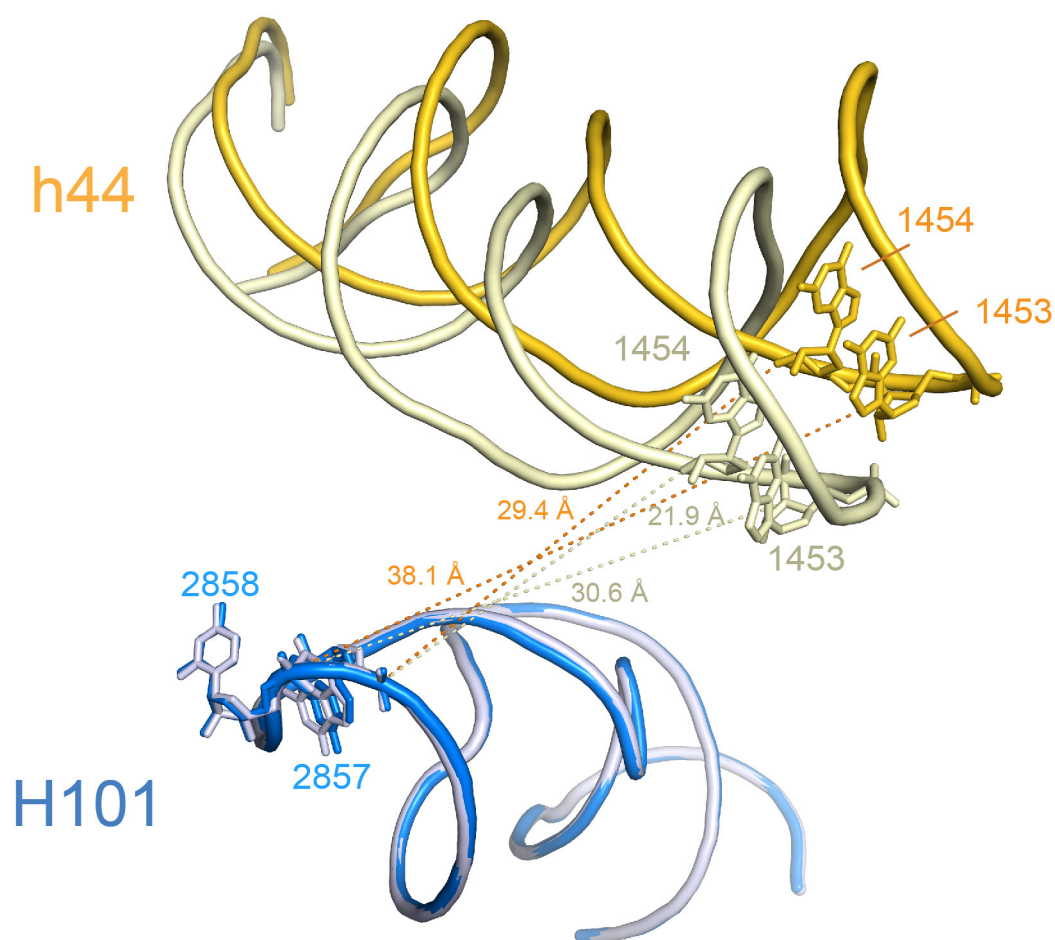
Extended Data Figure 1 | Key plasmids used in the study. **a**, The pAM552 plasmid is a derivative of pLK35 (ref. 27), from which the unessential segments of the pBR322 cloning vector have been removed. pAM552 contains the entire *rrnB* operon of *E. coli* under the control of the phage lambda P_L promoter, which is constitutively active in the conventional *E. coli* strains but is silent at 30 °C in the strain POP2136 (30 °C) carrying the *cl857* gene of the temperature-sensitive lambda repressor. The 16S rRNA gene is shown in orange, and the 16S rRNA processing stem sequences indicated in yellow. The 23S rRNA gene is blue, and the corresponding processing stem sequences are light blue. The intergenic tRNA^{Glu} gene is shown in dark grey. **b**, The map of the pRibo-T8/9 plasmid derived from pAM552. The native 5' and 3' ends of the 23S

rRNA were linked via a tetranucleotide sequence GAGA (connector C shown in green), and circularly permuted 23 rRNA gene, 'opened' in the apex loop of H101, was inserted in the apex loop of 16S rRNA helix h44 via an A₈ linker T1 and an A₉ linker T2 (red bars). **c**, The map of the backbone plasmid pT7wtK and the reporter plasmids pT7oGFP and pLpp5oGFP, expressing *sf-gfp* controlled by an orthogonal Shine–Dalgarno sequence (orange semi-circle) under T7 or *lpp5* promoters (black triangles). **d**, The map of the pACYC177-derived plasmid containing the *secM-lacZ α* reporter gene controlled by the T7 promoter (black triangle) and alternative Shine–Dalgarno sequence (orange semi-circle). The sequence of the *secM-lacZ α* reporter matches that in the originally described plasmid pNH122 (ref. 18).



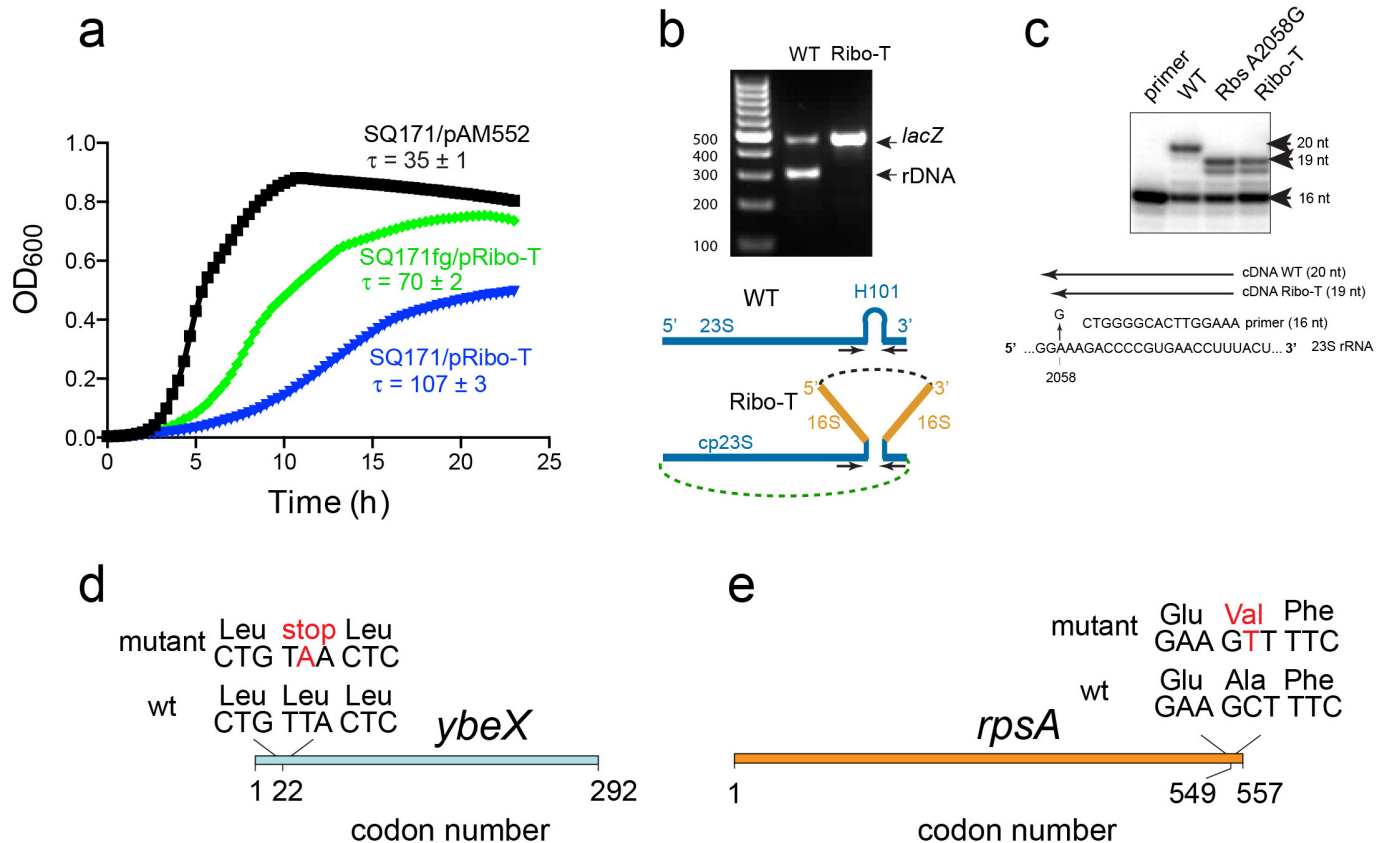
Extended Data Figure 2 | The experimental scheme of preparing and testing circularly permuted 23S rRNA gene library. **a**, The CP23S template is generated from pCP23S-EagI plasmid by EagI digestion and ligation. Each CP23S variant is generated by PCR using circularized 23S rRNA gene as a template and a unique primer pair, with added sequences overlapping the destination plasmid backbone. **b**, The plasmid backbone is prepared by digestion of pAM552-Δ23S-AfIII with the AfIII restriction enzyme, which linearizes the backbone at the 23S processing stem site. **c**, Gibson assembly is

used to incorporate each CP23S variant into the plasmid backbone to generate the 91 target circular permutants. **d**, The pAM-CP23S plasmids are transformed into the SQ171 strain lacking chromosomal rRNA operons and carrying the pCSacB plasmid with the wild-type rRNA operon, and transformants resistant to ampicillin, erythromycin and sucrose are selected. **e**, A complete replacement of pCSacB with pAM-CP23S is verified by a three-primer diagnostic PCR.



Extended Data Figure 3 | The Ribo-T tethers allow for the ribosome ratcheting. Distance changes (Å) between the 16S rRNA and 23S rRNA residues h44 and H101 connected by the oligo(A) linkers in Ribo-T when the ribosome undergoes the transition from the classic to the rotated state. The distances between the 5' phosphorus atoms of the corresponding nucleotides

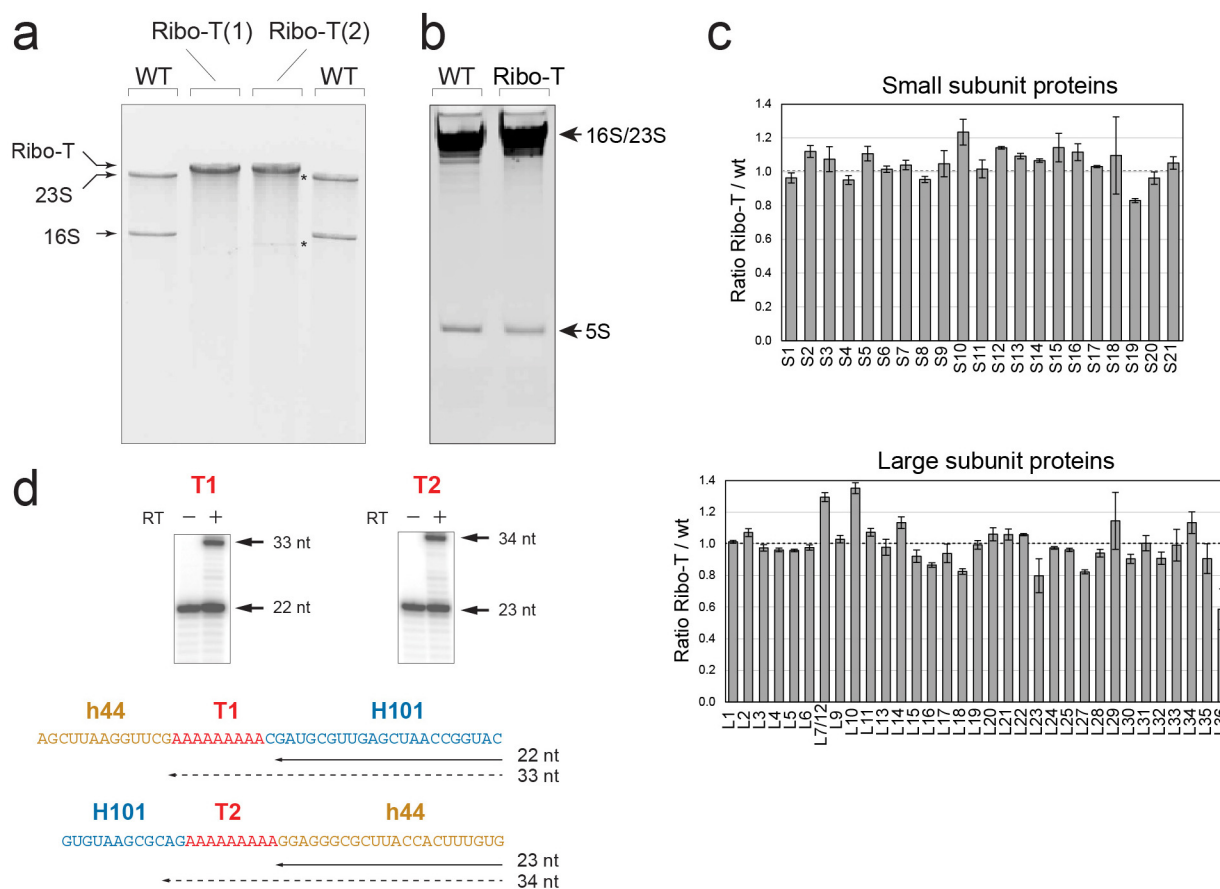
are shown. 16S and 23S rRNAs in the non-rotated state are tan and pale blue, and in the rotated state are gold and blue, respectively. The structures of the *E. coli* ribosomes used for measuring the distances and generating the figure have PDB accession numbers 3R8T and 4GD2 (non-rotated state) and 3R8S and 4GD1 (rotated state).



Extended Data Figure 4 | Chromosomal mutations enhance growth of SQ171 cells in which Ribo-T completely replace wild-type ribosomes.

a, Growth curves of the parental SQ171 cells transformed with the pAM552(G2058) plasmid (black curve) or pRibo-T8/9 plasmid (blue curve) or selected fast growing mutant (SQ171fg) transformed with pRibo-T8/9 (green curve). The cells express homogeneous populations of ribosomes (wt for pAM552 transformants or Ribo-T for the pRibo-T8/9 transformants, see panels b and c). **b**, PCR analysis of rDNA in the SQ171fg strain transformed with pRibo-T8/9 (the SQ110 strain that carries a single chromosomal copy of the *rrn* allele served as a wild-type control). The PCR primers amplify the 302-base-pair 23S rRNA gene segment 'across' the H101 hairpin in wild-type rDNA. In pRibo-T, the primer annealing sites are more than 4.8 kb apart (black dashed line), which prevents formation of the PCR product. Two additional primers designed to amplify a 467-bp fragment from the *lacZ* gene were included in the same PCR reaction as an internal control. The gel is

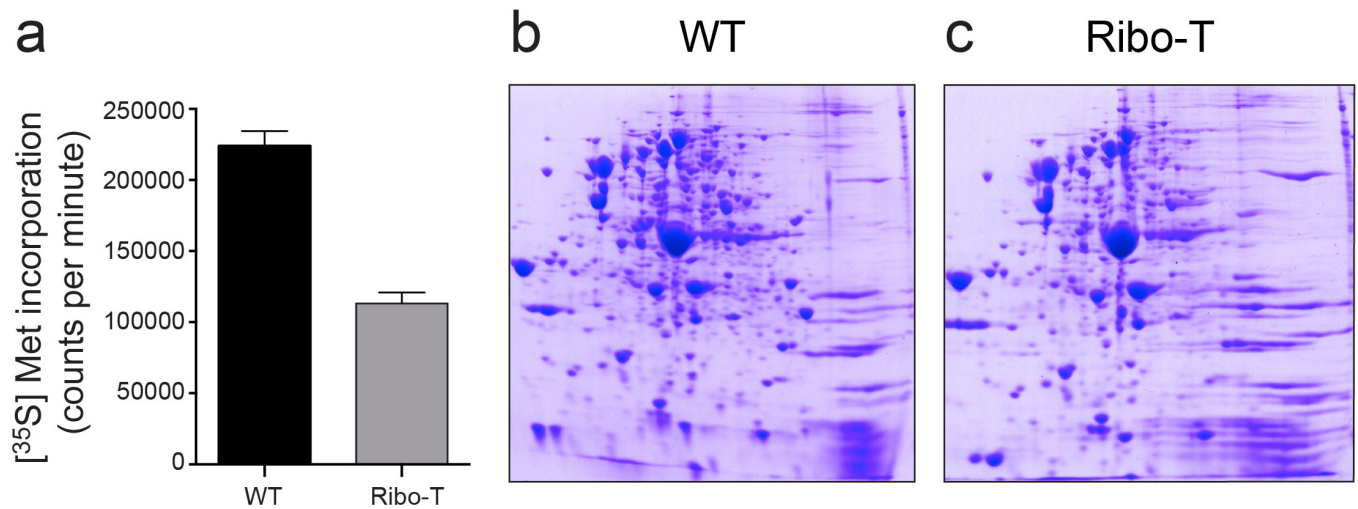
representative of two independent biological experiments. **c**, Primer extension analysis of rRNA expressed in the SQ171fg cells transformed with pAM552 (WT), pAM552 with the A2058G mutation, or pRibo-T8/9, which carries the A2058G mutation. Primer extension was carried out in the presence of dTTP and ddCTP. Because Ribo-T contains the A2058G mutation in the 23S rRNA sequence, the generated cDNA is one nucleotide shorter than the one generated on the wild-type 23S rRNA template. The lack of the 20-nucleotide cDNA band in the Ribo-T sample demonstrates the absence of wild-type 23S rRNA in the SQ171fg cells transformed with pRibo-T8/9. The gel is representative of three independent biological experiments. **d**, **e**, Chromosomal mutations in SQ171fg: a nonsense mutation in the Leu codon 22 of the *ybeX* gene encoding a protein similar to Mg^{2+}/Co^{2+} efflux transporter (**d**); and a missense mutation in codon 549 of the *rpsA* gene encoding ribosomal protein S1 (**e**).



Extended Data Figure 5 | Ribo-T composition and integrity of the linkers.

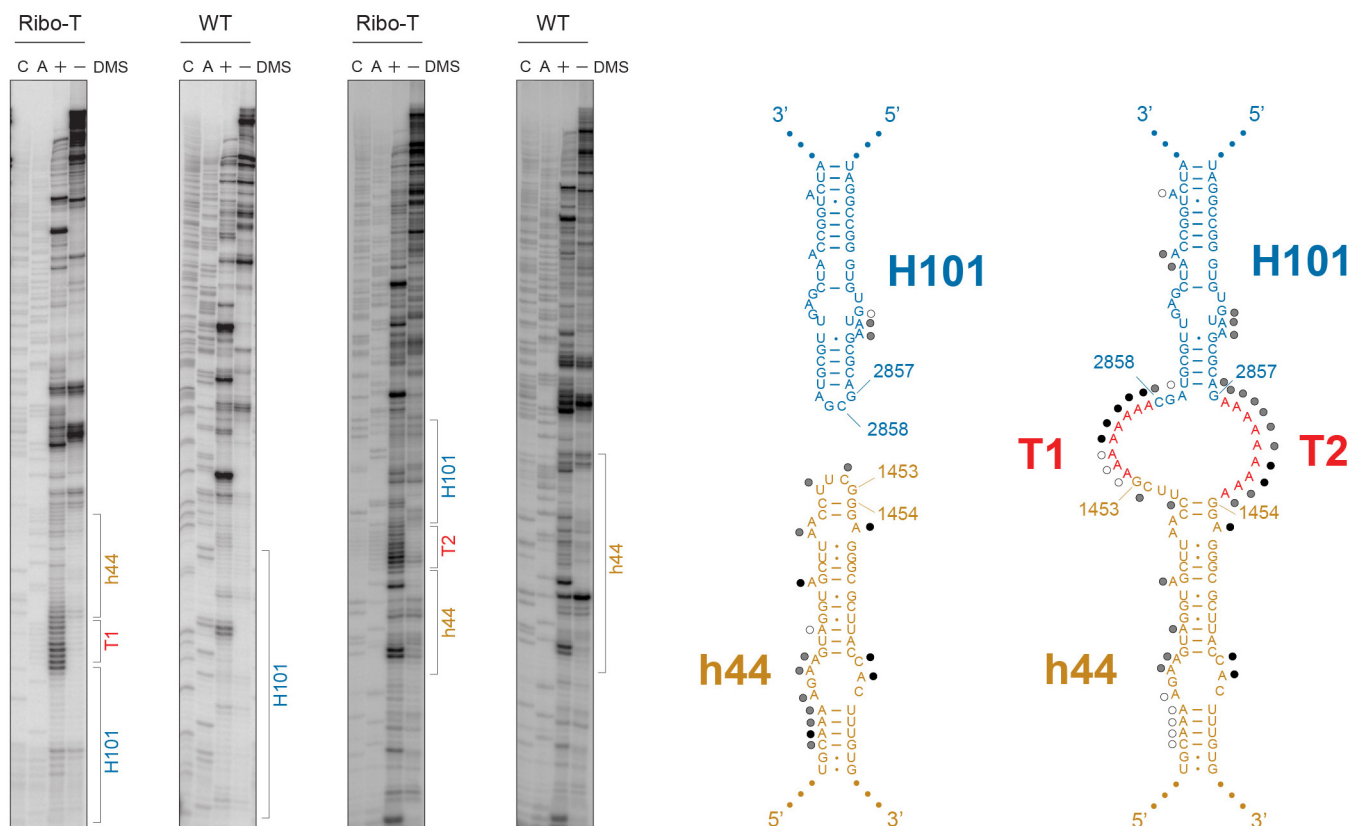
a, b, Analysis of rRNA extracted from the isolated wild-type ribosomes or Ribo-T in a denaturing 4% (**a**) or 8% (**b**) polyacrylamide gel. **a**, Ribo-T(1) and Ribo-T(2) represent two individual preparations with Ribo-T(2) isolated following the standard procedure (see Methods), and Ribo-T(1) isolated by immediate pelleting through the sucrose cushion after the cell lysis. The faint bands in the Ribo-T2 preparation indicated by the asterisks could be occasionally seen in some preparations; they probably represent rRNA fragments generated by cleavage of the linkers in a small fraction of Ribo-T either in the cell or during Ribo-T preparation. **b**, 5S rRNA is present in Ribo-T.

c, The relative abundance of small and large subunit proteins in Ribo-T in comparison with wild-type ribosome as determined by mass spectrometry (protein L26 could not be reliably quantified in Ribo-T and wild-type ribosomes). The data represent the average of three technical replicates, and error bars indicate the s.d. **d**, Analysis of the integrity of the T1 and T2 linkers in a Ribo-T preparation by primer extension. The 22-nucleotide-long primer was extended across the T1 linker in the presence of ddCTP terminator and the 23S-nucleotide-long primer was extended across the T2 linker in the presence of ddGTP terminator. Control samples (–) represent the unextended primers. The gels are representative of two independent experiments.



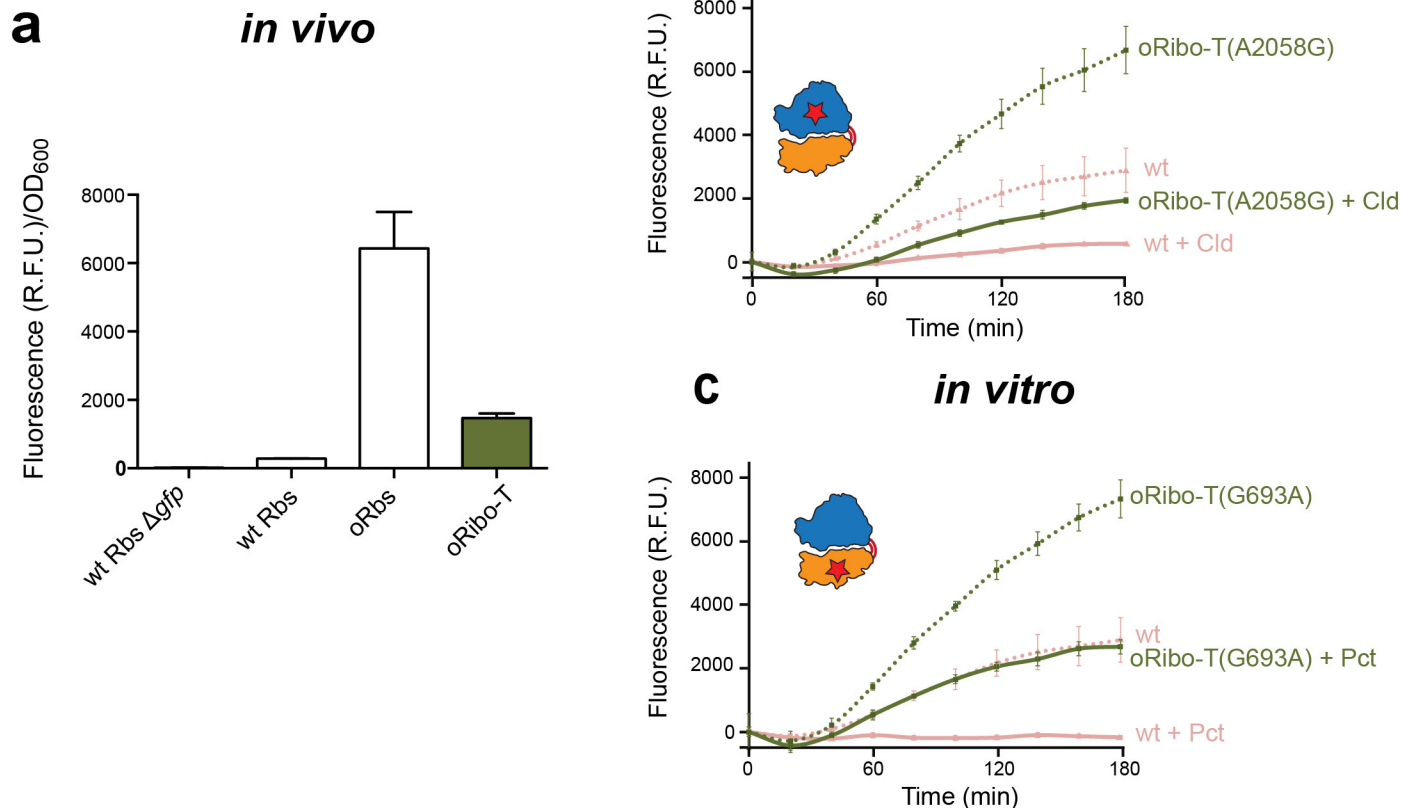
Extended Data Figure 6 | Ribo-T can successfully translate most cellular polypeptides. **a**, Protein synthesis rate in SQ171fg cells expressing wild-type ribosomes or Ribo-T. Protein synthesis was measured by quantifying the incorporation of [³⁵S] L-methionine into TCA-insoluble protein fraction during a 45-s incubation at 37 °C in minimal medium. The bar graphs represent

the average values of experiments performed in two biological replicates each done in two technical duplicates. Error bars denote s.d. **b**, **c**, 2D gel electrophoresis analysis of the proteins expressed in exponentially growing SQ171fg transformed with pAM552 (A2058G) (**b**) or pRibo-T (**c**).



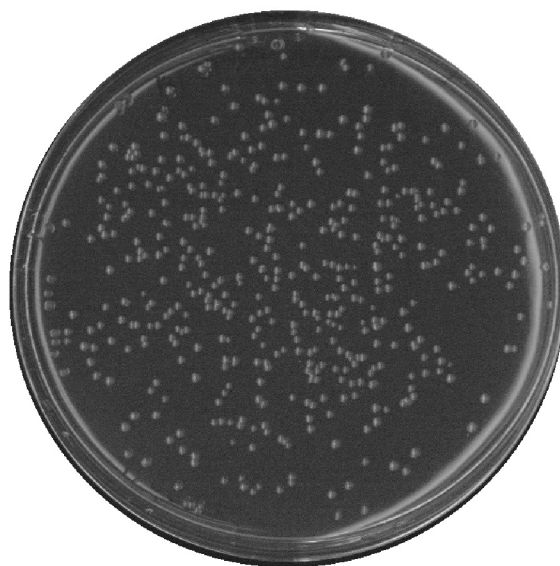
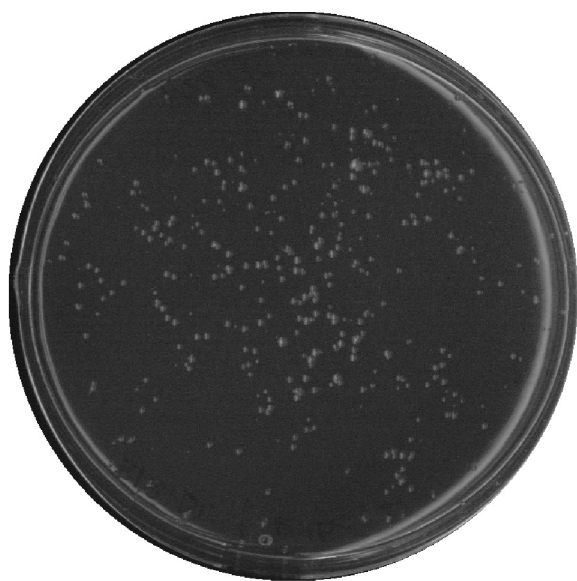
Extended Data Figure 7 | Chemical probing of the structure of the Ribo-T linkers. Ribo-T or wild-type ribosomes were modified by dimethylsulfate, and extracted rRNA was subjected to primer extension analysis. In each gel, the left two lanes ('C' and 'A') represent sequencing reactions followed by dimethylsulfate-modified sample and control (unmodified) RNA. The

diagrams on the right represent the secondary structures of helices H101 and h44 in wild-type ribosomes (left) and Ribo-T (right), with the nucleotide residues modified strongly, moderately and weakly indicated by black, grey and white circles, respectively. The gels are representative of two independent experiments.



Extended Data Figure 8 | Translation of the orthogonal *sf-gfp* gene by oRibo-T *in vivo* and *in vitro*. **a**, Expression of an orthogonal *sf-gfp* reporter in the *E. coli* POP2136 cells transformed with pAM552 plasmid encoding wild-type rRNA (wt Rbs), pAM552 with an orthogonal Shine–Dalgarno sequence in 16S rRNA of a non-tethered ribosome (oRbs) or poRibo-T1 expressing an orthogonal Ribo-T (green bar). Cells lacking *gfp* reporter gene (wt Rbs Δ gfp) were used as a background fluorescence control. The data represent the average value of six biological replicates in technical triplicates; error bars indicate the s.d. **b**, *In vitro* translation of the orthogonal *sf-gfp* reporter by non-tethered

non-orthogonal wt ribosomes (pink lines), or oRibo-T(A2058G) (which also contained cellular wild-type ribosomes) (green lines). The dotted lines correspond to the translation reactions without antibiotic and solid lines represent reactions supplemented with 50 μ M clindamycin (Cld). **c**, Same as in **b**, but oRibo-T contained a G693A mutation instead of A2058G and clindamycin was replaced with 100 μ M pactamycin (Pct). The red stars indicate the ribosomal subunit carrying the antibiotic-resistance mutation. Graphs in **b** and **c** are each representative of two biological replicates each performed in technical triplicates, and error bars indicating the s.d.

a poRibo-T1 (16 hr)**c** poRibo-T2 (16 hr)**b** poRibo-T1 (32 hr)

Extended Data Figure 9 | Promoter mutation in oRibo-T improves transformation of the *E. coli* cells. **a, b,** Several *E. coli* strains, including BL21 shown in this figure, as well as JM109 and C41, produced slowly growing, heterogeneous colonies when transformed with poRibo-T1. **c,** Fortuitously, in the course of the experiments we isolated a spontaneous mutant plasmid, poRibo-T2, which showed improved transformation efficiency, producing evenly sized colonies after a single overnight incubation. Sequencing of

poRibo-T2 revealed a single mutation in the P_L promoter controlling Ribo-T expression, altering the '-10' box from GATACT to TATACT bringing it closer to the TATAAT consensus. It is unclear why the promoter mutation improves performance of poRibo-T (as well as of non-orthogonal pRibo-T) in 'unselected' *E. coli* cells. The plates show representative results of three independent biological experiments.

Extended Data Table 1 | Characterization of the growth of *E. coli* SQ171 cells expressing a pure population of ribosomes with circularly permuted 23S rRNA

	Doubling time (min) *		Cell density (OD ₆₀₀) at saturation [†]		n [¶]
	30 °C	37 °C	30 °C	37 °C	
pAM552 [‡]	61.0 ± 3.2	53.9 ± 1.0	1.04 ± 0.06	0.93 ± 0.03	4
pAM552-AfIII [§]	67.4 ± 1.0	53.3 ± 2.4	1.07 ± 0.01	0.97 ± 0.00	4
CP67	106.4 ± 5.4	69.6 ± 2.1	0.83 ± 0.05	0.41 ± 0.07	3
CP95	144.9 ± 35.9	82.4 ± 24.4	0.66 ± 0.31	0.51 ± 0.18	6
CP104	90.8 ± 10.3	52.7 ± 3.2	0.98 ± 0.03	0.95 ± 0.02	3
CP168	123.8 ± 27.9	57.7 ± 1.9	0.70 ± 0.22	0.88 ± 0.12	10
CP281	100.1 ± 11.0	54.6 ± 10.1	1.01 ± 0.04	0.93 ± 0.13	3
CP549	101.7 ± 18.2	46.5 ± 3.9	1.00 ± 0.02	0.98 ± 0.03	3
CP617	231.7 ± 20.5	91.5 ± 18.5	0.16 ± 0.03	0.85 ± 0.05	4
CP634	162.0 ± 34.2	212.5 ± 58.1	0.46 ± 0.19	0.50 ± 0.10	3
CP879	106.6 ± 4.7	51.4 ± 4.6	1.03 ± 0.02	0.99 ± 0.04	3
CP891	144.5 ± 41.8	60.7 ± 4.1	0.56 ± 0.43	0.76 ± 0.23	6
CP1112	89.6 ± 6.0	57.8 ± 12.2	0.96 ± 0.02	0.91 ± 0.12	3
CP1178	102.5 ± 11.0	46.2 ± 1.3	0.96 ± 0.02	0.99 ± 0.01	3
CP1498	167.5 ± 17.5	118.0 ± 17.1	0.56 ± 0.32	0.52 ± 0.19	3
CP1511	131.5 ± 4.2	76.7 ± 1.5	0.88 ± 0.01	0.88 ± 0.01	3
CP1587	98.1 ± 12.4	55.1 ± 6.6	0.93 ± 0.05	0.92 ± 0.08	3
CP1716	174.4 ± 31.9	117.8 ± 16.5	0.44 ± 0.16	0.62 ± 0.34	3
CP1733	117.3 ± 8.2	83.8 ± 2.2	0.95 ± 0.01	0.80 ± 0.01	3
CP1741	230.0 ± 14.7	269.0 ± 50.3	0.28 ± 0.00	0.66 ± 0.09	3
CP1873	108.4 ± 6.5	52.9 ± 0.8	0.94 ± 0.01	0.91 ± 0.01	3
CP2148	83.0 ± 2.9	52.4 ± 3.9	0.73 ± 0.09	0.82 ± 0.02	4
CP2800	85.9 ± 15.7	53.5 ± 9.7	1.04 ± 0.03	0.91 ± 0.12	3
CP2861	138.4 ± 10.7	93.7 ± 4.5	0.88 ± 0.00	0.83 ± 0.04	3

*Growth in 100 µl LB media supplemented with 50 µg ml⁻¹ carbenicillin in 96-well plate with shaking.

[†]After 18 h of growth.

[‡]pAM552: wild-type *rnb* operon.

[§]pAM552-AfIII: *rnb* operon with the 23S rRNA mutations G2C and C2901G used to introduce the AfIII restriction sites.

^{||}CPx: *rnb* with 23S circular permutations and G2C/C2901G mutations; x indicates the 5' starting nucleotide of the circularly permuted 23S gene.

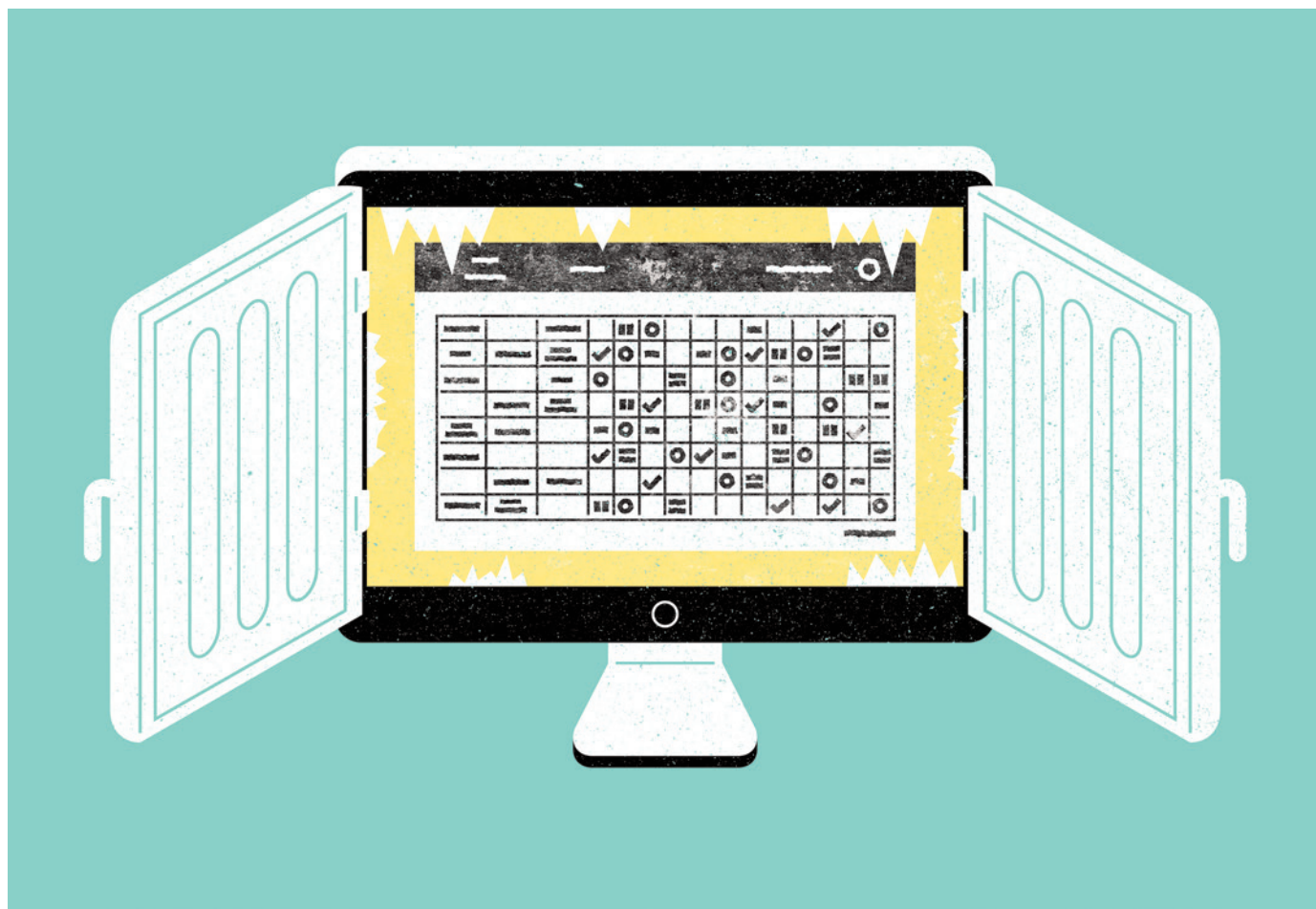
[¶]Biological replicates are indicated in the 'n' column, which is the number of separate colonies that were used for each mean number and s.d.

TOOLBOX

TIME TO TAKE STOCK

Inventory-tracking systems range from paper filing to custom-made databases. Using the right system can save researchers time, money and frustration.

ILLUSTRATION BY THE PROJECT TWINS



BY JEFFREY M. PERKEL

When Marilyn Goudreault received a request for plasmids stored in the repository of the laboratory she manages at the Lunenfeld–Tanenbaum Research Institute in Toronto, Canada, there was never any question whether she would honour it. Reagent sharing is typically a precondition of publication in peer-reviewed journals, and is fundamental to the scientific process. But first, Goudreault would have to find the plasmids — circular strings of DNA.

In many labs, the task might have required a tortuous search through old notebooks, out-of-date spreadsheets and frost-encrusted freezer boxes. But in Goudreault's lab, reagents are tracked with OpenFreezer: a free, web-based system designed to document data such as the location, source, creator and biological properties of every reagent in a user's possession — including not just plasmids, but also antibodies and stretches of DNA, RNA and protein. Goudreault needed only to run a quick search for the materials, then retrieve the indicated boxes from storage. “I had

everything within 15 minutes,” she says.

OpenFreezer is one of a number of computerized inventory systems developed to simplify lab management. They range from simple homespun databases for individual labs to enterprise-level systems, and accommodate a range of budgets. Some are designed for documenting frozen samples; others for tracking chemicals or lab animals. Some facilitate purchasing and equipment scheduling; others are limited to simple descriptions. But in all cases, the goal is to ensure that lab workers know what resources are available ►

► to them, and where to find them.

Many labs track their inventories with nothing more than sheets of paper in a binder or entries in an Excel spreadsheet. But some are using more-sophisticated database software. In the late 1990s, for example, virologist Joe Mymryk created a Microsoft Access database to track key reagents when he set up his lab at Western University in London, Canada. In 2007, his graduate student Ahmed Yousef joined Ibrahim Baggili, a computer-science graduate student then at Purdue University in West Lafayette, Indiana, to develop a friendlier, Windows-based interface to the system, called LINA (Laboratory Inventory Network Application; A. F. Yousef *et al.* *J. Lab. Automat.* **16**, 82–89; 2011).

LINA draws from a series of Access databases — one for each class of reagent, including bacterial and yeast strains and short sequences of DNA and RNA known as oligonucleotides. As new reagents are developed or acquired, they are logged in the system, which assigns each one a unique identifier. Samples are then organized in freezer boxes according to those numbers and users can search the database by keyword, source and function.

SEARCH AND RESCUE

For Mymryk, LINA's most useful feature is a tool to search and compare DNA sequences. This means that he can enter a gene sequence and check whether the library contains any oligonucleotides that could be used to amplify it, rather than just ordering new ones. "The oligo thing has really saved my bacon," he says.

LINA is free and simple to use, which makes it particularly attractive for small molecular-biology labs. But more-advanced options are also available at no cost. Marie Ebersole, who manages the chemistry preparation room at Wellesley College in Massachusetts, opted to upgrade her Excel-based system to Quartz, a free cloud-based system that allows her to track purchases for her 1,000-reagent collection. Quartz's zero cost figured prominently in her decision. "I didn't have to have 'buy-in' from 12 different people in 3 departments, and I could upload my existing spreadsheets," she says.

Ebersole uses Quartz mainly for tracking dry and liquid chemicals. But it can also track freezer boxes, so that users know precisely what each slot of a given container holds. When stocks run low, users click on a button to reorder, and the system automatically alerts the manager so that she or he can track the order's status. (The system is able to offer its service for free because it incorporates catalogues from several reagent vendors, and suggests those products when orders are placed.) Other features include support for tracking barcodes attached to individual samples, as well as equipment scheduling and document management for maintaining lab manuals and the like.

For Ebersole, Quartz's features not only

improve the efficiency of the lab, they cut down on her costs. "I've saved about a third of my budget," she says. In part, that is because there is less waste: by knowing precisely what chemicals she has to hand, Ebersole can use up old reagents before buying fresh ones. And when she does buy new chemicals, she says, she can do so in smaller quantities than before.

Another option is StrainControl, which has been developed by DNA Globe of Umeå, Sweden. The software is free for individual researchers in small labs; a professional licence for 10 users costs US\$79.95; and a 50-user licence costs \$649.95. Both of the paid versions allow the software to be used on a computer network or cloud-based service.

"We believe that providing high-quality metadata for reagents and methods coupled with linkage to experimental data will help to improve the reproducibility problem."

proteins, plasmids, antibodies and chemicals, and like some other tools, is compatible with sample barcoding. Users can rename any of the fields to suit their needs, Lindell says; as a result, StrainControl can be used to catalogue anything, whether lab-related or not. An imminent update will allow users to add one or two custom modules to the database (not just reconfigure existing ones), for tasks such as tracking references.

Other systems are more specialized. A lab information-management system (LIMS) called mLIMS, developed by BioInfoRx in Madison, Wisconsin, is designed to track rodent colonies, for instance. Some also offer connectivity to electronic notebooks. Labguru, for instance, is a cloud-based application that tracks plasmids, bacteria, antibodies, plants, rodents and proteins and has a built-in electronic notebook, says product specialist Xavier Armand. Developed with investment from *Nature's* parent company, Holtzbrinck Publishing Group in Stuttgart, Germany, Labguru costs \$120 per user per year for academics and \$450 per user per year for industry labs and is produced by BioData in Cambridge, Massachusetts.

Usually, Armand explains, inventories and electronic lab notebooks connect details about each sample to experimental results, so users can track which reagents were used in which experiments. "We believe that providing high-fidelity metadata for reagents and methods coupled with linkage to experimental data will help to improve the reproducibility problem," he explains. It should make it easier for researchers

to duplicate the findings of their own and other labs' experiments. Similarly, Freezer Web Access and Lab Inventory, both from ATGC Labs in Potomac, Maryland, allow users to link their reagents to a LIMS. Software developer Pavel Bolotov says that both applications cost \$150 per user and \$350 per server installation — plus \$1,000–20,000 for customization.

LINKED-UP APPROACH

Some research institutes and companies centralize inventory management at a large scale. The office of Environmental Health & Radiation Safety (EHRS) at the University of Pennsylvania in Philadelphia has spent the past several years moving its 700 lab groups to the unified system CISPro, which is developed by BIOVIA (formerly Accelrys) in San Diego, California. According to EHRS lab-safety specialist Kimberly Bush, institution-wide tracking facilitates three key tasks: compliance reporting (for example, whether the university is meeting building-code limits on flammable materials), cross-lab material sharing and university-wide reagent monitoring. "Those are difficult or impossible to accomplish if there are 700 standalone inventory systems," she says.

In 2011, the EHRS received \$50,000 from the Penn Green Fund, a university sustainability initiative, to implement CISPro as part of an effort to reduce waste and consolidate inventory management. Today, only about one in eight labs is on-board. The roll-out has been anything but smooth, Bush says, and exemplifies the challenges of inventory tracking. Because the university's chemical purchases do not go through a central office, each lab has to be trained to create and upload its own inventories. And the process of creating the database is cumbersome and error-prone. For instance, a chemical might have multiple names, and inconsistencies in database set-up and material logging can make the chemical difficult to recall at a later date, leading to unnecessary reordering. Thus, she notes, some users actually maintain two systems, "but that's duplicate effort".

Furthermore, CISPro is designed to give every chemical container a unique barcode. But for users that consume bottle after bottle of a given solvent, the repetitive logging can become tedious. In that case, says Bush, users might reserve and reuse a handful of barcodes on the door of the flammables cabinet. "To keep an inventory as accurate as possible you have to consider both the chemicals and the users' workflow," she advises.

Whichever tracking system researchers choose, they can be confident at least of this: they need never be at a loss for their lab's resources again. If nothing else, says Mymryk, that could save researchers some awkward moments: "There's nothing more embarrassing than having to ask for the same reagent twice." ■

Jeffrey M. Perkel is a freelance writer in Pocatello, Idaho

STRIPPED TO ZERO

Someone to watch over you.

BY STEPHEN S. POWER

I don't know why we bother waiting on the stoop. After an hour, I grab Tommy's Caillou backpack and reach for his hand. He tucks it against his chest. It kills me, but I can't blame him. I'd call his mother if she would carry a phone. Or answer if she did.

Tommy follows me inside and asks: "Do I still get chips for being good?"

"Sure," I say, turning, "if you can beat me. Go!"

We race across the lobby and down a hall to the 24Shop, a small room lined with video displays. I let him dart in just ahead of me, and the shop says: "Good morning, Tommy."

"How does she always know my name, Daddy?"

I shrug. To a four-year-old, even the most mundane technology is indistinguishable from magic.

The shop has a woman's voice, soft and warm. I imagine her kneeling when she asks him: "What would you like, Tommy?"

He looks from screen to screen. Dancing chips. Splashing sodas. Cookies, ice cream and comfort foods. The shop says: "How about corn flakes with milk?" A bowl of cereal appears.

"No, chips," he says.

"It's much too early. Oatmeal with cinnamon?" Steaming oatmeal appears.

"No, chips! Daddy..."

Stupid nutrition protocols. "He can have a snack."

The shop says nothing. Instead, images flow down a screen like a slot machine before settling on a MoonPie.

"Yes!"

"And a coke?" the shop asks.

"Why not?" I say.

A red light blinks above the bill slot. Standing behind Tommy, I nod, and the light turns green. A MoonPie tumbles into one tray, a can of RC into another.

"What do you want, Henry?"

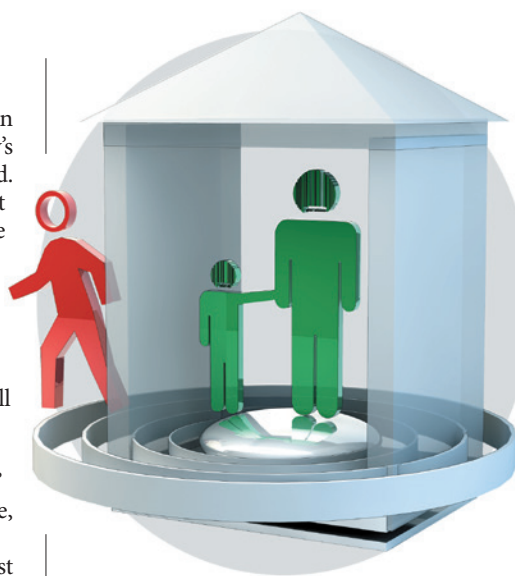
Tommy takes my hand. "Nothing," I say. "I'm good."

Upstairs, Tommy turns on the TV and tears into his food. He's promptly shown commercials for MoonPies and RC, a fact to which he pays no attention.

I head for my reading room and find

Karen sitting on the toilet tank. The mirror's unplugged and draped with towels.

I close the door.



"What are you doing in here? How did you even get in?"

"I spoofed a pass card."

"I'd get you a real card."

"Worse than phones." She glances through the high, small window.

"He waited an hour for you."

"I know. I watched."

"From the shadows? Jesus. He can't remember most of your shit, but it's starting to stick."

"It's not shit."

I hold up my hands. "Look. He misses you. Come on out. I'll tell him you —"

"Don't make excuses for me. And I'm not going near that TV. This toilet's bad enough. Probably reporting my weight." She lifts her boots off the lid.

"Fine. I'll call him."

"No."

"Then why get his hopes up? Why ... this?"

"I wanted to see him, but I needed to speak with you."

She slides down and stands close. She seems taller. And thinner. Probably the boots.

"I'm leaving," she says. "For good. I won't be coded anymore. I won't be tagged. It's killing me."

"So you'll kill him instead."

"He's another tag, Henry."

"He's a little boy."

"No. We're just data sets here. Why can't you see that? Is that all you want him to be?" Now I get it. "You're not taking him."

"We could live clean. Stripped to zero. Anonymous. This place I'm going —"

"I'll get him to his room," I say and grip the door knob. "Slither out, and the TV won't see you either."

I don't worry about her snatching Tommy. It'd be easier for her disappear if no one wanted to find her, and I would.

"Then tell him," she says, "when he's old enough, tell him that I'm not crazy."

"He'll never be that old."

My watch screen flares. Tommy knocks. "Daddy, I don't feel well."

I look at Karen. She's already ducking behind the black shower curtain.

I open the door. Tommy's face is pale, sweaty and smeared with MoonPie. With a whirl, the toilet lifts its lid.

"Quickly." We kneel together on the mat, and Tommy spews brown-black vomit.

I can hear my mother say: "You just *had* to let him eat all that junk, didn't you?"

The toilet expresses a milky foam that bonds with the vomit, then it vacuums both away. I wipe Tommy's mouth with a tissue as the scent of vanilla fills the room.

"Smells like Mommy," he says.

"Yeah." I used to love her vanilla perfume. "I could set the vents to vanilla too."

"No, I want Mommy."

"I know." I rub his back.

"Why didn't she come?" Tommy slams the toilet lid down. "Where is she?"

I take his wrists and turn him so I can look him in the eyes. "Do you love her?"

He nods.

"Then she's always nearby."

"Like in the shower?"

"Ha! Exactly. Come on. Let's get a new shirt on you."

I pick Tommy up and take him through to his room. While he paws through a drawer, I hear her footstep outside. I smell the vanilla again, my stomach twists, and, despite everything, I want her to rush in and grab us both. So when the front door clicks, I'm horribly relieved, like someone watching his terminal partner finally die.

Tommy pulls out his Batman T-shirt. I bend him into it. We go to the living room and flop down in a heap before the TV. The first commercial is for vanilla air fresheners.

It's on every channel. ■

Stephen S. Power's novel *The Dragon Round* will be published by Simon&Schuster in June 2016. His stories have recently appeared at AE and Daily Science Fiction with many forthcoming. He tweets at @stephenspower and his site is stephenspower.com.

ILLUSTRATION BY JACEY